

Dissertation zur Erlangung des
Doktorgrades der Fakultät für
Chemie und Pharmazie
der Ludwig-Maximilians-Universität München

**Novel Strategies in Chemical Tool Development
for the Nuclear Receptors Nurr1, RXR and PPAR**

Nhat Minh Sai

aus

Erbach (Odenwald), Deutschland

2024

Erklärung

Diese Dissertation wurde im Sinne von § 7 der Promotionsordnung vom 28. November 2011 von Herrn Prof. Dr. Daniel Merk betreut.

Eidesstattliche Versicherung

Diese Dissertation wurde eigenständig und ohne unerlaubte Hilfe erarbeitet.

München, 09.09.2024

.....
Nhat Minh Sai

Dissertation eingereicht am 20.09.2024

1. Gutachter: Prof. Dr. Daniel Merk

2. Gutachter: Prof. Dr. Franz Paintner

Mündliche Prüfung am 28.10.2024

„The journey of a thousand miles begins with one step“

Lao Tzu

Inhaltsverzeichnis

1	Introduction.....	- 7 -
1.1	Nuclear receptor related 1 – Nurr1	- 10 -
1.1.1	Structure and function.....	- 10 -
1.1.2	Physiological function.....	- 15 -
1.1.3	Nurr1 ligands	- 20 -
1.2	Retinoid X receptors (RXRs)	- 29 -
1.2.1	Physiological function.....	- 30 -
1.2.2	RXR ligands	- 32 -
1.3	Peroxisome proliferator-activated receptors (PPARs) - PPARα	- 35 -
1.3.1	Physiological and pathophysiology function.....	- 36 -
1.3.2	PPAR α ligands.....	- 37 -
1.4	Photopharmacology.....	- 38 -
2	Aim of the doctoral thesis	- 41 -
3	Results and Discussion	- 43 -
3.1	Structure-Guided Design of Nurr1 Agonists Derived from the Natural Ligand Dihydroxyindole.....	- 43 -
3.2	Development of Nurr1 agonists from amodiaquine by scaffold hopping and fragment growing	- 50 -
3.3	Tuning RXR modulators for PGC1α recruitment	- 58 -
3.4	Azologs of the fatty acid mimetic drug cinalukast enable light-induced PPARα activation	- 64 -
4	Summary.....	- 73 -
5	References	- 79 -
6	List of abbreviations.....	- 95 -
7	List of figures	- 97 -
8	List of tables.....	- 103 -
9	List of publications	- 104 -
10	Author contribution	- 105 -
11	Acknowledgments.....	- 107 -
12	Reprints of the publications and manuscript for peer-review.....	- 109 -
12.1	Structure-Guided Design of Nurr1 Agonists Derived from the Natural Ligand Dihydroxyindole.....	- 109 -

12.2 Development of Nurr1 agonists from amodiaquine by scaffold hopping and fragment growing.....	- 138 -
12.3 Tuning RXR modulators for PGC1α recruitment	- 267 -
12.4 Azologs of the fatty acid mimetic drug cinalukast enable light-induced PPARα activation	- 346 -

1 Introduction

Neurodegenerative diseases, such as Alzheimer's and Parkinson's, are characterized by progressive neuronal degeneration, loss of neuronal function, associated neuroinflammation and abnormal neuronal disposal of certain aggregated proteins in the central nervous system (CNS)^{1,2}. These disorders have major impact on the life quality of those affected as well as their families, and on healthcare systems globally¹.

The Global Burden of Disease Study estimated that a remarkable number of 3.40 billion individuals were afflicted by neurological disorders in 2021, representing 43% of the world's population¹. Among them, 57 million had Alzheimer's disease (AD) and 11.8 million had Parkinson's disease (PD)¹. In Germany approximately 1.8 million people were affected by dementia and an estimated 300,000 were affected by PD^{3,4}. With the rising number of elderly individuals in Germany, neurodegenerative diseases will become even more significant medical challenges in the coming decades^{3,4}. It is estimated that the total number of patients with neurodegenerative diseases in Germany will reach 3 million or more cases by 2050 due to demographic changes^{3,4} (Figure 1).

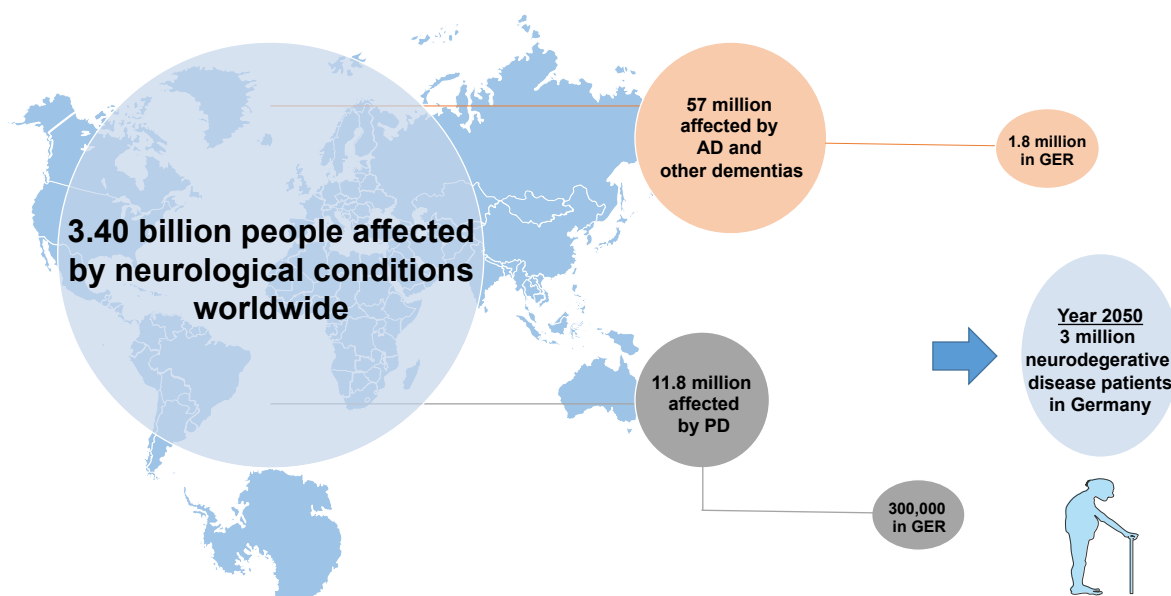


Figure 1. The prevalence of neurodegenerative diseases on a global scale, with a particular focus on Germany (now and estimated for 2050).

Dementia is defined as a decline and loss of cognitive functions and the ability to perform activities of daily living. The disease's progressive course leads to impairments in temporal and spatial orientation, communication skills, autobiographical identity, and personality traits⁵. AD represents the most common cause of dementia⁶. Its pathogenesis can be described as the accumulation of amyloid β ($A\beta$) plaques and tau tangles within the brain, resulting via various mechanisms of neuronal damage in a cognitive decline and memory loss^{6,7}. In contrast, PD is characterized by the accumulation of Lewy bodies and

Lewy neurites within the nervous system, comprising aggregated and misfolded α -synuclein species. This is accompanied by a decline of dopamine-producing neurons in the substantia nigra and other regions of the brain⁸. This leads to motor symptoms including tremors, rigidity and bradykinesia⁹.

For both AD and PD, age is a significant risk factor, since the prevalence of these conditions increases with advancing age^{3-5,8}. Current therapeutic interventions for AD and PD focus on symptom management, rather than on disease cure. Pharmacological agents such as acetylcholinesterase inhibitors (e.g. Donepezil, Rivastigmine), NMDA antagonist (e.g. Memantine) and dopamine agonists (e.g. Levodopa, Pramipexole) can alleviate symptoms and enhance the quality of life^{4,5}. Nevertheless, these treatment options are not without adverse effects and do not halt disease progression. New therapeutic approaches and mechanisms of action are required to tackle neurodegeneration, which pose a major medical challenge for the future^{3,4}. Currently, the role of nuclear receptors (NRs) in neurodegenerative diseases is garnering increased attention^{2,10}.

NRs are a superfamily of 48 transcription factors, most of which are involved in regulating gene expression by binding to their endogenous and exogenous ligands¹¹. They play a significant role in developmental processes and the maintenance of physiological homeostasis. Furthermore, they have been implicated in numerous pathological conditions, including obesity, diabetes, and cancer¹².

There is a growing body of evidence that certain NRs could represent potential molecular targets for the treatment of neurodegenerative diseases². Nuclear receptor related 1 (Nurr1), a transcription factor with neuroprotective properties that is predominantly expressed in the CNS, has demonstrated considerable potential in the context of neurodegenerative diseases^{2,13,14}. Altered levels of Nurr1 have been detected in patients with PD, AD, and multiple sclerosis (MS), as well as in rodent models of these conditions¹⁵⁻¹⁷. A reduction in neuronal Nurr1 activity in mice resulted in a phenotype with features reminiscent of PD^{18,19}, and led to an exacerbation of the pathology observed in AD models^{14,20} and experimental autoimmune encephalomyelitis in MS²¹. Therefore, Nurr1 represents a promising target for developing new treatments for neurodegenerative disorders^{14,22}.

A notable feature of the NR family is their propensity to function as dimers. Retinoid X receptors (RXRs) serve as the archetypal partners for forming heterodimers with a diverse range of NRs and homodimers with themselves²³⁻²⁵. The modulation of RXRs offers a potential avenue for the development of new therapeutic strategies for a variety of neurodegenerative diseases, such as AD and MS². The use of bexarotene (a RXR agonist) in a mouse model of AD has been demonstrated to repress inflammation and prevent

neuronal loss²⁶. This, in turn, has been shown to improve cognitive and behavioral performance in the subjects²⁶. Furthermore, recent findings have indicated a potential link between the activation of RXR γ and the promotion of CNS remyelination^{27,28}.

A heterodimer partner for RXR is the peroxisome proliferator-activated receptor (PPAR) α ²⁹. PPAR α is a primary regulator of β -oxidation and lipid transport in the liver and other tissues with high levels of lipid metabolism^{29,30}. Additionally, it can modulate genes involved in glutamate homeostasis and cholinergic/dopaminergic signaling in the brain³¹. In AD, there is a notable reduction in PPAR α expression, which may contribute to diminished anti-oxidative and anti-inflammatory processes, as well as disturbances in fatty acid transport, lipid metabolism, and mitochondrial function³¹. Moreover, preclinical studies have demonstrated that treatment with PPAR α agonists enhances cognitive function and mitigates neuronal loss³¹.

Although preclinical models of neurodegeneration have shown promising results, there is a lack of high-quality and selective compounds to validate the modulation of NRs as a therapeutic strategy and to fully understand their biological function. This thesis aimed to address this gap by developing novel, high-quality chemical tools that would improve our biological and physiological understanding of these NRs. Moreover, novel approaches for the selective activation of NRs by coregulators, as well as alternative methods for modulating these receptors using photopharmacology, will be investigated. This thesis is divided into four parts: structure-guided design of Nurr1 agonists based on a natural ligand, the development of high-quality Nurr1 modulators by scaffold hopping and fragment growing, tuning RXR modulators for specific coregulator recruitment and finally the development of photohormones for light induced PPAR α activation.

1.1 Nuclear receptor related 1 – Nurr1

Nuclear receptor related 1 (Nurr1¹³, NOT³², TINUR³³, RNR-1³⁴, HZF-3³⁵, NR4A2) was identified in the 1990s as a transcription factor with a degree of homology^{13,14} to the nerve growth-factor induced clone B^{36,37} (NGFI-B, Nur77, NR4A1). Together with the neuron-derived orphan receptor 1 (NOR-1, NR4A3) the three transcription factors form the NR4A subfamily of NRs which is crucial for the development and survival of neurons¹⁴. In terms of their architecture, they align with the domain structure of NRs comprising five domains (A-E, Figure 2a)^{12,14}. The A/B domain is a variable N-terminal domain (NTD), C domain is the highly conserved DNA-binding domain (DBD), D domain represents a hinge region and domain E is a conserved ligand-binding domain (LBD).

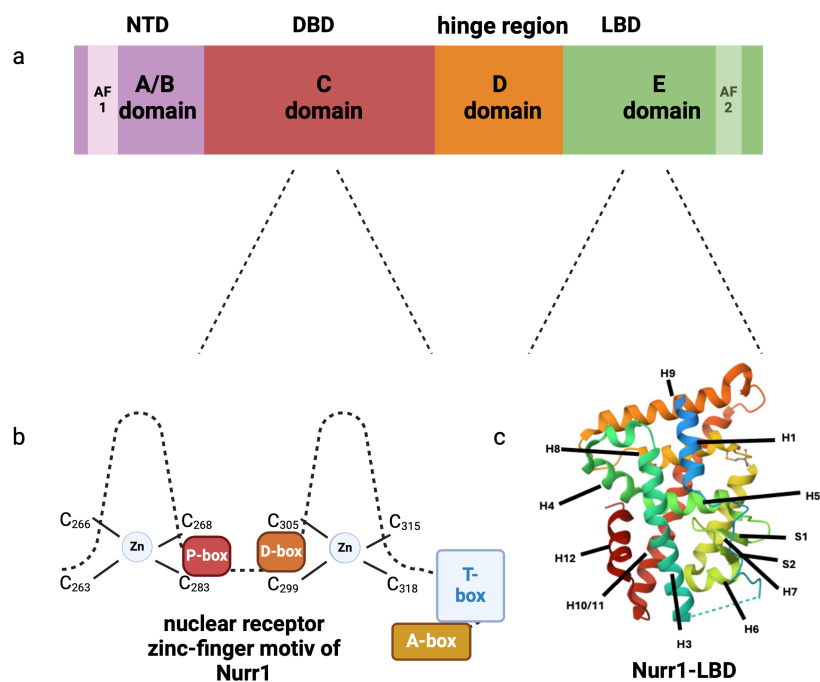


Figure 2. (a) Structural architecture of Nurr1 containing five domains. A/B-domain with ligand-independent transcriptional activation function 1 (AF1), C-domain with Zn-finger and P-,D-,T- and A-box ((b), adapted from ³⁸), D-domain with hinge region, E-domain with ligand-dependent transcriptional activation function 2 (AF2 = H12) and Nurr1-LBD X-ray structure and his helices (H1-H12) ((c), PDB: 1OVL)³⁹. Created with Biorender.com.

1.1.1 Structure and function

The NTD (Figure 2a) is not highly conserved and has variable length and sequence within the superfamily⁴⁰. For some orphan receptors like TLX, the NTD is very short (14 amino acids) compared to the NR4A family (250-280 amino acids)⁴⁰. It is typically unordered and contains a ligand-independent transcriptional activation function 1 (AF1). AF1 contributes to the constitutive ligand-independent activation of the receptor⁴¹ and interacts with a variety of coregulator proteins¹² such as coactivators and other

transcription factors¹¹. Post-translational modifications in the NTD, such as phosphorylation, SUMOylation and acetylation, can modulate receptor activity⁴².

In the case of Nurr1, it has been demonstrated that the activity of Nurr1 is dependent on phosphorylation by MAP-kinases (including ERK1/2 (Ser126, Thr132) and ERK5 (Thr168, Ser177)⁴³, and AKT (Ser347)⁴⁴. Phosphorylation by AKT can result in proteasomal degradation⁴⁴. SUMOylation, which is the reversible covalent attachment of one or more SUMO proteins to a lysine residue (Lys91 in Nurr1), has been demonstrated to repress Nurr1 transcriptional activity⁴⁴. Moreover, additional lysine residues (K558 and K577) have been identified as potential SUMOylation sites for Nurr1. The SUMOylation of K558 and K576 resulted in the recruitment of the corepressor CoREST⁴⁴. The Nurr1/CoREST-mediated transrepression complex inhibits NFκB p65 activity, thereby reducing the expression of proinflammatory genes, including tumor necrosis factor-alpha (TNF-α)^{44,45}. This mechanism may provide insights into the role of Nurr1 in neuroinflammatory processes^{44,45}.

In the structural architecture of the superfamily the A/B domain is followed by the DBD (C domain, Figure 2a), which is highly conserved across the NRs. The DBD is capable of binding directly to specific DNA binding sites and responsible for the recognition of a specific sequences, namely hormone response elements (REs)¹¹. The DBD is composed of 66 amino acids and features two cysteine-rich zinc finger motifs, two α helices and a C-terminal extension (CTE)⁴⁶. The cysteine residues, together with other amino acids and two zinc ions, form two zinc finger motifs via tetrahedral complexes that allow binding to DNA in the nucleus. The amino acids required for discrimination of DNA recognition motifs are located on the underside of the first finger in a region known as the P-box⁴⁷. The P-box is a highly conserved region and is critical for the differentiation of DNA recognition motifs⁴⁸. The amino acid residues of the second zinc finger form the D-box and are involved in the dimerization process⁴⁹. In the case of Nurr1, the A-box is of significance in binding to the NGFI-B response element (NBRE) and capable of recognizing adenine residues of NBRE^{33,34} (Figure 2b). The poorly conserved CTE (= T-box) across the superfamily serves as a significant motif for a specific and increased binding affinity to the REs by contacting the minor groove of the DNA⁵⁰, especially in Nurr1³⁸ (Figure 2b). Additionally, the CTE plays a role in the selective recognition of RXR-NR heterodimers by facilitating the completion of the contact point between the dimers and specifying the optimal distance between the repeats of the REs based on their length⁵¹.

Nurr1 can act as a monomer, homodimer or heterodimer with RXR or Nur77 as heterodimer partner on different REs (Figure 3)^{14,52-54}. The monomer binds to NBRE represented by the extended motif AAAGGTCA⁵⁵ (Figure 3a). The homodimer or heterodimer with Nur77 can recognize the so-called Nur response element (NurRE), which contains two half-sites as an inverted repeat (TGATATTTACCTCCAAATGCCA)^{54,56} (Figure 3b). This was initially discovered in the promoter region of the proopiomelanocortin (POMC) gene^{54,56}, which is important as a precursor protein for several neuropeptides in the hypothalamic pituitary adrenal axis⁵⁶. The binding of Nurr1 and RXR to the DR5

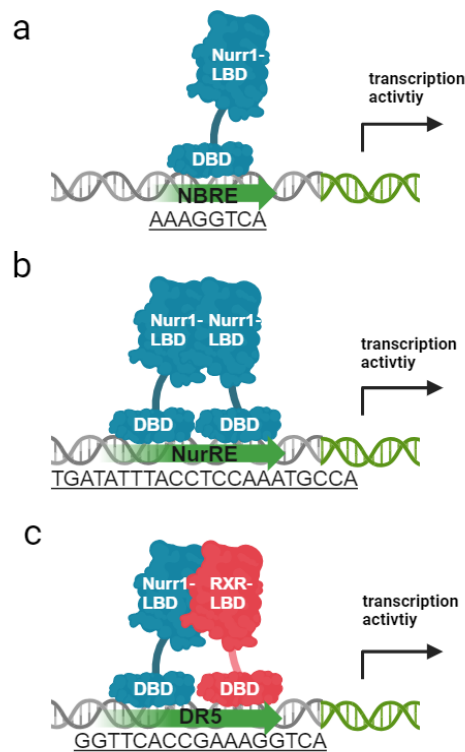


Figure 3. Schematic illustration of Nurr1 with its REs as a monomer (a), homodimer (b) and heterodimer with RXR (c). Created with Biorender.com.

sequence GGTTCACCGAAAGGTCA is similar to other RXR heterodimers that interact with REs comprising a direct repeat, which is separated by a distance of five bases in case of Nurr1^{52,53} (Figure 3c).

The hinge region (D domain, Figure 2a) is located between the DBD and the LBD. It is a poorly conserved region that allows the DBD to rotate, enabling different conformations without steric hindrance to form dimers⁴⁶.

The LBD (E domain, Figure 2a) within NRs is a multifunctional domain that binds ligands, mediates homo- and heterodimerization, interacts with heat-shock proteins, and exhibits ligand-dependent transcriptional activity^{41,57}. It also allows interactions with various corepressors, coactivators and other cofactors involved in the signaling of basal transcription⁵⁸. In general, the LBD has a characteristic structure consisting of a short beta-sheet region (s1 and s2) and usually twelve α -helices (H1-H12), which form a three-layered antiparallel alpha-helical sandwich^{12,46}. The lower region of this sandwich usually harbors the canonical hydrophobic ligand-binding pocket (LBP) in NRs^{59,60}. This LBP is highly variable in NRs and can vary in size and shape, ranging from almost non-existent, to very large volumes exceeding $> 1600 \text{ \AA}^3$ (e.g. pregnane X receptor (PXR))^{39,58,61,62}.

In the case of Nurr1, the X-ray crystallography (PDB: 1OVL) has revealed that the typical LBP is blocked, with bulky hydrophobic side chains filling the cavity³⁹ (Figure 4). These

residues, which are also found within the NR4A subfamily and the *Drosophila* ortholog DHR38, exhibit a high degree of conservation^{63,64}. For this reason, the NR4A receptors have been classified as orphan receptors for a long time^{14,40}. However, in the case of Nurr1, unsaturated fatty acids were identified as binding and modulating Nurr1 transcriptional activity, although the physiological relevance of this discovery remains unclear^{14,65} (see chapter 1.1.3.1).

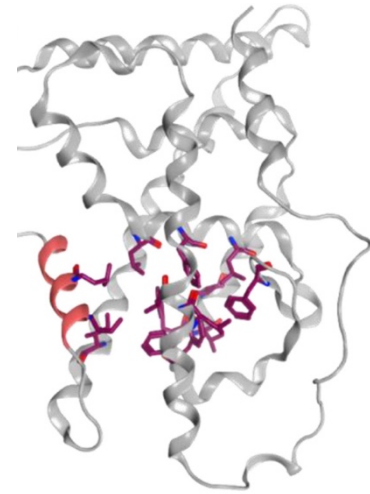


Figure 4. The apo structure of the Nurr1 LBD (PDB: 1OVL³⁹) revealed that the canonical LBP region is blocked by bulky hydrophobic side chains filling the cavity. Adapted from ¹⁴.

The mechanism for activating NRs by binding agonists involves several components¹⁴. The capacity of NRs LBDs to initiate transcription is regulated by the H12, also known as activation function 2 (AF2)⁴⁶. H12 demonstrates a high degree of conformational flexibility in the LBD⁴⁶. In the apo-form (unliganded state), the H12 is typically unordered and not bound to the LBD core, thus allowing the formation of a hydrophobic surface on the H3/H4 region^{14,46}. This provides a corepressor binding site that can bind α -helical structures with the so-called CoRNR box. This surface can bind various corepressors like nuclear receptor corepressor 1 (NCoR1) and silencing mediator of retinoid and thyroid hormone receptors (SMRT). Corepressors are proteins that recruit and activate epigenetic regulators, such as histone deacetylases and demethylases, to form multiprotein complexes that block transcription. Ligand binding to the LBD induces conformational changes eventually leading to stabilization of H12 bound to the core of the LBD⁶¹. Based on a holoRAR γ (active state) crystal structure in which the ligand binding site entry was sealed by H12, a so-called mouse trap-like mechanism has been established^{14,60}. Nevertheless, further studies of NRs have demonstrated a more dynamic stabilization mechanism, whereby H12 is not fixed in any single position, but rather exhibits mobility over several conformations, resembling a molten state⁶¹. Ligands that bind to the LBD have the effect of stabilizing the receptor folding process globally, thereby reducing the degree of conformational dynamics and promoting an active conformation and position of H12⁶¹. The binding of H12 to the LBD core affects the LBD surface, resulting in the release (i.e., reduction in affinity) of corepressors and the generation of a new coactivator binding epitope typically located between H12 and H3. This process results in a number of changes in the geometry of the LBD core. Firstly, a glutamate in H12 and a lysine in H3 form a “charge clamp”, which typically has a distance of 18-20 Å⁶⁶. Secondly a hydrophobic groove between helices H3, H4, H5 and H12 forms which can bind a consensus LXXLL motif (NR box) contained in coactivators like steroid receptor coactivators (SRC) and the PPAR γ coactivator 1alpha (PGC1 α)⁴⁶. These coactivators are

proteins that recruit epigenetic regulators, such as histone acetyltransferases and methyltransferases, to form multiprotein complexes that activates transcription^{14,61}.

If a NR is already conformationally stable in the absence of a ligand, it is likely to exhibit constitutive transcriptional activity⁶¹. Nurr1 and its relatives Nur77 and Nor1 provide a useful example of this phenomenon^{13,36,53}. A structural explanation for the constitutive activity can be found in an autoactivated conformation of the Nurr1 LBD³⁹. The first X-ray crystal structure of Nurr1 (PDB: 1OVL) demonstrated that H12 was bound to the core of the LBD in absence of a ligand and formed an autoactivated conformation, analogous to the ligand-activated states of other NRs³⁹. The presence of a lysine residue (Lys590) in H12 forms a strong ionic interaction with a glutamate residue (Glu440) in H4³⁹. This interaction has been proposed to facilitate the autoactivated conformation and lead to the constitutive activity of Nurr1^{14,39}. It should be noted that a crystal structure provides only a static snapshot of the protein at a specific conformation. Consequently, it may not fully reflect the protein's full range of dynamic states, as observed in its natural environment^{67,68}. The structural superimposition of Nurr1 (PDB: 1OVL) and Nur77 (PDB: 2QW4) demonstrated a significant shift in H12 (2.8 Å), which could explain Nurr1's higher constitutive activity compared to Nur77^{39,58,64}.

Another factor to consider are the polar and charged characteristics of the NR box binding region in Nurr1, precluding the formation of a hydrophobic surface that would enable interaction with the leucine residues of coactivators^{14,39}. The presence of bulky residues (R418/F439/K590 and K370/F392/N543) at the AF2 region suggests a lack of affinity for common coregulators^{39,58}. Moreover, the residues of lysine and glutamate in helices H3 and H12, which serve to stabilize the binding of the coactivator α -helix in ligand-activated NR (charge clamp), are interchanged with glutamate situated in H3 and lysine in H12 in Nurr1. This missing interaction of charge clamp and hydrophobic surface, in conjunction with the ionic interplay between H4 (Glu440) and H12 (Lys590), impedes the interaction with coregulators at the canonical binding site^{14,39}. However, a hydrophobic groove between H11 and H12 has been identified as a potential alternative coregulator binding site in Nurr1, Nur77 and Nor1 for NCoR1 and SMRT (Figure 5). It has been demonstrated that the coregulators NCoR1, SMRT, nuclear receptor coactivator 6 (NCoA6), forkhead family of winged-helix transcription factor (Foxa2) and SUMO E3 ligase protein inhibitor of activated STAT (PIASy) bind to Nurr1^{44,69-71}. However, the binding mode and molecular mechanism of the coregulators of the NR4A family remain mostly elusive¹⁴.

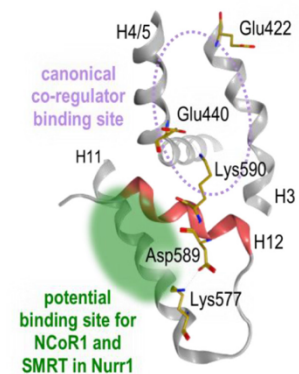


Figure 5. Potential binding sites of coregulators in the LBD of Nurr1 (PDB:1OVL³⁹). Adapted from¹⁴.

1.1.2 Physiological function

Nurr1 was first linked to dopaminergic neuron function through its critical involvement in the development of midbrain neurons^{17,18}. Nevertheless, the expression of Nurr1 has been observed not only in the CNS but also in other tissues, including smooth muscle, endothelial cells, bone, synovial tissues, adrenal glands, intestine, liver cells, and immune cells (e.g., macrophages)^{14,22}. Within the CNS, the expression of Nurr1 is particularly high^{2,18}. It is widely expressed in the substantia nigra, ventral tegmental area, and limbic system^{18,72}. Moreover, Nurr1 has been identified in the olfactory bulb, hippocampus, temporal cortex, subiculum, cerebellum, posterior hypothalamus, and habenular nuclei^{22,73}.

The results of knockout studies on Nurr1 have demonstrated that this gene is associated with the loss of dopaminergic neurons in the substantia nigra and ventral tegmental area, as well as severe respiratory dysfunction and, ultimately, death¹⁷. In newborn mice with global homozygous Nurr1 deficiency (Nurr1^{-/-}) where death occurred within the first two days after birth, there was an absence of dopaminergic neurons in the substantia nigra and ventral tegmental area¹⁷. Furthermore, alterations in gene expression were noted in the dorsal motor nucleus of the brainstem^{14,17}. This resulted in a notable reduction in respiratory activity and a pronounced decrease in the animals' overall level of activity^{14,17}. The elimination of Nurr1 in adult dopaminergic neurons in mice was achieved through a process of genetic cross-breeding, whereby Nurr1 floxed mice were crossed with mice harboring a CreERT2 allele under the control of the DAT locus, which enables tamoxifen-induced ablation of the Nurr1 gene^{18,19}. Ablation of Nurr1 resulted in the development of a progressive pathological phenotype^{18,19}. This was characterized by a reduction of dopaminergic neuron markers in the ventral midbrain and striatum, a decrease in dopamine in the striatum and eventually motor deficits, which closely resembled the features of early PD^{18,19}. Due to its critical function in the growth and maintenance of dopaminergic neurons, Nurr1 represents a promising objective for the treatment of PD^{18,19}.

The expression of essential proteins involved in the dopamine metabolism, differentiation, axonal growth and survival in dopaminergic neurons is regulated by Nurr1^{14,18} (Figure 6). Nurr1 regulates the expression of genes involved in dopamine synthesis, packaging, and reuptake. This includes the tyrosine hydroxylase (TH), dopamine decarboxylase (DDC), vesicular monoamine transporter 2 (VMAT2), and dopamine transporter (DAT) genes. By controlling the expression of these genes, Nurr1 plays a crucial role in maintaining homeostasis in dopamine levels within the brain^{14,18,74}. Moreover, Nurr1 controls the expression of genes involved in neuronal differentiation and axonal growth, including delta-like homologue 1 (DLK1), alcohol dehydrogenase 2 (ADH2), protein tyrosine phosphatase receptor U (PTPRU), and kelch-like protein 1

(KLHL1). In addition, Nurr1 affects the proto-oncogene tyrosine-protein kinase receptor Ret (Ret)^{14,18,75}. Ret is a crucial component of the signal transduction pathway for neurotrophic factors, such as glial cell-derived neurotrophic factor (GDNF), which is essential for the survival of dopaminergic neurons^{14,18,75}.

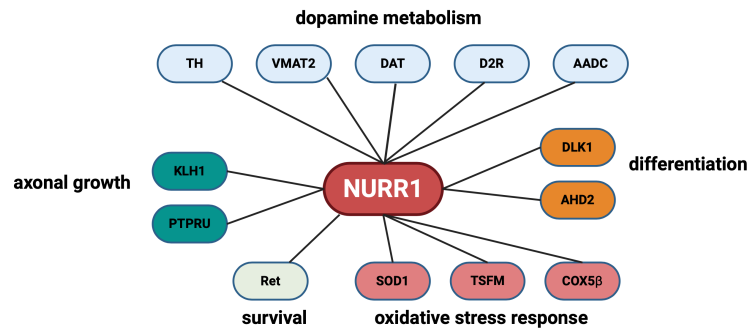


Figure 6. Nurr1 regulates genes of dopamine metabolism, axonal growth, survival, oxidative stress response and differentiation. Created with Biorender.com.

The regulation of mitochondrial gene expression, including superoxide dismutase 1 (SOD1), mitochondrial elongation factor Ts (TSFM), and crucial oxidative phosphorylation genes such as cytochrome c oxidase subunit 5β (COX5β), is a pivotal role of Nurr1 in protecting neurons from oxidative stress and maintaining the respiratory chain^{14,19}. Furthermore, Nurr1 functions as a mediator of cAMP response element-binding protein (CREB) dependent neuroprotection in neurons exposed to excitotoxic and oxidative stress^{18,22}. CREB is a transcription factor that is essential for neuronal protection^{18,22}.

In addition to its role in oxidative stress, Nurr1 is also involved in the inflammatory response of the nervous system^{14,18,22}. In lipopolysaccharide (LPS)-treated mice, it can restrict the production of neurotoxic mediators, including TNF-α, IL-1β, and iNOS^{14,18,22}. In astrocytes and microglia, Nurr1 acts as a negative regulator of NFκB-induced inflammatory genes, stabilizing the CoREST corepressor complex which restores the expression of NFκB-activated genes to basal levels^{14,18,22}.

1.1.2.1 Nurr1 in Parkinson's disease

As previously outlined in chapter 1, PD is defined by a progressive degeneration of midbrain dopamine neurons containing misfolded α-synuclein¹⁸. The expression of Nurr1 is found to be reduced in post-mortem human brain tissue from cases of sporadic PD^{18,76}. This is particularly noticeable in the substantia nigra dopamine neurons with α-synuclein inclusions. A reduction in Nurr1 expression is associated with a loss of TH-positive neurons, which implies that decreased Nurr1 expression may underlie reduced dopamine production and dopamine neuron death^{18,76}. In addition, research data have been indicated that the overexpression of Nurr1 has the capacity to protect neurons from the toxic effects of α-synuclein *in vitro* and *in vivo*^{14,18,22,77}.

It has been observed that the number of dopaminergic neurons that express Nurr1 declines with age^{18,78}. This decline was accompanied by a reduction in TH expression within individual neurons^{18,78}. As the ageing process is linked to a reduction in the number of dopamine neurons in the substantia nigra, and advancing age constitutes a significant risk factor for PD, age-related declines in Nurr1 expression may play a contributory role in the pathogenesis of PD¹⁸.

Further support for the role of Nurr1 in PD is provided by genetic association studies^{14,15,79}. Single nucleotide polymorphisms (SNPs) in the Nurr1 gene have been identified in several patients with familial and sporadic PD^{14,15,79}. Among these, the polymorphism rs35479735 in intron 6, which can affect splicing, correlates significantly with sporadic and familial PD^{14,15,79}. Nevertheless, subsequent studies involving other PD patient cohorts have not replicated these findings, indicating a need for further systematic genetic association studies on Nurr1 in the context of PD^{14,15}.

Amodiaquine (AQ, **1**, Figure 7) and chloroquine (CQ, **2**, Figure 7) are known to act as Nurr1 agonists (see chapter 1.1.3.2), and several studies have indicated that both have therapeutic effects based on Nurr1 modulation in PD^{14,77,80}. In rat dopaminergic neurons, treatment with AQ was demonstrated to increase the mRNA levels of Nurr1-target genes, including TH, DAT, VMAT and AADC, in a concentration-dependent manner^{77,80}. Furthermore, AQ and CQ demonstrated neuroprotective properties against the neurotoxin 6-hydroxydopamine (6-OHDA) in both *in vitro* and *in vivo* models, resulting for example in the alleviation of motor deficits characteristic of PD in rats with 6-OHDA-induced lesions^{77,80}. In a rotenone rat model study^{77,81}, where exposure of rotenone (an inhibitor of complex I of the mitochondrial respiratory chain) has been observed to result in the development of parkinsonian features, including the loss of dopaminergic neurons in the substantia nigra and motor impairment⁸², the less toxic derivative hydroxychloroquine (HCQ) has been demonstrated to exert an anti-inflammatory effect that is associated with increased Nurr1 expression and diminished expression levels of inflammatory mediators (NFκB, TNF-α, and IL-1β)^{77,81}. Consequently, treatment with HCQ resulted in the alleviation of the motor deficits induced by rotenone^{77,81}. Nevertheless, there is currently no evidence that HCQ binds and activates Nurr1 directly. The *in vitro* treatment of MN9D (murine dopamine neuron cell line) and N27-A (rat dopaminergic neurons) cells from 1-methyl-4-phenylpyridinium (MPP+)-induced toxicity with natural Nurr1 ligands prostaglandin A1 (PGA1, **3**, Figure 7, see chapter 1.1.3.1) and E1 (PGE1, **4**, Figure 7, see chapter 1.1.3.1) was demonstrated to provide protection in a Nurr1-dependent manner^{77,83}. Furthermore, PGE1 and PGA1 mitigated the loss of TH-positive dopaminergic neurons induced by MPP+ and LPS in primary dopaminergic neuron-glia cocultures derived from the embryonic ventral mesencephalic region of the rat^{77,83}. Additionally, intraperitoneal injection of PGE1 (2 mg/kg) or PGA1 (2 mg/kg) was observed

to significantly rescue dopaminergic neurons in the substantia nigra and the striatum, as well as to alleviate the impaired motor behaviors exhibited in a subchronic MPTP-induced animal model of PD^{77,83}. In conclusion, modulation of Nurr1 by agonists may represent a promising avenue for therapeutic intervention in PD.

1.1.2.2 *Nurr1 in Alzheimer's disease*

Nurr1 also seems to play a role in the pathogenesis of AD and is a potential target for therapeutic intervention^{14,20}. A post-mortem analysis revealed a reduction in Nurr1 levels in the substantia nigra of AD patients, which correlated with the loss of TH-positive neurons, as observed in PD^{14,20,76}. Similar reductions in Nurr1 mRNA levels were observed in APP_{swe/lnd} mutant mice⁸⁴, a model of early memory loss in AD, while the number of Nurr1-positive cells in the subiculum of 5xFAD mice, a model with a number of AD-related phenotypes⁸⁵, also decreased in an age-dependent manner^{14,20,86}. In addition, Nurr1 protein co-expressed with A β in early disease stages in 5xFAD mice^{14,20,86}. This co-expression suggested that Nurr1 may be involved in the early pathological changes of AD^{14,20,86}. Recent studies have demonstrated that A β ₁₋₄₂ fibrils result in the upregulation of tau hyperphosphorylation and presenilin 1 mRNA, which are considered to be hallmarks of AD pathology^{20,87}. In cortical neurons treated with A β ₁₋₄₂ fibrils, a reduction in Nurr1 protein and mRNA expression was observed. This finding was replicated in a human mesenchymal stem cell (hMSC) line *in vitro*^{14,20,87}.

The impairment of memory observed in AD can be attributed to the effects of A β , which has been demonstrated to induce neuroinflammation, neuronal death and synaptic dysfunction^{20,88}. The role of Nurr1 in cognitive function regulation has been proposed, with evidence indicating that mice with Nurr1 knockdown (hippocampal infusions of Nurr1 antisense oligodeoxynucleotides (ODNs)) exhibited impaired hippocampus-dependent memories and increased Nurr1 mRNA expression during spatial learning tasks^{20,89,90}. Furthermore, it has been demonstrated that siRNA-mediated knockdown of Nurr1^{20,91} and the generation of heterozygosity for the Nurr1 gene impaired memory functions^{20,92}. The regulation of learning and memory by Nurr1 is mediated by the CREB signaling pathway, which controls the transcription of genes associated with memory^{20,93,94}. The CREB-related pathways are essential for the formation of long-term memory in the hippocampus^{20,95}. The expression of the Nurr1 in hippocampal subregions is increased by behavioral task training^{20,90}, and in rats that have undergone long-term potentiation^{20,96}. While the exact mechanism underlying cognitive enhancement remains elusive, a placebo-controlled trial has demonstrated that the intermittent preventive administration of AQ led to enhanced cognitive performance in semi-immune schoolchildren^{20,97}. In another study, the overexpression and activation of Nurr1 in 5xFAD mice treated with AQ showed significant benefits, including lower A β levels, reduced hippocampal neurodegeneration, and improved cognitive function^{14,84}. Moreover, a

recently published study has provided evidence that the administration of AQ restored impaired spatial working memory in A β -overexpressing mice which alleviates AD-related pathology^{20,98}.

Although only a limited number of studies have assessed the role of Nurr1 in the context of AD, the existing evidence regarding Nurr1 in AD and its general neuroprotective and anti-inflammatory properties suggests that Nurr1 activation may offer significant therapeutic potential^{14,20}.

1.1.2.3 *Nurr1 in multiple sclerosis*

MS is defined as a heterogeneous autoimmune chronic disease of the CNS. MS is distinguished by its characteristic immune-mediated inflammatory processes which result in demyelination and subsequent axonal damage^{21,99}. The aberrant lymphocyte attacks that occur in the context of CNS autoimmune disorders result in damage not only to the myelin sheath but also to neuronal structures, including axons, dendrites and synapses^{21,100}.

The existence of a genetic link between Nurr1 and MS has yet to be substantiated in genome-wide association studies (GWAS)^{21,101}. However, several studies show altered expression patterns of Nurr1 in MS patient^{21,102}. The observed alterations are particularly pronounced in various blood components, including whole blood, peripheral mononuclear cells, CD14⁺ monocytes, and CD4⁺ T cells^{14,21}. The results revealed a decline in the concentrations of all members of the NR4A family for MS patients when compared to those of the healthy control cohort^{21,102}. In an additional patient trial, low levels of Nurr1 were found to correlate with an aggressive form of the disease and a higher degree of disability^{21,103}.

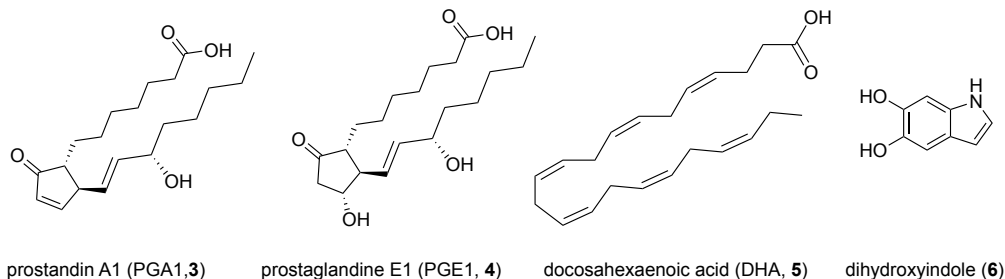
The most prevalent mouse model for MS studies is experimental autoimmune encephalomyelitis (EAE), which is induced by immunization with CNS-specific antigens such as MOG35-55 (peptide fragment 35-55 of myelin oligodendrocyte glycoprotein)^{21,104}. Nurr1 deficiency in mice (heterozygous Nurr1-knockout) led to an earlier onset and more severe course of EAE, suggesting increased recruitment of immune cells to the CNS^{21,105}. Conversely activation of Nurr1 delayed the onset of EAE and reduced inflammation and neurodegeneration in the spinal cord^{21,105}. Treatment with the so-called Nurr1 agonist IP7e (see chapter 1.1.3.2) after the onset of EAE had no effect on the progression of the disease^{21,106}. The administration of IP7e prior to the onset of EAE has been demonstrated to mitigate the severity of the disease by impeding the aggregation of vital cellular elements, including T lymphocytes and macrophages, within the spinal cord, which are indispensable for the onset of EAE^{21,106}. This suggested that, particularly in the early stages of the disease, Nurr1 plays a critical role^{21,106}. It is important to note that a direct binding of IP7e to Nurr1 has not yet been conclusively proven¹⁰⁷ (see chapter 1.1.3.2), and

that this lack of proof could lead to misunderstanding. The administration of dendritic cells overexpressing Nurr1 to EAE mice resulted in a delay in disease progression, which was accompanied by an enhancement in the differentiation of regulatory T cells (Tregs) and a reduction in neuroinflammation^{14,108}. In contrast, the systemic administration of Nurr1-specific siRNA in mice resulted in a notable reduction in EAE symptoms^{14,109}. This outcome was deemed indicative of Nurr1's potential involvement in Th17 cell differentiation, as evidenced by its capacity to influence IL-21 and IL-23 expression^{14,109}. The findings on Nurr1 in the context of MS are, on the whole, encouraging and suggest that Nurr1 modulation may have therapeutic potential. However, further studies are required in order to fully capture the role and potential of Nurr1 in this disease^{14,21}.

1.1.3 Nurr1 ligands

As previously described in chapter 1.1.1, Nurr1 occupies a unique position within the NR superfamily, characterized by the absence of a binding pocket, the absence of a classical binding site for coregulators and the constitutive activity of Nurr1, whose activity was thought to be regulated through alternative mechanisms^{13,14}. Nevertheless, a range of strategies, such as high-throughput screening (HTS) and the advancement of structure-activity relationships (SAR), as well as techniques including mass spectrometry, nuclear magnetic resonance (NMR), molecular docking, and cellular assays, have been effectively employed in ligand discovery to identify compounds capable of modulating Nurr1.

Natural ligands



Synthetic ligands

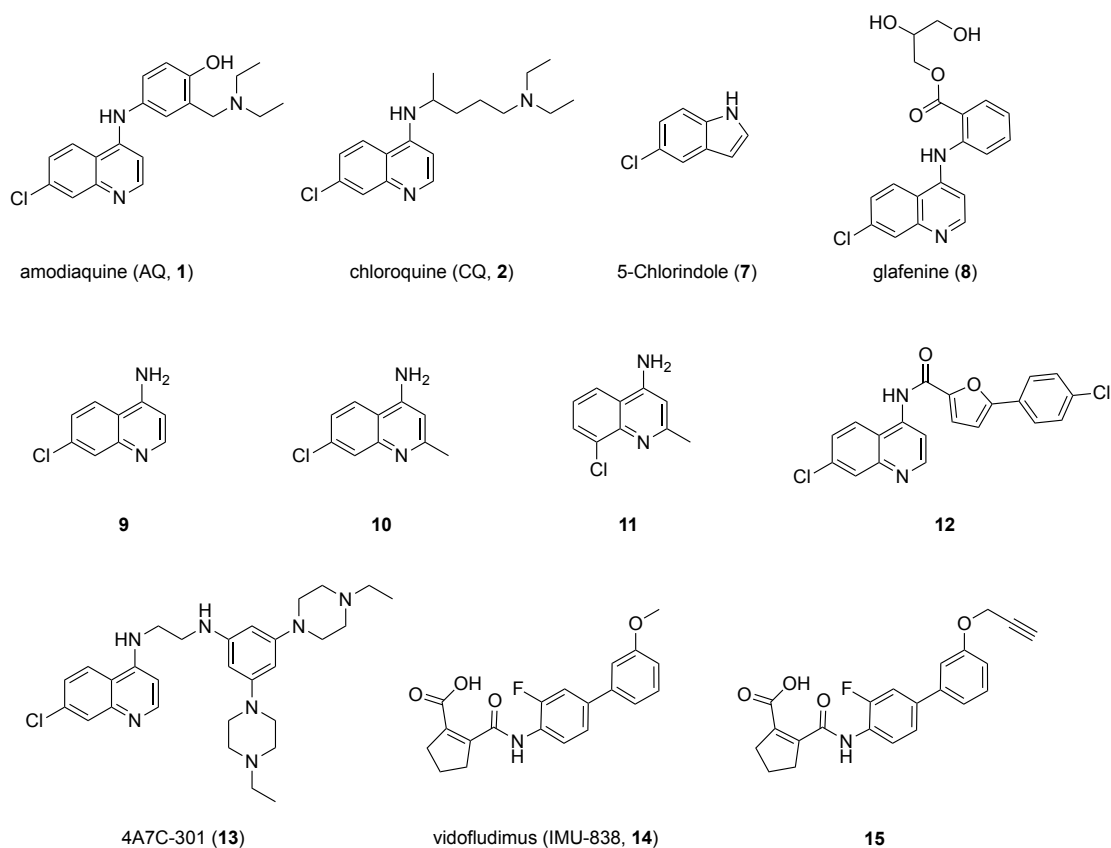


Figure 7. Chemical structures of natural and synthetic Nurr1 ligands.

1.1.3.1 Natural ligands for Nurr1

A metabolomics study of immobilized Nur77-LBD (His6-tagged Nur77 LBD on resins) demonstrated an interaction between Nur77 and arachidonic acid and docosahexaenoic acid (DHA, **5**, Figure 7)¹¹⁰. Based on these results, *de Vera and colleagues* employed a pull-down assay to show that **5** also interacted with Nurr1-LBD⁶⁵. A NMR study revealed that the binding of **5** affects the methyl groups of Leu410, Ile483 and Ile486 in H3 and H11 in the LBD⁶⁵. This resulted in a conformational change of H5, H7 and H12⁶⁵. In HEK293T and MN9D cells, **5** was found to repress Nurr1 transcriptional activity (remaining activity 75%) using a NBRE-based reporter gene assay⁶⁵. Furthermore, it was observed that **5** promoted interactions between Nurr1 LBD and the coregulator PIAS χ (SUMO-E3 ligase) in a

fluorescence polarization and time-resolved fluorescence resonance energy transfer (HFTR) assay⁶⁵. Further studies using NMR, hydrogen-deuterium exchange mass spectrometry (HDX-MS) and molecular dynamics simulations have suggested that the region of the canonical LBP in Nurr1 (bulky residues blocking the pocket) is dynamic with high solvent accessibility. It can expand markedly to bind unsaturated fatty acids including **5**, arachidonic acid, linoleic acid and oleic acid (volume from 30 Å to 500 Å)^{14,77,111}.

Prostaglandin E1 (PGE1, **3**, Figure 7) and A1 (PGA1, **4**, Figure 7) have been identified to interact directly with the LBD of Nurr1⁸³. In SK-N-BE(2)C (human neuroblastoma cells), MN9D and N27-A, PGE1 and PGA1 were observed to induce Nurr1 transcriptional activity in a dose-dependent manner, with varying activation efficacies between 10 to 25-fold for PGE1, contingent on the assay setup^{14,83}.

The cocrystal structure of Nurr1 LBD with PGA1 (PDB: 5Y41, Figure 8) has been elucidated, demonstrating PGA1 binds covalently between its cyclopentenone ring and the thiol group of Cys566 as a Michael adduct^{14,83}. Furthermore, the fatty acid tails have been shown to occupy a hydrophobic space, situated between H4/5, H11, and H12, which results in an outward movement of H12 from the core of Nurr1^{14,83}. The hydroxyl group engages in hydrogen bonds with the backbones of Glu440 and Leu44^{14,83}. The carboxylic acid chain of PGA1 exhibits conformational flexibility, and the carboxylate motif forms ionic interaction with Arg515 and His516 (H8-9 loop) as well as a water-mediated hydrogen bond with Arg563 (H11)^{14,83}. In the case of PGE1, the acidic (pH 5.5) crystallization conditions resulted in the conversion to the corresponding anhydride PGA1^{14,83}.

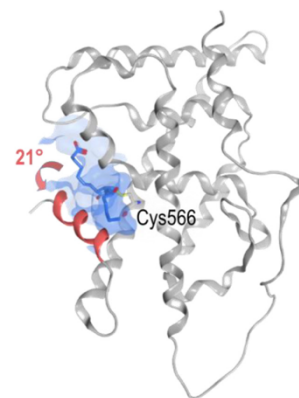


Figure 8. Crystal structure of Nurr1 LBD and PGA1 (PDB: 5Y41⁸³). Adapted from ¹⁴.

A further potential endogenous ligand for Nurr1 may be the dopamine metabolite dihydroxyindole (DHI, **6**, Figure 7), which interacted with Nurr1 as proven with biophysical assays, including differential scanning fluorimetry (DSF) and surface plasmon resonance (SPR) spectroscopy, as well as X-ray crystallography and cell assays⁷⁴. As an oxidized 5,6-indolquinone DHI forms a covalent reversible adduct with Cys566 in the region of H11 and H12, resulting in a 10° outward movement of H12 (PDB: 6DDA), which is less pronounced than the one observed in the PGA1-bound structure. Furthermore, DHI is stabilized by an H-bond with the Glu445 (H4/5) side chain. It also interacts with Arg515 (H8/9 loop) and Arg563 (H11) in cation- π interactions and exhibits weak contacts with Arg515 via the hydroxyl/carbonyl groups of DHI^{14,74} (Figure 9a). In a quantum mechanical model, DHI bound noncovalently within the same manner as the covalent one¹¹² (Figure 9b). Here

also, a cation- π interaction with Arg563 appears to be of significant importance for the stabilization of the aromatic indole system¹¹². The use of DSF revealed that DHI induced a concentration-dependent increase in the melting temperature (T_m) of the Nurr1 LBD, with a 1°C rise observed at a concentration of 50 mM. Additionally, direct binding of a biotinylated Nurr1 LBD immobilized on a streptavidin-coated biosensor chip was observed in a concentration-dependent manner for DHI in a SPR assay⁷⁴. In a cell-based reporter gene assay using a Gal4-DBD fused Nurr1 construct, DHI induced a 1.6-fold activation (100 μ M) in JEG3 cells (human choriocarcinoma cells)⁷⁴. Furthermore, DHI has been demonstrated to induce the expression of DAT, VMAT2 (both after 6 h incubation) and TH (after 24 h incubation) in zebrafish⁷⁴. However, due to the high reactivity of DHI, which involves autooxidation and polymerization to neuromelanin, a chromogenic and toxic pigment found in neurons, it is not suitable for the study of Nurr1 *in vivo* nor *in vitro*^{14,74,112}. Nevertheless, the discovery of the binding site for DHI has provided a potential avenue for the identification of novel ligands based on the indole scaffold¹¹².

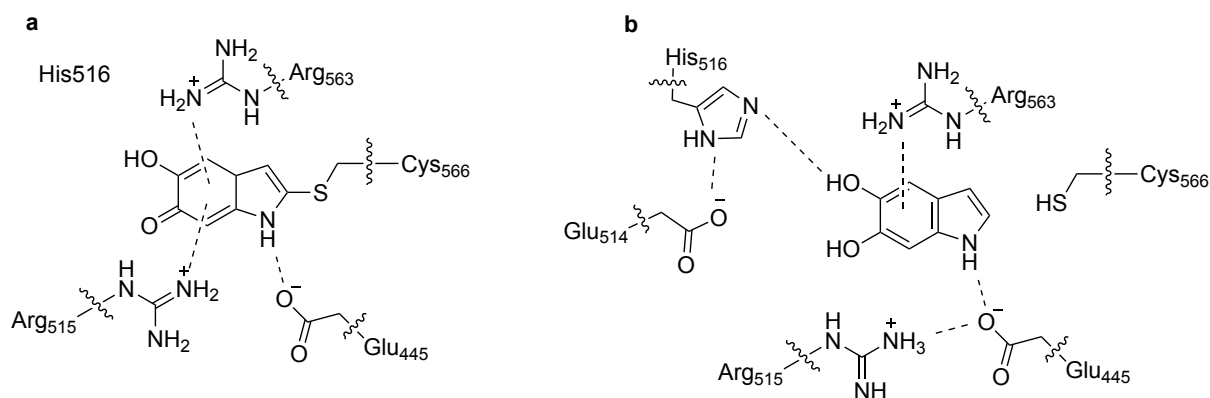


Figure 9. (a) Molecular interactions between the Nurr1 LBD residues and the ligand DHI as a covalent adduct. (b) Molecular interactions between the Nurr1 LBD residues and DHI as a non-covalent adduct. Adapted from support information of ¹¹².

1.1.3.2 Synthetic ligands for Nurr1

Based on DHI, *Kholodar and colleagues* have identified 5-chloroindole (**7**, Figure 7) as Nurr1 agonist with confirmed binding to the Nurr1 LBD¹¹². In this study, a computational evaluation was conducted on 19 indole derivatives, substituted at the 5 and 6 positions, with the objective of predicting their binding to the Nurr1 LBD¹¹² and their ability to form a favorable cation- π interaction. The compounds' binding affinity to the LBD was determined using microscale thermophoresis (MST)¹¹². **7** demonstrated micromolar affinity ($K_d = 15 \mu$ M), comparable to that of DHI, and activated Nurr1's transcriptional activity in a reporter gene assay using a Nurr1-LBD-Gal4-DBD (Gal4-Nurr1 hybrid) construct. In MN9D cells, **7** increased TH and VMAT2 expression in a concentration-dependent manner at 2.5, 5.0 and 10.0 μ M¹¹². A cytotoxicity assay suggested that **7** exhibited less toxicity when compared to the other substituted indoles¹¹². Consequently,

7 represents a promising lead compound for further development and optimization through medicinal chemistry¹¹².

The first orthogonally validated Nurr1 ligands were the antimalarials AQ and CQ (Figure 7)⁸⁰. A high-throughput screening of 960 FDA-approved drugs was conducted using a reporter gene assay based on the full-length Nurr1 and the monomer response element NBRE in SK-N-BE(2) C cells. Three compounds promoting Nurr1 activity were discovered: AQ, CQ and glafenine (**8**, Figure 7). They all share the 4-amine-7-chloroquinoline scaffold⁸⁰. The Nurr1 activation by AQ and CQ was approximately 3.0-fold, while that of **8** was only 1.5-fold^{14,80}. Consequently, **8** was not subjected to further evaluation⁸⁰. To ascertain whether AQ and CQ bind to the Nurr1 LBD, a Gal4 hybrid reporter gene assay was conducted, utilizing a construct comprising the human Nurr1-DBD or Nurr1-LBD with Gal4-DBD. AQ and CQ were found to induce Nurr1 transcriptional activity through the LBD construct with an EC₅₀ of approximately 20 and 50 μM , respectively^{14,80}.

Furthermore, a radioligand binding assay using radiolabeled (³H)-CQ demonstrated a saturable binding to Nurr1 LBD with a K_d value of 0.27 μM and a maximal binding capacity (B_{max}) of 13.9 μM ⁸⁰. A competition assay with unlabeled AQ and (³H)-CQ revealed that AQ binds to a similar region of the Nurr1 LBD. Using ¹H/¹⁵N-HSQC NMR in conjunction with a ¹⁵N-labelled Nurr1 LBD and mutagenesis study, the binding epitope of AQ was located^{14,80}. The observed binding was focused on the amino acids H402, I403, Q404, Q405, D408 and L409 in the lower section of helix H3 and on the H6/ β -sheet region as well as residues in helices H11 and H12 (V468, Y575 and D580)^{14,80}. In another 2D (¹H, ¹⁵N) TROSY-HSQC NMR study, AQ and CQ were observed to directly bind to Nurr1 LBD¹⁰⁷. It has been shown that the binding of AQ and CQ to H3, H6, H10/11 and H12 was affected by residues that were within or in close proximity to the canonical orthosteric LBP¹⁰⁷. Nevertheless, studies of AQ and CQ also demonstrated that they mediated Nurr1-independent, nonspecific transcriptional effects in the control experiment VP16-Gal4 in SK-N-BE(2)-C cells¹⁰⁷. Gal4-VP16 is a fusion protein that exhibits high constitutive transcriptional activity¹⁰⁷. Ligands that cause decreased or increased activity of this chimeric transcription factor exert their influence on general transcription in a target-independent manner or are toxic¹⁰⁷. Nevertheless, AQ has been demonstrated to display greater Nurr1-activating efficacy than CQ, indicating the potential for the development of SAR on this scaffold to achieve greater specificity towards Nurr1 while reducing the nonspecific effects¹⁰⁷.



Figure 10. Proposed binding region of AQ (orange) to Nurr1 LBD based on NMR binding studies. Adapted from ¹⁴.

A fragment-based study of AQ using a Gal4-Nurr1 hybrid reporter gene assay by former doctoral student Dr. Sabine Willems revealed that 4-amino-7-chloroquinoline (**9**, Figure 7) fragment shared by AQ, CQ and **8** weakly induced Nurr1 activity at high micromolar potency ($EC_{50} = 259 \mu\text{M}$)¹¹³. The systematic variation of the quinoline substitution pattern led to the discovery of 4-amino-7-chloro-2-methyl-quinoline (**10**, Figure 7) as a fragment-like Nurr1 agonist, exhibiting low micromolar potency ($EC_{50} = 33 \mu\text{M}$)^{14,113}. By shifting the chlorine to position 8, the quinoline **11** (Figure 7) exhibited a twofold increase in potency, with an EC_{50} value of $17 \mu\text{M}$ ¹¹³. **11** induced Nurr1 transcriptional activity in all three full-length reporter gene assays, using NBRE, NurRE and DR5 in HEK293T cells, and promoted the expression of TH and VMAT2 in T98G (human astrocytes). In a HFTR assay utilizing a Tb^{3+} -cryptate-labeled NCoR1 or NCoR2 and a superfolder green fluorescent protein (sGFP)-labeled Nurr1 LBD, **11** induced the recruitment of coregulatory proteins to the LBD and the homodimerization of Nurr1^{14,113}. In addition, **11** exhibited no Nurr1-independent effects on transcriptional activity in contrast to AQ and CQ in a Gal4-VP16 reporter gene assay^{107,113}.

A further study based on a microscale analogue library synthesis and computational pharmacophore evaluation of **9** indicated its possible extension with various substituents on the amine and revealed the 5-(4-chlorophenyl)furan-2-ylamide derivative as a promising novel Nurr1 ligand (**12**, Figure 7) moiety^{14,114}. **12** was found to induce Nurr1 transcriptional activity in a Gal4 hybrid reporter gene assay with an EC_{50} of $3.0 \mu\text{M}$ ¹¹⁴.

In light of the identification of AQ, CQ and **9** binding on Nurr1^{113,115}, *Kim and colleagues* proceeded to develop 4A7C-301 (**13**, Figure 7) through a systematic optimization process of 4A7C-101 which was designed as a potent anti-malarial hybrid for *Plasmodium falciparum* strains and demonstrated Nurr1 transcriptional activation in a Gal4 reporter gene assay¹¹⁵. This study involved the generation and characterization of 570 derivatives, resulting in the identification of the optimized, brain-penetrating Nurr1 agonist **13**. **13** induced Nurr1 transcriptional activity in a Gal4-Nurr1 reporter gene assay with 8 repeats of the upstream activation sequence (UAS) RE¹¹⁵. The EC_{50} was found to be low micromolar ($6.53 \mu\text{M}$), with an activation efficacy of 18-fold¹¹⁵. In SK-N-BE(2)C cells, **13** activated full-length Nurr1 in a dose-dependent manner ($EC_{50} = 7\text{-}8 \mu\text{M}$), demonstrating greater potency than CQ ($EC_{50} = 70 \mu\text{M}$)¹¹⁵. Previous mutagenesis studies of AQ/CQ and PGA1/PGE1 interaction with Nurr1 LBD have indicated that different synthetic and native agonists of Nurr1 interact with shared as well as distinct residues within the Nurr1 LBD¹¹⁵. It has been observed that the agonist effect of **13** is reduced in the Nurr1 mutants of I573, I588, L593, D594, T595, L596 and F598¹¹⁵ indicating that these residues, which are situated at the C-terminal H12, are critical for activation and interaction with the Nurr1 LBD for **13**¹¹⁵. Furthermore, the binding assay using (³H)-CQ fluorescent-labelled hydroxy-CQ for TR-FRET has demonstrated that **13** has a 20-fold higher binding affinity to the

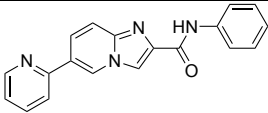
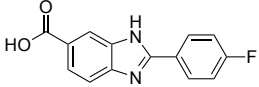
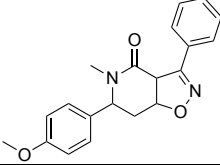
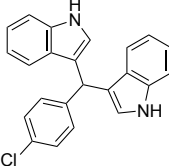
Nurr1-LBD than CQ ($IC_{50} = 107.71$ nM (**13**) and 2.33 μ M (CQ))¹¹⁵. *In vivo*, **13** protected midbrain dopamine neurons in the MPTP-induced male mouse model of PD and improved both motor and non-motor olfactory deficits without causing dyskinesia-like behaviors¹¹⁵. Furthermore, **13** significantly ameliorated neuropathological abnormalities and improved motor and olfactory dysfunctions in AAV2-mediated α -synuclein-overexpressing male mice¹¹⁵. The authors propose that these disease-modifying properties of **13** may warrant clinical evaluation of this or analogous compounds for the treatment of PD-patients¹¹⁵.

In a screening for NRs selectivity, the dihydroorotate dehydrogenase (DHODH) inhibitor vidofludimus (IMU838, **14**, Figure 7) demonstrated Nurr1 activation in a Gal4 hybrid reporter gene assay¹¹⁶. A comprehensive dose-response characterization of IMU838 revealed Nurr1 activation with an EC_{50} of 0.4 μ M and a Nurr1 preference compared to its NR4A relatives ($EC_{50} = 3.1$ μ M (Nur77), $EC_{50} = 2.9$ μ M (Nor1)) which markedly exceeded available Nurr1 activators¹¹⁶. Furthermore, IMU838 was observed to activate human Nurr1 in its native full-length form as a monomer, displaying an EC_{50} of 0.3 μ M (NBRE), and as an RXR/Nurr1 heterodimer, exhibiting an EC_{50} of 0.4 μ M (DR5)¹¹⁶. Additionally, IMU838 demonstrated a remarkable binding affinity for the Nurr1 LBD, with a K_d value of 0.7 μ M, as determined through isothermal titration calorimetry (ITC)¹¹⁶. In order to identify regions offering potential for optimization towards potent Nurr1 agonists with selectivity over DHODH, a broad survey of the structural variations on all parts of the scaffold was conducted in order to probe the SAR, leading to the discovery of **15** (Figure 7)¹¹⁶. **15** demonstrated both boosting potency ($EC_{50} = 0.11$ μ M) and efficacy (6.2-fold activation) on Nurr1, while exhibiting reduced DHODH inhibitory potency ($IC_{50} = 1.7$ μ M vs. $IC_{50} = 0.61$ μ M (IMU838))¹¹⁶. Additionally, **15** demonstrated a high degree of affinity binding to the Nurr1 LBD in ITC ($K_d = 0.3$ μ M)¹¹⁶. Furthermore, **15** activated full-length human Nurr1 on both the monomer (NBRE) and the RXR-heterodimer (DR5) with comparable efficiency, with respective EC_{50} values of 0.22 μ M and 0.36 μ M¹¹⁶. In T98G cells, **15** induced mRNA expression of the Nurr1-regulated genes TH and VMAT2, thereby demonstrating cellular target engagement¹¹⁶. Consequently, **15** emerges as an improved Nurr1 agonist and as a next-generation chemical tool for this receptor¹¹⁶.

Some further Nurr1 so-called agonist scaffolds have been reported, including derivatives of imidazopyridines (e.g. SR24237 (**16**) and SA00025), benzimidazoles (e.g. SR10098 (**17**)), isoxazolpyridinones (e.g. SR10658 (**18**) and IP7e), bis(indolyl)methane (e.g. C-DIM12 (**19**))^{14,107} (Table 1). All of these so-called agonists have been observed to induce Nurr1-mediated activation in a variety of *in vitro* and *in vivo* contexts^{107,117-120}. The systematic *in vitro* evaluation, comprising a reporter gene assay (full-length Nurr1 and VP16 control) and a viability assay, as well as profiling in a NMR spectroscopy structural footprinting assay, of these compounds did not reveal any direct interaction with Nurr1^{14,107,116}. The results indicated that these ligands may influence Nurr1 activity in a manner that is

dependent on the type of cell in question, as well as via interactions with upstream effector proteins, such as kinases. This in turn could result in alterations to Nurr1 cellular activity through the exertion of downstream effects^{14,107}.

Table 1. Further so-called Nurr1 modulators (**16-19**).

ID	Structure	Nurr1 activation reported	Binding evidence
SR24237 (16)		EC ₅₀ = ~ 1-240 nM ¹²⁰	No binding detected ¹⁰⁷
SR10098 (17)		EC ₅₀ = 24 nM ¹¹⁷	No binding detected ¹⁰⁷
SR10658 (18)		EC ₅₀ = 4.1 nM ¹¹⁹	No binding detected ¹⁰⁷
C-DIM2 (19)		Dose dependent activation, approximately 60-fold (20 μM) ¹¹⁸	No binding detected ¹⁰⁷

The development of Nurr1 agonists is hindered by two significant challenges: the lack of detailed structural data on ligand-binding sites and the incomplete understanding of the molecular mechanisms behind Nurr1^{14,107}. In contrast to other NRs, the crystal structures of the Nurr1 LBD have not revealed the presence of a well-defined LBP, which has impeded the discovery and design of Nurr1-binding ligands¹⁰⁷. While some ligands, including DHI and the antimalarials AQ and CQ, have been observed to interact with the Nurr1 LBD, the majority of NR4A ligands appear to act through indirect binding to Nurr1. These findings highlight the necessity for further structural and mechanistic studies to facilitate the development of Nurr1 agonists that are both specific and selective^{14,107}. Despite the identification of Nurr1 ligands, there is still a lack of potent and selective modulators that can reliably capture the therapeutic effects of Nurr1^{14,107}. It is therefore essential that further research is conducted to gain a deeper insight into the structural characteristics of the Nurr1 LBD and to develop novel techniques for the identification of direct Nurr1 ligands, in order to fully realize the potential therapeutic benefits of Nurr1.

1.1.3.3 *Nurr1-RXR heterodimer-specific RXR agonist activation*

An alternative approach to modulating Nurr1 activity is through ligands that specifically target its heterodimer-binding partner, RXR¹²¹. For example, Nurr1-RXR selective agonists include BRF110 (**20**, Figure 11)¹²² and dibenzodiazepine HX600 (**21**, Figure 11)¹²³. **20** was observed to prevent dopaminergic neuron demise and striatal denervation *in vivo* against PD-causing toxins in a Nurr1-dependent manner¹²². In a Gal4 reporter gene assay, **21** effectively activated the Nurr1/RXR heterodimer (also Nur77/RXR) in a concentration-dependent manner, but not other RXR heterodimers¹²³. In addition, it has been shown that RXR ligands can increase the number of dopaminergic cells and other neurons in the embryonic rodent CNS in a process mediated by the Nurr1-RXR heterodimer¹²⁴.

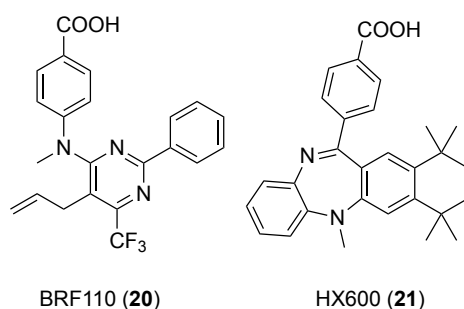


Figure 11. Chemical structures of selective Nurr1-RXR heterodimer ligands BRF110 (**20**) and HX600 (**21**).

Another potential mechanism for Nurr1-RXR heterodimerization involves the release of Nurr1 as a monomer from this complex¹²¹. When Nurr1 forms a heterodimer with RXR α , it represses transcription on monomeric NBRE¹²¹, which are found in the promoter regions of genes regulating dopaminergic signaling, including TH¹²⁵. It has been observed that classical RXR agonists enhance activity of NBRE reporters^{52,126}, leading to the discovery of RXR-binding ligands that preferentially activate Nurr1-RXR heterodimers over other NR-RXR heterodimers or RXR homodimers^{121,127,128}. A recent study has demonstrated that RXR ligands can act as allosteric protein-protein interaction inhibitors, binding to the canonical ligand-binding pocket within the RXR LBD and influencing Nurr1-mediated transcription via Nurr1-RXR heterodimer dissociation¹²¹. NMR spectroscopy, protein-protein interaction, and cellular transcription assays demonstrated that Nurr1-RXR α transcriptional activation by RXR ligands is not correlated with classical RXR agonism¹²¹. Instead, it is correlated with weakening the Nurr1-RXR α LBD heterodimer affinity and heterodimer dissociation, which results in the release of Nurr1 as a monomer and subsequent regulation of gene transcription¹²¹. These findings may open a new avenue for selective activation of the RXR/Nurr1 heterodimer as a potential target in the treatment of neurodegenerative diseases¹²²⁻¹²⁴.

1.2 Retinoid X receptors (RXRs)

The first retinoid X receptor (RXR, NR2B) to be identified, RXR α (NR2B1), was initially described as an orphan receptor, lacking an endogenous ligand^{24,129}. 9-cis retinoid acid (9cisRA, **22**, Figure 14), DHA (**5**) and several fatty acids (e.g. oleic acid and palmitic acid) were later discovered as potential endogenous ligands for RXR^{24,130,131}. There are three subtypes of RXR, which are encoded by separate genes: RXR α , RXR β , and RXR γ ^{23,24}. As with the other members of the superfamily of NRs, all subtypes of RXRs exhibit a variable NTD, a highly conserved DBD, a hinge region that is not conserved, and a highly conserved C-terminal LBD^{23-25,59}. The amino acids responsible for forming the ligand binding site are identical in all three RXR subtypes and are highly lipophilic^{132,133}. There are almost exclusively lipophilic interactions with the ligands, apart from a strong interaction with an arginine of the ligand-binding site deep in the interior¹³⁴. Consequently, the development of selective ligands for a specific subtype is challenging^{2,131}. All three RXR subtypes are known to act as common heterodimerization partners for numerous members of the NR1 (TRs, RARs, VDR, PPARs, LXRs, FXR, PXR, CAR) and NR4 (Nurr1, Nur77) subfamily or with themselves as homodimers²³⁻²⁵ (Figure 12). This interaction between the dimer partners is ligand-dependent and occurs at the surface of the LBD and is facilitated by H10, with minor contributions from H9 and the loop between helices 8 and 9²⁵. Moreover, specific recognition of RE, including DR1, DR3, DR4, and DR5, also plays a pivotal role in the dimerization²³⁻²⁵. The spacing within these RE plays an important role in the binding process, influencing the specificity of the interaction of the dimer with the DNA²³⁻²⁵. The RXR heterodimers can be divided into three distinct functional categories: permissive and nonpermissive heterodimers (and conditional heterodimers)^{24,130} (Figure 13). Permissive RXR heterodimers (RXRs/PPARs, RXRs/LXRs, RXRs/FXR, RXRs/PXR) can be activated by agonists of both RXR and the partner receptor, either independently or in combination, to induce a synergistic activation^{24,41,46,130}. In contrast, nonpermissive heterodimers (RXRs/RARs, RXRs/TRs, RXRs/VDR) are unable to be activated by an RXR agonist, but only by the agonist of the partner receptor^{24,41,46,130}. Nevertheless, in the case of a liganded partner, the RXR agonist can trigger an activation, resulting in a synergistic activation^{24,41,46,130}.

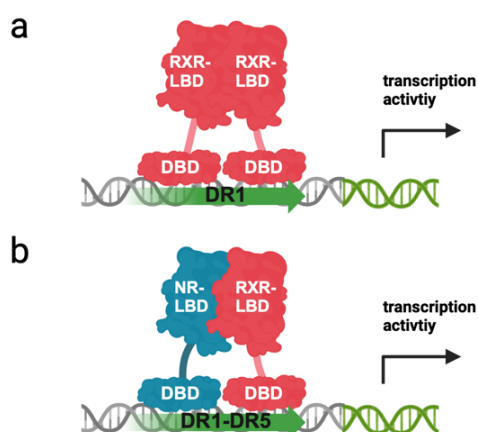


Figure 12. Schematic illustration of RXR with its REs as a homodimer (a) and heterodimer (b) with other NRs. Created with Biorender.com.

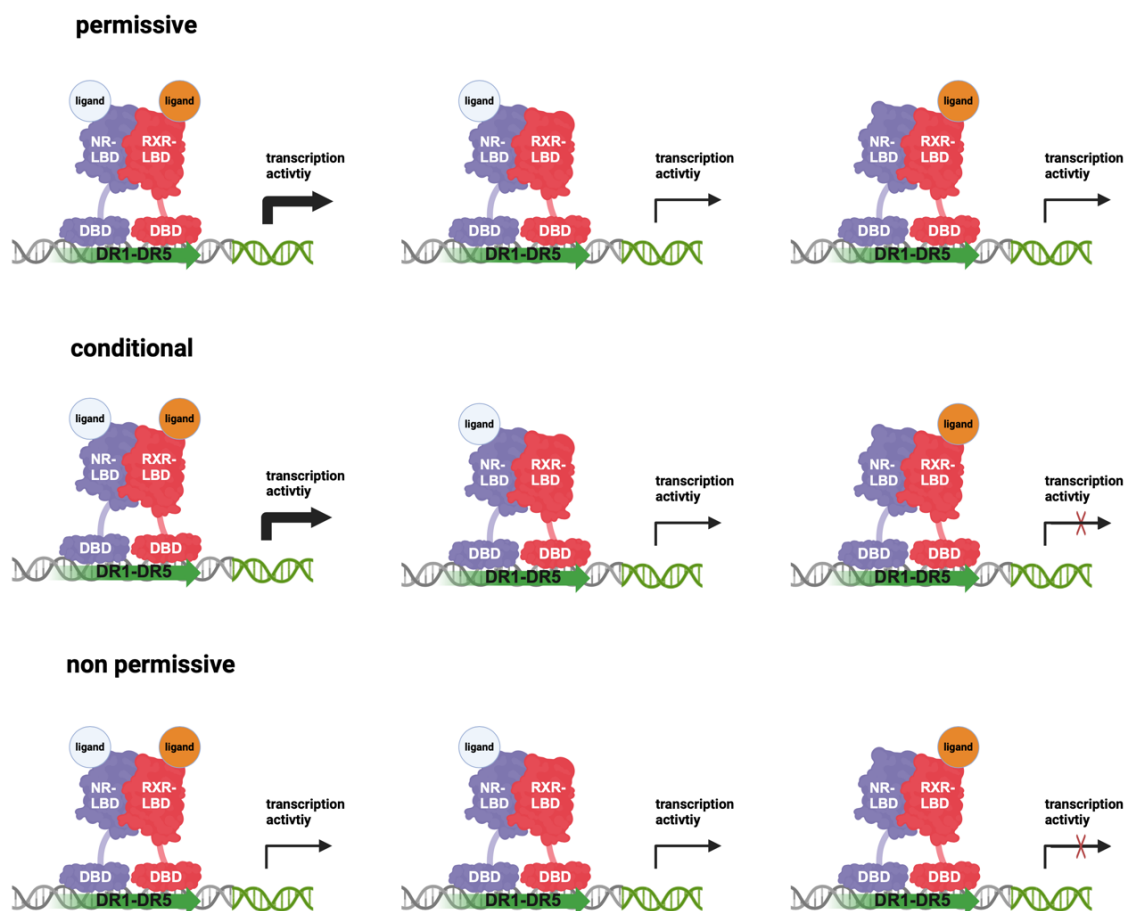


Figure 13. Schematic illustration of the mechanism of RXR as permissive, non-permissive and conditional heterodimer partner. *Created with Biorender.com.*

The transcriptional activity of the RXRs is regulated by the LBD, which facilitates the binding of small, lipophilic molecules to the LBP located in the canonical binding site region of NRs^{23,24,131}. This leads to a conformational change of H12, the exchange of coregulators, and finally gene transcription as previously described (see chapter 1.1.1)^{23,24,131}. In the absence of ligands, RXR heterodimers can still bind with high affinity to DNA, which can result in the repression of transcriptional activity (e.g., RAR)¹³⁵.

1.2.1 Physiological function

The expression profiles of the RXRs display significant disparities²³⁻²⁵. RXR α is expressed at a high level in liver, kidney, epidermis and intestine, and constitutes the major RXR isoform in skin tissue^{23-25,129}. RXR β is distributed widely and is detectable in almost every tissue, while RXR γ is mostly restricted to muscle tissue and selected parts of the brain, as well as the pituitary gland^{24,25}. In the context of neurodegenerative diseases, a higher CNS localization was observed for RXR γ in contrast to the other two subtypes^{2,24}. Within the CNS, RXR γ exhibits a non-specific distribution². It is expressed in the striatum, parts of

the amygdala, the spinal cord, and the hypothalamus^{2,136}. A particularly elevated level of expression was observed in the basal ganglia, where it appears to be associated with motor function and addiction^{137,138}. It is particularly noteworthy that RXR γ exhibits a high level of expression in glial cells, which are known to play a role in the pathological processes associated with neurodegenerative disorders^{2,27}.

Given its pivotal role in numerous (patho-)physiological processes as a universal NR heterodimer partner, the pharmacological potential of RXR is considerable^{2,24,131}. In addition to its established role in cancer therapy, RXR has been the subject of intense study in recent years regarding its involvement in neurodegenerative diseases^{2,131,134}. In this context, RXR is implicated in neuroprotective, neuroinflammatory, and regenerative processes, which are regulated by its heterodimers^{2,10}.

1.2.1.1 RXRs in Alzheimer's disease

As previously indicated (chapter 1), AD can be defined as a pathological condition characterized by the accumulation and aggregation of A β peptides, which are derived from the sequential cleavage of the amyloid precursor protein (APP) by the β -secretase (BACE) and γ -secretase enzymes⁶. Initial observations in an AD mouse model (APP/PS1) have indicated that treatment with bexarotene (**23**, Figure 14), a RXR agonist, resulted in elevated levels of apolipoprotein E (ApoE) expression in astrocytes, which was associated with enhanced clearance of A β peptides via an ApoE-mediated pathway²⁶. This was accompanied by a reduction in the burden of A β in the brain, as well as a reversal of cognitive deficits²⁶. Furthermore, the activation of RXRs induces the expression of ABCA1 (ATP-binding cassette transporter A1), which is involved in the cellular efflux of phospholipids and cholesterol^{2,139}. This results in an increased ABCA1-mediated lipidation of ApoE and elevated HDL levels in the brain^{140,141}. An elevated cholesterol level in the brain is associated with an elevated risk of developing AD^{142,143}. Cholesterol has been demonstrated to facilitate the production and deposition of A β peptides^{142,143}. ApoE-containing HDLs (high-density lipoproteins) have been shown to induce the proteolytic degradation of A β peptides through microglial neprilysin and extracellular insulin-degrading enzyme¹⁴⁴. ApoE and ABCA1 are both transcriptionally controlled by the heterodimers of PPAR γ /RXR and LXR/RXR^{2,139}. Due to their permissive nature, both heterodimers can be induced by RXR agonists and exhibit simultaneous activation^{2,24}. Another study demonstrated that **23** induces A β phagocytosis by brain myeloid cells, which is associated with an increase in the expression of phagocytic receptors MerTK, Ax1 and Trem2²⁶. Additionally, **23** exhibited neuroprotective effects in an AD mouse model (5xFAD), where it repressed inflammation and prevented neuronal loss accompanied by an increase in synaptic markers and behavioral improvement²⁶. Although **23** has been shown to exhibit great potential as a therapeutic agent for AD in numerous experimental models, its performance in clinical trials has been less encouraging due to the

compound's limited penetration of the blood-brain barrier, as well as the occurrence of significant adverse effects such as hypertriglyceridaemia^{2,134}. Nevertheless, a small-scale clinical trial involving AD patients with ApoE3 alleles has demonstrated that the administration of **23** can lead to a notable reduction in amyloid burden within a 30-day period¹⁴⁵.

1.2.1.2 RXRs in Parkinson's disease

Similar to AD, the involvement of RXR in PD is associated with beneficial activity of permissive RXR heterodimers^{14,113,122}. In the context of PD, the permissive RXR/Nurr1 heterodimer is of particular significance, given the pivotal role of Nurr1 in the pathogenesis of PD^{14,113,122} (see chapter 1.1.2.1 and 1.1.3.3).

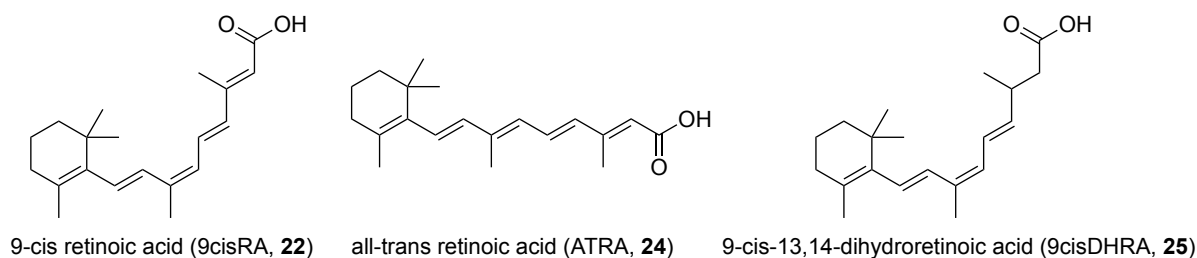
1.2.1.3 RXRs in Multiple sclerosis

Recent evidence suggests that RXR γ plays a role in protecting and remyelinating the CNS^{2,28}. RXR γ is minimally expressed in glial cells of the uninjured CNS, but is upregulated in microglia, macrophages and astrocytes after CNS injury^{2,27,28}. RXR γ knockout studies showed its absence to result in inefficient differentiation of oligodendrocyte precursor cells (OPCs) to mature myelinating oligodendrocytes (OLs)^{27,28}. Moreover, administration of **22** promoted remyelination in rats following toxin-induced demyelination^{28,146} and inhibited the expression of pro-inflammatory molecules, suggesting an anti-inflammatory role for RXR in microglia and astrocytes^{28,146}. *In vitro* treatment with **23** restored the phagocytic efficiency of myelin debris clearance in monocytes from MS patients to levels seen in young healthy individuals¹⁴⁷.

1.2.2 RXR ligands

Selective activation of RXRs in the CNS with a small molecule is challenging^{28,134}. This is due to the ubiquitous nature and critical role of RXRs in multiple tissues^{28,134}. RXR agonists that have been clinically investigated, such as **23**, cause serious adverse effects, including elevated blood triglycerides, hepatomegaly and hypothyroidism^{2,25,28,134}. Nonetheless, studies with **23** have shown promising therapeutic effects in neurodegenerative diseases^{2,28,134}. This highlights the potential of RXRs for CNS protection, but also the risk for undesirable effects^{2,28,134}. Therefore, subtype- or tissue-selective RXR agonists or alternative, more selective mechanisms of RXR activation are needed to evaluate the full potential of RXR as a therapeutic target in neurodegenerative diseases.

Natural ligands



Synthetic ligands

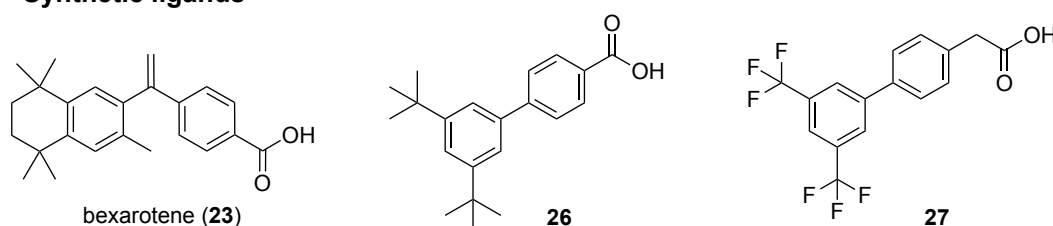


Figure 14. Chemical structures of natural and synthetic RXR ligands.

1.2.2.1 Natural ligands

Initially, RXR was identified as an orphan receptor that responded to high concentrations of all-trans retinoic acid (ATRA, **24**, Figure 14) via a heterodimeric complex of a retinoic acid receptors (RARs) and RXR^{23,24}. It was therefore hypothesized at an early stage that metabolites of vitamin A, such as the oxidized vitamin A analogue ATRA, could act as ligands for RXR^{148,149}. It was demonstrated that ATRA does not bind to RXR, but rather its isomer, 9cisRa (**22**, Figure 14)^{24,25,150}. **22** is a high-affinity ligand for RXRs ($EC_{50} = 140\text{-}200$ nM, depending on the assay) with an unclear physiological role^{134,151}. A metabolite of **22**, 9-cis-13,14-dihydroretinoic acid (9cisDHRA, **25**, Figure 14), was identified as naturally occurring and physiologically pertinent RXR ligand, exhibiting moderate efficacy in RXR activation^{134,152}. **22** is highly hydrophobic and can exhibit a pronounced L-shape which aligns with the structural requirements of the RXR LBP^{24,130,131,134}. The acidic group forms a strong salt bridge with Arg316 as only polar contact stabilizing the binding^{130,131,134}. This L-shaped geometry is preserved in synthetic RXR ligands (rexinoids) such as **23**^{130,131,134}. Several other fatty acids including linoleic acid, palmitoleic acid, arachidonic acid and **5** were identified as further endogenous ligands for RXR with significantly lower potency^{131,134}. The naturally occurring sesquiterpenoid valerenic acid^{134,153} was discovered in a computer-assisted screen as subtype-preferential RXR β agonist ($EC_{50}(\text{RXR}\alpha/\text{RXR}\beta/\text{RXR}\gamma) = 27 \mu\text{M}$ (9-fold) / $5 \mu\text{M}$ (69-fold) / $43 \mu\text{M}$ (4-fold)) indicating the possibility to achieve selectivity between the subtypes with ligands¹⁵³.

1.2.2.2 Synthetic ligands

The majority of synthetic RXR ligands share a common fatty acid mimetic backbone with an acidic head group in an L-shaped hydrophobic scaffold mimicking **22**¹³⁴. Among the synthetic rexinoids, only **23** has received drug approval and is currently used for the treatment of cutaneous T-cell lymphoma as a second-line therapy^{131,134}. **23** exhibits structural similarities with **22**, containing a highly hydrophobic scaffold and an acidic head group¹⁵⁴. The L-shaped geometry is derived from the ethylene moiety^{134,154}. **23** similarly has activated all RXRs with EC₅₀(RXR α /RXR β /RXR γ) values of 33/24/25 nM and has exhibited high selectivity towards RARs, unlike **22**¹⁵⁴. Nevertheless, it is important to note that **23** has unfavorable physicochemical properties^{131,134}. The solubility of **23** in water is limited, it exhibits high lipophilicity and has been demonstrated to have cytotoxic properties, which are not optimal characteristics for an efficacious pharmaceutical^{134,155}.

To address the limited chemical diversity of RXR ligands, virtual screening and computational de novo design have identified a potential avenue for the discovery of new ligands with innovative molecular frameworks¹⁵⁶. The computational de novo design software, design of genuine structures (DOGS), was employed to construct novel molecules from a collection of commercially available building blocks and a set of synthetic reaction schemes¹⁵⁶. This approach led to the discovery of the biphenyl **26** (Figure 14), which activated all RXR subtypes in a Gal4 hybrid reporter gene assay (EC₅₀ (RXR α /RXR β /RXR γ) = 11.8/11.7/14.1 μ M)¹⁵⁶ and revealed a subtype preference for RXR β /RXR γ in terms of transactivation efficacy (5.7-fold RXR α / 70.6-fold RXR β / 58.3-fold RXR γ)¹⁵⁶. Consequently, **26** represented an attractive starting point for the development of novel RXR modulators^{156,157}.

In the light of the discovery that **26** represents a novel chemotype for RXR, Dr. Julius Pollinger, a former doctoral student, explored the scaffold's SAR in relation to RXR potency, subtype preference and heterodimer selectivity, resulting in the identification of biphenyl **27** (Figure 14)¹⁵⁷. It has been demonstrated that 3',5'-substituents of the biphenyl affect RXR subtype preference¹⁵⁷. In particular, bulky lipophilic residues were found to be essential for RXR γ activation, while the RXR α and RXR β subtypes revealed greater tolerance to smaller moieties¹⁵⁷. By chain elongation of the benzoic acid component, remarkable increases in potency were achieved¹⁵⁷. **27** activated RXRs with EC₅₀ (RXR α /RXR β /RXR γ) values of 0.08/0.15/0.22 μ M in Gal4 hybrid reporter gene assays in HEK293T cells¹⁵⁷. The X-ray structure of the RXR α LBD in complex with **27** (PDB: 6SJM, Figure 15) demonstrated that **27** binds in the classical orthosteric LBP, with a binding mode resembling 9CR α and bexarotene but without the typical L-shaped configuration¹⁵⁷. The carboxylic acid of **27** engages in an ionic interaction with Arg316, while the entire biphenyl scaffold is surrounded by a cluster of lipophilic residues within the LBP. In contrast to other known RXR agonists, **27** does not extend towards H12¹⁵⁷. The findings of

the current study indicated that the unique binding mode of **27** demonstrates that the typical L-shape is not essential for RXR activation and provides an opportunity for structure-based optimization, which may also elucidate the particular activity exhibited by this novel RXR ligand chemotype¹⁵⁷.

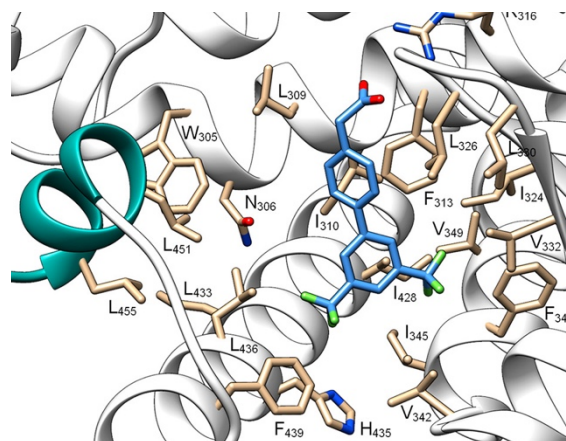


Figure 15. X-ray structure of RXR α in complex with **27** (PDB: 6SJM)¹⁵⁷. Reprinted from ¹⁵⁷.

1.3 Peroxisome proliferator-activated receptors (PPARs) - PPAR α

A significant heterodimer partner of RXR, which can also be activated by fatty acids, is the peroxisome proliferator-activated receptor α (PPAR α , NR1C1)²⁹. PPAR α was identified as the initial member¹⁵⁸ of a triad of PPARs (PPAR β/δ (NR1C2), and PPAR γ (NR1C3)), which collectively constitute a subfamily of NRs^{29,159}. All three PPARs exhibit a protein domain organization that is similar

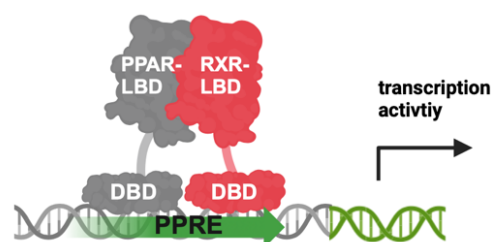


Figure 16. Schematic illustration of PPAR and RXR to bind as a heterodimer on PPRE. Created with Biorender.com.

to most members of the superfamily, comprising a NTD, a DBD, a hinge region and a LBD^{29,30}. PPAR α forms a heterodimer with RXR, which is obligate in nature and permissive^{29,30}. Consequently, RXR agonists facilitate the formation of the heterodimer complex^{29,30}. However, simultaneous binding of agonists to both receptors results in a synergistic activation effect^{29,30}. The PPAR α -RXR heterodimer interacts with PPAR response elements (PPREs), which are organized as a DR1^{29,160,161} (Figure 16). A DR1 RE consists of two copies of the hexameric 5'-AGGTCA-3' motif separated by a single nucleotide, with an additional consensus AACT motif positioned 5' to the DR1^{29,160,161}. PPAR α binds to the 5' extended half-site of the RE, whereas RXR occupies the 3' half-site^{29,160,161}. In the unliganded state this heterodimer recruits corepressors (e.g. NCoR, SMRT) and inhibits transcription^{29,30}. As described for other NR (chapter 1.1.1), ligand binding induces corepressor dissociation from the heterodimer surface, and a newly

formed surface (coactivator motif) recruits coactivators (e.g. PGC1 α), initiating gene transcription^{29,30}. The LBP of the PPAR α is more lipophilic than in the other PPAR subtypes, but its shape and size are similar to that of PPAR γ ¹⁶²⁻¹⁶⁴. In general, the LBP of PPARs represents a large, Y-shaped hydrophobic cavity¹⁶²⁻¹⁶⁴ that can bind a wide range of lipophilic ligands, including fatty acids^{29,162}.

1.3.1 Physiological and pathophysiology function

PPAR α is expressed in tissues with high metabolic activity, such as the liver, heart, kidney, intestine and adipose tissue^{29,30}. It regulates fatty acid catabolism by β -oxidation, lipid transport and gluconeogenesis^{29,30}. PPAR α agonists such as fibrates influence β oxidation in the liver, resulting in a reduction of triglyceride levels in the blood^{29,161}. This effect is similar to the processes initiated by the body during starvation¹⁶⁵. The increased supply of fatty acids to the liver and the increased β -oxidation, which promotes gluconeogenesis and thus leads to energy production, are physiological processes to counteract the breakdown of proteins^{29,165,166}. In addition, PPAR α activation leads to a reduction in unstable low-density lipoprotein (LDL) and a simultaneous increase in HDL¹⁶⁷. With the reduction of triglyceride levels and the conversion of LDL to stable HDL, the formation of sclerotic plaques is minimized^{167,168}. Given their relatively limited effectiveness in reducing LDL levels, fibrates are primarily employed for the management of hypertriglyceridemia¹⁶⁹ while statins are considered the primary therapeutic option for the treatment of hypercholesterolemia and dyslipidemia¹⁷⁰.

1.3.1.1 PPAR α in neurodegenerative diseases

PPAR α was also identified in the CNS^{31,171}. Apart from robust expression in the thalamus, an accumulation in glial cells, and particularly in astrocytes, is noteworthy^{171,172} although the precise role of PPAR α in these cell types remains unclear³¹. Nevertheless, studies have indicated that PPAR α may represent a promising target for the treatment of neurodegenerative diseases³¹. PPAR α regulates genes involved in glutamate homeostasis and cholinergic/dopaminergic signaling in the brain³¹. Furthermore, PPAR α regulates the expression of enzymes engaged in the metabolism of APP^{31,173} including the α and γ secretases, which are responsible for the non-amyloidogenic pathway of APP degradation and the release of A β peptide in AD^{31,173}. In the context of AD, the expression of genes encoding PPAR α and PGC1 α was found to be significantly diminished, thereby underscoring a possible role of the receptor and its coregulator^{31,174}.

1.3.1.2 PPAR in skin diseases

Another significant role for PPAR α as a therapeutic target is in the skin¹⁷⁵. In the epidermis, PPAR α expression increases with keratinocyte differentiation¹⁷⁵⁻¹⁷⁷. A lack of PPAR α in knockout mice resulted in delayed stratum corneum formation during pregnancy,

postnatal hypoplasia of the stratum granulosum with reduced expression of epidermal differentiation markers and delayed wound healing, particularly during the early inflammatory phase^{175,176,178,179}. PPAR α ligands possess anti-inflammatory properties^{175,180,181}. They reduce inflammation in the skin by inhibiting the maturation, migration and cytokine expression of Langerhans cells^{175,180,181}. In mouse models of irritant-toxic eczema, allergic contact dermatitis and atopic dermatitis, topical application of various PPAR α ligands led to a reduction in inflammatory infiltrates and cytokine release¹⁸²⁻¹⁸⁴. Moreover, the expression of PPAR α is reduced in psoriasis lesions and UV-exposed healthy skin¹⁸⁵ and topical application of PPAR α ligands has been demonstrated to reduce UV erythema¹⁸⁵. This suggests potential of photopharmacology (see chapter 1.3) in PPAR α -targeted therapy.

1.3.2 PPAR α ligands

1.3.2.1 Natural ligands

In accordance with their role in fatty acid metabolism and their lipophilic LBDs, a variety of fatty acids have been proposed to act as physiological ligands of PPARs^{29,30,163,165}. Thereby, these ligands facilitate their own degradation or metabolism, for example, through PPAR α -induced β -oxidation or enhanced storage in adipose tissue mediated by PPAR γ activation^{30,186}. Self-regulation and feedback loops represent common mechanisms among NRs and their ligands^{30,186}.

Activation frequently leads to a reduced concentration of the endogenous ligands, thereby acting as an intrinsic feedback mechanism^{30,186}. The endogenous ligands of PPAR α include a number of unsaturated fatty acids such as oleic acid (**28**, Figure 17), stearic acid (**29**, Figure 17), palmitic acid (**30**, Figure 17) and leukotriene B₄ (**31**, Figure 17), a metabolite of arachidonic acid with moderate binding affinity in the micromolar range^{159,162,187}.

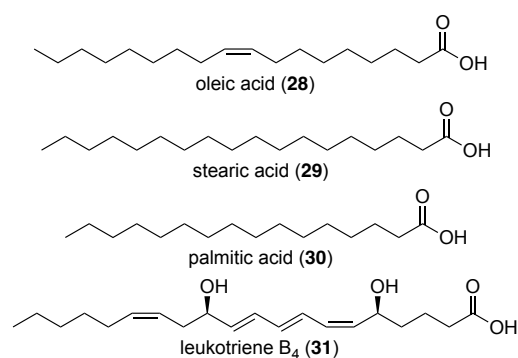


Figure 17. Chemical structure of fatty acids (oleic acid (**28**), stearic acid (**29**), palmitic acid (**30**) and leukotriene B₄(**31**).

1.3.2.2 Synthetic ligands

Synthetic PPAR α ligands include fibrates, a class of lipid-lowering agents that have been in use since the 1960s¹⁶⁹. Their primary function is the reduction of triglyceride levels. In addition to bezafibrate, which is a moderately potent pan-PPAR agonist, fibrates represent a group of selective PPAR α activators exhibiting activities in the micromolar range^{188,189}. They share a common structural motif, 2-methyl-2-phenoxy-propanoic acid, and include drugs such as fenofibrate (**32**, Figure 18), which is frequently used as a prodrug¹⁸⁸. Nevertheless, fibrates have become less prominent in clinical practice due to their limited long-term benefits on cardiovascular events¹⁹⁰.

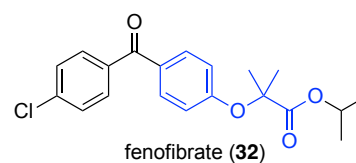


Figure 18. Chemical structure of fenofibrate (**32**). In blue the 2-methyl-2-phenoxypropanoic acid

1.4 Photopharmacology

The field of photopharmacology represents an innovative approach to the optical control of biological processes^{191,192}. The incorporation of light-responsive moieties into the structure of drugs enables the modulation of their activity, whether reversible or irreversible¹⁹². The principal advantage of photopharmacology is its capacity to regulate biological systems in a precise, reversible/irreversible, and non-invasive manner^{191,192}. The utilization of light with defined wavelengths (λ) enables the precise transition between different states of photosensitive drugs, which are ideally characterized by two distinct bioactivities (active and inactive)^{191,192}. This allows for targeted interventions at specific sites and times, enhancing the precision and efficacy of therapeutic interventions^{138,191}. This degree of precision could minimize off-target effects and reduce systemic exposure, thereby enhancing the safety and efficacy of therapeutic interventions¹⁹²⁻¹⁹⁴.

The most commonly utilized tools of reversible photopharmacology are *E-Z* photoswitches, which undergo isomerization between their (*E*)- and (*Z*)-configurations as a consequence of irradiation with light^{191,192,195}. A number of strategies have been developed with the objective of facilitating the design of photoswitches¹⁹⁵. The incorporation of photoactive structural motifs into bioactive molecules represents a promising strategy for the development of photoswitches¹⁹⁵. Two examples of commonly used photoactive motifs are stilbene and azobenzene¹⁹².

Stilbenes are bistable photoswitches¹⁹² (Figure 19a). In order for the (*E*) to (*Z*) isomerization to occur, lower λ (about 300 nm¹⁹⁶) of UV light is required for exposure, and the reverse process ((*Z*) to (*E*)) is considerably more challenging and less efficient. (*Z*)-stilbenes are susceptible to a range of additional reactions (Figure 19a)¹⁹⁷. A π -electrocyclic rearrangement can be induced in these compounds, resulting in the

formation of dihydrophenanthrene (> 10% yield) which can subsequently be oxidized to phenanthrene¹⁹⁷. In addition to other potential photooxidation and photocyclization routes, this electrocyclization process has considerably hindered the implementation of stilbene as a molecular photoswitch¹⁹⁷. As a consequence of their structural similarity to azobenzenes, stilbenes are often replaced by azobenzene^{191,192}.

In the presence of light irradiation, azobenzene undergoes a process of isomerization, whereby it transitions between a thermodynamically stable (*E*)-isomer and a metastable (*Z*)-isomer¹⁹² (Figure 19b). Subsequently, the latter is able to revert to the (*E*)-isomer when exposed to light or thermal relaxation¹⁹². In the (*E*)-configuration, azobenzenes exhibit planar orientation, whereas in the (*Z*)-configuration, they display globular characteristics^{192,198}. In photopharmacology, azobenzenes are the preferred option due to their superior photophysical properties, which allow for 95% switching (*E* to *Z*)¹⁹⁸. Moreover, azobenzenes facilitate slow and steady thermal isomerization (with a half-life time of 2 days at room temperature) and exhibit resistance to excessive reversible photoisomerization¹⁹⁹.

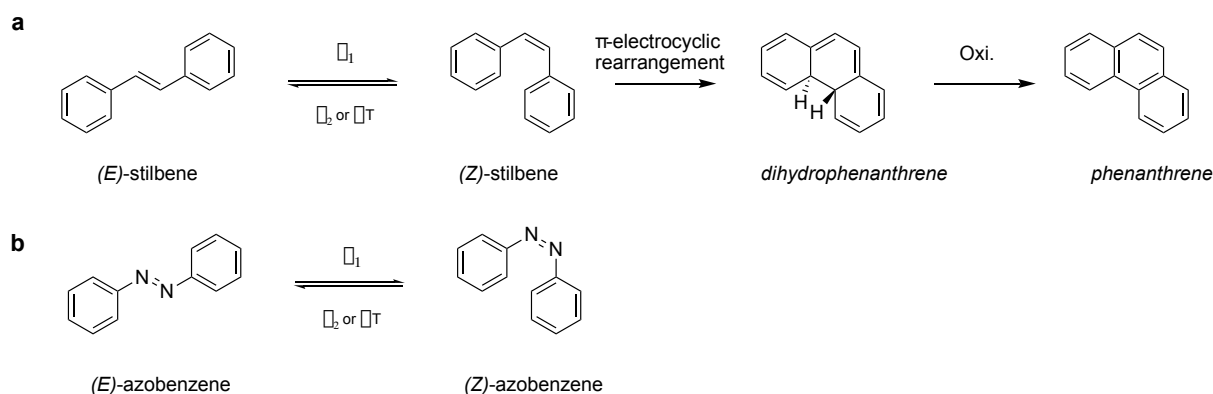


Figure 19. (a) Photoswitchable stilbene isomerization by UV-light with its π -electrocyclic rearrangement and oxidation. (b) Photoswitchable azobenzene by UV-light.

The potential of photopharmacology has been demonstrated by recent advances in its application across various fields, including neuroscience, cancer therapy, and infectious diseases¹⁹⁴. For example, photoswitchable inhibitors have been developed to regulate ion channels and receptors in neuronal cells, providing insights into neural circuits and potential treatments for neurological disorders. In the context of cancer therapy, light-activated drugs can be directed to tumor sites with greater precision, sparing healthy tissues and reducing the incidence of side effects^{193,194}.

In the field of NRs, a number of photoswitchable modulators have also been developed. (Table 2)^{138,200-202}. These studies demonstrated that optogenetic and photopharmacological technologies can be applied to NRs²⁰¹. These photoswitchable modulators ("photohormones") have emerged as an attractive new class of tools that allow light-dependent modulation of transcription factors to achieve spatio-temporal control of transcriptional activity^{138,200-202}.

Table 2. Photohormones for NRs. NRs modulations were determined by a Gal4 hybrid reporter gene assay.

ID	structure	EC ₅₀ (NR modulation)	
		<i>E</i> -isomer	<i>Z</i> -isomer
AzoGW ²⁰¹ (33)		1.1 × 10 ⁻⁶ M (FXR) ²⁰¹	9.5 × 10 ⁻⁵ M (FXR) ²⁰¹
34		Inactive (30 μM) (LXRα and β) ²⁰²	13 μM (LXRα and β) ²⁰²
AzoRosi-4 ²⁰⁰ (35)		2.8 μM (PPARγ) ²⁰⁰	6.4 μM (PPARγ) ²⁰⁰
36		7 nM (PPARα) ¹³⁸	244 nM (PPARα) ¹³⁸

Despite its potential, the field of photopharmacology faces a number of significant challenges, including the development of photoswitches with suitable absorption properties for deep tissue penetration and the need for precise light delivery systems^{191,192,194,203}. There is also a need to improve the biocompatibility and stability of photoswitchable molecules under physiological conditions²⁰⁴. Further research is also required to better understand the long-term effects and safety of using light-activated compounds in clinical settings^{191,205}. However, the innovation of photopharmacology lies in its ability to control biological processes with unprecedented precision. This offers new possibilities for targeted therapy and reduces the side effects associated with conventional treatments.

2 Aim of the doctoral thesis

As previously described in chapter 1, the number of patients with neurodegenerative diseases is increasing at a constant rate in the future^{3,4}. New therapeutic approaches and mechanisms of action are required to effectively address these diseases. Despite numerous efforts, no satisfactory treatment option is yet available for neurodegenerative diseases^{3,4}. To close this gap, NR modulation^{3,4} could be a promising avenue for further investigation (see chapter 1.1 to 1.3). The objective of this thesis was to develop novel chemical tools for NRs linked to neurodegeneration using different techniques and strategies of medicinal chemistry, with the aim of improving our biological and mechanistic understanding of these NRs.

The primary focus of this thesis is modulation of Nurr1. As previously described in chapter 1.2, Nurr1 has great potential as a target for the treatment of neurodegenerative diseases such as PD, AD and MS. However, there is a lack of high-quality chemical tools to study Nurr1 and an urgent need for the identification and development of Nurr1 ligands.

The first approach to develop novel high-quality Nurr1 modulators was based on the ligand-bound cocrystal structure of the Nurr1 LBD in complex with DHI. Despite recent advances in Nurr1 ligand discovery, only a few ligand-bound Nurr1 LBD cocrystal structures are available^{74,83}. Among these, the Nurr1:DHI complex (PDB: 6dda)⁷⁴ was identified as the most suitable for structure-based design due to the favorable features of the indole scaffold. Structural analysis indicated the potential for further extension of DHI, particularly in the 5- and 6-positions of the indole, while the five-membered ring was situated in a narrow pocket⁷⁴ (Figure 20). The objective was to demonstrate that the binding site of the natural DHI ligand is druggable by employing a structure-guided virtual screening and design approach combined with microscale synthesis. The results were published in the article entitled "Structure-Guided Design of Nurr1 Agonists Derived from the Natural Ligand Dihydroxyindol" (*Journal of Medicinal Chemistry*, 66 (19), 13556-13567 (2023))²⁰⁶ and are presented in chapter 3.1.

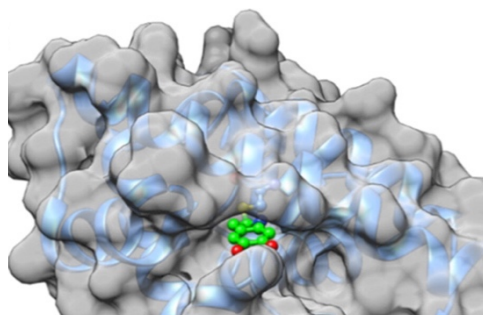


Figure 20. Cocrystal structure of DHI bound to the Nurr1 LBD (PDB: 6dda⁷⁴). The 5- and 6-positions of DHI are oriented towards the solvent. Adapted from ²⁰⁶.

One of the first validated Nurr1 agonists was AQ (see chapter 1.1.3.2), which emerged as an early tool to study therapeutic effects of Nurr1 activation. The administration of AQ has been demonstrated to counteract neuroinflammation and ameliorate behavioral deficits in a PD model, as well as to reduce neuronal loss and A β deposition in an AD model^{98,115}. Nevertheless, AQ is unspecific^{107,113,207,208} and hepatotoxic²⁰⁹, and its pharmacological

effects cannot be confidently attributed to Nurr1 modulation. Moreover, AQ and many analogues contain PAINS^{210,211} elements, which further have compromised their value as a chemical tool. Consequently, it is necessary to develop AQ derivatives with enhanced efficacy and selectivity in order to substantiate the encouraging findings regarding the Nurr1-mediated therapeutic actions of this pharmacological agent. As previously described in chapter 1.1.3.2 *Willems and colleagues* identified a fragment-like agonist **11**¹¹³, which enhanced the transcriptional activity of Nurr1. **11** has been notable for its relatively small size and low molecular weight, which make it an attractive starting point for further optimization¹¹³. Based on the findings of the study, novel Nurr1 agonists should be developed systematically through scaffold hopping and fragment growing. The results are presented in chapter 3.2 and were published in the article entitled "Development of Nurr1 agonists from amodiaquine by scaffold hopping and fragment growing" (*Communications Chemistry*, 7, 149 (2024))²¹².

In addition, this doctoral thesis addressed the NR RXR. RXRs are involved in numerous physiological processes and RXR modulators have been identified as a potentially promising avenue for therapeutic intervention in the treatment of neurodegenerative diseases (see chapter 1.2). Nevertheless, the current range of RXR ligands exhibits suboptimal physicochemical properties and an absence of subtype selectivity amongst RXRs, which limits their potential for therapeutic application due to the occurrence of adverse effects^{131,134}. The selective modulation of NRs by influencing protein-protein interactions with partner receptors or coregulators is increasingly being recognized as a promising avenue for therapeutic innovation²¹³. The objective of this approach was to design and test a chemically diverse set of analogues based on the biphenyl scaffold **27**, demonstrating that minor structural changes can lead to selective effects on coregulator interactions. The results of the SAR of **27** are summarized in chapter 3.3 and the article entitled "Tuning RXR modulators for PGC1 α recruitment" is accepted after peer-review process in *Journal of Medicinal Chemistry*.

In the field of NRs, temporal control is of particular relevance, given that these receptors are endogenously activated by short-lived molecules such as hormones and reactive metabolites¹³⁸. Temporal control over pharmacological effects has represented a significant challenge, even when highly selective and potent ligands are employed²¹⁴. In some cases, this objective cannot be achieved, even when pharmacokinetic properties are favorable, due to the delayed genomic effects²¹⁴. The field of photopharmacology provides an avenue for achieving precise spatial and temporal control over protein activity, which could prove an invaluable strategy in addressing this challenge^{191,192}. By incorporating stilbene or azobenzene motifs into a previously optimized PPAR α ligand, the objective was to create a light-activated PPAR α agonist and expand the toolbox of photoswitchable ligands that would enable the study of PPAR α biology and facilitate the

development of selective and safer therapeutic interventions. The results of this study are presented in chapter 3.4 and were published in the article entitled "Azologs of the fatty acid mimetic drug cinalukast enable light-induced PPAR α activation" (*ChemMedChem*, e20240032 (2024))²¹⁵.

3 Results and Discussion

3.1 Structure-Guided Design of Nurr1 Agonists Derived from the Natural Ligand Dihydroxyindole

The use of natural ligands of NRs as templates for drug design has yielded promising results for several members of the NR family. Steroidal ligands like prednisolone for NR3 receptors and the FXR agonist obeticholic acid are notable examples of such drugs^{216,217}. The fatty acids PGA1 and PGE1, as well as DHI, have been identified as natural ligands for Nurr1 (see chapter 1.1.3.1)^{74,83}. Given its status as a putative endogenous ligand, DHI is an attractive lead for the development of Nurr1 agonists. The analysis of the Nurr1 complex with DHI (PDB: 6dda) revealed that the 5- and 6-positions of the indole are solvent-exposed, presenting opportunities to explore adjacent grooves formed by helices H4/H12 and H10/H11 on the surface of the Nurr1 LBD⁷⁴. This suggested potential for structural modifications to enhance binding interactions. A small previous study on the SAR of DHI indicated a preference for a chlorine substituent at the 5-position of the indole (**7**, see chapter 1.1.3.2). Consequently, extension in the 6-position appeared as promising avenue for the development of novel optimized Nurr1 agonists.

A virtual library was constructed utilizing **7** as a central motif, which was subsequently extended at the 6-position through the incorporation of an amide linker coupled with 14 K commercially available primary amines (molecular weight \leq 240, Figure 21). The amide linkage was selected on the basis of its potential to form hydrogen bonds with the His516 backbone amine and the Pro597 backbone carbonyl, as evidenced by preliminary docking assessments.

The virtual library was docked into the DHI-binding site of the Nurr1 LBD (Figure 21) using the Glide docking program. The results of the docking procedure demonstrated that the molecules populated the grooves on the protein surface in accordance with the hypothesis of the design. The binding modes of the top-scoring 100 docking candidates were analyzed manually, and subsequently 24 structurally diverse molecules were identified for synthesis and biological evaluation. This process was undertaken with the objective of selecting molecules that exhibited favorable binding modes and were deemed suitable for microscale amide synthesis.

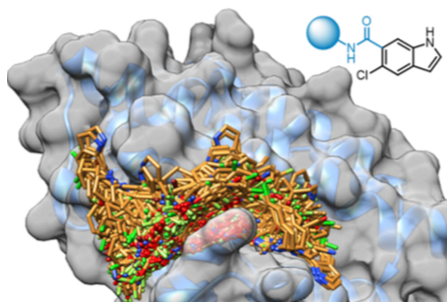


Figure 21. The virtual amide library was docked to the Nurr1 LBD (PDB: 6dda⁷⁴). The virtual designs were extended to address the grooves on the Nurr1 LBD surface that surround the DHI-binding site. *Adapted from* ²⁰⁶.

In order to efficiently and economically explore the Nurr1 agonist potential of the virtually favored designs, the compounds were initially prepared in microscale quantities (100 μ mol). The amide synthesis was conducted in 1.5 mL reaction tubes utilizing 5-chloro-1*H*-indole-6-carboxylic acid (**41**) and a range of primary amines (**24**) in conjunction with EDC·HCl in ethyl acetate (Figure 22a). The products were then roughly purified by washing them with aqueous sodium bicarbonate solution. Mass spectrometry was employed to confirm the formation of the desired amides. The building block (**41**) was synthesized from 2-chloro-4-methylbenzoic acid (**37**) by Batcho-Leimgruber indole synthesis. This synthesis involved nitration (**38**), esterification (**39**), cyclisation (**40**), and ester hydrolysis (**41**), as illustrated in Figure 22b.

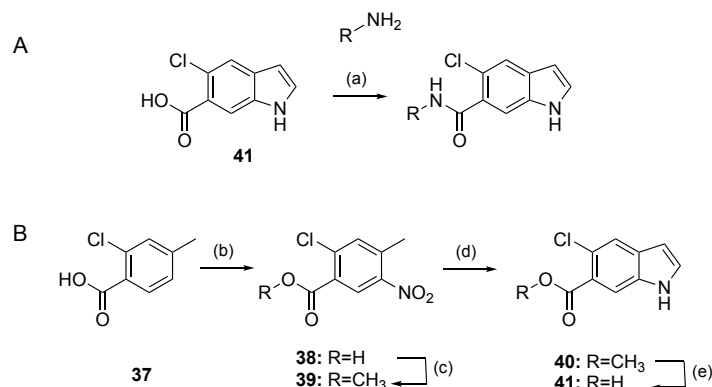


Figure 22. Microscale amide synthesis (A) and synthesis of building block (**41**) (B). Reagents and conditions: (a) EDC·HCl, EtOAc, rt, 36 h; (b) HNO₃/H₂SO₄, 5 °C, 0.5 h, 59%; (c) acetyl chloride, MeOH, 50 °C, 4 h, 96%; (d) DMF-DMA, DMF, 120 °C, 2 h; then Zn, AcOH/H₂O, 80 °C, 2 h, 40%; (e) LiOH·H₂O, EtOH/H₂O, rt, 18 h, 94%. *Adapted from* ²⁰⁶.

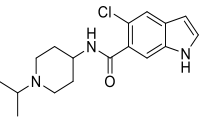
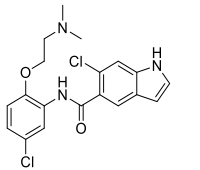
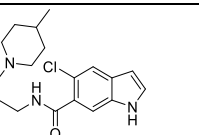
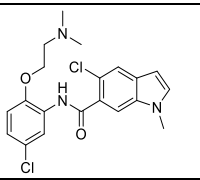
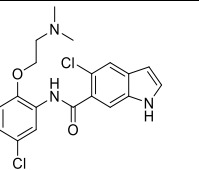
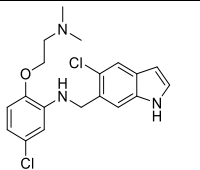
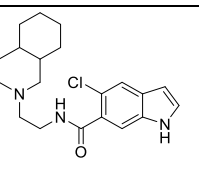
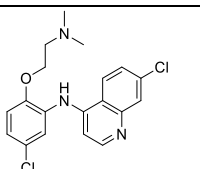
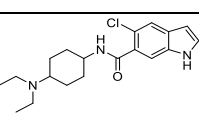
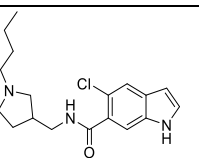
The biological activity of the virtual screening hits was evaluated using a Gal4 hybrid reporter gene assay conducted in HEK293T cells. The cells are transfected with plasmids encoding a fusion protein consisting of the human Nurr1 LBD and a Gal4 DBD. The fusion protein activates a firefly luciferase reporter gene. To control for transfection efficiency and cytotoxicity, renilla luciferase plasmid is used. Following treatment with the test compounds, luciferase activity of both firefly and renilla are measured. The data are normalized to relative light units (RLU), and the relative activation is determined by comparing the RLUs to those of the negative control (DMSO) and positive control (AQ).

The microscale synthesis products were tested for Nurr1 modulation in the Gal4–Nurr1 hybrid reporter gene assay at 100 μM , assuming full conversion. The actual concentrations were likely lower. To account for the activity of any remaining amine building blocks, these amines were also tested at 100 μM . The possibility of false negatives due to the microscale synthesis format, purification procedure, and assay settings was acknowledged.

Among the 24 computationally favored designs, six compounds (**42-47**) were identified as primary hits, representing a significant proportion of the total number of compounds tested (Table 3). The compounds demonstrated Nurr1 activation of over 140% (159% (**42**), 149% (**43**), 160% (**44**), 146% (**45**), 146% (**46**), 147% (**47**)) compared to the DMSO-treated cells, with no pronounced effects on cell viability and their corresponding amines exhibiting either no effect or diminished Nurr1 activity. Subsequently, the six compounds were prepared in larger quantities, isolated and subjected to comprehensive characterization.

In order to validate the primary hits, orthogonal methods were employed. These commenced with ITC, through which direct interaction with the Nurr1 LBD could be observed in an effort to determine binding affinities. Of the six primary hits, three (**42**, **43**, and **46**) exhibited no discernible interaction with the Nurr1 LBD, while three (**44**, **45** and **47**) demonstrated binding with K_d values of 0.5 μM (**43**), 3.2 μM (**45**), and 16 μM (**47**), respectively (Table 3). In accordance with these findings, compounds **42**, **43**, and **46** were unable to activate Nurr1 in a Gal4–Nurr1 hybrid reporter gene assay at concentrations up to 100 μM , whereas compounds **44**, **45**, and **47** were identified as Nurr1 agonists (Table 3). Compound **44** was identified as most active DHI derivative with a K_d value of 0.5 μM and an EC_{50} value of 3 μM representing a substantial improvement in activity compared to DHI ($\text{EC}_{50} > 100 \mu\text{M}^{74}$).

Table 3. Nurr1 modulation and binding affinity to the Nurr1 LBD of **42-47** and **48-51**.

ID	structure	K _d	EC ₅₀	ID	structure	K _d	EC ₅₀
42		no binding	inactive (100 μM)	48		1.6 μM	6 ± 3 μM (1.4 ± 0.1-fold act.)
43		no binding	inactive (100 μM)	49		1 μM	16 ± 6 μM (1.4 ± 0.1-fold act.)
44		0.5 μM	3 ± 1 μM (1.4 ± 0.1-fold act.)	50		1.8 μM	5 ± 2 μM (1.4 ± 0.1-fold act.)
45		3.2 μM	12 ± 2 μM (1.4 ± 0.1-fold act.)	51		1.5 μM	3 ± 1 μM (1.5 ± 0.1-fold act.)
46		no binding	inactive (100 μM)				
47		16 μM	28 ± 6 μM (1.3 ± 0.1-fold act.)				

The predicted binding modes of the three active hits (**44**, **45** and **47**) suggested binding to a hydrophobic groove on the Nurr1 LBD surface lined by H12 (Figure 23a). The indole moiety was positioned between residues Arg515 and Arg563, in a manner that allowed it to interact with Cys566. The amide substituents primarily formed hydrophobic contacts.

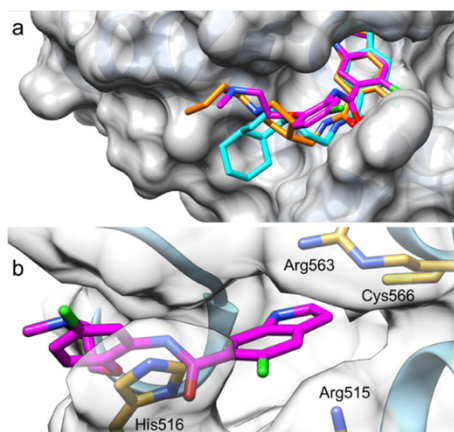


Figure 23. Predicted binding modes of **44** (magenta), **45** (cyan), and **47** (orange) to the Nurr1 LBD (PDB: 6dda⁷⁴). (a) It was predicted that the three active DHI descendants, **44**, **45**, and **47**, would bind to the DHI-binding site and extend towards a hydrophobic groove lining H12. (b) The most active Nurr1 agonist, **45**, formed a face-to-face contact with His516. Reprinted from²⁰⁶.

The most active compound (**44**) additionally formed a face-to-face π -interaction with His516, which may be responsible for its enhanced potency (Figure 23b).

Mutagenesis of the binding site cysteine (Cys566 to Ser566) resulted in a reduction in the activity of **44**, which supported the interaction with this epitope and highlighted the importance of Cys566 in ligand-Nurr1 contacts (Figure 24a). Stability tests demonstrated that **44** exhibited high stability against glutathione (GSH), which can be used to form a covalent disulfide adduct, and that no observable adduct formation occurred between recombinant Nurr1 LBD and **44** in LC-MS/MS. These findings indicated that the interaction was non-covalent, despite the importance of Cys566 (Figure 24b).

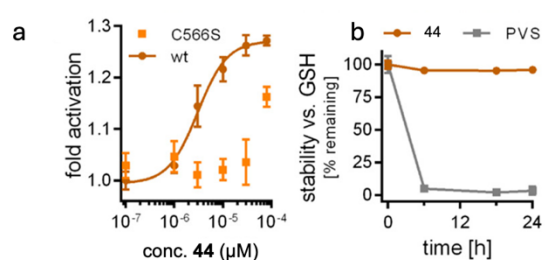


Figure 24. (a) Mutagenesis indicated that **45** was less active on a Nurr1-C566S mutant, which provided support for an interaction with the proposed epitope. The data are presented as the mean \pm S.E.M., $n \geq 3$. (b) **45** demonstrated stability against reaction with glutathione (GSH). Phenyl vinyl sulfone (PVS) was used as a positive control (125 μ M **45** or PVS were incubated with 2.5 mM GSH in PBS at 37 °C). $n = 3$. Reprinted from²⁰⁶.

Compared to the natural DHI, **44** exhibited a significant increase in Nurr1 transcriptional activity, with an EC_{50} value of 3 μ M for **44** and $> 100 \mu$ M⁷⁴ for DHI. **44** was observed to induce Nurr1 regulated expression of TH and VMAT2 in T98G cells, indicating cellular target engagement (Figure 26b). In order to further elucidate the SAR of this novel Nurr1 agonist scaffold, additional derivatives were synthesized and evaluated.

An inverted analogue (**48**), comprising the opposite indole regiochemistry, exhibited comparable activity to **44** ($K_d = 1.6 \mu$ M, $EC_{50} = 6 \mu$ M, Table 3) indicating that the orientation of the indole scaffold in the binding site was not a determining factor. The methylation of the indole nitrogen in **49** had a minimal effect on affinity ($K_d = 1 \mu$ M, $EC_{50} = 16 \mu$ M, Table 3), although a fivefold decrease in cellular potency was observed. The reduction of the amide in **44** to a secondary amine linker (**50**) was tolerated, yet it did not result in an improvement in affinity or potency ($K_d = 1.8 \mu$ M, $EC_{50} = 5 \mu$ M, Table 3). These findings indicated that both 6-chloro-1*H*-indole-5-carboxamide and 5-chloro-1*H*-indole-6-carboxamide (along with its reduced amide form) were suitable and readily available scaffolds for the development of Nurr1 ligands that bind to the LBD surface.

A number of Nurr1 ligands have contained a chloroquinoline motif derived from AQ and it was observed for other Nurr1 ligand chemotypes that a scaffold hop from indole to the quinoline (fluvastatin (**52**), $EC_{50} = 1.9 \mu$ M) to quinoline (pitavastatin (**53**), $EC_{50} = 0.12 \mu$ M) resulted in a notable increase in potency (Figure 25a). Therefore, the structural components of **44** and AQ were combined by merging the 7-chloroquinolin-4-amine motif of AQ and the amide substituent of **44** to possibly enhance potency and affinity (Figure 25b). The resulting compound exhibited considerably higher potency as a Nurr1 agonist

(**51**, $EC_{50} = 3 \mu\text{M}$) than AQ ($EC_{50} = 36 \mu\text{M}$) and a binding affinity (K_d) of $1.5 \mu\text{M}$ to the Nurr1 LBD (Table 3, Figure 26a). However, its performance was not appreciably superior to that of the DHI-derived compounds, particularly **44**. In order to assess whether **44** and **51** are binding to the same site, a combined treatment of **44/51** with the Nurr1 agonist **15** (see chapter 1.1.3.2) was employed in a Gal4-Nurr1 hybrid reporter gene assay. The presence of **44** or **51** ($20 \mu\text{M}$ each) did not result in a change to the EC_{50} value of **15** (Figure 25c). However, it did increase the maximum effect by 34–77%. This non-competitive behavior with additive Nurr1 activation suggested that the ligands occupy different, non-overlapping binding sites, which opens up new possibilities for the modulation of Nurr1.

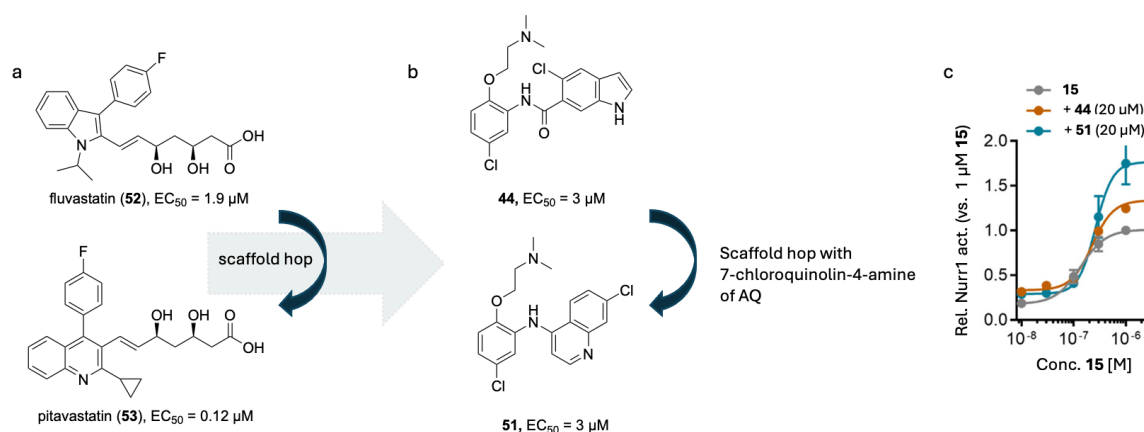


Figure 25. (a) Comparison of fluvastatin (**52**) and pitavastatin (**53**) on Nurr1 transcriptional activity. A scaffold hop from indole (**52**) to the quinoline (**53**) resulted in a notable increase in potency. (b) Merging of the amide motif of **44** and 7-chloroquinolin-4-amine motif of AQ. (c) The data demonstrate that **44** and **51** enhanced the maximal activation of Nurr1 by agonist **15** to 134% (**44**) and 177% (**51**) of its maximal effect when administered alone. The data are presented as the mean \pm S.E.M. relative Nurr1 act. vs $1 \mu\text{M}$ **15**, with $n \geq 3$.

The structure-guided approach to Nurr1 modulator development led to the identification of compounds **44** and its AQ-hybrid (**51**) as the most potent DHI descendants. Further *in vitro* profiling confirmed that **44** and **51** induced Nurr1-dependent transcriptional activity on NBRE with an EC_{50} of $2 \mu\text{M}$ (**44**) and $4 \mu\text{M}$ (**51**) (Figure 26c). In the immortalized rat dopaminergic neural cell line N27, **44** and **51** induced expressions of TH, VMAT, SOD1 and SOD2 in a dose-dependent manner (Figure 26d).

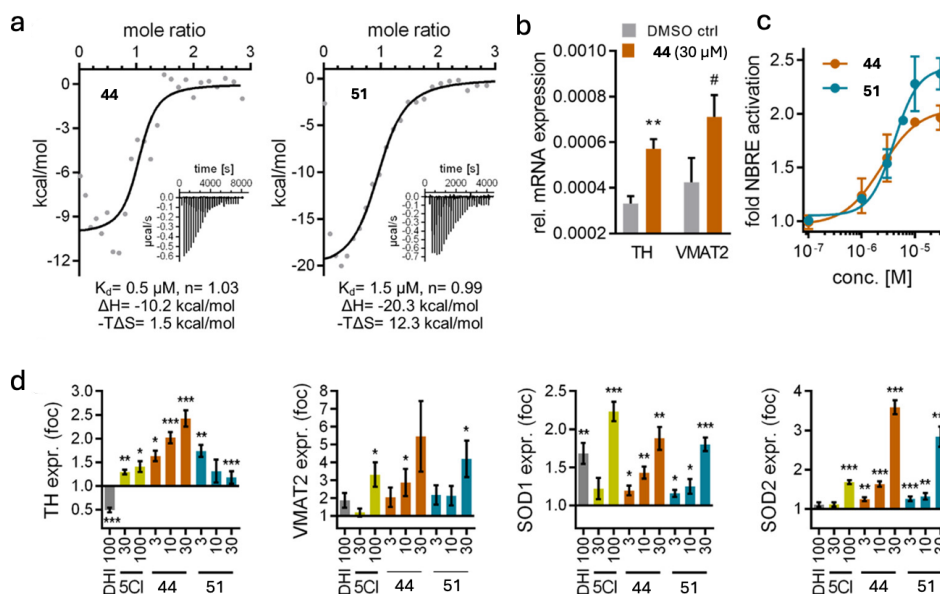


Figure 26. In vitro profiling of DHI-derived Nurr1 agonists. (a) ITC demonstrated that compounds **44** and **51** exhibited binding to the recombinant Nurr1 LBD. The fitting of the heat of binding is illustrated, and the isotherms at 25 °C are presented as insets. (b) Treatment with **44** (30 µM) resulted in Nurr1-regulated mRNA expression of TH and VMAT2 in T98G cells. The data are presented as the mean ± S.E.M. relative mRNA expression ($2^{-\Delta\Delta C_t}$), $n = 4$. # $p < 0.1$, ** $p < 0.01$ (t-test vs. DMSO control). (c) **44** ($EC_{50} = 2 \pm 1 \mu\text{M}$) and **51** ($EC_{50} = 4 \pm 1 \mu\text{M}$) were observed to activate full-length human Nurr1 on the NBRE. The data are presented as the mean ± S.E.M. fold activity relative to the DMSO control, $n \geq 4$. (d) DHI, 5-chloroindole (5Cl, **7**) and the descendants **44** and **51** were observed to modulate Nurr1-regulated gene expression in dopaminergic neural cells (N27). TH; VMAT2; SOD1/2. The data represent the mean ± S.E.M. relative mRNA expression in comparison to 0.1% DMSO, with $n = 7-8$. Statistical significance was determined using the Wilcoxon test or t-test, with the following levels of significance: * $p < 0.05$, ** $p < 0.01$, *** $p < 0.001$. Adapted from²⁰⁶.

The findings of our study illustrate that the crystal structure of DHI with Nurr1 serves as a valuable foundation for the development of new ligands through the principle of structure-guided design. By targeting the binding site, we were able to develop compounds like **44**, which exhibit improved transcriptional Nurr1 potency compared to DHI. However, it should be noted that crystal structures are static and only represent the binding mode of a specific ligand. Therefore, we cannot be entirely certain of the precise binding mode of compound **44** within this site. Further investigations are necessary to ascertain this information in order to develop further compounds with the base. The predicted binding mode of the phenylmotif of **44** is oriented outward (solvent-exposed), which suggests further development potential, such as the creation of PROTACs (proteolysis targeting chimeras) to facilitate a deeper understanding of the physiological biology of Nurr1. In contrast to DHI, **44** exhibited enhanced molecular stability and diminished toxicity. DHI is unsuitable for rigorous biological studies due to its tendency for autooxidation, polymerization, and the generation of a chromogenic pigment in solution, which in neurons contributes to the formation of neuromelanin^{14,74,112}. However, the development of **44** indicated the feasibility of creating a stable and less toxic compound based on the indole scaffold.

In summary **44** is a highly potent and selective Nurr1 agonist. This compound exhibited robust Nurr1 activation, high binding affinity, and pronounced neuroprotective effects in dopaminergic neurons, thus underscoring its potential for therapeutic development in neurodegenerative diseases such as PD. Further optimization and *in vivo* studies will be essential to fully elucidate the therapeutic potential of **44** and other related compounds in modulating Nurr1 activity and protecting against neurodegeneration.

3.2 Development of Nurr1 agonists from amodiaquine by scaffold hopping and fragment growing

As described in chapters 1.1.2.1 and 1.1.3.2, AQ emerged as an early tool for investigating the therapeutic effects of Nurr1 activation. Nevertheless, AQ is unspecific, which demonstrated the inhibition of human histamine *N*-methyltransferase and several human cytochrome P450 enzymes^{207,208} and non-specific transcriptional effects^{107,113} (see chapter 1.1.3.2), and it is unclear whether these pharmacological effects can be attributed to Nurr1 modulation, highlighting the necessity for AQ derivatives that possess enhanced potency and selectivity.

The antimalarial activity of AQ and related compounds has been mainly attributed to the common chloroquinoline scaffold²¹⁸, while the 4-hydroxyaniline moiety has been postulated to contribute to the observed cytotoxicity and hepatotoxicity which are thought to result from metabolic activation to a reactive quinoneimine^{209,219}. Optimization of the AQ scaffold for Nurr1 agonism thus required the substitution of both the chloroquinoline amine motif and the 4-aminophenol residue. Willems and colleagues showed that the fragment-like chloroquinolineamine **11** is a promising starting point for the development of novel Nurr1 agonists that can potentially overcome the limitations of AQ¹¹³.

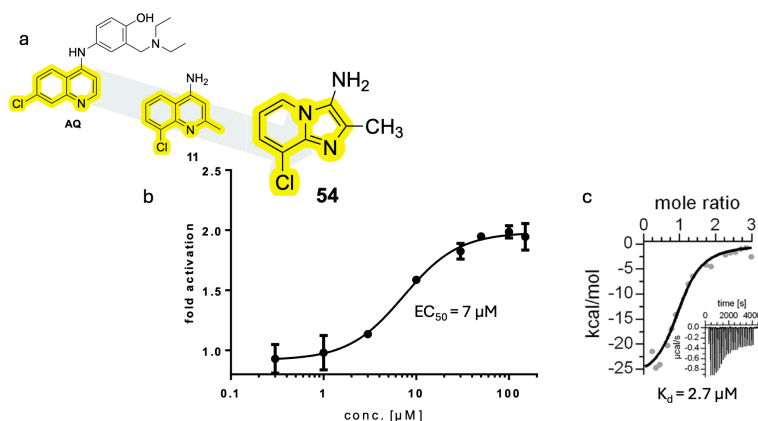


Figure 27. (a) Scaffold hop from the chloroquinoline amine motif of AQ to the imidazo[1,2-*a*]pyridine scaffold **54**. (b) **54** exhibited Nurr1 activity with an EC₅₀ of 7 μM in a Gal4-Nurr1 hybrid reporter gene assay. Data are presented as the mean ± S.E.M. fold activity relative to the DMSO control, n ≥ 3. (c) **54** bound to the Nurr1 LBD (K_d 0.17 μM) determined by ITC. The fitting of the heat of binding is shown and the isotherm at 25 °C is shown as inset.

The development of novel AQ-derived Nurr1 modulators began with the replacement of the quinoline scaffold by alternative heterocycles. Among several tested aromatic two-ring systems (not shown), the imidazo[1,2-*a*]pyridine scaffold (**54**) emerged with improved potency ($EC_{50} = 7 \mu\text{M}$) and efficacy (2.0-fold activation) compared to **11** ($EC_{50} = 17 \mu\text{M}$, 1.71-fold activation) (Figure 27). This smaller skeleton was incompatible with the original regiochemistry of the chlorine substituent (7-Position, **55**, Table 4). Furthermore, systematic deconstruction of **54** revealed a tight SAR in which all substituents (**56-59**, Table 4) were needed for Nurr1 agonism. Despite the weak or absent Nurr1 activation by compounds **55-59**, ITC showed that compounds **57** and **58**, which contain the 8-chloro substituent, still bound to the Nurr1 LBD with low micromolar affinity. In contrast, compounds **56** and **59**, which lack the chlorine atom, showed weaker binding. These results highlighted the importance of the 8-chloro substituent in the control of affinity and the importance of the amino motif for Nurr1 activation.

Table 4. SAR evaluation of imidazo[1,2-*a*]pyridine **54** for Nurr1 modulation.

ID	structure	EC_{50}	K_d
54		2.7 μM	7 μM
55		inactive (100 μM)	weak binding
56		inactive (100 μM)	weak binding
57		inactive (100 μM)	7.2 μM
58		< 1.2-fold activation	5.1 μM
59		inactive (100 μM)	weak binding

To improve potency, fragment growing strategies were employed and modifications to the 2-methyl substituent of **54** were evaluated first. The synthesis of these compounds was accomplished by the Groebke–Blackburn reaction, which involved the combination of 3-chloropyridine-2-amine (**60**), the corresponding aldehyde, and 1,1,3,3-tetramethylbutyl isocyanide (**61**), resulting in the formation of the imidazo[1,2-*a*]pyridine scaffold, as depicted in Figure 28. Subsequently, the respective imidazo[1,2-*a*]pyridine underwent acid-mediated cleavage, yielding the free amine.

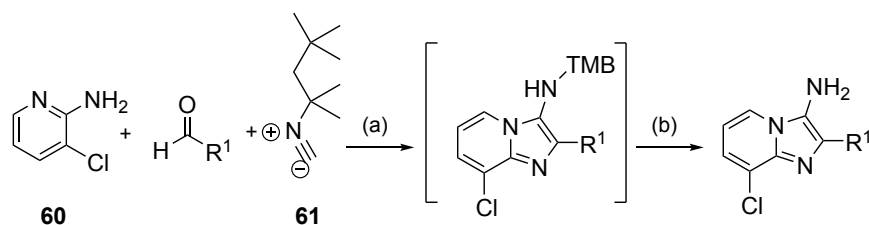


Figure 28. General synthesis of the imidazo[1,2-*a*]pyridine scaffold. Reagents and conditions: (a) AcOH, MeOH, rt, 24-48 h; (b) TFA/DCM, rt, 30 min to overnight, 3-30% over two steps.

Extension of the 2-methyl group to phenyl and systematic evaluation of substituents on the ring resulted in the 3,4-dichlorophenyl **62** (Figure 29) as most favored analogue which

achieved a considerable increase in Nurr1 agonist potency ($EC_{50} = 0.4 \mu\text{M}$) and affinity to the Nurr1 LBD ($K_d = 0.7 \mu\text{M}$) as confirmed by ITC. However, in terms of ligand efficiency (LE) which is a measure of a ligand's binding affinity relative to its size, the structural extension from **54** (LE = 0.59) to **62** (0.46) did not provide a substantial improvement, but the 2-(3,4-dichlorophenyl) substituent of **62** may still be a valuable potency enhancing extension in fused derivatives (Figure 33).

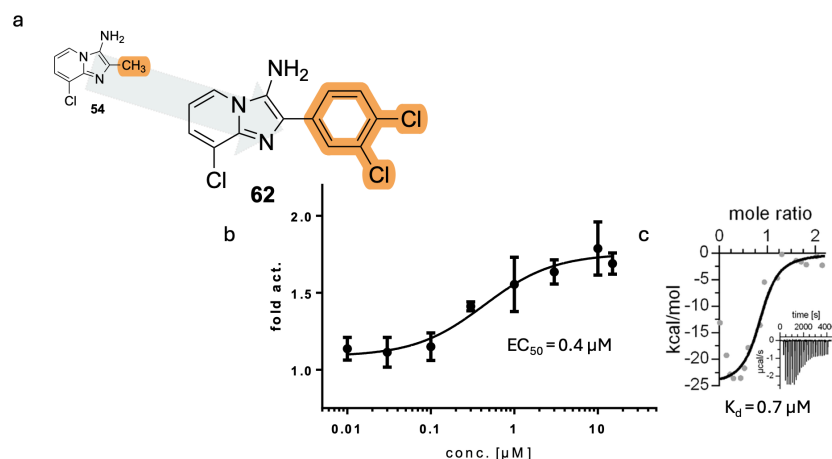


Figure 29. Fragment growing of the 2-methyl substituent of **54** (a). **62** exhibited Nurr1 activity with an EC_{50} of $0.4 \mu\text{M}$ in a Gal4-Nurr1 hybrid reporter gene assay. Data are presented as the mean \pm S.E.M. fold activity relative to the DMSO control, $n \geq 3$. (c) **62** bound to the Nurr1 LBD (K_d $0.7 \mu\text{M}$) determined by ITC. The fitting of the heat of binding is shown and the isotherm at 25°C is shown as inset.

Further optimization involved the transfer of known SAR knowledge using the 5-(4-chlorophenyl)furan-2-carboxamide¹¹⁴ residue as an alternative motif (see chapter 1.1.3.2) to replace the aminophenol of AQ to the imidazo[1,2-a]pyridine (**54**) scaffold. This yielded compound **65** which showed improved Nurr1 agonist potency in a Gal4 hybrid reporter gene assay ($EC_{50} = 1.6 \mu\text{M}$) and binding affinity to the Nurr1 LBD ($K_d = 0.7 \mu\text{M}$, Figure 31) in an ITC. Subsequently, a systematic evaluation was conducted on the furan motif and the 4-chloro substituent of the phenyl ring of the 5-(4-chlorophenyl)furan-2-carboxamide motif. The syntheses of these compounds were accomplished with **54** by employing amid coupling or, alternatively, a combination of amid coupling with **63** followed by a Suzuki reaction, as depicted in Figure 30.

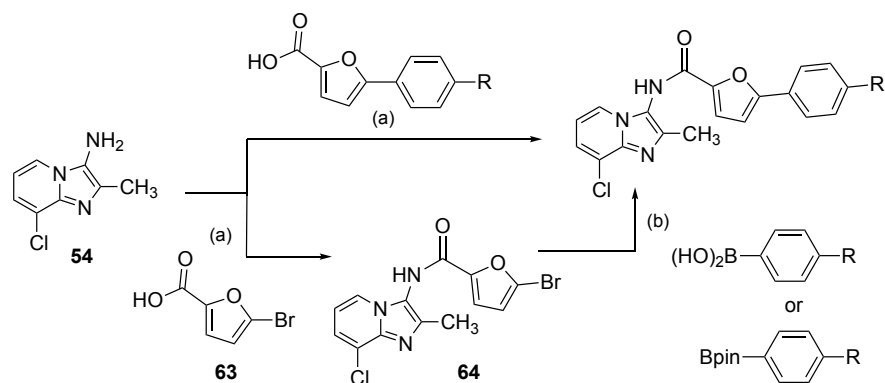


Figure 30. General synthesis of *N*-carboxamide of **54**. Reagents and conditions: (a) HATU, DIPEA, DMF, rt, overnight; (b) tetrakis(triphenylphosphane)palladium(0), Na₂CO₃, water/dioxane, reflux, overnight.

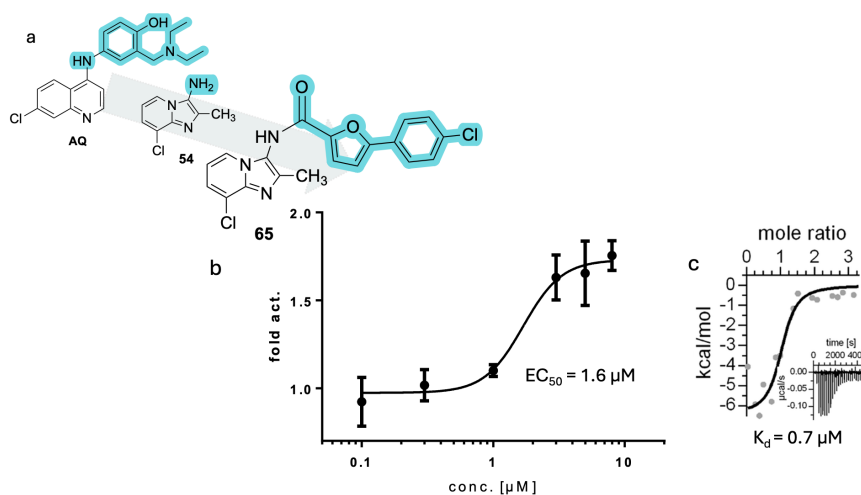


Figure 31. Replacement of the aminophenol of AQ by 5-(4-chlorophenyl)furan-2-carboxamide motif (**65**) (a). **65** exhibited Nurr1 activity with an EC₅₀ of 0.4 μM in a Gal4-Nurr1 hybrid reporter gene assay. Data are presented as the mean ± S.E.M. fold activity relative to the DMSO control, n ≥ 3. (c) **65** bound to the Nurr1 LBD (K_d 0.7 μM) determined by ITC. The fitting of the heat of binding is shown and the isotherm at 25 °C is shown as inset.

SAR evaluation of **65** led to the identification of **66** (Figure 32a) which demonstrated potent Nurr1 agonist transcriptional activity (EC₅₀ = 0.090 μM), high affinity binding (K_d = 0.17 μM, Figure 32d) to the Nurr1 LBD and robust induction of Nurr1 regulated genes (TH, VMAT2, SOD2, Figure 32e) in T98G cells. Additionally, **66** caused robust activation of the human full-length Nurr1 in reporter gene assays for the Nurr1 homodimer (NuRE, EC₅₀ = 0.094 μM) and the Nurr1 RXR heterodimer (DR5, EC₅₀ = 0.165 μM), while showing no activity on the Nurr1 monomer (NBRE) (Figure 32b,c). It displayed a preference for Nurr1 over Nur77, and - in contrast to the template AQ - had no toxic effects in neuronal (N27 cells) and HEK293T cells (Figure 32g). Complementing **66**, compound **67** was identified as a structurally matched negative control without Nurr1 agonism or binding (Figure 32a).

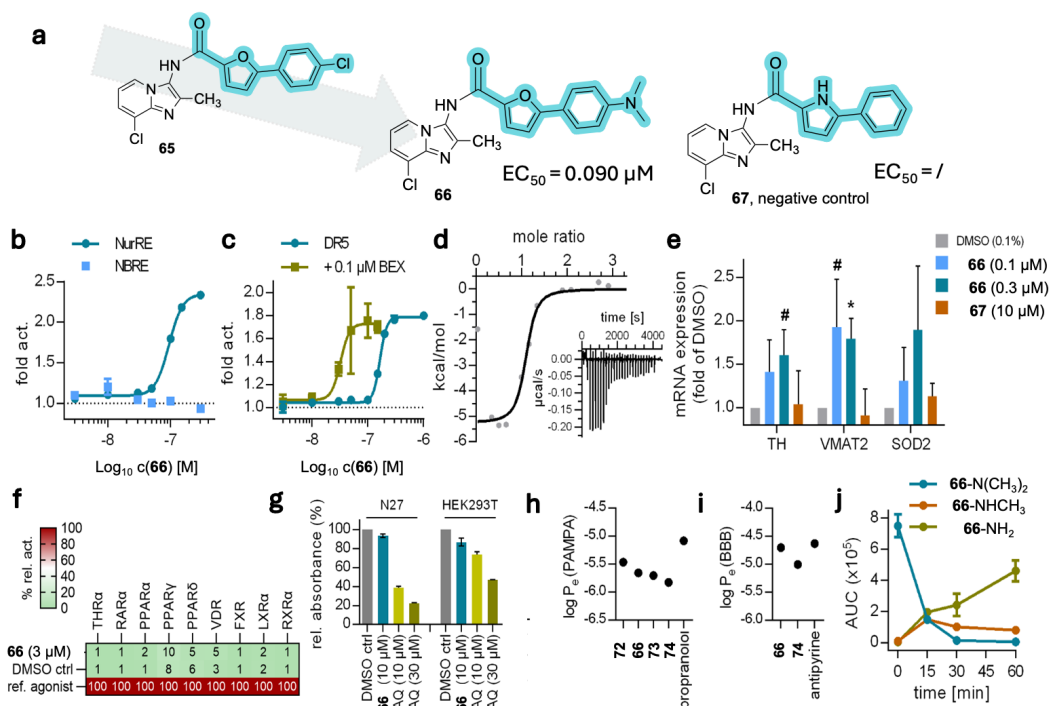


Figure 32. In vitro characterization of the optimized Nurr1 agonist **66**. (a) Optimization of **65** resulted in **66** with an EC_{50} of 0.090 μM and inactive **67** which can be used as negative control. (b) Effects of **66** on the human full-length Nurr1 homodimer (NurRE) and monomer (NBRE) in reporter gene assays. The data are presented as the mean \pm S.E.M. fold activation relative to the DMSO control, $n \geq 3$. (c) The effects of **66** on the Nurr1-RXR heterodimer (DR5) in the absence and presence of bexarotene (0.1 μM) are shown. The data are presented as the mean \pm S.E.M. fold activation relative to the DMSO control or 0.1 μM BEX, $n \geq 3$. (d) Binding of **66** to the Nurr1 LBD ($K_d = 0.17 \mu\text{M}$) was determined by ITC. The fitting of the heat of binding is illustrated, and the isotherm at 25 $^{\circ}\text{C}$ is shown as an insert. (e) Effects of **66** and **67** on the expression of the Nurr1-regulated TH, VMAT2, and SOD2 in T98G. The data represent the mean \pm S.E.M. fold mRNA induction relative to the DMSO control, with $n = 3$. # $p < 0.1$, * $p < 0.05$ (t-test vs. DMSO ctrl). (f) Selectivity screening of **66** on NRs. The heatmap illustrates the mean relative activation in comparison to reference ligands, $n = 3$. (g) **66** (10 μM) was not toxic in a WST-8 assay in N27 rat neurons and HEK293T cells. AQ (1, 10 and 30 μM) was found to be toxic. The data represent the mean \pm S.E.M. relative absorbance (450 nm), $n \geq 3$. (h,i) Permeability of Nurr1 agonists in a parallel artificial membrane permeability assay (PAMPA) and in a cellular model of the blood-brain barrier (BBB). Propranolol and the brain-penetrant reference antipyrine were used for comparison. The data are presented as the mean \pm S.D., $n = 6$. (j) Metabolism of **66** by rat liver microsomes resulted in demethylation of the dimethylamino group. The data are presented as the mean \pm S.D., $n = 4$. Adapted from ²¹².

Despite favorable membrane permeability and blood-brain penetration *in vitro* (Figure 32h,i), the metabolic stability of **66** was limited due to demethylation of the dimethylamino motif (Figure 32j). Although the free amine **68** still showed weak Nurr1 activation (Table 5), the metabolic liability should be overcome. Therefore, cyclic amino substituents (**69** and **70**, Table 5) were incorporated, yet there was no evidence of Nurr1 agonistic activity. However, replacement of the dimethylamine by a methoxy group (**72**) and related motifs (**73**, **74**) enhanced metabolic stability, while retaining Nurr1 agonist potency as well as favorable membrane permeability and brain penetration, suggesting potential for *in vivo* application (Table 5, Figure 32h,i).

Table 5. Optimization of **66** for microsomal stability and Nurr1 modulation. Microsomal stability against degradation by rat liver microsomes was determined by LCMS.

ID	R ³ =	EC ₅₀ (Nurr1) (max. act.) μM (fold)	microsomal half-life min.
66		0.090±0.005 μM (2.1±0.1-fold)	6.3±0.3
68		< 1.2-fold activation	n.d.
69		inactive (10 μM)	n.d.
70		inactive (10 μM)	n.d.
71		0.16±0.06 μM (1.7±0.1-fold)	18±2 min.
72		0.12±0.03 μM (2.1±0.2-fold)	42±5 min.
73		0.12±0.06 μM (1.5±0.2-fold)	78±7 min.

The SAR evaluation showed that a 3,4-dichlorophenyl substituent at the 2-position of the imidazopyridine scaffold and a 5-(4-(dimethylamino)phenyl)furan-2-carboxamide motif at the 3-position were favorable for the Nurr1 agonist potency. The combination of these modifications in **74** resulted in a high affinity Nurr1 modulator with a K_d of 0.08 μM (Nurr1 LBD) and strong agonist potency in a Gal4-Nurr1 hybrid reporter gene assay (EC₅₀ = 0.04 μM, Figure 33). However, **74** did not significantly outperform **66** and had a much higher lipophilicity (SlogP = 7.54). This suggests that while the structural fusion increased affinity and potency, it also increased lipophilicity, negatively affecting the drug-like properties of the compound.

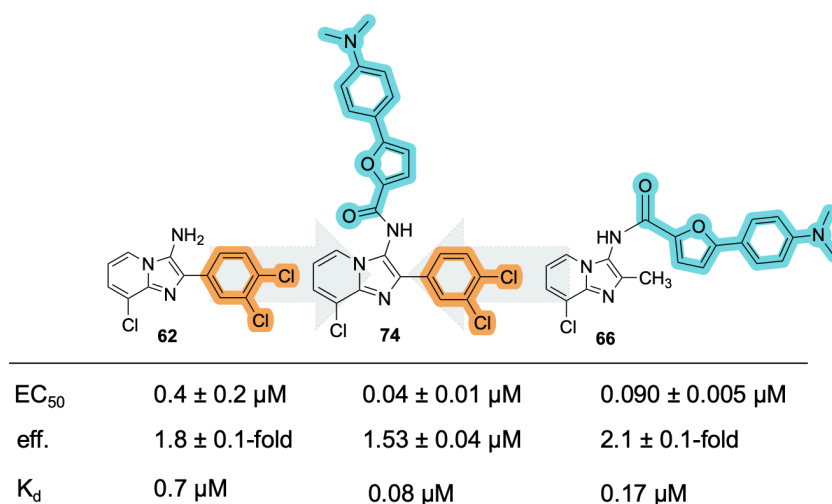


Figure 33. Structural fusion of **62** and **66** in **74** enhanced Nurr1 agonist potency and binding affinity. *Reprinted from* ²¹².

In order to evaluate the potential of the new Nurr1 agonist scaffold in a relevant setting, a model of PD using three-dimensional organoids derived from iPSCs was used. Organoids were generated from wild-type isogenic pluripotent stem cells (iPSCs)²²⁰ and iPSCs bearing a G2019S LRRK2 mutation. LRRK2 mutations are a common genetic cause of PD and the G2019S mutation enhancing the kinase activity of LRRK2 has been correlated with increased α -synuclein accumulation, mitochondrial dysfunction, impaired dopamine signaling, and ultimately progressive dopamine neuron loss in the human brain^{221,222}. The Nurr1 agonist **66** was observed to significantly rescue TH mRNA levels and (almost) histological TH staining in LRRK2 mutant organoids to the wild type, indicating a promising therapeutic potential (Figure 34d). In contrast, **67** demonstrated no effect. The weaker effect of **66** on wild-type organoids suggested that therapeutic activation of Nurr1 may be more beneficial in cases where Nurr1 activity has been pathologically reduced. The levels of Nurr1 did not change after treatment with **66**, confirming that the effects were due to the direct activation of Nurr1.

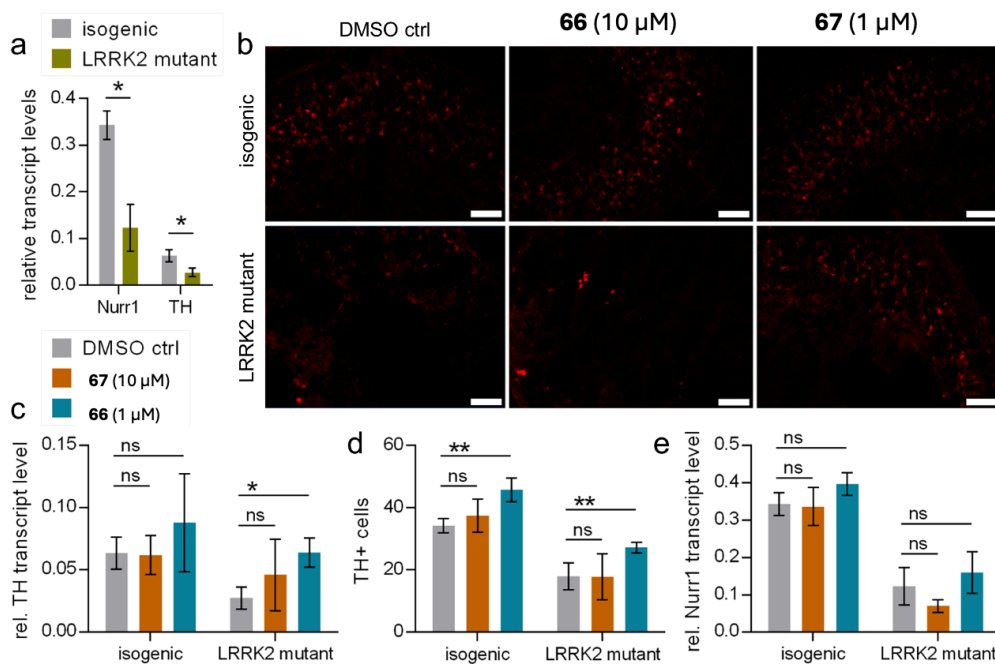


Figure 34. Treatment of midbrain organoids with the Nurr1 agonist **66** and the negative control analogue **67**. (a) Organoids derived from human iPSC carrying a gain-of-function mutation in the leucine-rich repeat kinase 2 (LRRK2) gene (G2019S) exhibited reduced Nurr1 and TH transcript levels when compared to isogenic controls after 45 days. (b) Immunofluorescence staining of midbrain organoid sections revealed the presence of TH-expressing cells. Scale bars represent 100 μm . (c) **66**, but not the negative control **67**, induced TH mRNA expression in LRRK2 mutant organoids and tended to enhance TH mRNA expression in isogenic controls. All data are presented as the mean \pm S.E.M., $n = 3$. * $p < 0.05$, ** $p < 0.01$ (unpaired, two-tailed Student's t-test). Reprinted from ²¹².

The development of **66** represents a significant advancement over the lead structure AQ in terms of potency, toxicity, and selectivity for Nurr1 activity. The structure-based optimization of AQ exemplifies that **66** represents a superior alternative to AQ for the investigation of Nurr1 as a potential therapeutic target in neurodegenerative diseases. The nanomolar potency of this compound in Nurr1 activation means that the need for high concentrations of the tested compound is minimized, thus reducing cellular stress and toxicity in subsequent *in vitro* and *in vivo* studies. In a 3D organoid PD model, **66** has already demonstrated encouraging effects in Nurr1 activation, indicating its potential utility in PD therapy. Nevertheless, further *in vitro* and *in vivo* studies are necessary to compare the positive effects demonstrated by AQ in various neurodegenerative disease models (see chapter 1.1.2.1 to 1.1.2.3) and to confirm that these effects are indeed mediated by Nurr1, rather than being nonspecific actions of AQ. Furthermore, the selectivity profile of **66** must be expanded in order to ascertain whether it interacts with G proteins, kinases, surface receptors, or other enzymes. Additional SAR studies may be required to determine whether higher selectivity within the NR4A family can be achieved with this scaffold. In light of the fact that **66** has been derived from AQ, it would be beneficial to gain clarity on whether this optimization still targets the same predicted

binding side of AQ or whether this has changed. The observation that **66** activated dimers on DR5 and NuRE, but not monomers on NBRE in the Gal4 assay, indicated that **66** may influence the conformation of Nurr1, which in turn may affect the recruitment of coregulators. This suggested that **66** may induce distinctive conformational states in Nurr1, thereby modulating its activity in a manner distinct from that of AQ, which demonstrated Nurr1 activation at NBRE (see chapter 1.1.3.2).

The development of **66**, a potent and selective AQ-derived Nurr1 agonist, provided a high-quality chemical tool to study Nurr1 modulation and advance neurodegenerative therapeutic strategies. Scaffold-hopping, fragment optimization and replacement of unfavorable motifs have resulted in a next-generation Nurr1 agonist with favorable chemical properties and experimentally confirmed high-affinity binding to Nurr1. **66** and its structurally matched negative control (**67**) met the highest chemical tool quality criteria (potency < 100 nM, selectivity for NR4A receptors within NR family > 30-fold, cellular on target activity < 1 μ M, 100-fold less potent control compound, no PAINS elements²²³) for robust biological studies on Nurr1 modulation and the receptor's therapeutic potential.

3.3 Tuning RXR modulators for PGC1 α recruitment

As previously outlined in chapter 1.2, RXR is a distinctive receptor due to its capacity to form heterodimers with a range of other NRs, thereby contributing to a multitude of physiological processes, including proliferation, differentiation, metabolic homeostasis, and inflammation. Despite the therapeutic potential of RXR ligands, their broad involvement in genomic regulation can lead to notable adverse effects. A notable example of this phenomenon has been the synthetic RXR agonist **23**, which has been found to exhibit great potential as a therapeutic agent for AD in numerous experimental models but is also associated with significant side effects such as hypertriglyceridemia (see chapter 1.2.2.1 and 1.2.2.2).

The concept of selective modulation through ligand-induced coregulator recruitment has the potential to facilitate more targeted RXR modulation (Figure 35). As NRs are typically capable of interacting with a multitude of coregulators, the selective recruitment of a specific subset of these partners by ligands could facilitate a tissue-specific or even gene-specific modulation. This approach may prove an efficacious method of reducing any adverse effects and may also be considered a more targeted therapeutic option.

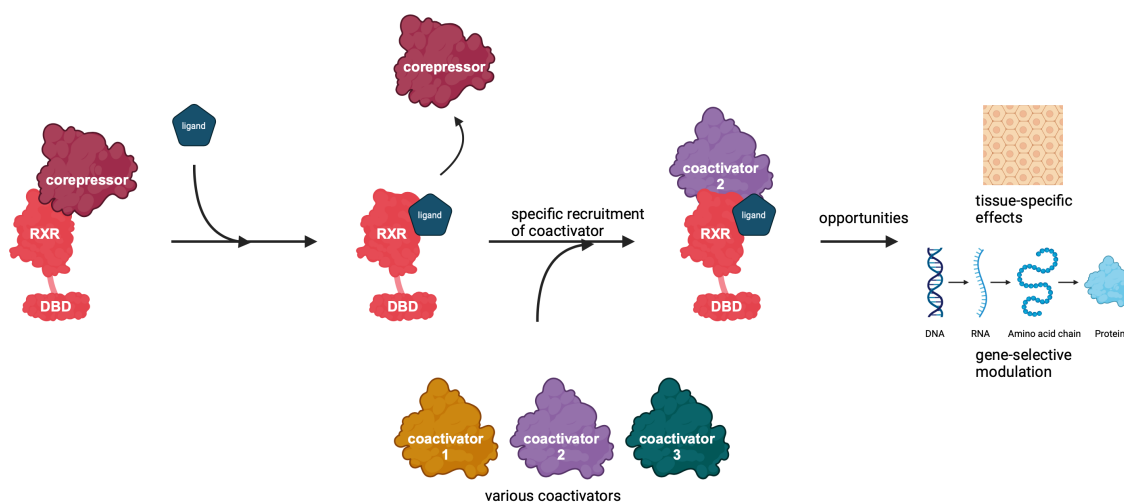


Figure 35. Selective modulation through ligand-induced coregulator recruitment. The binding of a ligand to the LBD-corepressor complex induces a conformational change, resulting in the release of the corepressor. The active conformation of the ligand-induced LBD recruits a selective coactivator, which may exert effects specific to tissues and genes expression. *Created with Biorender.com.*

In order to ascertain the potential for ligand-induced coregulator recruitment for RXR, a HTRF assay was conducted using two distinct RXR ligands. The HTRF assay comprising the RXR α LBD (Tb³⁺-cryptate labelled, FRET donor) and a panel of common NR coregulator peptides (fluorescein-labelled, FRET acceptor) revealed pronounced differences in the RXR-coregulator recruitment profiles of 9cisRA (**22**) and the synthetic agonist **27** (Figure 36, see chapter 1.1.2.2). While 9cisRA was observed to recruit several coactivators (e.g., SRCs, NCoA6) with intermediate efficacy and strongly displaced the corepressor silencing mediator for retinoid and thyroid-hormone receptor (SMRT, NCoR2), **27** exhibited a strong preference for PGC1 α recruitment with minimal impact on SMRT binding (Figure 36). This differential recruitment profile indicates that RXR ligands can be tuned to selectively modulate interaction with specific co-regulators.

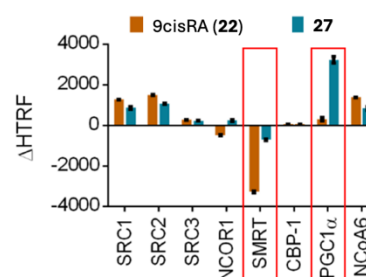


Figure 36. Effects of 9cisRA and **27** on coregulator recruitment to the RXR α LBD. Compounds were tested at 1 μ M.

In light of the impact of **27** on the RXR-PGC1 α interaction, a chemically diverse set of analogues of **27** was designed through a structure-guided approach to explore the impact of structural modifications on coregulator recruitment. A virtual library comprising 15 K biphenylacetic acid derivatives was created by combining 4-boronophenylacetic acid (**75**) with commercially available aryl halides through an in silico fusion process (Figure 37a). The resulting designs were then docked to the RXR α LBD in complex with **27** (PDB: 6sjm¹⁵⁷, Figure 37b) and the top-ranking molecules were selected for synthesis based on their docking scores and structural diversity.

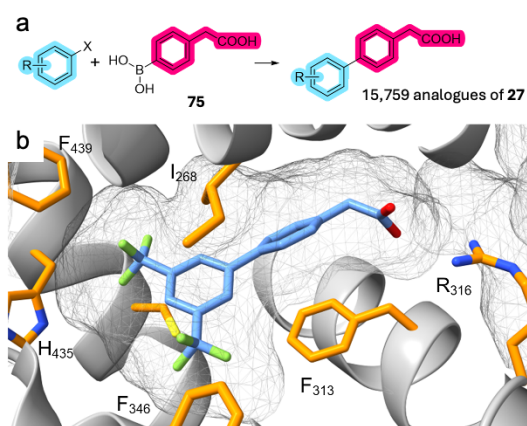


Figure 37. (a) A virtual library of 15,759 biphenylacetic acids was constructed docked to the binding site of **27** in RXR α , with the objective of identifying novel RXR modulators related to **27**. (b) **27** binds to the highly hydrophobic orthosteric site of RXR α (PDB: 6sjm¹⁵⁷) and forms a single polar contact to Arg316.

The synthesis of these biphenyls was achieved through a Suzuki reaction of (4-(2-methoxy-2-oxoethyl)phenyl)boronic acid (**76**) or ethyl 2-(4-(4,4,5,5-tetramethyl-1,3,2-dioxaborolan-2-yl)phenyl)acetate (**77**) with aryl bromides, followed by alkaline hydrolysis (Figure 38). The Suzuki coupling was achieved using XPhos Pd G2 pre-catalyst in good to excellent yields. However, in some cases, the synthesis of biphenyls proved to be challenging. As a result, the synthesis pathway was modified by employing the carboxylic acid of **77** for Suzuki coupling or by utilizing the bromide of **77** as an alternative to the boronic acid pinacol ester motif and the corresponding boronic acid for coupling (not shown).

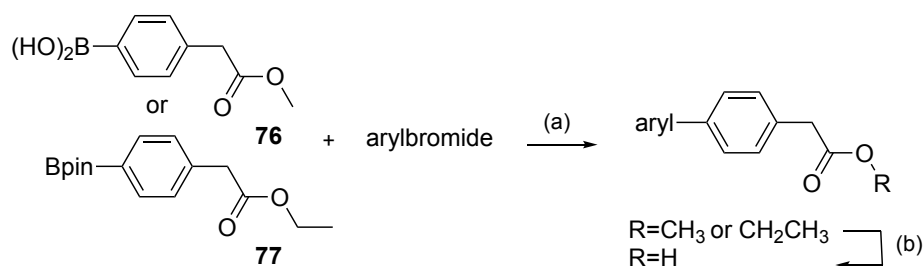


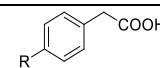
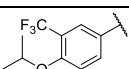
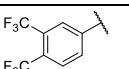
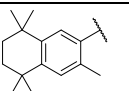
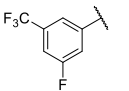
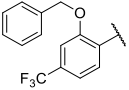
Figure 38. General synthesis of phenylacetic acid derivatives of **27**. Reagents and conditions (a) K_3PO_4 , XPhos Pd G2, 1,4-dioxane/ H_2O , reflux, 1.5–24 h or Cs_2CO_3 , XPhos Pd G2, toluene/ H_2O , reflux, 1.5–24 h, 4–96%; (b) LiOH, MeOH/ H_2O , rt, 18 h, 16–90%.

In order to investigate the SAR of RXR modulators, a total of 28 analogues were synthesized and tested via a Gal4-RXR hybrid reporter gene assay, which evaluated their activity on the three RXR subtypes. Additionally, a HFTR assay was utilized in order to assess their effects on coregulator recruitment.

Notable findings included the discovery that derivatives containing a 3,4-substituted and 3,5-substituted benzene ring exhibited potent RXR agonist activity. For example, the 4-isopropoxy-3-trifluoromethyl derivative (**78**) and the 3,4-bistrifluoromethyl derivative (**79**) demonstrated remarkable potency as RXR agonists (EC_{50} (RXR $\alpha/\beta/\gamma$) = 0.29/1.3/3.4 μM (**78**) and EC_{50} (RXR $\alpha/\beta/\gamma$) = 0.060/0.4/0.24 μM (**79**)), displaying slight preferences for RXR α .

(Table 6). The bexarotene related design **80** exhibited considerable RXR agonist potency (EC_{50} (RXR α / β / γ) = 0.53/0.55/0.52 μ M), too (Table 6).

Table 6. RXRs modulation of selected analogues of RXR agonist **27** from structure-guided design.

ID	 R =	EC_{50} (max. rel. activation refer to 1 μ M bexarotene)		
		RXR α	RXR β	RXR γ
78		0.29 \pm 0.03 μ M (29 \pm 1%)	1.3 \pm 0.1 μ M (22 \pm 1%)	3.4 \pm 0.3 μ M (20 \pm 1%)
79		0.060 \pm 0.004 μ M (22 \pm 1%)	0.4 \pm 0.1 μ M (22 \pm 1%)	0.24 \pm 0.03 μ M (21 \pm 1%)
80		0.53 \pm 0.04 μ M (53 \pm 3%)	0.55 \pm 0.04 μ M (55 \pm 3%)	0.52 \pm 0.07 μ M (52 \pm 3%)
81		2.6 \pm 0.3 μ M (28 \pm 2%)	0.54 \pm 0.06 μ M (26 \pm 1%)	6.1 \pm 0.9 μ M (25 \pm 1%)
82		1.0 \pm 0.2 μ M (34 \pm 1%)	1.1 \pm 0.2 μ M (24 \pm 1%)	2.9 \pm 0.1 μ M (13 \pm 1%)

Comparative profiling of RXR modulators **78**, **79**, and **80** in HTRF-based assays revealed significant differences in their effects on the binding of coregulators, SRC1, SMRT, and PGC1 α to RXR α (Figure 39a), despite their structural similarity. **78** did not affect PGC1 α binding, while **79** and **80** retained the ability of **27** to promote PGC1 α recruitment, with **79** demonstrating substantially higher efficacy in inducing PGC1 α binding than **80**. These findings were corroborated through dose-response profiling, which demonstrated that **79** exhibited stronger recruitment of PGC1 α compared to **80** (Figure 39b).

The wider profiling of structurally disparate analogues demonstrated that minor structural alterations in RXR ligands could result in markedly distinct coregulator recruitment profiles. For instance, **81** (Table 6), which demonstrated slight RXR β preference (EC_{50} (RXR α / β / γ) = 2.6/0.54/6.1 μ M) and **82** (Table 6), which exhibited a markedly more angled shape, were unable to enhance PGC1 α recruitment to RXR although both compounds were potent RXR agonists in cellular setting (Figure 39c). These findings highlight the potential of structural modification to achieve selective RXR modulation.

To validate the biological relevance of these findings, the activity profiles of compounds **78**, **79**, and **80** were subjected to further characterization. All three compounds were found to be inactive on lipid-activated NRs related to RXR, thereby demonstrating favorable selectivity (Figure 39d). Furthermore, these compounds consistently inhibited the interaction of RXR α with other NRs (THR α , RAR α , LXRA, and PPAR γ , Figure 39e),

thereby demonstrating the absence of activity differences on related NRs that would compromise the use of this compound set as a tool.

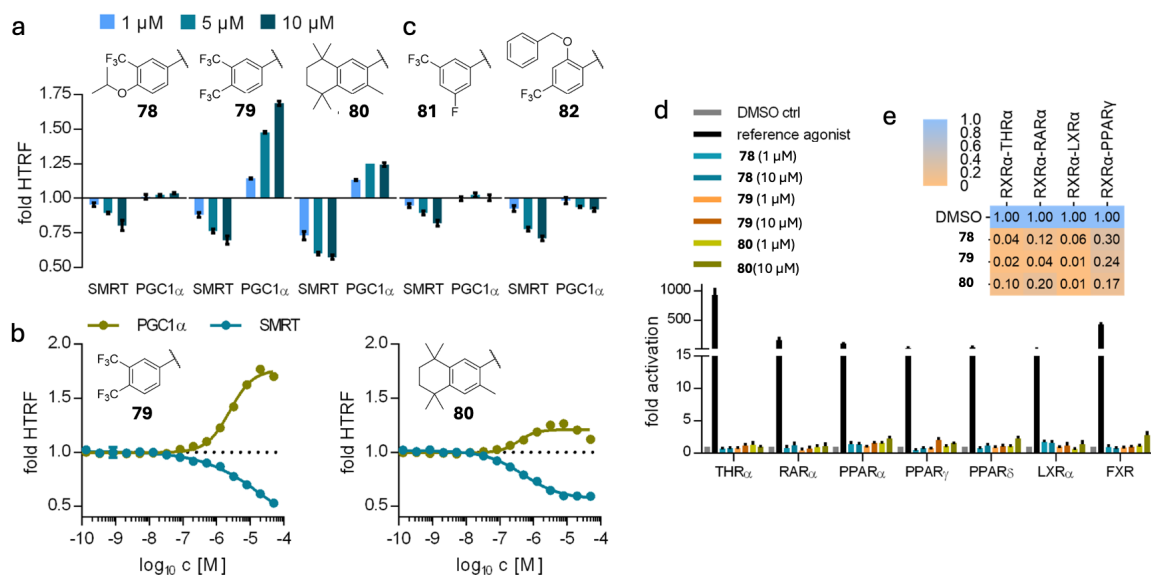


Figure 39. Effects of RXR ligands on the recruitment of co-regulators to the RXR α LBD in HTRF-based systems. The data are presented as the mean \pm S.E.M., $n = 3$. Despite their high structural similarity, **78-82** revealed pronounced differences in their effects on coregulator recruitment. (b) Dose-response profiling demonstrated that **79** and **80** induce recruitment of PGC1 α , with **79** exhibiting considerably higher efficacy. (c) **81** and **82** were ineffective in inducing PGC1 α recruitment. (d) **78**, **79** and **80** demonstrated no transcriptional activity at 1 and 10 μ M on lipid-sensing NRs associated with RXR. The data are presented as the mean \pm S.E.M., $n = 3$. (e) The effects of **78**, **79** and **80** (10 μ M each) on the interaction of RXR α with the heterodimer partners THR α , RAR α , LXR α and PPAR γ were observed in a cellular assay, in which the binding of VP16-RXR α -LBD to the corresponding Gal4 hybrid receptors of the dimer partners was monitored. The heat map depicts the mean relative reporter activity in comparison to the control substance DMSO, $n = 3$.

In order to confirm the ability of **79** and **80** to induce the interaction of RXR with PGC1 α within a cellular context, a reporter gene assay was employed utilizing a Gal4-PGC1 α fusion protein and an RXR α -LBD-VP16 fusion protein (Figure 40a). This assay permitted the observation of the interaction between PGC1 α and RXR α LBD in a cellular context via a reporter gene assay. The RXR modulators **79** and **80** were found to robustly enhance reporter gene expression in the presence of RXR α -LBD-VP16, thereby demonstrating their ability to induce RXR α -PGC1 α interaction with high potency. As observed in the cell-free HTRF assay, **79** demonstrated a greater efficacy in promoting RXR α -PGC1 α binding than **80**. In contrast, the reference RXR agonist bexarotene exhibited only a minimal effect on reporter activity.

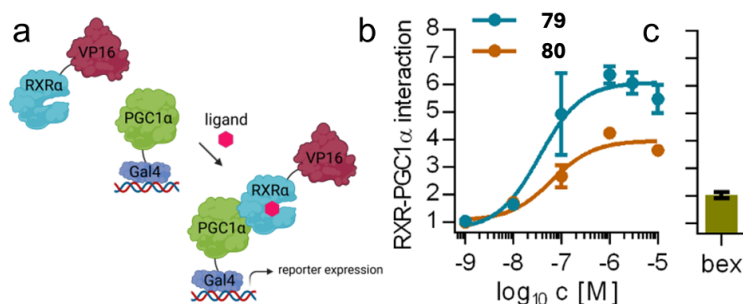


Figure 40. The RXR modulators **79** and **80** induced the interaction between RXR α and PGC1 α in a cellular context. (a) A Gal4-PGC1 α fusion protein, a Gal4-responsive reporter construct and an RXR α -LBD-VP16 fusion protein were employed to observe ligand-induced RXR α -PGC1 α interaction in HEK293T cells. (b) RXR α -PGC1 α interaction was robustly enhanced by **79** and **80**, resulting in enhanced reporter activity ($EC_{50} = 0.04 \pm 0.02 \mu\text{M}$ (**79**); $0.06 \pm 0.03 \mu\text{M}$ (**80**)). In contrast, the reference RXR agonist bexarotene ($1 \mu\text{M}$) had only a weak effect (c). The data represent the mean \pm S.D. of reporter activity in the presence of Gal4-PGC1 α and RXR α -LBD-VP16, with the readings normalized to the RXR α -LBD-VP16-free setting, $n = 3$.

A more detailed analysis of the predicted binding modes of compounds **27**, **78**, **79**, and **80** (Figure 41a) revealed no notable differences. However, it was observed that compounds **78** and **80** extend further towards His435 in H11 in comparison to **27** and **79** (Figure 41b). H11 forms numerous interactions with H12, which is responsible for AF2 of RXR and plays a role in mediating the activation process by ligands (Figure 41c, see chapter 1.1.1). It can be hypothesized that variations in the positioning of H11 exert an influence on H12, resulting in alterations to the shape and size of the coactivator binding site. Consequently, the predicted binding differences in the His435 region may induce subtle allosteric changes in the coactivator binding site, which could explain the differential effects on PGC1 α recruitment.

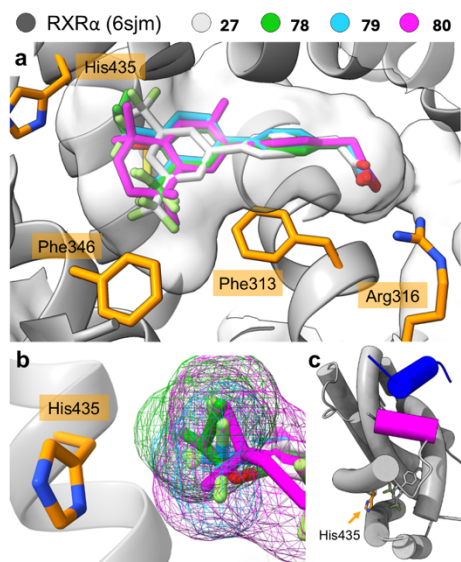


Figure 41. A comparison of the binding modes of **27**, **78**, **79** and **80**. (a) Predicted binding modes of **78**, **79** and **80** in the binding site of **27** in the RXR α LBD (PDB: 6sjm¹⁵⁷). The binding modes of **27**, **78**, **79** and **80** to RXR α are highly similar, involving a strong ionic contact with Arg316. (b) The differences in the binding of **27**, **78**, **79** and **80** in the His435 region are illustrated with the ligand surfaces shown as a mesh. The structural demands in the His435 region are higher for **78** (green mesh) and **80** (magenta mesh) than for **27** (grey mesh) and **79** (blue mesh), which may affect the position of H11. (c) The structural overview of the ternary complex of **27** and nuclear receptor co-activator 2 (blue) bound to the RXR α LBD (PDB: 6sjm¹⁵⁷) is presented here. H12 is depicted in magenta. The interaction of different ligands with H11 is likely to affect the position of H12, consequently impacting the region responsible for the binding of co-activators via allosteric crosstalk.

Despite their high structural similarity, the RXR ligands **78**, **79**, and **80** exhibited significant mechanistic differences in terms of PGC1 α recruitment, with **79** displaying a strong effect, **80** a weak effect, and **78** no ligand-induced PGC1 α binding. While this structural similarity may present a challenge for the further development of the scaffold and complicate the discovery of other coregulator-selective RXR ligand chemotypes, it also serves as a valuable feature for mechanistic studies. The different abilities to recruit PGC1 α can lead to distinct gene expression patterns and tissue-specific effects, which may influence varying therapeutic outcomes. The present study focused on a limited number of coregulators; however, at least 350 additional coregulators of NRs have been identified in the past²²⁴. This highlights the necessity for future research to include screening a broader range of coregulators in order to gain a comprehensive understanding of the ligand-induced recruitment pattern. This comprehensive approach is needed to fully unlock the potential of RXR ligands and understand their diverse effects, which will ultimately contribute to the development of more selective and effective therapeutic agents.

These findings demonstrate that RXR ligands can be engineered to function as molecular glues, modulating the binding and release of individual coregulators. Such differences in ligand-induced coregulator recruitment could enable tissue-selective RXR activation based on cell-type-specific expression and roles of certain coregulators. These findings suggested that future innovations in targeting RXRs may rely on a more thorough understanding of ligands and their structural modifications to achieve desired activation mechanisms. The RXR ligands **78**, **79**, and **80**, despite sharing a similar structure, exhibited significantly divergent effects on PGC1 α recruitment. In addition to providing evidence that RXR ligands can be tuned to modulate certain coregulator interactions, the set of **78**, **79**, and **80** is a valuable chemical tool to explore the biological relevance of the RXR-PGC1 α interaction and the therapeutic potential of its selective modulation.

3.4 Azologs of the fatty acid mimetic drug cinalukast enable light-induced PPAR α activation

Using virtual activity prediction, the fatty acid mimetic cysteinyl leukotriene receptor 1 (CysLT1R) antagonist cinalukast (**83**, Figure 42a) was found to activate PPAR α with an EC₅₀ value of 10 μ M (5.3-fold activation) in a Gal4 hybrid reporter gene assay²²⁵. Based on the selective optimization of side activities (SOSA) concept, in which (weak) off-target activities are converted into the major activity of a new, closely related structural analogue, while reducing the original target activity²²⁵, **83** was optimized towards PPAR α agonism. An optimized analogue **84** (Figure 42a) achieved a considerable activity shift with approximately 3-fold enhanced PPAR α activation efficacy (13.7-fold versus 5.3-fold) and strongly reduced CysLT1R antagonism (by approximately 100-fold)²²⁵.

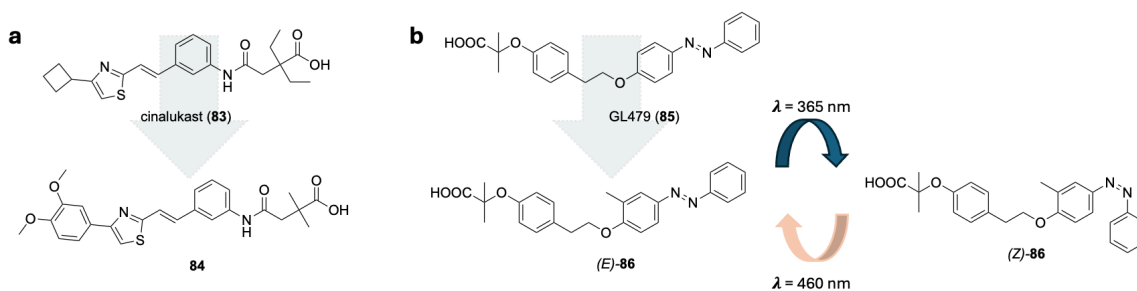


Figure 42. (a) The development of a weak PPAR α agonist, cinalukast (**83**), based on the SOSA concept, resulted in the synthesis of **84**. (b) A structure-guided approach was employed to develop the weak PPAR α agonist, GL479 (**85**), into the photohormone **86**. Irradiation with UV light enabled the formation of *E/Z*-**86**.

Another potent and selective PPAR α agonist relevant to this thesis is the photohormone **86** (Figure 42b)¹³⁸. Photohormones represent a novel class of attractive tool compounds that enable light-dependent modulation of transcription factors, thereby achieving spatiotemporal control of transcriptional activity¹³⁸. **86** was developed via a structure-guided approach from the weak pan-PPAR agonist GL479 (**85**, EC₅₀ (PPAR α , *E/Z*) = 1.09/0.8 μ M, Figure 42b)¹³⁸. This photohormone exhibited considerable greater potency (EC₅₀ (*E/Z*) = 0.007/0.24 μ M, factor > 150) and selectivity towards PPAR α than **85** and was also capable of being switched off by light-induced isomerization to its (*Z*)-conformer, which was less active on the intended target by a factor of 35 in a Gal4 hybrid reporter gene assay¹³⁸. In a live-cell fluorescence (mCherry) reporter gene assay in HEK293T cells, **86** was observed to alter transcriptional activity in a light-dependent fashion, indicating the potential of this compound as a valuable *in vitro* tool for functional studies¹³⁸.

However, the development of (*Z*)-active photohormones has been preferable for optical control, as azobenzenes have been unable to achieve full photo-switching to 100% (*Z*)-configuration¹⁹¹. Thus, the objective was to create a novel light-controlled PPAR α ligand which was active in (*Z*)-configuration based on **84** by replacing the styrylthiazole motif with a stilbene or azobenzene motif.

The synthesis of the *E*-stilbene analogue **87** of **84** was carried out in accordance with Figure 43. Initially, the Suzuki reaction was employed to couple 3-bromobenzaldehyde (**88**) with 3,4-dimethoxyphenylboronic acid (**89**) to **90**. Subsequently, **90** was subjected to a Wittig reaction with methyltriphenylphosphonium bromide, resulting in the formation of **91**. Simultaneously, 3-iodoaniline (**92**) was coupled with ethyl 2,2-dimethylmalonate (**93**)

to form the amide **94**. Subsequently, Heck coupling of **94** with **91** resulted in the formation of ester precursor **95**, which, following alkaline hydrolysis, yielded **87**.

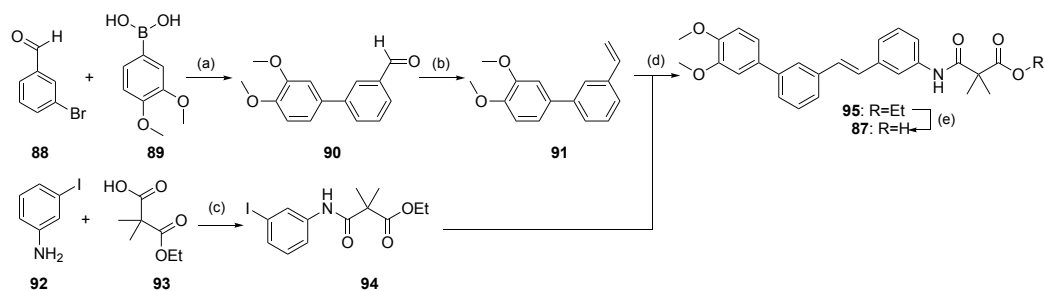


Figure 43. Synthesis of **82**. Reagents and conditions: (a) XPhos Pd G2, K_3PO_4 , water/dioxane, reflux, overnight, 83%; (b) methyltriphenylphosphonium bromide, $KOtBu$, THF, $0^\circ C \rightarrow rt$, overnight, 94%; (c) HATU, DIPEA, DMF, rt, overnight, 95%; (d) $Pd(OAc)_2$, K_3PO_4 , DMA, $140^\circ C$, overnight, 42%; (e) $LiOH$, water/THF, rt, overnight, 72%. Reprinted from ²¹⁵.

Irradiation of *E*-**87** with UV light ($\lambda = 365$ nm) resulted in the formation of 62% *Z*-isomer (38% remained *E*-isomer). In order to separate the two isomeric forms (*E/Z*) and remove any impurities identified through an analysis of 1H -NMR during (*E*) to (*Z*) photoisomerization of **87**, a preparative HPLC method was employed. This approach was deemed necessary due to indications of potential undesired irreversible electrocyclization by oxidation of (*Z*)-**87**. Unfortunately, it was not possible to separate the two isomers, however the impurities were successfully removed. Consequently, the mixture of 62% (*Z*)-**87** was used as the (*Z*)-isomer for further *in vitro* characterization. The screening of *E/Z*-**87** in a Gal4 hybrid reporter gene assay on various lipid-sensing NRs revealed agonistic activity on $RAR\alpha$, PPARs, and FXR, with PPAR α agonism being the most pronounced (Figure 44a). This profile prompted the synthesis of the azobenzene analogue with the objective of improving the light-dependent switching properties.

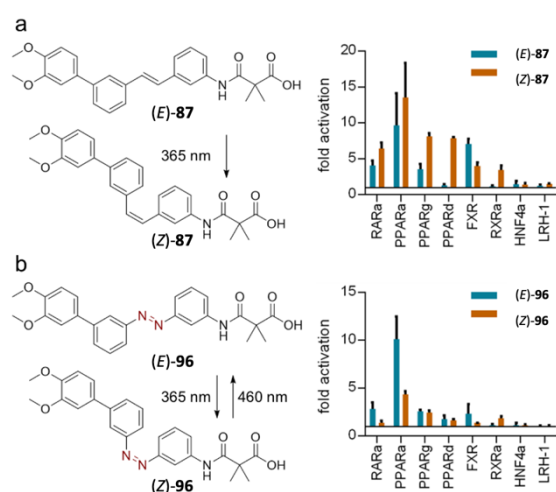


Figure 44. Modulation of NRs of **87** and **96**. (a) The stilbene analogue **87** ($3 \mu M$) exhibited agonistic activity on $RAR\alpha$, PPARs and FXR, with the most prominent effect observed in the case of PPAR α . (b) The azobenzene **96** ($10 \mu M$) demonstrated a more pronounced preference for PPAR α . The data are presented as the mean \pm S.E.M. fold NR activation relative to the DMSO control, $n \geq 3$. Reprinted from ²¹⁵.

The synthesis of the azobenzene derivatives **96-106** was carried out involving the Suzuki reaction, the Baeyer–Mills coupling, and alkaline ester hydrolysis according to Figure 45 and 46. The initial synthesis, which contains an acidic head group (**109**), involved an amide coupling between **93** and *N*-BOC-3-phenylenediamine (**107**), followed by BOC deprotection. The corresponding amines **118-125**, which represent the lipophilic backbones, were prepared through Suzuki coupling of the corresponding bromoanilines **110-112** with the boronic acids **113-115**, **117** and boronic acid pinacol ester **116**. Subsequently, a Baeyer-Mills reaction was performed by oxidizing **109** with Oxone® to form a nitroso intermediate, which was then reacted with amines **118-125** to give intermediates **126-133**. The final step in the synthesis involved alkaline ester hydrolysis, which produced the desired photoswitchable PPAR modulators **96-98** and **101-105** (Figure 45).

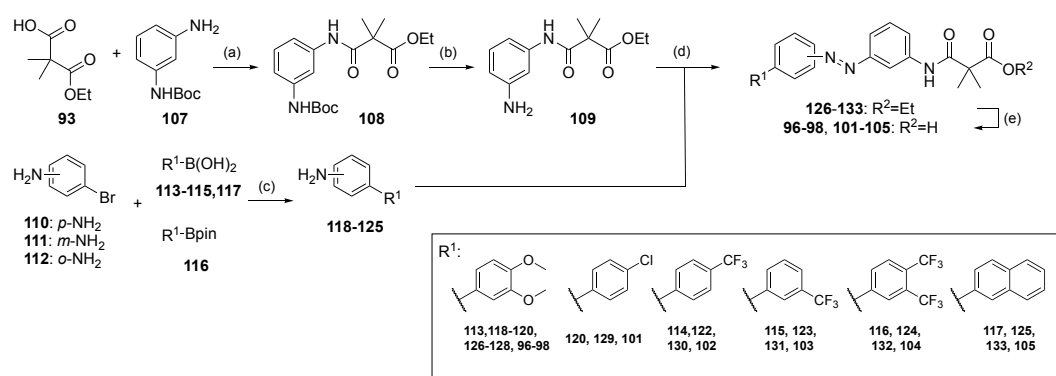


Figure 45. Synthesis of azobenzenes **96-98**, **101-105**. Reagents and conditions: (a) HATU, DIPEA, DMF, rt, overnight, quant.; (b) TFA, rt, overnight, quant.; (c) XPhos Pd G2, K₃PO₄, water/dioxane, reflux, overnight, 44-95%; (d) Oxone, DCM, rt, 1-3h, workup, DCM, HOAc, rt, 1-2 days, 3-59%; (e) LiOH, water/THF, rt, overnight, 40-95%. *Reprinted from* ²¹⁵.

A modified synthetic approach was employed to skip one synthesis step (instead of two Suzuki reactions) in the case of azobenzenes **99** and **100** (Figure 46). The initial step involved the Baeyer-Mills coupling between **107** and **111** which resulted in the formation of diazobenzene **134**. Subsequently, the Suzuki coupling of **134** with boronic acids **135** and **136** yielded **137** and **138**, which were then subjected to ester hydrolysis, affording compounds **99** and **100**. Similarly, azobenzene **106** was synthesized by coupling **107** with 9,9-dimethyl-9*H*-fluoren-3-amine (**139**) to obtain **140**, which was then subjected to ester hydrolysis to yield **106**.

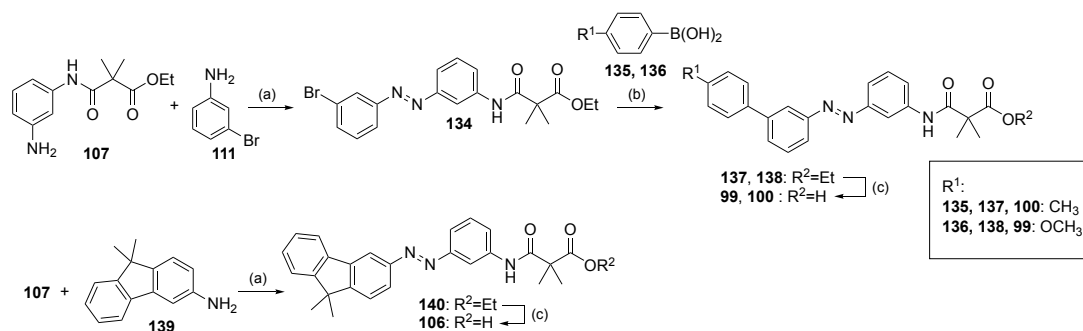


Figure 46. Synthesis of azobenzenes **99**, **100**, **106**. Reagents & Conditions: (a) Oxone, DCM, rt, 1h, workup, DCM, HOAc, rt, 2 days, 59-60%; (b) XPhos Pd G2, K₃PO₄, water/dioxane, reflux, overnight, 91-94%; (c) LiOH, water/THF, rt, overnight, 77-99%. Reprinted from ²¹⁵.

PPAR α agonism was determined in a Gal4-PPAR α hybrid reporter gene assay. A cell DISCO System¹⁹³ was employed to maintain the (*Z*)-configuration which exhibited 75 ms light pulses with a specific λ every 15 s. The azobenzene derivative **96** of **87** demonstrated PPAR agonism, with a preference for PPAR α and greater selectivity over RAR α and FXR compared to **87** (Figure 44b). The full dose-response profiling of **96** confirmed that (*E*)-**96** was a potent PPAR α agonist (EC₅₀ = 3 μ M, 26% relative activation), with the (*Z*)-isomer exhibiting reduced efficacy (EC₅₀ = 4 μ M, 17% relative activation) (Table 8). **96** demonstrated favorable photophysical characteristics (irradiating with λ = 365 nm for (*E*) to (*Z*), λ = 435 nm for (*Z*) to (*E*), Figure 47a), enabling efficient and repeated photo-switching (Figure 47b), and thus represented a suitable lead for further photohormone development.

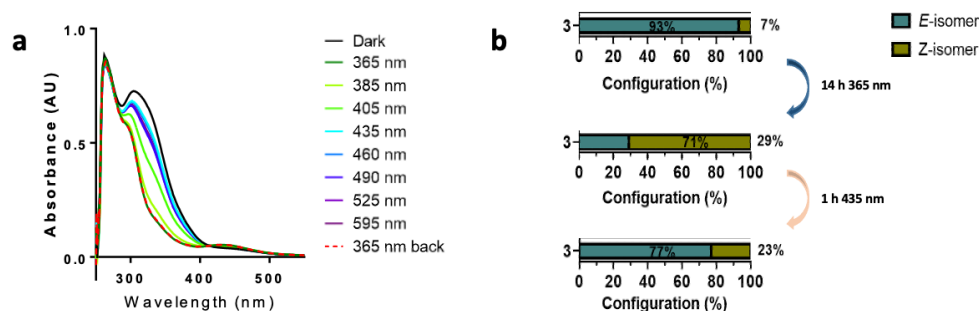


Figure 47. UV-Profiling of the PPAR α targeted photohormone **96**. (a) UV absorbance spectra of **96** (30 μ M in DMSO) measured after irradiation at the indicated wavelengths. (b) *E/Z*-configuration ratios of **96** in the dark adapted, state and after irradiation at 365 nm or 435 nm determined by ¹H-NMR based on the (CH₃)₂-integral of the oxopropanoic acid motif. Adapted from ²¹⁵.

To identify the optimal geometry for structural optimization, the scaffold geometry of **96** was systematically varied. The para-analogue (**97**) exhibited improved photophysical characteristics, with a red-shifted absorption maximum for (*E*) to (*Z*) switching (λ = 405 nm) yet exhibited diminished PPAR α agonism (Table 7). The ortho-derivative (**98**) displayed poor switching efficiency and was devoid of any activity on PPAR α (Table 7).

Given the favorable meta-regiochemistry of **96**, attention was directed towards the influence of substituents on the lipophilic backbone.

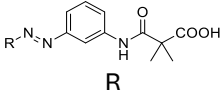
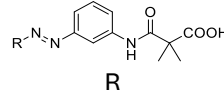
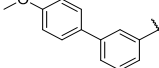
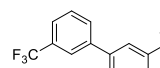
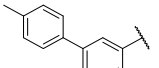
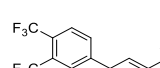
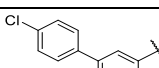
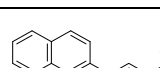
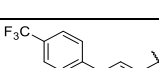
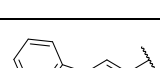
Table 7. Photoswitchable analogues of **84**. A cell DISCO¹⁹³ was used to maintain the (*Z*)-configuration.

ID	structure	EC ₅₀ (max. rel. activation refer to 1 μM GW7647)	
		(<i>E</i>)	(<i>Z</i>)
87		2.4 ± 0.4 μM (17 ± 2%)	1.3 ± 0.1 μM (48 ± 2%)
96		3 ± 1 μM (26 ± 1%)	4 ± 2 μM (17 ± 4%)
97		6 ± 1 μM (15 ± 2%)	7 ± 1 μM (8.1 ± 0.8%)
98		inactive (10 μM)	inactive (10 μM)

The removal of the 3'-methoxy substituent (**99**) resulted in a slight increase in potency (EC₅₀ (*E/Z*) = 2.3/3.1 μM), indicating that double substitution was not necessary. The introduction of alternative groups in the 4-position, such as methyl (**100**) and chloro (**101**), enhanced potency (EC₅₀ (*E/Z*) = 2.2/1.5 μM (**100**), 3.6/1.2 μM (**101**)) and provided (*Z*)-preference. The 4-trifluoromethyl derivative (**102**) was identified as a light-activated PPARα agonist with high potency in the light-induced (*Z*)-configuration and significantly reduced activity of the dark-adapted (*E*)-isomer (EC₅₀ (*E/Z*) > 20/1.5 μM (**102**)) (Table 8).

Additional variations, such as the relocation of the trifluoromethyl group to the 3-position (**103**), a 3,4-bistrifluoromethyl substitution (**104**) and β-naphthyl motif (**105**) retained PPARα agonism but lacked the favorable (*Z*)-preference of **102** (EC₅₀ (*E/Z*) = 4/3 μM (**103**), 5/3.1 μM (**104**)). The bulkier 9,9-dimethyl-9*H*-fluoren-2-yl substituent (**106**) was not tolerated (Table 8). The results of this SAR analysis indicated that the PPARα agonistic activity was tolerant of a range of substitution patterns on the 3-substituent scaffold but only a bulky, electron-withdrawing, and hydrophobic 4-substituent was found to provide the desired (*Z*)-preference.

Table 8. Evaluation of the lipophilic substitution pattern of **96**. A cell DISCO¹⁹³ was used to maintain the (*Z*)-configuration.

ID		EC ₅₀ (max. rel. activation refer to 1 μM GW7647)		ID		EC ₅₀ (max. rel. activation refer to 1 μM GW7647)	
		(<i>E</i>)	(<i>Z</i>)			(<i>E</i>)	(<i>Z</i>)
99		2.3 ± 0.4 μM (18 ± 2%)	3.1 ± 0.5 μM (20 ± 2%)	103		4 ± 1 μM (37 ± 8%)	3 ± 1 μM (38 ± 7%)
100		2.2 ± 0.2 μM (36 ± 2%)	1.5 ± 0.1 μM (32 ± 1%)	104		5 ± 1 μM (15 ± 3%)	3.1 ± 0.2 μM (33 ± 1%)
101		3.6 ± 0.5 μM (40 ± 3%)	1.2 ± 0.1 μM (30 ± 1%)	105		4.8 ± 0.4 μM (23 ± 2%)	3.7 ± 0.5 μM (21 ± 2%)
102		> 20 μM	1.5 ± 0.2 μM (39 ± 2%)	106		inactive (10 μM)	inactive (10 μM)

Overall, **102** demonstrated efficient switching between (*E*)- and (*Z*)-configurations without fatigue over multiple cycles and a long thermal relaxation half-life of 28.5 hours for the light-induced (*Z*)-isomer (Figure 48a-d). *In vitro* profiling in a Gal4 hybrid reporter gene assay demonstrated favorable selectivity for PPARα over related lipid-activated NRs for both (*E*)- and (*Z*)-**102** (Figure 48e). In order to verify the efficacy of **102** as a light-activatable tool in cellular environments, a live-cell fluorescence (mCherry) reporter gene assay in HEK293T cells was conducted over a temporal period to compare the effects of (*E*)-**102** and light-activated (*Z*)-**102** on PPARα. In the absence of light, dark-adapted (*E*)-**102** did not induce PPARα-dependent mCherry expression at 10 μM (Figure 48f, *grey line*). In contrast, light-activated (*Z*)-**102** mediated a continuously increasing reporter expression (Figure 48f, *blue line*), confirming its applicability as a light-activated tool.

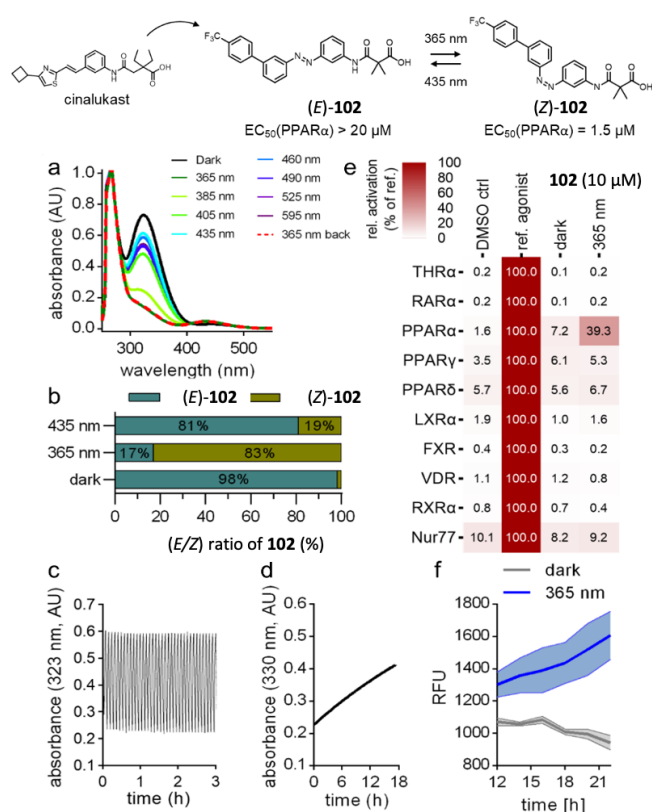


Figure 48. Profiling of the PPAR α targeted photohormone **102**. (a) UV/Vis absorbance spectra of **102** (30 μM in DMSO) were recorded following irradiation at the specified wavelengths. (b) The *E/Z*-configuration ratios of **102** in the dark-adapted state and after irradiation at 365 nm or 435 nm were determined by 1H -NMR based on the $(CH_3)_2$ -integral of the oxopropanoic acid motif. (c) **102** was demonstrated to be reversibly switchable between the (*E*)- and (*Z*)-configurations over multiple cycles by alternating irradiation at 365 and 435 nm. The absorbance was measured at a wavelength of 323 nm. (d) (*Z*)-**102** exhibited slow thermal relaxation at 37 $^{\circ}C$, with a half-life of 28.5 hours. (e) **102** demonstrated selective activation of PPAR α over related lipid-activated NRs. The data represent the mean \pm S.E.M. of the NR activation, $n = 3$. (f) The light-activated (*Z*)-**102** caused continuous PPAR α activation over time, while the (*E*)-**102** had no effect. The compounds were tested at a concentration of 10 μM in a fluorescent reporter gene assay utilising the mCherry protein, with fluorescence intensity (FI) measured at two-hour intervals. The fluorescence intensity (FI) of (*Z/E*)-**102** was normalized to that of the untreated control (DMSO) and multiplied by 1000 to obtain the relative fluorescence units (RFU). A cell DISCO was employed to induce the active (*Z*)-configuration of **102**. The graph depicts the mean (lines) and S.E.M. (shadows); $n = 3$. Adapted from ²¹⁵.

The development of photohormone **102** represented a notable achievement in the creation of a (*Z*)-active isomer for PPAR α , confirming its applicability as a light-activated tool in live-cell fluorescence reporter gene assays. It is, however, important to note that the difference in activity between the (*Z*)- and (*E*)-isomers is approximately 10-fold, with the (*Z*)-isomer showing PPAR α activation only within the low micromolar range. In order to address these limitations, further SAR studies for **102** are required. In this study, the SAR was primarily focused on the lipophilic backbone. Additional optimization strategies could include modifications such as extending or replacing the amide group or incorporating bulkier substituents (e.g., instead of the dimethyl group) in the linker region of the acidic head motif. These have the potential to facilitate the development of a more

potent and efficacious (*Z*)-photohormones, thereby enhancing the utility of this precise, light-controlled modulator of PPAR α activity.

A new class of light-switchable PPAR α agonists by modifying a cinalukast-derived ligand (**84**) with an azobenzene motif was developed. The resulting photohormone (**102**) offers > 10-fold activity difference between (*E*)- and (*Z*)-configurations and efficient photoswitching properties. This novel photohormone can be employed as a tool for precise studies of PPAR α biology, allowing for an investigation of the role and potential of the transcription factor in phenotypic *in vitro* settings. In addition, the spatially resolved activity of potential future light-controlled PPAR α agonist drugs may provide an effective means of overcoming the side effects of PPAR α activation, such as rhabdomyolysis²²⁶ and gallstone formation²²⁷, which are particularly relevant for applications where topical administration is feasible²²⁸. **102**, therefore, has emerged as a valuable addition to previously developed PPAR α modulators and a promising photohormone scaffold for further optimization.

4 Summary

Nuclear receptors (NRs) are ligand-activated transcription factors that belong to a superfamily of 48 human members¹¹. For many decades, these have represented an attractive field of research for drug development, given their involvement in a wide range of physiological (e.g., metabolism, immune response, cell differentiation) and pathological (e.g., cancer, metabolic dysfunction, chronic inflammation, asthma) processes in the human body¹². A growing body of evidence suggests that certain NRs may represent promising molecular targets for the treatment of neurodegenerative diseases². Among them, nuclear receptor related 1 (Nurr1, NR4A2) is expressed predominantly in neurons and in immune cells of the brain^{2,13,14} and plays a pivotal role in the regulation of dopaminergic neuronal development and maintenance, as well as in the modulation of brain inflammatory processes^{2,13,14}. Observations of reduced Nurr1 levels in patients with Alzheimer's disease (AD) and Parkinson's disease (PD)¹⁵⁻¹⁷, as well as in corresponding animal models, suggest that Nurr1 activation may represent a promising approach in the treatment of neurodegenerative diseases^{18,19}. Despite this potential, potent and selective Nurr1 modulators are lacking which impedes comprehensive research on Nurr1's biological roles and therapeutic application^{14,22}.

Like Nurr1, the nuclear retinoid X receptors (RXRs)²³⁻²⁵ and peroxisome proliferator-activated receptors (PPARs) are also involved in several pathologies and linked to neurodegenerative processes. RXRs form heterodimers with many other NRs²³⁻²⁵ including Nurr1 and might offer access to potential treatments for AD and multiple sclerosis (MS), but available RXR ligands suffer from poor pharmacokinetic properties and lack selectivity². PPAR α regulates lipid metabolism and insulin sensitivity^{29,30} in various tissues including the brain. Although there are many PPAR α agonists, understanding of the receptor's role in the CNS remains limited^{31,229}. Current drugs targeting these receptors often have significant side effects, highlighting the need for safer, more selective modulators to fully exploit their therapeutic potential^{2,14,134,214}. The aim of this thesis was to identify new ligands as innovative tools for Nurr1, RXR and PPAR α .

The discovery of the dopamine metabolite 5,6-dihydroxyindole⁷⁴ (DHI, **6**, Figure 49) as an endogenous ligand for Nurr1, along with the validation of the antimalarial drug amodiaquine⁸⁰ (AQ, **1**, Figure 50) as the first synthetic Nurr1 agonist, represents a notable advancement in the field of Nurr1 ligand research. Nevertheless, the high reactivity of DHI, which results in autooxidation and polymerization into neuromelanin, and the lack of specificity of AQ, despite its promising effects and role in early studies on Nurr1 activation, highlight the necessity for more selective and high-quality chemical tools to facilitate confident target validation and further pharmacological research on Nurr1^{2,14,107}.

The initial strategy in this thesis to develop novel Nurr1 agonists was based on the natural ligand DHI. Natural NR ligands have proven as valuable lead structures for drug development as exemplified by glucocorticoids and the FXR agonist obeticholic acid^{216,217}. The analysis of the Nurr1 complex with DHI (PDB: 6dda⁷⁴) revealed that the 5- and 6-positions of the indole are solvent-exposed⁷⁴, thereby offering the possibility of exploring adjacent grooves formed by helices H4/H12 and H10/H11 on the surface of the Nurr1 ligand binding domain (LBD). This suggested the potential for structural modifications of DHI to enhance binding interactions. A prior study on the SAR of DHI suggested a preference for a chlorine substituent at the 5-position of the indole (**7**)¹¹². Therefore, an extension in the 6-position seemed a promising avenue for developing novel Nurr1 agonists. A virtual library was constructed utilizing **7** as the core structure, with an amide linker attached at the 6-position to 14 K commercially available primary amines (molecular weight \leq 240). The amide linkage was selected for its potential to form hydrogen bonds with the His516 backbone nitrogen and the Pro597 backbone carbonyl, as indicated by preliminary docking studies. Subsequently, the virtual library was docked into the DHI-binding site of the Nurr1 LBD, and the top 24 candidates were synthesized on a microscale for testing their biological activity in a Gal4-Nurr1 hybrid reporter gene assay. This screening process identified six compounds with notable Nurr1 agonism. Batch synthesis and further validation of these candidates confirmed direct binding and modulation of Nurr1 for three compounds (**44**, **45**, and **47**). **44** was identified as most potent, exhibiting a binding affinity (K_d) of 0.5 μ M and an EC_{50} value of 3 μ M, which represented a significant improvement in activity compared to the natural ligand DHI ($EC_{50} > 100 \mu$ M) (Figure 49). Notably, **44** also demonstrated reduced toxicity, overcoming the limitations of DHI. Further analysis of the binding mode indicated that **44** formed specific interactions with the Nurr1 LBD, including a critical π -interaction with His516 which likely contributed to the enhanced potency of **44**. *In vitro* profiling also confirmed the cellular target engagement of **44** which induced the Nurr1-regulated and neuroprotective genes TH, VMAT2, SOD1 and SOD2 in astrocytes (T98G cells) and in dopaminergic neurons (N27 cells). These results highlight **44** as validated Nurr1 agonist tool and the potential of structure-guided design in the development of potent Nurr1 agonists.

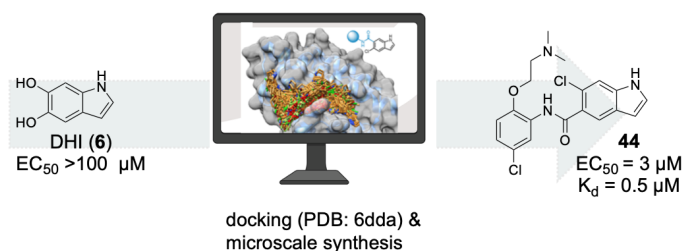


Figure 49. Structure-guided design of Nurr1 agonist **44** derived from DHI.

Based on previous observations indicating that the 7-chloroquinoline-4-amine substructure of AQ and chloroquine is adequate for Nurr1 activation⁸⁰, alternative heterobicycles were investigated for their ability to activate Nurr1. A scaffold hop resulted in 8-chloro-2-methylimidazo[1,2-*a*]pyridin-3-amine (**54**) as a promising fragment-like Nurr1 agonist, with considerable affinity (K_d 2.7 μ M) to the Nurr1 LBD and an EC_{50} value of 7 μ M for Nurr1 activation in a Gal4 hybrid reporter gene assay. Subsequent fragment growth and systematic exploration of substituents in favored positions guided the development of the high-affinity Nurr1 agonist **66** (K_d = 0.17 μ M, EC_{50} = 0.09 μ M, Figure 50) exhibiting strong selectivity for NR4A over other NRs, favorable physicochemical properties and low toxicity. Furthermore, a structurally analogous negative control compound **67** (Figure 50) was identified, which does not bind to Nurr1 and is suitable to complement the agonist **66** in biological studies. **66** efficiently induced Nurr1-regulated genes (TH, VMAT2, SOD2) in T98G cells, whereas **67** had no effect, demonstrating cellular target engagement and supporting the suitability of the pair of **66** and **67** as a chemical tool for *in vitro* experiments on the biology of Nurr1. This was further evidenced in a phenotypic experiment in human midbrain organoids generated from induced pluripotent stem cells (iPSC)²²⁰ bearing a G2019S mutation in the leucine-rich repeat kinase 2 (LRRK2) gene, or without the mutation (wild-type). LRRK2 mutations are among the most common genetic causes of PD^{221,222} giving this model pathological relevance. Accordingly, organoids bearing the mutation displayed diminished expression of Nurr1 and the dopaminergic neuron marker gene TH. Treatment with **66** rescued TH transcript levels in LRRK2 mutant organoids and enhanced the number of TH-positive cells in both mutant and wild-type. The negative control **67** had no effect. These results highlight the potential of Nurr1 activation for PD treatment and validate **66** and **67** as chemical tool. **66** and its structurally matched negative control (**67**) meet the highest chemical tool quality criteria (potency < 100 nM, selectivity for NR4A receptors within NR family > 30-fold, cellular on target activity < 1 μ M, 100-fold less potent control compound, no PAINS elements²²³), making them robust tools for studying Nurr1 modulation and its therapeutic potential. The optimization of AQ fragments and the replacement of unfavorable motifs have led to the development of **66**, which demonstrates notable improvements over the original lead structure AQ, particularly in terms of potency, selectivity and toxicity. These advancements position **66** as a next-generation Nurr1 agonist, offering a superior alternative for investigating Nurr1 as a potential therapeutic target in neurodegenerative diseases.

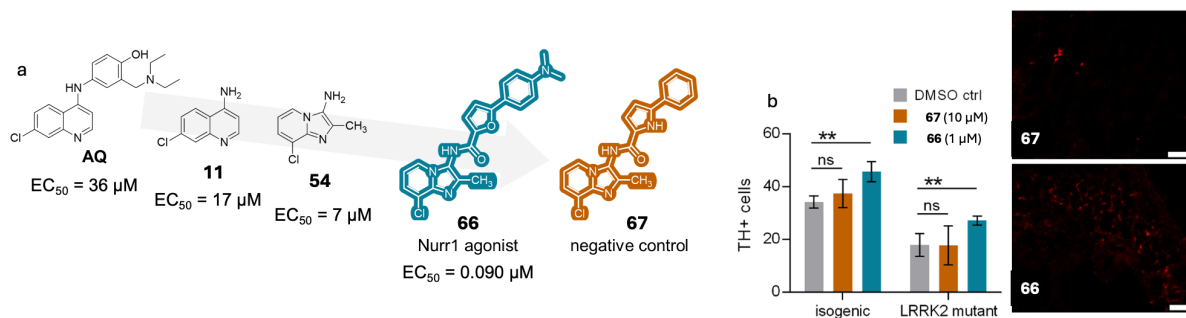


Figure 50. (a) Development of Nurr1 agonist **66** and the matching negative control **67** from AQ by scaffold hopping and fragment growing. (b) **66** rescued tyrosine hydroxylase (TH) expression in LRRK2 mutant midbrain organoids, **67** had no effect.

The dimer partner of Nurr1 RXR has the unique ability to form heterodimers with many NRs and is thus involved in a wide variety of physiological processes²³⁻²⁵. However, the wide transcriptional impact of RXR ligands can also result in considerable adverse effects, such as hypertriglyceridemia, as exemplified by synthetic RXR agonists like bexarotene (**23**)^{134,155}. Selective RXR modulation by ligand-induced recruitment of specific coregulators may be an avenue to address this issue and was explored in this thesis. Coregulators interact with RXR to mediate gene transcription or repression and could potentially have gene-specific effects as well as tissue-specific expression patterns. A homogeneous time-resolved fluorescence (HTRF) assay was used to compare the effects of natural 9cisRA (**22**) and a synthetic agonist **27** for their impact on ligand-induced coregulator recruitment by RXR. While **22** recruited several coactivators (e.g., SRC1, SRC2) with intermediate efficacy, **27** demonstrated a marked preference for recruiting PGC1 α . These findings supported the hypothesis that RXR ligands can be structurally tuned to modulate interactions with specific coregulators. Building on this, the study proceeded to design and synthesize a series of analogues of **27**, with the objective of exploring the impact of structural modifications on coregulator recruitment. A virtual library of 15,000 biphenylacetic acid derivatives was constructed, and the most promising 28 molecules were selected for synthesis based on their docking scores and structural diversity. The general synthesis of these compounds was carried out via a Suzuki reaction followed by alkaline hydrolysis, after which they were tested for RXR activation in Gal4-RXR hybrid reporter gene assay. The most active RXR ligands from this series were further profiled for their effects on the coregulator recruitment to RXR in a HFTR assay. The biological evaluation of **78**, **79** and **80** showed potent RXR agonist activity (EC₅₀ (RXR α / β / γ) = 0.29/1.3/3.4 μM (**78**), 0.060/0.4/0.24 μM (**79**), 0.53/0.55/0.52 μM (**80**)) and robust PGC1 α recruitment with **79** showing considerably higher recruitment efficacy than **80** (Figure 51) and **78** having no affect on PGC1 α binding. Despite their structural similarities and similar potency on RXR in cellular setting, these compounds thus exhibited distinct effects on PGC1 α recruitment, indicating the potential for selective modulation through the fine-tuning of RXR ligands. This may be explained by the predicted

binding mode of these compounds, where **80** extends further towards His435 in helix 11 (H11) compared to **79**. This change in positioning of H11 may influence H12, resulting in changes in the shape and size of the coactivator binding site. As a result, the predicted differences in binding in the His435 region may induce subtle allosteric changes in the coactivator binding site, which could mediate the different effects on PGC1 α recruitment. These findings demonstrated that RXR ligands can be engineered as molecular glues to selectively modulate coregulator interactions, possibly paving the way for tissue-selective RXR activation and more targeted therapeutic strategies.

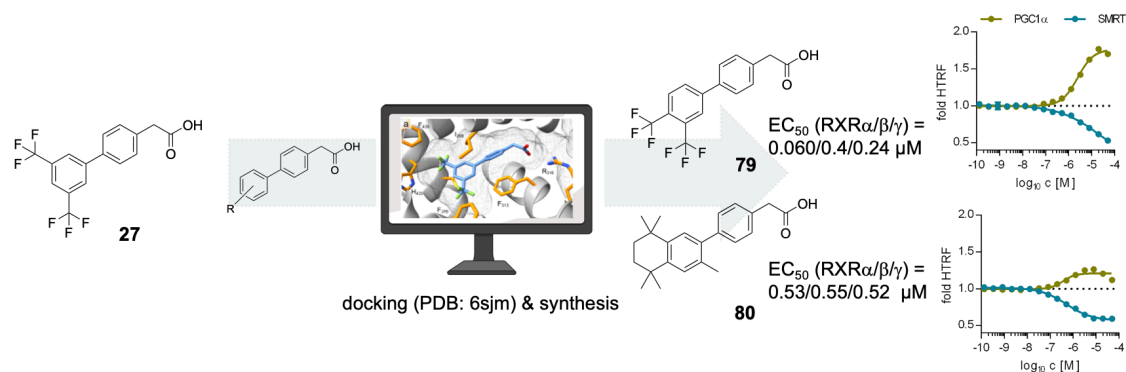


Figure 51. Structure-guided tuning of RXR agonists **79** and **80** derived from **27** for differential PGC1 α recruitment.

Photohormones have emerged as a promising class of tools¹³⁸ enabling an alternative approach to NR modulation. These molecules allow light-dependent control of transcription factors, providing precise spatio-temporal regulation of transcriptional activity^{191,192}. The focus has been on the development of (*Z*)-active photohormones since traditional azobenzenes have struggled to achieve complete photo-switching to 100% (*Z*)-configuration¹⁹¹. Through the introduction of photoswitchable motifs and subsequent optimization of the lipophilic backbone of the cinalukast-derived PPAR α ligand **84**, this thesis aimed to design a novel light-controlled PPAR α ligand that is active in its (*Z*)-configuration. The resulting compound **102** exhibited efficient photo-switching between its (*E*)- and (*Z*)-isomers, with the (*Z*)-isomer showing a markedly enhanced PPAR α agonistic activity in a Gal4 hybrid reporter gene assay. The light-induced (*Z*)-isomer showed high potency ($EC_{50} = 1.5 \mu\text{M}$), whereas the dark-adapted (*E*)-isomer showed reduced activity ($EC_{50} > 20 \mu\text{M}$). The (*Z*)-isomer also had a long thermal relaxation half-life of 28.5 hours and maintained its switching efficiency over multiple cycles without fatigue, making it suitable for further *in vitro* studies. To characterize the efficacy of **102** as a light-activated tool in a cellular environment, a live-cell fluorescence (mCherry) reporter gene assay was performed in HEK293T cells. The results showed that dark-adapted (*E*)-**102** (10 μM) did not induce PPAR α -dependent mCherry expression, whereas light-activated (*Z*)-**102** (10 μM) mediated a continuous increase in reporter expression, confirming its potential as a light-controlled tool. However, it is important to note despite favorable

activity difference between (*E*)- and (*Z*)-**102** and good photophysical properties that the new light-activated photohormone exhibits only moderate potency. To overcome these limitations, further SAR studies on **102** are required to develop more potent and effective (*Z*)-active photohormones, thereby increasing the utility of this precise, light-controlled PPAR α modulator scaffold.

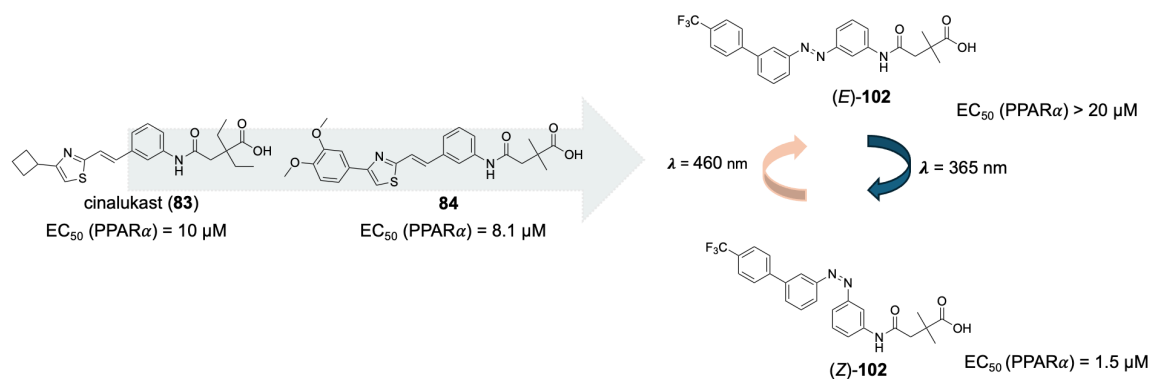


Figure 52. Azobenzene incorporation and SAR optimization of cinalukast for development of photohormone **102**.

This doctoral thesis presents the development of novel ligands for Nurr1, employing two distinct approaches. Firstly, a structure-guided approach was employed, which revealed that the binding site occupied by the natural ligand DHI in Nurr1 is indeed druggable. In addition, established strategies, including scaffold hopping, fragment optimization and the replacement of unfavorable structural elements, were employed for AQ as Nurr1 agonist lead. Both approaches have achieved substantial improvements in Nurr1 agonist development and contribute to advancing this NR as promising target. Particularly compound **66** has been identified as a highly optimized chemical tool, providing considerable scope for further investigation of Nurr1 as a potential therapeutic target in neurodegenerative disease. Furthermore, this thesis emphasizes alternative mechanisms for modulating PPAR and RXR, including selective coregulator recruitment for RXR and the use of photohormones for spatial and temporal control of PPAR activity. Such strategies and the tools optimized in this thesis provide new opportunities to explore the mechanisms and biology of NRs and to assess their potential for innovative therapeutic applications. The findings of this thesis underscore both the opportunities and challenges in developing new NR modulators to harness the full therapeutic potential of these receptors.

5 References

- 1 Steinmetz, J. D. *et al.* Global, regional, and national burden of disorders affecting the nervous system, 1990–2021: a systematic analysis for the Global Burden of Disease Study 2021. *The Lancet Neurology* **23**, 344-381 (2024). [https://doi.org/10.1016/s1474-4422\(24\)00038-3](https://doi.org/10.1016/s1474-4422(24)00038-3)
- 2 Willems, S., Zaienne, D. & Merk, D. Targeting Nuclear Receptors in Neurodegeneration and Neuroinflammation. *J Med Chem* **64**, 9592-9638 (2021). <https://doi.org/10.1021/acs.jmedchem.1c00186>
- 3 Blotenberg, I., Hoffmann, W. & Thyrian, J. R. Dementia in Germany: Epidemiology and Prevention Potential. *Dtsch Arztebl Int* **120**, 470-476 (2023). <https://doi.org/10.3238/arztebl.m2023.0100>
- 4 Heinzl, S. *et al.* Do We Need to Rethink the Epidemiology and Healthcare Utilization of Parkinson's Disease in Germany? *Front Neurol* **9**, 500 (2018). <https://doi.org/10.3389/fneur.2018.00500>
- 5 Livingston, G. *et al.* Dementia prevention, intervention, and care: 2020 report of the Lancet Commission. *The Lancet* **396**, 413-446 (2020). [https://doi.org/10.1016/s0140-6736\(20\)30367-6](https://doi.org/10.1016/s0140-6736(20)30367-6)
- 6 Scheltens, P. *et al.* Alzheimer's disease. *Lancet* **397**, 1577-1590 (2021). [https://doi.org/10.1016/S0140-6736\(20\)32205-4](https://doi.org/10.1016/S0140-6736(20)32205-4)
- 7 Lane, C. A., Hardy, J. & Schott, J. M. Alzheimer's disease. *European Journal of Neurology* **25**, 59-70 (2018). <https://doi.org/10.1111/ene.13439>
- 8 Tolosa, E., Garrido, A., Scholz, S. W. & Poewe, W. Challenges in the diagnosis of Parkinson's disease. *Lancet Neurol* **20**, 385-397 (2021). [https://doi.org/10.1016/S1474-4422\(21\)00030-2](https://doi.org/10.1016/S1474-4422(21)00030-2)
- 9 Bloem, B. R., Okun, M. S. & Klein, C. Parkinson's disease. *The Lancet* **397**, 2284-2303 (2021). [https://doi.org/10.1016/s0140-6736\(21\)00218-x](https://doi.org/10.1016/s0140-6736(21)00218-x)
- 10 Skerrett, R., Malm, T. & Landreth, G. Nuclear receptors in neurodegenerative diseases. *Neurobiol Dis* **72 Pt A**, 104-116 (2014). <https://doi.org/10.1016/j.nbd.2014.05.019>
- 11 Gronemeyer, H., Gustafsson, J. A. & Laudet, V. Principles for modulation of the nuclear receptor superfamily. *Nat Rev Drug Discov* **3**, 950-964 (2004). <https://doi.org/10.1038/nrd1551>
- 12 Weikum, E. R., Liu, X. & Ortlund, E. A. The nuclear receptor superfamily: A structural perspective. *Protein Sci* **27**, 1876-1892 (2018). <https://doi.org/10.1002/pro.3496>
- 13 Law, S. W., Conneely, O. M., DeMayo, F. J. & O'Malley, B. W. Identification of a new brain-specific transcription factor, NURR1. *Mol Endocrinol* **6**, 2129-2135 (1992). <https://doi.org/10.1210/mend.6.12.1491694>
- 14 Willems, S. & Merk, D. Medicinal Chemistry and Chemical Biology of Nurr1 Modulators: An Emerging Strategy in Neurodegeneration. *J Med Chem* **65**, 9548-9563 (2022). <https://doi.org/10.1021/acs.jmedchem.2c00585>
- 15 Liu, H. *et al.* NR4A2 genetic variation and Parkinson's disease: Evidence from a systematic review and meta-analysis. *Neurosci Lett* **650**, 25-32 (2017). <https://doi.org/10.1016/j.neulet.2017.01.062>

- 16 Liu, W., Gao, Y. & Chang, N. Nurr1 overexpression exerts neuroprotective and anti-inflammatory roles via down-regulating CCL2 expression in both in vivo and in vitro Parkinson's disease models. *Biochem Biophys Res Commun* **482**, 1312-1319 (2017). <https://doi.org/10.1016/j.bbrc.2016.12.034>
- 17 Zetterstrom, R. H. *et al.* Dopamine neuron agenesis in Nurr1-deficient mice. *Science* **276**, 248-250 (1997). <https://doi.org/10.1126/science.276.5310.248>
- 18 Decressac, M., Volakakis, N., Bjorklund, A. & Perlmann, T. NURR1 in Parkinson disease--from pathogenesis to therapeutic potential. *Nat Rev Neurol* **9**, 629-636 (2013). <https://doi.org/10.1038/nrneurol.2013.209>
- 19 Kadkhodaei, B. *et al.* Transcription factor Nurr1 maintains fiber integrity and nuclear-encoded mitochondrial gene expression in dopamine neurons. *Proc Natl Acad Sci U S A* **110**, 2360-2365 (2013). <https://doi.org/10.1073/pnas.1221077110>
- 20 Jeon, S. G. *et al.* The Critical Role of Nurr1 as a Mediator and Therapeutic Target in Alzheimer's Disease-related Pathogenesis. *Aging Dis* **11**, 705-724 (2020). <https://doi.org/10.14336/AD.2019.0718>
- 21 Montarolo, F., Martire, S., Perga, S. & Bertolotto, A. NURR1 Impairment in Multiple Sclerosis. *Int J Mol Sci* **20** (2019). <https://doi.org/10.3390/ijms20194858>
- 22 Jakaria, M. *et al.* Molecular Insights into NR4A2(Nurr1): an Emerging Target for Neuroprotective Therapy Against Neuroinflammation and Neuronal Cell Death. *Mol Neurobiol* **56**, 5799-5814 (2019). <https://doi.org/10.1007/s12035-019-1487-4>
- 23 Evans, R. M. & Mangelsdorf, D. J. Nuclear Receptors, RXR, and the Big Bang. *Cell* **157**, 255-266 (2014). <https://doi.org/10.1016/j.cell.2014.03.012>
- 24 Germain, P. *et al.* International Union of Pharmacology. LXIII. Retinoid X receptors. *Pharmacol Rev* **58**, 760-772 (2006). <https://doi.org/10.1124/pr.58.4.7>
- 25 Szanto, A. *et al.* Retinoid X receptors: X-ploring their (patho)physiological functions. *Cell Death Differ* **11 Suppl 2**, S126-143 (2004). <https://doi.org/10.1038/sj.cdd.4401533>
- 26 Cramer, P. E. *et al.* ApoE-directed therapeutics rapidly clear beta-amyloid and reverse deficits in AD mouse models. *Science* **335**, 1503-1506 (2012). <https://doi.org/10.1126/science.1217697>
- 27 Huang, J. K. *et al.* Retinoid X receptor gamma signaling accelerates CNS remyelination. *Nat Neurosci* **14**, 45-53 (2011). <https://doi.org/10.1038/nn.2702>
- 28 Merk, D. Chances and challenges of retinoid X receptor gamma targeting for regenerative multiple sclerosis treatment. *Future Med Chem* **7**, 2411-2413 (2015). <https://doi.org/10.4155/fmc.15.163>
- 29 Michalik, L. *et al.* International Union of Pharmacology. LXI. Peroxisome proliferator-activated receptors. *Pharmacol Rev* **58**, 726-741 (2006). <https://doi.org/10.1124/pr.58.4.5>
- 30 Bougarne, N. *et al.* Molecular Actions of PPARalpha in Lipid Metabolism and Inflammation. *Endocr Rev* **39**, 760-802 (2018). <https://doi.org/10.1210/er.2018-00064>
- 31 Wojtowicz, S., Strosznajder, A. K., Jezyna, M. & Strosznajder, J. B. The Novel Role of PPAR Alpha in the Brain: Promising Target in Therapy of Alzheimer's Disease and Other Neurodegenerative Disorders. *Neurochem Res* **45**, 972-988 (2020). <https://doi.org/10.1007/s11064-020-02993-5>

- 32 Mages, H. W., Rilke, O., Bravo, R., Senger, G. & Kroczeck, R. A. NOT, a human immediate-early response gene closely related to the steroid/thyroid hormone receptor NAK1/TR3. *Mol Endocrinol* **8**, 1583-1591 (1994). <https://doi.org/10.1210/mend.8.11.7877627>
- 33 Okabe, T. *et al.* cDNA cloning of a NGFI-B/nur77-related transcription factor from an apoptotic human T cell line. *J Immunol* **154**, 3871-3879 (1995).
- 34 Scarce, L. M., Laz, T. M., Hazel, T. G., Lau, L. F. & Taub, R. RNR-1, a nuclear receptor in the NGFI-B/Nur77 family that is rapidly induced in regenerating liver. *J Biol Chem* **268**, 8855-8861 (1993).
- 35 Pena de Ortiz, S., Cannon, M. M. & Jamieson, G. A., Jr. Expression of nuclear hormone receptors within the rat hippocampus: identification of novel orphan receptors. *Brain Res Mol Brain Res* **23**, 278-283 (1994). [https://doi.org/10.1016/0169-328x\(94\)90235-6](https://doi.org/10.1016/0169-328x(94)90235-6)
- 36 Milbrandt, J. Nerve growth factor induces a gene homologous to the glucocorticoid receptor gene. *Neuron* **1**, 183-188 (1988). [https://doi.org/10.1016/0896-6273\(88\)90138-9](https://doi.org/10.1016/0896-6273(88)90138-9)
- 37 Hazel, T. G., Nathans, D. & Lau, L. F. A gene inducible by serum growth factors encodes a member of the steroid and thyroid hormone receptor superfamily. *Proc Natl Acad Sci U S A* **85**, 8444-8448 (1988). <https://doi.org/10.1073/pnas.85.22.8444>
- 38 Jiang, L. *et al.* Structural basis of binding of homodimers of the nuclear receptor NR4A2 to selective Nur-responsive DNA elements. *J Biol Chem* **294**, 19795-19803 (2019). <https://doi.org/10.1074/jbc.RA119.010730>
- 39 Wang, Z. *et al.* Structure and function of Nurr1 identifies a class of ligand-independent nuclear receptors. *Nature* **423**, 555-560 (2003). <https://doi.org/10.1038/nature01645>
- 40 Benoit, G. *et al.* International Union of Pharmacology. LXVI. Orphan nuclear receptors. *Pharmacol Rev* **58**, 798-836 (2006). <https://doi.org/10.1124/pr.58.4.10>
- 41 Aranda, A. & Pascual, A. Nuclear hormone receptors and gene expression. *Physiol Rev* **81**, 1269-1304 (2001). <https://doi.org/10.1152/physrev.2001.81.3.1269>
- 42 Anbalagan, M., Huderson, B., Murphy, L. & Rowan, B. G. Post-translational modifications of nuclear receptors and human disease. *Nucl Recept Signal* **10**, e001 (2012). <https://doi.org/10.1621/nrs.10001>
- 43 Nordzell, M., Aarnisalo, P., Benoit, G., Castro, D. S. & Perlmann, T. Defining an N-terminal activation domain of the orphan nuclear receptor Nurr1. *Biochem Biophys Res Commun* **313**, 205-211 (2004). <https://doi.org/10.1016/j.bbrc.2003.11.079>
- 44 Garcia-Yague, A. J. & Cuadrado, A. Mechanisms of NURR1 Regulation: Consequences for Its Biological Activity and Involvement in Pathology. *Int J Mol Sci* **24** (2023). <https://doi.org/10.3390/ijms241512280>
- 45 Saijo, K. *et al.* A Nurr1/CoREST pathway in microglia and astrocytes protects dopaminergic neurons from inflammation-induced death. *Cell* **137**, 47-59 (2009). <https://doi.org/10.1016/j.cell.2009.01.038>

- 46 Germain, P., Staels, B., Dacquet, C., Spedding, M. & Laudet, V. Overview of nomenclature of nuclear receptors. *Pharmacol Rev* **58**, 685-704 (2006). <https://doi.org/10.1124/pr.58.4.2>
- 47 Luisi, B. F. *et al.* Crystallographic analysis of the interaction of the glucocorticoid receptor with DNA. *Nature* **352**, 497-505 (1991). <https://doi.org/10.1038/352497a0>
- 48 Zilliacus, J., Carlstedt-Duke, J., Gustafsson, J. A. & Wright, A. P. Evolution of distinct DNA-binding specificities within the nuclear receptor family of transcription factors. *Proc Natl Acad Sci U S A* **91**, 4175-4179 (1994). <https://doi.org/10.1073/pnas.91.10.4175>
- 49 Umesono, K. & Evans, R. M. Determinants of target gene specificity for steroid/thyroid hormone receptors. *Cell* **57**, 1139-1146 (1989). [https://doi.org/10.1016/0092-8674\(89\)90051-2](https://doi.org/10.1016/0092-8674(89)90051-2)
- 50 Schoenmakers, E. *et al.* Differential DNA binding by the androgen and glucocorticoid receptors involves the second Zn-finger and a C-terminal extension of the DNA-binding domains. *Biochem J* **341 (Pt 3)**, 515-521 (1999).
- 51 Rastinejad, F., Perlmann, T., Evans, R. M. & Sigler, P. B. Structural determinants of nuclear receptor assembly on DNA direct repeats. *Nature* **375**, 203-211 (1995). <https://doi.org/10.1038/375203a0>
- 52 Perlmann, T. & Jansson, L. A novel pathway for vitamin A signaling mediated by RXR heterodimerization with NGFI-B and NURR1. *Genes Dev* **9**, 769-782 (1995). <https://doi.org/10.1101/gad.9.7.769>
- 53 Zetterstrom, R. H., Solomin, L., Mitsiadis, T., Olson, L. & Perlmann, T. Retinoid X receptor heterodimerization and developmental expression distinguish the orphan nuclear receptors NGFI-B, Nurr1, and Nor1. *Mol Endocrinol* **10**, 1656-1666 (1996). <https://doi.org/10.1210/mend.10.12.8961274>
- 54 Maira, M., Martens, C., Philips, A. & Drouin, J. Heterodimerization between members of the Nur subfamily of orphan nuclear receptors as a novel mechanism for gene activation. *Mol Cell Biol* **19**, 7549-7557 (1999). <https://doi.org/10.1128/MCB.19.11.7549>
- 55 Paulsen, R. F., Granas, K., Johnsen, H., Rolseth, V. & Sterri, S. Three related brain nuclear receptors, NGFI-B, Nurr1, and NOR-1, as transcriptional activators. *J Mol Neurosci* **6**, 249-255 (1995). <https://doi.org/10.1007/BF02736784>
- 56 Murphy, E. P. & Conneely, O. M. Neuroendocrine regulation of the hypothalamic pituitary adrenal axis by the nurr1/nur77 subfamily of nuclear receptors. *Mol Endocrinol* **11**, 39-47 (1997). <https://doi.org/10.1210/mend.11.1.9874>
- 57 Pratt, W. B. & Toft, D. O. Steroid receptor interactions with heat shock protein and immunophilin chaperones. *Endocr Rev* **18**, 306-360 (1997). <https://doi.org/10.1210/edrv.18.3.0303>
- 58 Gallastegui, N., Mackinnon, J. A., Fletterick, R. J. & Estebanez-Perpina, E. Advances in our structural understanding of orphan nuclear receptors. *Trends Biochem Sci* **40**, 25-35 (2015). <https://doi.org/10.1016/j.tibs.2014.11.002>
- 59 Bourguet, W., Ruff, M., Chambon, P., Gronemeyer, H. & Moras, D. Crystal structure of the ligand-binding domain of the human nuclear receptor RXR-alpha. *Nature* **375**, 377-382 (1995). <https://doi.org/10.1038/375377a0>

- 60 Wurtz, J. M. *et al.* A canonical structure for the ligand-binding domain of nuclear
receptors. *Nat Struct Biol* **3**, 87-94 (1996). <https://doi.org/10.1038/nsb0196-87>
- 61 Rastinejad, F., Huang, P., Chandra, V. & Khorasanizadeh, S. Understanding nuclear
receptor form and function using structural biology. *J Mol Endocrinol* **51**, T1-T21
(2013). <https://doi.org/10.1530/JME-13-0173>
- 62 Ingraham, H. A. & Redinbo, M. R. Orphan nuclear receptors adopted by
crystallography. *Curr Opin Struct Biol* **15**, 708-715 (2005).
<https://doi.org/10.1016/j.sbi.2005.10.009>
- 63 Baker, K. D. *et al.* The *Drosophila* orphan nuclear receptor DHR38 mediates an
atypical ecdysteroid signaling pathway. *Cell* **113**, 731-742 (2003).
[https://doi.org/10.1016/s0092-8674\(03\)00420-3](https://doi.org/10.1016/s0092-8674(03)00420-3)
- 64 Flaig, R., Greschik, H., Peluso-Iltis, C. & Moras, D. Structural basis for the cell-
specific activities of the NGFI-B and the Nurr1 ligand-binding domain. *J Biol Chem*
280, 19250-19258 (2005). <https://doi.org/10.1074/jbc.M413175200>
- 65 de Vera, I. M. *et al.* Identification of a Binding Site for Unsaturated Fatty Acids in the
Orphan Nuclear Receptor Nurr1. *ACS Chem Biol* **11**, 1795-1799 (2016).
<https://doi.org/10.1021/acscchembio.6b00037>
- 66 Molnar, F., Matilainen, M. & Carlberg, C. Structural determinants of the agonist-
independent association of human peroxisome proliferator-activated receptors
with coactivators. *J Biol Chem* **280**, 26543-26556 (2005).
<https://doi.org/10.1074/jbc.M502463200>
- 67 Davis, A. M., St-Gallay, S. A. & Kleywegt, G. J. Limitations and lessons in the use of
X-ray structural information in drug design. *Drug Discov Today* **13**, 831-841 (2008).
<https://doi.org/10.1016/j.drudis.2008.06.006>
- 68 Zheng, H., Hou, J., Zimmerman, M. D., Wlodawer, A. & Minor, W. The future of
crystallography in drug discovery. *Expert Opin Drug Discov* **9**, 125-137 (2014).
<https://doi.org/10.1517/17460441.2014.872623>
- 69 Galleguillos, D. *et al.* PIASgamma represses the transcriptional activation induced
by the nuclear receptor Nurr1. *J Biol Chem* **279**, 2005-2011 (2004).
<https://doi.org/10.1074/jbc.M308113200>
- 70 Willems, S. *et al.* The orphan nuclear receptor Nurr1 is responsive to non-steroidal
anti-inflammatory drugs. *Commun Chem* **3**, 85 (2020).
<https://doi.org/10.1038/s42004-020-0331-0>
- 71 Yi, S. H. *et al.* Foxa2 acts as a co-activator potentiating expression of the Nurr1-
induced DA phenotype via epigenetic regulation. *Development* **141**, 761-772
(2014). <https://doi.org/10.1242/dev.095802>
- 72 Zetterstrom, R. H., Williams, R., Perlmann, T. & Olson, L. Cellular expression of the
immediate early transcription factors Nurr1 and NGFI-B suggests a gene
regulatory role in several brain regions including the nigrostriatal dopamine
system. *Brain Res Mol Brain Res* **41**, 111-120 (1996). [https://doi.org/10.1016/0169-328x\(96\)00074-5](https://doi.org/10.1016/0169-328x(96)00074-5)
- 73 Saucedo-Cardenas, O. & Conneely, O. M. Comparative distribution of NURR1 and
NUR77 nuclear receptors in the mouse central nervous system. *J Mol Neurosci* **7**,
51-63 (1996). <https://doi.org/10.1007/BF02736848>

- 74 Bruning, J. M. *et al.* Covalent Modification and Regulation of the Nuclear Receptor Nurr1 by a Dopamine Metabolite. *Cell Chem Biol* **26**, 674-685 e676 (2019). <https://doi.org/10.1016/j.chembiol.2019.02.002>
- 75 Wallen, A. A. *et al.* Orphan nuclear receptor Nurr1 is essential for Ret expression in midbrain dopamine neurons and in the brain stem. *Mol Cell Neurosci* **18**, 649-663 (2001). <https://doi.org/10.1006/mcne.2001.1057>
- 76 Chu, Y. *et al.* Nurr1 in Parkinson's disease and related disorders. *J Comp Neurol* **494**, 495-514 (2006). <https://doi.org/10.1002/cne.20828>
- 77 Jang, Y., Kim, W., Leblanc, P., Kim, C. H. & Kim, K. S. Potent synthetic and endogenous ligands for the adopted orphan nuclear receptor Nurr1. *Exp Mol Med* **53**, 19-29 (2021). <https://doi.org/10.1038/s12276-021-00555-5>
- 78 Chu, Y., Kompoliti, K., Cochran, E. J., Mufson, E. J. & Kordower, J. H. Age-related decreases in Nurr1 immunoreactivity in the human substantia nigra. *J Comp Neurol* **450**, 203-214 (2002). <https://doi.org/10.1002/cne.10261>
- 79 Le, W. D. *et al.* Mutations in NR4A2 associated with familial Parkinson disease. *Nat Genet* **33**, 85-89 (2003). <https://doi.org/10.1038/ng1066>
- 80 Kim, C. H. *et al.* Nuclear receptor Nurr1 agonists enhance its dual functions and improve behavioral deficits in an animal model of Parkinson's disease. *Proc Natl Acad Sci U S A* **112**, 8756-8761 (2015). <https://doi.org/10.1073/pnas.1509742112>
- 81 Hedy, S. A., Safar, M. M. & Bahgat, A. K. Hydroxychloroquine antiparkinsonian potential: Nurr1 modulation versus autophagy inhibition. *Behav Brain Res* **365**, 82-88 (2019). <https://doi.org/10.1016/j.bbr.2019.02.033>
- 82 von Wrangel, C., Schwabe, K., John, N., Krauss, J. K. & Alam, M. The rotenone-induced rat model of Parkinson's disease: behavioral and electrophysiological findings. *Behav Brain Res* **279**, 52-61 (2015). <https://doi.org/10.1016/j.bbr.2014.11.002>
- 83 Rajan, S. *et al.* PGE1 and PGA1 bind to Nurr1 and activate its transcriptional function. *Nat Chem Biol* **16**, 876-886 (2020). <https://doi.org/10.1038/s41589-020-0553-6>
- 84 Moon, M. *et al.* Correlation between orphan nuclear receptor Nurr1 expression and amyloid deposition in 5XFAD mice, an animal model of Alzheimer's disease. *J Neurochem* **132**, 254-262 (2015). <https://doi.org/10.1111/jnc.12935>
- 85 Forner, S. *et al.* Systematic phenotyping and characterization of the 5xFAD mouse model of Alzheimer's disease. *Sci Data* **8**, 270 (2021). <https://doi.org/10.1038/s41597-021-01054-y>
- 86 Moon, M. *et al.* Ghrelin ameliorates cognitive dysfunction and neurodegeneration in intrahippocampal amyloid-beta1-42 oligomer-injected mice. *J Alzheimers Dis* **23**, 147-159 (2011). <https://doi.org/10.3233/JAD-2010-101263>
- 87 Terzioglu-Usak, S., Negis, Y., Karabulut, D. S., Zaim, M. & Isik, S. Cellular Model of Alzheimer's Disease: Aβ1-42 Peptide Induces Amyloid Deposition and a Decrease in Topo Isomerase IIβ and Nurr1 Expression. *Curr Alzheimer Res* **14**, 636-644 (2017). <https://doi.org/10.2174/1567205014666170117103217>
- 88 Heneka, M. T. *et al.* Neuroinflammation in Alzheimer's disease. *Lancet Neurol* **14**, 388-405 (2015). [https://doi.org/10.1016/S1474-4422\(15\)70016-5](https://doi.org/10.1016/S1474-4422(15)70016-5)

- 89 Colon-Cesario, W. I. *et al.* Knockdown of Nurr1 in the rat hippocampus: implications to spatial discrimination learning and memory. *Learn Mem* **13**, 734-744 (2006). <https://doi.org/10.1101/lm.407706>
- 90 Pena de Ortiz, S., Maldonado-Vlaar, C. S. & Carrasquillo, Y. Hippocampal expression of the orphan nuclear receptor gene hzf-3/nurr1 during spatial discrimination learning. *Neurobiol Learn Mem* **74**, 161-178 (2000). <https://doi.org/10.1006/nlme.1999.3952>
- 91 McNulty, S. E. *et al.* Differential roles for Nr4a1 and Nr4a2 in object location vs. object recognition long-term memory. *Learn Mem* **19**, 588-592 (2012). <https://doi.org/10.1101/lm.026385.112>
- 92 Rojas, P., Joodmardi, E., Hong, Y., Perlmann, T. & Ogren, S. O. Adult mice with reduced Nurr1 expression: an animal model for schizophrenia. *Mol Psychiatry* **12**, 756-766 (2007). <https://doi.org/10.1038/sj.mp.4001993>
- 93 Hawk, J. D. *et al.* NR4A nuclear receptors support memory enhancement by histone deacetylase inhibitors. *J Clin Invest* **122**, 3593-3602 (2012). <https://doi.org/10.1172/JCI64145>
- 94 Pittenger, C. *et al.* Reversible inhibition of CREB/ATF transcription factors in region CA1 of the dorsal hippocampus disrupts hippocampus-dependent spatial memory. *Neuron* **34**, 447-462 (2002). [https://doi.org/10.1016/s0896-6273\(02\)00684-0](https://doi.org/10.1016/s0896-6273(02)00684-0)
- 95 Josselyn, S. A. & Nguyen, P. V. CREB, synapses and memory disorders: past progress and future challenges. *Curr Drug Targets CNS Neurol Disord* **4**, 481-497 (2005). <https://doi.org/10.2174/156800705774322058>
- 96 Ryan, M. M., Mason-Parker, S. E., Tate, W. P., Abraham, W. C. & Williams, J. M. Rapidly induced gene networks following induction of long-term potentiation at perforant path synapses in vivo. *Hippocampus* **21**, 541-553 (2011). <https://doi.org/10.1002/hipo.20770>
- 97 Clarke, S. E. *et al.* Effect of intermittent preventive treatment of malaria on health and education in schoolchildren: a cluster-randomised, double-blind, placebo-controlled trial. *Lancet* **372**, 127-138 (2008). [https://doi.org/10.1016/S0140-6736\(08\)61034-X](https://doi.org/10.1016/S0140-6736(08)61034-X)
- 98 Moon, M. *et al.* Nurr1 (NR4A2) regulates Alzheimer's disease-related pathogenesis and cognitive function in the 5XFAD mouse model. *Aging Cell* **18**, e12866 (2019). <https://doi.org/10.1111/accel.12866>
- 99 Frohman, E. M., Racke, M. K. & Raine, C. S. Multiple sclerosis--the plaque and its pathogenesis. *N Engl J Med* **354**, 942-955 (2006). <https://doi.org/10.1056/NEJMra052130>
- 100 Compston, A. & Coles, A. Multiple sclerosis. *Lancet* **372**, 1502-1517 (2008). [https://doi.org/10.1016/S0140-6736\(08\)61620-7](https://doi.org/10.1016/S0140-6736(08)61620-7)
- 101 International Multiple Sclerosis Genetics, C. *et al.* Analysis of immune-related loci identifies 48 new susceptibility variants for multiple sclerosis. *Nat Genet* **45**, 1353-1360 (2013). <https://doi.org/10.1038/ng.2770>
- 102 Achiron, A. *et al.* Microarray analysis identifies altered regulation of nuclear receptor family members in the pre-disease state of multiple sclerosis. *Neurobiol Dis* **38**, 201-209 (2010). <https://doi.org/10.1016/j.nbd.2009.12.029>

- 103 Gilli, F. *et al.* Loss of braking signals during inflammation: a factor affecting the development and disease course of multiple sclerosis. *Arch Neurol* **68**, 879-888 (2011). <https://doi.org/10.1001/archneurol.2011.32>
- 104 Constantinescu, C. S., Farooqi, N., O'Brien, K. & Gran, B. Experimental autoimmune encephalomyelitis (EAE) as a model for multiple sclerosis (MS). *Br J Pharmacol* **164**, 1079-1106 (2011). <https://doi.org/10.1111/j.1476-5381.2011.01302.x>
- 105 Montarolo, F., Perga, S., Martire, S. & Bertolotto, A. Nurr1 reduction influences the onset of chronic EAE in mice. *Inflamm Res* **64**, 841-844 (2015). <https://doi.org/10.1007/s00011-015-0871-4>
- 106 Montarolo, F. *et al.* Effects of isoxazolo-pyridinone 7e, a potent activator of the Nurr1 signaling pathway, on experimental autoimmune encephalomyelitis in mice. *PLoS One* **9**, e108791 (2014). <https://doi.org/10.1371/journal.pone.0108791>
- 107 Munoz-Tello, P. *et al.* Assessment of NR4A Ligands That Directly Bind and Modulate the Orphan Nuclear Receptor Nurr1. *J Med Chem* **63**, 15639-15654 (2020). <https://doi.org/10.1021/acs.jmedchem.0c00894>
- 108 Saini, A., Mahajan, S. & Gupta, P. Nuclear receptor expression atlas in BMDCs: Nr4a2 restricts immunogenicity of BMDCs and impedes EAE. *Eur J Immunol* **46**, 1842-1853 (2016). <https://doi.org/10.1002/eji.201546229>
- 109 Raveney, B. J., Oki, S. & Yamamura, T. Nuclear receptor NR4A2 orchestrates Th17 cell-mediated autoimmune inflammation via IL-21 signalling. *PLoS One* **8**, e56595 (2013). <https://doi.org/10.1371/journal.pone.0056595>
- 110 Vinayavekhin, N. & Saghatelian, A. Discovery of a protein-metabolite interaction between unsaturated fatty acids and the nuclear receptor Nur77 using a metabolomics approach. *J Am Chem Soc* **133**, 17168-17171 (2011). <https://doi.org/10.1021/ja208199h>
- 111 de Vera, I. M. S. *et al.* Defining a Canonical Ligand-Binding Pocket in the Orphan Nuclear Receptor Nurr1. *Structure* **27**, 66-77 e65 (2019). <https://doi.org/10.1016/j.str.2018.10.002>
- 112 Kholodar, S. A. *et al.* Analogs of the Dopamine Metabolite 5,6-Dihydroxyindole Bind Directly to and Activate the Nuclear Receptor Nurr1. *ACS Chem Biol* **16**, 1159-1163 (2021). <https://doi.org/10.1021/acscchembio.1c00326>
- 113 Willems, S., Ohrndorf, J., Kilu, W., Heering, J. & Merk, D. Fragment-like Chloroquinolineamines Activate the Orphan Nuclear Receptor Nurr1 and Elucidate Activation Mechanisms. *J Med Chem* **64**, 2659-2668 (2021). <https://doi.org/10.1021/acs.jmedchem.0c01779>
- 114 Willems, S. *et al.* Scaffold Hopping from Amodiaquine to Novel Nurr1 Agonist Chemotypes via Microscale Analogue Libraries. *ChemMedChem* **17**, e202200026 (2022). <https://doi.org/10.1002/cmdc.202200026>
- 115 Kim, W. *et al.* An optimized Nurr1 agonist provides disease-modifying effects in Parkinson's disease models. *Nat Commun* **14**, 4283 (2023). <https://doi.org/10.1038/s41467-023-39970-9>
- 116 Vietor, J. *et al.* Development of a Potent Nurr1 Agonist Tool for In Vivo Applications. *J Med Chem* **66**, 6391-6402 (2023). <https://doi.org/10.1021/acs.jmedchem.3c00415>

- 117 Dubois, C., Hengerer, B. & Mattes, H. Identification of a potent agonist of the orphan nuclear receptor Nurr1. *ChemMedChem* **1**, 955-958 (2006). <https://doi.org/10.1002/cmdc.200600078>
- 118 Hammond, S. L. *et al.* The Nurr1 Ligand, 1,1-bis(3'-Indolyl)-1-(p-Chlorophenyl)Methane, Modulates Glial Reactivity and Is Neuroprotective in MPTP-Induced Parkinsonism. *J Pharmacol Exp Ther* **365**, 636-651 (2018). <https://doi.org/10.1124/jpet.117.246389>
- 119 Hintermann, S. *et al.* Identification of a series of highly potent activators of the Nurr1 signaling pathway. *Bioorg Med Chem Lett* **17**, 193-196 (2007). <https://doi.org/10.1016/j.bmcl.2006.09.062>
- 120 Lesuisse, D. *et al.* Development of a novel NURR1/NOT agonist from hit to lead and candidate for the potential treatment of Parkinson's disease. *Bioorg Med Chem Lett* **29**, 929-932 (2019). <https://doi.org/10.1016/j.bmcl.2019.01.024>
- 121 Yu, X., Shang, J. & Kojetin, D. J. Molecular basis of ligand-dependent Nurr1-RXR α activation. *Elife* **12** (2023). <https://doi.org/10.7554/eLife.85039>
- 122 Spathis, A. D. *et al.* Nurr1:RXR α heterodimer activation as monotherapy for Parkinson's disease. *Proc Natl Acad Sci U S A* **114**, 3999-4004 (2017). <https://doi.org/10.1073/pnas.1616874114>
- 123 Morita, K. *et al.* Selective allosteric ligand activation of the retinoid X receptor heterodimers of NGFI-B and Nurr1. *Biochem Pharmacol* **71**, 98-107 (2005). <https://doi.org/10.1016/j.bcp.2005.10.017>
- 124 Wallen-Mackenzie, A. *et al.* Nurr1-RXR heterodimers mediate RXR ligand-induced signaling in neuronal cells. *Genes Dev* **17**, 3036-3047 (2003). <https://doi.org/10.1101/gad.276003>
- 125 Kim, K. S. *et al.* Orphan nuclear receptor Nurr1 directly transactivates the promoter activity of the tyrosine hydroxylase gene in a cell-specific manner. *J Neurochem* **85**, 622-634 (2003). <https://doi.org/10.1046/j.1471-4159.2003.01671.x>
- 126 Aarnisalo, P., Kim, C. H., Lee, J. W. & Perlmann, T. Defining requirements for heterodimerization between the retinoid X receptor and the orphan nuclear receptor Nurr1. *J Biol Chem* **277**, 35118-35123 (2002). <https://doi.org/10.1074/jbc.M201707200>
- 127 Giner, X. C., Cotnoir-White, D., Mader, S. & Levesque, D. Selective ligand activity at Nur/retinoid X receptor complexes revealed by dimer-specific bioluminescence resonance energy transfer-based sensors. *FASEB J* **29**, 4256-4267 (2015). <https://doi.org/10.1096/fj.14-259804>
- 128 Scheepstra, M. *et al.* Ligand Dependent Switch from RXR Homo- to RXR-NURR1 Heterodimerization. *ACS Chem Neurosci* **8**, 2065-2077 (2017). <https://doi.org/10.1021/acschemneuro.7b00216>
- 129 Mangelsdorf, D. J., Ong, E. S., Dyck, J. A. & Evans, R. M. Nuclear receptor that identifies a novel retinoic acid response pathway. *Nature* **345**, 224-229 (1990). <https://doi.org/10.1038/345224a0>
- 130 Brtko, J. & Dvorak, Z. Natural and synthetic retinoid X receptor ligands and their role in selected nuclear receptor action. *Biochimie* **179**, 157-168 (2020). <https://doi.org/10.1016/j.biochi.2020.09.027>

- 131 Dawson, M. I. & Xia, Z. The retinoid X receptors and their ligands. *Biochim Biophys Acta* **1821**, 21-56 (2012). <https://doi.org/10.1016/j.bbaliip.2011.09.014>
- 132 de Lera, A. R., Bourguet, W., Altucci, L. & Gronemeyer, H. Design of selective nuclear receptor modulators: RAR and RXR as a case study. *Nat Rev Drug Discov* **6**, 811-820 (2007). <https://doi.org/10.1038/nrd2398>
- 133 Dominguez, M., Alvarez, S. & de Lera, A. R. Natural and Structure-based RXR Ligand Scaffolds and Their Functions. *Curr Top Med Chem* **17**, 631-662 (2017). <https://doi.org/10.2174/1568026616666160617072521>
- 134 Schierle, S. & Merk, D. Therapeutic modulation of retinoid X receptors - SAR and therapeutic potential of RXR ligands and recent patents. *Expert Opin Ther Pat* **29**, 605-621 (2019). <https://doi.org/10.1080/13543776.2019.1643322>
- 135 Mangelsdorf, D. J. & Evans, R. M. The RXR heterodimers and orphan receptors. *Cell* **83**, 841-850 (1995). [https://doi.org/10.1016/0092-8674\(95\)90200-7](https://doi.org/10.1016/0092-8674(95)90200-7)
- 136 Zetterstrom, R. H. *et al.* Role of retinoids in the CNS: differential expression of retinoid binding proteins and receptors and evidence for presence of retinoic acid. *Eur J Neurosci* **11**, 407-416 (1999). <https://doi.org/10.1046/j.1460-9568.1999.00444.x>
- 137 Moreno, S., Farioli-Vecchioli, S. & Ceru, M. P. Immunolocalization of peroxisome proliferator-activated receptors and retinoid X receptors in the adult rat CNS. *Neuroscience* **123**, 131-145 (2004). <https://doi.org/10.1016/j.neuroscience.2003.08.064>
- 138 Willems, S., Morstein, J., Hinnah, K., Trauner, D. & Merk, D. A Photohormone for Light-Dependent Control of PPARalpha in Live Cells. *J Med Chem* **64**, 10393-10402 (2021). <https://doi.org/10.1021/acs.jmedchem.1c00810>
- 139 Koster, K. P. *et al.* Rexinoids as Therapeutics for Alzheimer's Disease: Role of APOE. *Curr Top Med Chem* **17**, 708-720 (2017). <https://doi.org/10.2174/1568026616666160617090227>
- 140 Koldamova, R., Fitz, N. F. & Lefterov, I. ATP-binding cassette transporter A1: from metabolism to neurodegeneration. *Neurobiol Dis* **72 Pt A**, 13-21 (2014). <https://doi.org/10.1016/j.nbd.2014.05.007>
- 141 Oram, J. F. & Vaughan, A. M. ATP-Binding cassette cholesterol transporters and cardiovascular disease. *Circ Res* **99**, 1031-1043 (2006). <https://doi.org/10.1161/01.RES.0000250171.54048.5c>
- 142 Rudajev, V. & Novotny, J. Cholesterol as a key player in amyloid beta-mediated toxicity in Alzheimer's disease. *Front Mol Neurosci* **15**, 937056 (2022). <https://doi.org/10.3389/fnmol.2022.937056>
- 143 Xiong, H. *et al.* Cholesterol retention in Alzheimer's brain is responsible for high beta- and gamma-secretase activities and Abeta production. *Neurobiol Dis* **29**, 422-437 (2008). <https://doi.org/10.1016/j.nbd.2007.10.005>
- 144 Tai, L. M. *et al.* Soluble apoE/Abeta complex: mechanism and therapeutic target for APOE4-induced AD risk. *Mol Neurodegener* **9**, 2 (2014). <https://doi.org/10.1186/1750-1326-9-2>
- 145 Cummings, J. L. *et al.* Double-blind, placebo-controlled, proof-of-concept trial of bexarotene in moderate Alzheimer's disease. *Alzheimers Res Ther* **8**, 4 (2016). <https://doi.org/10.1186/s13195-016-0173-2>

- 146 Pombo, P. M., Baretino, D., Ibarrola, N., Vega, S. & Rodriguez-Pena, A. Stimulation of the myelin basic protein gene expression by 9-cis-retinoic acid and thyroid hormone: activation in the context of its native promoter. *Brain Res Mol Brain Res* **64**, 92-100 (1999). [https://doi.org/10.1016/s0169-328x\(98\)00311-8](https://doi.org/10.1016/s0169-328x(98)00311-8)
- 147 Natrajan, M. S. *et al.* Retinoid X receptor activation reverses age-related deficiencies in myelin debris phagocytosis and remyelination. *Brain* **138**, 3581-3597 (2015). <https://doi.org/10.1093/brain/awv289>
- 148 Heyman, R. A. *et al.* 9-cis retinoic acid is a high affinity ligand for the retinoid X receptor. *Cell* **68**, 397-406 (1992). [https://doi.org/10.1016/0092-8674\(92\)90479-v](https://doi.org/10.1016/0092-8674(92)90479-v)
- 149 Levin, A. A. *et al.* 9-cis retinoic acid stereoisomer binds and activates the nuclear receptor RXR alpha. *Nature* **355**, 359-361 (1992). <https://doi.org/10.1038/355359a0>
- 150 Mangelsdorf, D. J. *et al.* A direct repeat in the cellular retinol-binding protein type II gene confers differential regulation by RXR and RAR. *Cell* **66**, 555-561 (1991). [https://doi.org/10.1016/0092-8674\(81\)90018-0](https://doi.org/10.1016/0092-8674(81)90018-0)
- 151 Fitzgerald, P., Teng, M., Chandraratna, R. A., Heyman, R. A. & Allegretto, E. A. Retinoic acid receptor alpha expression correlates with retinoid-induced growth inhibition of human breast cancer cells regardless of estrogen receptor status. *Cancer Res* **57**, 2642-2650 (1997).
- 152 Ruhl, R. *et al.* 9-cis-13,14-Dihydroretinoic Acid Is an Endogenous Retinoid Acting as RXR Ligand in Mice. *PLoS Genet* **11**, e1005213 (2015). <https://doi.org/10.1371/journal.pgen.1005213>
- 153 Merk, D., Grisoni, F., Friedrich, L., Gelzinyte, E. & Schneider, G. Computer-Assisted Discovery of Retinoid X Receptor Modulating Natural Products and Isofunctional Mimetics. *J Med Chem* **61**, 5442-5447 (2018). <https://doi.org/10.1021/acs.jmedchem.8b00494>
- 154 Boehm, M. F. *et al.* Synthesis and structure-activity relationships of novel retinoid X receptor-selective retinoids. *J Med Chem* **37**, 2930-2941 (1994). <https://doi.org/10.1021/jm00044a014>
- 155 Pollinger, J. *et al.* Tuning Nuclear Receptor Selectivity of Wy14,643 towards Selective Retinoid X Receptor Modulation. *J Med Chem* **62**, 2112-2126 (2019). <https://doi.org/10.1021/acs.jmedchem.8b01848>
- 156 Merk, D., Grisoni, F., Friedrich, L., Gelzinyte, E. & Schneider, G. Scaffold hopping from synthetic RXR modulators by virtual screening and de novo design. *Medchemcomm* **9**, 1289-1292 (2018). <https://doi.org/10.1039/c8md00134k>
- 157 Pollinger, J. *et al.* A Novel Biphenyl-based Chemotype of Retinoid X Receptor Ligands Enables Subtype and Heterodimer Preferences. *ACS Med Chem Lett* **10**, 1346-1352 (2019). <https://doi.org/10.1021/acsmedchemlett.9b00306>
- 158 Issemann, I. & Green, S. Activation of a member of the steroid hormone receptor superfamily by peroxisome proliferators. *Nature* **347**, 645-650 (1990). <https://doi.org/10.1038/347645a0>
- 159 Dreyer, C. *et al.* Control of the peroxisomal beta-oxidation pathway by a novel family of nuclear hormone receptors. *Cell* **68**, 879-887 (1992). [https://doi.org/10.1016/0092-8674\(92\)90031-7](https://doi.org/10.1016/0092-8674(92)90031-7)

- 160 Kliewer, S. A. *et al.* Differential expression and activation of a family of murine peroxisome proliferator-activated receptors. *Proc Natl Acad Sci U S A* **91**, 7355-7359 (1994). <https://doi.org/10.1073/pnas.91.15.7355>
- 161 Schoonjans, K., Staels, B. & Auwerx, J. Role of the peroxisome proliferator-activated receptor (PPAR) in mediating the effects of fibrates and fatty acids on gene expression. *J Lipid Res* **37**, 907-925 (1996).
- 162 Kamata, S. *et al.* PPARAlpha Ligand-Binding Domain Structures with Endogenous Fatty Acids and Fibrates. *iScience* **23**, 101727 (2020). <https://doi.org/10.1016/j.isci.2020.101727>
- 163 Lin, Q., Ruuska, S. E., Shaw, N. S., Dong, D. & Noy, N. Ligand selectivity of the peroxisome proliferator-activated receptor alpha. *Biochemistry* **38**, 185-190 (1999). <https://doi.org/10.1021/bi9816094>
- 164 Xu, H. E. *et al.* Structural determinants of ligand binding selectivity between the peroxisome proliferator-activated receptors. *Proc Natl Acad Sci U S A* **98**, 13919-13924 (2001). <https://doi.org/10.1073/pnas.241410198>
- 165 Kersten, S. *et al.* Peroxisome proliferator-activated receptor alpha mediates the adaptive response to fasting. *J Clin Invest* **103**, 1489-1498 (1999). <https://doi.org/10.1172/JCI6223>
- 166 Reddy, J. K. & Hashimoto, T. Peroxisomal beta-oxidation and peroxisome proliferator-activated receptor alpha: an adaptive metabolic system. *Annu Rev Nutr* **21**, 193-230 (2001). <https://doi.org/10.1146/annurev.nutr.21.1.193>
- 167 Fruchart, J. C., Duriez, P. & Staels, B. Peroxisome proliferator-activated receptor-alpha activators regulate genes governing lipoprotein metabolism, vascular inflammation and atherosclerosis. *Curr Opin Lipidol* **10**, 245-257 (1999). <https://doi.org/10.1097/00041433-199906000-00007>
- 168 Berger, J. P., Akiyama, T. E. & Meinke, P. T. PPARs: therapeutic targets for metabolic disease. *Trends Pharmacol Sci* **26**, 244-251 (2005). <https://doi.org/10.1016/j.tips.2005.03.003>
- 169 Goldenberg, I., Benderly, M. & Goldbourt, U. Update on the use of fibrates: focus on bezafibrate. *Vasc Health Risk Manag* **4**, 131-141 (2008). <https://doi.org/10.2147/vhrm.2008.04.01.131>
- 170 Karr, S. Epidemiology and management of hyperlipidemia. *Am J Manag Care* **23**, S139-S148 (2017).
- 171 Warden, A. *et al.* Localization of PPAR isotypes in the adult mouse and human brain. *Sci Rep* **6**, 27618 (2016). <https://doi.org/10.1038/srep27618>
- 172 Roy, A. *et al.* Regulation of cyclic AMP response element binding and hippocampal plasticity-related genes by peroxisome proliferator-activated receptor alpha. *Cell Rep* **4**, 724-737 (2013). <https://doi.org/10.1016/j.celrep.2013.07.028>
- 173 Corbett, G. T., Gonzalez, F. J. & Pahan, K. Activation of peroxisome proliferator-activated receptor alpha stimulates ADAM10-mediated proteolysis of APP. *Proc Natl Acad Sci U S A* **112**, 8445-8450 (2015). <https://doi.org/10.1073/pnas.1504890112>
- 174 Wenz, T. Mitochondria and PGC-1alpha in Aging and Age-Associated Diseases. *J Aging Res* **2011**, 810619 (2011). <https://doi.org/10.4061/2011/810619>

- 175 M. Schmuth, S. D. Nukleäre Hormonrezeptoren: Perspektiven der Dermatotherapie* Nuclear Hormone Receptors: Perspectives for Dermatotherapy. *Aktuelle Dermatologie* **38(03)**, 80-84 (2012). <https://doi.org/10.1055/s-0031-1291554>
- 176 Michalik, L. *et al.* Impaired skin wound healing in peroxisome proliferator-activated receptor (PPAR)alpha and PPARbeta mutant mice. *J Cell Biol* **154**, 799-814 (2001). <https://doi.org/10.1083/jcb.200011148>
- 177 Rivier, M. *et al.* Differential expression of peroxisome proliferator-activated receptor subtypes during the differentiation of human keratinocytes. *J Invest Dermatol* **111**, 1116-1121 (1998). <https://doi.org/10.1046/j.1523-1747.1998.00439.x>
- 178 Komuves, L. G. *et al.* Stimulation of PPARalpha promotes epidermal keratinocyte differentiation in vivo. *J Invest Dermatol* **115**, 353-360 (2000). <https://doi.org/10.1046/j.1523-1747.2000.00073.x>
- 179 Schmuth, M. *et al.* Role of peroxisome proliferator-activated receptor alpha in epidermal development in utero. *J Invest Dermatol* **119**, 1298-1303 (2002). <https://doi.org/10.1046/j.1523-1747.2002.19605.x>
- 180 Dubrac, S. & Schmuth, M. PPAR-alpha in cutaneous inflammation. *Dermatoendocrinol* **3**, 23-26 (2011). <https://doi.org/10.4161/derm.3.1.14615>
- 181 Dubrac, S. *et al.* Peroxisome proliferator-activated receptor-alpha activation inhibits Langerhans cell function. *J Immunol* **178**, 4362-4372 (2007). <https://doi.org/10.4049/jimmunol.178.7.4362>
- 182 Hatano, Y. *et al.* Murine atopic dermatitis responds to peroxisome proliferator-activated receptors alpha and beta/delta (but not gamma) and liver X receptor activators. *J Allergy Clin Immunol* **125**, 160-169 e161-165 (2010). <https://doi.org/10.1016/j.jaci.2009.06.049>
- 183 Sheu, M. Y. *et al.* Topical peroxisome proliferator activated receptor-alpha activators reduce inflammation in irritant and allergic contact dermatitis models. *J Invest Dermatol* **118**, 94-101 (2002). <https://doi.org/10.1046/j.0022-202x.2001.01626.x>
- 184 Staumont-Salle, D. *et al.* Peroxisome proliferator-activated receptor alpha regulates skin inflammation and humoral response in atopic dermatitis. *J Allergy Clin Immunol* **121**, 962-968 e966 (2008). <https://doi.org/10.1016/j.jaci.2007.12.1165>
- 185 Kippenberger, S. *et al.* Activators of peroxisome proliferator-activated receptors protect human skin from ultraviolet-B-light-induced inflammation. *J Invest Dermatol* **117**, 1430-1436 (2001). <https://doi.org/10.1046/j.0022-202x.2001.01537.x>
- 186 Kersten, S., Desvergne, B. & Wahli, W. Roles of PPARs in health and disease. *Nature* **405**, 421-424 (2000). <https://doi.org/10.1038/35013000>
- 187 Krey, G. *et al.* Fatty acids, eicosanoids, and hypolipidemic agents identified as ligands of peroxisome proliferator-activated receptors by coactivator-dependent receptor ligand assay. *Mol Endocrinol* **11**, 779-791 (1997). <https://doi.org/10.1210/mend.11.6.0007>

- 188 Giampietro, L., Ammazzalorso, A., Amoroso, R. & De Filippis, B. Development of Fibrates as Important Scaffolds in Medicinal Chemistry. *ChemMedChem* **14**, 1051-1066 (2019). <https://doi.org/10.1002/cmdc.201900128>
- 189 Willson, T. M., Brown, P. J., Sternbach, D. D. & Henke, B. R. The PPARs: from orphan receptors to drug discovery. *J Med Chem* **43**, 527-550 (2000). <https://doi.org/10.1021/jm990554g>
- 190 Abourbih, S. *et al.* Effect of fibrates on lipid profiles and cardiovascular outcomes: a systematic review. *Am J Med* **122**, 962 e961-968 (2009). <https://doi.org/10.1016/j.amjmed.2009.03.030>
- 191 Fuchter, M. J. On the Promise of Photopharmacology Using Photoswitches: A Medicinal Chemist's Perspective. *J Med Chem* **63**, 11436-11447 (2020). <https://doi.org/10.1021/acs.jmedchem.0c00629>
- 192 Kobauri, P., Dekker, F. J., Szymanski, W. & Feringa, B. L. Rational Design in Photopharmacology with Molecular Photoswitches. *Angew Chem Int Ed Engl* **62**, e202300681 (2023). <https://doi.org/10.1002/anie.202300681>
- 193 Borowiak, M. *et al.* Photoswitchable Inhibitors of Microtubule Dynamics Optically Control Mitosis and Cell Death. *Cell* **162**, 403-411 (2015). <https://doi.org/10.1016/j.cell.2015.06.049>
- 194 Hull, K., Morstein, J. & Trauner, D. In Vivo Photopharmacology. *Chem Rev* **118**, 10710-10747 (2018). <https://doi.org/10.1021/acs.chemrev.8b00037>
- 195 Zhu, W. F. *et al.* Photochemistry in Medicinal Chemistry and Chemical Biology. *J Med Chem* **67**, 4322-4345 (2024). <https://doi.org/10.1021/acs.jmedchem.3c02109>
- 196 Peddie, V. & Abell, A. D. Photocontrol of peptide secondary structure through non-azobenzene photoswitches. *Journal of Photochemistry and Photobiology C* **40**, 1-20 (2019). <https://doi.org/10.1016/j.jphotochemrev.2019.05.001>
- 197 Villaron, D. & Wezenberg, S. J. Stiff-Stilbene Photoswitches: From Fundamental Studies to Emergent Applications. *Angew Chem Int Ed Engl* **59**, 13192-13202 (2020). <https://doi.org/10.1002/anie.202001031>
- 198 Beharry, A. A. & Woolley, G. A. Azobenzene photoswitches for biomolecules. *Chem Soc Rev* **40**, 4422-4437 (2011). <https://doi.org/10.1039/c1cs15023e>
- 199 Broichhagen, J., Frank, J. A. & Trauner, D. A roadmap to success in photopharmacology. *Acc Chem Res* **48**, 1947-1960 (2015). <https://doi.org/10.1021/acs.accounts.5b00129>
- 200 Hinnah, K. *et al.* Photohormones Enable Optical Control of the Peroxisome Proliferator-Activated Receptor gamma (PPARgamma). *J Med Chem* **63**, 10908-10920 (2020). <https://doi.org/10.1021/acs.jmedchem.0c00654>
- 201 Morstein, J. *et al.* Optical control of the nuclear bile acid receptor FXR with a photohormone. *Chem Sci* **11**, 429-434 (2020). <https://doi.org/10.1039/c9sc02911g>
- 202 Mukhopadhyay, T. K. *et al.* Development of Light-Activated LXR Agonists. *ChemMedChem* **18**, e202200647 (2023). <https://doi.org/10.1002/cmdc.202200647>
- 203 Dunkel, P. & Ilas, J. Targeted Cancer Therapy Using Compounds Activated by Light. *Cancers (Basel)* **13** (2021). <https://doi.org/10.3390/cancers13133237>

- 204 Volaric, J., Szymanski, W., Simeth, N. A. & Feringa, B. L. Molecular photoswitches in aqueous environments. *Chem Soc Rev* **50**, 12377-12449 (2021). <https://doi.org/10.1039/d0cs00547a>
- 205 Yun, S. H. & Kwok, S. J. J. Light in diagnosis, therapy and surgery. *Nat Biomed Eng* **1** (2017). <https://doi.org/10.1038/s41551-016-0008>
- 206 Sai, M. *et al.* Structure-Guided Design of Nurr1 Agonists Derived from the Natural Ligand Dihydroxyindole. *J Med Chem* **66**, 13556-13567 (2023). <https://doi.org/10.1021/acs.jmedchem.3c00852>
- 207 De Bruyn, T. *et al.* Structure-based identification of OATP1B1/3 inhibitors. *Mol Pharmacol* **83**, 1257-1267 (2013). <https://doi.org/10.1124/mol.112.084152>
- 208 Ren, S. *et al.* Discovery and characterization of novel, potent, and selective cytochrome P450 2J2 inhibitors. *Drug Metab Dispos* **41**, 60-71 (2013). <https://doi.org/10.1124/dmd.112.048264>
- 209 den Braver-Sewradj, S. P. *et al.* Reduction and Scavenging of Chemically Reactive Drug Metabolites by NAD(P)H:Quinone Oxidoreductase 1 and NRH:Quinone Oxidoreductase 2 and Variability in Hepatic Concentrations. *Chem Res Toxicol* **31**, 116-126 (2018). <https://doi.org/10.1021/acs.chemrestox.7b00289>
- 210 Baell, J. & Walters, M. A. Chemistry: Chemical con artists foil drug discovery. *Nature* **513**, 481-483 (2014). <https://doi.org/10.1038/513481a>
- 211 Baell, J. B. & Nissink, J. W. M. Seven Year Itch: Pan-Assay Interference Compounds (PAINS) in 2017-Utility and Limitations. *ACS Chem Biol* **13**, 36-44 (2018). <https://doi.org/10.1021/acscchembio.7b00903>
- 212 Sai, M. *et al.* Development of Nurr1 agonists from amodiaquine by scaffold hopping and fragment growing. *Commun Chem* **7**, 149 (2024). <https://doi.org/10.1038/s42004-024-01224-0>
- 213 De Bosscher, K., Desmet, S. J., Clarisse, D., Estebanez-Perpina, E. & Brunsveld, L. Nuclear receptor crosstalk - defining the mechanisms for therapeutic innovation. *Nat Rev Endocrinol* **16**, 363-377 (2020). <https://doi.org/10.1038/s41574-020-0349-5>
- 214 Cheng, H. S. *et al.* Exploration and Development of PPAR Modulators in Health and Disease: An Update of Clinical Evidence. *Int J Mol Sci* **20** (2019). <https://doi.org/10.3390/ijms20205055>
- 215 Sai, M., van Herwijnen, N. & Merk, D. Azologs of the Fatty Acid Mimetic Drug Cinalukast Enable Light-Induced PPARalpha Activation. *ChemMedChem*, e202400327 (2024). <https://doi.org/10.1002/cmdc.202400327>
- 216 Isigkeit, L. & Merk, D. Opportunities and challenges in targeting orphan nuclear receptors. *Chem Commun (Camb)* **59**, 4551-4561 (2023). <https://doi.org/10.1039/d3cc00954h>
- 217 Pellicciari, R. *et al.* 6alpha-ethyl-chenodeoxycholic acid (6-ECDCA), a potent and selective FXR agonist endowed with anticholestatic activity. *J Med Chem* **45**, 3569-3572 (2002). <https://doi.org/10.1021/jm025529g>
- 218 Kaur, K., Jain, M., Reddy, R. P. & Jain, R. Quinolines and structurally related heterocycles as antimalarials. *Eur J Med Chem* **45**, 3245-3264 (2010). <https://doi.org/10.1016/j.ejmech.2010.04.011>

- 219 Zhang, Y. *et al.* Glutathione S-Transferase P1 Protects Against Amodiaquine Quinoneimines-Induced Cytotoxicity but Does Not Prevent Activation of Endoplasmic Reticulum Stress in HepG2 Cells. *Front Pharmacol* **9**, 388 (2018). <https://doi.org/10.3389/fphar.2018.00388>
- 220 Smits, L. M. *et al.* Modeling Parkinson's disease in midbrain-like organoids. *NPJ Parkinsons Dis* **5**, 5 (2019). <https://doi.org/10.1038/s41531-019-0078-4>
- 221 Cookson, M. R. alpha-Synuclein and neuronal cell death. *Mol Neurodegener* **4**, 9 (2009). <https://doi.org/10.1186/1750-1326-4-9>
- 222 Kim, H. *et al.* Modeling G2019S-LRRK2 Sporadic Parkinson's Disease in 3D Midbrain Organoids. *Stem Cell Reports* **12**, 518-531 (2019). <https://doi.org/10.1016/j.stemcr.2019.01.020>
- 223 Consortium, S. G. *Brochure_Donated Chemical Probes (May 2024)*, <<https://www.thesgc.org/donated-chemical-probes>> (2024).
- 224 Broekema, M. F. *et al.* Profiling of 3696 Nuclear Receptor-Coregulator Interactions: A Resource for Biological and Clinical Discovery. *Endocrinology* **159**, 2397-2407 (2018). <https://doi.org/10.1210/en.2018-00149>
- 225 Pollinger, J. *et al.* Computer-Assisted Selective Optimization of Side-Activities-from Cinalukast to a PPARalpha Modulator. *ChemMedChem* **14**, 1343-1348 (2019). <https://doi.org/10.1002/cmdc.201900286>
- 226 Wu, J., Song, Y., Li, H. & Chen, J. Rhabdomyolysis associated with fibrate therapy: review of 76 published cases and a new case report. *Eur J Clin Pharmacol* **65**, 1169-1174 (2009). <https://doi.org/10.1007/s00228-009-0723-7>
- 227 Botta, M. *et al.* PPAR Agonists and Metabolic Syndrome: An Established Role? *Int J Mol Sci* **19** (2018). <https://doi.org/10.3390/ijms19041197>
- 228 Banno, A., Reddy, A. T., Lakshmi, S. P. & Reddy, R. C. PPARs: Key Regulators of Airway Inflammation and Potential Therapeutic Targets in Asthma. *Nucl Receptor Res* **5** (2018). <https://doi.org/10.11131/2018/101306>
- 229 Lee, D. *et al.* PPARalpha Modulation-Based Therapy in Central Nervous System Diseases. *Life (Basel)* **11** (2021). <https://doi.org/10.3390/life11111168>

6 List of abbreviations

λ wavelenghts

5xFAD AD mouse model

6-OHDA 6-hydroxydopamine

9cisDHRA 9-cis-13,14-dihydroretinoic acid

9cisRA 9-cis retinoid acid

A β amyloid beta

AAV adeno-associated viruses

ABCA1 ATP-binding cassette transporter A1

AcOH acetic acid

AD Alzheimer's disease

ADH2 alcohol dehydrogenase 2

AF1 activation function 1

AF2 activation function 2

AKT protein kinase B

ApoE apolipoprotein E

APP amyloid precursor protein

APP/PS1 transgenic mouse model of AD

AQ amodiaquine

Arg argenine

ATRA all-trans retinoic acid

Ax1 adhesion related kinase

BACE β -secretase

B_{max} maximal binding capacity

BOC tert-butylloxycarbonyl

CARs constitutive androstane receptor

CNS central nervous system

CoREST REST corepressor

COX5 β cytochrome c oxidase subunit 5 β

CQ chloroquine

CREB ... cAMP response element-binding protein

Cs₂CO₃ caesium carbonate

CTE C-terminal extension

Cys cysteine

CysLT1R cysteinyl leukotriene receptor 1

DAT dopamine transporter

DBD DNA-binding domain

DCM dichlormethane

DDC dopamine decarboxylase

DHA docosahexaenoic acid

DHI dihydroxyindole

DHODH dihydroorotate dehydrogenase

DHR38 Drosophila Hormone Receptor 38

DIPEA N,N-diisopropylethylamine

DLK1 delta-like homologue 1

DMA dimethylacetale

DMF dimethylformamide

DMSO dimethylsulfoxide

DOGS design of genuine structures

DR direct repeat

DSF differential scanning fluorimetry

EAE experimental autoimmune encephalomyelitis

EC₅₀ Half maximal effective concentration

EDC 1-ethyl-3-(3-dimethylaminopropyl)carbodiimide

ERK extracellular signal-regulated kinase 1/2

EtOAc ethyl acetate

EtOH ethanol

Foxa2 forkhead family of winged-helix transcription factor

FRET Förster resonance energy transfer

FXR farnesoid X receptor

GDNF glial cell-derived neurotrophic factor

Glu glutamic acid

GWAS genome-wide association studies

H₂SO₄ sulfuric acid

HATU hexafluorophosphate azabenzotriazole tetramethyl uronium

HCl hydrogen chloride

HCQ hydroxychloroquine

HDL high-density lipoprotein

HDX-MS hydrogen-deuterium exchange mass spectrometry

HEK human embryonic kidney

HFTR..... time-resolved fluorescence resonance energy transfer

His..... histidine

HNO₃..... nitric acid

IL-1βinterleukin-1 beta

iNOS..... nitric oxide synthase

iPSCs..... isogenic pluripotent stem cells

JEG3 human choriocarcinoma cells

K₃PO₄..... tripotassium phosphate

KLHL1kelch-like protein 1

LBD ligand-binding domain

LBP.....ligand-binding pocket

LDL.....low-density lipoprotein

LE ligand efficiency

Leu leucine

LiOH lithium hydroxide

LPS lipopolysaccharide

LRRK2 leucine rich repeat kinase 2

LXRs liver X receptors

Lys..... lysine

MAP mitogen-activated protein

MeOHmethanol

MerTK ...Proto-oncogene tyrosine-protein kinase
MER

MN9Dmurine dopamine neuron cell line

MOG35-55peptide fragment 35-55 of myelin oligodendrocyte glycoprotein

MPP 1-methyl-4-phenylpyridinium

MPTP 1-methyl-4-phenyl-1,2,3,6-tetrahydropyridine

mRNA messenger RNA

MS..... multiple sclerosis

MSTmicroscale thermophoresis

N27-Arat dopaminergic neurons

NBRE NGFI-B response element

NCoA6 nuclear receptor coactivator 6

NCoR1 nuclear receptor corepressor 1

NFκB nuclear factor kappa-light-chain-enhancer of activated B cells

NGFI-B.....nerve growth-factor induced clone B

NOR-1 neuron-derived orphan receptor 1

NR nuclear receptor

NR1C nuclear receptor supfamily C

NR2B nuclear receptor subfamily 2 B

NR4A nuclear receptor subfamily 4A

NRs..... nuclear receptors

NTD N-terminal domain

Nurr1 nuclear receptor related 1

NurRE Nur response element

ODNs.....oligodeoxynucleotide

OLs oligodendrocytes

OPCs oligodendrocyte precursor cells

PAINS..... pan-assay interference compounds

PAMPA parallel artificial membrane permeability assay

PD..... Parkinson's disease

PGA1..... prostaglandin A1

PGE1.....prostaglandin E1

PIASy SUMO E3 ligase protein inhibitor of activated STAT

POMC proopiomelanocortin

PPAR.....proliferator-activated receptor

PPARγ coactivator 1alpha..... PPAR coactivator 1alpha

PPREs PPAR response elements

PROTACs.....proteolysis targeting chimeras

PTPRU. protein tyrosine phosphatase receptor U

PXRpregnane X receptor

RAR.....retinoid acid receptor

REs response elements

Ret tyrosine-protein kinase receptor Ret

rt room temperature

RXRs retinoid X receptors

Serserine

sGFP superfolder green fluorescent protein

siRNA..... small interfering RNA

SK-N-BE(2)Chuman neuroblastoma cells

SMRT.. silencing mediator of retinoid and thyroid hormone receptors

SNPs single nucleotide polymorphisms

SOD1 superoxide dismutase 1

SOSA the selective optimization of side activities

SPR..... surface plasmon resonance

SRC..... steroid receptor coactivators

T98G	human astrocytes	TR-FRET	time-resolved fluorescence energy transfer
TFA	trifluoroacetic acid	TRs.....	thyroid hormone receptors
TH.....	tyrosine hydroxylase	TSFM.....	mitochondrial elongation factor Ts
Th17	T helper cells 17	UAS.....	upstream activation sequence
Thr	threonine	VDR	vitamin D receptor
T _m	melting temperature	VMAT2.....	vesicular monoamine transporter 2
TNF-α.....	tumor necrosis factor-alpha	Zn	zinc
Tregs	regulatory T cells		
Trem2 .	triggering receptor expressed on myeloid cells 2		

7 List of figures

Figure 1. The prevalence of neurodegenerative diseases on a global scale, with a particular focus on Germany (now and estimated for 2050).	- 7 -
Figure 2. (a) Structural architecture of Nurr1 containing five domains. A/B-domain with ligand-independent transcriptional activation function 1 (AF1), C-domain with Zn-finger and P-,D-,T- and A-box ((b), adapted from ³⁸), D-domain with hinge region, E-domain with ligand-dependent transcriptional activation function 2 (AF2 = H12) and Nurr1-LBD X-ray structure and his helices (H1-H12) ((c), PDB: 1OVL) ³⁹ . Created with Biorender.com..	- 10 -
Figure 3. Schematic illustration of Nurr1 with its REs as a monomer (a), homodimer (b) and heterodimer with RXR (c). Created with Biorender.com.	- 12 -
Figure 4. The apo structure of the Nurr1 LBD (PDB: 1OVL ³⁹) revealed that the canonical LBP region is blocked by bulky hydrophobic side chains filling the cavity. Adapted from ¹⁴	- 13 -
Figure 5. Potential binding sites of coregulators in the LBD of Nurr1 (PDB:1OVL). Adapted from ¹⁴	- 14 -
Figure 6. Nurr1 regulates genes of dopamine metabolism, axonal growth, survival, oxidative stress response and differentiation. Created with Biorender.com.....	- 16 -
Figure 7. Chemical structures of natural and synthetic Nurr1 ligands.	- 21 -
Figure 8. Crystal structure of Nurr1 LBD and PGA1 (PDB: 5Y41 ⁸³). Adapted from ¹⁴	- 22 -
Figure 9. (a) Molecular interactions between the Nurr1 LBD residues and the ligand DHI as a covalent adduct. (b) Molecular interactions between the Nurr1 LBD residues and DHI as a non-covalent adduct. Adapted from support information of ¹¹²	- 23 -
Figure 10. Proposed binding region of AQ (orange) to Nurr1 LBD based on NMR binding studies. Adapted from ¹⁴	- 24 -
Figure 11. Chemical structures of selective Nurr1-RXR heterodimer ligands BRF110 (20) and HX600 (21).	- 28 -

Figure 12. Schematic illustration of RXR with its REs as a homodimer (a) and heterodimer (b) with other NRs. Created with Biorender.com.	- 29 -
Figure 13. Schematic illustration of the mechanism of RXR as permissive, non-permissive and conditional heterodimer partner. Created with Biorender.com.....	- 30 -
Figure 14. Chemical structures of natural and synthetic RXR ligands.	- 33 -
Figure 15. X-ray structure of RXR α in complex with 27 (PDB: 6SJM) ¹⁵⁷ . Reprinted from ¹⁵⁷	- 35 -
Figure 16. Schematic illustration of PPAR and RXR to bind as a heterodimer on PPRE. Created with Biorender.com.....	- 35 -
Figure 17. Chemical structure of fatty acids (oleic acid (28), stearic acid (29), palmitic acid (30) and leukotriene B ₄ (31))......	- 37 -
Figure 18. Chemical structure of fenofibrate (32). In blue the 2-methyl-2-phenoxypropanoic acid motif.	- 38 -
Figure 19. (a) Photoswitchable stilbene isomerization by UV-light with its π -electrocyclic rearrangement and oxidation. (b) Photoswitchable azobenzene by UV-light.	- 39 -
Figure 20. Cocrystal structure of DHI bound to the Nurr1 LBD (PDB: 6dda ⁷⁴). The 5- and 6-positions of DHI are oriented towards the solvent. Adapted from ²⁰⁶	- 41 -
Figure 21. The virtual amide library was docked to the Nurr1 LBD (PDB: 6dda ⁷⁴). The virtual designs were extended to address the grooves on the Nurr1 LBD surface that surround the DHI-binding site. Adapted from ²⁰⁶	- 44 -
Figure 22. Microscale amide synthesis (A) and synthesis of building block (41) (B). Reagents and conditions: (a) EDC·HCl, EtOAc, rt, 36 h; (b) HNO ₃ /H ₂ SO ₄ , 5 °C, 0.5 h, 59%; (c) acetyl chloride, MeOH, 50 °C, 4 h, 96%; (d) DMF-DMA, DMF, 120 °C, 2 h; then Zn, AcOH/H ₂ O, 80 °C, 2 h, 40%; (e) LiOH·H ₂ O, EtOH/H ₂ O, rt, 18 h, 94%. Adapted from ²⁰⁶	- 44 -
Figure 23. Predicted binding modes of 44 (magenta), 45 (cyan), and 47 (orange) to the Nurr1 LBD (PDB: 6dda ⁷⁴). (a) It was predicted that the three active DHI descendants, 44 , 45 , and 47 , would bind to the DHI-binding site and extend towards a hydrophobic groove lining H12. (b) The most active Nurr1 agonist, 45 , formed a face-to-face contact with His516. Reprinted from ²⁰⁶	- 46 -
Figure 24. (a) Mutagenesis indicated that 45 was less active on a Nurr1-C566S mutant, which provided support for an interaction with the proposed epitope. The data are presented as the mean \pm S.E.M., n \geq 3. (b) 45 demonstrated stability against reaction with glutathione (GSH). Phenyl vinyl sulfone (PVS) was used as a positive control (125 μ M 45 or PVS were incubated with 2.5 mM GSH in PBS at 37 °C). n = 3. Reprinted from ²⁰⁶	- 47 -
Figure 25. (a) Comparison of fluvastatin (52) and pitavastatin (53) on Nurr1 transcriptional activity. A scaffold hop from indole (52) to the quinoline (53) resulted in a notable increase in potency. (b) Merging of the amide motif of 44 and 7-chloroquinolin-4-amine motif of AQ. (c) The data demonstrate that 44 and 51 enhanced the maximal activation of Nurr1	

by agonist **15** to 134% (**44**) and 177% (**51**) of its maximal effect when administered alone. The data are presented as the mean \pm S.E.M. relative Nurr1 act. vs 1 μ M **15**, with $n \geq 3$ - 48 -

Figure 26. In vitro profiling of DHI-derived Nurr1 agonists. (a) ITC demonstrated that compounds **44** and **51** exhibited binding to the recombinant Nurr1 LBD. The fitting of the heat of binding is illustrated, and the isotherms at 25 °C are presented as insets. (b) Treatment with **44** (30 μ M) resulted in Nurr1-regulated mRNA expression of TH and VMAT2 in T98G cells. The data are presented as the mean \pm S.E.M. relative mRNA expression ($2^{-\Delta\text{Ct}}$), $n = 4$. # $p < 0.1$, ** $p < 0.01$ (t-test vs. DMSO control). (c) **44** ($\text{EC}_{50} = 2 \pm 1 \mu\text{M}$) and **51** ($\text{EC}_{50} = 4 \pm 1 \mu\text{M}$) were observed to activate full-length human Nurr1 on the NBRE. The data are presented as the mean \pm S.E.M. fold activity relative to the DMSO control, $n \geq 4$. (d) DHI, 5-chloroindole (5Cl, **7**) and the descendants **44** and **51** were observed to modulate Nurr1-regulated gene expression in dopaminergic neural cells (N27). TH; VMAT2; SOD1/2. The data represent the mean \pm S.E.M. relative mRNA expression in comparison to 0.1% DMSO, with $n = 7-8$. Statistical significance was determined using the Wilcoxon test or t-test, with the following levels of significance: * $p < 0.05$, ** $p < 0.01$, *** $p < 0.001$. Adapted from ²⁰⁶. - 49 -

Figure 27. (a) Scaffold hop from the chloroquinoline amine motif of AQ to the imidazo[1,2-a]pyridine scaffold **54**. (b) **54** exhibited Nurr1 activity with an EC_{50} of 7 μM in a Gal4-Nurr1 hybrid reporter gene assay. Data are presented as the mean \pm S.E.M. fold activity relative to the DMSO control, $n \geq 3$. (c) **54** bound to the Nurr1 LBD (K_d 0.17 μM) determined by ITC. The fitting of the heat of binding is shown and the isotherm at 25 °C is shown as inset.... - 50 -

Figure 28. General synthesis of the imidazo[1,2-a]pyridine scaffold. Reagents and conditions: (a) AcOH, MeOH, rt, 24-48 h; (b) TFA/DCM, rt, 30 min to overnight, 3-30% over two steps..... - 51 -

Figure 29. Fragment growing of the 2-methyl substituent of **54** (a). **62** exhibited Nurr1 activity with an EC_{50} of 0.4 μM in a Gal4-Nurr1 hybrid reporter gene assay. Data are presented as the mean \pm S.E.M. fold activity relative to the DMSO control, $n \geq 3$. (c) **62** bound to the Nurr1 LBD (K_d 0.7 μM) determined by ITC. The fitting of the heat of binding is shown and the isotherm at 25 °C is shown as inset..... - 52 -

Figure 30. General synthesis of N-carboxamide of **54**. Reagents and conditions: (a) HATU, DIPEA, DMF, rt, overnight; (b) tetrakis(triphenylphosphane)palladium(0), Na_2CO_3 , water/dioxane, reflux, overnight. - 53 -

Figure 31. Replacement of the aminophenol of AQ by 5-(4-chlorophenyl)furan-2-carboxamide motif (**65**) (a). **65** exhibited Nurr1 activity with an EC_{50} of 0.4 μM in a Gal4-Nurr1 hybrid reporter gene assay. Data are presented as the mean \pm S.E.M. fold activity relative to the DMSO control, $n \geq 3$. (c) **65** bound to the Nurr1 LBD (K_d 0.7 μM) determined

by ITC. The fitting of the heat of binding is shown and the isotherm at 25 °C is shown as inset. - 53 -

Figure 32. In vitro characterization of the optimized Nurr1 agonist **66**. (a) Optimization of **65** resulted in **66** with an EC₅₀ of 0.090 μM and inactive **67** which can be used as negative control. (b) Effects of **66** on the human full-length Nurr1 homodimer (NurRE) and monomer (NBRE) in reporter gene assays. The data are presented as the mean ± S.E.M. fold activation relative to the DMSO control, n ≥ 3. (c) The effects of **66** on the Nurr1-RXR heterodimer (DR5) in the absence and presence of bexarotene (0.1 μM) are shown. The data are presented as the mean ± S.E.M. fold activation relative to the DMSO control or 0.1 μM BEX, n ≥ 3. (d) Binding of **66** to the Nurr1 LBD (K_d = 0.17 μM) was determined by ITC. The fitting of the heat of binding is illustrated, and the isotherm at 25 °C is shown as an insert. (e) Effects of **66** and **67** on the expression of the Nurr1-regulated TH, VMAT2, and SOD2 in T98G. The data represent the mean ± S.E.M. fold mRNA induction relative to the DMSO control, with n = 3. #p < 0.1, *p < 0.05 (t-test vs. DMSO ctrl). (f). Selectivity screening of **66** on NRs. The heatmap illustrates the mean relative activation in comparison to reference ligands, n = 3. (g) **66** (10 μM) was not toxic in a WST-8 assay in N27 rat neurons and HEK293T cells. AQ (1, 10 and 30 μM) was found to be toxic. The data represent the mean ± S.E.M. relative absorbance (450 nm), n ≥ 3. (h,i) Permeability of Nurr1 agonists in a parallel artificial membrane permeability assay (PAMPA) and in a cellular model of the blood-brain barrier (BBB). Propranolol and the brain-penetrant reference antipyrine were used for comparison. The data are presented as the mean ± S.D., n = 6. (j) Metabolism of **66** by rat liver microsomes resulted in demethylation of the dimethylamino group. The data are presented as the mean ± S.D., n = 4. Adapted from ²¹². - 54 -

Figure 33. Structural fusion of **62** and **66** in **74** enhanced Nurr1 agonist potency and binding affinity. Reprinted from ²¹². - 56 -

Figure 34. Treatment of midbrain organoids with the Nurr1 agonist **66** and the negative control analogue **67**. (a) Organoids derived from human iPSC carrying a gain-of-function mutation in the leucine-rich repeat kinase 2 (LRRK2) gene (G2019S) exhibited reduced Nurr1 and TH transcript levels when compared to isogenic controls after 45 days. (b) Immunofluorescence staining of midbrain organoid sections revealed the presence of TH-expressing cells. Scale bars represent 100 μm. (c) **66**, but not the negative control **67**, induced TH mRNA expression in LRRK2 mutant organoids and tended to enhance TH mRNA expression in isogenic controls. All data are presented as the mean ± S.E.M., n = 3. *p < 0.05, **p < 0.01 (unpaired, two-tailed Student's t-test). Reprinted from ²¹². - 57 -

Figure 35. Selective modulation through ligand-induced coregulator recruitment. The binding of a ligand to the LBD-corepressor complex induces a conformational change, resulting in the release of the corepressor. The active conformation of the ligand-induced LBD recruits a selective coactivator, which may exert effects specific to tissues and genes expression. Created with Biorender.com. - 59 -

Figure 36. Effects of 9-cis RA and **27** on coregulator recruitment to the RXR α LBD. Compounds were tested at 1 μ M. - 59 -

Figure 37. (a) A virtual library of 15,759 biphenylacetic acids was constructed docked to the binding site of **27** in RXR α , with the objective of identifying novel RXR modulators related to **27** (b) **27** binds to the highly hydrophobic orthosteric site of RXR α (PDB: 6sjm¹⁵⁷) and forms a single polar contact to Arg316. - 60 -

Figure 38. General synthesis of phenylacetic acid derivatives of **27**. Reagents and conditions (a) K₃PO₄, XPhos Pd G2, 1,4-dioxane/H₂O, reflux, 1.5–24 h or Cs₂CO₃, XPhos Pd G2, toluene/H₂O, reflux, 1.5–24 h, 4–96%; (b) LiOH, MeOH/H₂O, rt, 18 h, 16–90%. - 60 -

Figure 39. Effects of RXR ligands on the recruitment of co-regulators to the RXR α LBD in HTRF-based systems. The data are presented as the mean \pm S.E.M., n = 3. Despite their high structural similarity, **78–82** revealed pronounced differences in their effects on coregulator recruitment. (b) Dose-response profiling demonstrated that **79** and **80** induce recruitment of PGC1 α , with **79** exhibiting considerably higher efficacy. (c) **81** and **82** were ineffective in inducing PGC1 α recruitment. (d) Compounds **78**, **79** and **80** demonstrated no transcriptional activity at 1 and 10 μ M on lipid-sensing NRs associated with RXR. The data are presented as the mean \pm S.E.M., n = 3. (e) The effects of **78**, **79** and **80** (10 μ M each) on the interaction of RXR α with the heterodimer partners THR α , RAR α , LXRA and PPAR γ were observed in a cellular assay, in which the binding of VP16-RXR α -LBD to the corresponding Gal4 hybrid receptors of the dimer partners was monitored. The heat map depicts the mean relative reporter activity in comparison to the control substance DMSO, n = 3. - 62 -

Figure 40. The RXR modulators **79** and **80** induced the interaction between RXR α and PGC1 α in a cellular context. a) A Gal4-PGC1 α fusion protein, a Gal4-responsive reporter construct and an RXR α -LBD-VP16 fusion protein were employed to observe ligand-induced RXR α -PGC1 α interaction in HEK293T cells. (b) RXR α -PGC1 α interaction was robustly enhanced by **79** and **80**, resulting in enhanced reporter activity (EC₅₀ = 0.04 \pm 0.02 μ M (**79**); 0.06 \pm 0.03 μ M (**80**)). In contrast, the reference RXR agonist bexarotene (1 μ M) had only a weak effect (c). The data represent the mean \pm S.D. of reporter activity in the presence of Gal4-PGC1 α and RXR α -LBD-VP16, with the readings normalized to the RXR α -LBD-VP16-free setting, n = 3. - 63 -

Figure 41. A comparison of the binding modes of **27**, **78**, **79** and **80**. (a) Predicted binding modes of **78**, **79** and **80** in the binding site of **27** in the RXR α LBD (PDB: 6sjm¹⁵⁷). The binding modes of **27**, **78**, **79** and **80** to RXR α are highly similar, involving a strong ionic contact with Arg316. (b) The differences in the binding of **27**, **78**, **79** and **80** in the His435 region are illustrated with the ligand surfaces shown as a mesh. The structural demands in the His435 region are higher for **78** (green mesh) and **80** (magenta mesh) than for **27** (grey mesh) and **79** (blue mesh), which may affect the position of H11. (c) The structural

overview of the ternary complex of **27** and nuclear receptor co-activator 2 (blue) bound to the RXR α LBD (PDB: 6sjm¹⁵⁷) is presented here. H12 is depicted in magenta. The interaction of different ligands with H11 is likely to affect the position of H12, consequently impacting the region responsible for the binding of co-activators via allosteric crosstalk. - 63 -

Figure 42. (a) The development of a weak PPAR α agonist, cinalukast (**83**), based on the SOSA concept, resulted in the synthesis of **84**. (b) A structure-guided approach was employed to develop the weak PPAR α agonist, GL479 (**85**), into the photohormone **86**. Irradiation with UV light enabled the formation of E/Z-**86**..... - 65 -

Figure 43. Synthesis of **82**. Reagents and conditions: (a) XPhos Pd G2, K₃PO₄, water/dioxane, reflux, overnight, 83%; (b) methyltriphenylphosphonium bromide, KOtBu, THF, 0 °C ->rt, overnight, 94%; (c) HATU, DIPEA, DMF, rt, overnight, 95%; (d) Pd(OAc)₂, K₃PO₄, DMA, 140 °C, overnight, 42%; (e) LiOH, water/THF, rt, overnight, 72%. Reprinted from ²¹⁵..... - 66 -

Figure 44. Modulation of NRs of **87** and **96**. (a) The stilbene analogue **87** (3 μ M) exhibited agonistic activity on RAR α , PPARs and FXR, with the most prominent effect observed in the case of PPAR α . (b) The azobenzene **96** (10 μ M) demonstrated a more pronounced preference for PPAR α . The data are presented as the mean \pm S.E.M. fold NR activation relative to the DMSO control, n \geq 3. Reprinted from ²¹⁵. - 66 -

Figure 45. Synthesis of azobenzenes **96-98**, **101-105**. Reagents and conditions: (a) HATU, DIPEA, DMF, rt, overnight, quant.; (b) TFA, rt, overnight, quant.; (c) XPhos Pd G2, K₃PO₄, water/dioxane, reflux, overnight, 44-95%; (d) Oxone, DCM, rt, 1-3h, workup, DCM, HOAc, rt, 1-2 days, 3-59%; (e) LiOH, water/THF, rt, overnight, 40-95%. Reprinted from ²¹⁵.... - 67 -

Figure 46. Synthesis of azobenzenes **99**, **100**, **106**. Reagents & Conditions: (a) Oxone, DCM, rt, 1h, workup, DCM, HOAc, rt, 2 days, 59-60%; (b) XPhos Pd G2, K₃PO₄, water/dioxane, reflux, overnight, 91-94%; (c) LiOH, water/THF, rt, overnight, 77-99%. Reprinted from ²¹⁵. - 68 -

Figure 47. UV-Profiling of the PPAR α targeted photohormone **96**. (a) UV absorbance spectra of **96** (30 μ M in DMSO) measured after irradiation at the indicated wavelengths. (b) E/Z-configuration ratios of **96** in the dark adapted, state and after irradiation at 365 nm or 435 nm determined by ¹H-NMR based on the (CH₃)₂-integral of the oxopropanoic acid motif. Adapted from ²¹⁵..... - 68 -

Figure 48. Profiling of the PPAR α targeted photohormone **102**. (a) UV/Vis absorbance spectra of **102** (30 μ M in DMSO) were recorded following irradiation at the specified wavelengths. (b) The E/Z-configuration ratios of **102** in the dark-adapted state and after irradiation at 365 nm or 435 nm were determined by ¹H-NMR based on the (CH₃)₂-integral of the oxopropanoic acid motif. (c) **102** was demonstrated to be reversibly switchable between the (E)- and (Z)-configurations over multiple cycles by alternating irradiation at 365 and 435 nm. The absorbance was measured at a wavelength of 323 nm. (d) (Z)-**102**

exhibited slow thermal relaxation at 37 °C, with a half-life of 28.5 hours. (e) **102** demonstrated selective activation of PPAR α over related lipid-activated NRs. The data represent the mean \pm S.E.M. of the NR activation, n = 3. (f) The light-activated (Z)-**102** caused continuous PPAR α activation over time, while the (E)-**102** had no effect. The compounds were tested at a concentration of 10 μ M in a fluorescent reporter gene assay utilising the mCherry protein, with fluorescence intensity (FI) measured at two-hour intervals. The fluorescence intensity (FI) of (Z/E)-**102** was normalized to that of the untreated control (DMSO) and multiplied by 1000 to obtain the relative fluorescence units (RFU). A cell DISCO was employed to induce the active (Z)-configuration of **102**. The graph depicts the mean (lines) and S.E.M. (shadows); n = 3. Adapted from ²¹⁵. - 71 -

8 List of tables

Table 1. Further so-called Nurr1 modulators (16-19).....	- 27 -
Table 2. Photohormones for NRs. NRs modulations were determined by a Gal4 hybrid reporter gene assay.....	- 40 -
Table 3. Nurr1 modulation and binding affinity to the Nurr1 LBD of 42-47 and 48-51 .	- 46 -
Table 4. SAR evaluation of imidazo[1,2-a]pyridine 54 for Nurr1 modulation.....	- 51 -
Table 5. Optimization of 66 for microsomal stability and Nurr1 modulation. Microsomal stability against degradation by rat liver microsomes was determined by LCMS.	- 55 -
Table 6. RXRs modulation of selected analogues of RXR agonist 27 from structure-guided design.....	- 61 -
Table 7. Photoswitchable analogues of 84 . A cell DISCO ¹⁹³ was used to maintain the (Z)-configuration.....	- 69 -
Table 8. Evaluation of the lipophilic substitution pattern of 96 . A cell DISCO ¹⁹³ was used to maintain the (Z)-configuration.	- 70 -

9 List of publications

Parts of this thesis have been published in peer-reviewed journals:

1. Sai, M.*; Vietor, J.*; Kornmayer, M.; Egner, M.; López-García, U.; Höfner, G.; Pabel, J.; Marschner, J.; Wein, T.; Merk, D. Structure-Guided Design of Nurr1 Agonists Derived from the Natural Ligand Dihydroxyindole. *J. Med. Chem.*, 2023, 13556–13567.

*these authors contributed equally to this work

Own contribution: planning of syntheses, synthesis of the building block **41** and **50-51**, determination of the stability of **44** against GSH, determination of toxicity of all compounds in a WST8 assay, quantification of Nurr1-regulated mRNA expression in N27 cells, supervision of Moritz Kornmayer's master's thesis on this topic.

2. Sai, M.; Hank, E. C.; Tai, H.M.; Kasch, T.; Lewandowski, M.; Vincendeau, M.; Marschner, J. A.; Merk, D. Development of Potent and Selective Nurr1 Agonists from Amodiaquine By Scaffold Hopping and Fragment Growing. *Commun. Chem.*, 2024, 7, 149.

Own contribution: design of SAR studies and syntheses, determination of activity data of all synthesized compounds in Gal4 hybrid and Nurr1 full-length reporter gene assays, performance of the Gal4 hybrid reporter gene assay to determine off-target effects, determination of toxicity in a WST8 assay, quantification of Nurr1-regulated mRNA expression in astrocytes.

3. Sai, M.; van Herwijnen, N.; Merk, D. Azologs of the fatty acid mimetic drug cinalukast enable light-induced PPAR α activation. *ChemMedChem*, 2024, e20240032 (2024).

Own contribution: planning of SAR studies and syntheses, synthesise of **99-100**, **105-106**, determination of photophysical properties, supervision of the internship of Niels van Herwijnen on this topic.

Part of this work is currently accepted after peer-review process:

4. Nawa, F.*; Sai, M.*; Vietor, J.*; Schwarzenbach, R.; Bitic, A.; Wolff, S.; Ildefeld, N.; Pabel, J.; Wein, T.; Marschner, J.A.; Heering, J.; Merk, D. Tuning RXR modulators for PGC1 α recruitment.

*these authors contributed equally to this work

Accepted in *J. Med. Chem.* (02.09.2024).

Own contribution: determination of activity data of all synthesized compounds in Gal4 hybrid assay, supervision of Anesa Bitic and Roman Schwarzenbach (bachelor thesis) on this topic.

Patent

5. Merk, D. and Sai, M. Nurr1 modulators. European patent application EP24155686.

Own contribution: see publication 2.

Further publications (published or in review process)

6. Hank, E.C.; Sai, M.; Kasch, T.; Meiyer, I.; Marschner, J.A.; Merk, D. Development of tailless homologue receptor (TLX) agonist chemical tools. Accepted in *J. Med. Chem.* after peer-review process (26.08.2024).
7. Lewandowski, M.; Carmina, M.; Knümann, L.; Sai, M.; Willems, S.; Kasch, T.; Pollinger, J.; Knapp, S.; Marschner, J. A.; Chaikuad, A.; Merk, D. Structure-Guided Design of a Highly Potent Partial RXR Agonist with Superior Physicochemical Properties. *J. Med. Chem.*, 2024, 67, 2152–2164.

10 Author contribution

Unless otherwise indicated by a reference or acknowledgment, the work presented here was written by me under the supervision of my supervisor (Prof. Dr. Daniel Merk) during my doctoral studies. All contributions by colleagues are explicitly identified in this dissertation. The following material was obtained in the context of collaborative research:

Structure-Guided Design of Nurr1 Agonists Derived from the Natural Ligand Dihydroxyindole

- Molecular docking on Nurr1:DHI complex (PDB: 6dda) by Thomas Wein (group of Prof. Daniel Merk, Department Pharmacy, Ludwig Maximilians University Munich).
- Supervision of the master thesis of Moritz Kornmayer with Jan Vietor (both group of Prof. Daniel Merk, Department Pharmacy, Ludwig Maximilians University Munich) who did the microscale synthesis and the biological evaluation of the microscale batch.
- Synthesis of **42**, **45-48** by Jan Vietor.
- Quantification of Nurr1-regulated mRNA expression in T98G cells by Julian Marschner (group of Prof. Daniel Merk, Department Pharmacy, Ludwig Maximilians University Munich).

- Gal4 hybrid reporter gene assay with Nurr1 mutant (C566S) by Ursula Lopez (group of Prof. Daniel Merk, Department Pharmacy, Ludwig Maximilians University Munich).
- Determination of the binding affinity to the Nurr1 LBD (ITC) by Daniel Merk (Department Pharmacy, Ludwig Maximilians University Munich).
- Manuscript and management of the study were prepared by Daniel Merk.

Development of Nurr1 agonists from amodiaquine by scaffold hopping and fragment growing

- Biological evaluation of Gal4 hybrid reporter gene assay together with Emily Hank and Max Lewandowski (both group of Prof. Daniel Merk, Department Pharmacy, Ludwig Maximilians University Munich).
- Pharmacokinetic experiments (microsomal degradation, PAMPA, blood-brain barrier) by Till Karsch and Julian Marschner (both group of Prof. Daniel Merk, Department Pharmacy, Ludwig Maximilians University Munich).
- Determination of the binding affinity to Nurr1 LBD (ITC) by Daniel Merk.
- *In vitro* evaluation in organoids by Hin-Man Tai and Michelle Vincendeau (Helmholtz Munich, Institute of Virology, Munich).
- Manuscript and management of the study were prepared by Daniel Merk.

Tuning RXR modulators for PGC1 α recruitment

- Molecular docking on RXR α :**27** complex (PDB: 6sjm33) by Thomas Wein.
- Synthesis and analytical characterization of all compounds from the study by Anesa Bitic, Roman Schwarzbach, Sina Wolff under the supervision of Felix Nawa, Jan Vietor and myself (all group of Prof. Daniel Merk, Department Pharmacy, Ludwig Maximilians University Munich).
- HFTR assays by Niklas Ildefeld (Goethe University Frankfurt, Institute of Pharmaceutical Chemistry, Frankfurt) and Jan Heering (Fraunhofer Institute for Translational Medicine and Pharmacology ITMP, Frankfurt).
- *In vitro* profiling of RXR α and PGC1 α in a cellular context by Julian Marschner.
- Manuscript and management of the study were prepared by Daniel Merk.

Azologs of the fatty acid mimetic drug cinalukast enable light-induced PPAR α activation

- Supervision of Niels van Herwijnen who did the synthesis and photophysical characterization of **87, 66-98, 102-104**.
- Manuscript and management of the study were authored by Daniel Merk.

The following parts of the dissertation have already been published:

- Figure 4, 5, 8, 10 are taken and adapted from reference 14 with permission. Copyright © 2022, American Chemical Society.
- Figure 15 are taken from reference 157 and reprinted with permission. Copyright © 2019, American Chemical Society.
- Figure 20-24, 26 are taken from reference 206 and does not require any further permission.
- Figure 32 and 33 have been adapted from reference 212 and does not require any further permission.
- Figure 43-48 are taken from reference 215 and does not require any further permission.

11 Acknowledgments

I would like to express my heartfelt gratitude to everyone who supported me throughout the journey of completing this doctoral thesis—my colleagues, partner, friends, and family.

First of all, I would like to thank Prof. Dr. Merk for his support and supervision of my work. Thank you for allowing me the freedom to develop my ideas and for the trust you placed in me. I am grateful to have started this adventure in Munich with you.

A special thanks to Prof. Dr. Paintner, who served as the second reviewer of this thesis.

I am also grateful to Silvia Arifi, who corrected my thesis and supported me through countless phone calls, both during and outside of work hours. Without you, this journey wouldn't have been as enjoyable. Thank you also for proofreading the thesis.

Thanks to Jan Vietor for the time we spent together in Frankfurt and Munich, and for the experiences we shared outside of work. I might not have gone to Munich without you. Thank you for everything.

Thanks to Emily Hank for all our work together and the party music we listened to.

I would also like to thank Max Lewandowski and Felix Nawa for the time and the fun we had together, especially in the early days in Munich.

My thanks also go to Markus Egner, Ursula Lopez, Tim Hörmann, Romy Busch, Katharina Scholz, Tanja Stiller, Xiu Ge, Till Kasch, and Loris Knümann for the wonderful time in Munich.

A special thanks goes to my students Niels van Herwijnen and Moritz Kornmayer for their work on our project and the fun we had in the lab.

A special thanks to the "Ex Wannern" and "new Merks" Jörg Pabel, Silke Duensing-Kropp, Tanja Franz, Georg Höfner, and Thomas Wein for warmly welcoming us upon our arrival and supporting us during our early days in Munich. I am very grateful for your help and support.

I would also like to thank the group of Prof. Manfred Schubert-Zsilavec in Frankfurt, particularly Mario Wurglics, Astrid Kaiser, as well as former Ph.D. students Silvia Arifi, Sabine Willems, Gustave Adouvi, Giuseppe Faudone, Simone Schierle, Daniel Zaienne, and Moritz Helmstädter and the new generation, including Espen Schallmayer, Laura Isigkeit, and Alisa Lang. You made my time in Frankfurt great.

A special heartfelt thanks goes to my girlfriend Yvonne, who has stood by me through both good times and challenging moments, always believing in me, being there for me, and showing endless understanding.

I would also like to thank my parents and sister, who supported me and helped me in every way.

To my friends, thank you for the non-academic conversations, your patience, and emotional support. Special thanks to Hannah and Nina for proofreading parts of my thesis. I would also like to say a big thank you to Hin-Man for being such a great friend and for working with me on Nurr1.

12 Reprints of the publications and manuscript for peer-review

12.1 Structure-Guided Design of Nurr1 Agonists Derived from the Natural Ligand Dihydroxyindole

Sai, M.; Vietor, J.; Kornmayer, M.; Egner, M.; López-García, U.; Höfner, G.; Pabel, J.; Marschner, J.; Wein, T.; Merk, D. Structure-Guided Design of Nurr1 Agonists Derived from the Natural Ligand Dihydroxyindole. *J. Med. Chem.*, **2023**, 13556–13567.

Reprinted with permission from Sai, M.; Vietor, J.; Kornmayer, M.; Egner, M.; López-García, U.; Höfner, G.; Pabel, J.; Marschner, J.; Wein, T.; Merk, D. Structure-Guided Design of Nurr1 Agonists Derived from the Natural Ligand Dihydroxyindole. *J. Med. Chem.*, **2023**, 13556–13567.

Structure-Guided Design of Nurr1 Agonists Derived from the Natural Ligand Dihydroxyindole

Minh Sai,[‡] Jan Vietor,[‡] Moritz Kornmayer, Markus Egner, Úrsula López-García, Georg Höfner, Jörg Pabel, Julian A. Marschner, Thomas Wein, and Daniel Merk*



Cite This: *J. Med. Chem.* 2023, 66, 13556–13567



Read Online

ACCESS |



Metrics & More

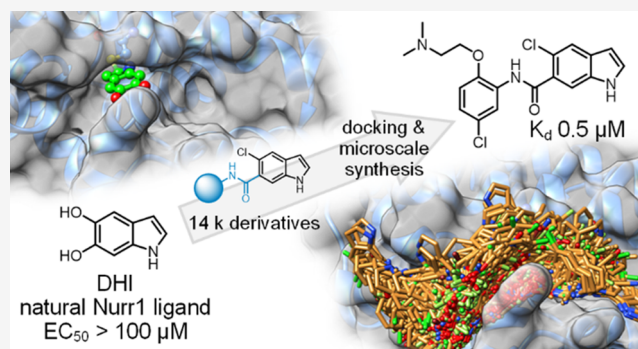


Article Recommendations



Supporting Information

ABSTRACT: The neuroprotective transcription factor Nurr1 was recently found to bind the dopamine metabolite 5,6-dihydroxyindole (DHI) providing access to Nurr1 ligand design from a natural template. We screened a custom set of 14 k extended DHI analogues in silico for optimized descendants to select 24 candidates for microscale synthesis and in vitro testing. Three out of six primary hits were validated as novel Nurr1 agonists with up to sub-micromolar binding affinity, highlighting the druggability of the Nurr1 surface region lining helix 12. In vitro profiling confirmed cellular target engagement of DHI descendants and demonstrated remarkable additive effects of combined Nurr1 agonist treatment, indicating diverse binding sites mediating Nurr1 activation, which may open new avenues in Nurr1 modulation.



INTRODUCTION

Nuclear receptor-related 1 (Nurr1) is a neuronal ligand-activated transcription factor with neuroprotective and anti-neuroinflammatory roles.^{1,2} Animal models have characterized Nurr1 as a critical for (dopaminergic) neuron development and survival and link the transcription factor with neurodegenerative diseases.^{1–5} Diminished neuronal Nurr1 activity in mice caused a phenotype with features of Parkinson's disease⁶ and exacerbated the pathology of Alzheimer's disease models⁷ and experimental autoimmune encephalomyelitis.⁸ Moreover, Nurr1 levels were decreased in human patients of Parkinson's and Alzheimer's disease and in rodent models of these pathologies.^{9–13} The transcription factor may therefore provide new opportunities in the treatment of neurodegeneration.

Despite the remarkable therapeutic potential of Nurr1, modulators are still rare.^{14,15} The antimalarials amodiaquine (AQ) and chloroquine (CQ), identified as the first direct Nurr1 agonists,¹⁶ have limited potency but served for studies on Nurr1 biology^{7,16} and as lead structures.^{17,18} We have recently developed Nurr1 agonist **1** with significantly enhanced potency as a next-generation chemical tool to elucidate the therapeutic potential of Nurr1.¹⁹ Still, new and chemically diverse Nurr1 agonist scaffolds with improved potency are needed to enable target validation of this remarkable nuclear receptor.

Prostaglandins A1 and E1²⁰ and the oxidized dopamine metabolite 5,6-dihydroxyindole (DHI, **2a**, Chart 1)²¹ have been discovered as potential endogenous Nurr1 ligands and were found to form covalent adducts with Cys566 of the Nurr1 ligand-binding domain (LBD). As a putative endogenous ligand,

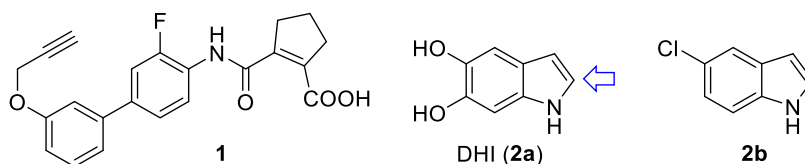
DHI is an attractive lead for Nurr1 agonist development. Structure–activity relationship (SAR) evaluation of DHI has yielded 5-chloro-1*H*-indole (**2b**) as a Nurr1 agonist with improved features and reduced toxicity,²² but an extension of the fragment-like **2a** and **2b** has not been studied.

Using DHI as lead and the Nurr1:DHI complex (PDB ID 6dda²¹) as a structural basis for docking-driven design and scoring, we have obtained derivatives of the natural Nurr1 ligand with enhanced affinity and potency. We employed a custom virtual library of 14,421 computationally generated DHI analogues, from which 24 top-scoring designs were prepared by microscale synthesis and tested for Nurr1 agonism. Six primary hits were prepared in batch and fully characterized to obtain three new validated and chemically diverse Nurr1 agonists. Additionally, structural fusion of the most active DHI analogue (**5o**, K_d 0.5 μM, EC₅₀ 3 μM) with the known ligand AQ produced another potent Nurr1 agonist (**13**, K_d 1.5 μM, EC₅₀ 3 μM). In vitro characterization confirmed cellular Nurr1 modulation by DHI descendants and interestingly revealed pronounced additive Nurr1 activation with the recently developed agonist **1**.¹⁹ Our structure-driven design and microscale synthesis approach successfully generated innovative

Received: May 12, 2023

Published: September 26, 2023



Chart 1. Nurr1 Agonists^a

^aThe blue arrow indicates the site for covalent interaction with Nurr1 (after oxidation of DHI).

Nurr1 ligand scaffolds based on a natural ligand, demonstrating druggability of the Nurr1 surface region lining helix 12.

RESULTS AND DISCUSSION

Structure-Guided Design. Despite recent progress in Nurr1 ligand discovery,¹ only a few ligand-bound Nurr1 LBD cocrystal structures are available among which the Nurr1:DHI complex (PDB ID 6dda²¹) appeared best suitable for structure-based design due to the favorable features of the indole scaffold. Structure analysis suggested space for structural extension of DHI (**2a**) or the related 5-chloroindole (**2b**), especially in the 5- and 6-positions of the indole, while the five-membered ring was buried in a narrow pocket (Figure 1a). The indole 5- and 6-positions are solvent exposed with opportunities to explore

adjacent grooves formed by helices H4/H12 and H10/H11 on the surface of the Nurr1 LBD. Previous structure–activity relationship analysis of the indole has demonstrated a preference for a chlorine substituent in the 5-position,²² prompting us to probe the extension of the indole in the 6-position to address the surface binding opportunities.

For a broad virtual exploration of potential substituents, we generated a virtual library based on 5-chloroindole as a common motif, which was extended in the 6-position by an amide linker and fused with 14,421 commercially available primary amines ($M_w \leq 240$) to obtain a virtual library of amides (full list in the Supporting Information). Amide linkage was chosen since potential for H-bond formation between the carbonyl group and the His516 backbone amine and between the amide nitrogen and the backbone carbonyl of Pro597 was observed in a preliminary docking assessment (Figure S1). Additionally, this approach enabled rapid and economic preparation of computationally preferred designs in microscale format even from very expensive amine building blocks. The full virtual library was docked with Glide to the DHI-binding site of the Nurr1 LBD. In line with the design hypothesis, the molecules populated the two grooves on the protein surface (Figure 1b). Docking scores varied widely over the entire virtual library (-7.71 to $+3.57$ for the best pose of each molecule) suggesting that the model was suitable to distinguish promising designs. We inspected the binding modes of the 100 top-ranking designs and selected 24 structurally diverse molecules (Table 1) for synthesis and testing based on a binding mode addressing the DHI pocket and suitability for microscale amide synthesis.

Microscale Library Preparation and Screening. To explore the Nurr1 agonist potential of the computationally preferred designs in a rapid and economical fashion, we initially prepared the compounds in a microscale format (100 μ mol). Amide synthesis was performed in 1.5 mL reaction tubes from 5-chloro-1*H*-indole-6-carboxylic acid (**3**) and the respective amines (**4a–x**) with EDC·HCl in ethyl acetate to obtain **5a–x** (Scheme 1a). Products from the microscale synthesis were roughly purified by a washing procedure with aqueous sodium bicarbonate, and amide formation was confirmed by mass spectrometry. The 5-chloro-1*H*-indole-6-carboxylic acid building block **3** was prepared from 2-chloro-4-methylbenzoic acid (**6**) by Batcho–Leimgruber indole synthesis (Scheme 1b) involving nitration to **7**, esterification (**8**), cyclization with DMF dimethylacetal to indole **9**, and ester hydrolysis to **3**.

A Gal4–Nurr1²³ hybrid reporter gene assay served for in vitro testing which is based on a chimeric receptor composed of the human Nurr1 LBD and the DNA-binding domain of Gal4 from yeast. A firefly luciferase construct with five tandem repeats of the Gal4 response element was used as the reporter gene and constitutively expressed (SV40 promoter) Renilla luciferase was employed for normalization and to capture potential test compound toxicity. The microscale synthesis products **5a–x** were tested for Nurr1 modulation in the Gal4–Nurr1 hybrid

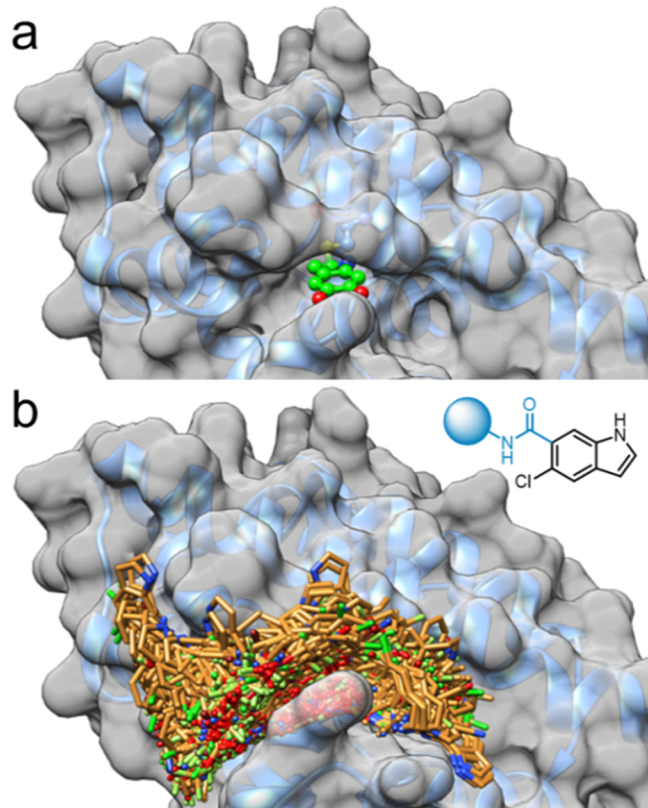
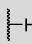
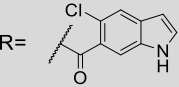
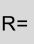
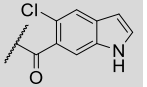
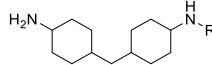
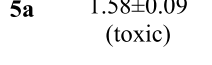
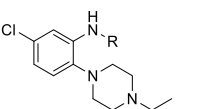
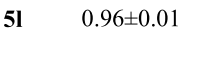
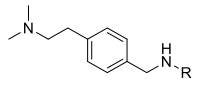
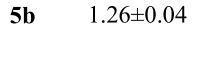
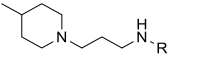
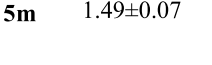
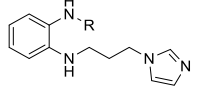
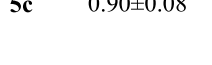
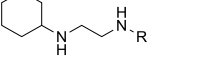
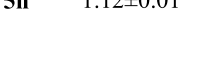
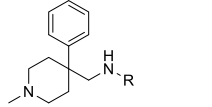
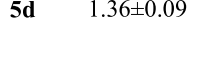
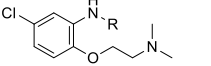
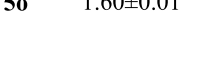
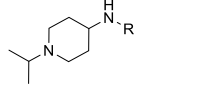
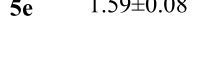
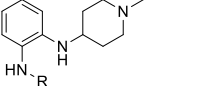
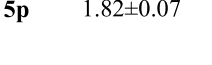
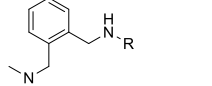
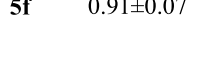
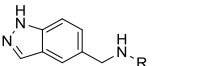
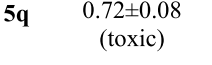
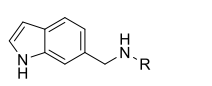
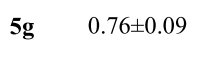
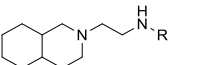
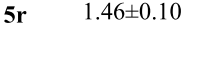
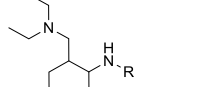
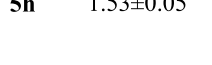
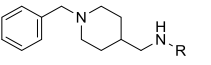
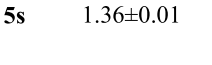
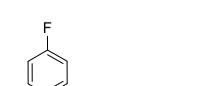
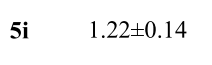
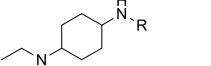
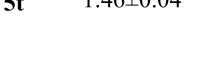
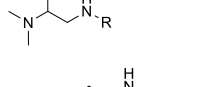

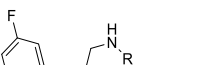
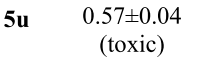
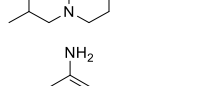
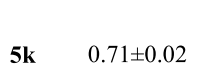
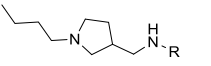
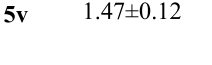
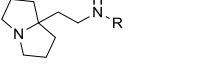
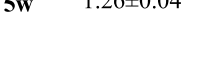
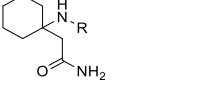
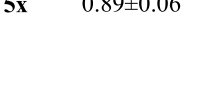


Figure 1. Structural basis for DHI-derived Nurr1 agonist design. (a) Cocrystal structure of the DHI-bound Nurr1 LBD (PDB ID 6dda,²¹ surface representation with bound DHI). DHI is bound in a narrow pocket with no space for extension around the five-membered ring, while the 5- and 6-positions are oriented toward the solvent. (b) General structure of the virtual amide library based on 5-chloro-1*H*-indole-6-carboxylic acid and 14,421 primary amines ($M_w \leq 240$) and docking of the virtual amide library to the Nurr1 LBD (PDB ID 6dda²¹). The virtual designs extended to the grooves on the Nurr1 LBD surface around the DHI-binding site.

Table 1. Gal4–Nurr1 Modulation by the Microscale DHI Analogue Library^a

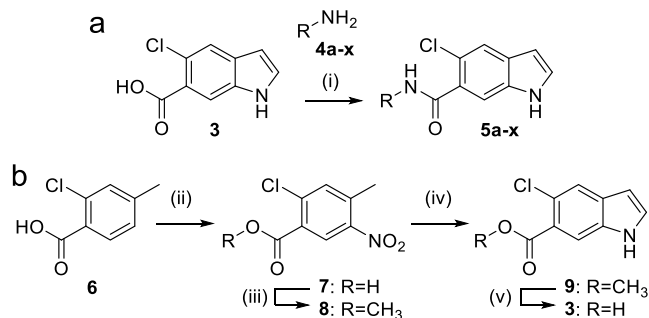
R = 		R = 		R = 		R = 	
ID	fold Nurr1 act.	ID	fold Nurr1 act.	ID	fold Nurr1 act.	ID	fold Nurr1 act.
 4a	1.10±0.08	 5a	1.58±0.09 (toxic)	 4l	0.89±0.07	 5l	0.96±0.01
 4b	1.62±0.15	 5b	1.26±0.04	 4m	1.08±0.04	 5m	1.49±0.07
 4c	1.29±0.09	 5c	0.90±0.08	 4n	0.96±0.12	 5n	1.12±0.01
 4d	1.60±0.14	 5d	1.36±0.09	 4o	1.19±0.05	 5o	1.60±0.01
 4e	1.10±0.12	 5e	1.59±0.08	 4p	1.51±0.19 (toxic)	 5p	1.82±0.07
 4f	0.97±0.10	 5f	0.91±0.07	 4q	1.20±0.18	 5q	0.72±0.08 (toxic)
 4g	1.24±0.05	 5g	0.76±0.09	 4r	1.05±0.13	 5r	1.46±0.10
 4h	1.6±0.4 (toxic)	 5h	1.53±0.05	 4s	1.72±0.28	 5s	1.36±0.01
 4i	1.02±0.14	 5i	1.22±0.14	 4t	0.83±0.13	 5t	1.46±0.04
 4j	1.60±0.27	 5j	1.29±0.08	 4u	1.34±0.04	 5u	0.57±0.04 (toxic)
 4k	1.09±0.05	 5k	0.71±0.02 (toxic)	 4v	1.39±0.30	 5v	1.47±0.12
				 4w	0.70±0.15	 5w	1.26±0.04
				 4x	0.86±0.08	 5x	0.89±0.06

^aCompounds were screened at 100 μ M assuming full conversion, actual concentrations were lower. Nurr1 activity data from the hybrid reporter gene assay are relative reporter activity vs DMSO-treated cells. Data are the mean \pm SD, $n = 3$. Compounds causing a decrease of the Renilla luminescence to $\leq 50\%$ of DMSO-treated cells were considered as potentially toxic (cf. Figure S2).

reporter gene assay at 100 μ M (assuming full conversion, actual concentrations were lower). To monitor the activity of the amine building blocks potentially remaining in the mixtures, the amines were also tested at 100 μ M to reveal true positive Nurr1 ligand hits. This enabled the discovery of promising scaffolds for further evaluation from a very diverse set in a rapid and cost-efficient manner despite expensive building blocks. The

possibility of false negatives resulting from the microscale synthesis format, purification procedure, and assay setting was accepted.

Of the 24 computationally favored designs 5a–x, six (5e, 5m, 5o, 5r, 5t, 5v; Table 1) were considered as primary hits as they activated Nurr1 by $\geq 140\%$ compared to DMSO-treated cells, exhibited no pronounced effect on cell viability as observed by

Scheme 1. Microscale Amide Synthesis (a) and Synthesis of Indole Building Block 3 (b)^a

^aReagents and conditions: (i) EDC·HCl, EtOAc, rt, 36 h; (ii) HNO₃/H₂SO₄, 5 °C, 0.5 h, 59%; (iii) acetyl chloride, MeOH, 50 °C, 4 h, 96%; (iv) DMF-DMA, DMF, 120 °C, 2 h; then Zn, AcOH/H₂O, 80 °C, 2 h, 40%; (v) LiOH·H₂O, EtOH/H₂O, rt, 18 h, 94%.

stable Renilla luciferase activity and in a WST-8 assay (Figure S2), and their corresponding amines were inactive/less active. These compounds were hence prepared in batch and isolated for full characterization.

Hit Validation. For orthogonal validation of the primary hits, we first employed isothermal titration calorimetry (ITC) to observe direct interaction and determine binding affinities (Table 2). Of the six hits in the primary screening, three (5e, 5m, 5t) exhibited no detectable interaction with the Nurr1 LBD and three revealed binding with K_d values of 0.5 μ M (5o), 3.2 μ M (5r), and 16 μ M (5v), respectively. In accordance with these results, 5e, 5m, and 5t failed to activate Nurr1 up to 100 μ M, while 5o, 5r, and 5v were confirmed as Nurr1 agonists (Table 2). 5o emerged as the most active DHI descendant with a K_d value of 0.5 μ M and an EC_{50} value of 3 μ M.

Binding Site Evaluation. Inspection of the predicted binding modes of the three active hits to Nurr1 revealed a similar orientation of 5o, 5r, and 5v with binding to a hydrophobic groove on the Nurr1 LBD surface lining helix 12 (Figure 2a), suggesting that this surface region of Nurr1 is druggable. The common indole motif was bound facing Cys566 and sandwiched between Arg515 and Arg563. Binding of the amide substituents was mainly mediated by hydrophobic contacts. The most active compound 5o additionally formed a face-to-face interaction with His516 (Figure 2b), rationalizing its enhanced potency.

Mutagenesis of the binding site cysteine 566 to serine diminished the activity of 5o (Figure 2c), supporting interaction with this epitope and the importance of Cys566 in ligand–Nurr1 contacts. High stability of 5o against glutathione (Figure 2d) and no observable adduct formation between recombinant Nurr1 LBD and 5o in LCMS (Figures S3 and S4) indicated that the interaction was non-covalent despite the prominent role of Cys566.

Structure–Activity Relationship of DHI Descendant 5o. The DHI descendant 5o presented markedly enhanced activity and affinity (Figure 3a) compared to the natural template 2a and induced Nurr1-regulated expression of tyrosine hydroxylase (TH) and vesicular amino acid transporter 2 (VMAT2) in astrocytes (T98G), indicative of cellular target engagement (Figure 3b). Based on this promising profile, we explored the structure–activity relationship of this new Nurr1 agonist scaffold (Table 3). The inverted analogue 10 comprising the opposite indole regiochemistry exhibited similar activity as 5o, indicating, in line with the predicted binding mode (Figure

Table 2. Binding Affinity to the Nurr1 LBD and Nurr1 Modulation of the Primary Hits (2a and 2b for Comparison)^{a–c}

ID	structure	K_d	EC_{50} (eff.)
DHI (2a)		- ^b	> 100 μ M ²¹
2b		15 μ M ²²	40±4 μ M (2.4±0.1-fold act.)
5e		no binding ^c	inactive at 100 μ M
5m		no binding ^c	inactive at 100 μ M
5o		0.5 μ M	3±1 μ M (1.3±0.1-fold act.)
5r		3.2 μ M	12±2 μ M (1.4±0.1-fold act.)
5t		no binding ^c	inactive at 100 μ M
5v		16 μ M	28±6 μ M (1.3±0.1-fold act.)

^aBinding affinity of 5e, 5m, 5o, 5r, 5t and 5v to the Nurr1 LBD was determined by ITC. Nurr1 modulation was determined in the Gal4–Nurr1 hybrid reporter gene assay; data are mean ± SD; $n \geq 3$. ^bCovalent binder. ^cNo interaction in ITC with 200 μ M ligand and 30 μ M protein.

2), that the orientation of the indole scaffold in the binding site is not critical. In accordance with this, methylation of the indole nitrogen of 5o in 11 had also little effect on affinity, albeit a fivefold decrease in cellular potency was observed. Reduction of the amide in 5o to a secondary amine linker in 12 was also tolerated, but it led to no improvement in affinity or potency. These results thus suggest 6-chloro-1H-indole-5-carboxamide and 5-chloro-1H-indole-6-carboxamide as suitable and easily accessible scaffolds to develop Nurr1 ligands binding to the LBD surface.

Several available Nurr1 ligands comprise a chloroquinoline motif derived from AQ,^{1,16,17} and we have observed that a scaffold hop from indole (fluvastatin, EC_{50} = 1.9 μ M) to quinoline (pitavastatin, EC_{50} = 0.12 μ M) produced a relevant

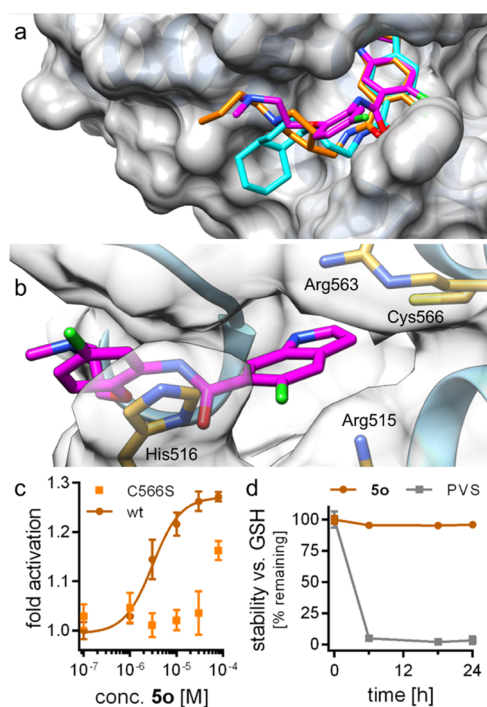


Figure 2. Predicted binding modes of **5o** (magenta), **5r** (cyan), and **5v** (orange) to the Nurr1 LBD (PDB ID 6dda³¹). (a) The three active DHI descendants **5o**, **5r**, and **5v** were predicted to bind to the DHI-binding site and extend toward a hydrophobic groove lining helix 12. (b) The most active Nurr1 agonist **5o** formed a face-to-face contact with His516, which is not observed for **5r** and **5v**, supporting the higher affinity of **5o**. (c) **5o** was less active on the Nurr1-C566S mutant, supporting interaction with the proposed epitope. Data are the mean \pm S.E.M.; $n \geq 3$. (d) **5o** was stable against reaction with glutathione (GSH). Phenyl vinyl sulfone (PVS) as positive control (125 μ M **5o** or PVS were incubated with 2.5 mM GSH in PBS at 37 $^{\circ}$ C). $n = 3$.

improvement in potency.² Thus, we evaluated the possibility of fusing the structural elements of **5o** and AQ. Interestingly, the merged compound **13** composed of the 7-chloroquinolin-4-amine motif of AQ and the amide substituent of **5o** acted as a Nurr1 agonist (K_d 1.5 μ M, EC_{50} 3 μ M) with considerably higher potency than AQ (EC_{50} 36 μ M).

In Vitro Profiling of Optimized DHI Descendants. **5o** and its AQ-hybrid **13** emerged as the most potent DHI descendants from the structure-guided approach to Nurr1 modulator development. Their further in vitro profiling confirmed Nurr1 agonism also on the human full-length receptor on the response element NBRE with similar potency to that observed in the hybrid reporter gene assay (**5o**: EC_{50} = $2 \pm 1 \mu$ M, 2.1 ± 0.2 -fold activation; **13**: EC_{50} = $4 \pm 1 \mu$ M, 2.4 ± 0.2 -fold activation; Figure 3c).

Selectivity profiling in Gal4 hybrid reporter gene assays (Figure 3d) revealed a preference of **5o** for Nurr1 over Nur77 (NR4A1) and, interestingly, no NOR-1 (NR4A3) activation, suggesting that the binding site of the DHI descendants is not conserved in NOR-1. **13** activated Nurr1 and Nur77 with equal potency but was less active on NOR-1. No nuclear receptor modulation by **5o** and **13** was observed outside the NR4A family (Figure 3e).

We also studied the response of Nurr1 to combined treatment with **5o**/**13** and the recently developed Nurr1 agonist **1** and, interestingly, detected additive Nurr1 activation (Figure 3f). The presence of **5o** or **13** (20 μ M each) did not alter the EC_{50}

value of **1** but increased its max. effect by 34–77%. This non-competitive behavior with additive Nurr1 activation suggests different, non-overlapping binding sites of the ligands, opening new avenues to modulation of Nurr1.

To assess the effects of the DHI descendants in a native cellular setting, we evaluated their effects on Nurr1-regulated gene expression in the immortalized rat dopaminergic neural cell line N27^{24,25} (Figure 3g). 5-Chloroindole (**2b**), **5o**, and **13** induced TH, VMAT, and superoxide dismutase 1 and 2 (SOD1/2) expression in a dose-dependent fashion. The efficacy of VMAT2 and SOD1 induction by **2b**, **5o**, and **13** was comparable, while TH and SOD2 upregulation by **5o** and **13** was stronger compared to that by **2b**. DHI (**2a**) had generally weaker effects and, interestingly, downregulated TH expression, suggesting that other regulatory mechanisms were involved.

CONCLUSIONS

Drug discovery based on natural ligands of nuclear receptors has been very fruitful in the past as exemplified by steroidal ligands for NR3 receptors or the FXR agonist obeticholic acid.^{15,26} Our results demonstrate that the binding site of the natural (covalent) Nurr1 ligand DHI (**2a**) is druggable and can be addressed by non-covalent binders with markedly enhanced potency compared to the natural template, opening a new avenue to Nurr1 agonist development.

Apart from the activity of 5-chloro-1H-indole (**2b**) and related fragment-like analogues,²² no SAR knowledge was available on DHI as Nurr1 agonist, prompting us to follow a structure-based virtual screening approach using a custom library of DHI derivatives. Modeling prioritized 24 molecules and experimental validation confirmed three DHI analogues as novel Nurr1 ligands. **5o** emerged from these DHI analogues with sub-micromolar affinity to Nurr1, preference over Nur77, and selectivity over NOR-1. Additionally, **5o** and its AQ-hybrid **13** caused additive Nurr1 activation with the recently discovered agonist **1**,¹⁹ indicating that Nurr1 can be simultaneously modulated through diverse ligand-binding sites, which may have additional therapeutic potential.

Despite recent progress in ligand discovery, molecular understanding of ligand binding to Nurr1 is still limited, and binding sites are elusive.¹ The binding site of DHI-derived Nurr1 ligands can be located with high confidence at the surface of the LBD close to helix 12 which opens new possibilities in Nurr1 ligand development. DHI descendants **5o** and **13** valuably expand the scarce collection of validated Nurr1 modulators and can serve as tools for chemogenomics and functional studies on the role of DHI and its binding site in Nurr1 modulation.

CHEMISTRY

The primary hits (**5e**, **5m**, **5o**, **5r**, **5t**, **5v**) were prepared according to Scheme 2 by amide coupling of **3** and the corresponding amines **4e**, **4m**, **4o**, **4r**, **4t**, and **4v**, respectively. The synthesis of **10** comprising an inverted substitution pattern on the indole was performed by the same route using the corresponding 6-chloro-1H-indole-5-carboxylic acid (**3a**) for amide coupling with **4o**. The *N*-methyl indole analogue **11** was obtained by *N*-methylation of the ester **9**, followed by ester hydrolysis to **9a** and amide coupling with **4o** using TCFH-NMI as coupling agent.

For the preparation of the secondary amine analogue **12**, **9** was reduced to the corresponding alcohol **14** using $LiAlH_4$ and

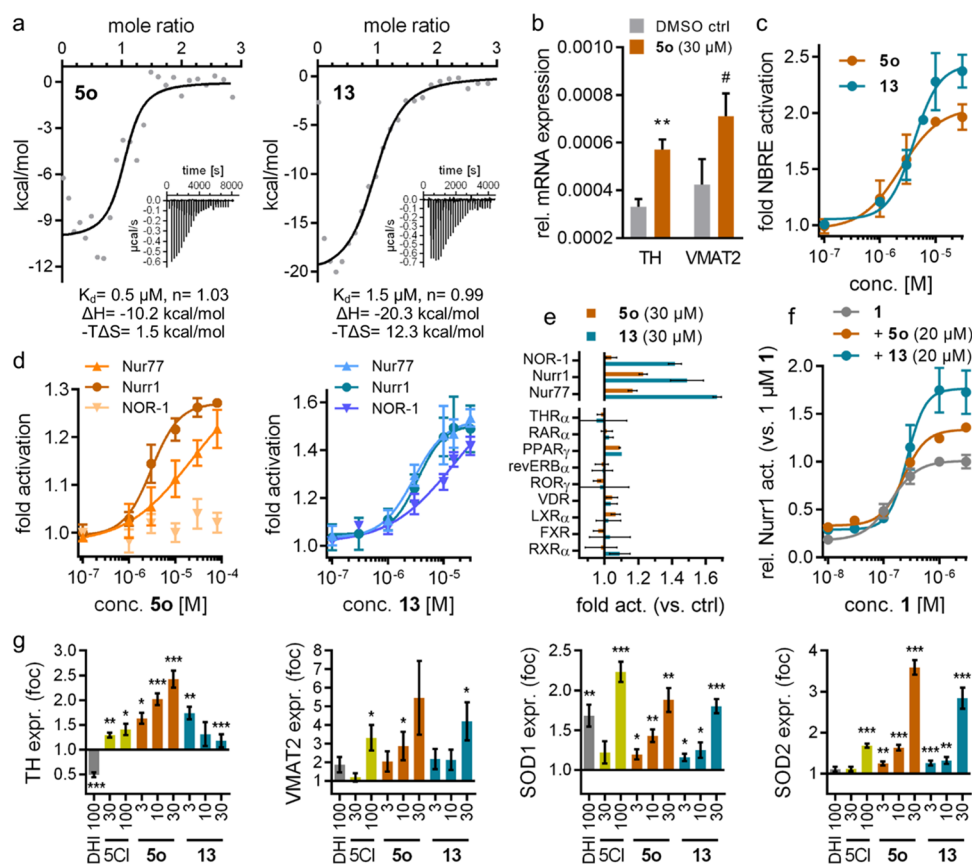


Figure 3. In vitro profiling of DHI-derived Nurr1 agonists. (a) Isothermal titration calorimetry (ITC) demonstrated binding of **5o** and **13** to the recombinant Nurr1 LBD. The fitting of the heat of binding is shown, and the isotherms at 25 °C are shown as insets. (b) **5o** (30 μ M) induced Nurr1-regulated mRNA expression of tyrosine hydroxylase (TH) and vesicular amino acid transporter 2 (VMAT2) in T98G cells. Data are the mean \pm S.E.M. rel. mRNA expression ($2^{-\Delta\Delta Ct}$), $n = 4$. # $p < 0.1$, ** $p < 0.01$ (t -test vs DMSO ctrl). (c) **5o** ($EC_{50} = 2 \pm 1 \mu$ M) and **13** ($EC_{50} = 4 \pm 1 \mu$ M) activated full-length human Nurr1 on the NBRE. Data are the mean \pm S.E.M. fold act. vs DMSO ctrl, $n \geq 4$. (d) **5o** exhibited preference for Nurr1 over the related NR4A receptors ($p < 0.001$ vs NOR-1; $p < 0.01$ vs Nur77; two-way analysis of variance (ANOVA) with multiple comparisons test); **13** activated Nurr1 and Nur77 with equal potency but revealed preference over NOR-1 ($p < 0.01$). Data are the mean \pm S.E.M. fold act. vs DMSO ctrl, $n \geq 4$. (e) **5o** and **13** did not modulate the activity of nuclear receptors outside the NR4A family. Data are the mean \pm S.E.M. fold activation vs DMSO ctrl, $n \geq 3$. (f) **5o** and **13** enhanced max. Nurr1 activation by agonist **1** to 134% (**5o**) and 177% (**13**) of its max. effect alone. Data are the mean \pm S.E.M. relative Nurr1 act. vs 1 μ M **1**, $n \geq 3$. (g) DHI (**2a**), *S*-chloroindole (**5Cl**, **2b**) and the descendants **5o** and **13** modulated Nurr1-regulated gene expression in dopaminergic neural cells (N27). TH, tyrosine hydroxylase; VMAT2, vesicular amino acid transporter 2; SOD1/2, superoxide dismutase 1/2. Data are the mean \pm S.E.M. relative mRNA expression compared to 0.1% DMSO; $n = 7-8$; * $p < 0.05$, ** $p < 0.01$, *** $p < 0.001$ (Wilcox test or t -test).

reoxidized to its aldehyde **15** with Dess–Martin periodinane, which reacted with amine **4o** in a reductive amination reaction to afford **12**. The AQ/**5o** hybrid **13** was prepared from 4-bromo-7-chloroquinoline (**16**) by Buchwald–Hartwig amination with amine **4o**.

EXPERIMENTAL SECTION

Chemistry. General. All chemicals were of reagent grade and used without further purification unless otherwise specified. All reactions were conducted in oven-dried Schlenk glassware under an argon atmosphere and in absolute solvents. Other solvents, especially for work-up procedures, were of reagent grade or purified by distillation (*iso*-hexane, ethyl acetate, ethanol). Reactions were monitored by thin-layer chromatography on TLC Silica gel 60 F₂₅₄ aluminum sheets by Merck and visualized under ultraviolet light (254 nm). Purification by column chromatography (CC) was performed on a puriFlash XSS20Plus system (Advion, Ithaca, NY) using high-performance spherical silica columns (SIHP, 50 μ M) by Interchim and a gradient of *iso*-hexane to EtOAc; reversed-phase CC was performed on a puriFlash 5.250 system (Advion) using C18HP columns (SIHP, 15 μ M) by Interchim and a gradient of 0.1% FA in H₂O, 10–100% acetonitrile (HPLC gradient grade). Preparative HPLC was also performed on the

puriFlash 5.250 system using a PREP-LC column (C18-HQ, 5 μ M) by Interchim and a gradient of 0.1% FA in H₂O, 10–100% methanol (HPLC gradient grade). Mass spectra were obtained on a puriFlash-CMS system (Advion) using atmospheric pressure chemical ionization (APCI). High-resolution mass spectrometry analysis (HRMS) was performed with a Thermo Finnigan LTQ FT instrument for electrospray ionization (ESI). NMR spectra were recorded on a Bruker Avance III HD 400 MHz or 500 MHz spectrometer equipped with a CryoProbe Prodigy broadband probe (Bruker). Chemical shifts are reported in δ values (ppm), and coupling constants (J) are reported in hertz (Hz). Purity was determined by quantitative ¹H NMR (qH NMR) according to a method described by Pauli et al. with internal calibration.²⁷ The qH NMR measurements were carried out under conditions allowing complete relaxation to assure the exact determination of peak area ratios. Used internal standards were ethyl 4-(dimethylamino)benzoate (LOT# BCCC6657, purity 99.63%) and maleic acid (LOT# BCBM8127V, purity 99.94%) in CDCl₃, MeOD-*d*₄, DMSO-*d*₆ or acetone-*d*₆. All compounds for biological testing had a purity $\geq 95\%$ according to qH NMR.

2-Chloro-4-methyl-5-nitrobenzoic acid (7).²⁸ 2-Chloro-4-methylbenzoic acid (**6**, 10.0 g, 55.8 mmol, 1.00 equiv) was suspended in sulfuric acid (100 mL) and cooled to 5 °C. Over a period of 40 min nitric acid (3.39 mL, 52.7 mmol, 0.90 equiv) was added dropwise so

Table 3. In Vitro Characterization of 10–12 Derived from Screening Hit 5o and 5o/AQ-Hybrid 13^a

ID	structure	K _d	EC ₅₀ (eff.)
5o		0.5 μM	3±1 μM (1.3±0.1-fold act.)
10		1.6 μM	6±3 μM (1.4±0.1-fold act.)
11		1 μM	16±6 μM (1.4±0.1-fold act.)
12		1.8 μM	5±2 μM (1.4±0.1-fold act.)
13		1.5 μM	3±1 μM (1.5±0.1-fold act.)

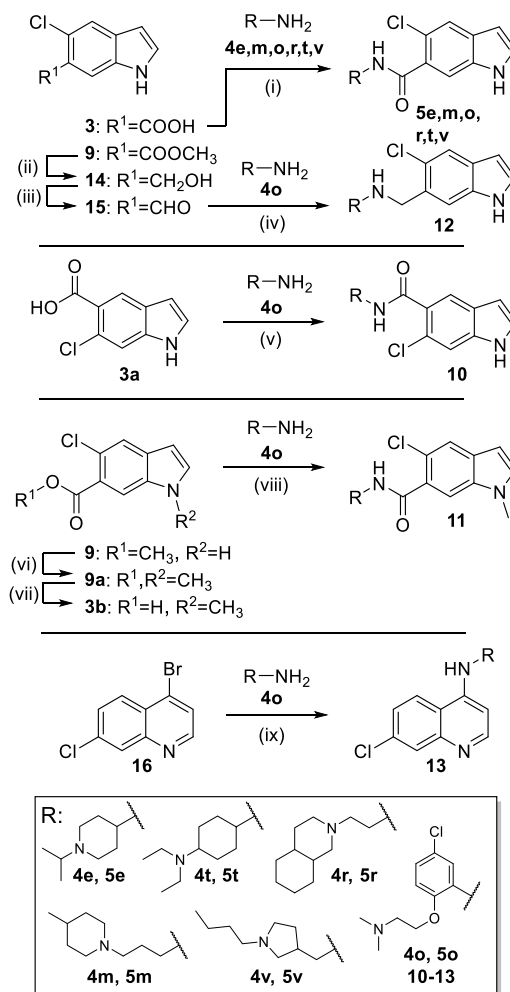
^aBinding affinity to the Nurr1 LBD was determined by ITC. Nurr1 modulation was determined in the Gal4–Nurr1 hybrid reporter gene assay; data are mean ± SD; *n* ≥ 3.

that the reaction mixture did not exceed a temperature of 15 °C. After complete addition of nitric acid, the reaction mixture was stirred at rt for 30 min and then poured into ice water. The solid that subsequently precipitated was filtered off, washed with cold water, and dissolved in EtOH. Water was added dropwise to the solution, whereupon a colorless solid precipitated. The solid was filtered off, washed with cold water, and dried under reduced pressure, yielding compound 7 as a colorless solid (7.57 g, 59%). *R_f* (*iso*-hexane/EtOAc = 8:2 + 2% AcOH) = 0.33. MS (–APCI): *m/z* 214.5 ([*M* – H][–]). ¹H NMR (400 MHz, acetone-*d*₆): δ = 8.54 (s, 1H), 7.72 (s, 1H), 2.65 (s, 3H) ppm. ¹³C NMR (101 MHz, acetone-*d*₆): δ = 164.70, 148.50, 139.43, 138.57, 136.14, 129.76, 128.72, 20.03 ppm.

Methyl 2-Chloro-4-methyl-5-nitrobenzoate (8).²⁸ Acetyl chloride (12.4 mL, 174 mmol, 5.00 equiv) was added dropwise to methanol (70 mL) at 5–10 °C. A solution of 2-chloro-4-methylnitrobenzoic acid (7, 7.50 g, 34.8 mmol, 1.00 equiv) in methanol (100 mL) was added in portions, and the reaction mixture was stirred at 50 °C for 4 h. After cooling to rt, the solvent was removed under reduced pressure. The yellow solid obtained was dissolved in DCM and washed with brine solution and water. The organic phase was dried over MgSO₄, filtered, and evaporated to yield 8 as a colorless solid (7.66 g, 96%). *R_f* (*iso*-hexane/EtOAc = 8:2) = 0.41. MS (+APCI): *m/z* 229.5 ([*M* + H]⁺). ¹H NMR (400 MHz, acetone-*d*₆): δ = 8.48 (s, 1H), 7.73 (s, 1H), 3.95 (s, 3H), 2.65 (s, 3H) ppm. ¹³C NMR (101 MHz, acetone-*d*₆): δ = 167.44, 148.34, 139.57, 138.30, 136.08, 129.51, 128.51, 53.18, 20.05 ppm.

Methyl 5-Chloro-1H-indole-6-carboxylate (9).²⁸ Methyl 2-chloro-4-methyl-5-nitrobenzoate (8, 7.66 g, 33.4 mmol, 1.00 equiv) was dissolved in DMF (50 mL). *N,N*-dimethylformamide dimethylacetate

Scheme 2. Batch Synthesis of 5e, 5m, 5o, 5r, 5t, 5v, and 10–13^a



^aReagents and conditions: (i) EDC·HCl, TEA, CHCl₃, rt, 18 h, 8–32%; (ii) LiAlH₄, THF, 0 °C, 1 h, 71%; (iii) Dess–Martin periodinane, DCM, DMF, 0 °C–rt, 1 h, 100%; (iv) NaBH(OAc)₃, AcOH, DCM, DCE, rt, 2 h, 36%; (v) EDC·HCl, TEA, CHCl₃, rt, 18 h, 5%; (vi) NaH, CH₃I, DMF, 0 °C, 10 min, rt, 2 h, 33%; (vii) LiOH·H₂O, EtOH, H₂O, rt, 18 h, 99%; (viii) NMI, TCFH, DMF, 80 °C, 18 h, 26%; (ix) Pd(OAc)₂, BINAP, K₃PO₄, dioxane, 90 °C, 24 h, 29%.

(10.4 mL, 49.9 mmol, 1.50 equiv) was added to the solution, and the reaction mixture was stirred for 2 h at 130 °C. The reaction mixture was concentrated under vacuum, dissolved in EtOAc, and washed with brine and water. The aqueous phases were extracted with EtOAc, and the combined organic phases were dried over MgSO₄. After removing the solvent, the obtained purple solid was dissolved in acetic acid (100 mL) and water (20 mL). Over a period of 40 min, zinc powder (13.06 g, 65.34 mmol, 6.0 equiv) was added in portions and the reaction mixture was heated to 80 °C for 2 h. After cooling to rt, the mixture was diluted with EtOAc and filtered. The organic phase was separated and washed with saturated NaHCO₃ solution and brine. The organic phase was dried over MgSO₄, filtered, and concentrated under reduced pressure. The brown oil was purified by CC and yielded compound 9 as a green solid (2.80 g, 40%). *R_f* (*iso*-hexane/EtOAc = 8:2) = 0.23. MS (+APCI): *m/z* 209.7 ([*M* + H]⁺). ¹H NMR (400 MHz, acetone-*d*₆): δ = 10.69 (s, 1H), 8.03 (s, 1H), 7.71 (s, 1H), 7.60 (t, *J* = 2.8 Hz, 1H), 6.54 (m, 1H), 3.87 (s, 3H) ppm. ¹³C NMR (126 MHz, acetone-*d*₆): δ = 167.20, 134.86, 132.86, 130.68, 124.13, 123.34, 122.65, 116.02, 102.38, 52.26 ppm.

5-Chloro-1H-indole-6-carboxylic acid (3). Methyl 5-chloro-1H-indole-6-carboxylate (**9**, 2.80 g, 13.4 mmol, 1.00 equiv) was dissolved in EtOH (25 mL) and water (25 mL). LiOH·H₂O (1.69 g, 40.2 mmol, 3.00 equiv) was added, and the reaction mixture was stirred at rt for 18 h. After removal of the solvent, the resulting solid was dissolved in water. The alkaline solution (pH ≥ 11) was extracted with EtOAc. The aqueous layer was acidified with aqueous hydrochloric acid (10%) and extracted with EtOAc. The latter organic layers were combined, washed with brine, dried over MgSO₄, and filtered. The solvent was removed under reduced pressure, and the residue was recrystallized from a mixture of DCM/diisopropylether (1:1), yielding compound **3** as a beige solid (2.47 g, 94%). *R*_f (iso-hexane/EtOAc = 8:2 + 2% AcOH) = 0.22. MS (+APCI): *m/z* 195.7 ([M + H]⁺). ¹H NMR (400 MHz, acetone-*d*₆): δ = 11.15 (s, 1H), 10.69 (s, 1H), 8.13 (s, 1H), 7.70 (s, 1H), 7.62–7.58 (m, 1H), 6.56–6.53 (m, 1H) ppm. ¹³C NMR (126 MHz, acetone-*d*₆): δ = 168.58, 134.20, 131.45, 129.74, 123.62, 122.39, 121.82, 115.47, 101.46 ppm.

5-Chloro-N-[5-chloro-2-[2-(dimethylamino)ethoxy]phenyl]-1H-indole-6-carboxamide (5o). 5-Chloro-1H-indole-6-carboxylic acid (**3**, 150 mg, 767 μmol, 1.00 equiv) and oxalyl chloride (69.0 μL, 767 μmol, 1.00 equiv) were dissolved in 4 mL of a mixture of one drop of DMF in DCM (14 mL). After 2 h, the solvent was removed under reduced pressure. The remaining residue was dissolved in DCM (6 mL), and 5-chloro-2-[2-(dimethylamino)ethoxy]aniline (**4o**, 165 mg, 767 μmol, 1.00 equiv) was added to the solution. The reaction mixture was stirred for 18 h at rt. Then, DCM (10 mL) and saturated NaHCO₃ solution (10 mL) were added. The separated organic layer was dried over MgSO₄, filtered, and concentrated under reduced pressure. The crude product was purified by CC, and subsequent recrystallization from methanol yielded compound **5o** as a colorless crystalline solid (23 mg, 8%). *R*_f (iso-hexane/EtOH = 1:1 + 2% TEA) = 0.24. MS (+APCI): *m/z* 391.3 ([M + H]⁺). HRMS (+EI): *m/z* calculated 391.08488 for [C₁₉H₁₉Cl₂N₃O₂]⁺, found: 391.08645 ([M]⁺). ¹H NMR (500 MHz, CDCl₃): δ = 10.17 (s, 1H), 8.78 (s, 1H), 8.71–8.66 (m, 1H), 7.90–7.86 (m, 1H), 7.68 (s, 1H), 7.38–7.33 (m, 1H), 7.03 (dd, *J* = 8.6, 2.6 Hz, 1H), 6.92 (d, *J* = 8.7 Hz, 1H), 6.54–6.50 (m, 1H), 4.09 (t, *J* = 5.4 Hz, 2H), 2.55 (t, *J* = 5.0 Hz, 2H), 2.02 (s, 6H) ppm. ¹³C NMR (126 MHz, CDCl₃): δ = 166.00, 146.62, 134.11, 131.66, 130.50, 129.03, 128.13, 128.09, 123.77, 122.13, 121.87, 120.81, 116.73, 113.63, 102.52, 69.45, 57.99, 45.18 ppm. qH NMR (400 MHz, MeOD-*d*₄, maleic acid as reference): purity = 95.4%.

7-Chloro-N-[5-chloro-2-[2-(dimethylamino)ethoxy]phenyl]-quinolin-4-amine (13). 4-Bromo-7-chloro-chloroquinoline (**16**, 170 mg, 699 μmol, 3.00 equiv), Pd(OAc)₂ (5.3 mg, 23 μmol, 0.1 equiv), (+/-)-2,2'-Bis(diphenylphosphino)-1,1'-binaphthalene (29 mg, 47 μmol, 0.2 equiv), K₃PO₄ (82.6 mg, 389 μmol, 1.67 equiv) and 5-chloro-2-[2-(dimethylamino)ethoxy]aniline (**5o**, 50.0 mg, 233 μmol, 1.00 equiv) were dissolved in 1,4-dioxane (10 mL). The suspension was stirred at 90 °C for 24 h. After completion of the reaction, the mixture was filtered through Celite and purified by CC, yielding compound **13** as a yellow solid (25 mg, 29%). *R*_f (DCM/MeOH = 95:5) = 0.13. MS (+APCI): *m/z* 375.7 ([M + H]⁺). HRMS (+ESI): *m/z* calculated 376.09779 for [C₁₉H₂₀Cl₂N₃O]⁺, found 376.09885 ([M + H]⁺). ¹H NMR (400 MHz, acetone-*d*₆): δ = 8.57 (d, *J* = 5.2 Hz, 1H), 8.54 (s, 1H), 8.27 (d, *J* = 9.0 Hz, 1H), 7.95 (d, *J* = 2.2 Hz, 1H), 7.55 (dd, *J* = 9.0, 2.2 Hz, 1H), 7.49 (d, *J* = 2.5 Hz, 1H), 7.22 (d, *J* = 8.7 Hz, 1H), 7.13 (dd, *J* = 8.7, 2.5 Hz, 1H), 7.01 (d, *J* = 5.2 Hz, 1H), 4.22 (t, *J* = 5.3 Hz, 2H), 2.57 (t, *J* = 5.4 Hz, 2H), 2.23 (s, 6H) ppm. ¹³C NMR (101 MHz, acetone-*d*₆): δ = 152.13, 150.06, 149.79, 147.27, 134.39, 132.89, 128.44, 126.28, 125.43, 124.07, 123.28, 121.72, 119.01, 117.67, 102.99, 68.52, 57.84, 44.8 ppm. qH NMR (400 MHz, acetone-*d*₆, Ethyl-4-(dimethylamino)-benzoate as reference): purity = 95.2%.

Computational Methods. Preparation of the Virtual Screening Library. Commercially available primary amines were retrieved from Reaxys with a molecular weight cutoff of ≤240, yielding 14,421 molecules. The “RDKit Two Component Reaction” node in KNIME²⁹ was used to generate a virtual library of amides by fusing compound **3** and the commercial amines. Three-dimensional (3D) structures of the resulting molecules were obtained using Schrödinger ligprep software with force field OPLS4. Protonation was calculated using Epik³⁰ in a pH

range of 6–8. Chiral information in the two-dimensional (2D) input structure was retained when present; otherwise, all possible stereoisomers were generated. The final amide library comprised 18,421 molecules for docking.

Docking. The 3D structure of Nurr1 LBD (PDB ID 6dda²¹) was prepared using the Schrödinger Protein Preparation Wizard in Maestro. The covalently bound ligand DHI was removed manually before docking. The center of the docking grid was centered at—40.62762552165796, 12.031786250745345, and 66.69510016401517. Docking was performed using Schrödinger GLIDE³¹ software in standard precision mode (SP). All parameters were left at the default values (SP; flexible ligands; sample ring conformations of ligand; add Epik state penalties to docking score; scaling of van der Waals radii = 0.8; postdocking minimization of five poses per ligand; write out of one pose per ligand). A total of 18,340 poses were generated with docking scores in the range between −7.71 and +5.73. A total of 18,313 poses had docking scores below zero. Structural analyses were visualized by UCSF Chimera.³²

Biological Characterization. Hybrid Reporter Gene Assays. Nurr1 modulation was determined in HEK293T cells (German Collection of Microorganisms and Cell Culture GmbH, DSMZ) by Gal4 hybrid reporter gene assays using pFR-Luc (Stratagene, La Jolla, CA; reporter), pRL-SV40 (Promega, Madison, WI; internal control), and pFA-CMV-hNurr1-LBD, as described previously.²³ Cells were cultured in Dulbecco's modified Eagle's medium (DMEM) high glucose supplemented with 10% fetal calf serum (FCS), sodium pyruvate (1 mM), penicillin (100 U/mL), and streptomycin (100 μg/mL) at 37 °C and 5% CO₂ and seeded in 96-well plates (3 × 10⁴ cells/well). After 24 h, the medium was changed to Opti-MEM without supplements, and cells were transiently transfected using Lipofectamine LTX reagent (Invitrogen) according to the manufacturer's protocol. Five hours after transfection, cells were incubated with the test compounds in Opti-MEM supplemented with penicillin (100 U/mL), streptomycin (100 μg/mL), and 0.1% DMSO for 16 h before luciferase activity was measured using the Dual-Glo Luciferase Assay System (Promega) according to the manufacturer's protocol on a Tecan Spark luminometer (Tecan Deutschland GmbH, Germany). Firefly luminescence was divided by Renilla luminescence and multiplied by 1000, resulting in relative light units (RLUs) to normalize for transfection efficiency and cell growth. Fold activation was obtained by dividing the mean RLU of the test compound by the mean RLU of the untreated control. All samples were tested in at least three biologically independent experiments in duplicate. For dose–response curve fitting and calculation of EC₅₀ values, the equation “[Agonist] versus response (three parameters)” was used in GraphPad Prism (version 7.00, GraphPad Software, La Jolla, CA). Selectivity profiling was performed with identical procedures using pFA-CMV-Nur77-LBD,²³ pFA-CMV-NOR-1-LBD,²⁵ pFA-CMV-THRα-LBD,³³ pFA-CMV-RARα-LBD,³⁴ pFA-CMV-PPARγ-LBD,³⁵ pFA-CMV-revERBα-LBD, pFA-CMV-RORγ-LBD,³⁶ pFA-CMV-VDR-LBD,³⁷ pFA-CMV-LXRα-LBD,³⁷ pFA-CMV-FXR-LBD,³⁸ and pFA-CMV-hRXRα-LBD.³⁹ Activity of test compounds on the Nurr1-C566S mutant was determined as described for wild-type Gal4–Nurr1 using pFA-CMV-Nurr1-C566S-LBD, which was constructed by site-directed mutagenesis using the Phusion Site-Directed Mutagenesis Kit (Thermo Scientific) and the following mutagenesis primer sequences: Pho-5'-TCG TAC CCT TAG CAC ACA GGG-3' and Pho-5'-AGT TCT GGG AGC TTC CCC AAC AGT TT-3'.

Reporter Gene Assay for Full-Length Human Nurr1. Activation of full-length human Nurr1 was studied in transiently transfected HEK293T cells as described previously²³ using the reporter plasmid pFR-Luc-NBRE, the full-length human nuclear receptor Nurr1 encoded by pcDNA3.1-hNurr1-NE (Addgene plasmid #102363), and pRL-SV40 (Promega) for normalization of transfection efficacy and to observe test compound toxicity. Cells were cultured in Dulbecco's modified Eagle's medium (DMEM) high glucose supplemented with 10% fetal calf serum (FCS), sodium pyruvate (1 mM), penicillin (100 U/mL), and streptomycin (100 μg/mL) at 37 °C and 5% CO₂ and seeded in 96-well plates (3 × 10⁴ cells/well). After 24 h, the medium was changed to Opti-MEM without supplements, and

cells were transiently transfected using Lipofectamine LTX reagent (Invitrogen) according to the manufacturer's protocol. Five hours after transfection, cells were incubated with the test compounds in Opti-MEM supplemented with penicillin (100 U/mL), streptomycin (100 μ g/mL), and 0.1% DMSO for 16 h before luciferase activity was measured using the Dual-Glo Luciferase Assay System (Promega) according to the manufacturer's protocol on a Tecan Spark luminometer (Tecan Deutschland GmbH, Germany). Firefly luminescence was divided by Renilla luminescence and multiplied by 1000, resulting in relative light units (RLUs) to normalize for transfection efficiency and cell growth. Fold activation was obtained by dividing the mean RLU of the test compound by the mean RLU of the untreated control. All samples were tested in at least three biologically independent experiments in duplicate. For dose–response curve fitting and calculation of EC₅₀ values, the equation “[Agonist] versus response (three parameters)” was used in GraphPad Prism (version 7.00, GraphPad Software, La Jolla, CA).

Isothermal Titration Calorimetry (ITC). ITC experiments were conducted as described previously¹⁹ on an Affinity ITC instrument (TA Instruments, New Castle, DE) at 25 °C and a stirring rate of 75 rpm. Nurr1 LBD protein (10 or 30 μ M) in buffer (20 mM Tris pH 7.5, 100 mM NaCl, 5% glycerol) containing 3–5% DMSO was titrated with the test compounds (100 or 200 μ M in the same buffer containing 3–5% DMSO) in 21–26 injections (1 \times 1 μ L and 20–25 \times 5 μ L) with an injection interval of 150 s. As control experiments, the test compounds were titrated to the buffer, and the buffer was titrated to the Nurr1 LBD protein under otherwise identical conditions. The heat rates of the compound–Nurr1 LBD titrations were analyzed using NanoAnalyze software (TA Instruments, New Castle, DE) with an independent binding model.

Glutathione Reactivity Assay. A hundred microliters of test compound solution (5o or PVS, 250 μ M each) in PBS buffer (pH 7.4 containing 2% DMSO) was mixed with 100 μ L of 5 mM glutathione solution in PBS buffer (pH 7.4) to obtain a final test compound concentration of 125 μ M and 2.5 mM glutathione in 200 μ L of sample volume. The samples were shaken at 37 °C. At different time points (0, 6, 18, 24 h), a 20 μ L aliquot of each reaction sample was diluted with 480 μ L of mobile phase (0.1% formic acid/acetonitrile = 40/60, v/v) containing 10 μ M 2-chloro-N-(5-chloro-2-(2-(dimethylamino)ethoxy)phenyl)benzamide as an internal standard. The resulting mixture was then analyzed by liquid chromatography–ultraviolet–electrospray ionization tandem mass spectrometry (LC–UV–ESI–MS) using an API 3200 QTrap triple quadrupole mass spectrometer (Sciex, Darmstadt, Germany) coupled to an Agilent 1100 HPLC system equipped with an Agilent 1100 diode array detector (G1315B, Agilent, Waldbronn, Germany) and a SIL-20A/HT autosampler (Shimadzu, Duisburg, Germany) controlled by Analyst software (v.1.6.3). A ZORBAX SB-Aq column (3.5 μ m, 3.0 mm \times 100 mm, Agilent, protected with a 0.5 μ m and a 0.2 μ m frit) was used as the stationary phase and 0.1% formic acid and acetonitrile (40:60, v/v) were used as the mobile phase at a flow rate of 400 μ L/min. The injection volume was 15 μ L per sample. MS detection was performed under positive ESI conditions in single-ion monitoring (SIM) mode recording *m/z* 392.1 (5o), *m/z* 353.0 (2-chloro-N-(5-chloro-2-(2-(dimethylamino)ethoxy)phenyl)benzamide), and *m/z* 169.1 (PVS). UV detection was performed at 254 nm. The AUC (area under the curve) values were determined by integration of LC–UV–ESI–MS chromatogram and then corrected using the internal standard for both MS and UV measurements. The experiment was repeated three times.

Evaluation of Covalent Nurr1 Ligand Adduct Formation. The Nurr1 LBD (10 μ M) was incubated in buffer (20 mM Tris pH 7.5, 100 mM NaCl, 5% glycerol, 1% DMSO) with 5o (100 μ M) or alone for 120 h at 4 °C and then analyzed by LC–UV/MS. LCMS spectra were recorded on a Bruker microTOF II in positive ionization mode. The instrument was calibrated in positive mode by direct infusion of a calibration solution (Agilent Technologies ESI-L Low Concentration Tuning Mix). The HPLC line was an Ultimate 3000 RP-HPLC System (Thermo Fisher Scientific) equipped with an Aeris C4 wide pore column (2.1 mm \times 150 mm, 6 μ m, Phenomenex) with 0.1% formic acid (A) and acetonitrile (B) as the mobile phase at a flow rate of 0.25 mL/

min. The gradient was 0–3 min at 5% B and then 5–95% B in 7 min plus 2 min of washing at 95% B. The column eluent was monitored by UV detection at 214, 254, and 280 nm with a diode array detector.

Cytotoxicity Assay. HEK293T cells were cultured at 37 °C and 5% CO₂ in DMEM high-glucose medium supplemented with sodium pyruvate (1 mM), penicillin (100 U/mL), streptomycin (100 μ g/mL), and 10% fetal calf serum (FCS) and seeded at a density of 10,000 cells in 96-well plates precoated with a 10 μ g/mL collagen G solution (Merck KgaA, L7213) at 37 °C for 30 min. After 24 h, the cells were treated with the test compounds in Opti-MEM medium supplemented with penicillin (100 U/mL), streptomycin (100 μ g/mL), and 0.1% DMSO or 0.1% DMSO alone as the untreated control. Each sample was prepared in four biologically independent repeats. After incubation for 24 h, the medium was removed and 10% water-soluble tetrazolium salt (Cell Counting Kit-8, MedChemExpress) in Opti-MEM supplemented with penicillin (100 U/mL) and streptomycin (100 μ g/mL) was added to assess metabolic activity. After 4 h, absorbance was measured at 450 nm using a Tecan Spark Cyto instrument (Tecan).

Evaluation of Nurr1-Regulated Gene Expression in T98G and N27 Cells. T98G cells (ATCC CRL-1690) were grown in DMEM high glucose supplemented with 10% FCS, sodium pyruvate (1 mM), penicillin (100 U/mL), and streptomycin (100 μ g/mL) at 37 °C and 5% CO₂ and seeded at a density of 250,000 cells per well in 12-well plates. After 24 h, the medium was changed to DMEM high glucose supplemented with 0.2% fetal calf serum (FCS), penicillin (100 U/mL), and streptomycin (100 μ g/mL), and the cells were incubated for another 24 h before stimulation with test compound 5o (30 μ M) solubilized with 0.1% DMSO or 0.1% DMSO as a negative control. After 16 h of incubation, the medium was removed and cells were washed with phosphate-buffered saline (PBS), and after full aspiration of residual liquids, cells were immediately frozen at –80 °C until further processing. N27 rat dopaminergic neural cells (SCC048, Sigma-Aldrich, Darmstadt, Germany) were grown in RPMI 1640 medium (Gibco, Thermo Fisher Scientific, Waltham) supplemented with 10% FCS, penicillin (100 U/mL), and streptomycin (100 μ g/mL) at 37 °C and 5% CO₂ and seeded at a density of 250,000 cells per well in 12-well plates. After 7 h, the medium was changed to RPMI 1640 medium supplemented with 0.2% FCS, penicillin (100 U/mL), and streptomycin (100 μ g/mL), and the cells were incubated for another 24 h before stimulation with the test compound solubilized with 0.1% DMSO or with 0.1% DMSO in RPMI 1640 medium with 0.2% FCS as a negative control. After 16 h of incubation, the medium was removed and cells were washed with phosphate-buffered saline (PBS), and after full aspiration of the residual liquids, cells were immediately frozen at –80 °C until further processing. Total RNA was isolated from T98G or N27 cells using the E.Z.N.A. Total RNA Kit I (Omega Bio-tek, Norcross) following the manufacturer's instructions. RNA concentration and purity were assessed using a NanoDrop One UV/VIS spectrophotometer (Thermo Fisher Scientific, Waltham) at 260/280 nm. Right before reverse transcription (RT), RNA was linearized at a concentration of 133 ng/ μ L (T98G) or 66.7 μ g/ μ L (N27) at 65 °C for 10 min and then immediately incubated on ice for at least 1 min. Reverse transcription was performed using 2 μ g (T98G) or 1 μ g (N27) of total RNA, 20 U Recombinant RNasin Ribonuclease Inhibitor (Promega, Mannheim, Germany), 100 U SuperScript IV Reverse Transcriptase including 5 \times First Strand Buffer and 0.1 M dithiothreitol (Thermo Fisher Scientific, Waltham), 3.75 ng of linear acrylamide, 625 ng of random hexamer primers (#11277081001, Merck, Darmstadt, Germany), and 11.25 nmol deoxynucleoside triphosphate mix (2.8 nmol each ATP, TTP, CTP, GTP; #R0186, Thermo Fisher Scientific, Waltham) at a volume of 22.45 μ L at 50 °C for 10 min and 80 °C for 10 min using a Thermal cycler XT⁹⁶ (VWR International, Darmstadt, Germany). Quantitative polymerase chain reaction (qPCR) was conducted using an Applied Biosystems QuantStudio 1 (Waltham) and a SYBR green-based detection method. Appropriately diluted cDNA was added to 6 pmol forward and reverse primers, respectively, 0.8 U Taq DNA Polymerase (#M0267, New England Biolabs, Ipswich), 40 ppm of SYBR Green I (#S9430, Sigma-Aldrich, St. Louis), 15 nmol deoxynucleoside triphosphate mix (as indicated above), 60 nmol MgCl₂, 4 μ g of bovine serum albumin (#B14, Thermo Fisher Scientific,

Waltham), 20% BioStab PCR Optimizer II (#53833, Merck, Darmstadt, Germany), and 10% Taq buffer without detergents (#B55, Thermo Fisher Scientific, Waltham) topped up to a final volume of 20 μ L with ddH₂O. Samples underwent 40 cycles of 15 s denaturation at 95 °C, 15 s of primer annealing at 59.4–62.4 °C (depending on the primer), and 20 s of elongation at 68 °C. PCR product specificity was evaluated using a melting curve analysis ranging from 65 to 95 °C. TH and VMAT2 mRNA expression was normalized to GAPDH mRNA expression per sample using the Δ Ct method. The following primers for the human genes were used for T98G cell samples: hVMAT2 (SLC18A2), 5'-GCT ATG CCT TCC TGC TGA TTG C-3' (fw) and 5'-CCA AGG CGA TTC CCA TGA CGT T-3' (rev); hTH, 5'-GCT GGA CAA GTG TCA TCA CCT G-3' (fw) and 5'-CCT GTA CTG GAA GGC GAT CTC A-3' (rev); and hGAPDH, 5'-AGG TCG GAG TCA ACG GAT TT-3' (fw) and 5'-TTC CCG TTC TCA GCC TTG AC-3' (rev). The following primers for the rat genes were used for N27 cell samples: rVMAT2 (SLC18A2), 5'-CAG AGT GCA GCA GAG CCA T-3' (fw) and 5'-CTG GGG ATG ATG GGA ACC AC-3' (rev); rTH, 5'-TGG GGA GCT GAA GGC TTA TG-3' (fw) and 5'-AGA GAA TGG GCG CTG GAT AC-3' (rev); rSOD1, 5'-GAA GGC GAG CAT GGG TTC C-3' (fw) and 5'-CAG GTC TCC AAC ATG CCT CTC T-3' (rev); rSOD2, 5'-CGG GGG CCA TAT CAA TCA CA-3' (fw) and 5'-TCC AGC AAC TCT CCT TTG GG-3' (rev); and rGAPDH, 5'-CAG CCG CAT CTT CTT GTG C-3' (fw) and 5'-AAC TTG CCG TGG GTA GAG TC-3' (rev). For statistical analysis, data were evaluated for normal distribution (Shapiro–Wilk test) and outliers (Grubb's test). Normally distributed data sets normalized to the respective vehicle control were tested for statistically significant differences to $H_0: \mu = 1$ with either a one-sample Wilcoxon rank-sum or a *t*-test depending on the respective Shapiro–Wilk test results. We considered a value of $p < 0.05$ to indicate statistical significance. *P*-values were indicated as * $p < 0.05$, ** $p < 0.01$, and *** $p < 0.001$.

■ ASSOCIATED CONTENT

Supporting Information

The Supporting Information is available free of charge at <https://pubs.acs.org/doi/10.1021/acs.jmedchem.3c00852>.

Initial docking experiments; toxicity evaluation of the screening compounds in a WST-8 assay; LC–UV chromatogram and MS pattern of the Nurr1 LBD with or without the ligand **5o**; and synthesis procedures, analytical data, and purity analyses (PDF)

Molecular formula strings containing molecular structures of **5e**, **5m**, **5o**, **5r**, **5t**, **5v**, and **10–13** with associated activity data (CSV)

Virtual DHI analogue library containing the structures of virtually generated DHI analogues (CSV)

Docking containing the results of docking **5a–x** to the Nurr1 LBD (ZIP)

■ AUTHOR INFORMATION

Corresponding Author

Daniel Merk – Department of Pharmacy, Ludwig-Maximilians-Universität München, 81377 Munich, Germany; orcid.org/0000-0002-5359-8128; Email: daniel.merk@cup.lmu.de

Authors

Minh Sai – Department of Pharmacy, Ludwig-Maximilians-Universität München, 81377 Munich, Germany; orcid.org/0009-0004-6053-9566

Jan Vietor – Department of Pharmacy, Ludwig-Maximilians-Universität München, 81377 Munich, Germany; orcid.org/0009-0008-0310-0804

Moritz Kornmayer – Department of Pharmacy, Ludwig-Maximilians-Universität München, 81377 Munich, Germany

Markus Egner – Department of Pharmacy, Ludwig-Maximilians-Universität München, 81377 Munich, Germany

Úrsula López-García – Department of Pharmacy, Ludwig-Maximilians-Universität München, 81377 Munich, Germany; orcid.org/0000-0003-2557-9584

Georg Höfner – Department of Pharmacy, Ludwig-Maximilians-Universität München, 81377 Munich, Germany

Jörg Pabel – Department of Pharmacy, Ludwig-Maximilians-Universität München, 81377 Munich, Germany; orcid.org/0000-0002-0174-9772

Julian A. Marschner – Department of Pharmacy, Ludwig-Maximilians-Universität München, 81377 Munich, Germany

Thomas Wein – Department of Pharmacy, Ludwig-Maximilians-Universität München, 81377 Munich, Germany

Complete contact information is available at:

<https://pubs.acs.org/10.1021/acs.jmedchem.3c00852>

Author Contributions

[‡]M.S. and J.V. contributed equally to this work.

Notes

The authors declare no competing financial interest.

■ ACKNOWLEDGMENTS

This research was co-funded by the European Union (ERC, NeuRoPROBE, 101040355). Views and opinions expressed are however those of the author(s) only and do not necessarily reflect those of the European Union or the European Research Council. Neither the European Union nor the granting authority can be held responsible for them. pcDNA3.1-hNurr1-NE (Addgene plasmid #102363) was a gift from Shu Leong Ho. Structural analyses were visualized with UCSF Chimera, developed by the Resource for Biocomputing, Visualization, and Informatics at the University of California, San Francisco. The authors thank Vasily Morozov and Céline Douat for their support.

■ ABBREVIATIONS USED

AQ, amodiaquine; CQ, chloroquine; DHI, 5,6-dihydroxyindole; ITC, isothermal titration calorimetry; LBD, ligand-binding domain; Nurr1, nuclear receptor-related factor 1; TH, tyrosine hydroxylase; VMAT2, vesicular amino acid transporter 2

■ REFERENCES

- (1) Willems, S.; Merk, D. Medicinal Chemistry and Chemical Biology of Nurr1 Modulators: An Emerging Strategy in Neurodegeneration. *J. Med. Chem.* **2022**, *65*, 9548–9563.
- (2) Willems, S.; Marschner, J. A.; Kilu, W.; Faudone, G.; Busch, R.; Duensing-Kropp, S.; Heering, J.; Merk, D. Nurr1 Modulation Mediates Neuroprotective Effects of Statins. *Adv. Sci.* **2022**, *9*, No. 2104640.
- (3) Saijo, K.; Winner, B.; Carson, C. T.; Collier, J. G.; Boyer, L.; Rosenfeld, M. G.; Gage, F. H.; Glass, C. K. A Nurr1/CoREST Pathway in Microglia and Astrocytes Protects Dopaminergic Neurons from Inflammation-Induced Death. *Cell* **2009**, *137*, 47–59.
- (4) Zetterström, R. H.; Solomin, L.; Jansson, L.; Hoffer, B. J.; Olson, L.; Perlmann, T. Dopamine Neuron Ageneration in Nurr1-Deficient Mice. *Science* **1997**, *276*, 248–250.
- (5) Willems, S.; Zaienne, D.; Merk, D. Targeting Nuclear Receptors in Neurodegeneration and Neuroinflammation. *J. Med. Chem.* **2021**, *64*, 9592–9638.
- (6) Decressac, M.; Volakakis, N.; Björklund, A.; Perlmann, T. NURR1 in Parkinson Disease—from Pathogenesis to Therapeutic Potential. *Nat. Rev. Neurol.* **2013**, *9*, 629–636.
- (7) Moon, M.; Jung, E. S.; Jeon, S. G.; Cha, M.-Y.; Jang, Y.; Kim, W.; Lopes, C.; Mook-Jung, I.; Kim, K.-S. Nurr1 (NR4A2) Regulates

Alzheimer's Disease-Related Pathogenesis and Cognitive Function in the 5XFAD Mouse Model. *Aging Cell* **2019**, *18*, No. e12866.

(8) Montarolo, F.; Perga, S.; Martire, S.; Bertolotto, A. Nurr1 Reduction Influences the Onset of Chronic EAE in Mice. *Inflammation Res.* **2015**, *64*, 841–844.

(9) Decressac, M.; Kadkhodaei, B.; Mattsson, B.; Laguna, A.; Perlmann, T.; Björklund, A. α -Synuclein-Induced down-Regulation of Nurr1 Disrupts GDNF Signaling in Nigral Dopamine Neurons. *Sci. Transl. Med.* **2012**, *4*, No. 163ra156.

(10) Liu, W.; Gao, Y.; Chang, N. Nurr1 Overexpression Exerts Neuroprotective and Anti-Inflammatory Roles via down-Regulating CCL2 Expression in Both in Vivo and in Vitro Parkinson's Disease Models. *Biochem. Biophys. Res. Commun.* **2017**, *482*, 1312–1319.

(11) Parra-Damas, A.; Valero, J.; Chen, M.; España, J.; Martín, E.; Ferrer, I.; Rodríguez-Alvarez, J.; Saura, C. A. Crcl1 Activates a Transcriptional Program Deregulated at Early Alzheimer's Disease-Related Stages. *J. Neurosci.* **2014**, *34*, 5776–5787.

(12) Chu, Y.; Le, W.; Kompolti, K.; Jankovic, J.; Mufson, E. J.; Kordower, J. H. Nurr1 in Parkinson's Disease and Related Disorders. *J. Comp. Neurol.* **2006**, *494*, 495–514.

(13) Satoh, J.-i.; Nakanishi, M.; Koike, F.; Miyake, S.; Yamamoto, T.; Kawai, M.; Kikuchi, S.; Nomura, K.; Yokoyama, K.; Ota, K.; Kanda, T.; Fukazawa, T.; Yamamura, T. Microarray Analysis Identifies an Aberrant Expression of Apoptosis and DNA Damage-Regulatory Genes in Multiple Sclerosis. *Neurobiol. Dis.* **2005**, *18*, 537–550.

(14) Munoz-Tello, P.; Lin, H.; Khan, P.; de Vera, I. M. S.; Kamenecka, T. M.; Kojetin, D. J. Assessment of NR4A Ligands That Directly Bind and Modulate the Orphan Nuclear Receptor Nurr1. *J. Med. Chem.* **2020**, *63*, 15639–15654.

(15) Isigkeit, L.; Merk, D. Opportunities and Challenges in Targeting Orphan Nuclear Receptors. *Chem. Commun.* **2023**, *59*, 4551–4561.

(16) Kim, C.-H.; Han, B.-S.; Moon, J.; Kim, D.-J.; Shin, J.; Rajan, S.; Nguyen, Q. T.; Sohn, M.; Kim, W.-G.; Han, M.; Jeong, I.; Kim, K.-S.; Lee, E.-H.; Tu, Y.; Naffin-Olivos, J. L.; Park, C.-H.; Ringe, D.; Yoon, H. S.; Petsko, G. A.; et al. Nuclear Receptor Nurr1 Agonists Enhance Its Dual Functions and Improve Behavioral Deficits in an Animal Model of Parkinson's Disease. *Proc. Natl. Acad. Sci. U.S.A.* **2015**, *112*, 8756–8761.

(17) Willems, S.; Ohrndorf, J.; Kilu, W.; Heering, J.; Merk, D. Fragment-like Chloroquinolineamines Activate the Orphan Nuclear Receptor Nurr1 and Elucidate Activation Mechanisms. *J. Med. Chem.* **2021**, *64*, 2659–2668.

(18) Willems, S.; Müller, M.; Ohrndorf, J.; Heering, J.; Proschak, E.; Merk, D. Scaffold Hopping from Amodiaquine to Novel Nurr1 Agonist Chemotypes via Microscale Analogue Libraries. *ChemMedChem* **2022**, *17*, No. e2022000.

(19) Vietor, J.; Gege, C.; Stiller, T.; Busch, R.; Schallmayer, E.; Kohlhof, H.; Höfner, G.; Pabel, J.; Marschner, J. A.; Merk, D. Development of a Potent Nurr1 Agonist Tool for in Vivo Applications. *J. Med. Chem.* **2023**, *66*, 6391–6402.

(20) Rajan, S.; Jang, Y.; Kim, C. H.; Kim, W.; Toh, H. T.; Jeon, J.; Song, B.; Serra, A.; Lescar, J.; Yoo, J. Y.; Beldar, S.; Ye, H.; Kang, C.; Liu, X. W.; Feitosa, M.; Kim, Y.; Hwang, D.; Goh, G.; Lim, K. L.; et al. PGE1 and PGA1 Bind to Nurr1 and Activate Its Transcriptional Function. *Nat. Chem. Biol.* **2020**, *16*, 876–886.

(21) Bruning, J. M.; Wang, Y.; Oltrabella, F.; Tian, B.; Kholodar, S. A.; Liu, H.; Bhattacharya, P.; Guo, S.; Holton, J. M.; Fletterick, R. J.; Jacobson, M. P.; England, P. M. Covalent Modification and Regulation of the Nuclear Receptor Nurr1 by a Dopamine Metabolite. *Cell Chem. Biol.* **2019**, *26*, 674–685.e6.

(22) Kholodar, S. A.; Lang, G.; Cortopassi, W. A.; Iizuka, Y.; Brah, H. S.; Jacobson, M. P.; England, P. M. Analogs of the Dopamine Metabolite 5,6-Dihydroxyindole Bind Directly to and Activate the Nuclear Receptor Nurr1. *ACS Chem. Biol.* **2021**, *16*, 1159–1163.

(23) Willems, S.; Kilu, W.; Ni, X.; Chaikuad, A.; Knapp, S.; Heering, J.; Merk, D. The Orphan Nuclear Receptor Nurr1 Is Responsive to Non-Steroidal Anti-Inflammatory Drugs. *Commun. Chem.* **2020**, *3*, No. 85.

(24) Clarkson, E. D.; La Rosa, F. G.; Edwards-Prasad, J.; Weiland, D. A.; Witta, S. E.; Freed, C. R.; Prasa, K. N. Improvement of Neurological

Deficits in 6-Hydroxydopamine-Lesioned Rats after Transplantation with Allogeneic Simian Virus 40 Large Tumor Antigen Gene-Induced Immortalized Dopamine Cells. *Proc. Natl. Acad. Sci. U. S. A.* **1998**, *95*, 1265–1270.

(25) Gao, L.; Zhou, W.; Symmes, B.; Freed, C. R. Re-Cloning the N27 Dopamine Cell Line to Improve a Cell Culture Model of Parkinson's Disease. *PLoS One* **2016**, *11*, No. e0160847.

(26) Pellicciari, R.; Fiorucci, S.; Camaioni, E.; Clerici, C.; Costantino, G.; Maloney, P. R.; Morelli, A.; Parks, D. J.; Willson, T. M. 6 α -Ethyl-Chenodeoxycholic Acid (6-ECDCa), a Potent and Selective FXR Agonist Endowed with Anticholestatic Activity. *J. Med. Chem.* **2002**, *45*, 3569–3572.

(27) Pauli, G. F.; Chen, S. N.; Simmler, C.; Lankin, D. C.; Gödecke, T.; Jaki, B. U.; Friesen, J. B.; McAlpine, J. B.; Napolitano, J. G. Importance of Purity Evaluation and the Potential of Quantitative ¹H NMR as a Purity Assay. *J. Med. Chem.* **2014**, *57*, 9220–9231.

(28) McCoull, W.; Barton, P.; Brown, A. J. H.; Bowker, S. S.; Cameron, J.; Clarke, D. S.; Davies, R. D. M.; Dossetter, A. G.; Ertan, A.; Fenwick, M.; Green, C.; Holmes, J. L.; Martin, N.; Masters, D.; Moore, J. E.; Newcombe, N. J.; Newton, C.; Pointon, H.; Robb, G. R.; et al. Identification, Optimization, and Pharmacology of Acylurea GHS-R1a Inverse Agonists. *J. Med. Chem.* **2014**, *57*, 6128–6140.

(29) Berthold, M. R.; Cebren, N.; Dill, F.; Gabriel, T. R.; Kötter, T.; Meinel, T.; Ohl, P.; Thiel, K.; Wiswedel, B. KNIME - the Konstanz Information Miner: Version 2.0 and Beyond. *SIGKDD Explor. Newsl.* **2006**, *11*, 26–31.

(30) Shelley, J. C.; Cholleti, A.; Frye, L. L.; Greenwood, J. R.; Timlin, M. R.; Uchimaya, M. Epik: A Software Program for PKa Prediction and Protonation State Generation for Drug-like Molecules. *J. Comput.-Aided. Mol. Des.* **2007**, *21*, 681–691.

(31) Friesner, R. A.; Banks, J. L.; Murphy, R. B.; Halgren, T. A.; Klicic, J. J.; Mainz, D. T.; Repasky, M. P.; Knoll, E. H.; Shelley, M.; Perry, J. K.; Shaw, D. E.; Francis, P.; Shenkin, P. S. Glide: A New Approach for Rapid, Accurate Docking and Scoring. 1. Method and Assessment of Docking Accuracy. *J. Med. Chem.* **2004**, *47*, 1739–1749.

(32) Pettersen, E. F.; Goddard, T. D.; Huang, C. C.; Couch, G. S.; Greenblatt, D. M.; Meng, E. C.; Ferrin, T. E. UCSF Chimera—a Visualization System for Exploratory Research and Analysis. *J. Comput. Chem.* **2004**, *25*, 1605–1612.

(33) Gellrich, L.; Heitel, P.; Heering, J.; Kilu, W.; Pollinger, J.; Goebel, T.; Kahnt, A.; Arifi, S.; Pogoda, W.; Paulke, A.; Steinhilber, D.; Proschak, E.; Wurglics, M.; Schubert-Zsilavecz, M.; Chaikuad, A.; Knapp, S.; Bischoff, I.; Fürst, R.; Merk, D. L-Thyroxin and the Nonclassical Thyroid Hormone TETRAC Are Potent Activators of PPAR γ . *J. Med. Chem.* **2020**, *63*, 6727–6740.

(34) Pollinger, J.; Gellrich, L.; Schierle, S.; Kilu, W.; Schmidt, J.; Kalinowsky, L.; Ohrndorf, J.; Kaiser, A.; Heering, J.; Proschak, E.; Merk, D. Tuning Nuclear Receptor Selectivity of Wy14,643 towards Selective Retinoid X Receptor Modulation. *J. Med. Chem.* **2019**, *62*, 2112–2126.

(35) Rau, O.; Wurglics, M.; Paulke, A.; Zitzkowski, J.; Meindl, N.; Bock, A.; Dingermann, T.; Abdel-Tawab, M.; Schubert-Zsilavecz, M. Carnosic Acid and Carnosol, Phenolic Diterpene Compounds of the Labiate Herbs Rosemary and Sage, Are Activators of the Human Peroxisome Proliferator-Activated Receptor Gamma. *Planta Med.* **2006**, *72*, 881–887.

(36) Moret, M.; Helmstädter, M.; Grisoni, F.; Schneider, G.; Merk, D. Beam Search for Automated Design and Scoring of Novel ROR Ligands with Machine Intelligence**. *Angew. Chem., Int. Ed.* **2021**, *60*, 19477–19482.

(37) Flesch, D.; Cheung, S.-Y.; Schmidt, J.; Gabler, M.; Heitel, P.; Kramer, J. S.; Kaiser, A.; Hartmann, M.; Lindner, M.; Lüddens-Dämgen, K.; Heering, J.; Lamers, C.; Lüddens, H.; Wurglics, M.; Proschak, E.; Schubert-Zsilavecz, M.; Merk, D.; Non-Acidic; Farnesoid, X. Receptor Modulators. *J. Med. Chem.* **2017**, *60*, 7199–7205.

(38) Schmidt, J.; Klingler, F.-M.; Proschak, E.; Steinhilber, D.; Schubert-Zsilavecz, M.; Merk, D. NSAIDs Ibuprofen, Indometacin, and Diclofenac Do Not Interact with Farnesoid X Receptor. *Sci. Rep.* **2015**, *5*, No. 14782.

(39) Heitel, P.; Gellrich, L.; Kalinowsky, L.; Heering, J.; Kaiser, A.; Ohrndorf, J.; Proschak, E.; Merk, D. Computer-Assisted Discovery and Structural Optimization of a Novel Retinoid X Receptor Agonist Chemotype. *ACS Med. Chem. Lett.* **2019**, *10*, 203–208.

- Supporting Information -

Structure-Guided Design of Nurr1 Agonists Derived from the Natural Ligand Dihydroxyindole

Minh Sai^{1,#}, Jan Vietor^{1,#}, Moritz Kornmayer¹, Markus Egner¹, Úrsula López-García¹, Georg Höfner¹, Jörg Pabel¹, Julian A. Marschner¹, Thomas Wein¹, Daniel Merk^{1*}

¹ Ludwig-Maximilians-Universität München, Department of Pharmacy, 81377 Munich, Germany

M.S. and J.V. contributed equally to this work

* daniel.merk@cup.lmu.de

Table of Contents

Supplementary Figures	S2
Experimental Procedures	S5
General	S5
General procedures	S5
Synthesis and analytical characterization of 5e,m,o,r,t,v, 10-13	S6
Synthesis and analytical characterization of intermediates	S9
qH NMR of 5e,m,o,r,t,v, 10-13 for purity analysis	S11
Supplementary References	S16

Supplementary Figures

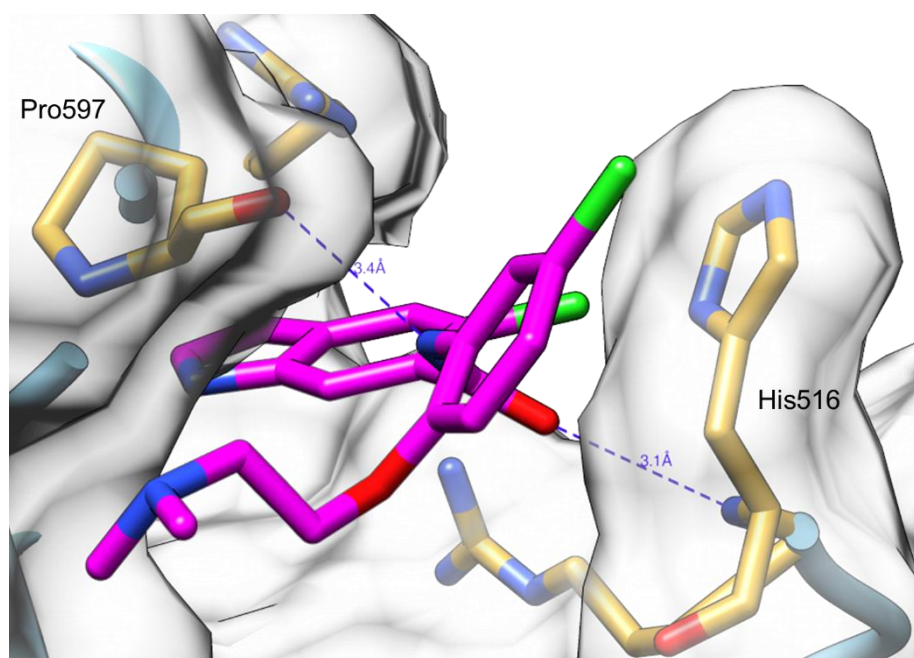


Figure S1. Initial evaluation by docking experiments suggested interactions of a carboxamide in 5- or 6-position of the 1*H*-indole scaffold with the backbone of His516 and Pro597 of the Nurr1 LBD (PDB ID 6dda¹, **5o** shown as example ligand) thus indicating potential of *N*-substituted carboxamides for extension of the natural ligand DHI.

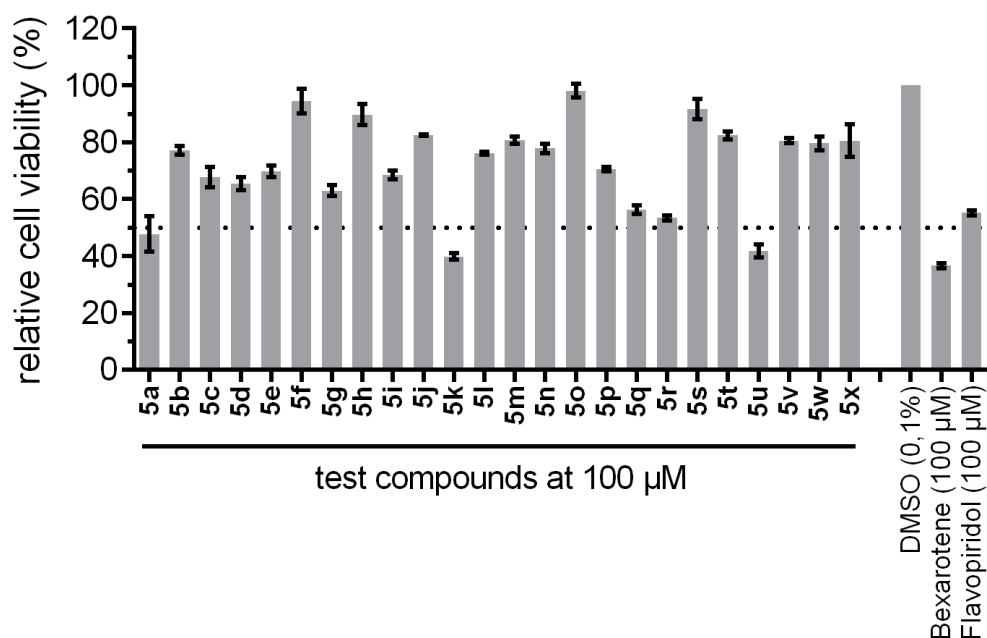


Figure S2. Toxicity evaluation of the screening compounds in a WST-8 assay in HEK293T cells at 100 μM (data are the mean±S.E.M.; n=4). Compounds **5a**, **5k** and **5u** causing <50% cell viability were excluded from follow-up studies. Like **5a**, **5k** and **5u**, compound **5q** diminished Renilla luciferase activity in the reporter gene assay to <50% and was also excluded despite slightly lower toxicity in the WST-8 assay.

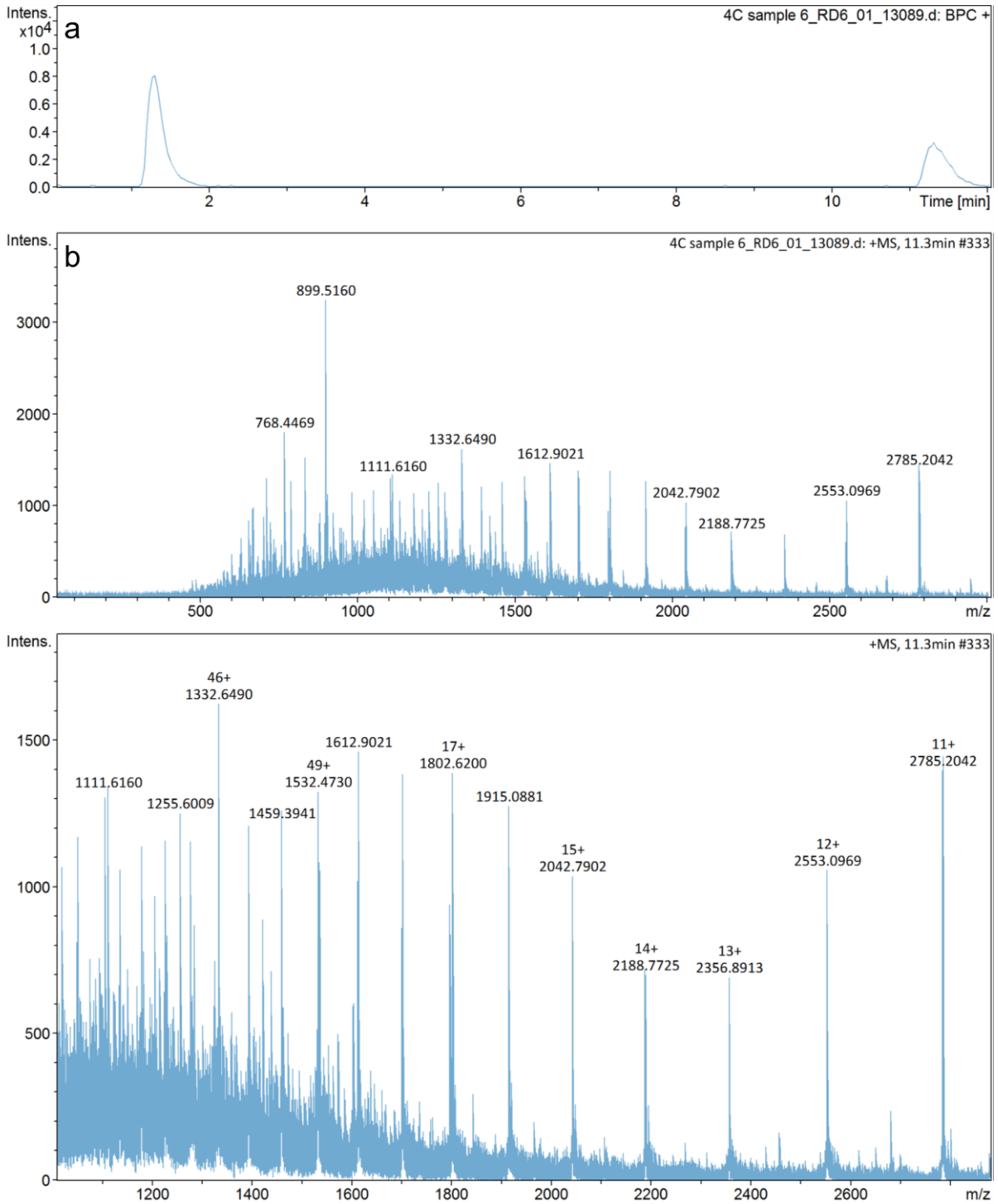


Figure S3. LC-UV (280 nm, a) and MS pattern (ESI+, b) of the Nurr1 LBD (10 μ M, M = 30.627 kDa) without ligand.

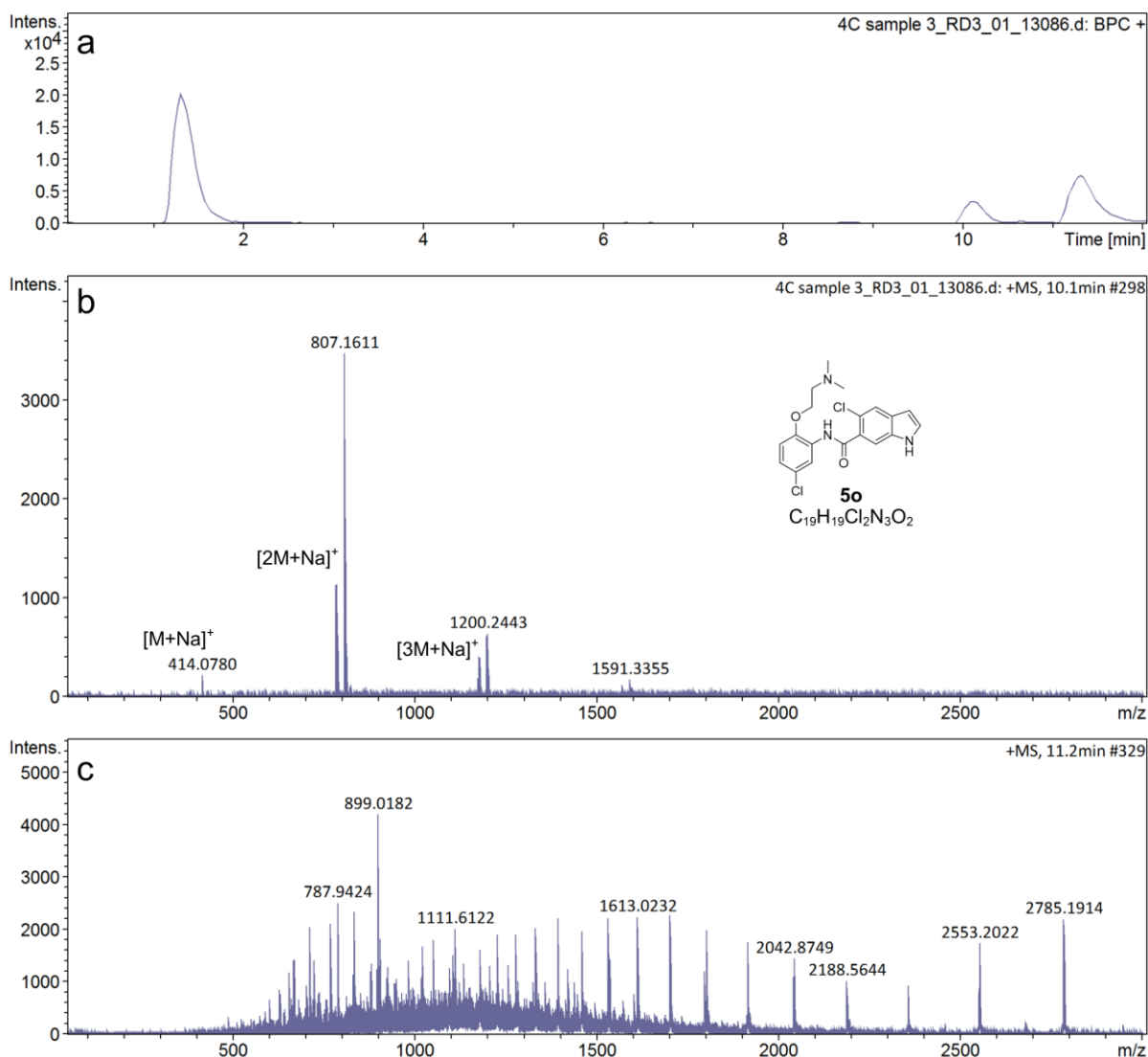


Figure S4. **5o** formed no covalent adduct with the Nurr1 LBD. (a) LC-UV (280 nm) of the Nurr1 LBD (10 μ M) + **5o** (100 μ M) mixture after 120 h incubation at 4 $^{\circ}$ C showed one signal for the ligand (10.1 min) and one for the intact Nurr1 LBD (11.2 min). (b) The MS pattern at 10.1 min corresponds to **5o**. (c) The MS pattern at 11.2 min corresponds to the intact Nurr1 LBD without covalent modification.

Experimental procedures

General. All chemicals were of reagent grade and used without further purification unless otherwise specified. All reactions were conducted in oven-dried Schlenk glassware under argon atmosphere and in absolute solvents. Other solvents, especially for work-up procedures, were of reagent grade or purified by distillation (*iso*-hexane, ethyl acetate, ethanol). Reactions were monitored by thin layer chromatography on TLC Silica gel 60 F₂₅₄ aluminium sheets by Merck and visualized under ultraviolet light (254 nm). Purification by CC was performed on a puriFlash® XS520Plus system (Advion, Ithaca, NY, USA) using high performance spherical silica columns (SIHP, 50 µM) by Interchim and a gradient of *iso*-hexane to EtOAc, reversed-phase CC was performed on a puriFlash® 5.250 system (Advion) using C18HP columns (SIHP, 15 µM) by Interchim and a gradient of 0.1% formic acid (FA) in water with 10 to 100% acetonitrile (HPLC gradient grade). Preparative HPLC was also performed on the puriFlash® 5.250 system using a PREP-LC column (C18-HQ, 5 µM) by Interchim and gradient of 0.1% FA in water with 10 to 100% methanol (HPLC gradient grade). Mass spectra were obtained on a puriFlash®-CMS system (Advion) using atmospheric pressure chemical ionization (APCI). HRMS were obtained with a Thermo Finnigan LTQ FT instrument for electrospray ionization (ESI). NMR spectra were recorded on Bruker Avance III HD 400 MHz or 500 MHz spectrometers equipped with CryoProbe™ Prodigy broadband probe (Bruker). Chemical shifts are reported in δ values (ppm), coupling constants (*J*) in hertz (Hz). Purity was determined by quantitative ¹H NMR (qH NMR) according to a method described by Pauli et al. with internal calibration.² The qH NMR measurements were carried out under conditions allowing complete relaxation to assure the exact determination of peak area ratios. Used internal standards were Ethyl 4-(dimethylamino)benzoate (LOT# BCCC6657, purity 99.63%) and maleic acid (LOT# BCBM8127V, purity 99.94%) in CDCl₃, MeOD-*d*₄, DMSO-*d*₆ or acetone-*d*₆. All compounds for biological testing had a purity >95% according to qH NMR.

General procedures

General procedure for amide coupling with EDC·HCl (GP1)

5-Chloro-1*H*-indole-6-carboxylic acid (**3**, 1.1 eq.) was suspended in chloroform (~0.04 M) and EDC·HCl (1.2 eq) was added. The mixture was stirred at rt for 1 h, whereby the solution cleared up. Then the respective amine (**4e,m,o,r,t,v**, 1.0 eq) and triethylamine (0.1 eq) were added and the resulting mixture was stirred at rt for 18 h. The solution was diluted with aqueous NaOH (2 M) and the aqueous layer was extracted with DCM (3 x). The combined organic layer was washed with aqueous NaOH (2 M), dried over Na₂SO₄, filtered and evaporated. The resulting residue was purified by CC and preparative HPLC.

Synthesis and analytical characterization of **5e,m,o,r,t,v**, 10-13

5-Chloro-*N*-(1-isopropylpiperidin-4-yl)-1*H*-indole-6-carboxamide (5e) Preparation according to GP1, using 5-chloro-1*H*-indole-6-carboxylic acid (**3**, 108 mg, 550 μ mol, 1.10 eq) and commercially available 4-amino-1-isopropylpiperidine (**4e**, 71.1 mg, 500 μ mol, 1.00 eq) yielded amide **5e** as a yellow oil (50 mg, 31%). R_f (EtOAc/EtOH = 1:1 + 2% TEA) = 0.55. MS (+APCI): m/z 319.9 ([$M+H$] $^+$). HRMS (+ESI): m/z calculated 320.15242 for [$C_{17}H_{23}ClN_3O$] $^+$, found 320.15277 ([$M+H$] $^+$). 1H NMR (400 MHz, MeOD- d_4): δ = 8.51 (s, 1H), 7.63 (s, 1H), 7.53–7.47 (m, 1H), 7.39 (d, J = 3.1 Hz, 1H), 6.47 (dd, J = 3.1, 0.9 Hz, 1H), 4.25–4.06 (m, 1H), 3.54–3.38 (m, 3H), 3.25–3.08 (m, 2H), 2.36–2.18 (m, 2H), 2.04–1.81 (m, 2H), 1.35 (d, J = 6.6 Hz, 6H) ppm. ^{13}C NMR (126 MHz, CD_2Cl_2): δ = 167.42, 134.44, 130.41, 128.77, 128.45, 121.85, 121.72, 113.30, 102.12, 56.20, 47.26, 46.38, 30.19, 17.24 ppm. qH NMR (400 MHz, MeOD- d_4 , Ethyl 4-(dimethylamino)benzoate as reference): purity = 98.9%.

5-Chloro-*N*-[3-(4-methylpiperidin-1-yl)propyl]-1*H*-indole-6-carboxamide (5m) Preparation according to GP1, using 5-chloro-1*H*-indole-6-carboxylic acid (**3**, 68.9 mg, 352 μ mol, 1.10 eq) and commercially available 3-(4-methylpiperidin-1-yl)propan-1-amine (**4m**, 50.0 mg, 320 μ mol, 1.00 eq) yielded amide **5m** as a yellow solid (28 mg, 26%). R_f (EtOAc/EtOH = 1:1 + 2% TEA) = 0.51. MS (+APCI): m/z 333.8 ([$M+H$] $^+$). HRMS (+ESI): m/z calculated 334.16807 for [$C_{18}H_{25}ClN_3O$] $^+$, found 334.16844 ([$M+H$] $^+$). 1H NMR (400 MHz, MeOD- d_4): δ = 8.45 (s, 1H), 7.64 (s, 1H), 7.56 (s, 1H), 7.41 (d, J = 3.1 Hz, 1H), 6.48 (d, J = 3.1 Hz, 1H), 3.61–3.44 (m, 4H), 3.26–3.15 (m, 2H), 3.06–2.87 (m, 2H), 2.14–1.99 (m, 2H), 1.99–1.86 (m, 2H), 1.81–1.64 (m, 1H), 1.59–1.41 (m, 2H), 1.02 (d, J = 6.4 Hz, 3H) ppm. ^{13}C NMR (126 MHz, MeOD- d_4): δ = 172.17, 135.42, 131.61, 129.47, 129.44, 122.09, 122.08, 112.95, 102.32, 55.69, 53.93, 37.90, 32.51, 29.95, 25.69, 21.27 ppm. qH NMR (400 MHz, MeOD- d_4 , Ethyl 4-(dimethylamino)benzoate as reference): purity = 97.0%.

5-Chloro-*N*-{5-chloro-2-[2-(dimethylamino)ethoxy]phenyl}-1*H*-indole-6-carboxamide (5o) 5-Chloro-1*H*-indole-6-carboxylic acid (**3**, 150 mg, 767 μ mol, 1.00 eq.) and oxalyl chloride (69.0 μ L, 767 μ mol, 1.00 eq.) were dissolved in 4 mL of a mixture of one drop of DMF in DCM (14 mL). After 2 h, the solvent was removed under reduced pressure. The remaining residue was dissolved in DCM (6 mL) and 5-chloro-2-[2-(dimethylamino)ethoxy]aniline (**4o**, 165 mg, 767 μ mol, 1.00 eq.) was added to the solution. The reaction mixture was stirred for 18 h at rt. Then DCM (10 mL) and saturated $NaHCO_3$ solution (10 mL) were added. The separated organic layer was dried over $MgSO_4$, filtered and concentrated under reduced pressure. The crude product was purified by CC and subsequent recrystallization from methanol yielded compound **5o** as a colorless crystalline solid (23 mg, 8%). R_f (iso-hexane/EtOH = 1:1 + 2% TEA) = 0.24. MS (+APCI): m/z 391.3 ([$M+H$] $^+$). HRMS (+EI): m/z calculated 391.08488 for [$C_{19}H_{19}Cl_2N_3O_2$] $^+$, found: 391.08645 ([M] $^+$). 1H NMR (500 MHz, $CDCl_3$) δ = 10.17 (s, 1H), 8.78 (s, 1H), 8.71–8.66 (m, 1H), 7.90–7.86 (m, 1H), 7.68 (s, 1H), 7.38–7.33 (m, 1H), 7.03 (dd, J = 8.6, 2.6 Hz, 1H), 6.92 (d, J = 8.7 Hz, 1H), 6.54–6.50 (m, 1H), 4.09 (t, J = 5.4 Hz, 2H), 2.55 (t, J = 5.0 Hz, 2H), 2.02 (s, 6H) ppm. ^{13}C NMR (126 MHz, $CDCl_3$) δ = 166.00, 146.62, 134.11, 131.66, 130.50, 129.03, 128.13, 128.09, 123.77, 122.13, 121.87, 120.81, 116.73, 113.63, 102.52, 69.45, 57.99, 45.18 ppm. qH NMR (400 MHz, MeOD- d_4 , maleic acid as reference): purity = 95.4%.

5-Chloro-*N*-{2-[decahydroisoquinolin-2(1*H*)-yl]ethyl}-1*H*-indole-6-carboxamide (5r) Preparation according to GP1, using 5-chloro-1*H*-indole-6-carboxylic acid (**3**, 73.2 mg, 374 μ mol, 1.10 eq) and commercially available 2-(decahydroisoquinolin-2-yl)ethan-1-amine (**4r**, mixture of diastereomers, 62.0 mg, 340 μ mol, 1.00 eq) yielded amide **5r** as a colourless solid (mixture of stereoisomers, 39 mg, 32%). R_f (EtOAc/EtOH = 1:1 + 2% TEA) = 0.52. MS (+APCI):

m/z 359.9 ($[M+H]^+$). HRMS (+ESI): m/z calculated 360.18372 for $[C_{20}H_{27}ClN_3O]^+$, found 360.18412 ($[M+H]^+$). 1H NMR (500 MHz, MeOD- d_4): δ = 8.53 (s, 1H), 7.64 (s, 1H), 7.59 (s, 1H), 7.41 (d, J = 3.1 Hz, 1H), 6.48 (d, J = 3.1 Hz, 1H), 3.72 (t, J = 6.2 Hz, 2H), 3.60–0.96 (m, 18H) ppm. ^{13}C NMR (126 MHz, MeOD- d_4) δ = 172.36, 135.40, 131.78, 129.61, 128.85, 122.20, 122.19, 113.21, 102.36, 59.86, 58.41, 55.04, 41.30, 36.98, 33.79, 33.33, 32.08, 30.89, 27.09, 26.74 ppm. qH NMR (400 MHz, MeOD- d_4 , Ethyl 4-(dimethylamino)benzoate as reference): purity = 97.9%.

5-Chloro-*N*-[4-(diethylamino)cyclohex-1-yl]-1*H*-indole-6-carboxamide (5t) Preparation according to GP1, using 5-chloro-1*H*-indole-6-carboxylic acid (**3**, 108 mg, 550 μ mol, 1.10 eq) and commercially available *N,N*-diethylcyclohexane-1,4-diamine (**4t**, mixture of diastereomers, 85.2 mg, 500 μ mol, 1.00 eq) yielded amide **5t** as a colorless solid (mixture of diastereomers: 6:4 *trans/cis*, 34 mg, 20%). R_f (EtOAc/EtOH = 1:1 + 2% TEA) = 0.51. MS (+APCI): m/z 347.9 ($[M+H]^+$). HRMS (+ESI): m/z calculated 348.18372 for $[C_{19}H_{27}ClN_3O]^+$, found 348.18419 ($[M+H]^+$). 1H NMR (500 MHz, MeOD- d_4): δ = 8.55 (s, 1H), 7.63 (s, 0.6·1H), 7.61 (s, 0.4·1H), 7.53 (s, 0.6·1H), 7.48 (s, 0.4·1H), 7.41–7.37 (m, 1H), 4.24 (quint, J = 3.3 Hz, 0.6·1H), 3.89 (tt, J = 11.8, 4.1 Hz, 0.4·1H), 3.27–2.97 (m, 5H), 2.26–2.04 (m, 3H), 1.90–1.81 (m, 4H), 1.56–1.41 (m, 1H), 1.38–1.25 (m, 6H) ppm. ^{13}C NMR (126 MHz, MeOD- d_4): δ = 171.23, 170.94, 135.52, 135.43, 131.44, 131.42, 130.24, 130.09, 129.23, 129.18, 122.20, 121.93, 121.84, 112.95, 112.71, 102.27, 62.09, 61.71, 46.22, 46.11, 45.93, 31.61, 29.45, 26.76, 23.00, 22.87, 11.04, 11.00 ppm. qH NMR (400 MHz, MeOD- d_4 , Ethyl 4-(dimethylamino)benzoate as reference): purity = 97.9%.

5-Chloro-*N*-[(1-butylpyrrolidin-3-yl)methyl]-1*H*-indole-6-carboxamide (5v) Preparation according to GP1, using 5-chloro-1*H*-indole-6-carboxylic acid (**3**, 94.7 mg, 484 μ mol, 1.10 eq) and commercially available (1-butylpyrrolidin-3-yl)methanamine (**4v**, mixture of enantiomers, 68.8 mg, 440 μ mol, 1.00 eq) yielded amide **5v** as a yellow oil (11 mg, 8%). R_f (EtOAc/EtOH = 1:1 + 2% TEA) = 0.48. MS (+APCI): m/z 333.7 ($[M+H]^+$). HRMS (+ESI): m/z calculated 334.16807 for $[C_{18}H_{25}ClN_3O]^+$, found 334.16848 ($[M+H]^+$). 1H NMR (500 MHz, MeOD- d_4): δ = 8.50 (s, 1H), 7.63 (s, 1H), 7.53 (s, 1H), 7.40 (d, J = 3.1 Hz, 1H), 6.47 (d, J = 2.9 Hz, 1H), 3.69–3.37 (m, 5H), 3.27–3.08 (m, 3H), 2.89–2.70 (m, 1H), 2.36–2.18 (m, 1H), 2.01–1.85 (m, 1H), 1.77–1.63 (m, 2H), 1.49–1.36 (m, 2H), 0.99 (t, J = 7.1 Hz, 3H) ppm. ^{13}C NMR (126 MHz, MeOD- d_4): δ = 171.94, 135.43, 131.54, 129.72, 129.39, 122.04, 122.02, 112.83, 102.30, 57.92, 56.39, 54.77, 42.74, 38.84, 28.95, 28.42, 20.88, 13.89 ppm. qH NMR (400 MHz, MEOD- d_4 , Ethyl 4-(dimethylamino)benzoate as reference): purity = 95.4%.

6-Chloro-*N*-[5-chloro-2-{2-(dimethylamino)ethoxy}phenyl]-1*H*-indole-5-carboxamide (10) Preparation according to GP1, using 6-chloro-1*H*-indole-5-carboxylic acid (**3a**, 108 mg, 550 μ mol, 1.10 eq) and commercially available 5-chloro-2-[2-(dimethylamino)ethoxy]aniline (**4o**, 107 mg, 500 μ mol, 1.00 eq) yielded amide **3a** as a colorless solid (9 mg, 5%). R_f (*iso*-hexane/EtOAc = 1:1) = 0.36. MS (+APCI): m/z 391.8 ($[M+H]^+$). HRMS (+ESI): m/z calculated 392.09271 for $[C_{19}H_{20}Cl_2N_3O_2]^+$, found 392.09335 ($[M+H]^+$). 1H NMR (400 MHz, acetone- d_6): δ = 10.62 (s, 1H), 10.45 (s, 1H), 8.66 (d, J = 2.6 Hz, 1H), 7.95 (s, 1H), 7.63–7.58 (m, 1H), 7.52–7.46 (m, 1H), 7.17 (d, J = 8.7 Hz, 1H), 7.08 (dd, J = 8.6, 2.6 Hz, 1H), 6.66–6.60 (m, 1H), 4.20–4.13 (m, 2H), 2.51–2.43 (m, 2H), 1.88 (s, 6H) ppm. ^{13}C NMR (101 MHz, acetone- d_6): δ = 166.92, 147.88, 138.03, 134.04, 128.87, 128.33, 128.14, 127.53, 124.60, 124.03, 122.56, 120.74, 119.93, 113.38, 103.28, 70.84, 58.37, 44.92 ppm. qH NMR (400 MHz, DMSO- d_6 , Ethyl 4-(dimethylamino)benzoate as reference): purity = 95.5%.

5-Chloro-*N*-{5-chloro-2-[2-(dimethylamino)ethoxy]phenyl}-1-methyl-1*H*-indole-6-carboxamide (11) 5-Chloro-1-methyl-1*H*-indole-6-carboxylic acid (**3b**, 14 mg, 67 μ mol, 1.00 eq.), 5-chloro-2-[2-(dimethylamino)ethoxy]aniline (**4o**, 19 mg, 87 μ mol, 1.3 eq.), 1-

methylimidazole (18.6 μL , 234 μmol , 3.5 eq.) and chloro-*N,N,N',N'*-tetramethylformamidinium hexafluorophosphate (22.5 mg, 80 μmol , 1.2 eq.) were dissolved in DMF (1 mL) and the reaction mixture was stirred at 80 °C overnight. Then the solution was diluted with 2N aqueous NaOH and the aqueous layer was extracted with EtOAc. The combined organic layer was dried over MgSO_4 , filtered and evaporated. The resulting residue was purified by CC and yielded compound **11** as a colorless solid (7 mg, 26%). R_f (iso-hexane/EtOAc = 8:2 + 2% TEA) = 0.3. MS (+APCI): m/z found 405.6 ($[\text{M}+\text{H}]^+$). HRMS (+ESI): m/z calculated 406.10836 for $[\text{C}_{20}\text{H}_{22}\text{Cl}_2\text{N}_3\text{O}_2]^+$, found 406.10908 ($[\text{M}+\text{H}]^+$). ^1H NMR (400 MHz, CDCl_3): δ 10.09 (s, 1H), 8.74–8.69 (m, 1H), 7.84 (s, 1H), 7.67 (s, 1H), 7.19 (d, J = 3.1 Hz, 1H), 7.03 (dd, J = 8.6, 2.6 Hz, 1H), 6.91 (d, J = 8.6 Hz, 1H), 6.49–6.43 (m, 1H), 4.11 (t, J = 5.5 Hz, 2H), 3.83 (s, 3H), 2.63–2.54 (m, 2H), 2.05 (s, 6H) ppm. ^{13}C NMR (101 MHz, CDCl_3): δ = 165.79, 146.40, 134.94, 132.47, 131.35, 130.81, 128.29, 127.85, 123.53, 121.85, 121.61, 120.64, 116.11, 112.00, 100.74, 69.08, 57.88, 45.10, 33.21 ppm. qH NMR (400 MHz, CDCl_3 , Ethyl-4-(dimethylamino)benzoate as reference): purity = 95.9%.

5-Chloro-*N*-[(5-chloro-1*H*-indol-6-yl)methyl]-2-[2-(dimethylamino)ethoxy]aniline (12) 5-Chloro-1*H*-indole-6-carbaldehyde (**15**, 0.045 g, 1.00 eq.) and 5-chloro-2-[2-(dimethylamino)ethoxy]aniline (**4o**, 59 mg, 276 μmol , 1.1 eq.) was dissolved in a mixture of DCM (3mL) and DCE (1 mL). Acetic acid (28 μL , 502 μmol , 2.00 eq.) was added to the solution and the reaction mixture was stirred for 2 h at rt. Then sodium triacetoxyborohydride (90 mg, 425 μmol , 1.69 eq) was added and the solution was stirred for further 2 h at rt. The reaction was quenched with saturated NaHCO_3 solution and the aqueous layer was extracted with EtOAc. The combined organic layer was dried over MgSO_4 , filtered and evaporated. The resulting residue was purified by reverse CC and yielded compound **12** as a beige solid. (34 mg, 36%). R_f (DCM/MeOH = 95:5) = 0.39. MS (+APCI): m/z 377.4 ($[\text{M}+\text{H}]^+$). HRMS (+ESI): m/z calculated 378.11344 for $[\text{C}_{19}\text{H}_{22}\text{Cl}_2\text{N}_3\text{O}]^+$, found 378.11344 ($[\text{M}+\text{H}]^+$). ^1H NMR (400 MHz, acetone- d_6): δ = 10.33 (s, 1H), 7.65 (s, 1H), 7.48 (s, 1H), 7.40–7.33 (m, 1H), 6.85 (d, J = 8.5 Hz, 1H), 6.52 (dd, J = 8.4, 2.5 Hz, 1H), 6.50–6.42 (m, 2H), 5.84 (s, 1H), 4.53 (d, J = 5.8 Hz, 2H), 4.10 (t, J = 5.7 Hz, 2H), 2.66 (t, J = 5.7 Hz, 2H), 2.23 (s, 6H).ppm. $^{13}\text{C}\{^1\text{H}\}$ -NMR (101 MHz, acetone- d_6) δ = 144.96, 140.56, 135.25, 128.73, 128.23, 126.60, 126.42, 123.88, 120.42, 114.92, 113.71, 111.27, 109.50, 101.04, 68.06, 58.25, 45.32, 45.15 ppm. qH NMR (400 MHz, acetone- d_6 , Ethyl 4-(dimethylamino)benzoate as reference): purity = 96.9%.

7-Chloro-*N*-{5-chloro-2-[2-(dimethylamino)ethoxy]phenyl}quinolin-4-amine (13) 4-Bromo-7-chloro-chloroquinoline (**16**, 170 mg, 699 μmol , 3.00 eq.), $\text{Pd}(\text{OAc})_2$ (5.3 mg, 23 μmol , 0.1 eq.), (+/-)-2,2'-Bis(diphenylphosphino)-1,1'-binaphthalene (29 mg, 47 μmol , 0.2 eq.), K_3PO_4 (82.6 mg, 389 μmol , 1.67 eq.) and 5-Chloro-2-[2-(dimethylamino)ethoxy]aniline (**5o**, 50.0 mg, 233 μmol , 1.00 eq.) were dissolved in 1,4-dioxane (10 mL). The suspension was stirred at 90 °C for 24 h. After completion of the reaction the mixture was filtered through Celite and purified by CC yielded compound **13** as a yellow solid (25 mg, 29%). R_f (DCM/MeOH = 95:5) = 0.13. MS (+APCI): m/z 375.7 ($[\text{M}+\text{H}]^+$). HRMS (+ESI): m/z calculated 376.09779 for $[\text{C}_{19}\text{H}_{20}\text{Cl}_2\text{N}_3\text{O}]^+$, found 376.09885 ($[\text{M}+\text{H}]^+$). ^1H NMR (400 MHz, acetone- d_6) δ = 8.57 (d, J = 5.2 Hz, 1H), 8.54 (s, 1H), 8.27 (d, J = 9.0 Hz, 1H), 7.95 (d, J = 2.2 Hz, 1H), 7.55 (dd, J = 9.0, 2.2 Hz, 1H), 7.49 (d, J = 2.5 Hz, 1H), 7.22 (d, J = 8.7 Hz, 1H), 7.13 (dd, J = 8.7, 2.5 Hz, 1H), 7.01 (d, J = 5.2 Hz, 1H), 4.22 (t, J = 5.3 Hz, 2H), 2.57 (t, J = 5.4 Hz, 2H), 2.23 (s, 6H) ppm. ^{13}C NMR (101 MHz, acetone- d_6) δ = 152.13, 150.06, 149.79, 147.27, 134.39, 132.89, 128.44, 126.28, 125.43, 124.07, 123.28, 121.72, 119.01, 117.67, 102.99, 68.52, 57.84, 44.8 ppm. qH NMR (400 MHz, acetone- d_6 , Ethyl-4-(dimethylamino)benzoate as reference): purity = 95.2%.

Synthesis and analytical characterization of intermediates

5-Chloro-1H-indole-6-carboxylic acid (3) Methyl 5-chloro-1H-indole-6-carboxylate (**9**, 2.80 g, 13.4 mmol, 1.00 eq.) was dissolved in EtOH (25 mL) and water (25 mL). LiOH·H₂O (1.69 g, 40.2 mmol, 3.00 eq.) was added and the reaction mixture was stirred at rt for 18 h. After removal of the solvent, the resulting solid was dissolved in water. The alkaline solution (pH > 11) was extracted with EtOAc. The aqueous layer was acidified with aqueous hydrochloric acid (10%) and extracted with EtOAc. The latter organic layers were combined, washed with brine, dried over MgSO₄ and filtered. The solvent was removed under reduced pressure and the residue was recrystallized from a mixture of DCM/diisopropylether (1:1) yielded compound **3** as a beige solid (2.47 g, 94 %). *R_f* (iso-hexane/EtOAc = 8:2 + 2% AcOH) = 0.22. MS (+APCI): *m/z* 195.7 ([M+H]⁺). ¹H NMR (400 MHz, acetone-*d*₆): δ = 11.15 (s, 1H), 10.69 (s, 1H), 8.13 (s, 1H), 7.70 (s, 1H), 7.62–7.58 (m, 1H), 6.56–6.53 (m, 1H) ppm. ¹³C NMR (126 MHz, acetone-*d*₆): δ = 168.58, 134.20, 131.45, 129.74, 123.62, 122.39, 121.82, 115.47, 101.46 ppm.

5-Chloro-1-methyl-1H-indole-6-carboxylic acid (3b) Methyl 5-chloro-1-methyl-1H-indole-6-carboxylate (**9a**, 30.3 mg, 135 μmol, 1.00 eq.) was dissolved in 2 mL of a mixture of EtOH/water (1:1). Lithium hydroxide (9.73 mg, 406 μmol, 3.00 eq) was added and the mixture was stirred at rt overnight. The solvent was removed and water was added. The alkaline solution (pH > 11) was extracted with EtOAc. The aqueous layer was acidified with aqueous hydrochloric acid (10%) and extracted with EtOAc. The latter organic layers were combined, dried over MgSO₄ filtered and concentrated under reduced pressure giving compound **3b** as a colorless solid (28 mg, 98.6%). *R_f* (i-hexane/EtOAc = 8:2 + 2% AcOH) = 0.25. MS (+APCI): *m/z* 209.7 ([M+H]⁺). ¹H NMR (400 MHz, acetone-*d*₆): δ = 8.04 (s, 1H), 7.68 (s, 1H), 7.49 (d, *J* = 3.0 Hz, 1H), 6.49 (dd, *J* = 3.0, 0.8 Hz, 1H), 3.93 (s, 3H) ppm. ¹³C NMR (101 MHz, acetone-*d*₆): δ = 166.58, 134.59, 133.86, 131.72, 123.57, 122.36, 122.02, 113.52, 100.34, 32.37 ppm.

2-Chloro-4-methyl-5-nitrobenzoic acid (7)³ 2-Chloro-4-methylbenzoic acid (**6**, 10.0 g, 55.8 mmol, 1.00 eq.) was suspended in sulfuric acid (100 mL) and cooled to 5 °C. Over a period of 40 min nitric acid (3.39 mL, 52.7 mmol, 0.90 eq.) was added dropwise so that the reaction mixture did not exceed a temperature of 15 °C. After complete addition of nitric acid the reaction mixture was stirred at rt for 30 min and then poured into ice water. The solid that subsequently precipitated was filtered off, washed with cold water and dissolved in EtOH. Water was added dropwise to the solution, whereupon a colorless solid precipitated. The solid was filtered off, washed with cold water and dried under reduced pressure yielded compound **7** as a colorless solid (7.57 g, 59%). *R_f* (iso-hexane/EtOAc = 8:2 + 2% AcOH) = 0.33. MS (-APCI): *m/z* 214.5 ([M-H]⁻). ¹H NMR (400 MHz, acetone-*d*₆): δ = 8.54 (s, 1H), 7.72 (s, 1H), 2.65 (s, 3H) ppm. ¹³C NMR (101 MHz, acetone-*d*₆): δ = 164.70, 148.50, 139.43, 138.57, 136.14, 129.76, 128.72, 20.03 ppm.

Methyl 2-chloro-4-methyl-5-nitrobenzoate (8)³ Acetyl chloride (12.4 mL, 174 mmol, 5.00 eq.) was added dropwise to methanol (70 mL) at 5-10 °C. A solution of 2-chloro-4-methylnitrobenzoic acid (**7**, 7.50 g, 34.8 mmol, 1.00 eq.) in methanol (100 mL) was added in portions and the reaction mixture was stirred at 50 °C for 4 h. After cooling to rt the solvent was removed under reduced pressure. The yellow solid obtained was dissolved in DCM and washed with brine solution and water. The organic phase was dried over MgSO₄, filtered and evaporated to yield **8** as a colorless solid (7.66 g, 96 %). *R_f* (iso-hexane/EtOAc = 8:2) = 0.41. MS (+APCI): *m/z* 229.5 ([M+H]⁺). ¹H NMR (400 MHz, acetone-*d*₆): δ = 8.48 (s, 1H), 7.73 (s, 1H), 3.95 (s, 3H), 2.65 (s, 3H) ppm. ¹³C NMR (101 MHz, acetone-*d*₆): δ = 167.44, 148.34, 139.57, 138.30, 136.08, 129.51, 128.51, 53.18, 20.05 ppm.

Methyl 5-chloro-1H-indole-6-carboxylate (9)³ Methyl 2-chloro-4-methyl-5-nitrobenzoate (**8**, 7.66 g, 33.4 mmol, 1.00 eq.) was dissolved in DMF (50 mL). *N,N*-dimethylformamide dimethylacetal (10.4 mL, 49.9 mmol, 1.50 eq.) was added to the solution and the reaction

mixture was stirred for 2 h at 130 °C. The reaction mixture was concentrated under vacuum, dissolved in EtOAc, washed with brine and water. The aqueous phases were extracted with EtOAc and the combined organic phases were dried over MgSO₄. After removing the solvent, the obtained purple solid was dissolved in acetic acid (100 mL) and water (20 mL). Over a period of 40 min, zinc powder (13.06 g, 65.34 mmol, 6.0 eq.) was added in portions and the reaction mixture was heated to 80 °C for 2 h. After cooling to rt, the mixture was diluted with EtOAc and filtered. The organic phase was separated and washed with saturated NaHCO₃ solution and brine. The organic phase was dried over MgSO₄, filtered and concentrated under reduced pressure. The brown oil was purified by CC and yielded compound **9** as a green solid (2.80 g, 40 %). *R_f* (iso-hexane/EtOAc = 8:2) = 0.23. MS (+APCI): *m/z* 209.7 ([M+H]⁺). ¹H NMR (400 MHz, acetone-*d*₆): δ = 10.69 (s, 1H), 8.03 (s, 1H), 7.71 (s, 1H), 7.60 (t, *J* = 2.8 Hz, 1H), 6.54 (m, 1H), 3.87 (s, 3H) ppm. ¹³C NMR (126 MHz, acetone-*d*₆): δ = 167.20, 134.86, 132.86, 130.68, 124.13, 123.34, 122.65, 116.02, 102.38, 52.26 ppm.

Methyl 5-chloro-1-methyl-1*H*-indole-6-carboxylate (9a) Sodium hydride (19.6 mg, 490 μmol, 1.20 eq.) was added portionwise to methyl 5-chloro-1*H*-indole-6-carboxylate (**9**, 85.6 mg, 0.408 mmol, 1.00 eq.) in DMF (1.5 mL) cooled to 0 °C over a period of 10 min. The resulting solution was stirred at 0 °C for further 10 min. Methyl iodide (30 μL, 49 μmol, 1.20 eq.) was added and the solution was stirred at rt for 2 h. The reaction mixture was quenched with saturated NH₄Cl solution and the aqueous layer was extracted with EtOAc. The combined organic layer was dried over MgSO₄, filtered and evaporated. The residue was purified by CC to yield compound **9a** as a colorless solid (30 mg, 33%). *R_f* (iso-hexane/EtOAc = 8:2) = 0.3. MS (+APCI): *m/z* 223.6 ([M+H]⁺). ¹H NMR (400 MHz, acetone-*d*₆): δ = 7.96 (s, 1H), 7.68 (s, 1H), 7.49 (d, *J* = 3.1 Hz, 1H), 6.52–6.48 (m, 1H), 3.92 (s, 3H), 3.89 (s, 3H) ppm. ¹³C NMR (101 MHz, CDCl₃): δ = 167.12, 134.47, 133.09, 131.73, 124.33, 122.65, 122.17, 113.29, 100.83, 52.23, 33.18 ppm.

5-Chloro-1*H*-indole-6-ylmethanol (14) Methyl 5-chloro-1*H*-indole-6-carboxylate (**3**, 0.5 g, 2.39 mmol, 1.00 eq.) was dissolved in THF (4 mL) under nitrogen. The solution was stirred at 0 °C and a solution of lithium aluminium hydride (596 μL, 2.39 mmol, 1.0 eq., 4 M in diethyl ether) was added dropwise. The reaction mixture was stirred for 1 h and quenched with EtOAc and water. The aqueous layer was extracted with EtOAc and the combined organic layer was dried over MgSO₄, filtered and evaporated. The residue was purified by CC yielded compound **14** as a colorless solid (115 mg, 71%). *R_f* (iso-hexane/EtOAc = 2:1) = 0.2. MS (+APCI): *m/z* 181.6 ([M+H]⁺). ¹H NMR (400 MHz, acetone-*d*₆): δ = 10.35 (s, 1H), 7.72–7.65 (m, 1H), 7.57 (s, 1H), 7.40–7.31 (m, 1H), 6.48–6.41 (m, 1H), 4.81–4.73 (m, 2H), 4.25 (t, *J* = 5.7 Hz, 1H) ppm. ¹³C NMR (101 MHz, acetone-*d*₆): δ = 135.25, 132.31, 127.92, 126.12, 123.00, 119.82, 110.65, 100.95, 61.77 ppm.

5-Chloro-1*H*-indole-6-carbaldehyde (15) 5-Chloro-1*H*-indole-6-ylmethanol (**14**, 0.091 g, 496 μmol, 1.00 eq.) was dissolved in a mixture of DCM (4 mL) and DMF (2 mL) at 0 °C. Dess-Martin-Periodinan (0.231 g, 546 μmol, 1.10 eq.) was added to the solution and the reaction mixture was allowed to warm to rt and stirred for 1 h. A solution of 1 N NaOH was added and the biphasic mixture was filtered through Celite. The biphasic mixture was extracted with EtOAc and the organic phase was dried over MgSO₄. The organic solvent was removed under reduced pressure and the residue was purified by CC to yield compound **14** as a brown solid (mixture of tautomers, 89 mg, 100%). *R_f* (iso-hexane/EtOAc = 2:1) = 0.5. MS (+APCI): *m/z* 179.7 ([M+H]⁺). ¹H NMR (400 MHz, acetone-*d*₆): δ = 10.91 (s, 1H), 10.48 (s, 1H), 8.07 (s, 1H), 7.75–7.67 (m, 2H), 6.63–6.56 (m, 1H) ppm. ¹³C NMR (101 MHz, acetone-*d*₆): δ = 190.14, 135.53, 135.38, 134.44, 134.40, 132.52, 132.35, 128.07, 126.82, 121.90, 113.88, 113.83, 102.87, 102.82 ppm.

gH NMR of 5e,m,o,r,t,v, 10-13 for purity analysis

Compound 5e:

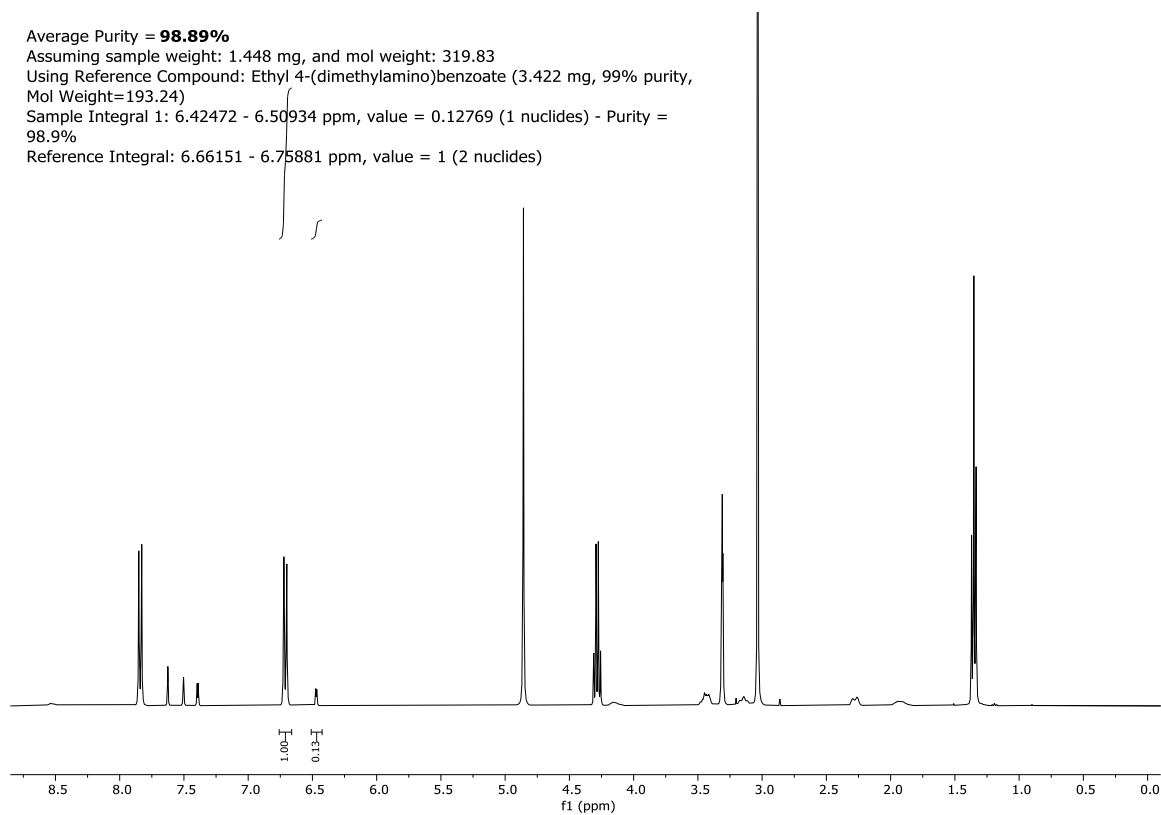
Average Purity = **98.89%**

Assuming sample weight: 1.448 mg, and mol weight: 319.83

Using Reference Compound: Ethyl 4-(dimethylamino)benzoate (3.422 mg, 99% purity, Mol Weight=193.24)

Sample Integral 1: 6.42472 - 6.50934 ppm, value = 0.12769 (1 nuclides) - Purity = 98.9%

Reference Integral: 6.66151 - 6.75881 ppm, value = 1 (2 nuclides)



Compound 5m:

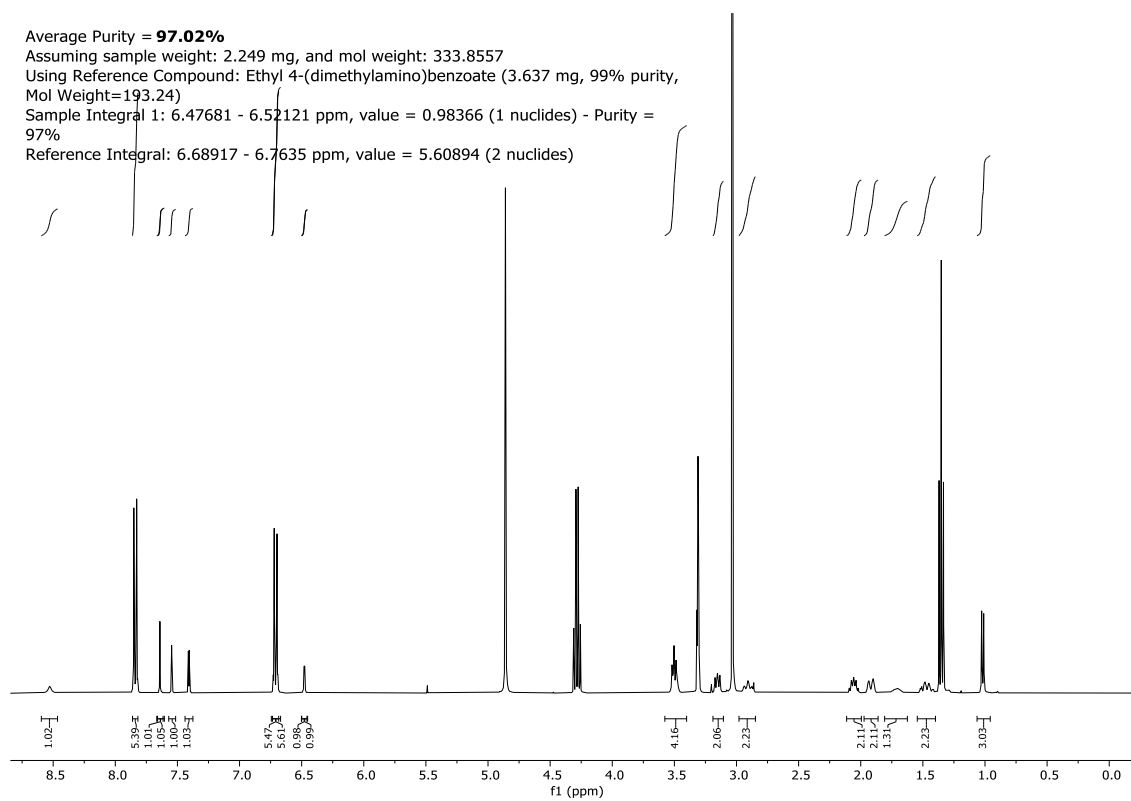
Average Purity = **97.02%**

Assuming sample weight: 2.249 mg, and mol weight: 333.8557

Using Reference Compound: Ethyl 4-(dimethylamino)benzoate (3.637 mg, 99% purity, Mol Weight=193.24)

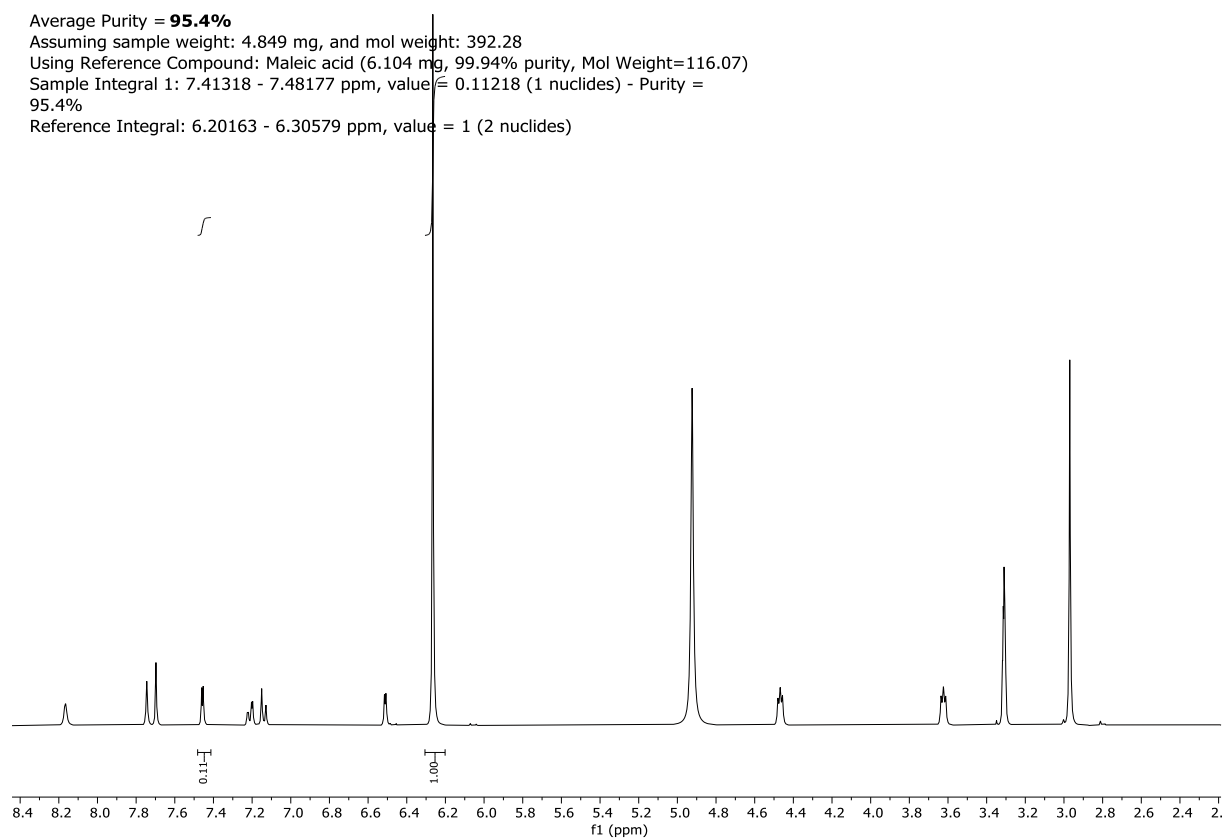
Sample Integral 1: 6.47681 - 6.52121 ppm, value = 0.98366 (1 nuclides) - Purity = 97%

Reference Integral: 6.68917 - 6.7635 ppm, value = 5.60894 (2 nuclides)



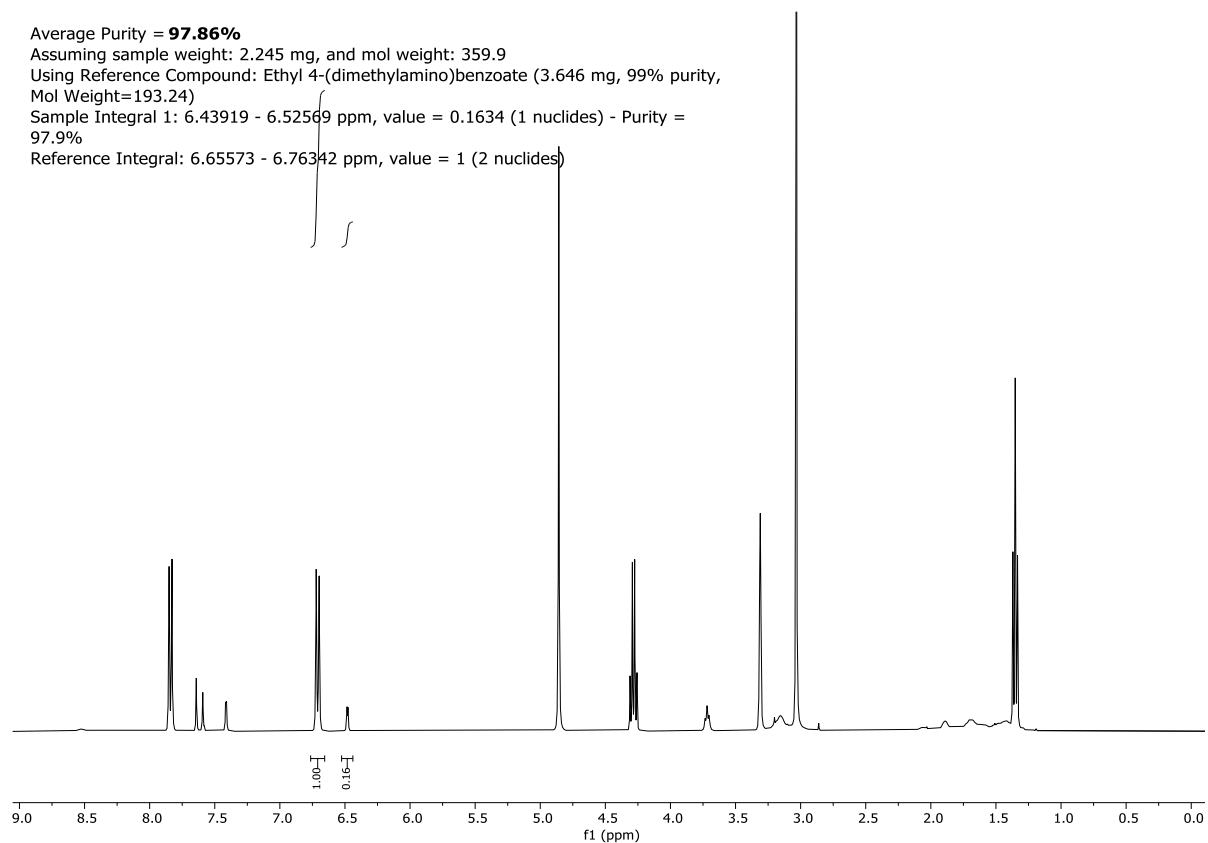
Compound 5o:

Average Purity = **95.4%**
Assuming sample weight: 4.849 mg, and mol weight: 392.28
Using Reference Compound: Maleic acid (6.104 mg, 99.94% purity, Mol Weight=116.07)
Sample Integral 1: 7.41318 - 7.48177 ppm, value = 0.11218 (1 nuclides) - Purity = 95.4%
Reference Integral: 6.20163 - 6.30579 ppm, value = 1 (2 nuclides)



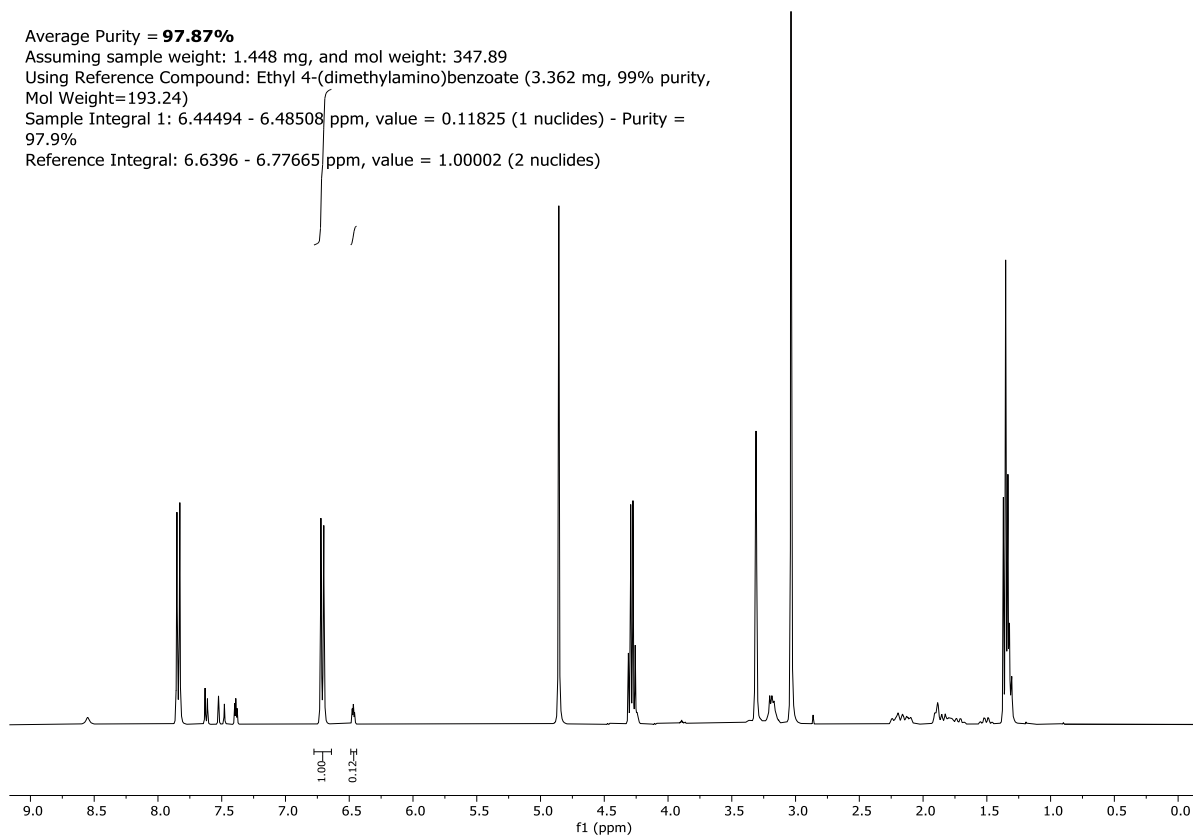
Compound 5r:

Average Purity = **97.86%**
Assuming sample weight: 2.245 mg, and mol weight: 359.9
Using Reference Compound: Ethyl 4-(dimethylamino)benzoate (3.646 mg, 99% purity, Mol Weight=193.24)
Sample Integral 1: 6.43919 - 6.52569 ppm, value = 0.1634 (1 nuclides) - Purity = 97.9%
Reference Integral: 6.65573 - 6.76342 ppm, value = 1 (2 nuclides)



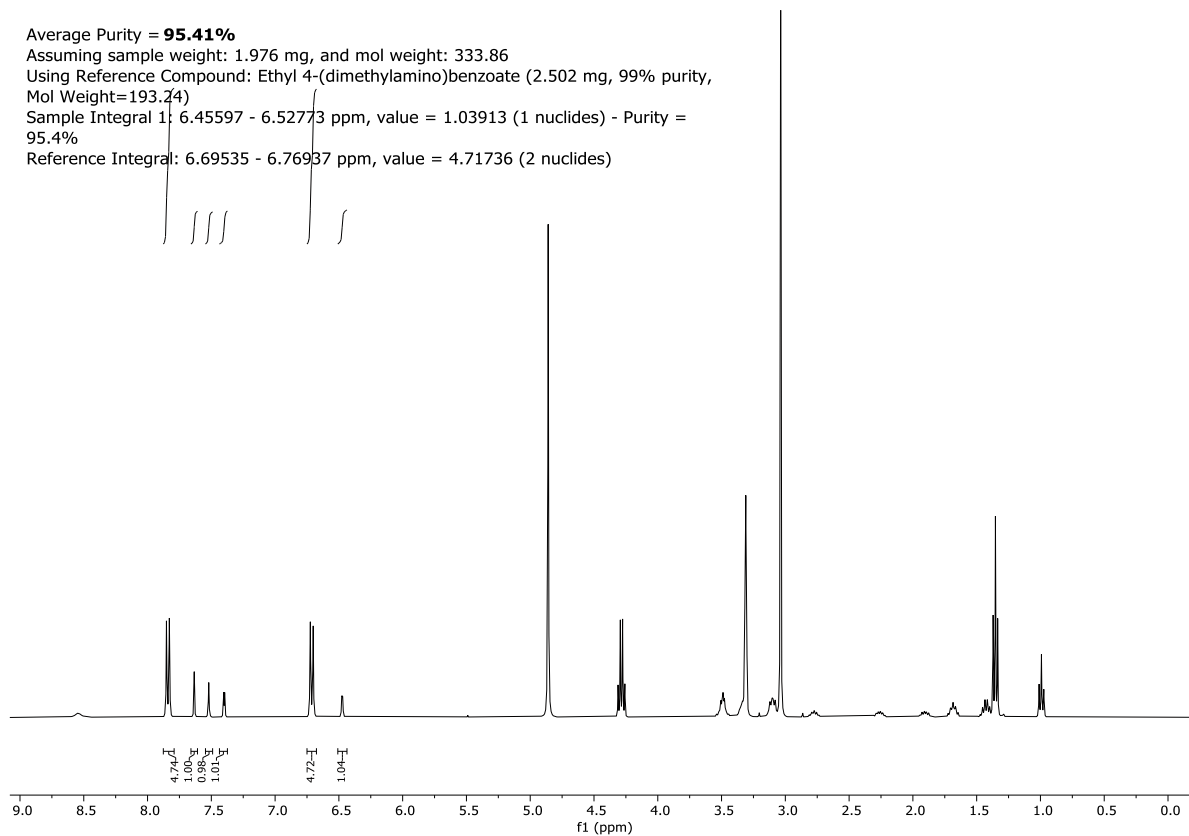
Compound 5t:

Average Purity = **97.87%**
Assuming sample weight: 1.448 mg, and mol weight: 347.89
Using Reference Compound: Ethyl 4-(dimethylamino)benzoate (3.362 mg, 99% purity, Mol Weight=193.24)
Sample Integral 1: 6.44494 - 6.48508 ppm, value = 0.11825 (1 nuclides) - Purity = 97.9%
Reference Integral: 6.6396 - 6.77665 ppm, value = 1.00002 (2 nuclides)



Compound 5v:

Average Purity = **95.41%**
Assuming sample weight: 1.976 mg, and mol weight: 333.86
Using Reference Compound: Ethyl 4-(dimethylamino)benzoate (2.502 mg, 99% purity, Mol Weight=193.24)
Sample Integral 1: 6.45597 - 6.52773 ppm, value = 1.03913 (1 nuclides) - Purity = 95.4%
Reference Integral: 6.69535 - 6.76937 ppm, value = 4.71736 (2 nuclides)



Compound 10:

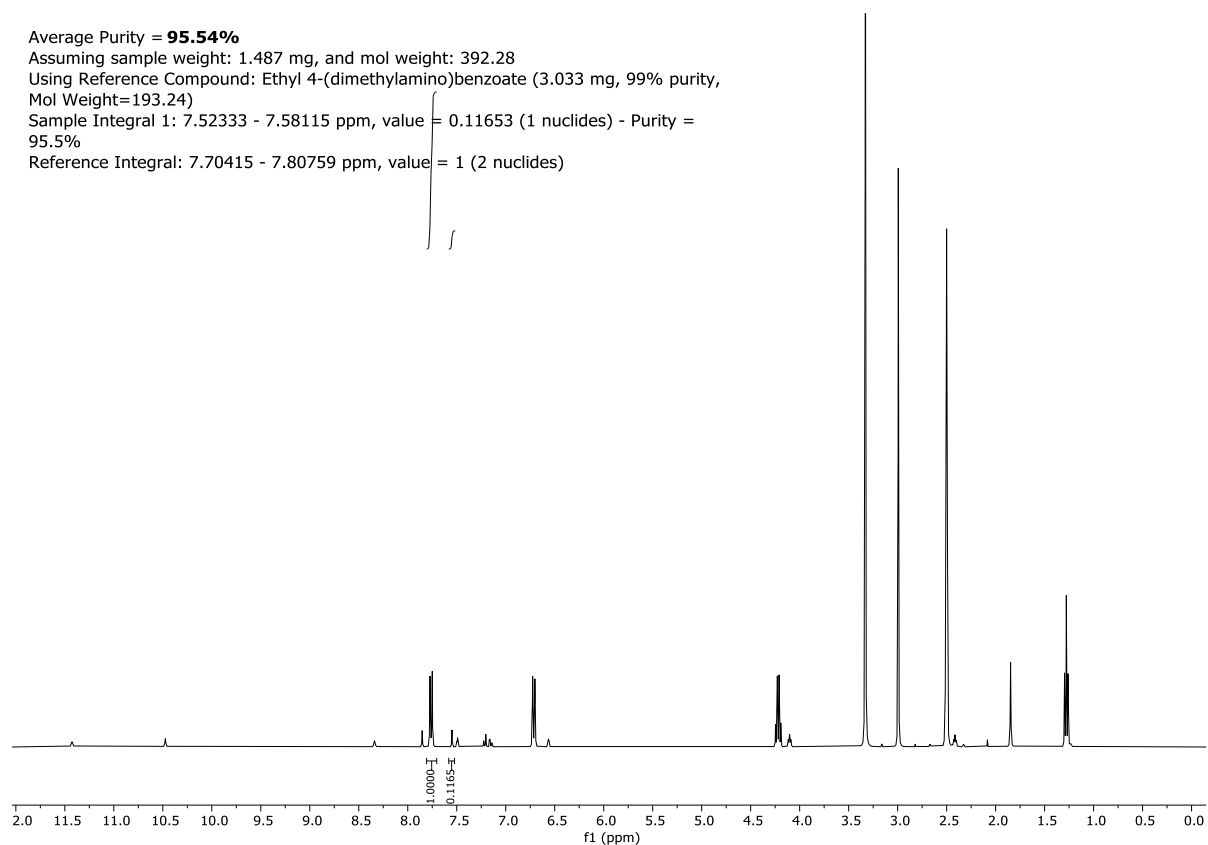
Average Purity = **95.54%**

Assuming sample weight: 1.487 mg, and mol weight: 392.28

Using Reference Compound: Ethyl 4-(dimethylamino)benzoate (3.033 mg, 99% purity, Mol Weight=193.24)

Sample Integral 1: 7.52333 - 7.58115 ppm, value = 0.11653 (1 nuclides) - Purity = 95.5%

Reference Integral: 7.70415 - 7.80759 ppm, value = 1 (2 nuclides)



Compound 11:

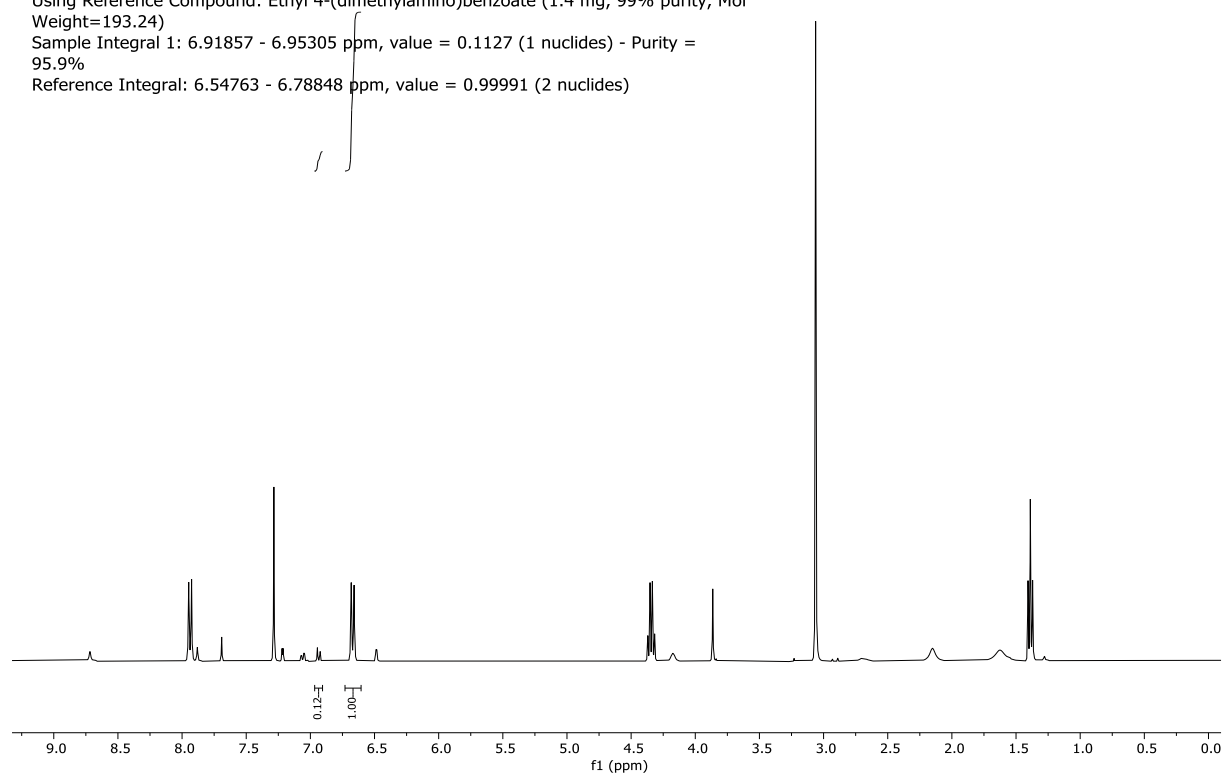
Average Purity = **95.9%**

Assuming sample weight: 0.685 mg, and mol weight: 406.31

Using Reference Compound: Ethyl 4-(dimethylamino)benzoate (1.4 mg, 99% purity, Mol Weight=193.24)

Sample Integral 1: 6.91857 - 6.95305 ppm, value = 0.1127 (1 nuclides) - Purity = 95.9%

Reference Integral: 6.54763 - 6.78848 ppm, value = 0.99991 (2 nuclides)



Compound 12:

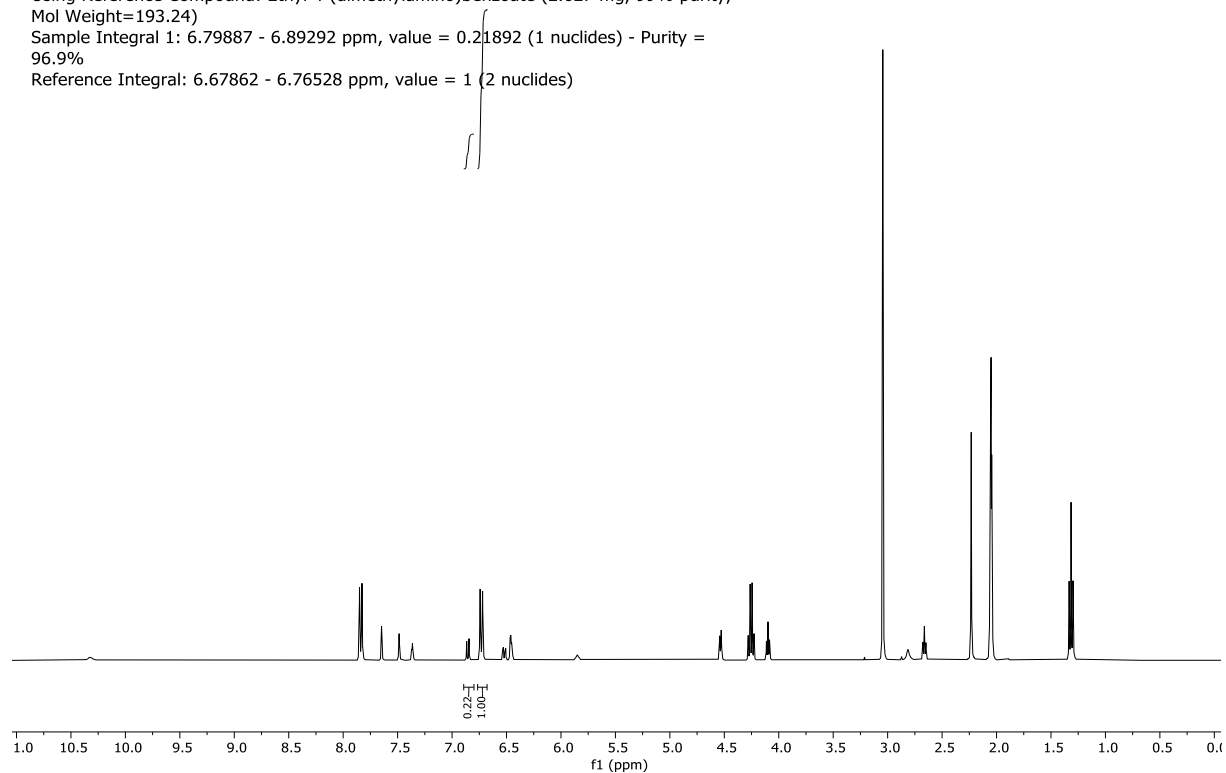
Average Purity = **96.88%**

Assuming sample weight: 2.301 mg, and mol weight: 378.3

Using Reference Compound: Ethyl 4-(dimethylamino)benzoate (2.627 mg, 99% purity, Mol Weight=193.24)

Sample Integral 1: 6.79887 - 6.89292 ppm, value = 0.21892 (1 nuclides) - Purity = 96.9%

Reference Integral: 6.67862 - 6.76528 ppm, value = 1 (2 nuclides)



Compound 13:

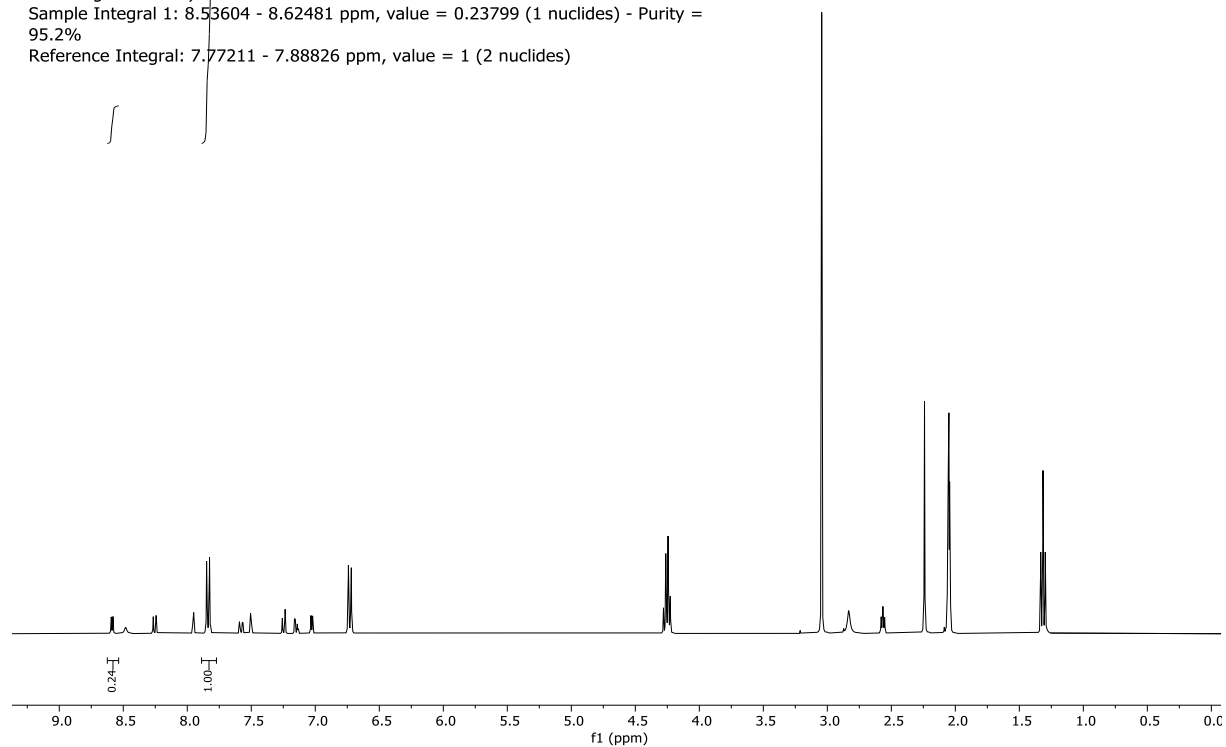
Average Purity = **95.2%**

Assuming sample weight: 2.903 mg, and mol weight: 376.28

Using Reference Compound: Ethyl 4-(dimethylamino)benzoate (3.012 mg, 99% purity, Mol Weight=193.24)

Sample Integral 1: 8.53604 - 8.62481 ppm, value = 0.23799 (1 nuclides) - Purity = 95.2%

Reference Integral: 7.77211 - 7.88826 ppm, value = 1 (2 nuclides)



Supplementary References

- (1) Bruning, J. M.; Wang, Y.; Oltrabella, F.; Tian, B.; Kholodar, S. A.; Liu, H.; Bhattacharya, P.; Guo, S.; Holton, J. M.; Fletterick, R. J.; Jacobson, M. P.; England, P. M. Covalent Modification and Regulation of the Nuclear Receptor Nurr1 by a Dopamine Metabolite. *Cell Chem. Biol.* **2019**, *26* (5), 674-685.e6.
- (2) Pauli, G. F.; Chen, S. N.; Simmler, C.; Lankin, D. C.; Gödecke, T.; Jaki, B. U.; Friesen, J. B.; McAlpine, J. B.; Napolitano, J. G. Importance of Purity Evaluation and the Potential of Quantitative ¹H NMR as a Purity Assay. *J. Med. Chem.* **2014**, *57* (22), 9220–9231.
- (3) McCoull, W.; Barton, P.; Brown, A. J. H.; Bowker, S. S.; Cameron, J.; Clarke, D. S.; Davies, R. D. M.; Dossetter, A. G.; Ertan, A.; Fenwick, M.; Green, C.; Holmes, J. L.; Martin, N.; Masters, D.; Moore, J. E.; Newcombe, N. J.; Newton, C.; Pointon, H.; Robb, G. R. et al. Identification, Optimization, and Pharmacology of Acylurea GHS-R1a Inverse Agonists. *J. Med. Chem.* **2014**, *57* (14), 6128–6140.

12.2 Development of Nurr1 agonists from amodiaquine by scaffold hopping and fragment growing

Sai, M.; Hank, E. C.; Tai, H.M.; Kasch, T.; Lewandowski, M.; Vincendeau, M.; Marschner, J. A.; Merk, D. Development of Potent and Selective Nurr1 Agonists from Amodiaquine By Scaffold Hopping and Fragment Growing. *Commun. Chem.*, **2024**, 7, 149.

Reprinted with permission from Sai, M.; Hank, E. C.; Tai, H.M.; Kasch, T.; Lewandowski, M.; Vincendeau, M.; Marschner, J. A.; Merk, D. Development of Potent and Selective Nurr1 Agonists from Amodiaquine By Scaffold Hopping and Fragment Growing. *Commun. Chem.*, **2024**, 7, 149.

<https://doi.org/10.1038/s42004-024-01224-0>

Development of Nurr1 agonists from amodiaquine by scaffold hopping and fragment growing

Check for updates

Minh Sai¹, Emily C. Hank¹, Hin-Man Tai², Till Kasch¹, Max Lewandowski¹, Michelle Vincendeau^{2,3}, Julian A. Marschner¹ & Daniel Merk¹ ✉

The neuroprotective transcription factor nuclear receptor-related 1 (Nurr1) has shown great promise as a therapeutic target in Parkinson's and Alzheimer's disease as well as multiple sclerosis but high-quality chemical tools for pharmacological target validation of Nurr1 are rare. We have employed the weak Nurr1 modulator amodiaquine (AQ) and AQ-derived fragments as templates to design a new Nurr1 agonist chemotype by scaffold hopping and fragment growing strategies. Systematic structural optimization of this scaffold yielded Nurr1 agonists with nanomolar potency and binding affinity. Comprehensive *in vitro* profiling revealed efficient cellular target engagement and compliance with the highest probe criteria. In human midbrain organoids bearing a Parkinson-driving LRRK2 mutation, a novel Nurr1 agonist rescued tyrosine hydroxylase expression highlighting the potential of the new Nurr1 modulator chemotype as lead and as a chemical tool for biological studies.

Nuclear receptor related 1 (Nurr1, NR4A2) is a ligand-activated transcription factor mainly expressed in neurons and immune cells of the brain^{1–3}. The receptor is critically involved in the regulation of (dopaminergic) neuron development and maintenance as well as inflammatory processes^{3–6}. Observations of diminished Nurr1 levels in patients⁷ and animal models^{8–10} of Alzheimer's (AD) and Parkinson's diseases (PD) underline the therapeutic potential of Nurr1 activation in neurodegenerative diseases. Moreover, recent findings suggest a protective and anti-inflammatory role of Nurr1 in retinal pigment epithelial cells in the eye with possible therapeutic relevance in age-related macular degeneration¹¹. Pharmacological activation of Nurr1 may therefore offer new therapeutic options in various degenerative diseases and potent Nurr1 agonists are needed¹².

Nurr1 acts as a monomer, homodimer, or heterodimer and has constitutive transcriptional activator activity also in the absence of ligands but can be modulated by agonists and inverse agonists in a bidirectional fashion^{13–15}. The dopamine metabolite 5,6-dihydroxyindole (DHI)¹⁶, polyunsaturated fatty acids¹⁷ and the prostaglandins A and E¹⁸ have been identified as natural Nurr1 ligands. A few synthetic Nurr1 ligand chemotypes have been recently identified^{19–23} among which the antimalarial amodiaquine (AQ; Fig. 1; EC₅₀~20 μM)²⁴ was the first validated Nurr1 agonist and emerged as an early tool to study therapeutic effects of Nurr1 activation²⁴. AQ treatment counteracted neuroinflammation and ameliorated behavioral deficits in a PD model²⁴, and reduced neuronal loss and amyloid-beta deposition in an AD model²⁵. However, while offering access

to Nurr1 ligand discovery, AQ is unspecific^{19,26–28} and hepatotoxic²⁹, and pharmacological effects with AQ cannot confidently be assigned to Nurr1 modulation. For example, AQ was found to inhibit autophagy, stabilize p53, block ribosome biogenesis, suppress PPARγ induced adipogenesis, and cause endoplasmic reticulum stress^{30–33} thus affecting multiple cellular processes. Moreover, AQ and many analogues contain pan-assay interference compounds (PAINS)^{34,35} elements further compromising their value as a chemical tool. Therefore, AQ descendants with improved potency and selectivity are needed to validate the promising observations on Nurr1-mediated therapeutic effects of this drug. So far, structural optimization efforts have yielded the AQ descendant **1** exhibiting improved Nurr1 agonist potency and protective effects in a PD model³⁶, simplified 7-chloroquinolin-4-amine (**2**) and 8-chloro-2-methylquinolin-4-amine (**3**) fragments with enhanced Nurr1 agonism²⁸, and a 5-(4-chlorophenyl)furan-2-carboxamide motif (**4**)³⁷ as replacement for the unfavorable 4-aminophenol residue of AQ.

Here, we aimed to develop AQ-derived Nurr1 agonists to enable target validation studies on the promising effects of AQ in neurodegeneration. Systematic optimization, scaffold-hopping, and fusion of AQ substructures yielded a next-generation Nurr1 ligand scaffold offering high potency and selectivity. Comprehensive characterization and validation demonstrated high affinity binding to Nurr1, cellular target engagement, low toxicity, favorable permeability, and tunable metabolic stability. A potent and extensively validated Nurr1 agonist of the AQ-derived chemotype and a structurally matched

¹Ludwig-Maximilians-Universität München, Department of Pharmacy, 81377 Munich, Germany. ²Helmholtz Munich, Institute of Virology, 85764 Munich, Germany.

³Technical University of Munich, Institute of Virology, School of Medicine, 81675 Munich, Germany. ✉e-mail: daniel.merk@cup.lmu.de

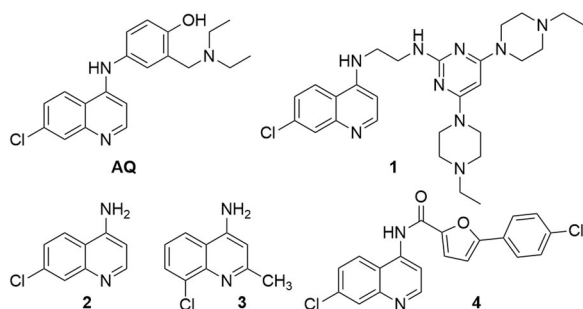


Fig. 1 | Nurr1 agonists. Amodiaquine (AQ)²⁴, the optimized AQ derivative **1**³⁶, the AQ-derived fragments **2** and **3**²⁸, and the AQ derivative **4** from microscale combinatorial chemistry³⁷.

negative control compound together provide a high-quality chemical tool for biological studies to validate Nurr1-dependent pharmacological effects of AQ and advance Nurr1 modulation as a therapeutic concept.

Results & Discussion

Design and structural optimization of Nurr1 agonists

Antimalarial activity of AQ and related compounds is mainly ascribed to the common chloroquinoline scaffold present in several antimalarials³⁸ while the 4-hydroxyaniline is considered mainly responsible for cyto- and hepatotoxicity after metabolic activation to a reactive quinoneimine^{29,32}. Additionally, cellular AQ effects, e.g., on autophagy and p53, surpassed the activity of chloroquinone (CQ)^{30,31} which is structurally related but lacks the 4-aminophenol moiety indicating that this substructure also mediates off-target activities of AQ.

Optimization of the AQ scaffold for Nurr1 agonism hence demanded the replacement of both the chloroquinolineamine and 4-aminophenol motifs. As we have previously found that 7-chloroquinoline-4-amine (**2**) is sufficient for Nurr1 activation and can be tuned in Nurr1 agonism by variation of its substitution pattern²⁸, we aimed for optimization of the chloroquinolineamine fragment by scaffold hopping and subsequent fragment extension. Thus, we commenced the development of AQ-derived Nurr1 modulators by probing replacement of the quinoline scaffold of the optimized AQ fragment **3** by alternative heterocycles (Table 1). The corresponding quinazoline **5** was inactive and 7-chloro-2-methyl-1H-indol-3-amine (**6**) was not stable. 4-Chloro-2-methyl-benzimidazole (**7**) also failed to activate Nurr1 suggesting that the amino substituent was required and could not be replaced by the ring NH.

The alternative imidazo[1,2-*a*]pyridine scaffold (**8**), in contrast, retained Nurr1 agonism and achieved a notable improvement in potency and efficacy compared to **4**. The smaller skeleton was not compatible with the original regiochemistry of the chloro substituent (**9**) and systematic deconstruction of **8** indicated a tight SAR with the importance of all substituents (**10–13**). Despite weak to no Nurr1 activation by **9–13**, isothermal titration calorimetry (ITC, Table 1, Supplementary Fig. 1) demonstrated that **11** and **12** containing the 8-chloro substituent still bound with low micromolar affinity to the Nurr1 LBD while **10** and **13** lacking the chlorine atom exhibited weaker binding. These results thus highlighted the 8-chloro substituent as a key factor driving affinity and the amino motif as relevant for Nurr1 activation. With single-digit micromolar potency (EC_{50} 7 μ M) and affinity (K_d 2.7 μ M, Fig. 2a), 8-chloro-2-methylimidazo[1,2-*a*]pyridine (**8**) emerged as an improved fragment-like Nurr1 agonist which was also evident from enhanced ligand efficiency (LE), lipophilic ligand efficiency (LLE), and size-independent ligand efficiency (SILE) compared to AQ and the lead fragment **3** (Table 2).

Imidazopyridine-based NR4A modulators have been reported previously^{39–41}, but independent evaluation by Munoz-Tello et al.¹⁹ provided no evidence for binding of a selected example of this chemotype (SR24237)⁴⁰ to Nurr1. For direct comparison, we profiled the previously reported imidazopyridine-based Nurr1 agonist SA00025 (EC_{50} (NBRE) 0.217 μ M)³⁹

Table 1 | Optimization of the chloroquinoline fragment

ID	structure	EC_{50} (Nurr1) (max. activation) ^a	K_d (Nurr1 LBD) ^b
3		17 \pm 6 μ M (1.7 \pm 0.1-fold)	n.d.
5		inactive (100 μ M)	n.d.
6		unstable	n.d.
7		inactive (100 μ M)	n.d.
8		7 \pm 1 μ M (2.0 \pm 0.1-fold)	2.7 μ M
9		inactive (100 μ M)	weak binding
10		inactive (100 μ M)	weak binding
11		inactive (100 μ M)	7.2 μ M
12		< 1.2-fold activation	5.1 μ M
13		inactive (100 μ M)	weak binding

^aNurr1 modulation was determined in a Gal4-Nurr1 hybrid reporter gene assay. Max. activation refers to the maximum effect vs. 0.1% DMSO control. Data are the mean \pm SD; $n \geq 3$. ^b K_d values were determined by isothermal titration calorimetry (cf. Fig. 2a Supplementary Fig. 1). n.d. - not determined; weak binding - titration of 15 μ M Nurr1 with 100 μ M ligand showed heat differences indicative of binding that could not be fitted, however.

in our test systems (refer to Supplementary Fig. 2 for assay setups; chemical structure and data for SA00025 in Supplementary Fig. 3). No activation of Nurr1 (or the related NR4A receptors Nur77 and NOR1) by SA00025 was detectable in the Gal4-hybrid reporter gene assay in the concentration range from 10 nM to 3 μ M (Supplementary Fig. 3b). At higher concentration, SA00025 was considerably cytotoxic. As literature³⁹ reported activation of full-length human Nurr1 by SA00025 on the NBRE response element, we also employed reporters for the human Nurr1 response elements (NBRE, NurRE, DR5)¹⁴ but detected no effect of SA00025 (Supplementary Fig. 3c). Orthogonal evaluation of SA00025 in cell-free setting by ITC indicated potential weak binding, but insufficient affinity to determine a K_d value with this technique (Supplementary Fig. 3d). In accordance with the findings of Munoz-Tello et al.¹⁹, these results do not support potent Nurr1 agonism of

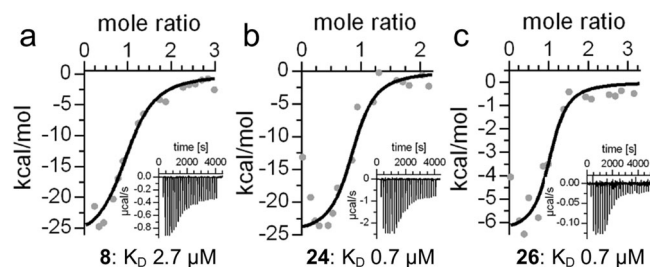


Fig. 2 | Orthogonal validation of ligand binding to Nurr1 by isothermal titration calorimetry (ITC). The fittings of the heat of binding are shown for **8** (a), **24** (b), and **26** (c) and the isotherms at 25 °C are shown as insets.

Table 2 | Ligand efficiency metrics of 1, 4, 8, 24, 26 and 36.^a

	1	4	8	24	26	36
pEC ₅₀	4.7	4.8	5.2	6.4	5.8	7.0
LE	0.26	0.50	0.59	0.46	0.31	0.34
LLE	-0.48	1.99	3.28	1.86	0.34	2.18
SILE	1.79	2.21	2.45	2.64	2.18	2.59

^aLigand efficiency (LE), lipophilic ligand efficiency (LLE), and size-independent ligand efficiency (SILE) were computed according to ref. 62.

SA00025 and related compounds and align with the lack of activity of **9** indicating that 8-substituted imidazopyridines like **8** are favored over analogues with substituents in 7-position.

Aiming to enhance potency by fragment growing, we next evaluated a potential optimization of the 2-methyl substituent of **8** (Table 3). Extension in this region caused a general reduction in Nurr1 activation efficacy. In a rough exploration of aliphatic (**14**) and aromatic (**15**, **16**) extensions, only the phenyl substituent (**15**) retained sufficient efficacy and provided a slight improvement over **8** in terms of potency (EC₅₀ 4 μM). Chloro substituents in 4- (**17**) and 3- (**18**) positions of the phenyl motif enhanced activation efficacy but diminished potency. 2-Chloro substitution (**19**) disrupted activity on Nurr1. Replacement of the chloro substituents (**17**, **18**) by a methyl group was tolerated in 4-position (**20**) but not in 3-position (**21**), and trifluoromethyl substituents (**22**, **23**) also caused a marked drop in efficacy. Double 3,4-chloro substitution (**24**), in contrast, was additive and resulted in enhanced potency (EC₅₀ 0.4 μM) and efficacy (1.8-fold activation). The corresponding dimethyl analogue **25** was less active.

Structural extension of the 2-methyl substituent in **8** thus provided no major gain in Nurr1 agonist activity. Only the 3,4-dichlorophenyl derivative **24** achieved a notable increase in potency over **8** which was in line with results from ITC confirming enhanced affinity of **24** (K_d 0.7 μM, Fig. 2b). In terms of ligand efficiency (Table 2), the structural extension from **8** to **24** represented no significant improvement but the 2-(3,4-dichlorophenyl) substituent of **24** may still be a valuable potency driving extension in fused derivatives.

The optimized Nurr1 agonist **8** obtained by fragment hopping from the chloroquinoline motif of AQ also appeared suitable for fragment growing by fusion with N-substituents. Our previous studies³⁷ have revealed a 5-(4-chlorophenyl)furan-2-carboxamide residue as alternative motif to replace the aminophenol of AQ. Transfer of this SAR knowledge to the new imidazo[1,2-*a*]pyridine scaffold of **8** in the fused 5-(4-chlorophenyl)furan-2-carboxamide derivative **26** provided an improvement in Nurr1 agonist potency (Table 4) but decreased ligand efficiency (Table 2). Simplification of **26** by removal of the chloro substituent (**27**) was tolerated but among alternative central aromatic systems, only thiophene (**28**) retained Nurr1 agonism. Replacement of furan (**27**) by pyrrole (**29**) or benzene (**30**) disrupted activity thus suggesting **26** as lead for further optimization which was also supported by improved binding affinity of **26** (K_d 0.7 μM, Fig. 2c). Further optimization potential seemed to rest in the 4-chloro substituent as its removal (**27**) hardly diminished potency. This indicated that space to accommodate substituents was

Table 3 | Extension of the imidazo[1,2-*a*]pyridine **8**

ID		EC ₅₀ (Nurr1) (max. activation) ^a
8		7 ± 1 μM (2.0 ± 0.1-fold)
14		< 1.2-fold act.
15		4 ± 2 μM (1.4 ± 0.1-fold)
16		< 1.2-fold act.
17		15 ± 3 μM (1.7 ± 0.2-fold)
18		9 ± 3 μM (1.7 ± 0.1-fold)
19		inactive (100 μM)
20		12 ± 2 μM (2.0 ± 0.2-fold)
21		< 1.2-fold act.
22		< 1.2-fold act.
23		< 1.2-fold act.
24		0.4 ± 0.2 μM (1.8 ± 0.1-fold)
25		14 ± 2 μM (1.6 ± 0.1-fold)

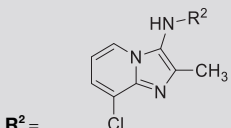
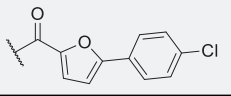
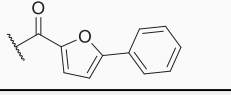
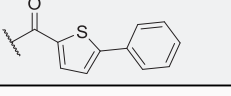
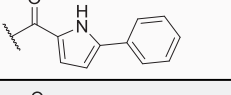
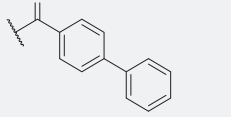
^aNurr1 modulation was determined in a Gal4-Nurr1 hybrid reporter gene assay. Max. activation refers to the maximum effect vs. 0.1% DMSO control. Data are the mean ± SD; n ≥ 3.

available in this region and we thus focused our attention on alternative motifs to replace the chlorine atom as 4-substituent of the phenylfuran-2-carboxamide residue (Table 5).

The 4-trifluoromethyl derivative **31** exhibited similar activity as **26** while the corresponding 4-methyl analogue **32** was substantially more potent. A similar trend was observed for the 4-trifluoromethoxy (**33**) and 4-methoxy (**34**) pair, which indicated the potential relevance of inductive effects. Like 4-methyl (**32**) and 4-methoxy (**34**), a 4-methylamino substituent (**35**) was highly favored and enhanced Nurr1 agonist potency to a sub-micromolar range. A 4-dimethylamino group (**36**) provided a further improvement to a double-digit nanomolar EC₅₀ value.

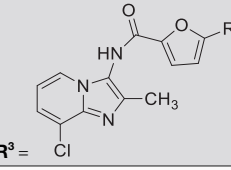
The SAR evaluation had revealed favorable contributions to Nurr1 agonist potency for a 3,4-dichlorophenyl substituent in 2-position of the imidazopyridine scaffold (**24**) and for the 5-(4-(dimethylamino)phenyl)furan-2-carboxamide motif in 3-position (**36**). Structural fusion of these modifications in the combined derivative **37** (Fig. 3) generated a high-affinity Nurr1 modulator (K_d 0.08 μM, Supplementary Fig. 4) with strong agonist potency (EC₅₀ = 0.04 ± 0.01 μM), but the fused compound **37** did

Table 4 | Fusion of 8 with N-substituents

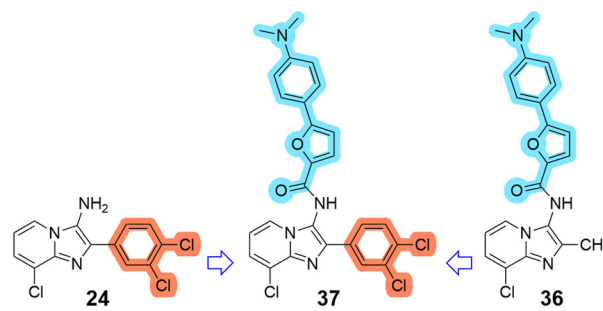
ID		EC ₅₀ (Nurr1) (max. activation) ^a
8	H	7 ± 1 μM (2.0 ± 0.1-fold)
26		1.6 ± 0.5 μM (1.8 ± 0.1-fold)
27		4 ± 1 μM (2.1 ± 0.1-fold)
28		3.2 ± 0.4 μM (2.1 ± 0.1-fold)
29		inactive (10 μM ^b)
30		inactive (10 μM ^b)

^aNurr1 modulation was determined in a Gal4-Nurr1 hybrid reporter gene assay. Max. activation refers to the maximum effect vs. 0.1% DMSO control. Data are the mean ± SD; *n* ≥ 3. ^bHighest non-toxic concentration.

Table 5 | Optimization of the fused derivative 26

ID		EC ₅₀ (Nurr1) (max. activation) ^a
27	phenyl	4 ± 1 μM (2.1 ± 0.1-fold)
26	4-chlorophenyl	1.6 ± 0.5 μM (1.8 ± 0.1-fold)
31	4-(trifluoromethyl)phenyl	1.1 ± 0.3 μM (1.8 ± 0.1-fold)
32	4-methylphenyl	0.13 ± 0.02 μM (2.0 ± 0.2-fold)
33	4-(trifluoromethoxy)phenyl	0.8 ± 0.2 μM (2.0 ± 0.1-fold)
34	4-methoxyphenyl	0.16 ± 0.06 μM (1.7 ± 0.1-fold)
35	4-(methylamino)phenyl	0.30 ± 0.02 μM (1.8 ± 0.1-fold)
36	4-(dimethylamino)phenyl	0.090 ± 0.005 μM (2.1 ± 0.1-fold)

^aNurr1 modulation was determined in a Gal4-Nurr1 hybrid reporter gene assay. Max. activation refers to the maximum effect vs. 0.1% DMSO control. Data are the mean ± SD; *n* ≥ 3.



	24	37	36
EC ₅₀	0.4 ± 0.2 μM	0.04 ± 0.01 μM	0.090 ± 0.005 μM
eff.	1.8 ± 0.1-fold	1.53 ± 0.04-fold	2.1 ± 0.1-fold
K _d	0.7 μM	0.08 μM	0.17 μM

Fig. 3 | Structural fusion of 24 and 36 in 37 enhanced Nurr1 agonist potency and binding affinity. Nurr1 modulation was determined in a Gal4-Nurr1 hybrid reporter gene assay. Max. activation refers to the maximum effect vs. 0.1% DMSO control. Data are the mean ± SD; *n* ≥ 3. Binding affinity was determined by ITC.

not substantially outmatch 36 and was significantly more lipophilic (37: SlogP 7.54).

Biological profiling of the Nurr1 agonist 36

These results highlighted 36 as preferred Nurr1 agonist from the scaffold hopping and fragment growing approach. Potent Nurr1 agonism of 36 was also evident in reporter gene assays to observe the activity of the full-length human Nurr1 (Fig. 4a, b) which better reflects the physiological setting than the hybrid reporter gene assay (cf. Supplementary Fig. 2). Nurr1 can act as a monomer, homodimer, and RXR heterodimer on different response elements¹⁴. 36 robustly activated the Nurr1 homodimer (NurRE, EC₅₀ 0.094 μM; Fig. 4a) and the Nurr1-RXR heterodimer (DR5, EC₅₀ 0.165 μM; Fig. 4b) but interestingly was inactive on the Nurr1 monomer (NBRE; Fig. 4a) indicating an unprecedented Nurr1 dimer preference. The RXR agonist bexarotene caused generally reduced activity of DR5 (Supplementary Fig. 5) but enhanced the potency of 36 by a factor of >5 (EC₅₀ 0.032 μM (DR5 w. 0.1 μM BEX)) suggesting potentially cooperative binding⁴² to and activation of the Nurr1-RXR heterodimer.

36 exhibited high-affinity binding (K_d 0.17 μM) to the Nurr1 LBD in ITC (Fig. 4c) orthogonally validating its potent Nurr1 agonism. In astrocytes (T98G), 36 induced expression of the Nurr1-regulated genes tyrosine hydroxylase (TH), vesicular amino acid transporter 2 (VMAT2), and superoxide dismutase 2 (SOD2) at low concentrations (0.1 μM, 0.3 μM) supporting cellular target engagement (Fig. 4d). Selectivity profiling revealed a preference of 36 for Nurr1 over Nur77 (Table 6) and no activity outside the NR4A family at 3 μM corresponding to >30-fold selectivity (Fig. 4e). Moreover, 36 was non-toxic in N27 rat neurons, which can be used for neurodegeneration models^{46,43}, and in HEK293T cells at 10 μM which is two orders of magnitude above its EC₅₀ value (Fig. 4f). AQ, in contrast, exhibited considerable toxicity with only ~20% remaining N27 metabolic activity at a concentration (30 μM) that may be considered necessary for confident target engagement given its low potency. With its favorable profile fulfilling the highest quality criteria for chemical tools^{44,45}, 36 thus emerges as a next-generation tool to study the effects of Nurr1 modulation by AQ-type ligands.

To boost the value of 36 as a chemical tool, we aimed to complement it with a structurally matched negative control compound for which 29 appeared suitable. 29 strongly resembles 36 in its chemical structure and physicochemical characteristics but exhibited no Nurr1 agonism in a cellular setting at 10 μM and revealed no detectable binding to Nurr1 in ITC (Table 6). Further profiling of 29 revealed no effect on Nur77 and NOR-1, no activation of full-length Nurr1, and no induction of Nurr1-regulated gene expression (Fig. 4d). Thus, 29 is at least 100-fold less active than 36 as Nurr1 modulator and suitable as negative control.

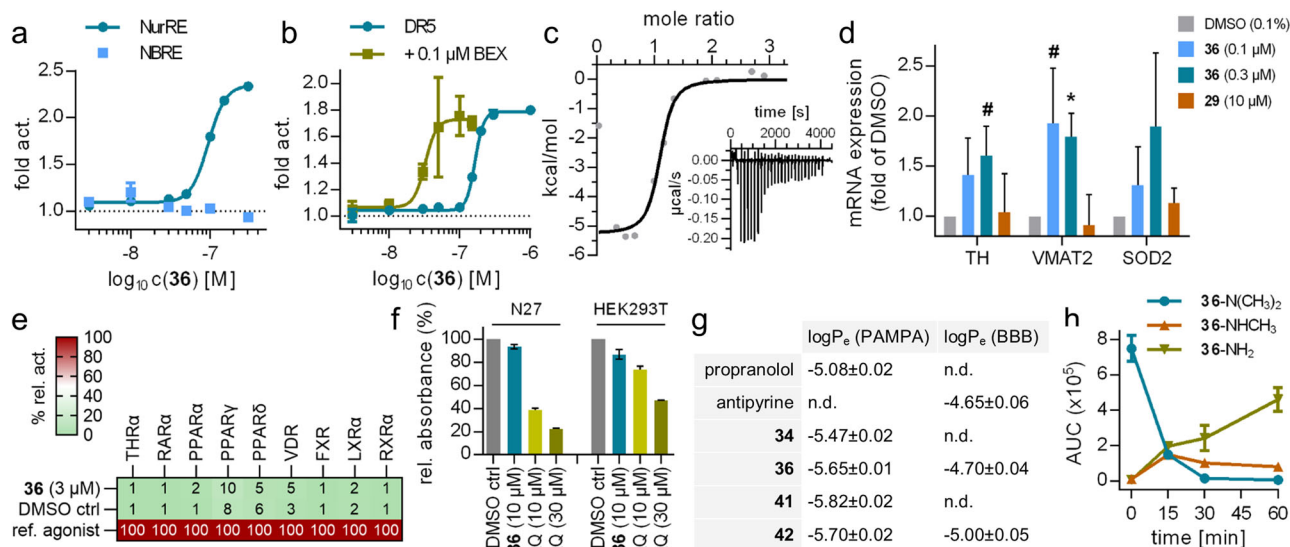


Fig. 4 | Orthogonal validation and profiling of 36. **a** Effects of 36 on the human full-length Nurr1 homodimer (NurRE) and monomer (NBRE). Data are the mean \pm S.E.M. fold activation vs. DMSO ctrl; $n \geq 3$. **b** Effects of 36 on the Nurr1-RXR heterodimer (DR5) in the absence and presence of bexarotene (0.1 μ M). Data are the mean \pm S.E.M. fold activation vs. DMSO ctrl or vs. 0.1 μ M BEX; $n \geq 3$. **c** Binding of 36 to the Nurr1 LBD (K_d 0.17 μ M, $n = 1.0$) determined by ITC. The fitting of the heat of binding is shown and the isotherm at 25 $^{\circ}$ C is shown as inset. **d** Effects of 36 and 29 on the expression of the Nurr1-regulated tyrosine hydroxylase (TH), vesicular amino acid transporter 2 (VMAT2), and superoxide dismutase 2 (SOD2) in astrocytes (T98G). Data are the mean \pm S.E.M. fold mRNA induction vs. DMSO ctrl;

$n = 3$; * $p < 0.1$, * $p < 0.05$ (t-test vs. DMSO ctrl). **e** Selectivity screening of 36 on nuclear receptors. Heatmap shows the mean relative activation compared to reference ligands (listed in the methods section); $n = 3$. **f** 36 (10 μ M) had no toxic effect in a WST-8 assay in N27 rat neurons and HEK293T cells. AQ (1, 10 and 30 μ M) was toxic. Data are the mean \pm S.E.M. rel. absorbance (450 nm); $n \geq 3$. **g** Permeability of Nurr1 agonists in a parallel artificial membrane permeability assay (PAMPA) and in a cellular model of the blood-brain-barrier (BBB). Propranolol and the brain-penetrant reference antipyryne for comparison. Data are the mean \pm SD; $n = 6$. **h** Metabolism of 36 by rat liver microsomes resulted in demethylation of the dimethylamino group. Data are the mean \pm SD; $n = 4$.

To further explore the potential of 36 as a chemical tool for in vivo applications, we evaluated its pharmacokinetic parameters. 36 exhibited favorable permeability in a parallel artificial membrane permeability assay (PAMPA) and a cellular model of the blood-brain barrier using the human brain endothelial cell-line HBEC-5i on trans-well plates⁴⁶ (Fig. 4g) as indicators of good absorption and brain penetration. The stability of 36 against degradation by rat liver microsomes was low, however, pointing to limited metabolic stability (Fig. 4h). Closer inspection suggested that 36 was almost exclusively degraded by demethylation of the dimethylamino motif. The initially formed monomethylamine (35) retained slightly reduced Nurr1 agonism (Table 5) while the eventually dominant fully demethylated amine 38 was less active (Table 7). We aimed to overcome the metabolic liability of 36 and obtain an analogue suitable for in vivo applications and hence probed replacement of the labile motif (Table 7). The introduction of cyclic amino substituents (39, 40) was not productive as Nurr1 agonism was lost with these bulkier residues. Therefore, we moved our attention to the methoxy analogue 34, which exhibited similar Nurr1 agonist potency as the labile dimethylamine 36 and threefold higher stability against microsomal degradation. Extension of the methoxy group of 34 to an isopropoxy (41) or cyclopropoxy (42) motif was well tolerated in terms of Nurr1 agonism and significantly improved metabolic stability while mostly retaining membrane and BBB permeability (Fig. 4g). These results, therefore, demonstrate that the pharmacokinetic profile of the new Nurr1 agonist scaffold can be tuned to obtain candidates for in vivo application.

The Nurr1 agonist 36 rescued tyrosine hydroxylase expression in LRRK2 mutant midbrain organoids

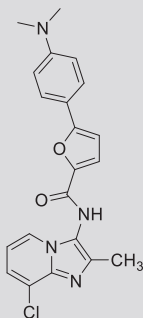
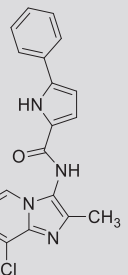
To evaluate the biological effects of the new Nurr1 agonist scaffold in a more (patho-)physiological setting and capture its full potential as a chemical tool and lead, we employed a PD model in a three-dimensional organoid system⁴⁷ derived from induced pluripotent stem cells (iPSC). Human midbrain organoids were generated from wildtype iPSC (isogenic control) and from iPSC bearing a G2019S mutation in the leucine-rich repeat kinase 2 (LRRK2) gene. LRRK2 mutation is among the most common genetic

causes of PD⁴⁸ and the G2019S mutation enhancing the kinase activity of LRRK2 has been correlated with increased α -synuclein accumulation, mitochondrial dysfunction, impaired dopamine signaling, and ultimately progressive dopamine neuron loss in the human brain^{48,49}. Using this in vitro disease model, we evaluated the impact of 36 and 29 on the dopamine neuron marker TH in 44 days old organoids (Fig. 5). Compared to the isogenic control, LRRK2 mutant organoids exhibited significantly diminished Nurr1 and TH mRNA expression (Fig. 5a, b). Treatment with the Nurr1 agonist 36 rescued the TH levels in LRRK2 mutant organoids as evident in mRNA transcript level (Fig. 5c) and histologically by staining for TH (Fig. 5b, d). TH transcript levels of mutant organoids treated with 36 reached the level of isogenic control organoids further supporting the therapeutic potential of Nurr1 activation in PD. A weaker efficacy of 36 on TH levels in wild-type organoids may indicate that Nurr1 activity in these organoids was sufficient and that therapeutic Nurr1 activation may unfold stronger when Nurr1 activity is pathologically diminished. Importantly, Nurr1 levels were not altered by treatment with 36 (Fig. 5e) underscoring that its effects on TH expression were mediated by direct Nurr1 activation. Compound 29 did not affect TH and Nurr1 levels in organoids supporting its suitability as negative control.

Conclusion

Nurr1 is attracting remarkable interest as a candidate target for neurodegenerative disease treatment¹². However, the therapeutic potential of the nuclear receptor is mainly supported by knockout studies and observations from patients¹², and target validation with high-quality chemical tools is pending. AQ was discovered as a direct Nurr1 modulator and used in several pharmacological studies^{24,25} but is only a weak Nurr1 agonist and exhibits unspecific effects¹⁹ disqualifying the antimalarial as a chemical tool. Despite recent progress with an optimized Nurr1 agonist providing further evidence for the therapeutic value of Nurr1 activation in PD models³⁶, the promising effects observed with AQ require validation. Here, we have developed potent Nurr1 agonists from AQ with extensively validated activity and lacking the structural elements of AQ mediating unspecific toxicity to enable robust

Table 6 | Characterization of NR4A agonist 36 and negative control 29 demonstrating high chemical tool quality^{44,45}

		
	36	29
EC ₅₀ (Nurr1)	0.090 ± 0.005 μM	no activation (10 μM)
EC ₅₀ (Nur77)	0.33 ± 0.04 μM	no activation (10 μM)
EC ₅₀ (NOR-1)	0.11 ± 0.03 μM	no activation (10 μM)
EC ₅₀ (NBRE)	no activation (1 μM)	no activation (10 μM)
EC ₅₀ (NurRE)	0.094 ± 0.003 μM	no activation (10 μM)
EC ₅₀ (DR5) [+0.1 μM BEX]	0.165 ± 0.004 μM [0.032 ± 0.007 μM]	no activation (10 μM)
K _d (Nurr1 LBD)	0.17 μM	no binding ^b
NR selectivity ^c	inactive (3 μM)	n.d.
toxicity ^d	inactive (10 μM)	inactive (10 μM)
aq. solubility	6.8 mg/L	4.1 mg/L
SlogP ^e	4.87	4.54

^aNurr1 modulation was determined in a Gal4-Nurr1 hybrid reporter gene assay. Max. activation refers to the maximum effect vs. 0.1% DMSO control. Data are the mean ± SD; *n* ≥ 3. ^bNo binding observable in ITC with 100 μM **29** and 30 μM protein (Supplementary Fig. 6). ^cNuclear receptor selectivity was determined in Gal4-hybrid reporter gene assays for THRα, RARα, PPARα/γ/δ, VDR, FXR, LXRα and RXRα (Fig. 4e). ^dCytotoxicity was evaluated in N27 (**36**) and HEK293T (**29**, **36**) cells using a WST-8 assay (Fig. 4f). ^eSlogP was computed with RDKit⁶³ software.

biological studies on Nurr1 modulation with AQ-derived agonists. Scaffold-hopping, fragment optimization, and replacement of unfavorable motifs generated potent Nurr1 agonists with preferable chemical features and experimentally confirmed high-affinity binding to the Nurr1 LBD. **36** and the structurally matched negative control **29** fulfil the highest quality criteria⁴⁴ as a next-generation chemical tool for biological studies on Nurr1 to advance Nurr1 modulation as a therapeutic strategy in neurodegeneration and beyond.

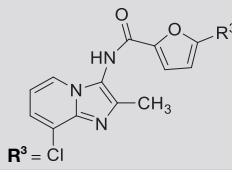
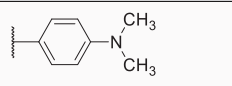
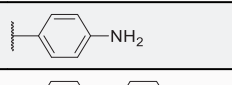
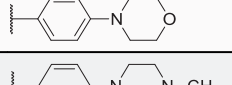
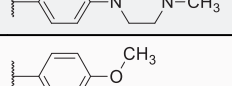
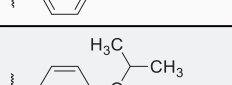
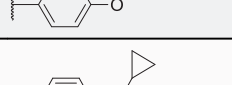
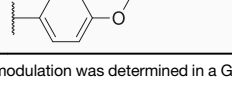
Chemistry

Compounds **7**, **8**, **12** and **14-24** were prepared by Groebke-Blackburn reaction according to Fig. 6. 3-Chloropyridine-2-amine (**43**) and 4-chloropyridine-2-amine (**44**) were cyclized with the aldehydes **45-57** and 1,1,3,3-tetramethylbutylisocyanide followed by acid-mediated cleavage to **7**, **8** and **14-24** using 4 N HCl in dioxane or TFA/CH₂Cl₂ (1:1). 1,1,3,3-Tetramethylbutylisocyanide (**63**) was commercially available. 3-Amino-8-chloroimidazo[1,2-*a*]pyridine (**12**) was prepared by nitration of 8-chloroimidazo[1,2-*a*]pyridine (**64**) followed by reduction with iron.

Compounds **26-36** were obtained by amide coupling of 3-amino-8-chloro-2-methylimidazo[1,2-*a*]pyridine (**8**) and the carboxylic acids **72-81** using HATU or thionyl chloride (Fig. 7). The carboxylic acids **72** and **73** were prepared by Suzuki coupling of aryl bromide **67** with the boronates **68**, **69** to **70**, **71** followed by alkaline ester hydrolysis. **74-81** were commercially available.

The fused derivative **37** was obtained from **24** via amide coupling with 5-bromofuran-2-carbonyl chloride (**82**) and subsequent Suzuki-Miyaura reaction with **73** according to Fig. 8. Similarly, **38-42** were synthesized from 3-amino-8-chloro-2-methylimidazo[1,2-*a*]pyridine (**8**) by amide coupling with 5-bromofuran-2-carboxylic acid (**81**) to **84** and Suzuki-Miyaura coupling with the boronates **85-89** (Fig. 9).

Table 7 | Optimization of 36 for microsomal stability

ID		EC ₅₀ (Nurr1) (max. act.) ^a	microsomal half-life ^b
36		0.090 ± 0.005 μM (2.1 ± 0.1-fold)	6.3 ± 0.3 min.
38		<1.2-fold activation	n.d.
39		inactive (10 μM ^c)	n.d.
40		inactive (10 μM ^c)	n.d.
34		0.16 ± 0.06 μM (1.7 ± 0.1-fold)	18 ± 2 min.
41		0.12 ± 0.03 μM (2.1 ± 0.2-fold)	42 ± 5 min.
42		0.12 ± 0.06 μM (1.5 ± 0.2-fold)	78 ± 7 min.

^aNurr1 modulation was determined in a Gal4-Nurr1 hybrid reporter gene assay. Max. activation refers to the maximum effect vs. 0.1% DMSO control. Data are the mean ± SD; *n* ≥ 3. ^bStability against degradation by rat liver microsomes was determined by LCMS. n.d. - not determined.

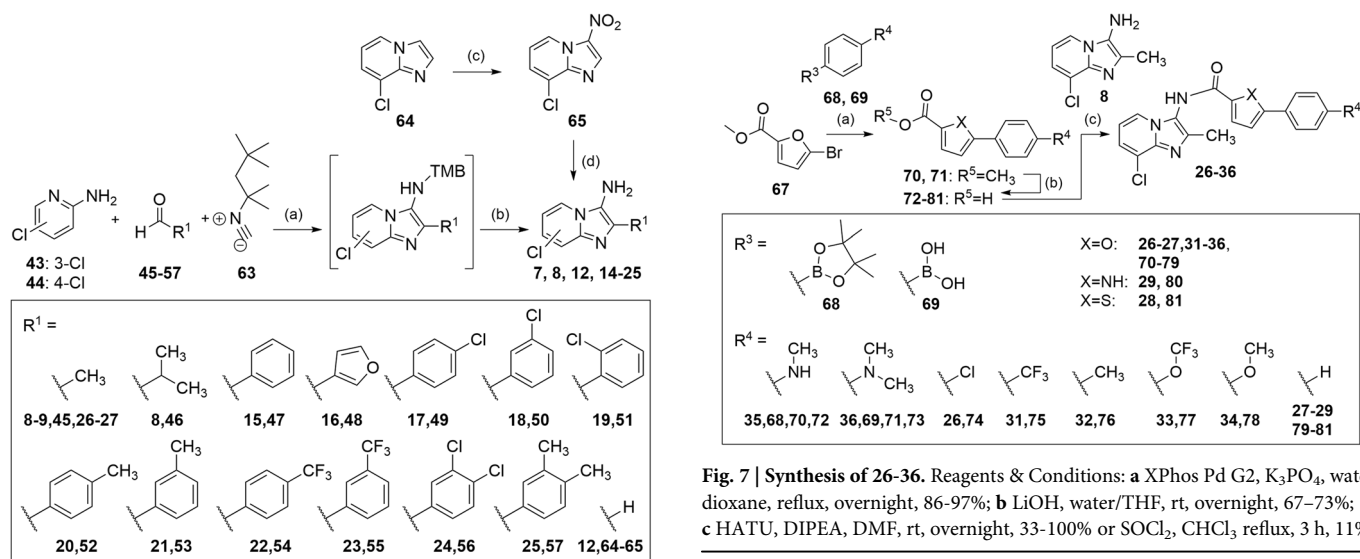
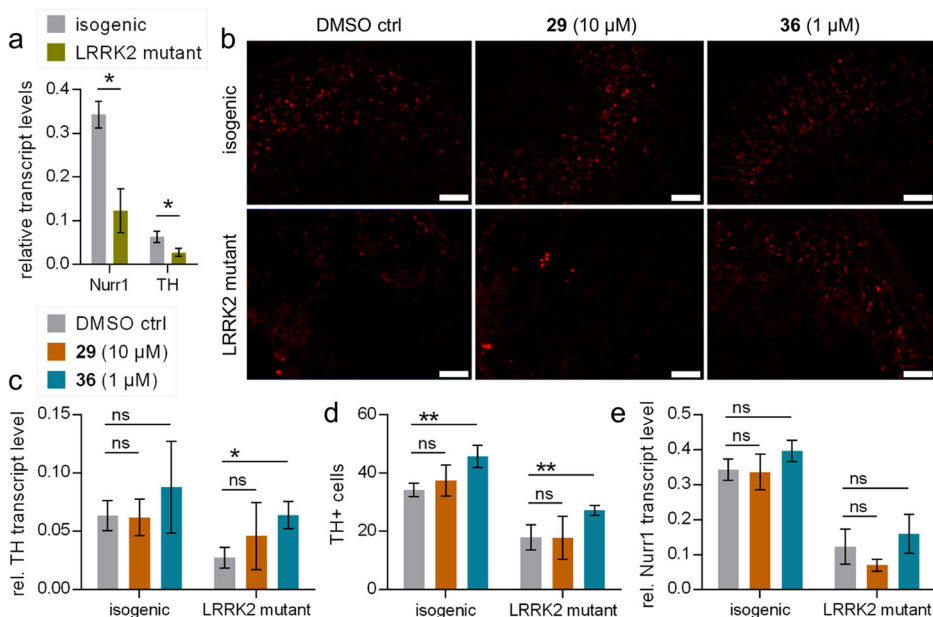
^cHighest non-toxic concentration.

Experimental procedures

Chemistry

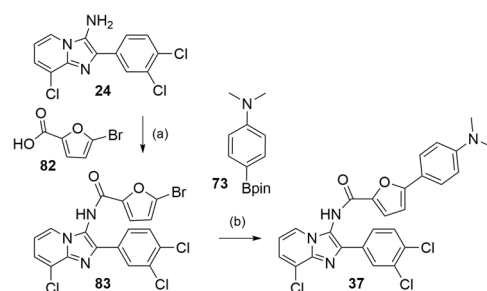
General. All chemicals were of reagent grade, purchased from commercial sources (e.g., Sigma-Aldrich, TCI, BLDpharm), and used without further purification unless otherwise specified. All reactions were conducted under a nitrogen or argon atmosphere and in absolute solvents purchased from Sigma-Aldrich. Other solvents, especially for work-up procedures, were of reagent grade or purified by distillation (*iso*-hexane, cyclohexane, ethyl acetate, EtOH). Reactions were monitored by thin layer chromatography (TLC) on TLC Silica gel 60 F254 coated aluminum sheets by Merck and visualized under ultraviolet light (254 nm) or by using ninhydrin or Ehrlich's reagent stains. Purification by column chromatography was performed on a puriFlash[®] XS520Plus system (Advion, Ithaca, NY, USA) using high-performance spherical silica columns (SIHP, 50 μm) by Interchim and a gradient of *iso*-hexane or cyclohexane to ethyl acetate. Reversed-phase column chromatography was performed on a puriFlash[®] 5.250 system (Advion) using C18HP columns (SIHP, 15 μm) by Interchim and a gradient of H₂O with 10% MeCN to 100% MeCN (HPLC gradient grade). Mass spectra were obtained on a puriFlash[®]-CMS system (Advion) using atmospheric pressure chemical ionization (APCI). HRMS were obtained with a Thermo Finnigan LTQ FT instrument for electron impact ionization (EI) or electrospray ionization (ESI). NMR spectra were recorded on Bruker Avance III HD 400 MHz or 500 MHz spectrometers equipped with a CryoProbe[™] Prodigy broadband probe (Bruker). Chemical shifts are reported in δ values (ppm) relative to residual protium signals in the NMR solvent (¹H-NMR: acetone-*d*₆: δ = 2.04 ppm; DMSO-*d*₆: δ = 2.50 ppm; MeOD-*d*₄: δ = 3.31 ppm, ¹³C-NMR: acetone-*d*₆: δ = 206.26, 29.84 ppm; DMSO-*d*₆: δ = 39.52 ppm; MeOD-*d*₄: δ = 49.0 ppm), coupling constants (*J*) in hertz (Hz). The purity of the compounds was determined by ¹H NMR (qHNMR) according to the method described by Pauli et al.⁵⁰ with internal calibration. To ensure accurate determination of peak area

Fig. 5 | Treatment of midbrain organoids with the Nurr1 agonist 36 increased the number of TH positive cells. **a** Midbrain organoids generated from human iPSC bearing a gain-of-function LRRK2 mutation (G2019S) displayed diminished Nurr1 and TH transcript levels compared to isogenic controls after 45 days. **b** Midbrain organoid sections stained for TH expressing cells by immunofluorescence. Scale bars represent 100 μm . **c** The Nurr1 agonist 36 but not the negative control 29 induced TH mRNA expression in LRRK2 mutant organoids and tended to enhance TH mRNA expression in isogenic controls. **d** The Nurr1 agonist 36 but not the negative control 29 enhanced the number of TH positive cells in LRRK2 mutant organoids and in isogenic controls. **e** Compound treatment did not affect Nurr1 levels. All data are the mean \pm SD; $n = 3$. * $p < 0.05$, ** $p < 0.01$ (unpaired, two-tailed Student's t -test).



ratio, the qHNMR measurements were conducted under conditions allowing for complete relaxation. Ethyl 4-(dimethylamino)benzoate (LOT#BCCB6657, purity 99.63%), dimethyl terephthalate (LOT#BCBT9974, purity 99.95%) and maleic acid (LOT#BCBM8127V, purity 99.94%) were used as internal standards in $\text{MeOD}-d_4$, $\text{DMSO}-d_6$, or acetone- d_6 . All compounds for biological testing had a purity >95% according to quantitative ^1H NMR (qHNMR).

General procedure A for Groebke-Blackburn-Bienaymé reaction and hydrolysis. 2-Amino-3-chloropyridine (**43**, 1.0 eq.) or 2-amino-4-chloropyridine (**44**, 1.0 eq.), the respective aldehyde (**45-57**, 1.0-1.1 eq.) and glacial acetic acid (1.5 eq.) were dissolved in dry methanol (0.7 M) under nitrogen atmosphere. The mixture was stirred for 30-45 min. at room temperature (rt) for imine formation. 1,1,3,3-Tetramethylbutylisocyanid (**63**, 1.5 eq.) was subsequently added, and the



mixture was stirred at rt for 17-48 h. When TLC monitoring indicated completion, the isocyanide was quenched by the addition of 2N aqueous HCl (2 mL) and further stirring for 30 min. 2 N aqueous NaOH solution and ethyl acetate (10 mL) were then added, and the phases were separated. The aqueous layer was extracted with ethyl acetate (3x). The

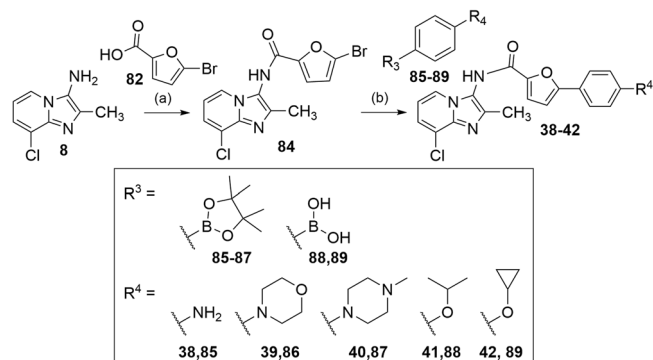


Fig. 9 | Synthesis of 38–42. Reagents & Conditions: **a** HATU, DIPEA, DMF, rt, overnight, 81%; **b** tetrakis(triphenylphosphane)palladium(0), Na₂CO₃, water/dioxane, reflux, overnight, 40–68%.

combined organic layers were dried over MgSO₄ and the solvent was evaporated under reduced pressure. The crude product was dissolved in a mixture of CH₂Cl₂ and trifluoroacetic acid (10 mL, 1:1) or 4 N HCl in dioxane (10 mL) and the mixture was stirred for 30–60 min. at rt. When TLC monitoring indicated completion, 2 N aqueous NaOH solution was added, phases were separated, and the aqueous layer was extracted with ethyl acetate (3x). The combined organic layers were dried over MgSO₄ and the solvents were evaporated under reduced pressure. The crude product was purified by flash column chromatography using a gradient of *iso*-hexane or cyclohexane/ethyl acetate as mobile phase, and potentially by reverse phase chromatography using a gradient of H₂O with 10% MeCN to 100% MeCN (HPLC gradient grade).

General procedure B for amide coupling with HATU. The respective carboxylic acid (**72–80**, 1.2 eq.) and 1-[bis(dimethylamino)methylene]-1*H*-1,2,3-triazolo[4,5-*b*]pyridinium 3-oxide hexafluorophosphate (HATU, 1.2 eq.) were dissolved in DMF (0.13 M). *N*-Ethyl-diisopropylamine (DIPEA, 0.13 M, 1.2 eq) was added and the mixture was stirred at rt for 40 min. 3-Aminoimidazo[1,2-*a*]pyridine (**8**, 1.0 eq.) was dissolved in DMF (0.11 M) and added to the activated carboxylic acid. The mixture was stirred at rt overnight. When TLC monitoring indicated completion, the solvent was removed under reduced pressure, the residue was dissolved in ethyl acetate and treated with 5% HCl (0.13 M). Phases were separated and the aqueous layer was extracted with ethyl acetate (3x). The combined organic layers were washed with 1 N aqueous NaOH solution and dried over MgSO₄. The solvent was evaporated under reduced pressure and the crude product was purified by flash column chromatography using a gradient of *iso*-hexane / ethyl acetate as mobile phase, and potentially by reverse phase chromatography using a gradient of H₂O with 10% MeCN to 100% MeCN (HPLC gradient grade).

8-Chloro-2-methylimidazo[1,2-*a*]pyridine-3-amine (8). Preparation according to general procedure A using 2-amino-3-chloropyridine (**43**, 821 mg, 6.39 mmol, 1.00 eq) and acetaldehyde (**45**, 39 μL, 7.03 mmol, 1.10 eq). **8** was obtained as a colorless solid (344 mg, 30%). ¹H-NMR (400 MHz, acetone-*d*₆): δ = 8.05 (dd, *J* = 6.8, 1.1 Hz, 1H), 7.11 (dd, *J* = 7.3, 1.0 Hz, 1H), 6.76 (t, *J* = 7.0 Hz, 1H), 4.17 (s, 2H), 2.33 (s, 3H). ¹³C-NMR (101 MHz, acetone-*d*₆): δ = 136.1, 130.1, 126.3, 121.5, 121.0, 119.8, 110.0, 11.9. MS (APCI+): *m/z* 181.9 ([M + H]⁺). HRMS (EI+): *m/z* calculated 181.0407 for C₈H₈ClN₃, found 181.0400 ([M + H]⁺). qHNMR (400 MHz, acetone-*d*₆, ethyl-4-(dimethylamino)benzoate as reference): purity = 97.5%.

8-Chloro-2-(3,4-dichlorophenyl)imidazo[1,2-*a*]pyridine-3-amine (24). Preparation according to general procedure A using 2-amino-4-chloropyridine (**43**, 1.29 g, 10.0 mmol, 1.00 eq) and 3,4-dichlorobenzaldehyde (**56**, 1.93 g, 11.0 mmol, 1.01 eq). **24** was obtained as a

yellow solid (197 mg, 6%). ¹H-NMR (400 MHz, acetone-*d*₆): δ = 8.41–8.35 (m, 1H), 8.30 – 8.23 (m, 1H), 8.20 – 8.12 (m, 1H), 7.630–7.56 (m, 1H), 7.27 (dd, *J* = 7.3, 1.1 Hz, 1H), 6.88 (t, *J* = 7.1 Hz, 1H), 4.83 (s, 2H). ¹³C-NMR (101 MHz, MeOD-*d*₄): δ = 137.2, 134.4, 132.1, 130.1, 130.0, 128.6, 128.0, 127.5, 126.3, 122.6, 121.7, 121.3, 111.3. MS (APCI+): *m/z* 311.9 ([M + H]⁺). HRMS (EI+): *m/z* calculated 310.9784 for C₁₃H₈Cl₃N₃, found 310.9778 ([M]⁺). qHNMR (400 MHz, acetone-*d*₆, ethyl-4-(dimethylamino)benzoate as reference) purity = 95.7%.

***N*-(8-Chloro-2-methylimidazo[1,2-*a*]pyridin-3-yl)-5-(4-(dimethylamino)phenyl)furan-2-carboxamide (36).** Preparation according to general procedure B using 8-chloro-2-methylimidazo[1,2-*a*]pyridine-3-amine (**8**, 50 mg, 0.28 mmol, 1.00 eq) and 5-(4-(dimethylamino)phenyl)furan-2-carboxylic acid (**73**, 76 mg, 0.33 mmol, 1.20 eq). **36** was obtained as a yellow solid (69 mg, 64%). ¹H-NMR (400 MHz, acetone-*d*₆): δ = 9.68 (s, 1H), 8.11 (d, *J* = 1.0 Hz, 1H), 7.77 (d, *J* = 8.5 Hz, 2H), 7.40 – 7.27 (m, 2H), 6.94 – 6.73 (m, 4H), 3.00 (s, 6H), 2.36 (s, 3H). ¹³C-NMR (101 MHz, acetone-*d*₆): δ = 157.7, 157.2, 151.0, 145.1, 139.1, 138.7, 125.9, 122.8, 122.6, 121.8, 118.0, 117.6, 117.0, 111.99, 111.0, 104.3, 39.4, 12.4. MS (APCI+): *m/z* 394.7 ([M + H]⁺). HRMS (EI+): *m/z* calculated 394.1197 for C₂₁H₁₉ClN₄O₂, found 394.1194 ([M]⁺). qHNMR (400 MHz, acetone-*d*₆, maleic acid as reference) purity = 95.1%.

***N*-(8-Chloro-2-methylimidazo[1,2-*a*]pyridin-3-yl)-5-phenyl-1*H*-pyrrole-2-carboxamide (29).** 5-Phenyl-1*H*-pyrrole-2-carboxylic acid (**80**, 74.0 mg, 396 μmol, 1.20 eq) was refluxed in thionyl chloride (4 mL) for 3 h. After cooling to rt, remaining thionyl chloride was removed under reduced pressure. 8-Chloro-2-methylimidazo[1,2-*a*]pyridine-3-amine (**8**, 60.0 mg, 330 μmol, 1.00 eq) dissolved in chloroform (5 mL) was added to the crude acyl chloride at 0 °C and the mixture was stirred at rt overnight. The solvent was removed under reduced pressure, the residue was dissolved in ethyl acetate and treated with 5% HCl (5 mL). Phases were separated, the aqueous layer was extracted with ethyl acetate (3x), and the combined organic layers were washed with 1 N aqueous NaOH solution and dried over MgSO₄. The solvent was removed under reduced pressure and the crude product was purified by flash column chromatography and reverse column chromatography giving compound **29** as a colorless solid (13 mg, 11%). ¹H-NMR (400 MHz, acetone-*d*₆): δ = 11.85 (s, 1H), 10.51 (s, 1H), 8.31 (d, *J* = 6.7 Hz, 1H), 7.98 (d, *J* = 7.5 Hz, 2H), 7.63 (d, *J* = 7.4 Hz, 1H), 7.41 (t, *J* = 7.7 Hz, 2H), 7.34–7.23 (m, 1H), 7.21–7.06 (m, 2H), 6.75–6.63 (m, 1H), 2.44 (s, 3H). ¹³C-NMR (101 MHz, acetone-*d*₆): δ = 159.6, 154.3, 154.1, 137.4, 136.7, 131.9, 128.7, 127.2, 126.2, 126.0, 125.0, 123.7, 118.9, 114.9, 113.1, 107.3, 11.2. qHNMR (400 MHz, acetone-*d*₆, dimethyl terephthalate as reference): purity = 97.1%. MS (APCI+): *m/z* 350.3 ([M]⁺). HRMS (ESI+): *m/z* calculated 351.0007 for C₁₉H₁₆ClN₄O⁺, found 351.10048 ([M + H]⁺).

***N*-(8-Chloro-2-(3,4-dichlorophenyl)imidazo[1,2-*a*]pyridin-3-yl)-5-(4-(dimethylamino)phenyl)furan-2-carboxamide (37).** *N,N*-Dimethyl-4-(4,4,5,5-tetramethyl-1,3,2-dioxaborolan-2-yl)aniline (**69**, 40.8 mg, 0.165 mmol, 1.00 eq), 5-bromo-*N*-(8-chloro-2-(3,4-dichlorophenyl)imidazo[1,2-*a*]pyridin-3-yl)furan-2-carboxamide (**84**, 80.0 mg, 0.165 mmol, 1.00 eq) and sodium carbonate (52.5 mg, 3.00 mol, 3.00 eq) were dissolved in dioxane/H₂O (10 mL, 9:1). The solution was degassed by freeze-pump-thaw cycles (3x). Pd(PPh₃)₄ (9.53 mg, 8.25 μmol, 0.05 eq) was added and the mixture was refluxed for 3 h under argon atmosphere. The resulting suspension was filtered, and the precipitate was washed with 2 N aqueous NaOH solution, EtOH, methylene chloride, and brine giving **37** as a colorless solid (59 mg, 68%). ¹H-NMR (400 MHz, DMSO-*d*₆): δ = 10.86 (s, 1H), 8.27–8.17 (m, 2H), 8.02–7.94 (m, 1H), 7.85–7.72 (m, 3H), 7.60 (d, *J* = 7.3 Hz, 1H), 7.57–7.50 (m, 1H), 7.02–6.92 (m, 2H), 6.80 (d, *J* = 8.8 Hz, 2H), 2.98 (s, 6H). ¹³C-NMR (126 MHz, DMSO-*d*₆): δ = 158.0, 151.1, 144.5, 139.7, 136.5, 136.0, 134.1, 132.0, 131.6, 128.6, 127.1, 126.4, 125.6, 124.1, 122.0, 119.4, 117.3, 115.3, 113.0, 112.4, 110.4, 105.2, 31.2. qHNMR (400 MHz, DMSO-*d*₆, maleic

acid as reference): purity = 96.1%. MS (APCI+): m/z 524.2 ($[M + H]^+$). HRMS (ESI+): m/z calculated 525.0646 for $C_{26}H_{20}Cl_3N_4O_2^+$, found 525.0641 ($[M + H]^+$).

***N*-(8-Chloro-2-methylimidazo[1,2-*a*]pyridin-3-yl)-5-(4-cyclopropoxyphenyl)furan-2-carboxamide (42).** 4-Cyclopropoxyphenylboronic acid (**89**, 30.1 mg, 169 μ mol, 1.00 eq), 5-bromo-*N*-(8-chloro-2-methylimidazo[1,2-*a*]pyridin-3-yl)furan-2-carboxamide (**84**, 60.0 mg, 0.169 mmol, 1.00 eq) and sodium carbonate (53.7 mg, 3.00 mol, 3.00 eq) were dissolved in dioxane/ H₂O (10 mL, 9:1). The solution was degassed by freeze-pump-thaw cycles (3x). Pd(PPh₃)₄ (9.76 mg, 8.45 μ mol, 0.05 eq) was added and the mixture was refluxed for 3 h under argon atmosphere. The resulting suspension was filtered through Celite and the solvent was removed under reduced pressure. The residue was dissolved in 2 N aqueous NaOH solution and was extracted with ethyl acetate (3x). The combined organic layers were dried over MgSO₄ and the solvent was removed under reduced pressure. The crude product was purified by flash column chromatography and reverse column chromatography giving **42** as a colorless solid (45 mg, 65%). ¹H-NMR (400 MHz, acetone-*d*₆): δ = 9.76 (s, 1H), 8.13 (d, J = 1.0 Hz, 1H), 7.89 (d, J = 8.5 Hz, 2H), 7.41–7.29 (m, 2H), 7.22–7.09 (m, 2H), 6.98 (d, J = 3.6 Hz, 1H), 6.88 (t, J = 6.8 Hz, 1H), 3.93–3.85 (m, 1H), 2.36 (s, 3H), 0.89–0.67 (m, 4H). ¹³C-NMR (126 MHz, acetone-*d*₆): δ = 159.8, 157.1, 156.5, 145.9, 139.1, 138.7, 126.1, 122.9, 122.8, 122.6, 121.9, 117.8, 116.9, 115.4, 111.0, 106.0, 50.8, 12.4, 5.7. qHNMR (400 MHz, acetone-*d*₆, ethyl-4-(dimethylamino)benzoate as reference): purity = 97.5%. MS (APCI+): m/z 407.7 ($[M + H]^+$). HRMS (ESI+): m/z calculated 408.1109 for $C_{22}H_{19}ClN_3O_3^+$, found 408.1103 ($[M + H]^+$).

5-Bromo-*N*-(8-chloro-2-(3,4-dichlorophenyl)imidazo[1,2-*a*]pyridin-3-yl)furan-2-carboxamide (83). 5-Bromofuran-2-carboxylic acid (**82**, 345 mg, 1.81 mmol, 3.14 eq) was dissolved in methylene chloride (2 mL) under Ar atmosphere. Oxalyl chloride (310 μ L, 3.62 mmol, 6.3 eq) was added dropwise to the solution at 0 °C. After 3 h the solvent was removed under reduced pressure and 8-chloro-2-(3,4-dichlorophenyl)imidazo[1,2-*a*]pyridine-3-amine (**24**, 180 mg, 576 μ mol, 1.00 eq) dissolved in a mixture of pyridine (1 mL) and toluene (4 mL) was added and the mixture was stirred at rt overnight. 2 N aqueous NaOH solution (10 mL) was added, phases were separated, and the aqueous layer was extracted with ethyl acetate (3x). The combined organic layers were dried over MgSO₄ and the solvent was removed under reduced pressure. The crude product was purified by flash column chromatography using a gradient of cyclohexane/ ethyl acetate as mobile phase giving **83** as a brown solid (180 mg, 64%). ¹H-NMR (400 MHz, DMSO-*d*₆): δ = 10.87 (s, 1H), 8.29–8.24 (m, 1H), 8.15 (d, J = 2.0 Hz, 1H), 7.92 (dd, J = 8.4, 2.1 Hz, 1H), 7.76 (d, J = 8.4 Hz, 1H), 7.62–7.57 (m, 1H), 7.50 (d, J = 3.6 Hz, 1H), 7.02–6.92 (m, 2H). ¹³C-NMR (101 MHz, DMSO-*d*₆): δ = 157.0, 148.8, 139.8, 136.5, 133.9, 132.0, 131.7, 131.1, 128.6, 127.1, 127.1, 125.7, 124.1, 122.0, 119.2, 117.2, 115.2, 113.1. MS (APCI+): m/z 483.3 ($[M + H]^+$).

5-Bromo-*N*-(8-chloro-2-methylimidazo[1,2-*a*]pyridin-3-yl)furan-2-carboxamide (84). Preparation according to general procedure B using 8-chloro-2-methylimidazo[1,2-*a*]pyridine-3-amine (**8**, 340 mg, 1.87 mmol, 1.00 eq) and 5-bromofuran-2-carboxylic acid (**82**, 429 mg, 2.24 mmol, 1.20 eq) yielded compound **84** as a colorless solid (536 mg, 81%). ¹H-NMR (400 MHz, MeOD-*d*₄): δ = 8.00 (d, J = 1.0 Hz, 1H), 7.43 (d, J = 1.0 Hz, 1H), 7.33 (d, J = 3.6 Hz, 1H), 6.91 (t, J = 7.1 Hz, 1H), 6.73 (d, J = 3.7 Hz, 1H), 2.39 (s, 3H). ¹³C-NMR (101 MHz, MeOD-*d*₄): δ = 157.5, 148.5, 139.5, 138.1, 126.6, 124.2, 122.2, 121.4, 118.5, 116.3, 114.4, 111.9, 11.2. MS (APCI+): m/z 355.4 ($[M + H]^+$).

Synthetic procedures and analytical data for **8-9**, **12**, **14-42** are provided as Supplementary Methods in the Supplementary Information (pdf). NMR spectra (¹H, ¹³C and qH) and HRMS of **8-9**, **12**, **14-42** are provided in Supplementary Data 1.

In vitro Characterization

Hybrid reporter gene assays. Nurr1 modulation was determined in a Gal4 hybrid reporter gene assay in HEK293T cells (German Collection of Microorganisms and Cell Culture GmbH, DSMZ) using pFR-Luc (Stratagene, La Jolla, CA, USA; reporter), pRL-SV40 (Promega, Madison, WI, USA; internal control) and pFA-CMV-hNurr1-LBD¹⁴, coding for the hinge region and ligand binding domain of the canonical isoform of human Nurr1. Cells were cultured in Dulbecco's modified Eagle's medium (DMEM), high glucose supplemented with 10% fetal calf serum (FCS), sodium pyruvate (1 mM), penicillin (100 U/mL), and streptomycin (100 μ g/mL) at 37 °C and 5% CO₂ and seeded in 96-well plates (3×10^4 cells/well). After 24 h, the medium was changed to Opti-MEM without supplements, and cells were transiently transfected using Lipofectamine LTX reagent (Invitrogen, Carlsbad, CA, USA) according to the manufacturer's protocol. Five hours after transfection, cells were incubated with the test compounds in Opti-MEM supplemented with penicillin (100 U/mL), streptomycin (100 μ g/mL), and 0.1% DMSO for 16 h before luciferase activity was measured using the Dual-Glo Luciferase Assay System (Promega) according to the manufacturer's protocol on a Tecan Spark luminometer (Tecan Deutschland GmbH, Crailsheim, Germany). Firefly luminescence was divided by Renilla luminescence and multiplied by 1000 resulting in relative light units (RLU) to normalize for transfection efficiency and cell growth. Fold activation was obtained by dividing the mean RLU of the test compound by the mean RLU of the untreated control. All samples were tested in at least three biologically independent experiments in duplicates. For dose-response curve fitting and calculation of EC₅₀ values, the equation "[Agonist] vs. response -- Variable slope (four parameters)" was used in GraphPad Prism (version 7.00, GraphPad Software, La Jolla, CA, USA). Selectivity profiling was performed with identical procedures using pFA-CMV-Nur77-LBD¹⁴, pFA-CMV-NOR-1-LBD¹⁴, pFA-CMV-THRA-LBD⁵¹, pFA-CMV-RAR α -LBD⁵², pFA-CMV-PPAR α -LBD⁵³, pFA-CMV-PPAR γ -LBD⁵³, pFA-CMV-PPAR δ -LBD⁵³, pFA-CMV-LXR α -LBD⁵⁴, pFA-CMV-FXR-LBD⁵⁵ and pFA-CMV-hRXR α -LBD⁵⁶.

Full-length Nurr1 reporter gene assays. Activation of full-length human Nurr1 was studied in transiently transfected HEK293T cells using the reporter plasmids pFR-Luc-NBRE¹⁴, pFR-Luc-POMC¹⁴ or pFR-Luc-DR5¹⁴ each containing one copy of the respective human Nurr1 response element NBRE N13, NurRE, or DR5. The full-length human nuclear receptor Nurr1 (pcDNA3.1-hNurr1-NE; Addgene plasmid #102363) and, for DR5, RXR α (pSG5-hRXR)⁵⁷ were overexpressed. pRL-SV40 (Promega) was used for the normalization of transfection efficacy and to observe test compound toxicity. Cells were cultured in Dulbecco's modified Eagle's medium (DMEM), high glucose supplemented with 10% fetal calf serum (FCS), sodium pyruvate (1 mM), penicillin (100 U/mL), and streptomycin (100 μ g/mL) at 37 °C and 5% CO₂ and seeded in 96-well plates (3×10^4 cells/well). After 24 h, the medium was changed to Opti-MEM without supplements, and cells were transiently transfected using Lipofectamine LTX reagent (Invitrogen) according to the manufacturer's protocol. Five hours after transfection, cells were incubated with the test compounds in Opti-MEM supplemented with penicillin (100 U/mL), streptomycin (100 μ g/mL) and 0.1% DMSO for 16 h before luciferase activity was measured using the Dual-Glo Luciferase Assay System (Promega) according to the manufacturer's protocol on a Tecan Spark luminometer (Tecan Deutschland GmbH). Firefly luminescence was divided by Renilla luminescence and multiplied by 1000 resulting in relative light units (RLU) to normalize for transfection efficiency and cell growth. Fold activation was obtained by dividing the mean RLU of the test compound by the mean RLU of the untreated control. All samples were tested in at least three biologically independent experiments in duplicates. For dose-response curve fitting and calculation of EC₅₀ values, the equation "[Agonist] vs. response -- Variable slope (four parameters)" was used in GraphPad Prism (version 7.00, GraphPad Software).

Isothermal Titration Calorimetry (ITC). ITC experiments were conducted on an Affinity ITC instrument (TA Instruments, New Castle, DE) at 25 °C with a stirring rate of 75 rpm. Nurr1 LBD protein (5–30 μM, expressed as described previously²¹) in buffer (20 mM Tris pH 7.5, 100 mM NaCl, 5% glycerol) containing 1–4% DMSO was titrated with the test compounds (30–150 μM in the same buffer containing 1–4% DMSO) in 26 injections (1 × 1 μL, 25 × 3–4 μL) with an injection interval of 120–150 s. As control experiments, the test compounds were titrated to the buffer, and the buffer was titrated to the Nurr1 LBD protein under otherwise identical conditions. Results were analyzed using NanoAnalyze software (version 3.11.0, TA Instruments, New Castle, DE) with independent binding models.

Evaluation of Nurr1-regulated VMAT2 expression in T98G cells.

T98G (ATCC, CRL-1690) were grown in DMEM, high glucose supplemented with 10% FCS, sodium pyruvate (1 mM), penicillin (100 U/mL), and streptomycin (100 μg/mL) at 37 °C and 5% CO₂ and seeded at a density of 250,000 cells per well in 12-well plates. After 24 h, medium was changed to DMEM, high glucose supplemented with 0.2% fetal calf serum (FCS), penicillin (100 U/mL), and streptomycin (100 μg/mL) and the cells were incubated for another 24 h before stimulation with the test compounds (**36** (0.3 μM), **29** (10 μM)) solubilized with 0.1% DMSO or with 0.1% DMSO as a negative control. After 16 h of incubation, the medium was removed, cells were washed with phosphate-buffered saline (PBS) and after full aspiration of residual liquids, they were immediately frozen at –80 °C until further processing. Total RNA was isolated using the E.Z.N.A.® Total RNA Kit I (Omega Bio-tek, Norcross, USA) following the manufacturer's instructions. RNA concentration and purity were assessed using a NanoDrop™ One UV/VIS spectrophotometer (Thermo Fisher Scientific, Waltham, USA) at 260/280 nm. Right before reverse transcription (RT), RNA was linearized at 65 °C for 10 min and then immediately incubated on ice for at least 1 min. Reverse transcription was performed using 2 μg total RNA, 20 U Recombinant RNasin® Ribonuclease Inhibitor (Promega, Mannheim, Germany), 100 U SuperScript® IV Reverse Transcriptase including 5x First Strand Buffer and 0.1 M dithiothreitol (Thermo Fisher Scientific, Waltham, USA), 3.75 ng linear acrylamide, 625 ng random hexamere primers (#11277081001, Merck, Darmstadt, Germany) and 11.25 nmol deoxynucleoside triphosphate mix (2.8 nmol each ATP, TTP, CTP, GTP; #R0186, Thermo Fisher Scientific, Waltham, USA) at a volume of 22.45 μL at 50 °C for 10 min and 80 °C for 10 min using a Thermal cycler XT⁹⁶ (VWR International, Darmstadt, Germany). Quantitative polymerase chain reaction (qPCR) was conducted using an Applied Biosystems™ QuantStudio 1 (Waltham, USA) and a SYBR green-based detection method. Appropriately diluted cDNA was added to 6 pmol of forward and reverse primer, respectively, 0.8 U Taq DNA Polymerase (#M0267, New England Biolabs, Ipswich, USA), 40 ppm SYBR® Green I (#S9430, Sigma Aldrich, St. Louis, USA), 15 nmol deoxynucleoside triphosphate mix (as indicated above), 60 nmol MgCl₂, 4 μg bovine serum albumin (#B14, Thermo Fisher Scientific, Waltham, USA), 20% BioStab PCR Optimizer II (#53833, Merck, Darmstadt, Germany), and 10% Taq buffer without detergents (#B55, Thermo Fisher Scientific, Waltham, USA) topped up at a final volume of 20 μL with ddH₂O. Samples underwent 40 cycles of 15 s denaturation at 95 °C, 15 s of primer annealing at 59.4 or 62.4 °C (depending on the primer), and 20 s of elongation at 68 °C. PCR product specificity was evaluated using a melting curve analysis ranging from 65 to 95 °C. VMAT2, TH and SOD2 mRNA expression was normalized to GAPDH mRNA expression per each sample using the ΔCt-method. The following primers for the human genes were used. hVMAT2 (SLC18A2): 5'-GCT ATG CCT TCC TGC TGA TTG C-3' (fw) and 5'-CCA AGG CGA TTC CCA TGA CGT T-3' (rev); hTH: 5'-GCT GAA CAA GTG TCA TCA CCT G-3' (fw) and 5'-CCT GTA CTG GAA GGC GAT CTC A-3' (rev); hSOD2: 5'-CCA AAG GGG AGT TGC TGG AA -3' (fw) and 5'-GAA ACC AAG CCA ACC CCA AC -3' (rev); hGAPDH: 5'-AGG TCG GAG TCA ACG GAT TT-3' (fw) and 5'-TTC CCG TTC TCA GCC TTG AC-3' (rev).

Determination of aqueous solubility. The aqueous solubility of **29** and **36** was assessed by mixing 1 mg of each test compound with an appropriate volume of water for a theoretical concentration of 4 mM to obtain an oversaturated mixture. The mixture was agitated in a VWR Thermal Shake lite (VWR International GmbH, Darmstadt, Germany) for 24 h at 600 rpm and a constant temperature of 25 °C. The supersaturated mixtures were subsequently centrifuged at 23,300 rpm for 15 min (25 °C). Part of the supernatant was taken off for quantification by UV absorbance at 312 nm with external calibration. The external calibration samples contained 1% DMSO and the test samples were spiked with DMSO to 1% concentration right before the measurement. Absorbance was measured with a Tecan Spark luminometer (Tecan Deutschland GmbH, Crailsheim, Germany). The solubility test was repeated in three independent experiments.

Cytotoxicity assays. HEK293T cells were cultured at 37 °C and 5% CO₂ in DMEM high-glucose supplemented with sodium pyruvate (1 mM), penicillin (100 U/mL), streptomycin (100 μg/mL), and 10% fetal calf serum (FCS) and seeded at a density of 10,000 cells in 96-well plates pre-coated with a 10 μg/mL collagen G solution (Merck KGaA, L7213) at 37 °C for 30 min. N27 rat dopaminergic neural cells (SCC048, Sigma-Aldrich, Darmstadt, Germany) were grown in RPMI 1640 (Gibco, Thermo Fisher Scientific, Waltham) supplemented with 10% FCS, penicillin (100 U/mL), and streptomycin (100 μg/mL) at 37 °C and 5% CO₂ and seeded at a density of 10,000 cells in 96-well plates. After 24 h, the cells were treated with the solubilized (0.1% DMSO) test compounds in Opti-MEM supplemented with penicillin (100 U/mL) and streptomycin (100 μg/mL) for HEK293T cells or in RPMI 1640 supplemented with penicillin (100 U/mL), streptomycin (100 μg/mL) and 0.2% FCS for N27 cells. Each sample was prepared in four biologically independent repeats. After incubation for 24 h, the medium was refreshed and 10% water-soluble tetrazolinium salt (Cell Counting Kit-8, MedChemExpress) was added to assess metabolic activity. After 4 h, absorbance was measured at 450 nm using a Tecan Spark Cyto instrument (Tecan).

Evaluation of microsomal stability. To determine microsomal stability, test compounds (10 μM) were incubated in 100 mM potassium phosphate buffer at pH 7.4 (total volume of 100 μL) containing 0.5 mg/mL male rat liver microsomes (Sprague-Dawley, no. M9066, Merck KGaA, Darmstadt) and 1 mM NADPH for 0, 15, 30, or 60 min. At the end of the incubation time, microsomal activity was terminated by the addition of 500 μL MeCN and subsequent centrifugation at 1700 g for 5 min. A reaction mixture containing heat-inactivated microsomes (95 °C, 10 min) was prepared as a control for each compound. 5 μL supernatant of each sample was analyzed and the remaining concentrations of the respective test compounds at each time point were determined by LC-MS/MS on an API-3200-QTrap (Sciex) with an Agilent Technologies 1100 series setup including a binary pump (G1311A), a degasser (G1322A), and a Shimadzu SIL 20 A HT autosampler under the control of Analyst 1.6 (Sciex). A XBridge BEH C18 (3.5 μm, 150 mm×3 mm, Waters, protected with a 0.5 μm frit) stationary phase was used in combination with a gradient method starting with 0.1% formic acid in water (A) and MeCN (B) as mobile phase (A:B = 80:20) for 6 min going to A: B = 50:50 after 8 min. 5 μL of supernatant diluted in mobile phase starting conditions was loaded onto the column, separated at a flow rate of 400 μL/min, and detected and quantified per Area of MRM (multiple reaction monitoring) with the following transitions: *m/z* 381.797/145.000 (**34**); *m/z* 395.125/158.200 (**36**); *m/z* 409.822/131.000 (**41**); *m/z* 407.838/171.100 (**42**).

Parallel artificial membrane permeability assay (PAMPA). Passive lipid membrane diffusion of test compounds was determined using Merck Millipore MultiScreen Filter Plates (0.45 μm pore diameter, hydrophobic PVDF). The filter inserts were coated with 1% L-α-phosphatidylcholine (Fluka Analytical) in *n*-dodecan. The test

compounds were then added to the donor compartment at a final concentration of 500 μM in a phosphate buffer pH 7.4 containing 5% DMSO with a total volume of 150 μL . The acceptor compartment was filled with 300 μL PBS containing 5% DMSO. Additionally, three equilibrium samples were prepared by directly adding the donor solution to the acceptor compartment for the calculation of log Pe values. The filter plates were incubated for 18 h before the test compound concentrations in the acceptor compartments and in the equilibrium, samples were determined by UV absorbance at 320 nm (34), 360 nm (36), 310 nm (41), or 315 nm (42) with external calibration in a 96 well quartz plate on a SpectraMax M2e microplate reader (Molecular Devices). logPe values were calculated according to the formula published by Sugano and colleagues⁵⁸.

In vitro blood-brain-barrier model. Permeation of test compounds through a human brain endothelial cell barrier was evaluated using the Corning Costar 3470 Transwell Plate system (0.4 μm pore diameter with 6.5 mm inserts) and HBEC-5i cells (ATCC, CRL-3245). Filter inserts were coated one day before seeding with 50 μL 0.01% rat-tail collagen type I (C7661, Sigma-Aldrich) in PBS. 60,000 HBEC-5i cells in 100 μL HBEC-5i-Medium (DMEM/F12 with 10% FCS and 40 $\mu\text{g}/\text{mL}$ ECGS) were seeded after aspiration of the coating-supernatant in each insert with 600 μL HBEC-5i-Medium in each receiver well. After 24 h incubation at 37 °C with 5% CO₂, the medium was exchanged to 600 μL T98G cell supernatant in receiver wells and 100 μL fresh HBEC-5i-Medium in inserts. The medium exchange was repeated every second day. On day 7 after seeding, the medium in the receiver wells was replaced by 600 μL Hank's balanced salt solution (HBSS) containing 10 mM HEPES and 0.1% DMSO and 100 μL test compound mixtures (antipyrine and test compound; each at 10 μM) in HBSS containing 10 mM HEPES and 0.1% DMSO were added to inserts. After 60 min incubation, 100 μL samples were taken from the receiver wells and diluted in 400 μL (75%/25% A/B; A=Formic acid 0.1% in water; B = Acetonitrile). Test compound concentrations in the samples were determined by LC-MS/MS on an API-3200-QTrap (Sciex) equipped with an Agilent Technologies 1100 series setup including a binary pump (G1311A), a degasser (G1322A), and a Shimadzu SIL 20 A HT autosampler under the control of Analyst 1.6 (Sciex). An XBridge BEH C18 (3.5 μm , 150 mm \times 3 mm, Waters, protected with a 0.5 μm frit) served as stationary phase in combination with a gradient method starting with 0.1% formic acid in water (A) and MeCN (B) as mobile phase (80%:20% = A: B) for 6 min going to (50%:50%) after 8 min. 5 μL of aspirated supernatant diluted in mobile phase starting conditions was loaded onto the column, separated at a flow rate of 400 $\mu\text{L}/\text{min}$, and quantified per Area of MRM (multiple reaction monitoring).

Organoid PD model. Cell lines: Human induced pluripotent stem cells (hiPSCs; iPSC-LRRK2 isogenic control and iPSC-LRRK2-G2019S) were cultured in Essential 8™ Flex Medium-Kit (Thermo Fisher) on vitronectin (VTN-N; Thermo Fisher) coated cell culture dishes. The cells were passaged every three days as clumps with 0.5 M EDTA (0.5 M EDTA, 5 M NaCl, PBS). The hiPSCs contained a NURR1 GFP reporter cassette and a single point mutation (G2019S) was incorporated into the LRRK2 gene, resulting in the generation of the PD iPSC-LRRK2-G2019S cell line⁴⁷ (cell lines were kindly provided by the Tchiew Lab, Cincinnati). Cells were regularly tested for pluripotency levels using the markers Nanog and Oct-4 and for mycoplasma contamination. Generation of human midbrain-like organoids: Human midbrain-like organoids (hMLOs) were formed according to the protocol of Jo et al.⁵⁹. In brief, hiPSCs were dissociated via accutase for 1 h at 37 °C into single cells after reaching 70% confluency. Subsequently, 10,000 cells were seeded in each well of a 96-well v-shaped ultra-low attachment plate (Sbio®) in neuronal induction media (NIC; DMEM/F12 (Thermo Fisher); Neurobasal media (Thermo Fisher) (1:1), 1:100 N2 supplement (Gibco), 1:50 B27 without Vitamin A (Gibco), 1% GlutaMAX (Gibco), 1% minimum essential media-essential amino acid (MEM-NEAA) (Gibco), 0.1% β -

mercaptoethanol (Gibco) supplemented with 1 $\mu\text{g}/\text{mL}$ heparin (Merck), 10 μM SB431542 (Miltenyi), 200 ng/mL human Noggin (Miltenyi), 0.8 μM CHIR99021 (R&D) and 10 μM Rock inhibitor Y27632 (R&D)). Following a two-day incubation period, the rock inhibitor was removed, and cells were cultured in NIC media until day 3. On day 4, hMLOs were supplemented with 100 ng/mL SHH-C25II (Miltenyi) and 100 ng/mL human FGF8b (Miltenyi). On day 7, the cells were embedded in 30 μL growth factor reduced matrigel (Merck) for 30 min. at 37 °C and cultured for 24 h in tissue growth induction media (Neurobasal media, 1:100 N2 supplement, 1:50 B27 without vitamin A, 1% GlutaMAX, 1% MEM-NEAA, 0.1% β -mercaptoethanol supplemented with 2.5 $\mu\text{g}/\text{mL}$ insulin, 200 ng/mL mouse laminin, 100 ng/mL SHH-C25II and 100 ng/mL human FGF8b. The following day, hMLOs were transferred into ultra-low-attachment 6-well plates (Corning) containing final differentiation media (Neurobasal media, 1:100 N2 supplement, 1:50 B27 without Vitamin A, 1% GlutaMAX, 1% MEM-NEAA, 0.1% β -mercaptoethanol, 1% Pen/Strep (Gibco), 10 ng/mL BDNF (Miltenyi), 10 ng/mL GDNF (Miltenyi), 100 μM ascorbic acid (Sigma) and 125 μM db-cAMP (Sigma). The hMLOs were cultured on a shaker and medium was changed every three days. hMLOs were treated on day 44 of organoid formation with the respective test compounds for 24 h. At day 45, organoids were harvested for further analysis. RNA isolation, reverse transcription and quantitative real-time PCR (qRT-PCR): Total RNA from hMLOs was isolated using TRIzol (Invitrogen) following the manufacturer's protocol. RNA extraction was performed using chloroform:isoamyl alcohol (24:1)(Thermo Scientific), precipitated in isopropanol and resuspended in nuclease-free ddH₂O. After DNase digestion, 500 μg total RNA was reverse transcribed using the RevertAid First-strand-cDNA-synthesis kit (Thermo Fisher) and random hexamers following the manufacturer's protocol. qRT-PCR was conducted with specific primers targeting hTH (5'-GCT GGA CAA GTG TCA TCA CCT G-3' (fw) and 5'-CCT GTA CTG GAA GGC GAT CTC A-3' (rev)), Nurr1 (5'-GGC TGA AGC CAT GCC TTG T-3' (fw) and 5'-GTG AGG TCC ATG CTA AAC TTG ACA-3' (rev)) and RNA polymerase 2 (5'-GCA CCA CGT CCA ATG ACA-3' (fw) and 5'-GTC GGC TGC TTC CAT AA-3' (rev)) using the LightCycler® 480 SYBR Green I (Roche) on a Roche LightCycler 480 II qPCR system. Relative gene expression was determined using the $-\Delta\Delta\text{Ct}$ method. All genes were normalized to RNA polymerase II values. Immunostaining of hMLOs: hMLOs were washed twice with PBS and fixed in 4% paraformaldehyde (PFA) overnight at 4 °C. On the following day, hMLOs were washed twice with PBS, cryoprotected and stored in 30% sucrose/PBS. Organoids were sectioned at 25 μm on a cryostat (Leica CM 3050 S, Leica Biosystems, Wetzlar, Germany). Immunostaining was performed within 1.5 mL Eppendorf tubes. Sections were permeabilized in 0.3% Triton X-100, blocked in 5% FBS, 0.1% Triton X-100/PBS and incubated as floating section in 1:200 dilution of primary antibody (rabbit anti-Tyrosine-Hydroxylase, Merck (AB152)) in blocking solution overnight. The next day, sections were washed twice with 0.1% Triton X-100, incubated in 1:500 dilution of secondary antibody (AlexaFluor™ 594 goat anti-rabbit IgG (H + L), Invitrogen) in blocking solution for 1.5 h and Hoechst 33342 (Chem-Cruz) was added in 1:10 000 dilution for 30 min for nuclear staining. Sections were mounted onto glass slides and imaged using a Zeiss LSM 980 microscope (Carl Zeiss AG, Oberkochen, Germany). The staining protocol was adapted from^{60,61}. Images were manually quantified by selecting a fixed area and counting TH+ neurons. The images used for quantification were acquired from four different sections of two different organoids for each condition. Statistical analysis: All experiments were performed at least in triplicate, if not otherwise indicated. Results are expressed as mean \pm SD. Statistical significance was analyzed using two-tailed Student's t-test (* p < 0.05, ** p < 0.01 and *** p < 0.001).

Reporting summary

Further information on research design is available in the Nature Portfolio Reporting Summary linked to this article.

Data availability

All data supporting the results of this study are available from the corresponding author. Source data for Figs. 1, 4, and 5 are provided in Supplementary Data 2.

Received: 28 December 2023; Accepted: 14 June 2024;

Published online: 29 June 2024

References

- Zetterström, R. H., Williams, R., Perlmann, T. & Olson, L. Cellular expression of the immediate early transcription factors Nurr1 and NGFI-B suggests a gene regulatory role in several brain regions including the nigrostriatal dopamine system. *Mol. Brain Res.* **41**, 111–120 (1996).
- Kummari, E., Guo-Ross, S. X., Partington, H. S., Nutter, J. M. & Eells, J. B. Quantitative immunohistochemistry to measure regional expression of Nurr1 in the brain and the effect of the Nurr1 heterozygous genotype. *Front. Neuroanat.* **15**, 563854 (2021).
- Saijo, K. et al. A Nurr1/CoREST pathway in Microglia and Astrocytes protects Dopaminergic neurons from inflammation-induced death. *Cell* **137**, 47–59 (2009).
- Zetterström, R. H. et al. Dopamine neuron agenesis in Nurr1-deficient mice. *Science* **276**, 248–250 (1997).
- Kadkhodaei, B. et al. Nurr1 is required for maintenance of maturing and adult midbrain dopamine neurons. *J. Neurosci.* **29**, 15923–15932 (2009).
- Willems, S. et al. Nurr1 modulation mediates neuroprotective effects of statins. *Adv. Sci.* **9**, e2104640 (2022).
- Chu, Y. et al. Nurr1 in Parkinson's disease and related disorders. *J. Comp. Neurol.* **494**, 495–514 (2006).
- Decressac, M. et al. α -synuclein-induced down-regulation of Nurr1 disrupts GDNF signaling in nigral dopamine neurons. *Sci. Transl. Med.* **4**, 163ra156 (2012).
- Liu, W., Gao, Y. & Chang, N. Nurr1 overexpression exerts neuroprotective and anti-inflammatory roles via down-regulating CCL2 expression in both in vivo and in vitro Parkinson's disease models. *Biochem. Biophys. Res. Commun.* **482**, 1312–1319 (2017).
- Parra-Damas, A. et al. Crtc1 activates a transcriptional program deregulated at early Alzheimer's disease-related stages. *J. Neurosci.* **34**, 5776–5787 (2014).
- Yao, P. L., Parmar, V. M., Choudhary, M. & Malek, G. NURR1 expression regulates retinal pigment epithelial-mesenchymal transition and age-related macular degeneration phenotypes. *Proc. Natl. Acad. Sci. USA.* **119**, e2202256119 (2022).
- Willems, S. & Merk, D. Medicinal chemistry and chemical biology of Nurr1 Modulators: An emerging strategy in neurodegeneration. *J. Med. Chem.* **65**, 9548–9563 (2022).
- Wang, Z. et al. Structure and function of Nurr1 identifies a class of ligand-independent nuclear receptors. *Nature* **423**, 555–560 (2003).
- Willems, S. et al. The orphan nuclear receptor Nurr1 is responsive to non-steroidal anti-inflammatory drugs. *Commun. Chem.* **3**, 85 (2020).
- Yu, X., Shang, J. & Kojetin, D. J. Molecular basis of ligand-dependent Nurr1-RXR α activation. *Elife* **12**, e85039 (2023).
- Bruning, J. M. et al. Covalent modification and regulation of the nuclear receptor Nurr1 by a Dopamine metabolite. *Cell Chem. Biol.* **26**, 674–685.e6 (2019).
- de Vera, I. M. S. et al. Identification of a binding site for unsaturated fatty acids in the orphan nuclear receptor Nurr1. *ACS Chem. Biol.* **11**, 1795–1799 (2016).
- Rajan, S. et al. PGE1 and PGA1 bind to Nurr1 and activate its transcriptional function. *Nat. Chem. Biol.* **16**, 876–886 (2020).
- Munoz-Tello, P. et al. Assessment of NR4A ligands that directly bind and modulate the orphan nuclear receptor Nurr1. *J. Med. Chem.* **63**, 15639–15654 (2020).
- Vietor, J. et al. Development of a potent Nurr1 agonist tool for in vivo applications. *J. Med. Chem.* **66**, 6391–6402 (2023).
- Ballarotto, M. et al. De Novo design of Nurr1 agonists via fragment-augmented generative deep learning in low-data regime. *J. Med. Chem.* **66**, 8170–8177 (2023).
- Sai, M. et al. Structure-guided design of Nurr1 agonists derived from the natural ligand dihydroxyindole. *J. Med. Chem.* **66**, 13556–13567 (2023).
- Stiller, T. & Merk, D. Exploring fatty acid mimetics as NR4A ligands. *J. Med. Chem.* **66**, 15362–15369 (2023).
- Kim, C.-H. et al. Nuclear receptor Nurr1 agonists enhance its dual functions and improve behavioral deficits in an animal model of Parkinson's disease. *Proc. Natl. Acad. Sci.* **112**, 8756–8761 (2015).
- Moon, M. et al. Nurr1 (NR4A2) regulates Alzheimer's disease-related pathogenesis and cognitive function in the 5XFAD mouse model. *Aging Cell* **18**, e12866 (2019).
- De Bruyn, T. et al. Structure-based identification of oap1b1/3 inhibitors. *Mol. Pharmacol.* **83**, 1257–1267 (2013).
- Ren, S. et al. Discovery and characterization of novel, potent, and selective cytochrome P450 2J2 inhibitors. *Drug Metab. Dispos.* **41**, 60–71 (2013).
- Willems, S., Ohmdorf, J., Kilu, W., Heering, J. & Merk, D. Fragment-like chloroquinolineamines activate the orphan nuclear receptor Nurr1 and elucidate activation mechanisms. *J. Med. Chem.* **64**, 2659–2668 (2021).
- Den Braver-Sewradj, S. P. et al. Reduction and scavenging of chemically reactive drug metabolites by NAD(P)H:Quinone Oxidoreductase 1 and NRH:Quinone Oxidoreductase 2 and variability in hepatic concentrations. *Chem. Res. Toxicol.* **31**, 116–126 (2018).
- Qiao, S. et al. The antimalarial amodiaquine causes autophagic-lysosomal and proliferative blockade sensitizing human melanoma cells to starvation- And chemotherapy-induced cell death. *Autophagy* **9**, 2087–2102 (2013).
- Espinoza, J. A. et al. The antimalarial drug amodiaquine stabilizes p53 through ribosome biogenesis stress, independently of its autophagy-inhibitory activity. *Cell Death Differ* **27**, 773–789 (2020).
- Zhang, Y. et al. Glutathione S-transferase P1 protects against Amodiaquine Quinoneimines-induced cytotoxicity but does not prevent activation of endoplasmic reticulum stress in HepG2 cells. *Front. Pharmacol.* **9**, 388 (2018).
- Kim, T. H., Kim, H. K. & Hwang, E. S. Novel anti-adipogenic activity of anti-malarial amodiaquine through suppression of PPAR γ activity. *Arch. Pharm. Res.* **40**, 1336–1343 (2017).
- Baell, J. & Walters, M. A. Chemistry: Chemical con artists foil drug discovery. *Nature* **513**, 481–483 (2014).
- Baell, J. B. & Nissink, J. W. M. Seven year itch: Pan-Assay Interference Compounds (PAINS) in 2017 – Utility and limitations. *ACS Chem. Biol.* **13**, 36–44 (2017).
- Kim, W. et al. An optimized Nurr1 agonist provides disease-modifying effects in Parkinson's disease models. *Nat. Commun.* **14**, 4283 (2023).
- Willems, S. et al. Scaffold hopping from amodiaquine to novel Nurr1 agonist chemotypes via microscale analogue libraries. *ChemMedChem* **17**, e2022000 (2022).
- Kaur, K., Jain, M., Reddy, R. P. & Jain, R. Quinolines and structurally related heterocycles as antimalarials. *Eur. J. Med. Chem.* **45**, 3245–3264 (2010).
- Almarío Garcia, A., Lardenois, P. & Olivier, A. Derivatives of 2-aryl-6-phenyl-imidazo [1, 2-a]pyridines, their preparation and their therapeutic use. WO 2008/034974A1. *Sanofi-Aventis* (2008).
- Lesuisse, D. et al. Development of a novel NURR1/NOT agonist from hit to lead and candidate for the potential treatment of Parkinson's disease. *Bioorg. Med. Chem. Lett.* **29**, 929–932 (2019).
- Smith, G. A. et al. A Nurr1 agonist causes neuroprotection in a Parkinson's disease Lesion model primed with the toll-like Receptor 3 dsRNA inflammatory stimulant Poly(I:C). *PLoS One* **10**, e0121072 (2015).

42. de Vink, P. J. et al. Cooperativity as quantification and optimization paradigm for nuclear receptor modulators. *Chem. Sci.* **13**, 2744–2752 (2022).
43. Gao, L., Zhou, W., Symmes, B. & Freed, C. R. Re-cloning the N27 dopamine cell line to improve a cell culture model of Parkinson's disease. *PLoS One* **11**, e0160847 (2016).
44. Hartung, I. V., Rudolph, J., Mader, M. M., Mulder, M. P. C. & Workman, P. Expanding chemical probe space: quality criteria for covalent and degrader probes. *J. Med. Chem.* **66**, 9297–9312 (2023).
45. <https://www.thesgc.org/chemical-probes/>.
46. Puech, C. et al. Assessment of HBEC-5i endothelial cell line cultivated in astrocyte conditioned medium as a human blood-brain barrier model for ABC drug transport studies. *Int. J. Pharm.* **551**, 281–289 (2018).
47. Smits, L. M. et al. Modeling Parkinson's disease in midbrain-like organoids. *npj Park. Dis.* **5**, 5 (2019).
48. Kim, H. et al. Modeling G2019S-LRRK2 sporadic Parkinson's disease in 3D midbrain Organoids. *Stem Cell Rep.* **12**, 518–531 (2019).
49. Cookson, M. R. α -Synuclein and neuronal cell death. *Mol. Neurodegener.* **4**, 9 (2009).
50. Pauli, G. F. et al. Importance of purity evaluation and the potential of quantitative ¹H NMR as a purity assay. *J. Med. Chem.* **57**, 9220–9231 (2014).
51. Gellrich, L. et al. L-Thyroxin and the nonclassical thyroid hormone TETRAC are potent activators of PPAR γ . *J. Med. Chem.* **63**, 6727–6740 (2020).
52. Pollinger, J. et al. Tuning nuclear receptor selectivity of Wy14,643 towards selective Retinoid X receptor modulation. *J. Med. Chem.* **62**, 2112–2126 (2019).
53. Rau, O. et al. Carnosic acid and carnosol, phenolic diterpene compounds of the labiate herbs rosemary and sage, are activators of the human peroxisome proliferator-activated receptor gamma. *Planta Med.* **72**, 881–887 (2006).
54. Flesch, D. et al. Non-acidic farnesoid X receptor modulators. *J. Med. Chem.* **60**, 7199–7205 (2017).
55. Schmidt, J. et al. NSAIDs Ibuprofen, Indometacin, and Diclofenac do not interact with Farnesoid X Receptor. *Sci. Rep.* **5**, 14782 (2015).
56. Heitel, P. et al. Computer-assisted discovery and structural optimization of a novel Retinoid X receptor agonist chemotype. *ACS Med. Chem. Lett.* **10**, 203–208 (2019).
57. Seuter, S., Väisänen, S., Rådmark, O., Carlberg, C. & Steinhilber, D. Functional characterization of vitamin D responding regions in the human 5-Lipoxygenase gene. *Biochim. Biophys. Acta* **1771**, 864–872 (2007).
58. Sugano, K., Hamada, H., Machida, M. & Ushio, H. High throughput prediction of oral absorption: improvement of the composition of the lipid solution used in parallel artificial membrane permeation assay. *SLAS Discov* **6**, 189–196 (2001).
59. Jo, J. et al. Midbrain-like Organoids from human Pluripotent stem cells contain functional Dopaminergic and Neuromelanin-producing neurons. *Cell Stem Cell* **19**, 248–257 (2016).
60. Cederquist, G. Y. et al. Specification of positional identity in forebrain organoids. *Nat. Biotechnol.* **37**, 436–444 (2019).
61. Watanabe, M. et al. Self-organized cerebral organoids with human-specific features predict effective drugs to combat Zika virus infection. *Cell Rep* **21**, 517–532 (2017).
62. Hopkins, A. L., Keserü, G. M., Leeson, P. D., Rees, D. C. & Reynolds, C. H. The role of ligand efficiency metrics in drug discovery. *Nat. Rev. Drug Discov.* **13**, 105–121 (2014).
63. RDKit: Open-source cheminformatics. Open-source cheminformatics. <http://www.rdkit.org>.

Acknowledgements

This research was co-funded by the European Union (ERC, NeuRoPROBE, 101040355). Views and opinions expressed are however those of the author(s) only and do not necessarily reflect those of the European Union or the European Research Council. Neither the European Union nor the granting authority can be held responsible for them. Further support was provided by Deutsche Forschungsgemeinschaft (DFG) (GRK2668 (435874434); 496872373; 498956525; 497803923). The authors thank Jason Tchieu for sharing the iPSC-LRRK2 isogenic control and iPSC-LRRK2-G2019S cell lines.

Author contributions

M.S. and D.M. conceived the project. M.S. performed the chemical synthesis. M.S., E.C.H., H.T., T.K., M.L., M.V. and J.A.M. performed the biological experiments. All authors were involved in the interpretation of results. D.M. supervised the project and wrote the manuscript with contributions from all authors.

Funding

Open Access funding enabled and organized by Projekt DEAL.

Competing interests

M.S. and D.M. are inventors of the European patent application EP24155686: "Nurr1 modulators" claiming compounds described in this study. There are no other conflicts to declare.

Additional information

Supplementary information The online version contains supplementary material available at <https://doi.org/10.1038/s42004-024-01224-0>.

Correspondence and requests for materials should be addressed to Daniel Merk.

Peer review information *Communications Chemistry* thanks Diwan Rawat, John Spencer, and the other, anonymous, reviewer(s) for their contribution to the peer review of this work.

Reprints and permissions information is available at <http://www.nature.com/reprints>

Publisher's note Springer Nature remains neutral with regard to jurisdictional claims in published maps and institutional affiliations.

Open Access This article is licensed under a Creative Commons Attribution 4.0 International License, which permits use, sharing, adaptation, distribution and reproduction in any medium or format, as long as you give appropriate credit to the original author(s) and the source, provide a link to the Creative Commons licence, and indicate if changes were made. The images or other third party material in this article are included in the article's Creative Commons licence, unless indicated otherwise in a credit line to the material. If material is not included in the article's Creative Commons licence and your intended use is not permitted by statutory regulation or exceeds the permitted use, you will need to obtain permission directly from the copyright holder. To view a copy of this licence, visit <http://creativecommons.org/licenses/by/4.0/>.

© The Author(s) 2024

- Supplementary Information -

Development of Nurr1 Agonists from Amodiaquine By Scaffold Hopping and Fragment Growing

Minh Sai¹, Emily C. Hank¹, Hin-Man Tai², Till Kasch¹, Max Lewandowski¹, Michelle Vincendeau^{2,3}, Julian A. Marschner¹, Daniel Merk^{1*}

¹ Ludwig-Maximilians-Universität München, Department of Pharmacy, 81377 Munich, Germany

² Helmholtz Munich, Institute of Virology, 85764 Munich, Germany

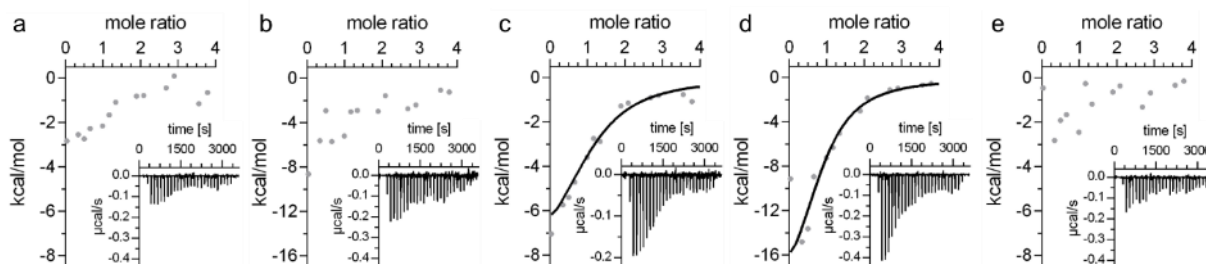
³ Technical University of Munich, Institute of Virology, School of Medicine, 81675 Munich, Germany

* daniel.merk@cup.lmu.de

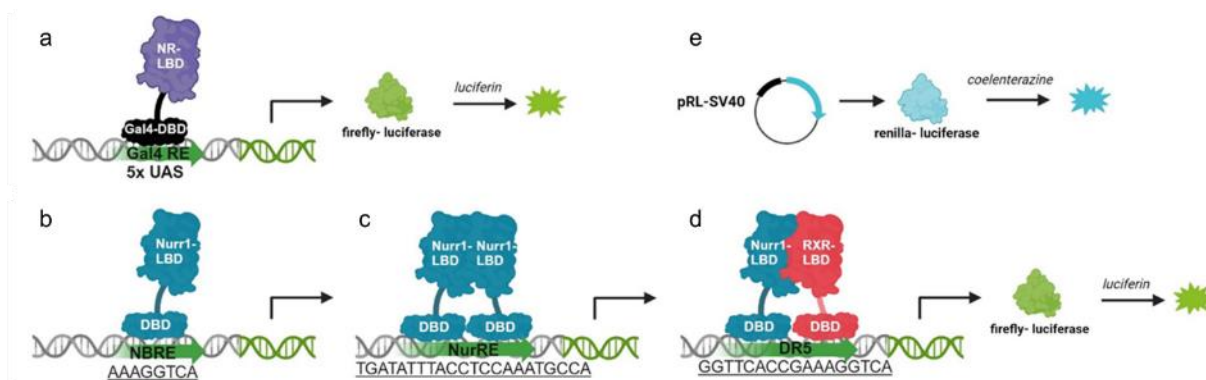
Table of Contents

Supplementary Figures	2
Supplementary Methods	5
Supplementary References	18

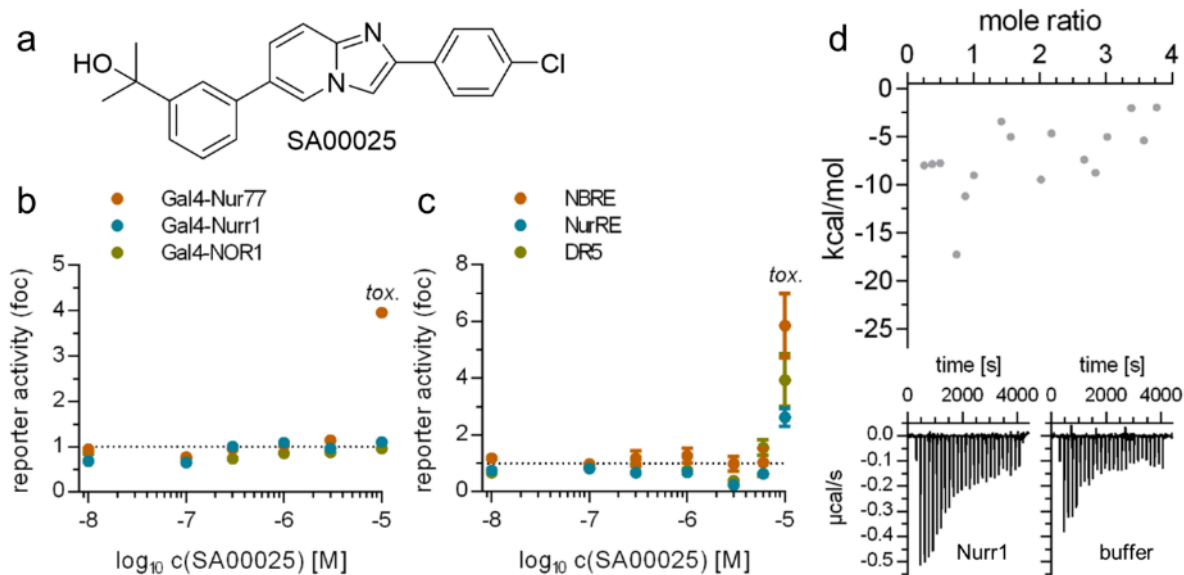
Supplementary Figures



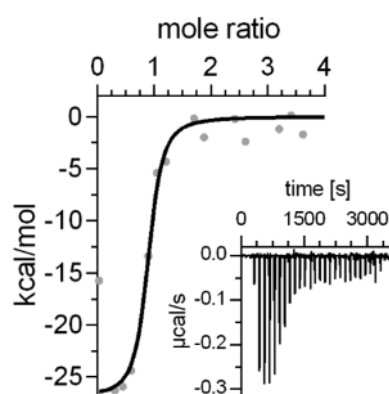
Supplementary Figure 1. Isothermal titration calorimetry (ITC) to determine binding of **9** (a), **10** (b), **11** (c), **12** (d) and **13** (e) to the Nurr1 LBD using 100 μM ligand and 15 μM protein. The fittings of the heat of binding are shown and the isotherms at 25°C are shown as insets.



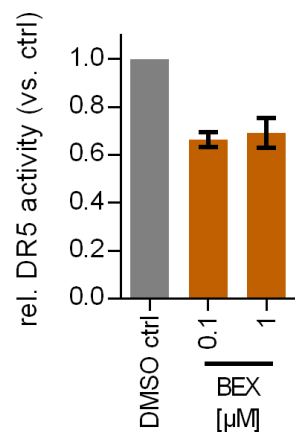
Supplementary Figure 2. Schematic illustration of reporter gene assays used in this study. All reporter gene assays were performed in transiently transfected HEK293T cells and firefly/renilla luminescence was measured using the Dual Glo kit from Promega. (a) Gal4-hybrid reporter gene assays used to characterize Nurr1 agonism during structural optimization and for selectivity profiling are based on chimeric receptors composed of the Gal4-DBD and the hinge region and LBD ("NR LBD") of the respective human nuclear receptor. A firefly luciferase construct with five repeats of the tandem Gal4 binding site UAS was used as reporter gene. (b-d) Selected compounds were studied in reporter gene assays testing the activity of the human full-length nuclear receptor Nurr1 which can act as monomer on the response element NBRE (b), as homodimer on NurRE (c), and as heterodimer with RXR on DR5 (d). For the reporter gene assays, Nurr1 and RXR (only for DR5) were overexpressed and firefly luciferase constructs each comprising a single repeat of either NBRE, NurRE or DR5 (sequences in figure) to control reporter gene expression were used as reporters. (e) A renilla luciferase construct with constitutively active SV40 promoter was co-transfected in all reporter gene assay settings as internal control for normalization of transfection efficiency and to monitor potential test compound toxicity. Created with BioRender.com.



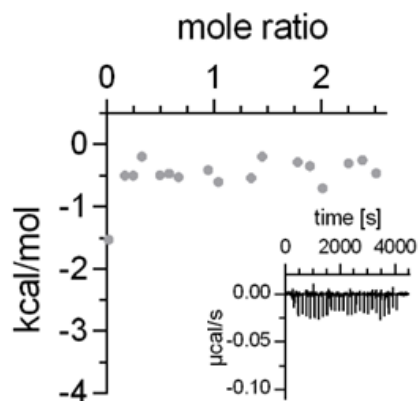
Supplementary Figure 3. In vitro characterization of the imidazo[1,2-a]pyridin-based Nurr1 modulator SA00025 (CAS# 1015231-98-7)¹. (a) Chemical structure of SA00025. (b) SA00025 caused no activation of NR4A receptors in Gal4 hybrid reporter gene assays in the concentration range from 10 nM to 3 μM . Higher concentrations were cytotoxic (tox.) leading to a drop in the control gene (renilla luciferase) luminescence and consequently increased firefly/renilla luminescence ratio that should not be misinterpreted as nuclear receptor activation. Data are the mean \pm S.E.M., $n\geq 3$. (c) SA00025 caused no activation of full-length Nurr1 on the human Nurr1 response elements NBRE, NurRE and DR5 in the concentration range from 10 nM to 3 μM . Higher concentrations were cytotoxic (tox.) leading to a drop in the control gene (renilla luciferase) luminescence and consequently increased firefly/renilla luminescence ratio that should not be misinterpreted as nuclear receptor activation. Data are the mean \pm S.E.M., $n\geq 3$. (d) ITC (50 μM SA00025, 10 μM Nurr1 LBD) indicated potential weak binding of SA00025 to the recombinant Nurr1 LBD but affinity was too low to determine a K_d value.



Supplementary Figure 4. The fused compound **37** bound to the recombinant Nurr1 LBD with high affinity (K_d 0.08 μM). The fitting of the heat of binding is shown and the isotherm at 25°C is shown as inset. 30 μM **37** and 5 μM Nurr1 LBD were used.



Supplementary Figure 5. Effect of bexarotene (BEX) on DR5 activity. Data are the mean \pm S.E.M.; n=3.



Supplementary Figure 6. **29** showed no binding to the Nurr1 LBD in ITC using 100 μM ligand and 30 μM protein. The fitting of the heat of binding is shown and the isotherm at 25 $^{\circ}\text{C}$ is shown as inset.

Supplementary Methods

Synthetic Procedures and Analytical Data

General. All chemicals were of reagent grade, purchased from commercial sources (e.g., Sigma-Aldrich, TCI, BLDpharm) and used without further purification unless otherwise specified. All reactions were conducted under nitrogen or argon atmosphere and in absolute solvents purchased from Sigma-Aldrich. Other solvents, especially for work-up procedures, were of reagent grade or purified by distillation (*iso*-hexane, cyclohexane, ethyl acetate, EtOH). Reactions were monitored by thin layer chromatography (TLC) on TLC Silica gel 60 F254 coated aluminum sheets by Merck and visualized under ultraviolet light (254 nm) or by using ninhydrin or Ehrlichs reagent stains. Purification by column chromatography was performed on a puriFlash® XS520Plus system (Advion, Ithaca, NY, USA) using high performance spherical silica columns (SIHP, 50 μ m) by Interchim and a gradient of *iso*-hexane or cyclohexane to ethyl acetate, Reversed-phase CC was performed on a puriFlash® 5.250 system (Advion) using C18HP columns (SIHP, 15 μ m) by Interchim and a gradient of H₂O with 10% MeCN to 100% MeCN (HPLC gradient grade). Mass spectra were obtained on a puriFlash®-CMS system (Advion) using atmospheric pressure chemical ionization (APCI). HRMS were obtained with a Thermo Finnigan LTQ FT instrument for electron impact ionization (EI) or electrospray ionization (ESI). NMR spectra were recorded on Bruker Avance III HD 400 MHz or 500 MHz spectrometers equipped with a CryoProbe™ Prodigy broadband probe (Bruker). Chemical shifts are reported in δ values (ppm) relative to residual protium signals in the NMR solvent (¹H-NMR: acetone-*d*₆: δ = 2.04 ppm; DMSO-*d*₆: δ = 2.50 ppm; MeOD-*d*₄: δ = 3.31 ppm, ¹³C-NMR: acetone-*d*₆: δ = 206.26, 29.84 ppm; DMSO-*d*₆: δ = 39.52 ppm; MeOD-*d*₄: δ = 49.0 ppm), coupling constants (*J*) in hertz (Hz). The purity of the compounds was determined by ¹H NMR (qHNMR) according to the method described by Pauli et al.² with internal calibration. To ensure accurate determination of peak area ratio, the qHNMR measurements were conducted under conditions allowing for complete relaxation. Ethyl 4-(diethylamino)benzoate (LOT#BCCC6657, purity 99.63%), dimethyl terephthalate (LOT#BCBT9974, purity 99.95%) and maleic acid (LOT#BCBM8127V, purity 99.94%) were used as internal standards in MeOD-*d*₄, DMSO-*d*₆, or acetone-*d*₆. All compounds for biological testing had a purity >95% according to quantitative NMR.

General procedure A for Groebke-Blackburn-Bienaymé reaction and hydrolysis.

2-Amino-3-chloropyridine (**43**, 1.0 eq.) or 2-amino-4-chloropyridine (**44**, 1.0 eq.), the respective aldehyde (**41-53**, 1.0-1.1 eq.) and glacial acetic acid (1.5 eq.) were dissolved in dry methanol (0.7 M) under nitrogen. The mixture was stirred for 30–45 min at room temperature (rt) for imine formation. 1,1,3,3-Tetramethylbutylisocyanid (**63**, 1.5 eq.) was subsequently added, and the mixture was stirred at rt for 17-48 h. When TLC monitoring indicated completion, the isocyanide was quenched by addition of 2 N aqueous HCl (2 mL) and further stirring for 30 min. 2 N aqueous NaOH solution and ethyl acetate (10 mL) were then added and the phases were separated. The aqueous layer was extracted with ethyl acetate (3x). The combined organic layers were dried over MgSO₄ and the solvent was evaporated under reduced pressure. The crude product was dissolved in a mixture of methylene chloride and trifluoroacetic acid (10 mL, 1:1) or 4 N HCl in dioxane (10 mL) and the mixture was stirred for 30-60 min at rt. When TLC monitoring indicated completion, 2 N aqueous NaOH solution was

added, phases were separated, and the aqueous layer was extracted with ethyl acetate (3x). The combined organic layers were dried over MgSO₄ and the solvents were evaporated under reduced pressure. The crude product was purified by flash column chromatography using a gradient of *iso*-hexane or cyclohexane / ethyl acetate as mobile phase, and potentially by reverse phase chromatography using a gradient of H₂O with 10% MeCN to 100% MeCN (HPLC grade).

General procedure B for amide coupling with HATU.

The respective carboxylic acid (**72-80**, 1.2 eq.) and 1-[bis(dimethylamino)methylene]-1*H*-1,2,3-triazolo[4,5-*b*]pyridinium 3-oxide hexafluorophosphate (HATU, 1.2 eq.) were dissolved in DMF (0.13 M). *N*-Ethyl-diisopropylamine (DIPEA, 0.13 M 1.2 eq) was added and the mixture was stirred at rt for 40 min. 3-Aminoimidazo[1,2-*a*]pyridine (**8**, 1.0 eq.) was dissolved in DMF (0.11 M) and added to the activated carboxylic acid. The mixture was stirred at rt overnight. When TLC monitoring indicated completion, the solvent was removed under reduced pressure, the residue was dissolved in ethyl acetate and treated with 5% HCl (0.13M). Phases were separated and the aqueous layer was extracted with ethyl acetate (3x). The combined organic layers were washed with 1 N aqueous NaOH solution and dried over MgSO₄. The solvent was evaporated under reduced pressure and the crude product was purified by flash column chromatography using a gradient of *iso*-hexane or cyclohexane / ethyl acetate as mobile phase, and potentially by reverse phase chromatography using a gradient of H₂O with 10% MeCN to 100% MeCN (HPLC gradient grade).

Synthesis and analytical characterization of **8-9**, **12**, **14-42** and precursors

8-Chloro-2-methylimidazo[1,2-a]pyridine-3-amine (8). Preparation according to general procedure A using 2-amino-3-chloropyridine (**43**, 821 mg, 6.39 mmol, 1.00 eq) and acetaldehyde (**45**, 39.0 μ L, 7.03 mmol, 1.10 eq) yielded compound **8** as a colorless solid (344 mg, 30%). $^1\text{H-NMR}$ (400 MHz, acetone- d_6): δ = 8.05 (dd, J = 6.8, 1.1 Hz, 1H), 7.11 (dd, J = 7.3, 1.0 Hz, 1H), 6.76 (t, J = 7.0 Hz, 1H), 4.17 (s, 2H), 2.33 (s, 3H). $^{13}\text{C-NMR}$ (101 MHz, acetone- d_6): δ = 136.1, 130.1, 126.3, 121.5, 121.0, 119.8, 110.0, 11.9. qHNMR (400 MHz, acetone- d_6 , ethyl-4-(dimethylamino)benzoate as reference): purity = 97.5%. MS (APCI+): m/z 181.9 ($[\text{M}+\text{H}]^+$). HRMS (EI+): m/z calculated 181.0407 for $\text{C}_8\text{H}_8\text{ClN}_3$, found 181.0400 ($[\text{M}]^{\bullet+}$).

7-Chloro-2-methylimidazo[1,2-a]pyridine-3-amine (9). Preparation according to general procedure A using 2-amino-4-chloropyridine (**44**, 87.0 mg, 0.68 mmol, 1.00 eq) and acetaldehyde (**46**, 0.04 μ L, 0.74 mmol, 1.10 eq) yielded compound **9** as a colorless solid (50 mg, 41%). $^1\text{H-NMR}$ (400 MHz, acetone- d_6): δ = 8.05 (dd, J = 7.2, 0.8 Hz, 1H), 7.32 (dd, J = 2.1, 0.8 Hz, 1H), 6.78 (dd, J = 7.3, 2.1 Hz, 1H), 4.08 (s, 2H), 2.29 (s, 3H). $^{13}\text{C-NMR}$ (101 MHz, acetone- d_6): δ = 138.9, 130.7, 126.4, 125.0, 122.7, 114.8, 111.4, 11.9. qHNMR (400 MHz, MeOH- d_6 , ethyl-4-(dimethylamino)benzoate as reference): purity = 97.8%. MS (APCI+): m/z 181.9 ($[\text{M}+\text{H}]^+$). HRMS (EI+): m/z calculated 181.0407 for $\text{C}_8\text{H}_8\text{ClN}_3$, found 181.0400 ($[\text{M}]^{\bullet+}$).

8-Chloroimidazo[1,2-a]pyridine-3-amine (12). 8-Chloro-3-nitroimidazo[1,2-a]pyridine (**65**, 156 mg, 0.08 mmol, 1.00 eq) was dissolved in $\text{H}_2\text{O}/\text{MeOH}$ (10 mL, 1:9). Iron powder (441 mg, 7.90 mmol, 10.0 eq) and ammonium chloride (296 mg, 5.53 mmol, 7.00 eq) were added to the solution and the resulting mixture was refluxed overnight. The mixture was filtered through Celite, diluted with ethyl acetate and neutralized with saturated NaHCO_3 solution. Phases were separated, the aqueous layer was extracted with ethyl acetate (10 mL), the combined organic layers were dried over MgSO_4 , and the solvents were removed under reduced pressure. The crude was purified by flash column chromatography and reverse phase chromatography to yield compound **12** as a yellow solid (75 mg, 57%). $^1\text{H-NMR}$ (400 MHz, acetone- d_6): δ = 8.08 (dd, J = 6.9, 1.0 Hz, 1H), 7.15 (dd, J = 7.2, 1.0 Hz, 1H), 7.03 (s, 1H), 6.80 (t, J = 7.0 Hz, 1H), 4.57 (s, 2H). $^{13}\text{C-NMR}$ (101 MHz, MeOD- d_4): δ = 138.8, 133.0, 123.2, 122.8, 122.4, 119.1, 112.43. qHNMR (400 MHz, MeOH- d_4 , ethyl-4-(dimethylamino)benzoate as reference): purity = 97.9%. MS (APCI+): m/z 168.0 ($[\text{M}+\text{H}]^+$). HRMS (EI+): m/z calculated 167.0250 for $\text{C}_7\text{H}_6\text{ClN}_3$, found 167.0244 ($[\text{M}]^{\bullet+}$).

8-Chloro-2-isopropylimidazo[1,2-a]pyridine-3-amine (14). Preparation according to general procedure A using 2-amino-4-chloropyridine (**43**, 395 mg, 3.07 mmol, 1.00 eq) and 2-methylpropanal (**46**, 336 μ L, 3.68 mmol, 1.20 eq) yielded compound **14** as a colorless solid (131 mg, 22%). $^1\text{H-NMR}$ (400 MHz, acetone- d_6): δ = 8.07 (dd, J = 6.8, 1.1 Hz, 1H), 7.12 (dd, J = 7.2, 1.1 Hz, 1H), 6.76 (t, J = 7.0 Hz, 1H), 4.15 (s, 2H), 3.30–3.21 (m, 1H), 1.30 (d, J = 6.9 Hz, 6H). $^{13}\text{C-NMR}$ (101 MHz, MeOD- d_4): δ = 140.1, 138.1, 126.2, 122.7, 122.5, 122.3, 112.0, 27.4, 22.4. qHNMR (400 MHz, acetone- d_6 , ethyl-4-(dimethylamino)benzoate as reference): purity = 95.0%. MS (APCI+): m/z 209.9 ($[\text{M}+\text{H}]^+$). HRMS (EI+): m/z calculated 209.0720 for $\text{C}_{10}\text{H}_{12}\text{ClN}_3$, found 209.0713 ($[\text{M}]^{\bullet+}$).

8-Chloro-2-phenylimidazo[1,2-a]pyridine-3-amine (15). Preparation according to general procedure A using 2-amino-4-chloropyridine (**43**, 390 mg, 3.03 mmol, 1.0 eq) and benzaldehyde (**47**, 322 mg, 3.03 mmol, 1.00 eq) yielded compound **15** as a brown solid (270 mg, 35%). ¹H-NMR (400 MHz, acetone-*d*₆): δ = 8.26–8.19 (m, 1H), 8.19–8.12 (m, 2H), 7.48–7.38 (m, 2H), 7.31–7.18 (m, 2H), 6.84 (t, *J* = 7.1 Hz, 1H), 4.68 (s, 2H). ¹³C-NMR (101 MHz, acetone-*d*₆): δ = 136.7, 135.1, 130.8, 128.3, 126.8, 126.2, 126.4, 122.2, 121.4, 121.2, 110.6. qHNMR (400 MHz, acetone-*d*₆, ethyl-4-(dimethylamino)benzoate as reference) purity = 97.1%. MS (APCI+): *m/z* 243.8 ([M+H]⁺). HRMS (EI+): *m/z* calculated 243.0563 for C₁₃H₁₀ClN₃, found 243.0557 ([M]^{•+}).

8-Chloro-2-(furan-2-yl)imidazo[1,2-a]pyridin-3-amine (16). Preparation according to general procedure A using 2-amino-4-chloropyridine (**43**, 300 mg, 2.33 mmol, 1.00 eq) and furan-3-carbaldehyde (**48**, 246 mg, 2.56 mmol, 1.10 eq) yielded compound **16** as a colorless solid (270 mg, 48%). ¹H-NMR (400 MHz, acetone-*d*₆): δ = 8.18 (dd, *J* = 6.9, 1.0 Hz, 1H), 8.15–8.13 (m, 1H), 7.63 (t, *J* = 1.7 Hz, 1H), 7.19 (dd, *J* = 7.2, 1.0 Hz, 1H), 7.13–7.06 (m, 1H), 6.82 (t, *J* = 7.0 Hz, 1H), 4.48 (s, 2H). ¹³C-NMR (101 MHz, acetone-*d*₆): δ = 143.1, 139.5, 136.9, 126.1, 125.8, 121.9, 121.3, 120.9, 120.7, 110.6, 109.3. qHNMR (400 MHz, acetone-*d*₆, ethyl-4-(dimethylamino)benzoate as reference): purity = 98.8%. MS (APCI+): *m/z* 233.6 ([M+H]⁺). HRMS (EI+): *m/z* calculated 233.0356 for C₁₁H₈ClN₃O, found 233.0350 ([M]^{•+}).

8-Chloro-2-(4-chlorophenyl)imidazo[1,2-a]pyridine-3-amine (17). Preparation according to general procedure A using 2-amino-4-chloropyridine (**43**, 123 mg, 960 μmol, 1.00 eq) and 4-chlorobenzaldehyde (**49**, 135 mg, 960 μmol, 1.00 eq) yielded compound **17** as a yellow solid (14 mg, 5%). ¹H-NMR (400 MHz, MeOH-*d*₄): δ = 8.16 (dd, *J* = 6.9, 1.0 Hz, 1H), 7.96–7.91 (m, 2H), 7.48–7.41 (m, 2H), 7.28 (dd, *J* = 7.3, 1.0 Hz, 1H), 6.86 (t, *J* = 7.0 Hz, 1H). ¹³C-NMR (101 MHz, MeOH-*d*₄): δ = 137.1, 132.6, 132.4, 128.9, 128.5, 128.2, 127.5, 122.2, 121.6, 121.2, 111.2. qHNMR (400 MHz, acetone-*d*₆, ethyl-4-(dimethylamino)benzoate as reference): purity = 95.7%. MS (APCI+): *m/z* 277.9 ([M+H]⁺). HRMS (EI+): *m/z* calculated 277.0174 for C₁₃H₉Cl₂N₃, found 277.0167 ([M]^{•+}).

8-Chloro-2-(3-chlorophenyl)imidazo[1,2-a]pyridine-3-amine (18). Preparation according to general procedure A using 2-amino-4-chloropyridine (**43**, 302 mg, 2.35 mmol, 1.00 eq) and 3-chlorobenzaldehyde (**50**, 328 mg, 2.33 mmol, 1.00 eq) yielded compound **18** as a yellow solid (25 mg, 4%). ¹H-NMR (400 MHz, acetone-*d*₆): δ = 8.29–8.20 (m, 2H), 8.17–8.08 (m, 1H), 7.44 (t, *J* = 7.9 Hz, 1H), 7.32–7.21 (m, 2H), 6.86 (t, *J* = 7.0 Hz, 1H), 4.79 (s, 2H). ¹³C-NMR (101 MHz, MeOD-*d*₄): δ = 138.6, 137.4, 135.5, 131.0, 129.8, 129.2, 128.2, 127.9, 126.5, 123.8, 123.1, 122.7, 112.6. qHNMR (400 MHz, acetone-*d*₆, ethyl-4-(dimethylamino)benzoate as reference) purity = 97.2%. MS (APCI+): *m/z* 278.0 ([M+H]⁺). HRMS (EI+): *m/z* calculated 277.0174 for C₁₃H₉Cl₂N₃, found 277.0168 ([M]^{•+}).

8-Chloro-2-(2-chlorophenyl)imidazo[1,2-a]pyridine-3-amine (19). Preparation according to general procedure A using 2-amino-4-chloropyridine (**43**, 300 mg, 2.33 mmol, 1.00 eq) and 2-chlorobenzaldehyde (**51**, 328 mg, 2.33 mmol, 1.00 eq) yielded compound **19** as a white solid (209 mg, 23%). ¹H-NMR (400 MHz, acetone-*d*₆): δ = 8.19 (dd, *J* = 6.9, 1.1 Hz, 1H), 7.70–7.63 (m, 1H), 7.55–7.48 (m, 1H), 7.47–7.36 (m, 2H), 7.24 (dd, *J* = 7.3, 1.0 Hz, 1H), 6.87 (t, *J* = 7.1 Hz, 1H), 4.53 (s, 2H). ¹³C-NMR (101 MHz, MeOD-*d*₄): δ = 142.0, 136.9, 133.6, 132.6, 129.4, 128.4, 128.3, 127.8, 126.6, 122.1, 121.7, 121.3, 111.2. qHNMR (400 MHz, acetone-*d*₆, ethyl-

4-(dimethylamino)benzoate as reference): purity = 95.6%. MS (APCI+): m/z 277.8 ($[M+H]^+$). HRMS (EI+): m/z calculated 277.0174 for $C_{13}H_9Cl_2N_3$, found 277.0167 ($[M]^{\bullet+}$).

8-Chloro-2-(*p*-tolyl)imidazo[1,2-*a*]pyridine-3-amine (20). Preparation according to general procedure A using 2-amino-4-chloropyridine (**43**, 309 mg, 2.40 mmol, 1.0 eq) and 4-methylbenzaldehyde (**52**, 289 mg, 2.40 mmol, 1.0 eq) yielded compound **20** as a yellow solid (178 mg, 29%). 1H -NMR (400 MHz, acetone- d_6): δ = 8.20 (dd, J = 6.9, 1.0 Hz, 1H), 8.07–7.99 (m, 2H), 7.28–7.17 (m, 3H), 6.83 (t, J = 7.1 Hz, 1H), 4.60 (s, 2H), 2.36 (s, 3H). ^{13}C -NMR (101 MHz, acetone- d_6): δ = 136.6, 136.1, 132.2, 131.2, 128.9, 126.8, 126.3, 122.1, 121.4, 121.0, 110.5, 20.3. qHNMR (400 MHz, acetone- d_6 , ethyl-4-(dimethylamino)benzoate as reference): purity = 96.5%. MS (APCI+): m/z 258.0 ($[M+H]^+$). HRMS (EI+): m/z calculated 257.0720 for $C_{14}H_{12}ClN_3$, und 257.0714 ($[M]^{\bullet+}$).

8-Chloro-2-(*m*-tolyl)imidazo[1,2-*a*]pyridine-3-amine (21). Preparation according to general procedure A using 2-amino-4-chloropyridine (**43**, 395 mg, 3.07 mmol, 1.00 eq) and 3-methylbenzaldehyde (**53**, 369 mg, 3.07 mmol, 1.00 eq) yielded compound **21** as a yellow solid (239 mg, 34%). 1H -NMR (400 MHz, acetone- d_6): δ = 8.24–8.16 (m, 1H), 7.98 (s, 1H), 7.93 (d, J = 7.9 Hz, 1H), 7.31 (td, J = 7.7, 1.4 Hz, 1H), 7.21 (d, J = 7.2 Hz, 1H), 7.13–7.05 (m, 1H), 6.87–6.79 (m, 1H), 4.68 (s, 2H), 2.39 (s, 3H). ^{13}C -NMR (101 MHz, acetone- d_6): δ = 137.7, 136.6, 135.0, 130.8, 128.2, 127.4, 127.3, 126.8, 123.9, 122.2, 121.4, 121.0, 110.6, 20.7. qHNMR (400 MHz, acetone- d_6 , dimethyl terephthalate as reference): purity = 95.3%. MS (APCI+): m/z 257.9 ($[M+H]^+$). HRMS (EI+): m/z calculated 257.0720 for $C_{14}H_{12}ClN_3$, found 257.0714 ($[M]^{\bullet+}$).

8-Chloro-2-(4-(trifluoromethyl)phenyl)imidazo[1,2-*a*]pyridine-3-amine (22). Preparation according to general procedure A using 2-amino-4-chloropyridine (**43**, 395 mg, 3.07 mmol, 1.00 eq) and 4-(trifluoromethyl)benzaldehyde (**54**, 535 mg, 3.07 mmol, 1.00 eq) yielded compound **22** as a yellow solid (33 mg, 3%). 1H -NMR (400 MHz, acetone- d_6): δ = 8.42–8.35 (m, 2H), 8.29–8.23 (m, 1H), 7.80–7.72 (m, 2H), 7.27 (dd, J = 7.3, 1.0 Hz, 1H), 6.88 (t, J = 7.1 Hz, 1H), 4.90 (s, 2H). ^{13}C -NMR (101 MHz, MeOH- d_4): δ = 137.9, 137.3, 128.5, 128.1 (q, J = 32.4 Hz), 127.8, 127.1, 124.5 (q, J = 270.8 Hz), 125.0 (q, J = 3.8 Hz), 122.5, 121.8, 121.3, 111.3. qHNMR (400 MHz, acetone- d_6 , dimethyl terephthalate as reference): purity = 98.2%. MS (APCI+): m/z 311.5 ($[M+H]^+$). HRMS (EI+): m/z calculated 311.0437 for $C_{14}H_9ClF_3N_3$, found 311.0431 ($[M]^{\bullet+}$).

8-Chloro-2-(3-(trifluoromethyl)phenyl)imidazo[1,2-*a*]pyridine-3-amine (23). Preparation according to general procedure A using 2-amino-4-chloropyridine (**43**, 405 mg, 3.15 mmol, 1.00 eq) and 3-(trifluoromethyl)benzaldehyde (**55**, 548 mg, 3.15 mmol, 1.00 eq) yielded compound **23** as a yellow solid (27 mg, 3%). 1H -NMR (400 MHz, acetone- d_6): δ = 8.60–8.52 (m, 1H), 8.48 (d, J = 8.2 Hz, 1H), 8.32–8.23 (m, 1H), 7.70–7.62 (m, 1H), 7.62–7.56 (m, 1H), 7.31–7.23 (m, 1H), 6.93–6.83 (m, 1H), 4.82 (s, 2H). ^{13}C -NMR (126 MHz, MeOD- d_4): δ = 137.4, 135.0, 130.5 (q, J = 31.78 Hz), 130.2, 128.9, 128.7, 127.9, 124.5 (q, J = 270.93), 123.6 (q, J = 4.0 Hz), 123.0 (q, J = 3.9 Hz), 122.6, 121.8, 121.4, 111.3. qHNMR (400 MHz, acetone- d_6 , dimethyl terephthalate as reference): purity = 95.3%. MS (APCI+): m/z 311.5 ($[M+H]^+$). HRMS (EI+): m/z calculated 311.0437 for $C_{14}H_9ClF_3N_3$, found 311.0429 ($[M]^{\bullet+}$).

8-Chloro-2-(3,4-dichlorophenyl)imidazo[1,2-a]pyridine-3-amine (24). Preparation according to general procedure A using 2-amino-4-chloropyridine (**43**, 1.30 g, 10.0 mmol, 1.00 eq) and 3,4-dichlorobenzaldehyde (**56**, 1.93 g, 11.0 mmol, 1.10 eq) yielded compound **24** as a yellow solid (197 mg, 6%). ¹H-NMR (400 MHz, acetone-*d*₆): δ = 8.41–8.35 (m, 1H), 8.30–8.23 (m, 1H), 8.20–8.12 (m, 1H), 7.63–7.56 (m, 1H), 7.27 (dd, *J* = 7.3, 1.1 Hz, 1H), 6.88 (t, *J* = 7.1 Hz, 1H), 4.83 (s, 2H). ¹³C-NMR (101 MHz, MeOD-*d*₄): δ = 137.2, 134.4, 132.1, 130.1, 130.0, 128.6, 128.0, 127.5, 126.3, 122.6, 121.7, 121.3, 111.3. qHNMR (400 MHz, acetone-*d*₆, ethyl-4-(dimethylamino)benzoate as reference): purity = 95.7%. MS (APCI+): *m/z* 311.9 ([M+H]⁺). HRMS (EI+): *m/z* calculated 310.9784 for C₁₃H₈Cl₃N₃, found 310.9778 ([M]^{•+}).

8-Chloro-2-(3,4-dimethylphenyl)imidazo[1,2-a]pyridine-3-amine (25). Preparation according to general procedure A using 2-amino-4-chloropyridine (**43**, 395 mg, 3.07 mmol, 1.00 eq) and 3,4-dimethylbenzaldehyde (**57**, 412 mg, 3.07 mmol, 1.00 eq) yielded compound **25** as a yellow solid (307 mg, 40%). ¹H-NMR (400 MHz, DMSO-*d*₆): δ = 8.27–8.20 (m, 1H), 7.81 (s, 1H), 7.79–7.72 (m, 1H), 7.20 (t, *J* = 7.7 Hz, 2H), 6.82 (t, *J* = 7.1 Hz, 1H), 5.30 (s, 2H), 2.30 (s, 3H), 2.25 (s, 3H). ¹³C-NMR (101 MHz, DMSO-*d*₆): δ = 136.5, 135.7, 134.7, 132.6, 130.0, 128.3, 128.2, 127.8, 124.3, 122.1, 121.4, 121.1, 111.0, 20.0, 19.6. qHNMR (400 MHz, acetone-*d*₆, dimethyl terephthalate as reference): purity = 99.8%. MS (APCI+): *m/z* 271.9 ([M+H]⁺). HRMS (EI+): *m/z* calculated 271.0876 for C₁₅H₁₄ClN₃, found 271.0870 ([M]^{•+}).

N-(8-Chloro-2-methylimidazo[1,2-a]pyridin-3-yl)-5-(4-chlorophenyl)furan-2-carboxamide (26). Preparation according to general procedure B using 8-chloro-2-methylimidazo[1,2-a]pyridine-3-amine (**8**, 50.0 mg, 275 μmol, 1.00 eq) and 5-(4-chlorophenyl)furan-2-carboxylic acid (**74**, 74.0 mg, 330 μmol, 1.20 eq) yielded compound **26** as a colorless solid (46 mg, 43%). ¹H-NMR (400 MHz, acetone-*d*₆): δ = 9.87 (s, 1H), 8.14 (d, *J* = 6.7 Hz, 1H), 7.98 (d, *J* = 8.3 Hz, 2H), 7.52 (d, *J* = 8.7 Hz, 2H), 7.40–7.34 (m, 2H), 7.18 (d, *J* = 3.7 Hz, 1H), 6.88 (t, *J* = 7.1 Hz, 1H), 2.36 (s, 3H). ¹³C-NMR (101 MHz, acetone-*d*₆): δ = 157.0, 154.9, 146.8, 139.2, 138.8, 134.1, 129.1, 128.5, 126.2, 122.9, 122.6, 121.9, 117.7, 116.7, 111.1, 108.3, 12.4. qHNMR (400 MHz, acetone-*d*₆, ethyl-4-(dimethylamino)benzoate as reference) purity = 95.2%. MS (APCI+): *m/z* 385.8 ([M+H]⁺). HRMS (EI+): *m/z* calculated 385.0385 for C₁₉H₁₃Cl₂N₃O₂, found 385.0380 ([M]^{•+}).

N-(8-Chloro-2-methylimidazo[1,2-a]pyridin-3-yl)-5-phenylfuran-2-carboxamide (27). Preparation according to general procedure B using 8-chloro-2-methylimidazo[1,2-a]pyridine-3-amine (**8**, 50.0 mg, 275 μmol, 1.00 eq) and 5-phenylfuran-2-carboxylic acid (**79**, 62.0 mg, 330 μmol, 1.20 eq) yielded compound **27** as a colorless solid (66 mg, 68%). ¹H-NMR (400 MHz, acetone-*d*₆): δ = 9.83 (s, 1H), 8.14 (d, *J* = 6.8 Hz, 1H), 7.96 (d, *J* = 7.1 Hz, 2H), 7.49 (t, *J* = 7.39 Hz, 2H), 7.45–7.37 (m, 2H), 7.37–7.33 (m, 1H), 7.13 (d, *J* = 3.6 Hz, 1H), 6.88 (t, *J* = 7.1 Hz, 1H), 2.36 (s, 3H). ¹³C-NMR (101 MHz, acetone-*d*₆): δ = 157.1, 156.2, 146.6, 139.1, 138.8, 129.7, 128.9, 128.9, 124.6, 122.9, 122.6, 121.9, 117.6, 116.8, 111.1, 107.6, 12.4. qHNMR (400 MHz, acetone-*d*₆, ethyl-4-(dimethylamino)benzoate as reference): purity = 96.1%. MS (APCI+): *m/z* 351.9 ([M+H]⁺). HRMS (EI+): *m/z* calculated 351.0775 for C₁₉H₁₄ClN₃O₂, found 351.0767 ([M]^{•+}).

N-(8-Chloro-2-methylimidazo[1,2-a]pyridin-3-yl)-5-phenylthiophene-2-carboxamide (28). Preparation according to general procedure B using 8-chloro-2-methylimidazo[1,2-a]pyridine-

3-amine (**8**, 50.0 mg, 275 μmol , 1.00 eq) and commercially available 5-phenylthiophene-2-carboxylic acid (**81**, 67.0 mg, 330 μmol , 1.20 eq) yielded compound **28** as a colorless solid (21 mg, 21%). $^1\text{H-NMR}$ (400 MHz, acetone- d_6): δ = 9.73 (s, 1H), 8.14 (d, J = 1.0 Hz, 1H), 8.08–8.02 (m, 1H), 7.79 (d, J = 7.6 Hz, 2H), 7.63–7.57 (m, 1H), 7.55–7.36 (m, 4H), 6.91 (t, J = 7.1 Hz, 1H), 2.38 (s, 3H). $^{13}\text{C-NMR}$ (101 MHz, acetone- d_6): δ = 160.8, 150.0, 139.1, 137.1, 133.4, 130.7, 129.3, 128.8, 126.0, 124.2, 123.0, 122.6, 121.9, 118.2, 117.2, 111.1, 12.3. qHNMR (400 MHz, acetone- d_6 , ethyl-4-(dimethylamino)benzoate as reference): purity = 96.9%. MS (APCI+): m/z 367.3 ($[\text{M}]^+$). HRMS (EI+): m/z calculated 367.0546 for $\text{C}_{19}\text{H}_{14}\text{ClN}_4\text{OS}$, found 367.0539 ($[\text{M}]^+$).

***N*-(8-Chloro-2-methylimidazo[1,2-*a*]pyridin-3-yl)-5-phenyl-1*H*-pyrrole-2-carboxamide (29).** 5-Phenyl-1*H*-pyrrole-2-carboxylic acid (**80**, 74.0 mg, 396 μmol , 1.20 eq) was refluxed in thionyl chloride (4 mL) for 3 h. After cooling to rt, remaining thionyl chloride was removed under reduced pressure. 8-Chloro-2-methylimidazo[1,2-*a*]pyridine-3-amine (**8**, 60.0 mg, 330 μmol , 1.00 eq) dissolved in chloroform (5 mL) was added to the crude acyl chloride at 0°C and the mixture was stirred at rt overnight. The solvent was removed under reduced pressure, the residue was dissolved in ethyl acetate and treated with 5% HCl (5 mL). Phases were separated, the aqueous layer was extracted with ethyl acetate (3x), the combined organic layers were washed with 1 N aqueous NaOH solution, and dried over MgSO_4 . The solvent was removed under reduced pressure and the crude product was purified by flash column chromatography and reverse column chromatography giving compound **29** as a colorless solid (13 mg, 11%). $^1\text{H-NMR}$ (400 MHz, acetone- d_6): δ = 11.85 (s, 1H), 10.51 (s, 1H), 8.31 (d, J = 6.7 Hz, 1H), 7.98 (d, J = 7.5 Hz, 2H), 7.63 (d, J = 7.4 Hz, 1H), 7.41 (t, J = 7.7 Hz, 2H), 7.34–7.23 (m, 1H), 7.21–7.06 (m, 2H), 6.75–6.63 (m, 1H), 2.44 (s, 3H). $^{13}\text{C-NMR}$ (101 MHz, acetone- d_6): δ = 159.6, 154.3, 154.1, 137.4, 136.7, 131.9, 128.7, 127.2, 126.2, 126.0, 125.0, 123.7, 118.9, 114.9, 113.1, 107.3, 11.2. qHNMR (400 MHz, acetone- d_6 , dimethyl terephthalate as reference): purity = 97.1%. MS (APCI+): m/z 350.3 ($[\text{M}]^+$). HRMS (ESI+): m/z calculated 351.0007 for $\text{C}_{19}\text{H}_{16}\text{ClN}_4\text{O}^+$, found 351.10048 ($[\text{M}+\text{H}]^+$).

***N*-(8-Chloro-2-methylimidazo[1,2-*a*]pyridin-3-yl)-[1,1'-biphenyl]-4-carboxamide (30).** Preparation according to general procedure B using 8-chloro-2-methylimidazo[1,2-*a*]pyridine-3-amine (**8**, 60.0 mg, 330 μmol , 1.00 eq) and [1,1'-biphenyl]-4-carboxylic acid (79.0 mg, 396 μmol , 1.20 eq) yielded compound **30** as a colorless solid (36 mg, 30%). $^1\text{H-NMR}$ (400 MHz, acetone- d_6): δ = 9.76 (s, 1H), 8.27–8.20 (m, 2H), 8.16–8.08 (m, 1H), 7.91–7.71 (m, 4H), 7.57–7.48 (m, 2H), 7.48–7.40 (m, 1H), 7.36 (dd, J = 7.3, 1.0 Hz, 1H), 6.88 (t, J = 7.1 Hz, 1H), 2.37 (s, 3H). $^{13}\text{C-NMR}$ (101 MHz, acetone- d_6): δ = 165.9, 144.7, 139.8, 139.1, 138.4, 132.2, 129.0, 129.0, 128.6, 128.2, 127.1, 127.0, 122.8, 122.7, 121.9, 111.0, 12.3. qHNMR (400 MHz, acetone- d_6 , ethyl-4-(dimethylamino)benzoate as reference): purity = 95.5%. MS (APCI+): m/z 361.3 ($[\text{M}]^+$). HRMS (ESI+): m/z calculated 362.1055 for $\text{C}_{21}\text{H}_{17}\text{ClN}_3\text{O}^+$, found 362.1054 ($[\text{M}+\text{H}]^+$).

***N*-(8-Chloro-2-methylimidazo[1,2-*a*]pyridin-3-yl)-5-(4-(trifluoromethyl)phenyl)furan-2-carboxamide (31).** Preparation according to general procedure B using 8-chloro-2-methylimidazo[1,2-*a*]pyridine-3-amine (**8**, 50.0 mg, 275 μmol , 1.00 eq) and 5-(4-(trifluoromethyl)phenyl)furan-2-carboxylic acid (**75**, 85.0 mg, 330 μmol , 1.20 eq) yielded compound **31** as a colorless solid (70 mg, 61%). $^1\text{H-NMR}$ (400 MHz, acetone- d_6): δ = 9.94 (s,

1H), 8.27–8.08 (m, 3H), 7.83 (d, $J = 8.3$ Hz, 2H), 7.47–7.28 (m, 3H), 6.88 (t, $J = 7.1$ Hz, 1H), 2.36 (s, 3H). ^{13}C -NMR (126 MHz, MeOD- d_4): $\delta = 158.5, 155.3, 146.5, 139.5, 138.2, 132.9, 130.1$ (q, $J = 32.5$ Hz), 125.6 (q, $J = 3.8$ Hz), 124.9, 124.2, 124.1 (q, $J = 271.43$), 122.2, 121.4, 118.2, 116.5, 112.0, 109.3, 11.2. qHNMR (400 MHz, acetone- d_6 , ethyl-4-(dimethylamino)benzoate as reference): purity = 98.9%. MS (APCI+): m/z 419.0 ($[\text{M}]^+$). HRMS (EI+): m/z calculated 419.0648 for $\text{C}_{20}\text{H}_{13}\text{ClF}_3\text{N}_3\text{O}_2$, found 419.0646 ($[\text{M}]^+$).

***N*-(8-Chloro-2-methylimidazo[1,2-*a*]pyridin-3-yl)-5-(*p*-tolyl)furan-2-carboxamide (32).** Preparation according to general procedure B using 8-chloro-2-methylimidazo[1,2-*a*]pyridine-3-amine (**8**, 50.0 mg, 275 μmol , 1.00 eq) and 5-(*p*-tolyl)furan-2-carboxylic acid (**76**, 67.0 mg, 330 μmol , 1.20 eq) yielded compound **32** as a colorless solid (69 mg, 69%). ^1H -NMR (400 MHz, acetone- d_6): $\delta = 9.78$ (s, 1H), 8.13 (d, $J = 6.7$ Hz, 1H), 7.85 (d, $J = 7.9$ Hz, 2H), 7.40–7.33 (m, 2H), 7.31 (d, $J = 8.0$ Hz, 2H), 7.06 (d, $J = 3.6$ Hz, 1H), 6.88 (t, $J = 7.1$ Hz, 1H), 2.43–2.31 (m, 6H). ^{13}C -NMR (101 MHz, acetone- d_6): $\delta = 157.1, 156.5, 146.2, 139.1, 138.9, 138.8, 129.5, 127.0, 124.6, 122.9, 122.6, 121.9, 117.7, 116.8, 111.0, 106.9, 20.4, 12.4$. qHNMR (400 MHz, acetone- d_6 , ethyl-4-(dimethylamino)benzoate as reference) purity = 97.8%. MS (APCI+): m/z 365.8 ($[\text{M}+\text{H}]^+$). HRMS (EI+): m/z calculated 365.0931 for $\text{C}_{20}\text{H}_{16}\text{ClN}_3\text{O}_2$, found 365.0923 ($[\text{M}]^+$).

***N*-(8-Chloro-2-methylimidazo[1,2-*a*]pyridin-3-yl)-5-(4-(trifluoromethoxy)phenyl)furan-2-carboxamide (33).** Preparation according to general procedure B using 8-chloro-2-methylimidazo[1,2-*a*]pyridine-3-amine (**8**, 50.0 mg, 275 μmol , 1.00 eq) and 5-(4-(trifluoromethoxy)phenyl)furan-2-carboxylic acid (**77**, 90.0 mg, 330 μmol , 1.20 eq) yielded compound **33** as a colorless solid (85 mg, 71%). ^1H -NMR (400 MHz, acetone- d_6): $\delta = 9.86$ (s, 1H), 8.19–8.09 (m, 3H), 7.48 (d, $J = 8.4$ Hz, 2H), 7.44–7.36 (m, 2H), 7.23 (d, $J = 3.7$ Hz, 1H), 6.90 (t, $J = 7.1$ Hz, 1H), 2.38 (s, 3H). ^{13}C -NMR (126 MHz, acetone- d_6): $\delta = 157.0, 154.7, 149.1$ –148.9 (m), 147.0, 139.2, 138.8, 128.9, 126.4, 123.0, 122.6, 121.9, 121.6, 120.5 (q, $J = 255.5$ Hz) 117.6, 116.7, 111.1, 108.5, 12.3. qHNMR (400 MHz, DMSO- d_6 , ethyl-4-(dimethylamino)benzoate as reference): purity = 95.6%. MS (APCI+): m/z 435.9 ($[\text{M}+\text{H}]^+$). HRMS (ESI+): m/z calculated 436.0670 for $\text{C}_{20}\text{H}_{14}\text{ClF}_3\text{N}_3\text{O}_3^+$, found 436.0663 ($[\text{M}+\text{H}]^+$).

***N*-(8-Chloro-2-methylimidazo[1,2-*a*]pyridin-3-yl)-5-(4-methoxyphenyl)furan-2-carboxamide (34).** Preparation according to general procedure B using 8-chloro-2-methylimidazo[1,2-*a*]pyridine-3-amine (**8**, 50.0 mg, 275 μmol , 1.00 eq) and 5-(4-methoxyphenyl)furan-2-carboxylic acid (**79**, 72.0 mg, 330 μmol , 1.20 eq) yielded compound **34** as a colorless solid (58 mg, 55%). ^1H -NMR (400 MHz, acetone- d_6): $\delta = 9.76$ (s, 1H), 8.12 (d, $J = 6.9$ Hz, 1H), 7.89 (d, $J = 8.5$ Hz, 2H), 7.41–7.30 (m, 2H), 7.04 (d, $J = 8.8$ Hz, 2H), 7.00–6.95 (m, 1H), 6.88 (t, $J = 7.1$ Hz, 1H), 3.86 (s, 3H), 2.36 (s, 3H). ^{13}C -NMR (101 MHz, acetone- d_6): $\delta = 160.5, 157.1, 156.5, 145.9, 139.1, 138.7, 126.2, 122.9, 122.6, 122.5, 121.9, 117.8, 116.9, 114.4, 111.0, 106.0, 54.9, 12.4$. qHNMR (400 MHz, acetone- d_6 , ethyl-4-(dimethylamino)benzoate as reference): purity = 95.9%. MS (APCI+): m/z 381.6 ($[\text{M}+\text{H}]^+$). HRMS (EI+): m/z calculated 381.0880 for $\text{C}_{20}\text{H}_{16}\text{ClN}_3\text{O}_3$, found 381.0875 ($[\text{M}]^+$).

***N*-(8-Chloro-2-methylimidazo[1,2-*a*]pyridin-3-yl)-5-(4-(methylamino)phenyl)furan-2-carboxamide (35).** Preparation according to general procedure B using 8-chloro-2-methylimidazo[1,2-*a*]pyridine-3-amine (**8**, 50.0 mg, 275 μmol , 1.00 eq) and 5-(4-

(methylamino)phenyl)furan-2-carboxylic acid (**72**, 72.0 mg, 330 μmol , 1.20 eq) yielded compound **35** as a yellow solid (35 mg, 33%). $^1\text{H-NMR}$ (400 MHz, acetone- d_6): δ = 9.65 (s, 1H), 8.11 (d, J = 1.1 Hz, 1H), 7.71 (d, J = 8.3 Hz, 2H), 7.36 (dd, J = 7.3, 1.0 Hz, 1H), 7.33–7.28 (m, 1H), 6.87 (t, J = 7.0 Hz, 1H), 6.79 (d, J = 3.6 Hz, 1H), 6.68 (d, J = 8.5 Hz, 2H), 5.41 (s, 1H), 2.85 (s, 3H), 2.35 (s, 3H). $^{13}\text{C-NMR}$ (400 MHz, DMSO- d_6): δ = 157.9, 157.7, 151.1, 144.5, 138.8, 138.3, 126.5, 123.7, 123.4, 121.3, 118.8, 117.6, 117.1, 111.9, 111.8, 104.5, 29.9, 13.4. qHNMR (400 MHz, acetone- d_6 , maleic acid as reference): purity = 96.2%. MS (APCI+): m/z 380.7 ($[\text{M}+\text{H}]^+$). HRMS (ESI+): m/z calculated 381.1113 for $\text{C}_{20}\text{H}_{18}\text{ClN}_4\text{O}_2^+$, found 381.1110 ($[\text{M}+\text{H}]^+$).

***N*-(8-Chloro-2-methylimidazo[1,2-*a*]pyridin-3-yl)-5-(4-(dimethylamino)phenyl)furan-2-carboxamide (36)**. Preparation according to general procedure B using 8-chloro-2-methylimidazo[1,2-*a*]pyridine-3-amine (**8**, 50.0 mg, 275 μmol , 1.00 eq) and 5-(4-(dimethylamino)phenyl)furan-2-carboxylic acid (**73**, 76.0 mg, 330 μmol , 1.20 eq) yielded compound **36** as a yellow solid (69 mg, 64%). $^1\text{H-NMR}$ (400 MHz, acetone- d_6) δ = 9.68 (s, 1H), 8.11 (d, J = 1.0 Hz, 1H), 7.77 (d, J = 8.5 Hz, 2H), 7.40–7.27 (m, 2H), 6.94–6.73 (m, 4H), 3.00 (s, 6H), 2.36 (s, 3H). $^{13}\text{C-NMR}$ (101 MHz, acetone- d_6) δ = 157.7, 157.2, 151.0, 145.1, 139.1, 138.7, 125.9, 122.8, 122.6, 121.8, 118.0, 117.6, 117.0, 112.0, 111.0, 104.3, 39.4, 12.4. qHNMR (400 MHz, acetone- d_6 , maleic acid as reference) purity = 95.1%. MS (APCI+): m/z 394.7 ($[\text{M}+\text{H}]^+$). HRMS (EI+): m/z calculated 394.1197 for $\text{C}_{21}\text{H}_{19}\text{ClN}_4\text{O}_2$, found 394.1194 ($[\text{M}]^{\bullet+}$).

***N*-(8-Chloro-2-(3,4-dichlorophenyl)imidazo[1,2-*a*]pyridin-3-yl)-5-(4-(dimethylamino)phenyl)furan-2-carboxamide (37)**. *N,N*-Dimethyl-4-(4,4,5,5-tetramethyl-1,3,2-dioxaborolan-2-yl)aniline (**69**, 40.8 mg, 0.165 mmol, 1.00 eq), 5-bromo-*N*-(8-chloro-2-(3,4-dichlorophenyl)imidazo[1,2-*a*]pyridin-3-yl)furan-2-carboxamide (**84**, 80.0 mg, 0.165 mmol, 1.00 eq) and sodium carbonate (52.5 mg, 3.00 mol, 3.00 eq) were dissolved in dioxane/ H_2O (10 mL, 9:1). The solution was degassed by freeze-pump-thaw cycles (3x). $\text{Pd}(\text{PPh}_3)_4$ (9.53 mg, 8.25 μmol , 0.05 eq) was added and the mixture was refluxed for 3 h under argon atmosphere. The resulting suspension was filtered, and the precipitate was washed with 2 N aqueous NaOH solution, EtOH, methylene chloride and brine giving **37** as a colorless solid (59 mg, 68%). $^1\text{H-NMR}$ (400 MHz, DMSO- d_6): δ = 10.86 (s, 1H), 8.27–8.17 (m, 2H), 8.02–7.94 (m, 1H), 7.85–7.72 (m, 3H), 7.60 (d, J = 7.3 Hz, 1H), 7.57–7.50 (m, 1H), 7.02–6.92 (m, 2H), 6.80 (d, J = 8.8 Hz, 2H), 2.98 (s, 6H). $^{13}\text{C-NMR}$ (126 MHz, DMSO- d_6): δ = 158.0, 151.1, 144.5, 139.7, 136.5, 136.0, 134.1, 132.0, 131.6, 128.6, 127.1, 126.4, 125.6, 124.1, 122.0, 119.4, 117.3, 115.3, 113.0, 112.4, 110.4, 105.2, 31.2. qHNMR (400 MHz, DMSO- d_6 , maleic acid as reference): purity = 96.1%. MS (APCI+): m/z 524.2 ($[\text{M}+\text{H}]^{\bullet+}$). HRMS (ESI+): m/z calculated 525.0646 for $\text{C}_{26}\text{H}_{20}\text{Cl}_3\text{N}_4\text{O}_2^+$, found 525.0641 ($[\text{M}+\text{H}]^{\bullet+}$).

5-(4-Aminophenyl)-*N*-(8-chloro-2-methylimidazo[1,2-*a*]pyridin-3-yl)furan-2-carboxamide (38). 4-(4,4,5,5-Tetramethyl-1,3,2-dioxaborolan-2-yl)aniline (**85**, 37 mg, 0.169 mmol, 1.00 eq), 5-bromo-*N*-(8-chloro-2-methylimidazo[1,2-*a*]pyridin-3-yl)furan-2-carboxamide (**84**, 60.0 mg, 0.169 mmol, 1.00 eq) and sodium carbonate (53.7 mg, 3.00 mol, 3.00 eq) were dissolved in dioxane/ H_2O (10 mL, 9:1). The solution was degassed by freeze-pump-thaw cycles (3x). $\text{Pd}(\text{PPh}_3)_4$ (9.76 mg, 8.45 μmol , 0.05 eq) was added and the mixture was refluxed for 3 h under argon atmosphere. The resulting suspension was filtered through Celite and the solvents were

removed under reduced pressure. The residue was dissolved in 2 N aqueous NaOH solution and extracted with ethyl acetate (3x). The combined organic layers were dried over MgSO₄ and the solvent was removed under reduced pressure. The crude product was purified by flash column chromatography, reverse column chromatography and preparative HPLC giving **38** as a yellow solid (25 mg, 40%). ¹H-NMR (400 MHz, DMSO-*d*₆) δ = 10.30 (s, 1H), 8.07 (d, *J* = 6.7 Hz, 1H), 7.65 (d, *J* = 8.2 Hz, 2H), 7.44 (d, *J* = 7.3 Hz, 1H), 7.37 (d, *J* = 3.6 Hz, 1H), 6.88 (t, *J* = 7.1 Hz, 1H), 6.82 (d, *J* = 3.6 Hz, 1H), 6.63 (d, *J* = 8.3 Hz, 2H), 5.54 (s, 2H), 2.31 (s, 3H). ¹³C-NMR (101 MHz, DMSO-*d*₆) δ = 158.0, 157.7, 150.3, 144.4, 138.8, 138.3, 126.5, 123.7, 123.4, 121.3, 118.8, 117.6, 117.3, 114.1, 111.9, 104.4, 13.4. qHNMR (400 MHz, DMSO-*d*₆, maleic acid as reference) purity = 99.1%. MS (APCI+): *m/z* 366.6 ([M+H]⁺). HRMS (ESI+): *m/z* calculated 367.0956 for C₁₉H₁₆ClN₄O₂⁺, found 367.0956 ([M+H]⁺).

***N*-(8-Chloro-2-methylimidazo[1,2-*a*]pyridin-3-yl)-5-(4-morpholinophenyl)furan-2-carboxamide (39).** 4-(4-(4,4,5,5-Tetramethyl-1,3,2-dioxaborolan-2-yl)phenyl)morpholine (**86**, 48.9 mg, 0.169 mmol, 1.00 eq), 5-bromo-*N*-(8-chloro-2-methylimidazo[1,2-*a*]pyridin-3-yl)furan-2-carboxamide (**84**, 60.0 mg, 0.169 mmol, 1.00 eq) and sodium carbonate (53.7 mg, 3.00 mol, 3.00 eq) were dissolved in dioxane/H₂O (10 mL, 9:1). The solution was degassed by freeze-pump-thaw cycles (3x). Pd(PPh₃)₄ (9.76 mg, 8.45 μmol, 0.05 eq) was added and the mixture was refluxed for 3 h under argon atmosphere. The resulting suspension was filtered through Celite and the solvents were removed under reduced pressure. The residue was dissolved in 2 N aqueous NaOH solution and extracted with ethyl acetate (3x). The combined organic layers were dried over MgSO₄ and the solvent was removed under reduced pressure. The crude product was purified by flash column chromatography and reverse column chromatography giving **39** as a yellow solid (33 mg, 45%). ¹H-NMR (400 MHz, acetone-*d*₆): δ = 9.72 (s, 1H), 8.12 (d, *J* = 1.1 Hz, 1H), 7.82 (d, *J* = 8.5 Hz, 2H), 7.40–7.31 (m, 2H), 7.05 (d, *J* = 8.8 Hz, 2H), 6.95–6.84 (m, 2H), 3.81–3.76 (m, 4H), 3.27–3.21 (m, 4H), 2.36 (s, 3H). ¹³C-NMR (101 MHz, acetone-*d*₆): δ = 157.9, 152.8, 152.5, 146.4, 140.0, 139.6, 126.7, 123.7, 123.5, 122.7, 121.4, 118.8, 117.8, 115.8, 111.9, 106.2, 67.2, 49.1, 13.3. qHNMR (400 MHz, acetone-*d*₆, ethyl-4(dimethylamino)benzoate as reference): purity = 95.2%. MS (APCI+): *m/z* 436.2 ([M]⁺). HRMS (ESI+): *m/z* calculated C₂₃H₂₂ClN₄O₃⁺ for 437.1375, found 437.1369 ([M+H]⁺).

***N*-(8-Chloro-2-methylimidazo[1,2-*a*]pyridin-3-yl)-5-(4-(4-methylpiperazin-1-yl)phenyl)furan-2-carboxamide (40).** 1-Methyl-4-(4-(4,4,5,5-tetramethyl-1,3,2-dioxaborolan-2-yl)phenyl)piperazine (**87**, 51.1 mg, 0.169 mmol, 1.00 eq), 5-bromo-*N*-(8-chloro-2-methylimidazo[1,2-*a*]pyridin-3-yl)furan-2-carboxamide (**84**, 60.0 mg, 0.169 mmol, 1.00 eq) and sodium carbonate (53.7 mg, 3.00 mol, 3.00 eq) were dissolved in dioxane/H₂O (10 mL, 9:1). The solution was degassed by freeze-pump-thaw cycles (3x). Pd(PPh₃)₄ (9.76 mg, 8.45 μmol, 0.05 eq) was added and the mixture was refluxed for 3 h under argon atmosphere. The resulting suspension was filtered through Celite and the solvents were removed under reduced pressure. The residue was dissolved in 2 N aqueous NaOH solution and extracted with ethyl acetate (3x). The combined organic layers were dried over MgSO₄ and the solvent was removed under reduced pressure. The crude product was purified by flash column chromatography and reverse column chromatography giving **40** as a yellow solid (30 mg, 40%). ¹H-NMR (400 MHz, acetone-*d*₆): δ = 9.71 (s, 1H), 8.12 (d, *J* = 6.6 Hz, 1H), 7.80 (d, *J* = 8.4 Hz, 2H), 7.39–7.30 (m, 2H), 7.03 (d, *J* = 8.7 Hz, 2H), 6.92–6.83 (m, 2H), 3.31–3.24 (m, 4H), 2.53–2.46 (m, 4H), 2.35 (s, 3H), 2.26 (s, 3H). ¹³C-NMR (101 MHz, acetone-*d*₆): δ = 157.1,

151.8, 145.5, 139.1, 138.7, 125.8, 122.8, 122.6, 121.8, 120.0, 117.9, 117.0, 115.0, 111.0, 105.1, 54.8, 47.8, 45.5, 12.4. qHNMR (400 MHz, acetone-*d*₆, ethyl-4(dimethylamino)benzoate as reference): purity = 96.5%. MS (APCI+): *m/z* 449.5 ([M+H]⁺). HRMS (ESI+): *m/z* calculated C₂₄H₂₅ClN₅O₂⁺ for 450.1691, found 450.1686 ([M+H]⁺).

***N*-(8-Chloro-2-methylimidazo[1,2-*a*]pyridin-3-yl)-5-(4-isopropoxyphenyl)furan-2-**

carboxamide (41). 4-Isopropoxyphenylboronic acid (**88**, 30.4 mg, 169 μmol, 1.00 eq), 5-bromo-*N*-(8-chloro-2-methylimidazo[1,2-*a*]pyridin-3-yl)furan-2-carboxamide (**84**, 60.0 mg, 0.169 mmol, 1.00 eq) and sodium carbonate (53.7 mg, 3.00 mol, 3.00 eq) were dissolved in dioxane/H₂O (10 mL, 9:1). The solution was degassed by freeze-pump-thaw cycles (3x). Pd(PPh₃)₄ (9.76 mg, 8.45 μmol, 0.05 eq) was added and the mixture was refluxed for 3 h under argon atmosphere. The resulting suspension was filtered through Celite and the solvents were removed under reduced pressure. The residue was dissolved in 2 N aqueous NaOH solution and extracted with ethyl acetate (3x). The combined organic layers were dried over MgSO₄ and the solvent was removed under reduced pressure. The crude product was purified by flash column chromatography and reverse column chromatography giving **41** as a colorless solid (47 mg, 68%). ¹H-NMR (500 MHz, acetone-*d*₆): δ = 9.76 (s, 1H), 8.13 (d, *J* = 6.8 Hz, 1H), 7.87 (d, *J* = 8.3 Hz, 2H), 7.39–7.32 (m, 2H), 7.02 (d, *J* = 8.4 Hz, 2H), 6.98–6.94 (m, 1H), 6.88 (t, *J* = 7.0 Hz, 1H), 4.77–4.66 (m, 1H), 2.36 (s, 3H), 1.35–1.30 (m, 6H). ¹³C-NMR (126 MHz, acetone-*d*₆): δ = 158.8, 157.1, 156.6, 145.8, 139.1, 138.7, 126.3, 122.8, 122.6, 122.2, 121.9, 117.8, 116.9, 116.0, 111.0, 105.9, 69.6, 21.3, 12.4. qHNMR (400 MHz, acetone-*d*₆, ethyl-4(dimethylamino)benzoate as reference): purity = 99.9%. MS (APCI+): *m/z* 409.7 ([M+H]⁺). HRMS (ESI+): *m/z* calculated C₂₂H₂₁ClN₃O₃⁺ for 410.1266, found 410.1260 ([M+H]⁺).

***N*-(8-Chloro-2-methylimidazo[1,2-*a*]pyridin-3-yl)-5-(4-cyclopropoxyphenyl)furan-2-**

carboxamide (42). 4-Cyclopropoxyphenylboronic acid (**89**, 30.1 mg, 169 μmol, 1.00 eq), 5-bromo-*N*-(8-chloro-2-methylimidazo[1,2-*a*]pyridin-3-yl)furan-2-carboxamide (**84**, 60.0 mg, 0.169 mmol, 1.00 eq) and sodium carbonate (53.7 mg, 3.00 mol, 3.00 eq) were dissolved in dioxane/H₂O (10 mL, 9:1). The solution was degassed by freeze-pump-thaw cycles (3x). Pd(PPh₃)₄ (9.76 mg, 8.45 μmol, 0.05 eq) was added and the mixture was refluxed for 3 h under argon atmosphere. The resulting suspension was filtered through Celite and the solvent was removed under reduced pressure. The residue was dissolved in 2 N aqueous NaOH and extracted with ethyl acetate (3x). The combined organic layers were dried over MgSO₄ and the solvent was removed under reduced pressure. The crude product was purified by flash column chromatography and reverse column chromatography giving **42** as a colorless solid (45 mg, 65%). ¹H-NMR (400 MHz, acetone-*d*₆): δ = 9.76 (s, 1H), 8.13 (d, *J* = 1.0 Hz, 1H), 7.89 (d, *J* = 8.5 Hz, 2H), 7.41–7.29 (m, 2H), 7.22–7.09 (m, 2H), 6.98 (d, *J* = 3.6 Hz, 1H), 6.88 (t, *J* = 6.8 Hz, 1H), 3.93–3.85 (m, 1H), 2.36 (s, 3H), 0.89–0.67 (m, 4H). ¹³C-NMR (126 MHz, acetone-*d*₆): δ = 159.8, 157.1, 156.5, 145.9, 139.1, 138.7, 126.1, 122.9, 122.8, 122.6, 121.9, 117.8, 116.9, 115.4, 111.0, 106.0, 50.8, 12.4, 5.7. qHNMR (400 MHz, acetone-*d*₆, ethyl-4(dimethylamino)benzoate as reference): purity = 97.5%. MS (APCI+): *m/z* 407.7 ([M+H]⁺). HRMS (ESI+): *m/z* calculated 408.1109 for C₂₂H₁₉ClN₃O₃⁺, found 408.1103 ([M+H]⁺).

8-chloro-3-nitroimidazo[1,2-*a*]pyridine (61). 8-Chloroimidazo[1,2-*a*]pyridine (**60**, 300 mg, 1.97 mmol, 1.00 eq) was dissolved in conc. sulfuric acid (10 mL) and cooled to 0°C. Nitric acid (65%, 358 μL, 5.60 mmol, 2.80 eq.) was added and the mixture was stirred for 1 h at 0°C. The

solution was then slowly poured into a H₂O-ice mixture leading to precipitation of the product. The precipitate was washed with cold H₂O to yield **61** as a yellow solid (363 mg, 93%). ¹H-NMR (400 MHz, acetone-*d*₆): δ = 9.39 (dd, *J* = 7.0, 1.0 Hz, 1H), 8.68 (s, 1H), 7.93 (dt, *J* = 7.7, 0.8 Hz, 1H), 7.48 (t, *J* = 7.3 Hz, 1H). ¹³C-NMR (101 MHz, acetone-*d*₆): 145.0, 138.5, 130.3, 127.5, 124.7, 120.1, 117.6. MS (APCI+): *m/z* 197.7 ([M+H]⁺).

Methyl 5-(4-(methylamino)phenyl)furan-2-carboxylate (66). *N*-Methyl-4-(4,4,5,5-tetramethyl-1,3,2-dioxaborolan-2-yl)aniline (**64**, 250 mg, 1.10 mmol, 1.10 eq) and tripotassium phosphate (637 mg, 3.00 mol, 3.00 eq) were dissolved in dioxane/H₂O (10 mL, 9:1). The solution was degassed by freeze-pump-thaw cycles (3x). Methyl 5-bromofuran-2-carboxylate (**63**, 205 mg, 1.00 mmol, 1.00 eq) and XPhos Pd G2 (79.0 mg, 0.10 mmol, 0.10 eq) were added and the mixture was refluxed for 3 h under nitrogen atmosphere. The resulting suspension was filtered through Celite and the solvents were removed under reduced pressure. The residue was dissolved in 2 N aqueous HCl and extracted with ethyl acetate (3x). The combined organic layers were dried over MgSO₄ and the solvent was removed under reduced pressure. The crude product was purified by flash column chromatography using a gradient of cyclohexane/ethyl acetate as mobile phase giving **66** as a brown solid (200 mg, 87%). ¹H-NMR (400 MHz, acetone-*d*₆): δ = 7.63–7.57 (m, 2H), 7.24 (d, *J* = 0.6 Hz, 1H), 6.72–6.65 (m, 3H), 5.42 (s, 1H), 3.84 (s, 3H), 2.83 (s, 3H). ¹³C-NMR (101 MHz, acetone-*d*₆): δ = 159.0, 158.6, 151.0, 142.1, 126.0, 120.3, 117.6, 111.8, 103.7, 50.8, 24.4. MS (APCI+): *m/z* 231.8 ([M+H]⁺).

Methyl 5-(4-(dimethylamino)phenyl)furan-2-carboxylate (67). 4-(Dimethylamino)phenylboronic acid (**65**, 198 mg, 1.20 mmol, 1.20 eq) and tripotassium phosphate (637 mg, 3.00 mmol, 3.00 eq) were dissolved in dioxane/H₂O (10 mL, 9:1). The solution was degassed by freeze-pump-thaw cycles (3x). Methyl 5-bromofuran-2-carboxylate (**63**, 205 mg, 1.00 mmol, 1.00 eq) and XPhos Pd G2 (79.0 mg, 0.10 mmol, 0.10 eq) were added and the mixture was refluxed for 3 h. The resulting suspension was filtered through Celite and the solvents were removed under reduced pressure. The residue was dissolved in 2 N aqueous HCl and extracted with ethyl acetate (3x). The combined organic layers were dried over MgSO₄ and the solvent was removed under reduced pressure. The crude product was purified by flash column chromatography using a gradient of cyclohexane/ethyl acetate as mobile phase giving **67** as a brown solid (237 mg, 97%). ¹H-NMR (400 MHz, acetone-*d*₆): δ = 7.70–7.61 (m, 2H), 7.26 (d, *J* = 3.6 Hz, 1H), 6.85–6.78 (m, 2H), 6.74 (d, *J* = 3.7 Hz, 1H), 3.84 (s, 3H), 3.01 (s, 6H). ¹³C-NMR (101 MHz, acetone-*d*₆): δ = 159.7, 159.5, 152.0, 143.1, 126.7, 121.2, 118.3, 112.9, 104.9, 51.8, 40.2. MS (APCI+): *m/z* 245.8 ([M+H]⁺).

5-(4-(Methylamino)phenyl)furan-2-carboxylic (68). Methyl 5-(4-(methylamino)phenyl)furan-2-carboxylate (**66**, 180 mg, 778 μmol, 1.00 eq) and LiOH (93.0 mg, 3.89 mmol, 5.00 eq) were dissolved in H₂O/THF (10 mL, 1:1). The mixture was stirred at rt overnight. The solvents were removed under reduced pressure and the crude product was purified by reverse column chromatography using a gradient of H₂O/MeCN as mobile phase giving **68** as a colorless solid (113 mg, 67%). ¹H-NMR (400 MHz, DMSO-*d*₆): δ = 7.45 (d, *J* = 8.7 Hz, 2H), 6.65–6.62 (m, 1H), 6.60–6.52 (m, 2H), 6.48 (d, *J* = 3.3 Hz, 1H), 5.93–5.85 (m, 1H), 2.69 (d, *J* = 5.0 Hz, 3H). ¹³C-NMR (101 MHz, DMSO-*d*₆): δ = 171.9, 162.6, 153.8, 149.9, 125.3, 119.2, 113.6, 112.1, 103.3, 30.1. MS (APCI+): *m/z* 217.9 ([M+H]⁺).

5-(4-(Dimethylamino)phenyl)furan-2-carboxylic acid (69). Methyl 5-(4-(dimethylamino)phenyl)furan-2-carboxylate (**67**, 189 mg, 771 μmol , 1.00 eq) and LiOH (92.0 mg, 3.89 mmol, 5.00 eq) were dissolved in $\text{H}_2\text{O}/\text{THF}$ (10 mL, 1:1). The solution was stirred at rt overnight. The solvents were removed under reduced pressure and the crude product was purified by reverse column chromatography using a gradient of $\text{H}_2\text{O}/\text{MeCN}$ as mobile phase giving **69** as a colorless solid (130 mg, 73%). $^1\text{H-NMR}$ (400 MHz, $\text{DMSO-}d_6$) δ = 7.57–7.48 (m, 2H), 6.79–6.71 (m, 2H), 6.63 (d, J = 3.2 Hz, 1H), 6.54 (d, J = 3.2 Hz, 1H), 2.93 (s, 6H). $^{13}\text{C-NMR}$ (101 MHz, $\text{MeOH-}d_6$) δ = 166.0, 156.0, 150.5, 148.6, 125.2, 119.3, 115.6, 112.2, 103.0, 39.3. MS (APCI+): m/z 232.1 ($[\text{M}+\text{H}]^+$).

5-Bromo-*N*-(8-chloro-2-(3,4-dichlorophenyl)imidazo[1,2-*a*]pyridin-3-yl)furan-2-carboxamide (83). 5-Bromofuran-2-carboxylic acid (**82**, 345 mg, 1.81 mmol, 3.14 eq) was dissolved in methylene chloride (2 mL) under Ar atmosphere. Oxalyl chloride (310 μL , 3.62 mmol, 6.3 eq) was added dropwise to the solution at 0 °C. After 3 h the solvent was removed under reduced pressure, 8-chloro-2-(3,4-dichlorophenyl)imidazo[1,2-*a*]pyridine-3-amine (**24**, 180 mg, 576 μmol , 1.00 eq) dissolved in a mixture of pyridine (1 mL) and toluene (4 mL) was added, and the mixture was stirred at rt overnight. 2 N aqueous NaOH solution (10 mL) was added, phases were separated, and the aqueous layer was extracted with ethyl acetate (3x). The combined organic layers were dried over MgSO_4 and the solvent was removed under reduced pressure. The crude product was purified by flash column chromatography using a gradient of cyclohexane/ ethyl acetate as mobile phase giving **83** as a brown solid (180 mg, 64%). $^1\text{H-NMR}$ (400 MHz, $\text{DMSO-}d_6$): δ = 10.87 (s, 1H), 8.29–8.24 (m, 1H), 8.15 (d, J = 2.0 Hz, 1H), 7.92 (dd, J = 8.4, 2.1 Hz, 1H), 7.76 (d, J = 8.4 Hz, 1H), 7.62–7.57 (m, 1H), 7.50 (d, J = 3.6 Hz, 1H), 7.02–6.92 (m, 2H). $^{13}\text{C-NMR}$ (101 MHz, $\text{DMSO-}d_6$): δ = 157.0, 148.8, 139.8, 136.5, 133.9, 132.0, 131.7, 131.1, 128.6, 127.1, 127.1, 125.7, 124.1, 122.0, 119.2, 117.2, 115.2, 113.1. MS (APCI+): m/z 483.3 ($[\text{M}+\text{H}]^+$).

5-Bromo-*N*-(8-chloro-2-methylimidazo[1,2-*a*]pyridin-3-yl)furan-2-carboxamide (84). Preparation according to general procedure B using 8-chloro-2-methylimidazo[1,2-*a*]pyridine-3-amine (**8**, 340 mg, 1.87 mmol, 1.00 eq) and 5-bromofuran-2-carboxylic acid (**82**, 429 mg, 2.24 mmol, 1.20 eq) yielded compound **84** as a colorless solid (536 mg, 81%). $^1\text{H-NMR}$ (400 MHz, $\text{MeOD-}d_4$): δ = 8.00 (d, J = 1.0 Hz, 1H), 7.43 (d, J = 1.0 Hz, 1H), 7.33 (d, J = 3.6 Hz, 1H), 6.91 (t, J = 7.1 Hz, 1H), 6.73 (d, J = 3.7 Hz, 1H), 2.39 (s, 3H). $^{13}\text{C-NMR}$ (101 MHz, $\text{MeOD-}d_4$): δ = 157.5, 148.5, 139.5, 138.1, 126.6, 124.2, 122.2, 121.4, 118.5, 116.3, 114.4, 111.9, 11.2. MS (APCI+): m/z 355.4 ($[\text{M}+\text{H}]^+$).

Supplementary References

1. Almaro Garcia, A., Lardenois, P. & Olivier, A. Derivatives of 2-aryl-6-phenyl-imidazo [1, 2- α]pyridines, their preparation and their therapeutic use. WO 2008/034974A1. *Sanofi-Aventis* (2008).
2. Pauli, G. F. *et al.* Importance of purity evaluation and the potential of quantitative ^1H NMR as a purity assay. *J. Med. Chem.* **57**, 9220–9231 (2014).

- Supplementary Data 1-

Development of Nurr1 Agonists from Amodiaquine By Scaffold Hopping and Fragment Growing

Minh Sai¹, Emily C. Hank¹, Hin-Man Tai², Till Kasch¹, Max Lewandowski¹, Michelle Vincendeau^{2,3}, Julian A. Marschner¹, Daniel Merk^{1*}

¹ Ludwig-Maximilians-Universität München, Department of Pharmacy, 81377 Munich, Germany

² Helmholtz Munich, Institute of Virology, 85764 Munich, Germany

³ Technical University of Munich, Institute of Virology, School of Medicine, 81675 Munich, Germany

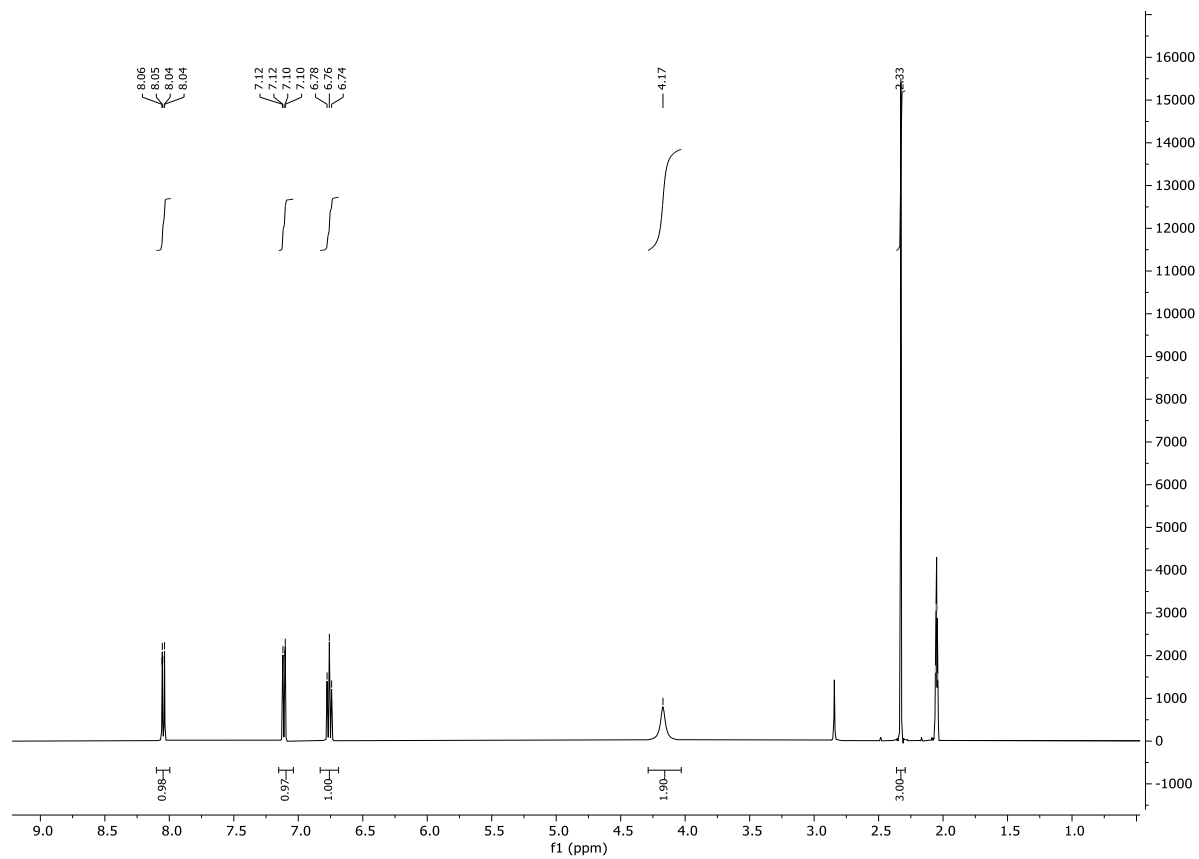
* daniel.merk@cup.lmu.de

Table of Contents

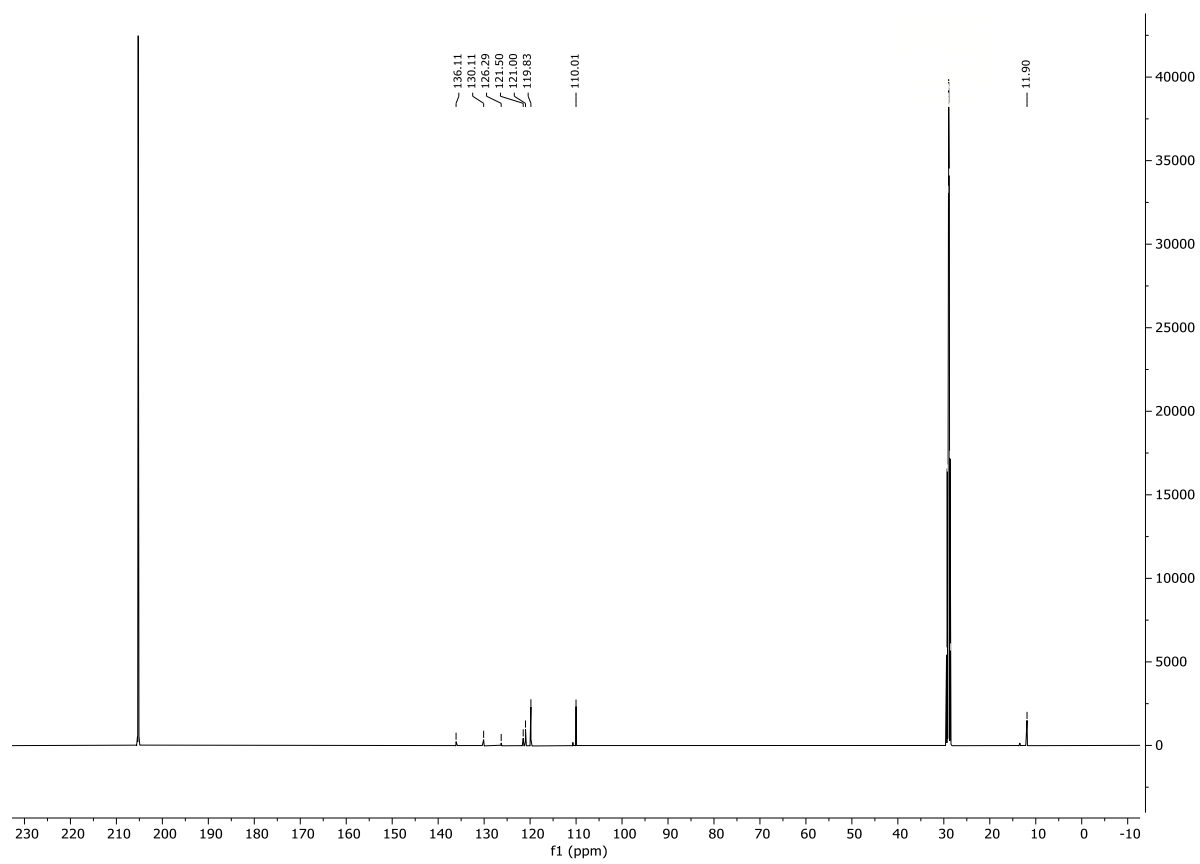
NMR spectra (¹ H, ¹³ C and qH) of 8-9, 12, 14-42	2
HRMS spectra of 8-9, 12, 14-42	98

NMR spectra (¹H, ¹³C and qH) of 8-9, 12 and 14-42

¹H spectrum of compound 8:

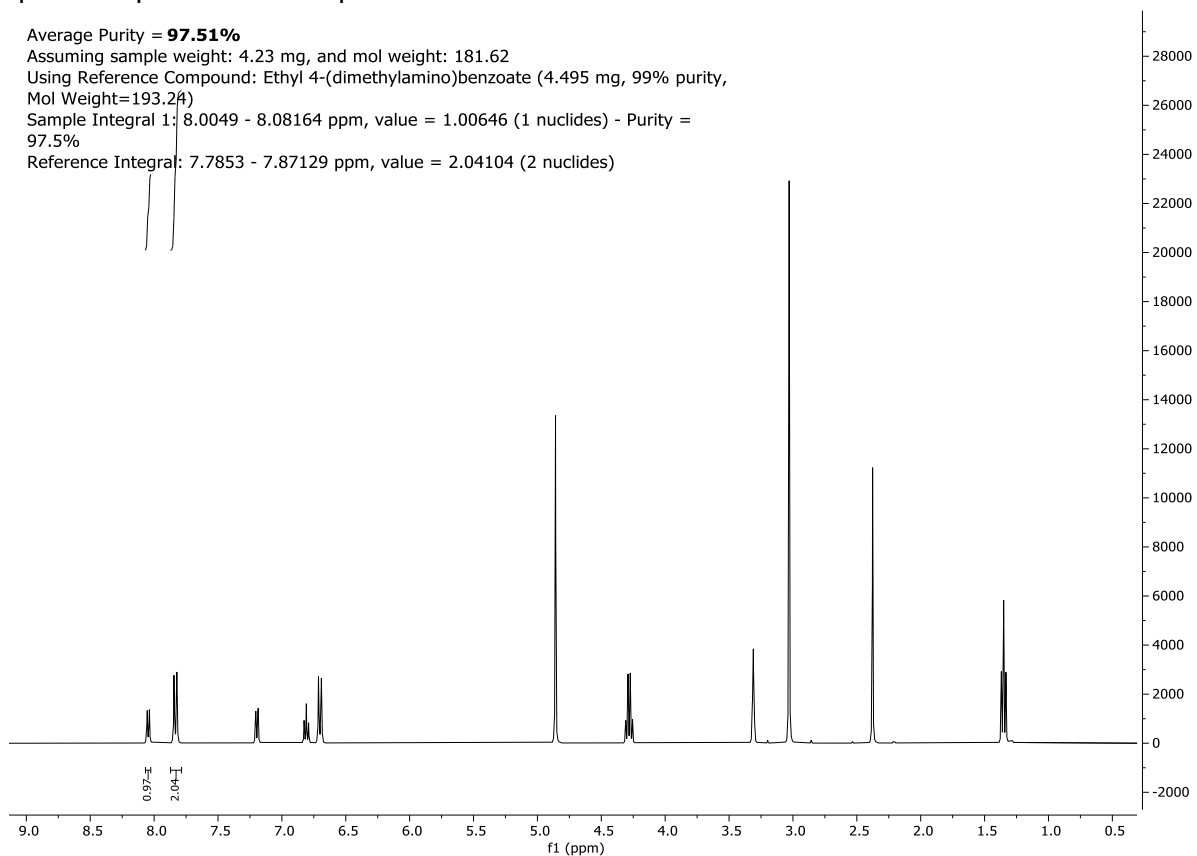


^{13}C spectrum of compound **8**:

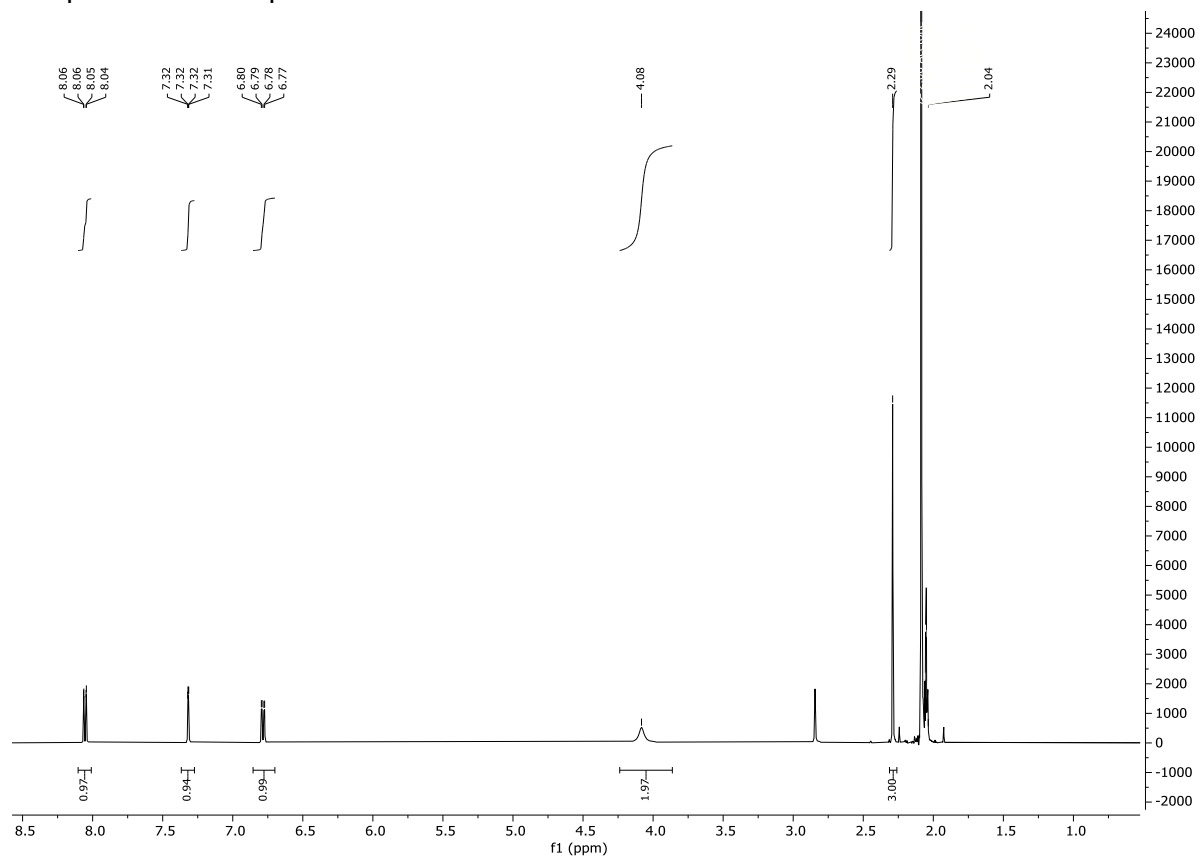


qHNMR spectrum of compound **8**:

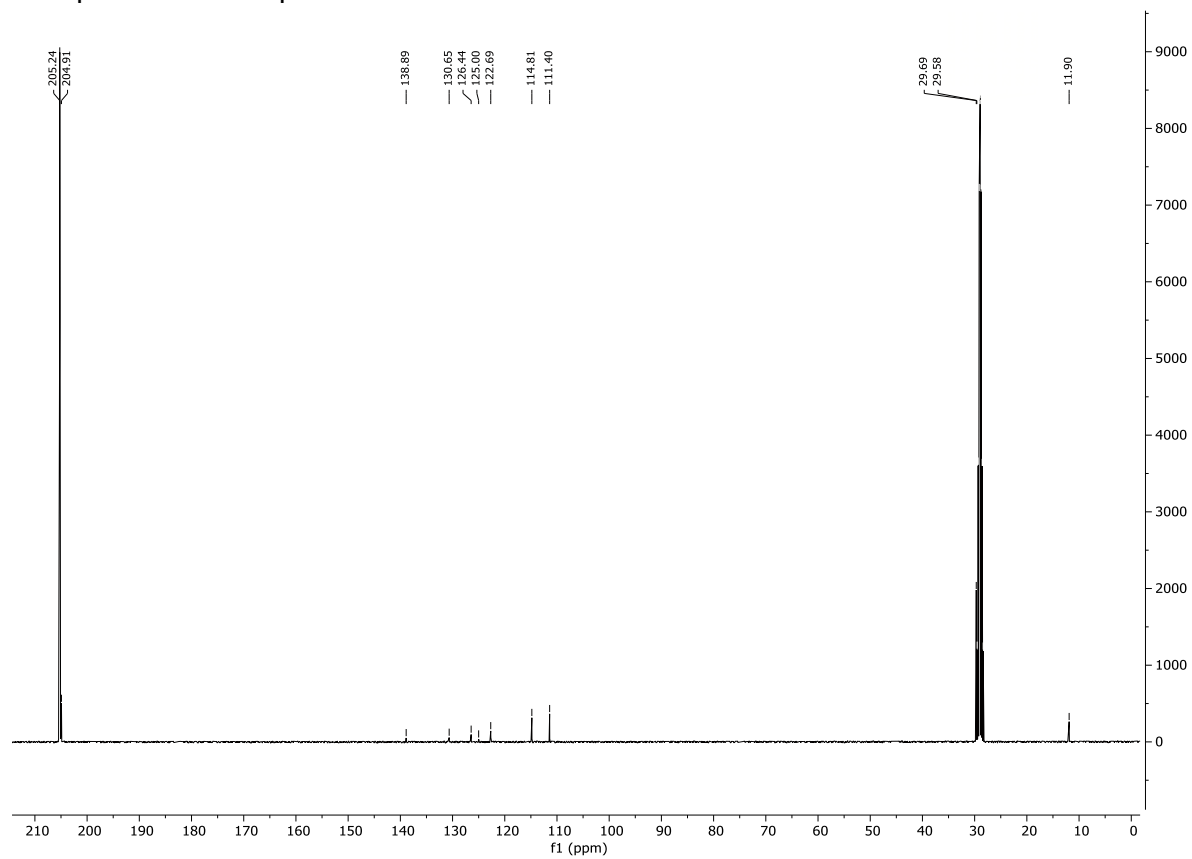
Average Purity = **97.51%**
Assuming sample weight: 4.23 mg, and mol weight: 181.62
Using Reference Compound: Ethyl 4-(dimethylamino)benzoate (4.495 mg, 99% purity,
Mol Weight=193.24)
Sample Integral 1: 8.0049 - 8.08164 ppm, value = 1.00646 (1 nuclides) - Purity = 97.5%
Reference Integral: 7.7853 - 7.87129 ppm, value = 2.04104 (2 nuclides)



¹H spectrum of compound **9**:



^{13}C spectrum of compound **9**:



qHNMR spectrum of compound **9**:

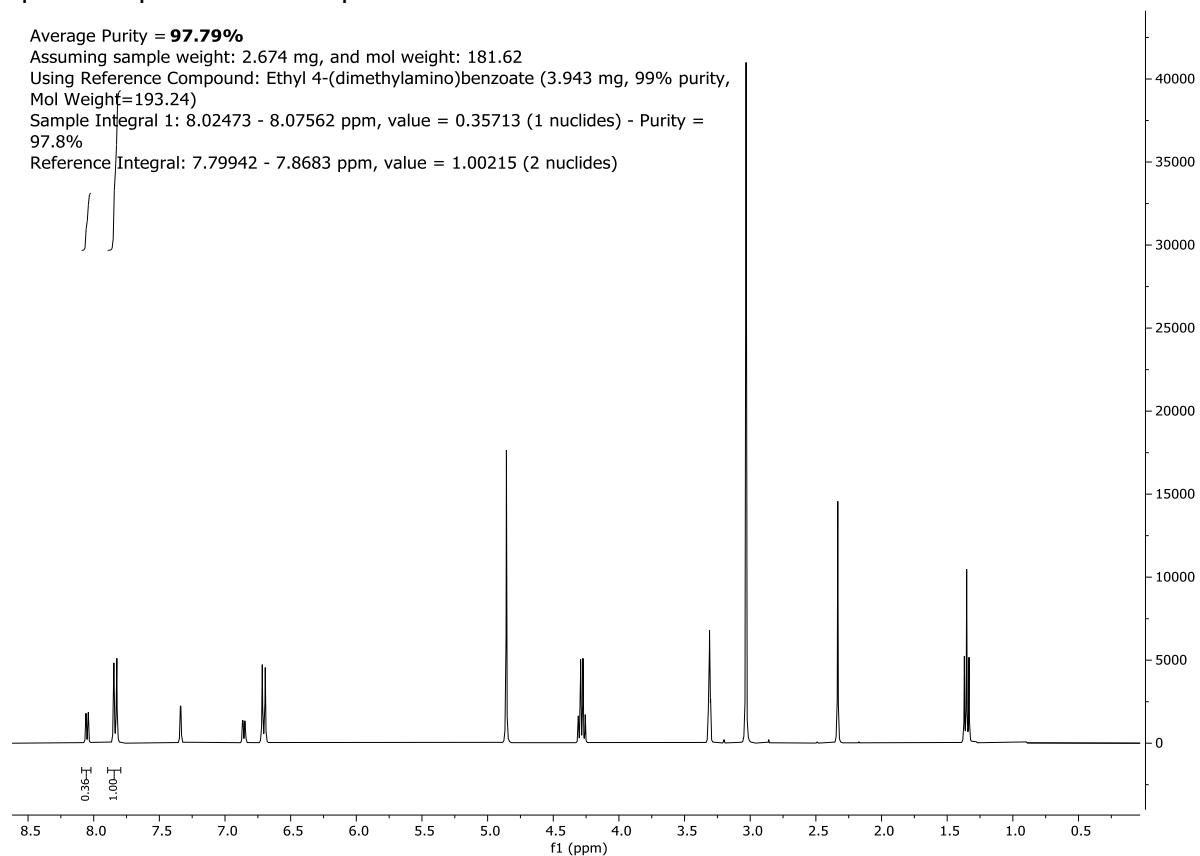
Average Purity = **97.79%**

Assuming sample weight: 2.674 mg, and mol weight: 181.62

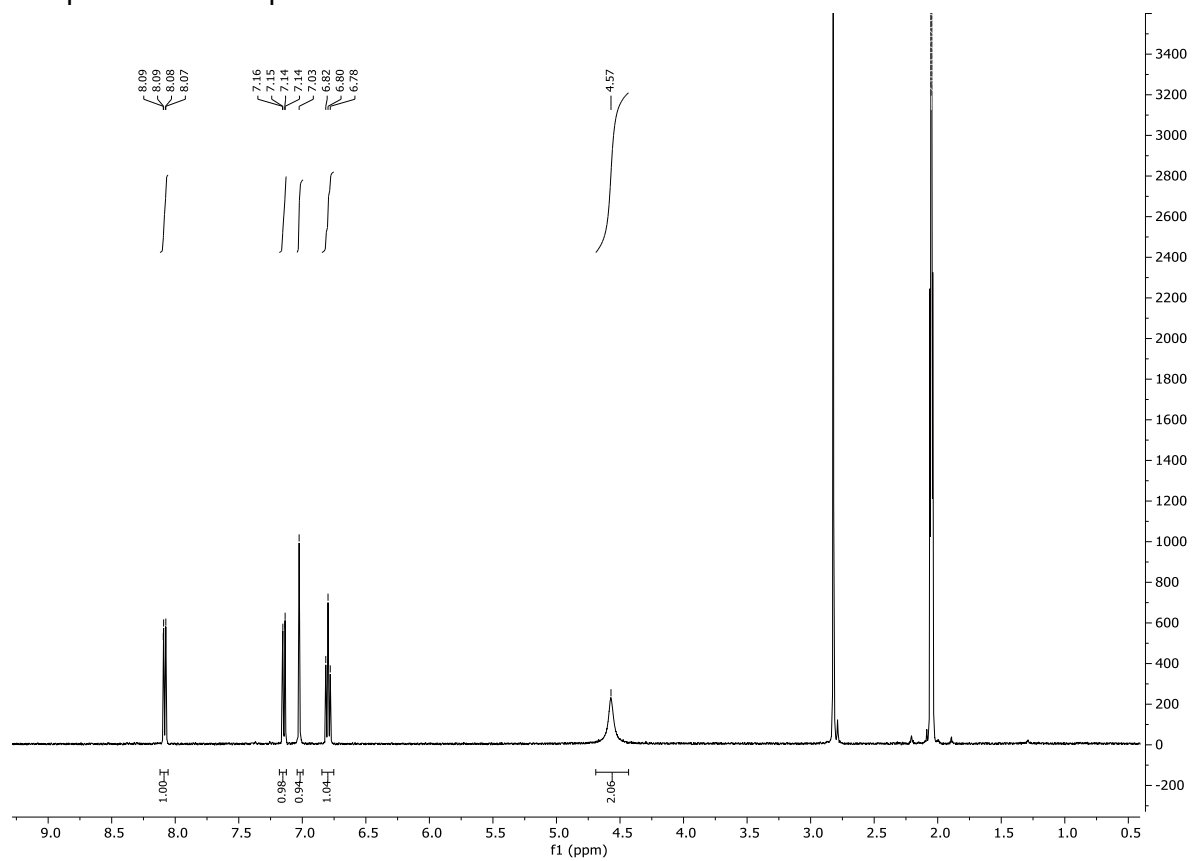
Using Reference Compound: Ethyl 4-(dimethylamino)benzoate (3.943 mg, 99% purity,
Mol Weight=193.24)

Sample Integral 1: 8.02473 - 8.07562 ppm, value = 0.35713 (1 nuclides) - Purity = 97.8%

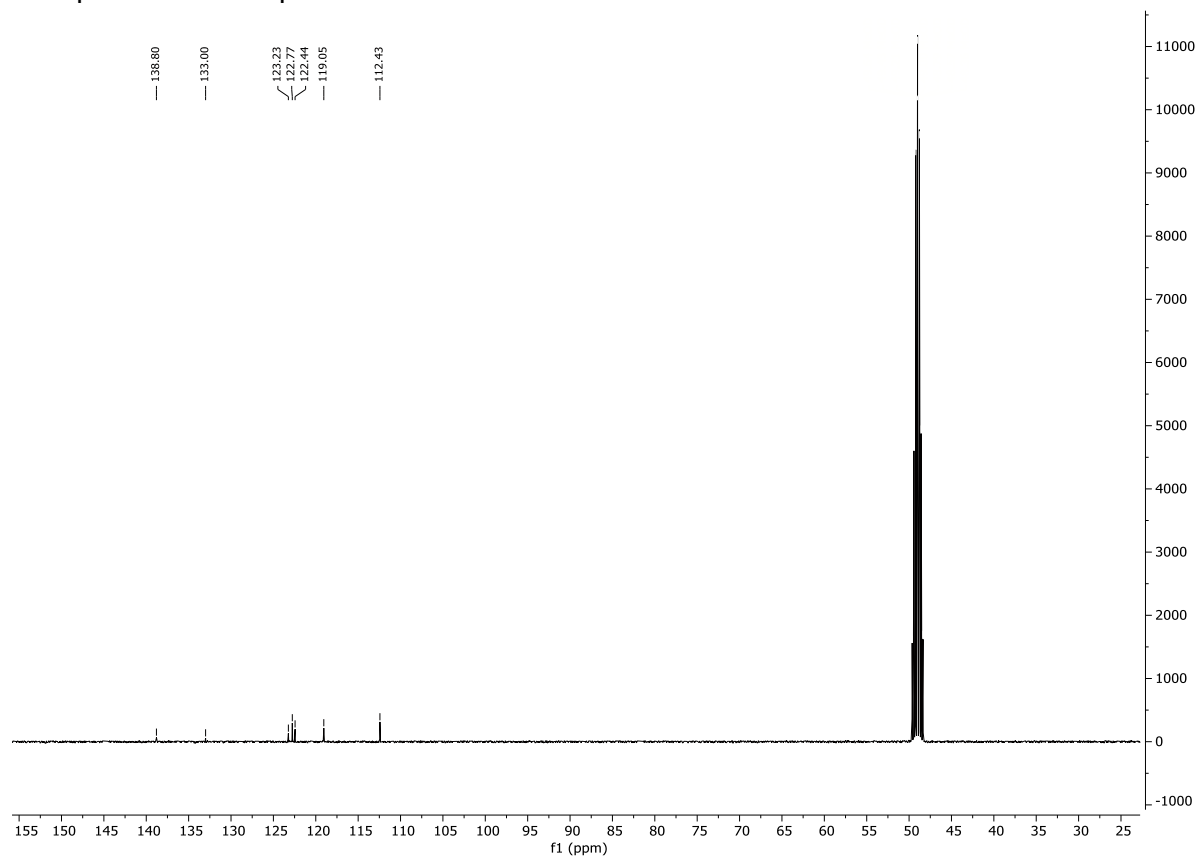
Reference Integral: 7.79942 - 7.8683 ppm, value = 1.00215 (2 nuclides)



¹H spectrum of compound 12:



¹³C spectrum of compound **12**:



qHNMR spectrum of compound **12**:

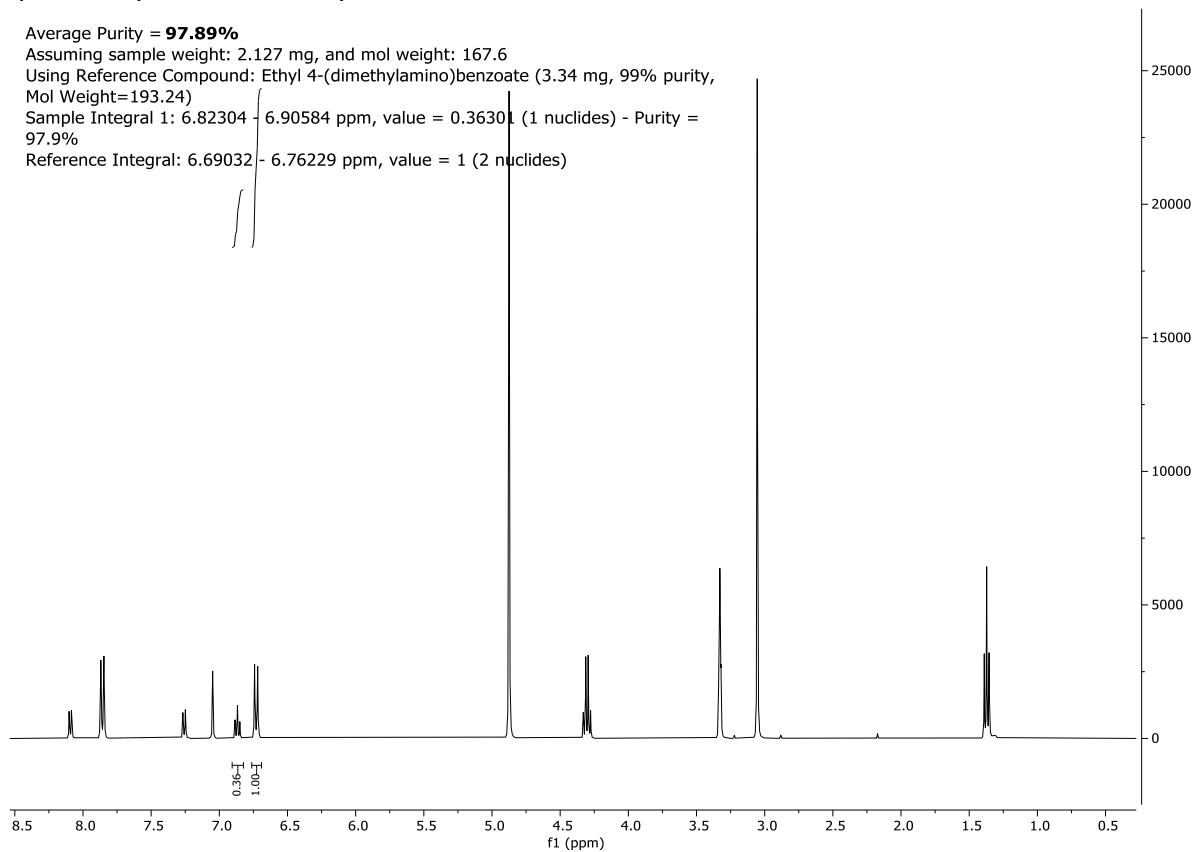
Average Purity = **97.89%**

Assuming sample weight: 2.127 mg, and mol weight: 167.6

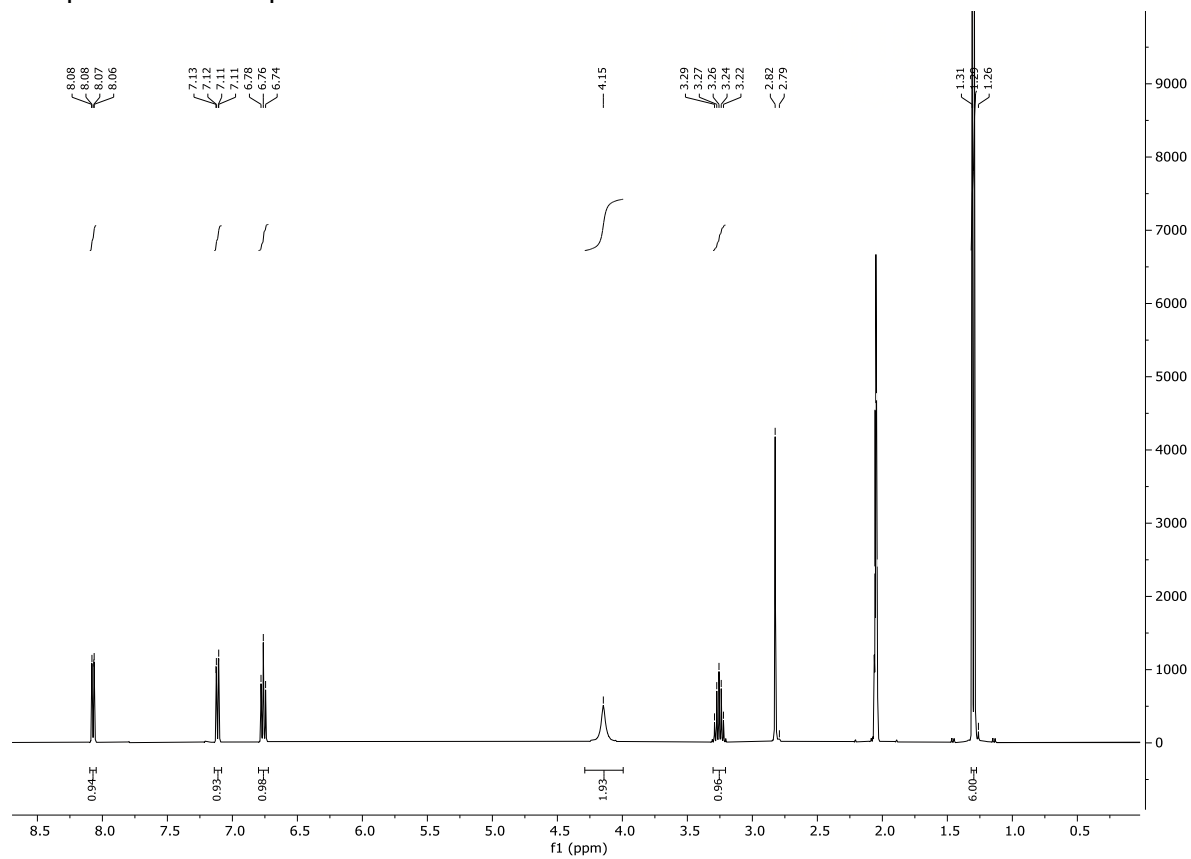
Using Reference Compound: Ethyl 4-(dimethylamino)benzoate (3.34 mg, 99% purity, Mol Weight=193.24)

Sample Integral 1: 6.82304 - 6.90584 ppm, value = 0.36301 (1 nuclides) - Purity = 97.9%

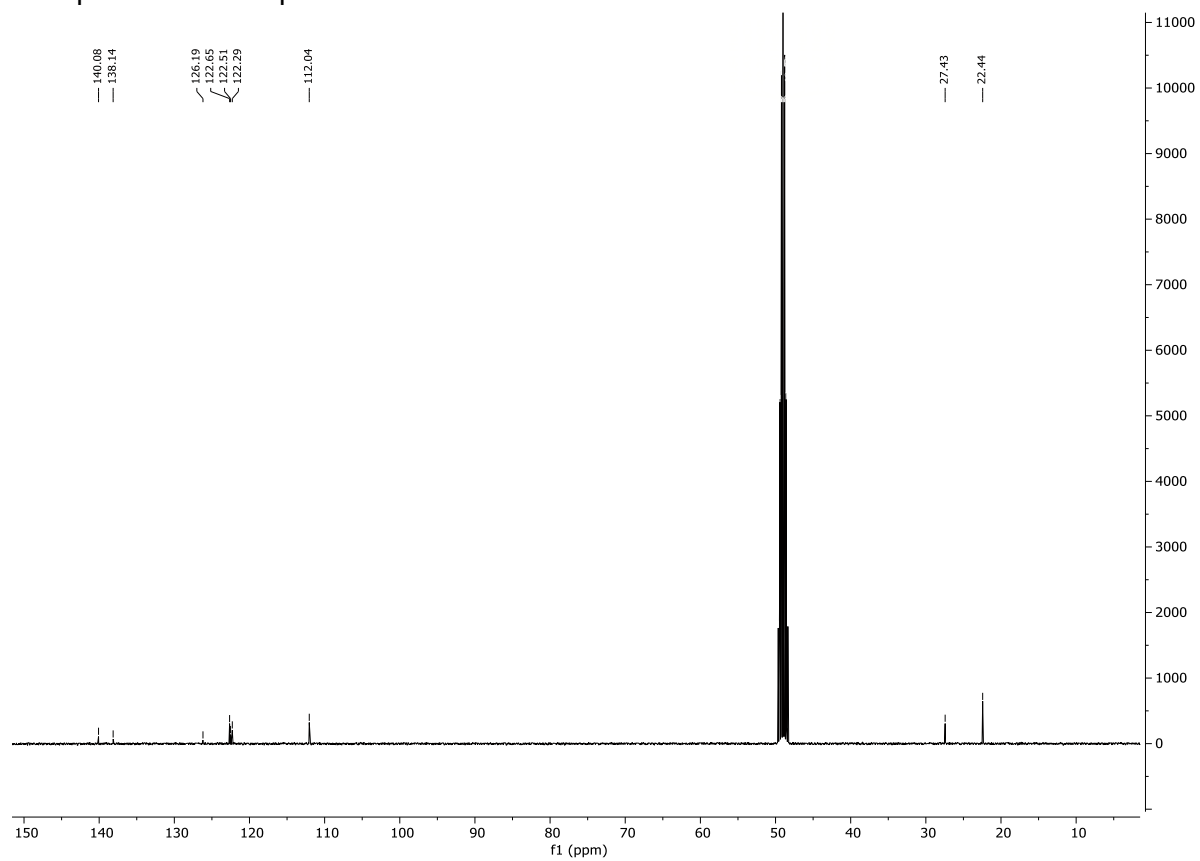
Reference Integral: 6.69032 - 6.76229 ppm, value = 1 (2 nuclides)



¹H spectrum of compound **14**:

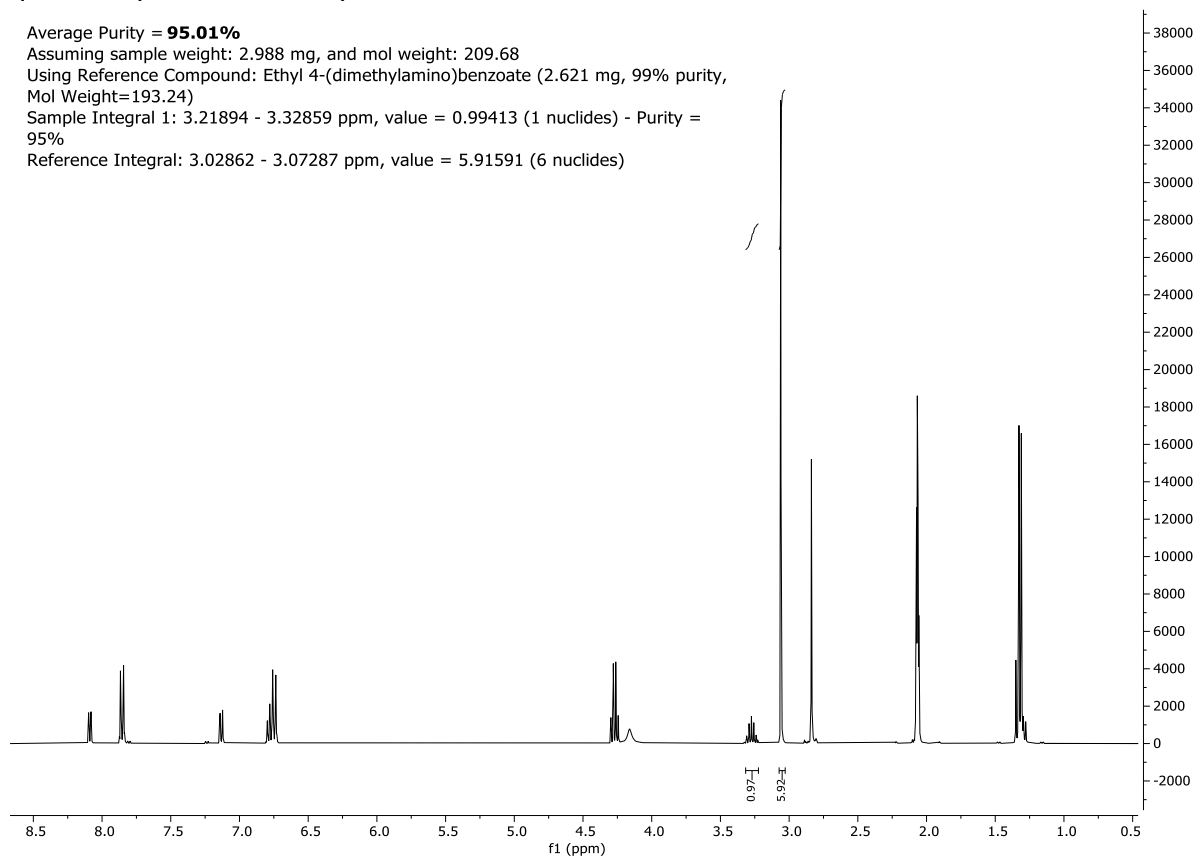


^{13}C spectrum of compound **14**:

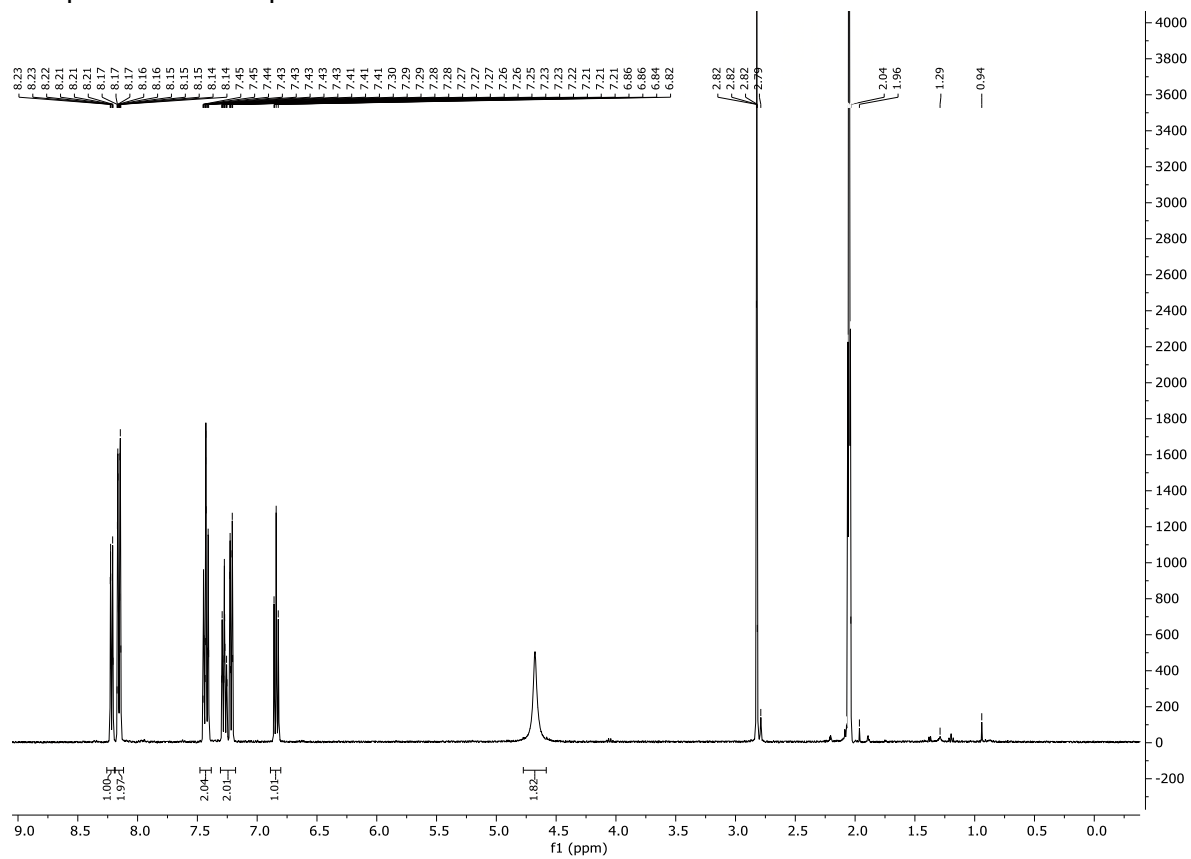


qHNMR spectrum of compound **14**:

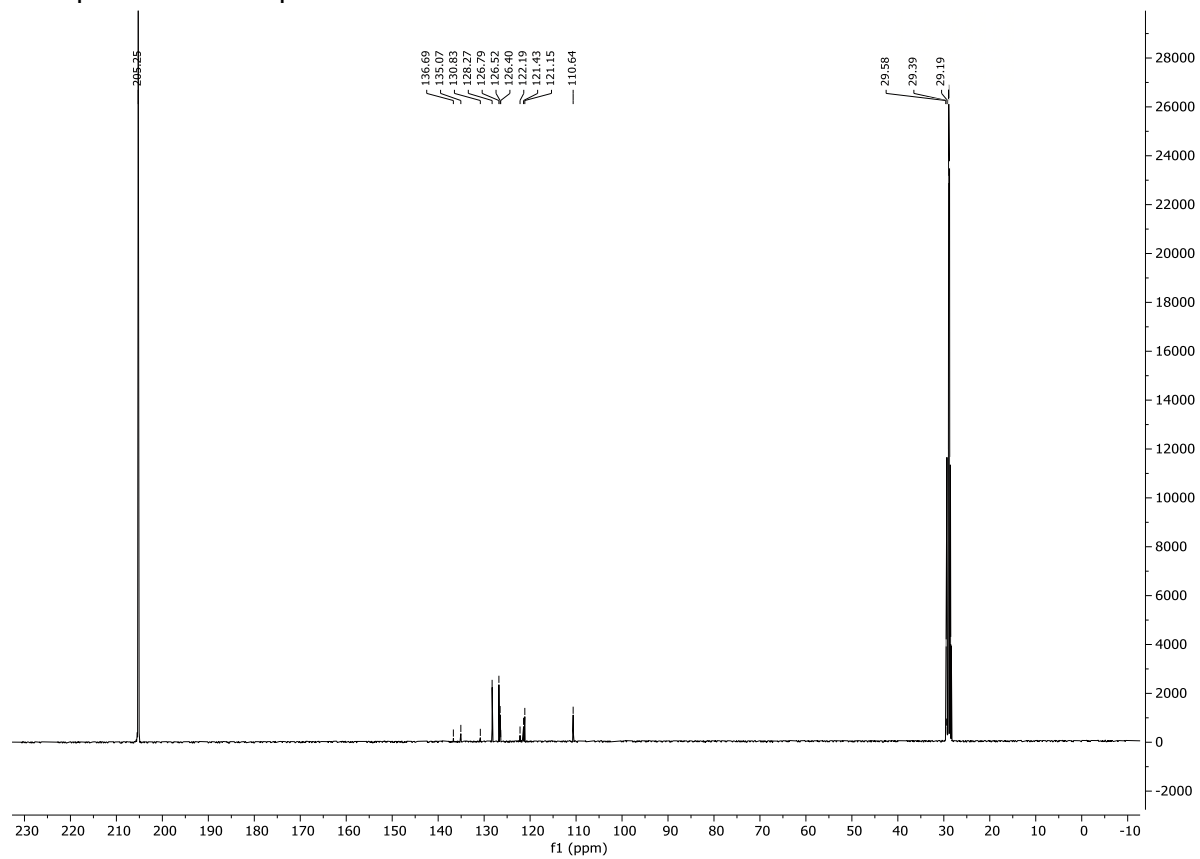
Average Purity = **95.01%**
Assuming sample weight: 2.988 mg, and mol weight: 209.68
Using Reference Compound: Ethyl 4-(dimethylamino)benzoate (2.621 mg, 99% purity,
Mol Weight=193.24)
Sample Integral 1: 3.21894 - 3.32859 ppm, value = 0.99413 (1 nuclides) - Purity =
95%
Reference Integral: 3.02862 - 3.07287 ppm, value = 5.91591 (6 nuclides)



¹H spectrum of compound 15:

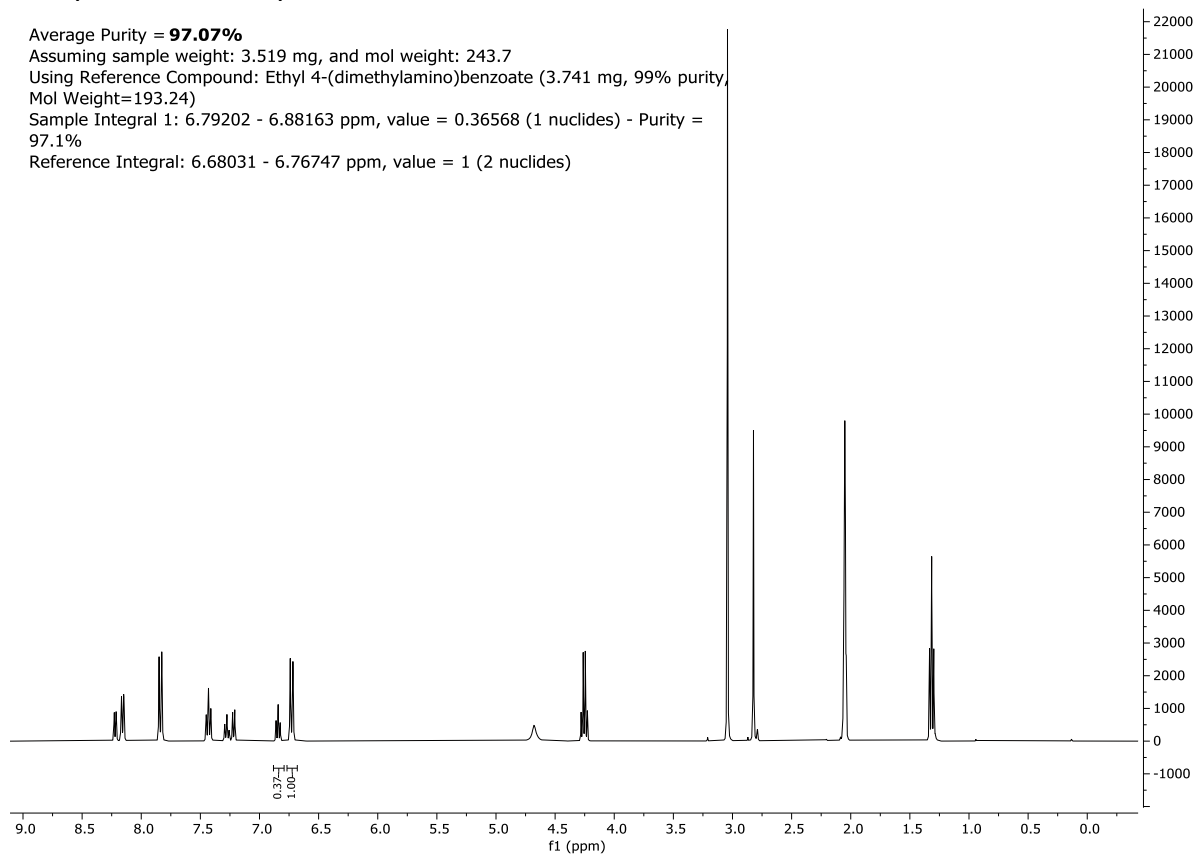


¹³C spectrum of compound **15**:

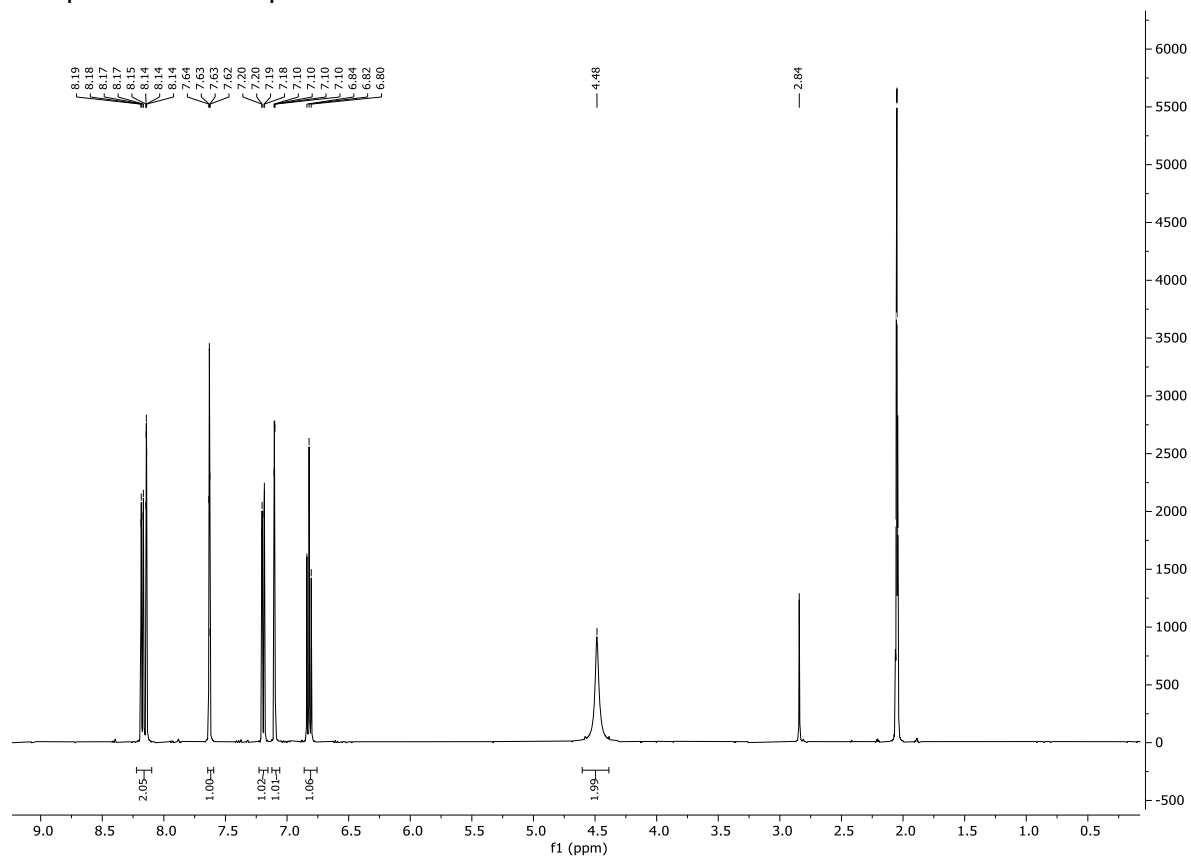


¹³C spectrum of compound **15**:

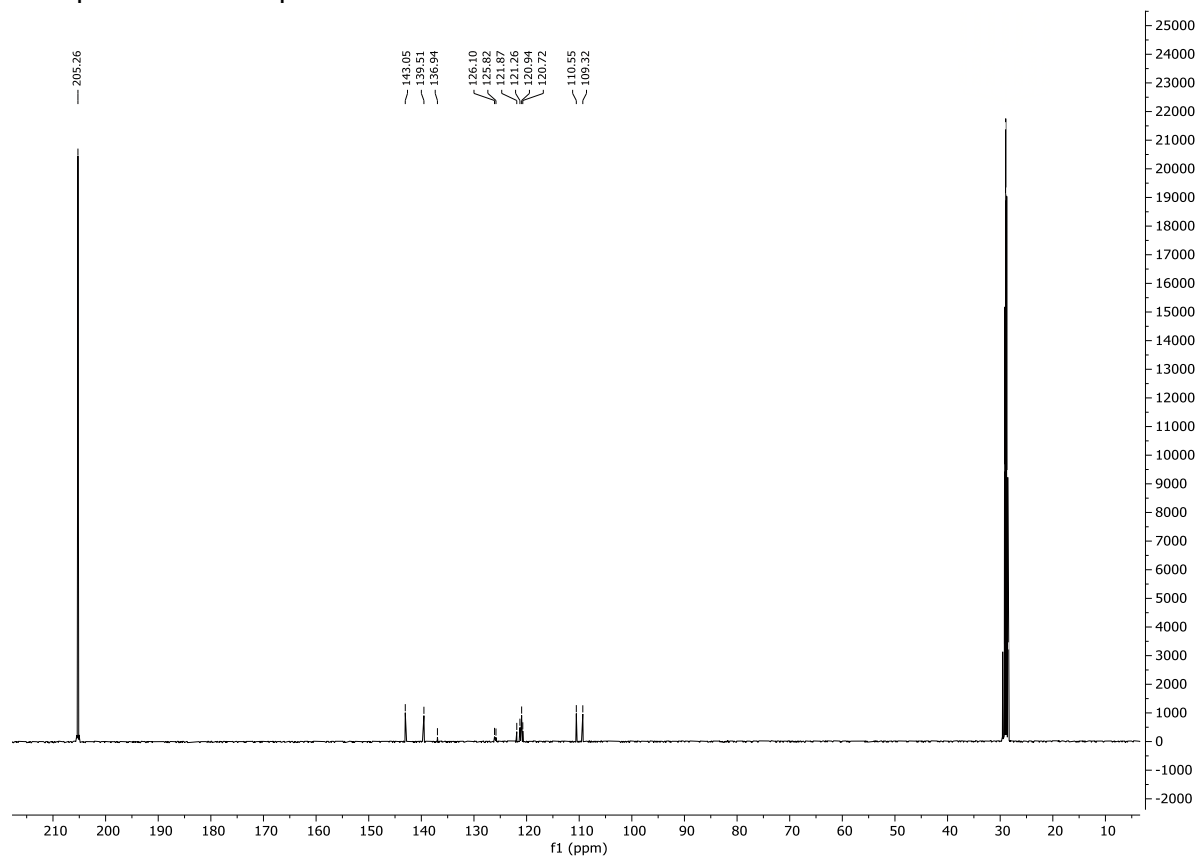
Average Purity = **97.07%**
Assuming sample weight: 3.519 mg, and mol weight: 243.7
Using Reference Compound: Ethyl 4-(dimethylamino)benzoate (3.741 mg, 99% purity,
Mol Weight=193.24)
Sample Integral 1: 6.79202 - 6.88163 ppm, value = 0.36568 (1 nuclides) - Purity =
97.1%
Reference Integral: 6.68031 - 6.76747 ppm, value = 1 (2 nuclides)



¹H spectrum of compound **16**:



¹³C spectrum of compound **16**:



qHNMR spectrum of compound **16**:

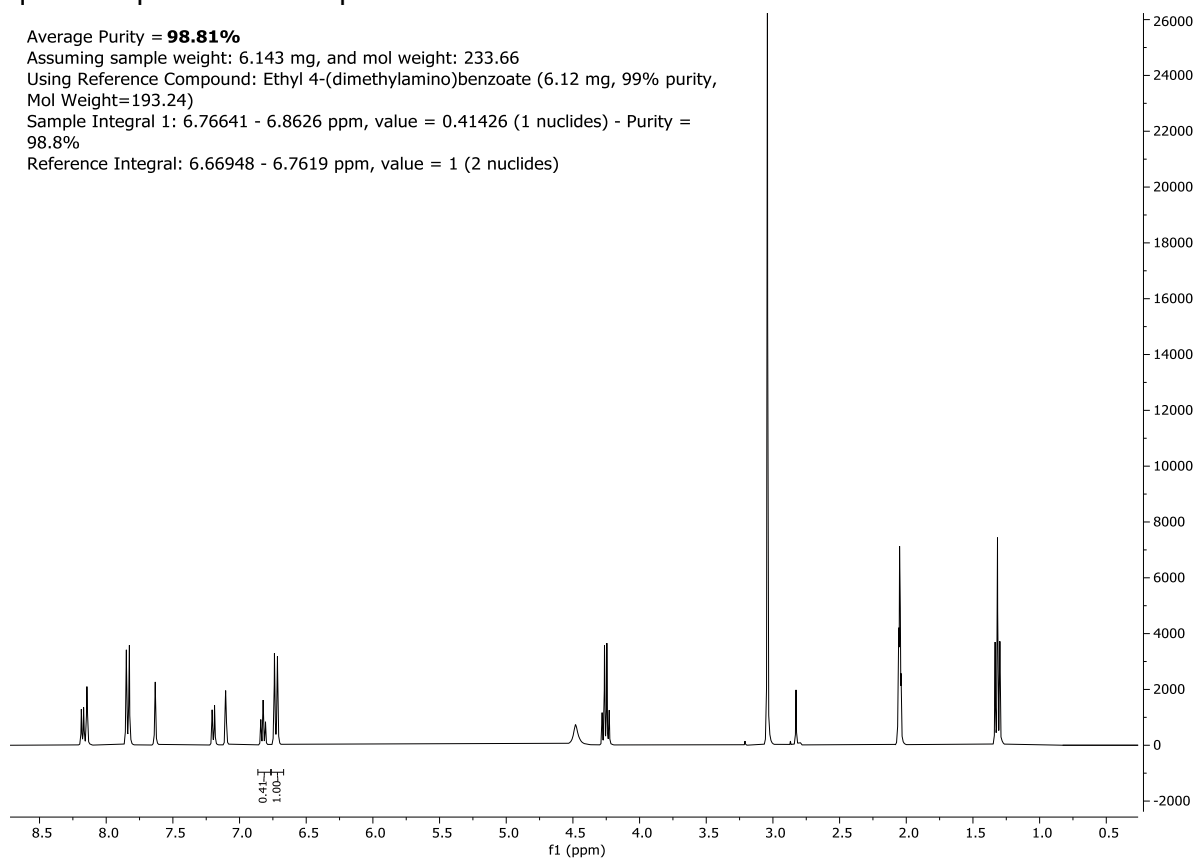
Average Purity = **98.81%**

Assuming sample weight: 6.143 mg, and mol weight: 233.66

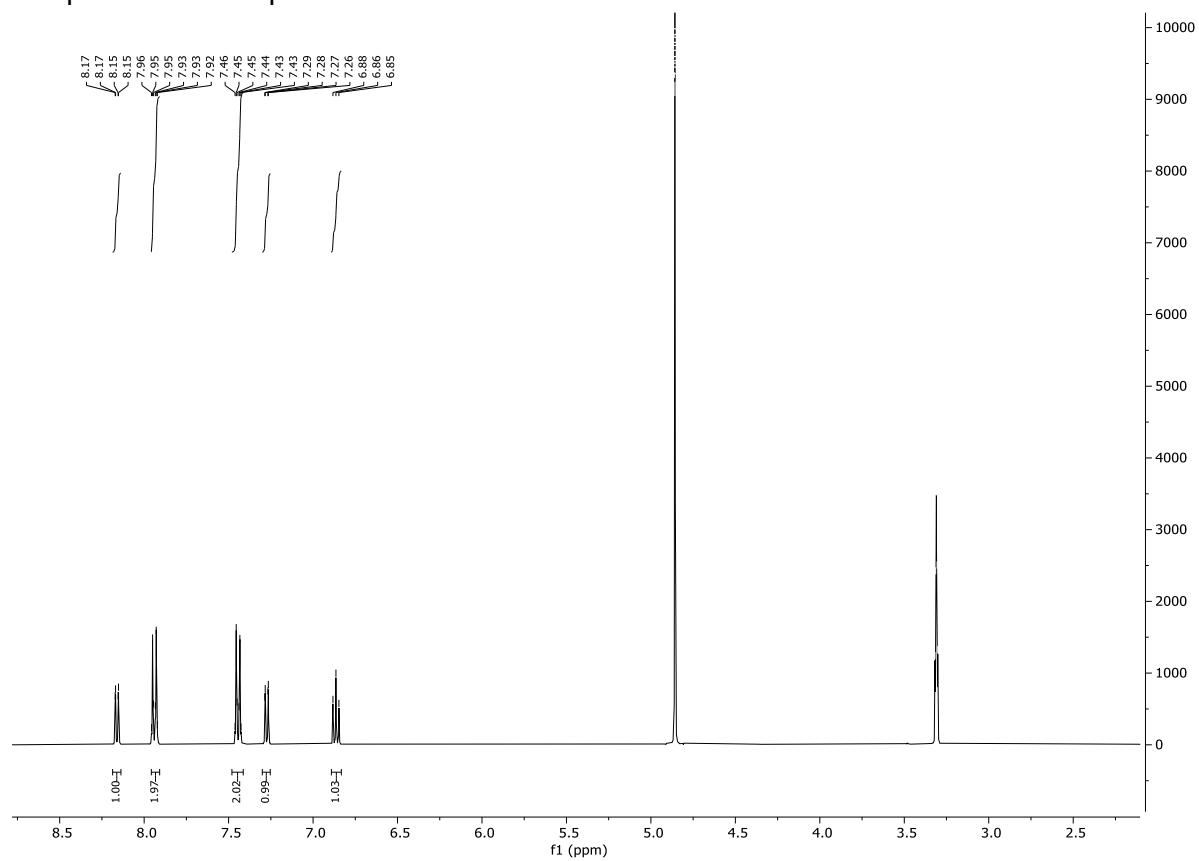
Using Reference Compound: Ethyl 4-(dimethylamino)benzoate (6.12 mg, 99% purity, Mol Weight=193.24)

Sample Integral 1: 6.76641 - 6.8626 ppm, value = 0.41426 (1 nuclides) - Purity = 98.8%

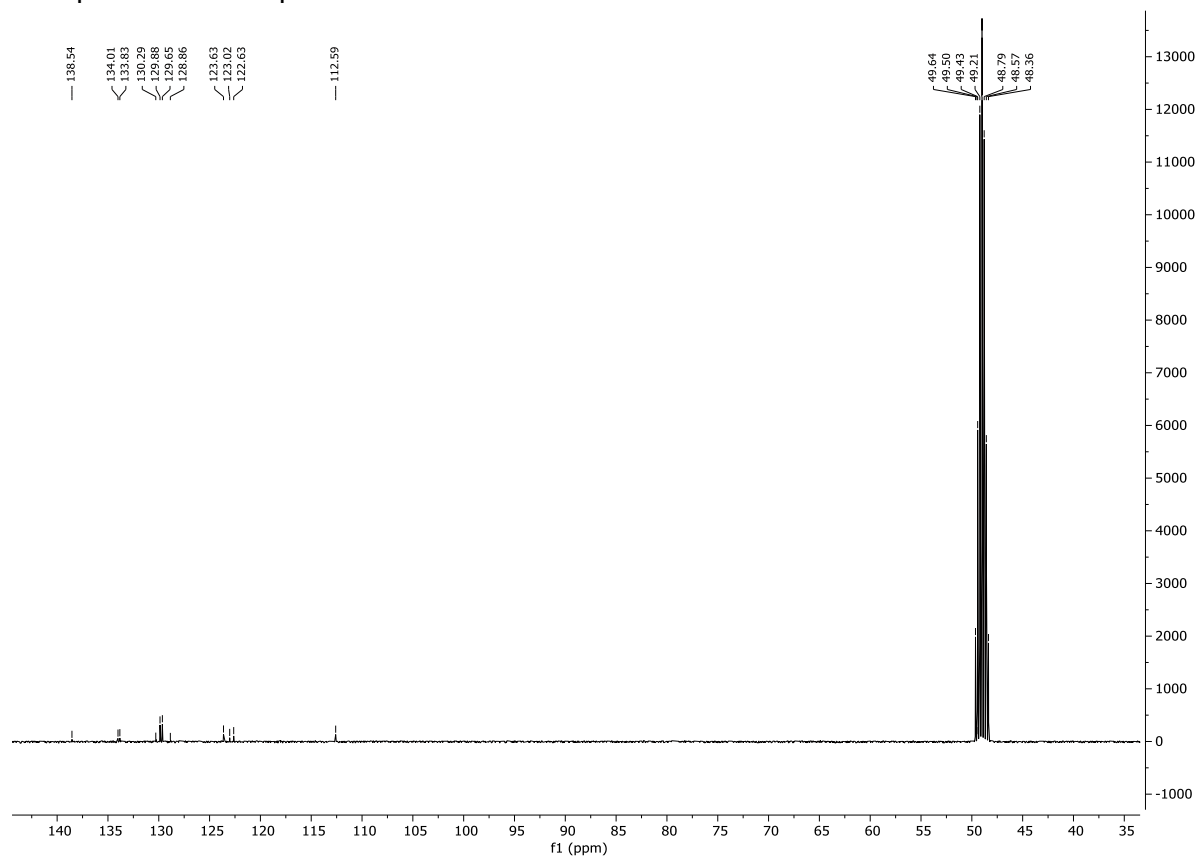
Reference Integral: 6.66948 - 6.7619 ppm, value = 1 (2 nuclides)



¹H spectrum of compound 17:

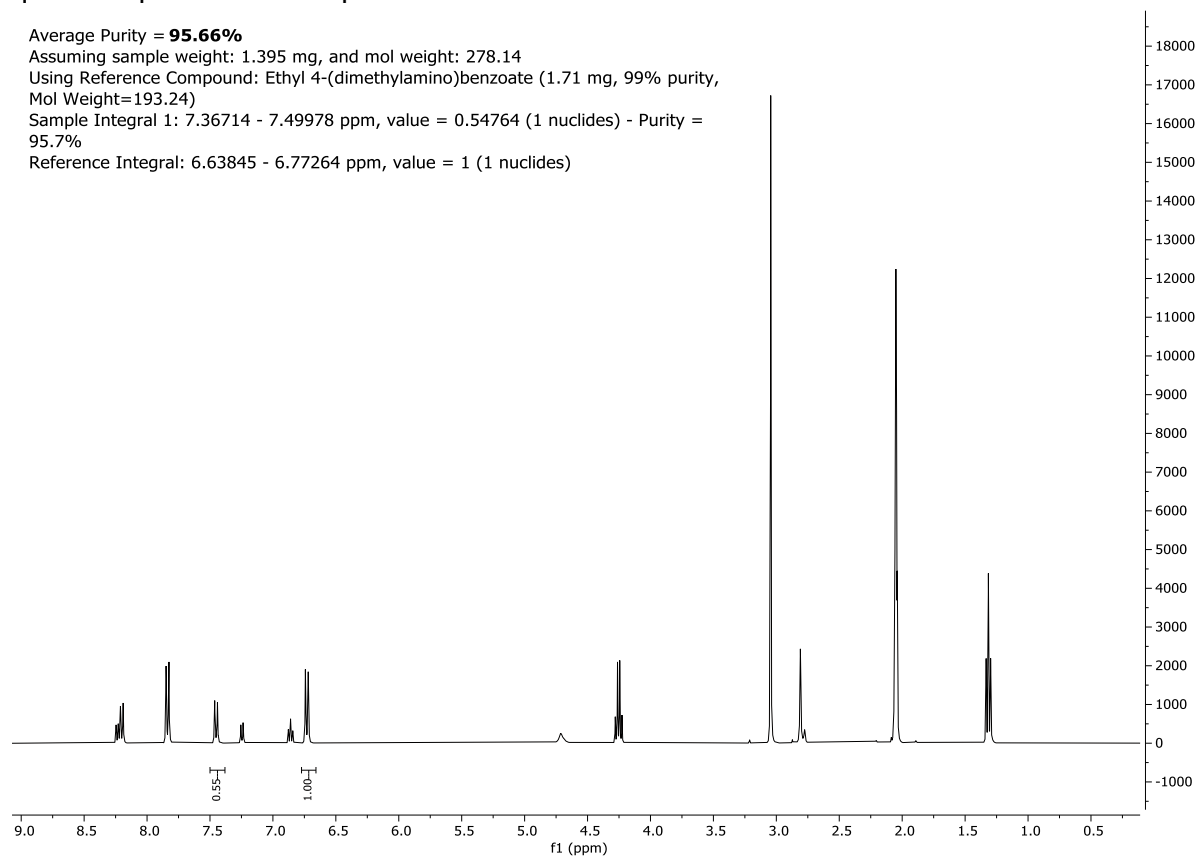


¹³C spectrum of compound **17**:

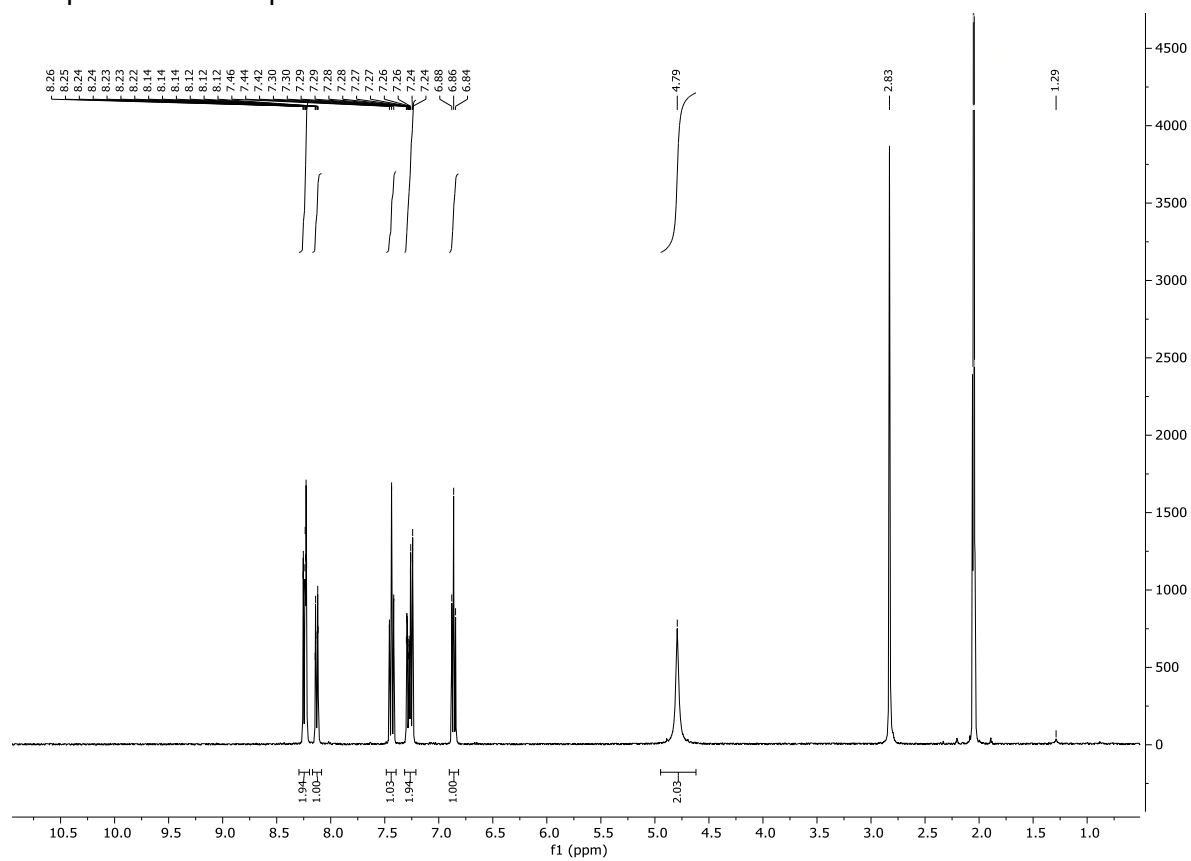


qHNMR spectrum of compound **17**:

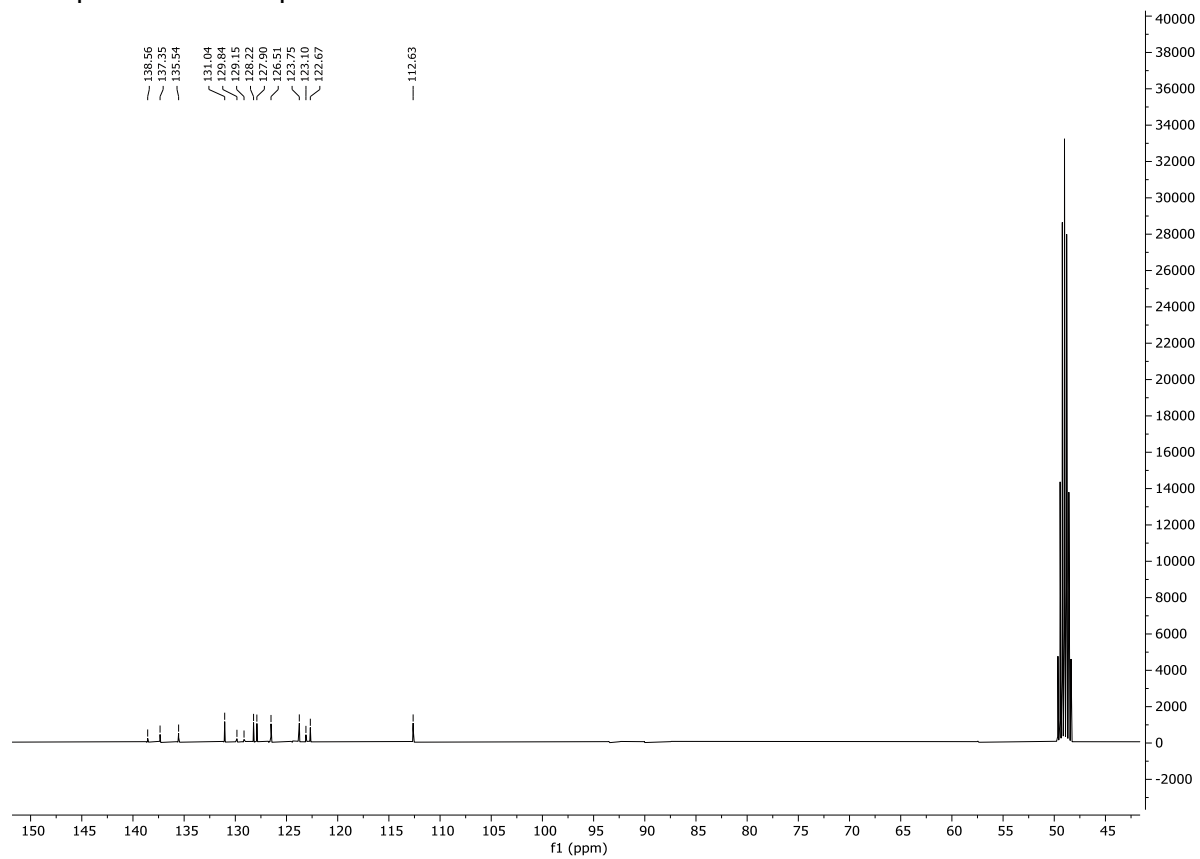
Average Purity = **95.66%**
Assuming sample weight: 1.395 mg, and mol weight: 278.14
Using Reference Compound: Ethyl 4-(dimethylamino)benzoate (1.71 mg, 99% purity, Mol Weight=193.24)
Sample Integral 1: 7.36714 - 7.49978 ppm, value = 0.54764 (1 nuclides) - Purity = 95.7%
Reference Integral: 6.63845 - 6.77264 ppm, value = 1 (1 nuclides)



¹H spectrum of compound 18:



¹³C spectrum of compound **18**:



qHNMR spectrum of compound **18**:

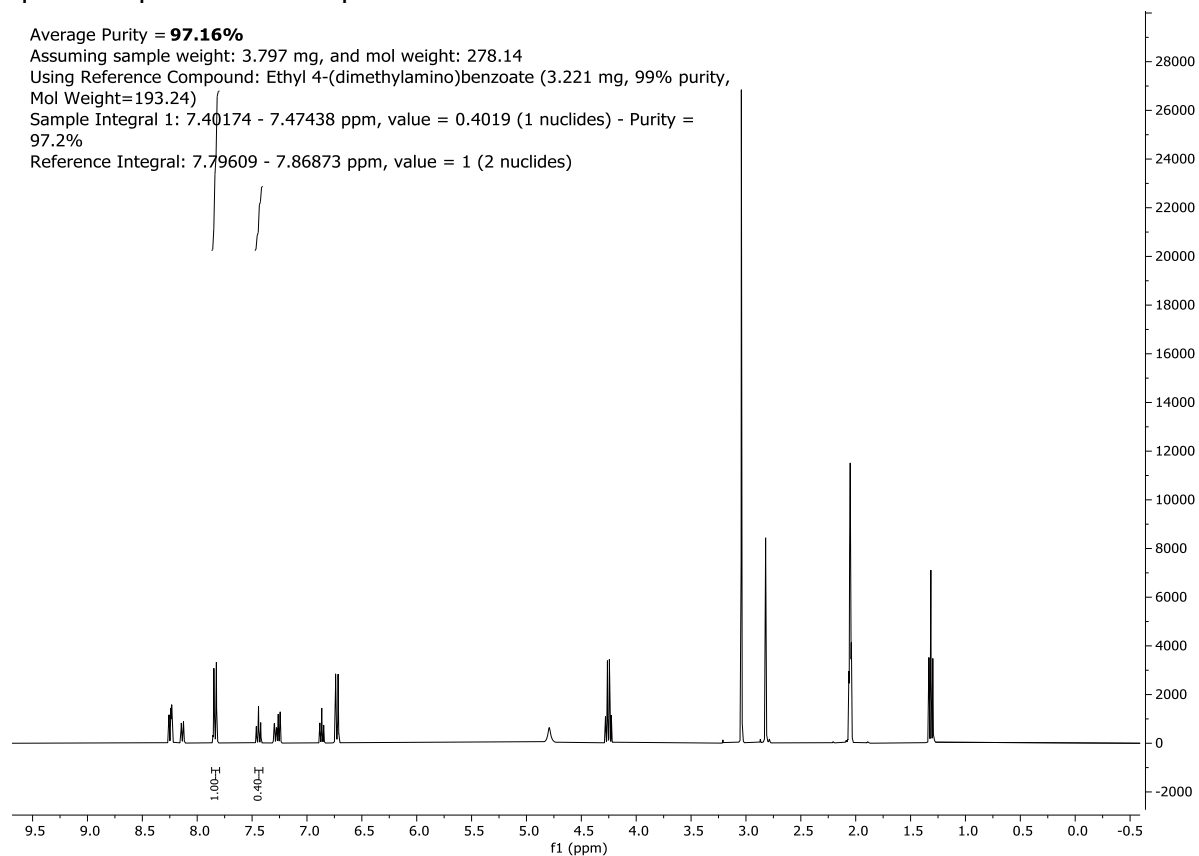
Average Purity = **97.16%**

Assuming sample weight: 3.797 mg, and mol weight: 278.14

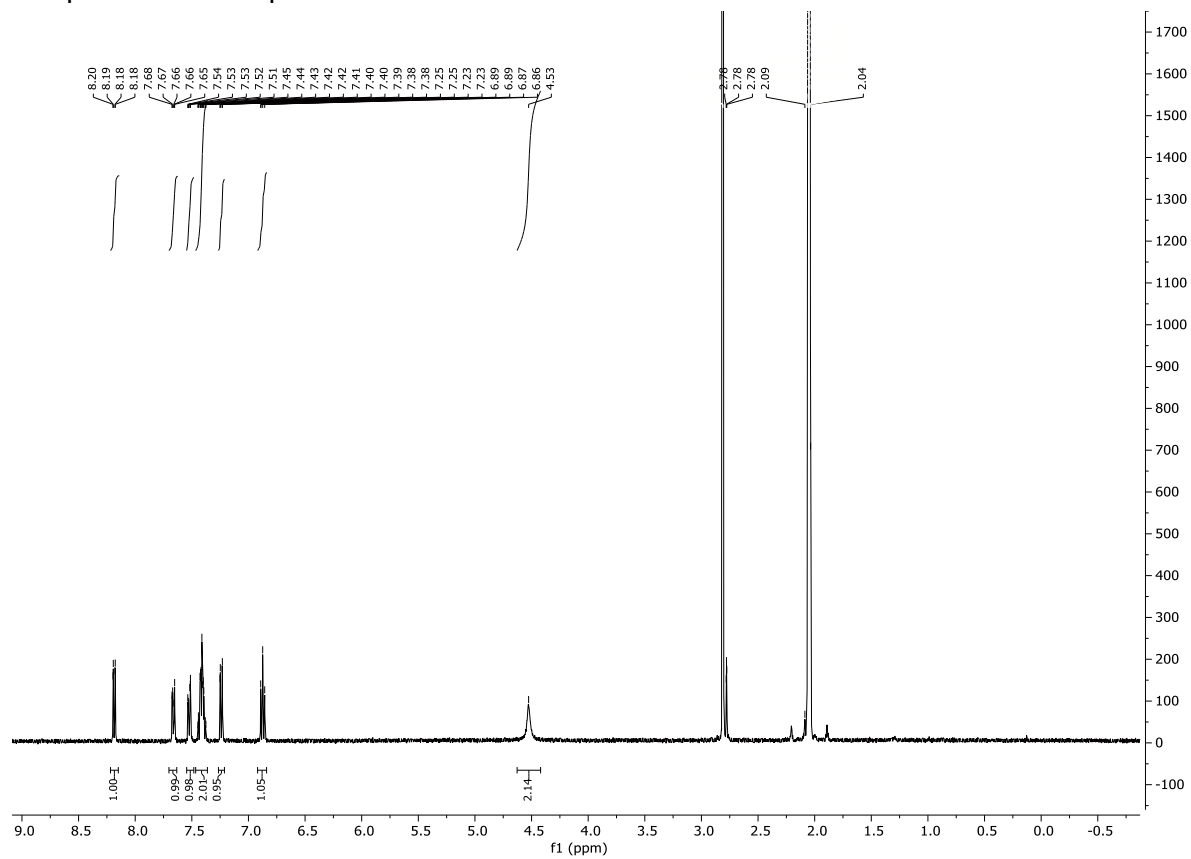
Using Reference Compound: Ethyl 4-(dimethylamino)benzoate (3.221 mg, 99% purity, Mol Weight=193.24)

Sample Integral 1: 7.40174 - 7.47438 ppm, value = 0.4019 (1 nuclides) - Purity = 97.2%

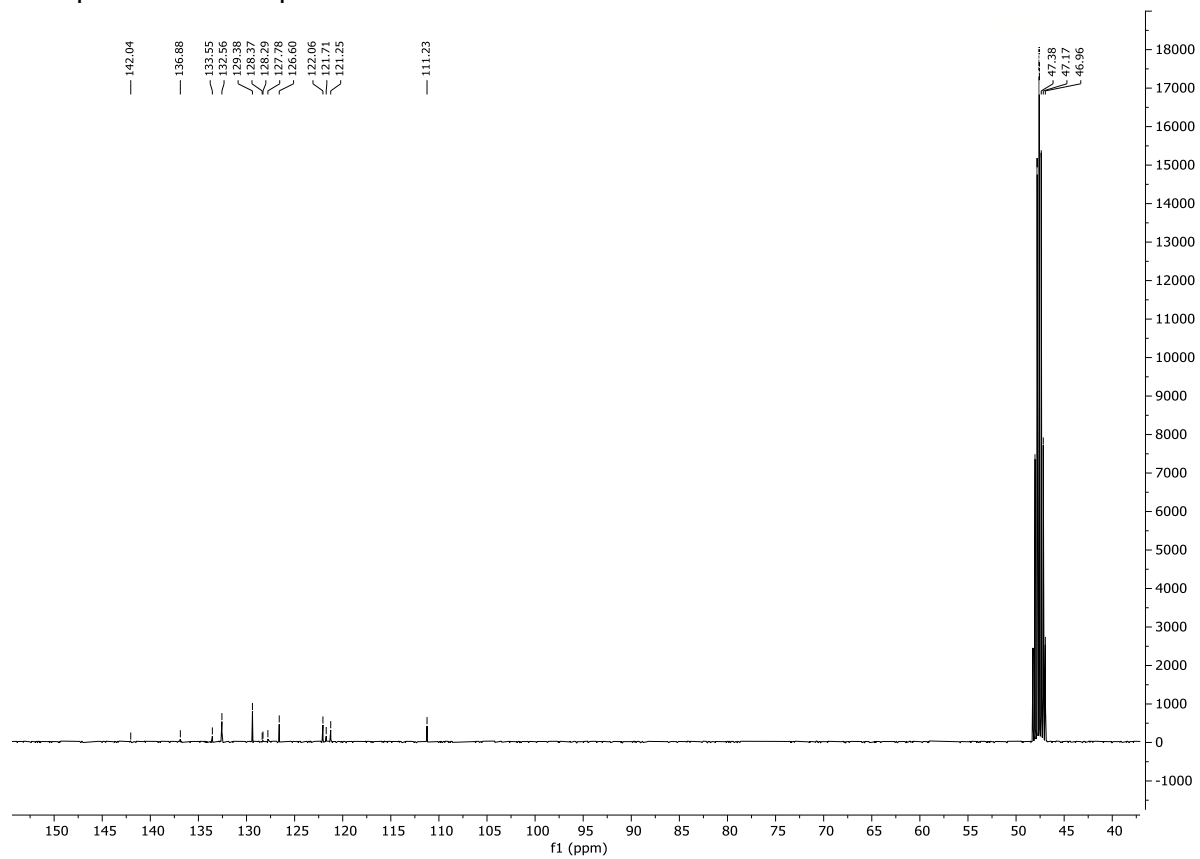
Reference Integral: 7.79609 - 7.86873 ppm, value = 1 (2 nuclides)



¹H spectrum of compound 19:



¹³C spectrum of compound **19**:



qHNMR spectrum of compound **19**:

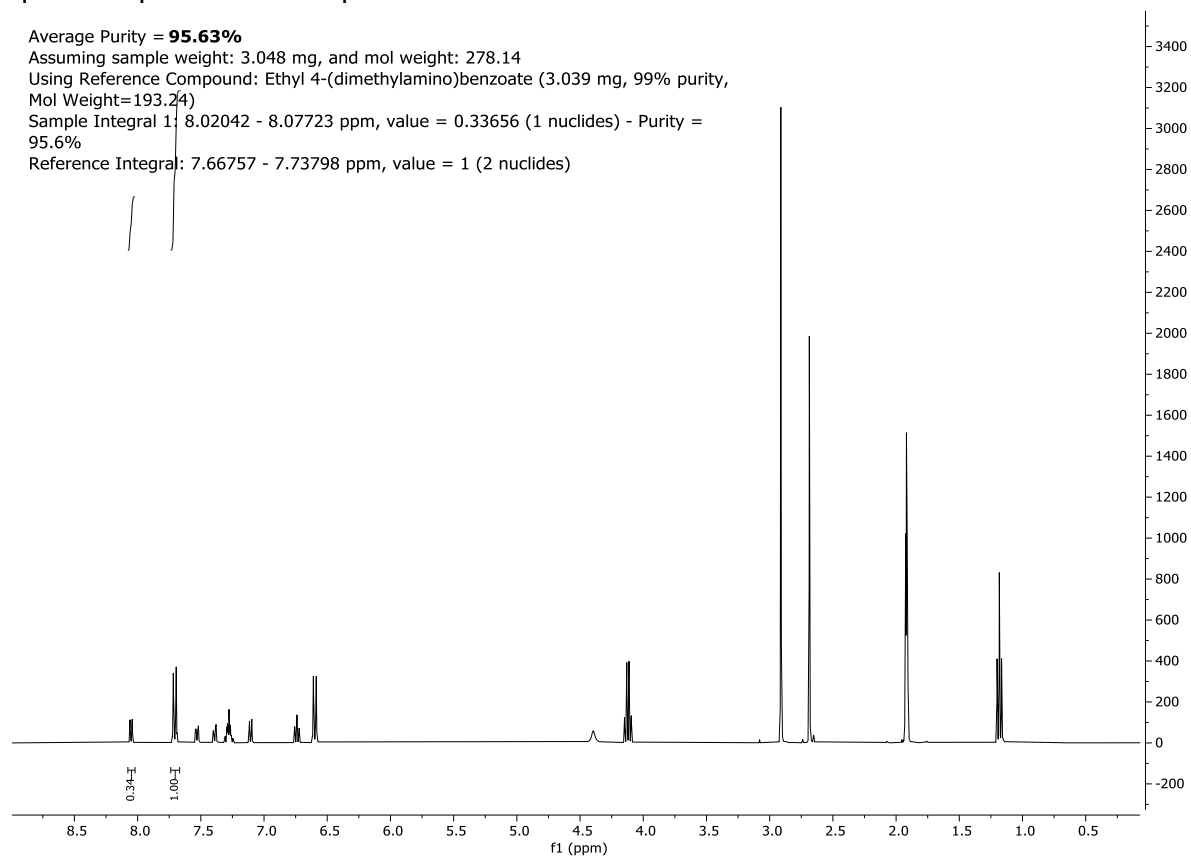
Average Purity = **95.63%**

Assuming sample weight: 3.048 mg, and mol weight: 278.14

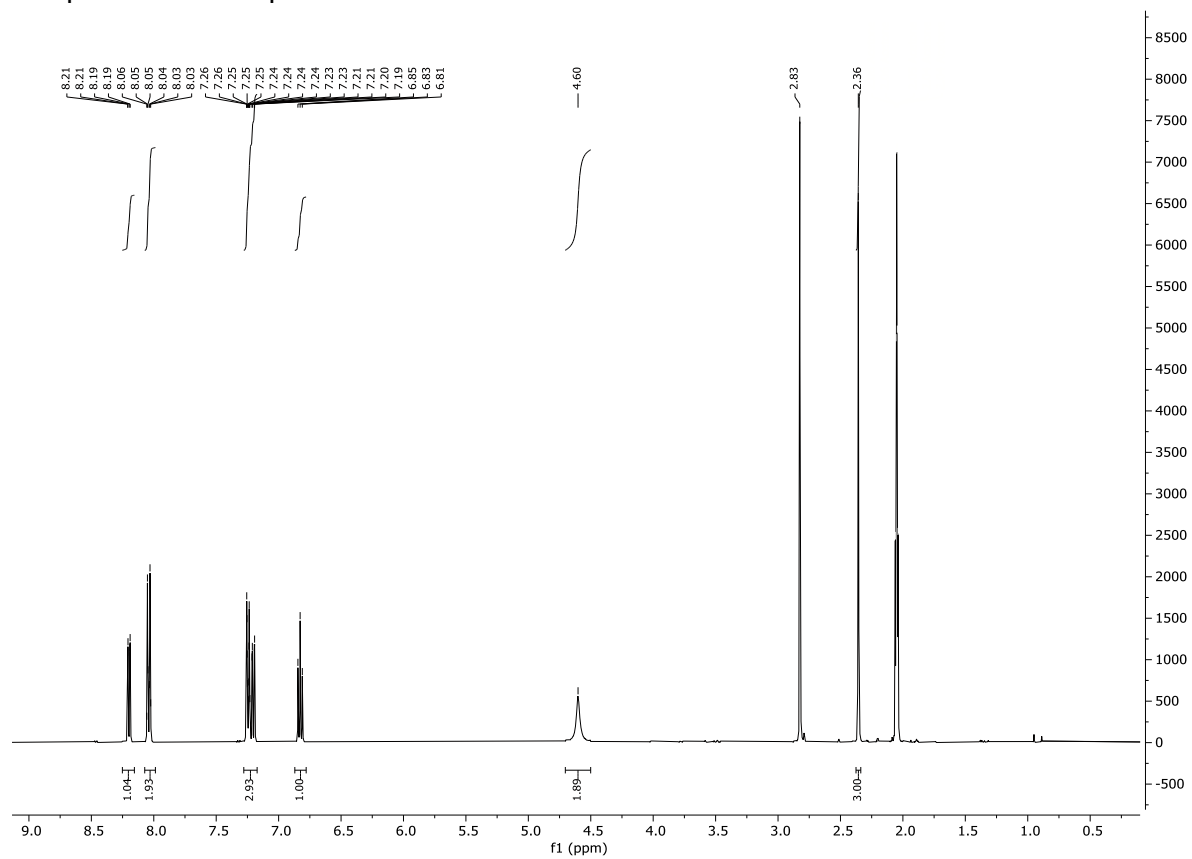
Using Reference Compound: Ethyl 4-(dimethylamino)benzoate (3.039 mg, 99% purity,
Mol Weight=193.24)

Sample Integral 1: 8.02042 - 8.07723 ppm, value = 0.33656 (1 nuclides) - Purity =
95.6%

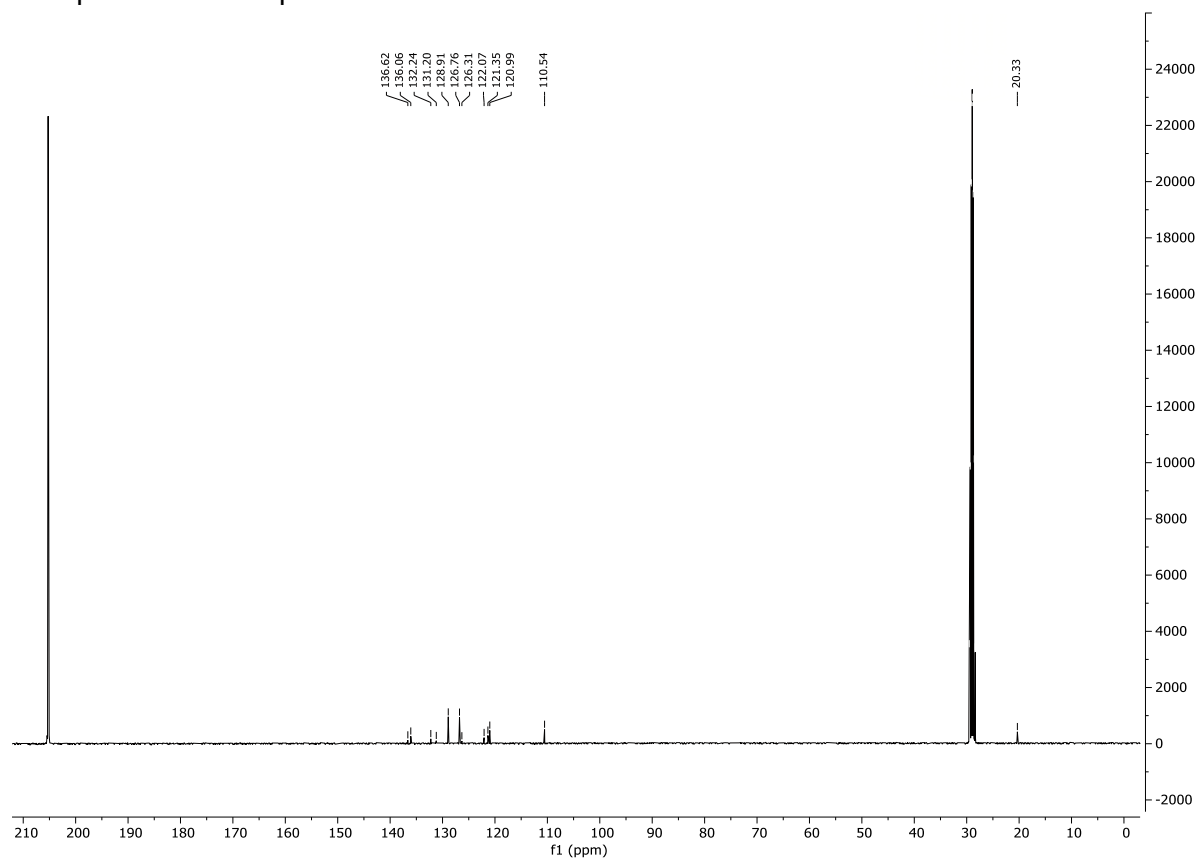
Reference Integral: 7.66757 - 7.73798 ppm, value = 1 (2 nuclides)



¹H spectrum of compound **20**:

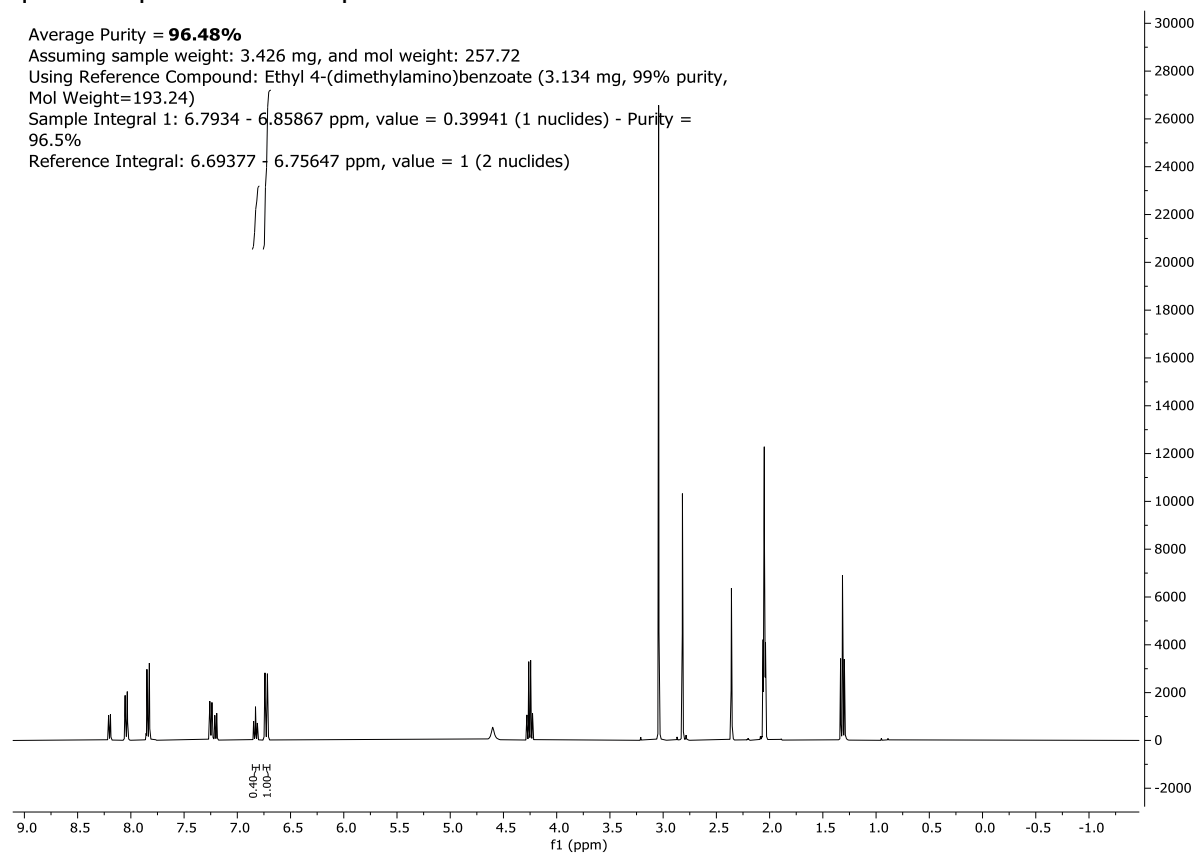


^{13}C spectrum of compound **20**:

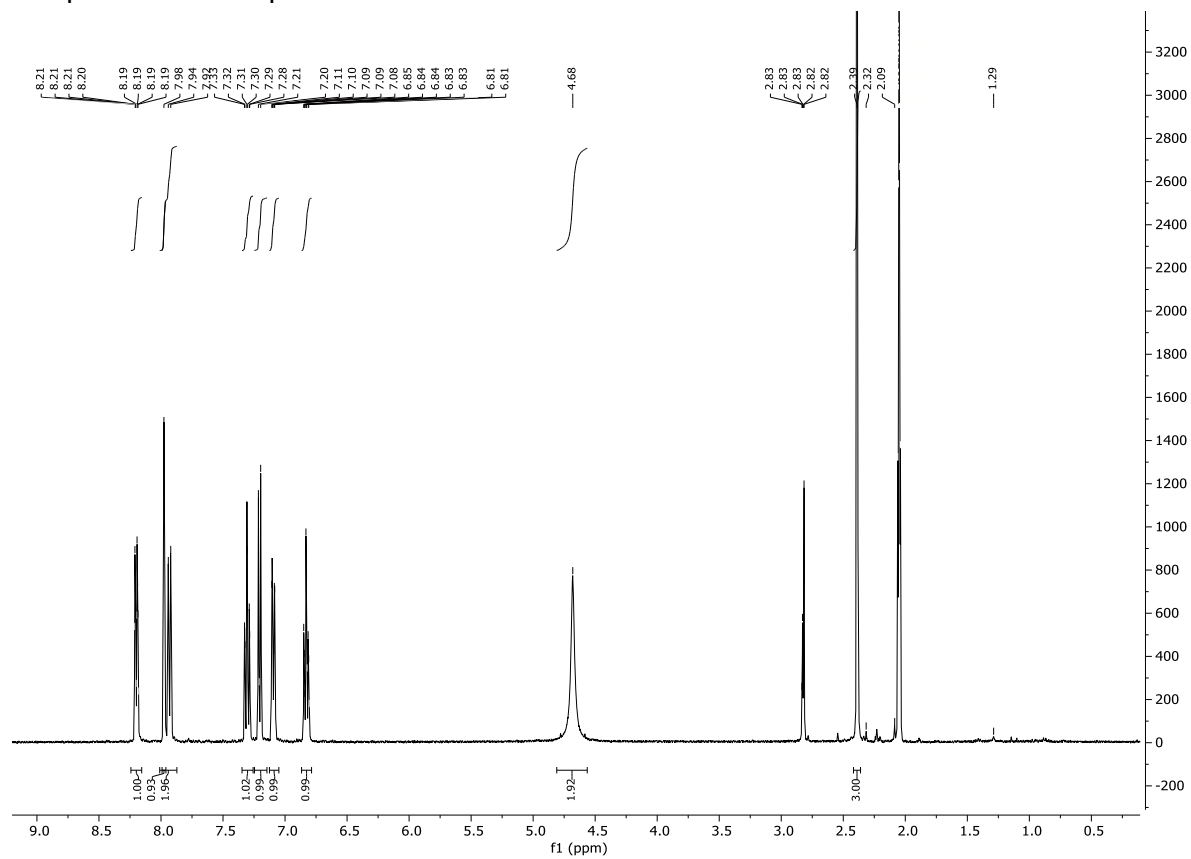


qHNMR spectrum of compound **20**:

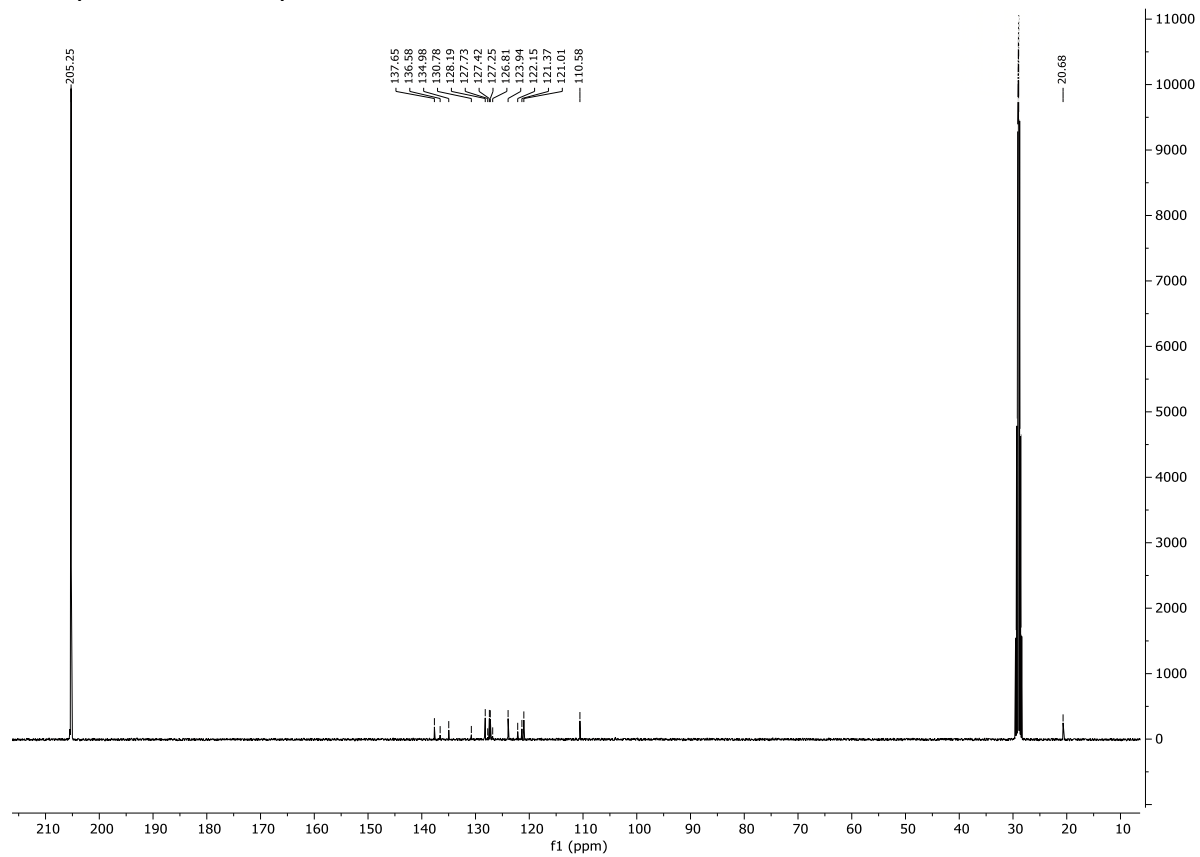
Average Purity = **96.48%**
Assuming sample weight: 3.426 mg, and mol weight: 257.72
Using Reference Compound: Ethyl 4-(dimethylamino)benzoate (3.134 mg, 99% purity,
Mol Weight=193.24)
Sample Integral 1: 6.7934 - 6.85867 ppm, value = 0.39941 (1 nuclides) - Purity = 96.5%
Reference Integral: 6.69377 - 6.75647 ppm, value = 1 (2 nuclides)



¹H spectrum of compound 21:



^{13}C spectrum of compound **21**:



qHNMR spectrum of compound **21**:

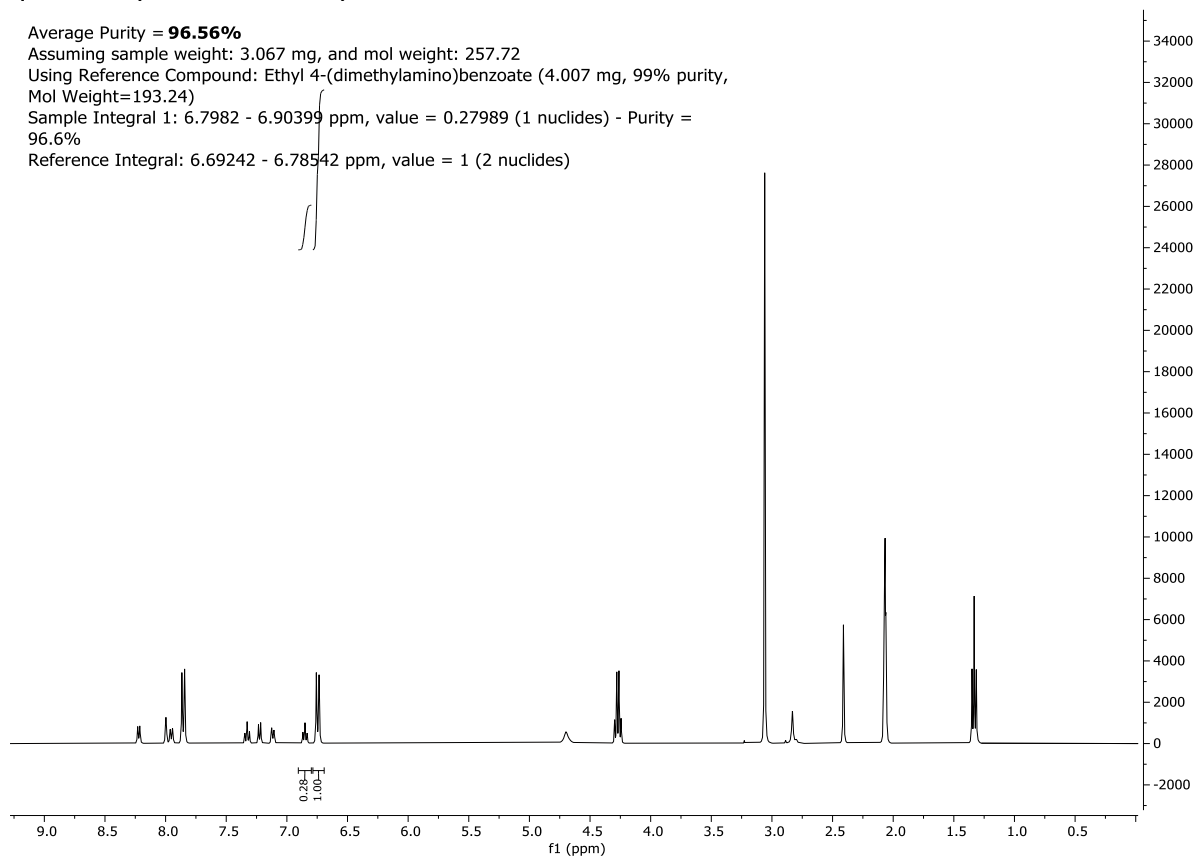
Average Purity = **96.56%**

Assuming sample weight: 3.067 mg, and mol weight: 257.72

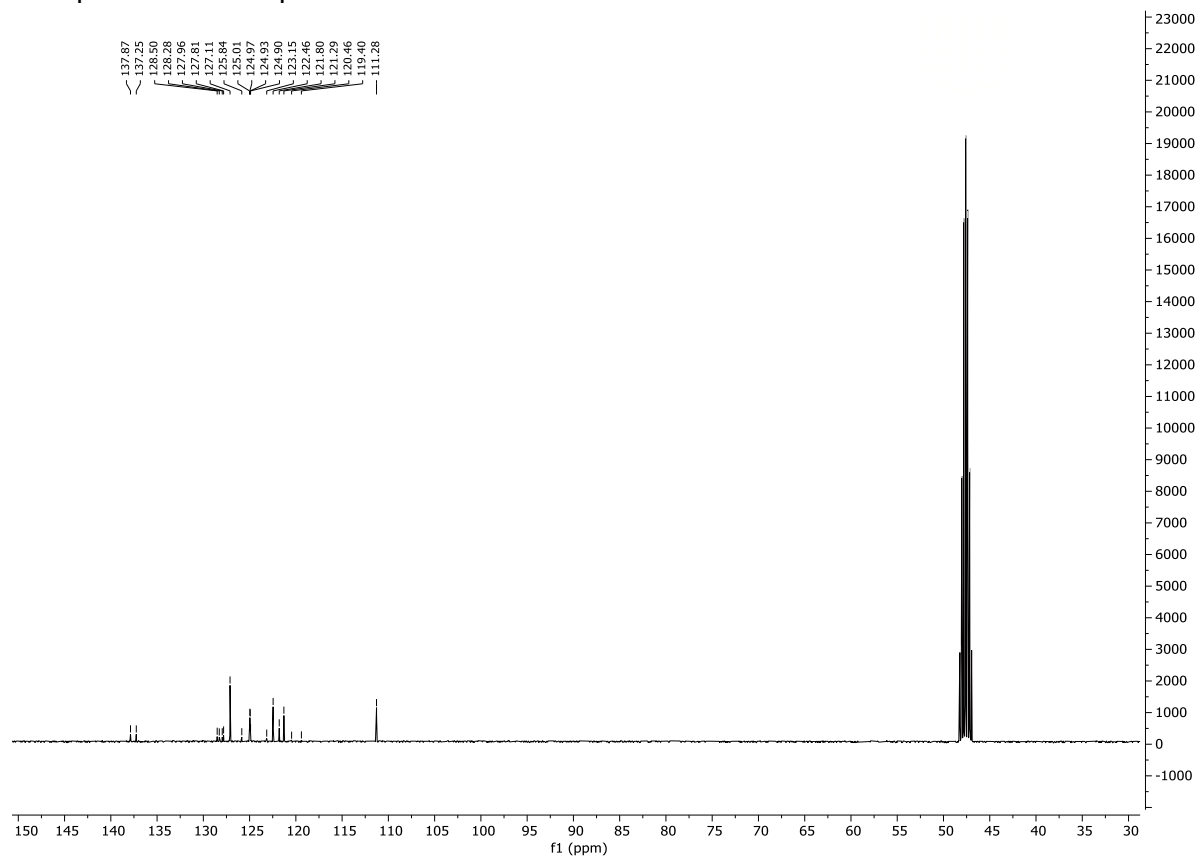
Using Reference Compound: Ethyl 4-(dimethylamino)benzoate (4.007 mg, 99% purity, Mol Weight=193.24)

Sample Integral 1: 6.7982 - 6.90399 ppm, value = 0.27989 (1 nuclides) - Purity = 96.6%

Reference Integral: 6.69242 - 6.78542 ppm, value = 1 (2 nuclides)



¹³C spectrum of compound **22**:



qHNMR spectrum of compound **22**:

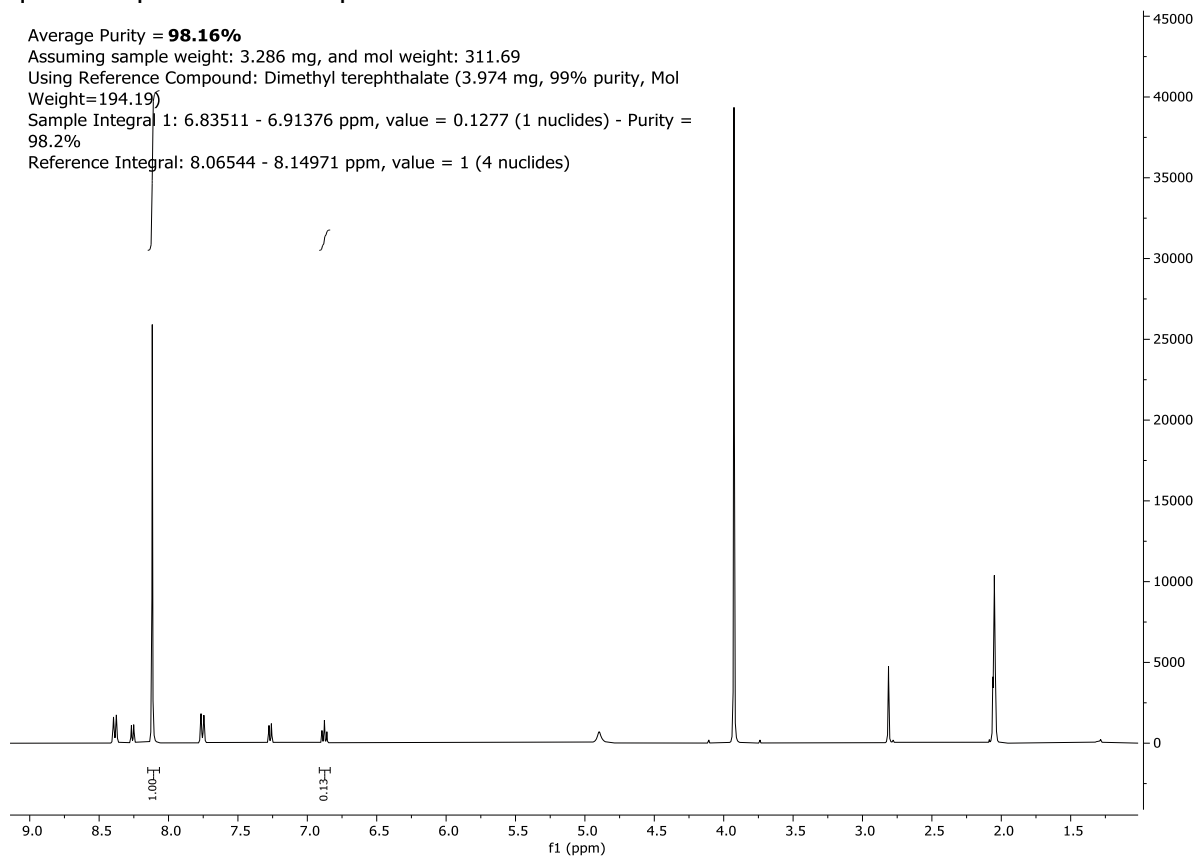
Average Purity = **98.16%**

Assuming sample weight: 3.286 mg, and mol weight: 311.69

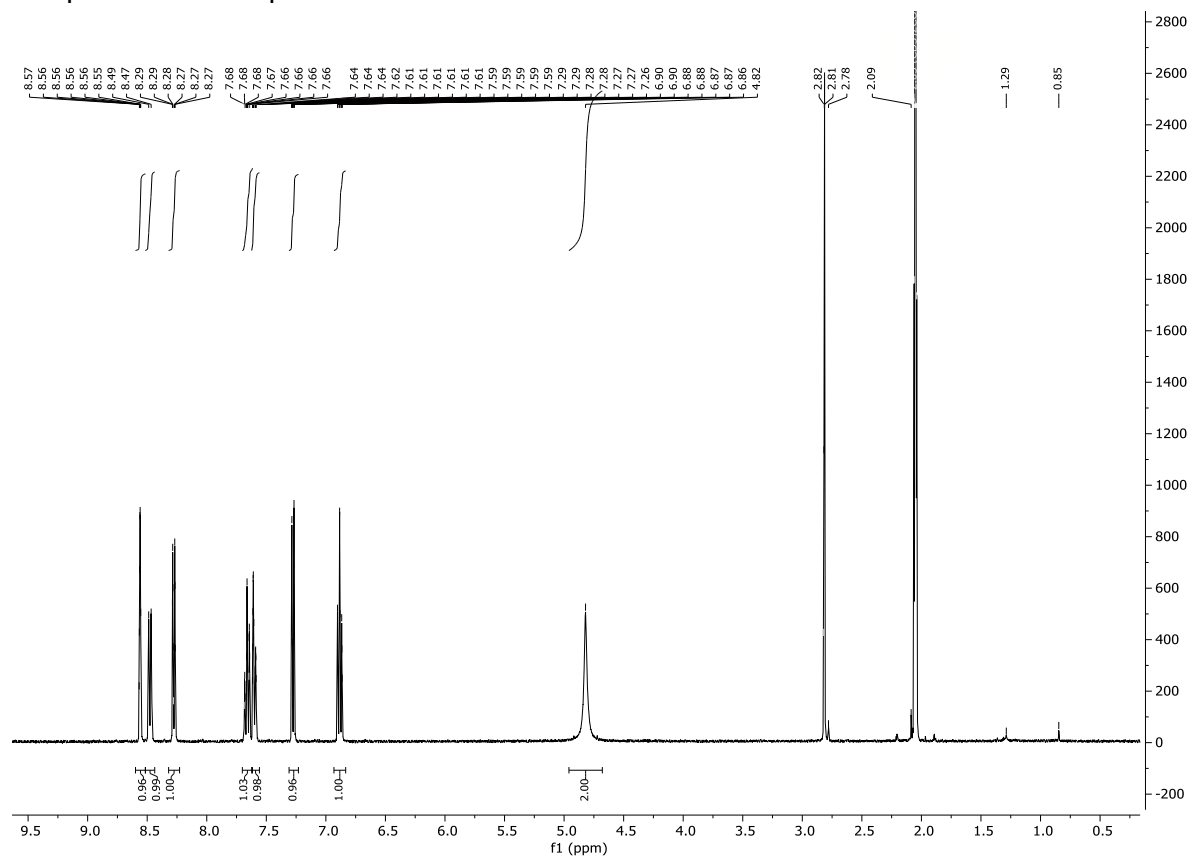
Using Reference Compound: Dimethyl terephthalate (3.974 mg, 99% purity, Mol Weight=194.19)

Sample Integral 1: 6.83511 - 6.91376 ppm, value = 0.1277 (1 nuclides) - Purity = 98.2%

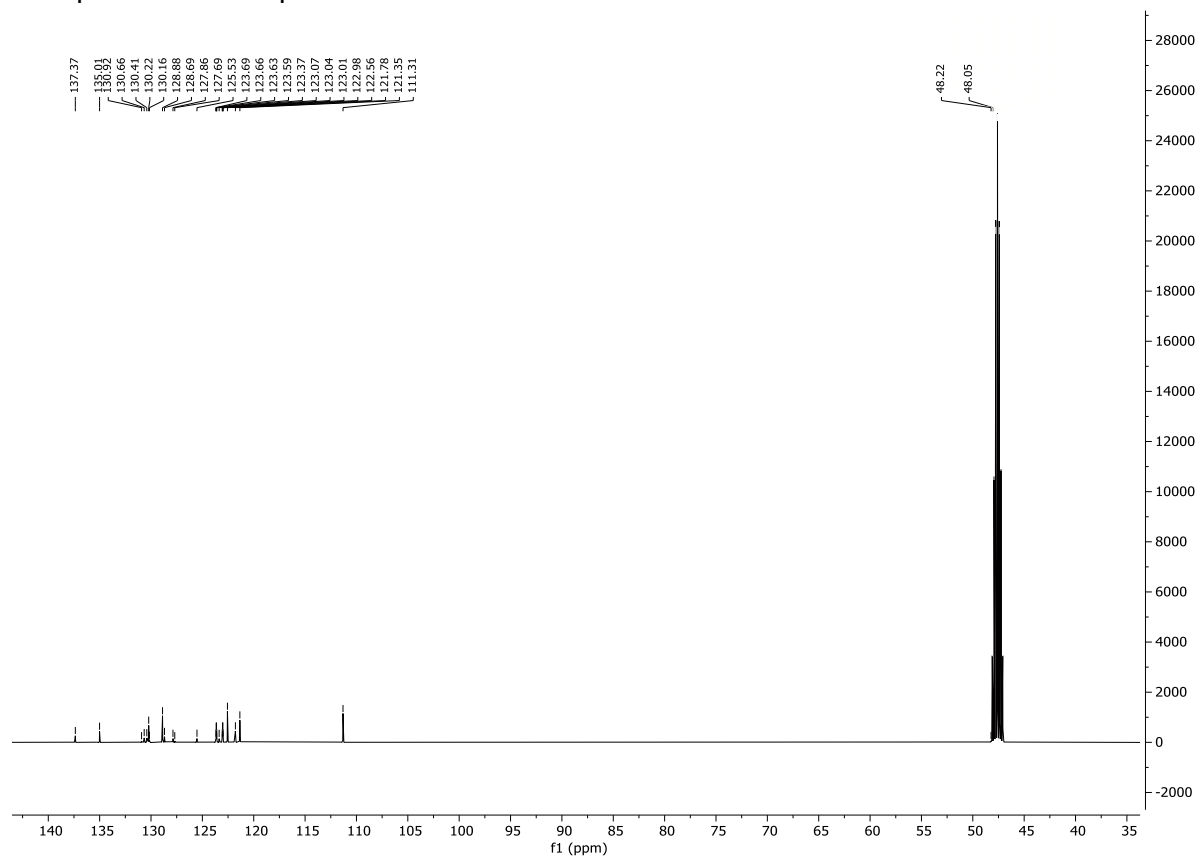
Reference Integral: 8.06544 - 8.14971 ppm, value = 1 (4 nuclides)



¹H spectrum of compound **23**:

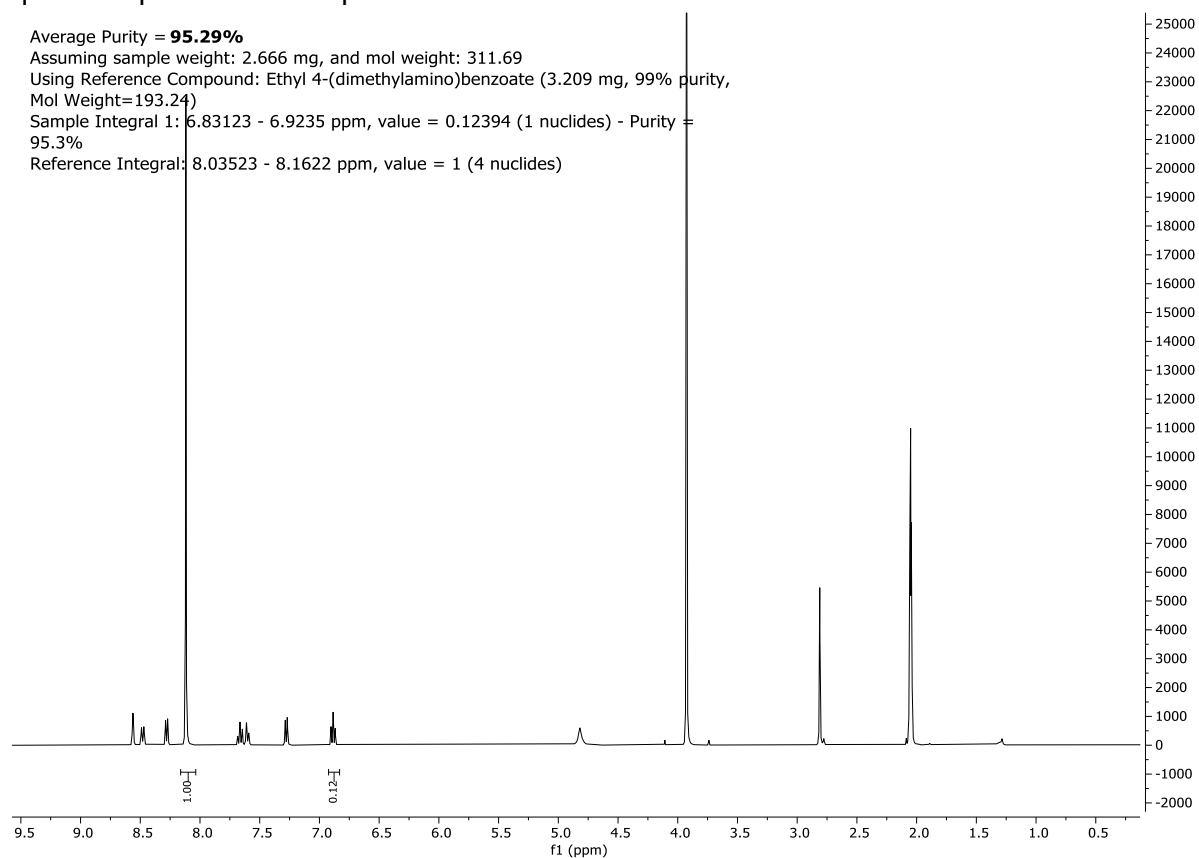


¹³C spectrum of compound **23**:

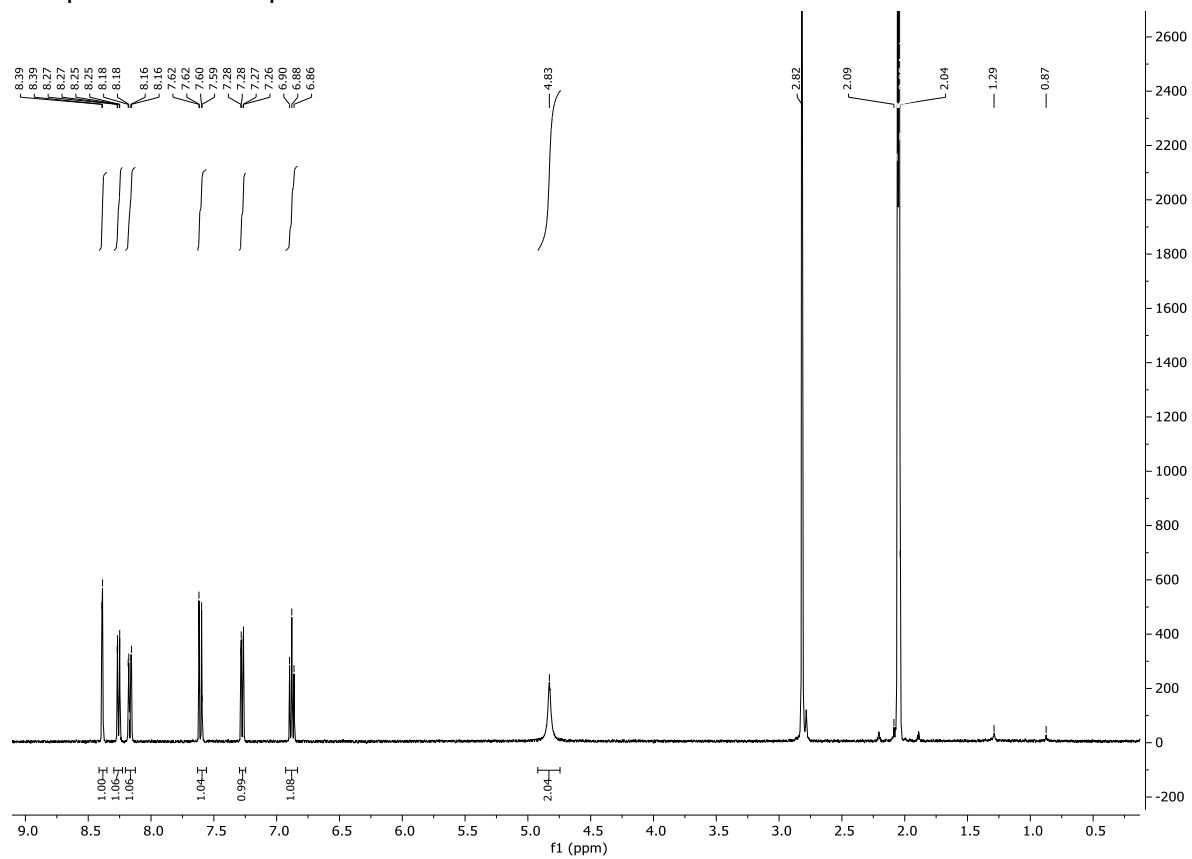


qHNMR spectrum of compound **23**:

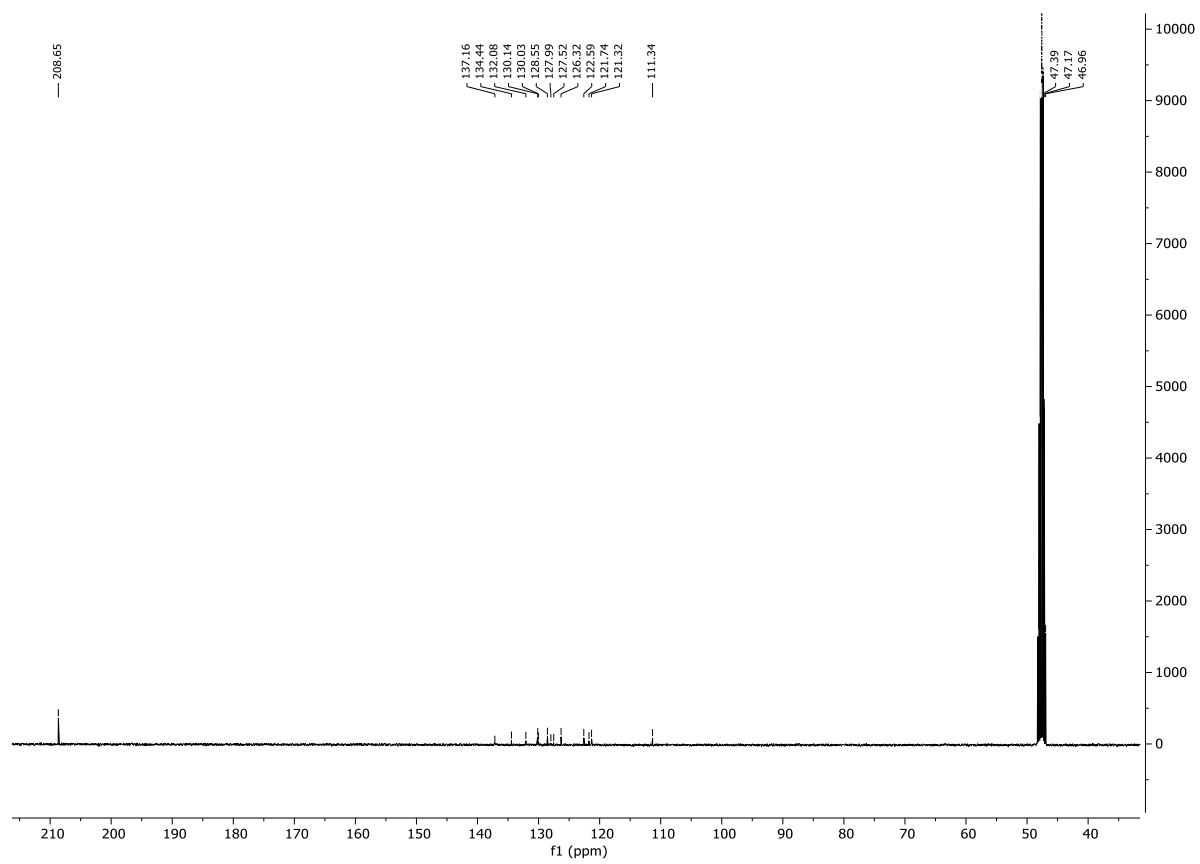
Average Purity = **95.29%**
Assuming sample weight: 2.666 mg, and mol weight: 311.69
Using Reference Compound: Ethyl 4-(dimethylamino)benzoate (3.209 mg, 99% purity,
Mol Weight=193.24)
Sample Integral 1: 6.83123 - 6.9235 ppm, value = 0.12394 (1 nuclides) - Purity =
95.3%
Reference Integral: 8.03523 - 8.1622 ppm, value = 1 (4 nuclides)



¹H spectrum of compound 24:



^{13}C spectrum of compound **24**:



qHNMR spectrum of compound **24**:

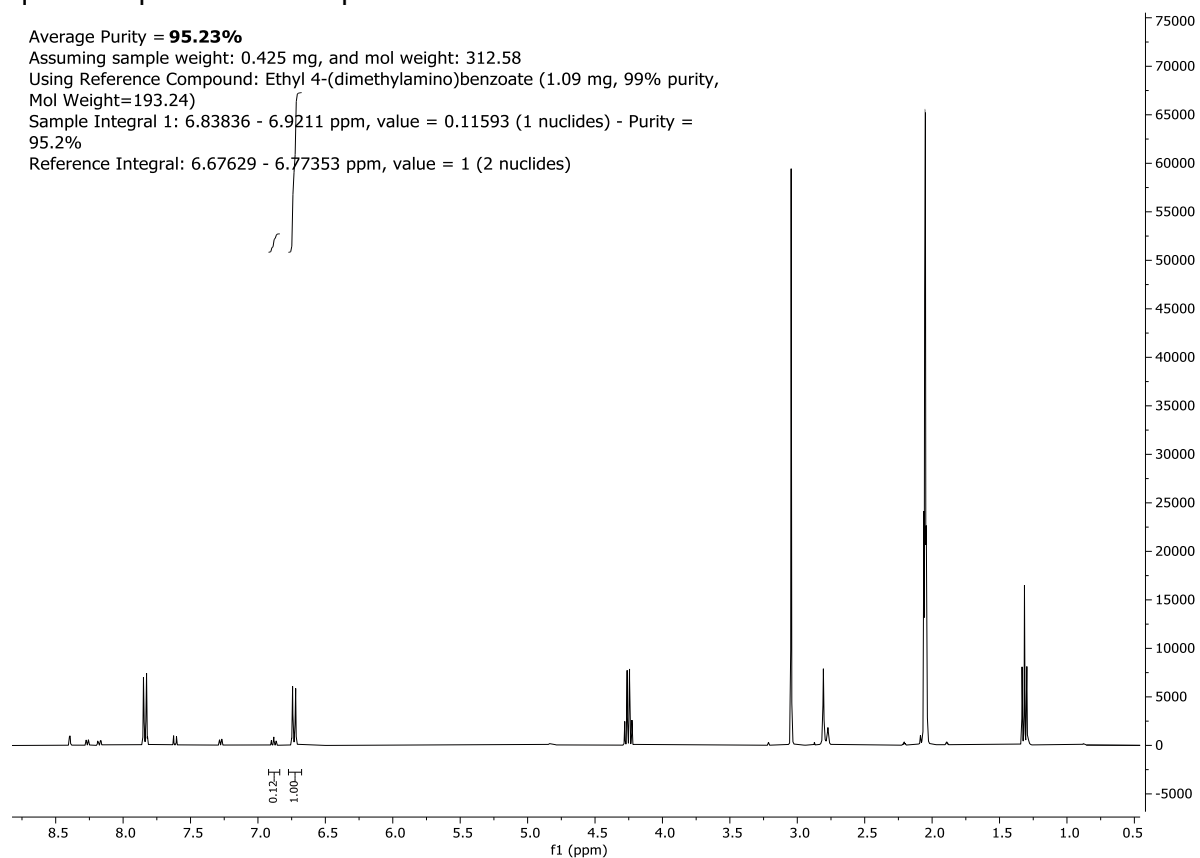
Average Purity = **95.23%**

Assuming sample weight: 0.425 mg, and mol weight: 312.58

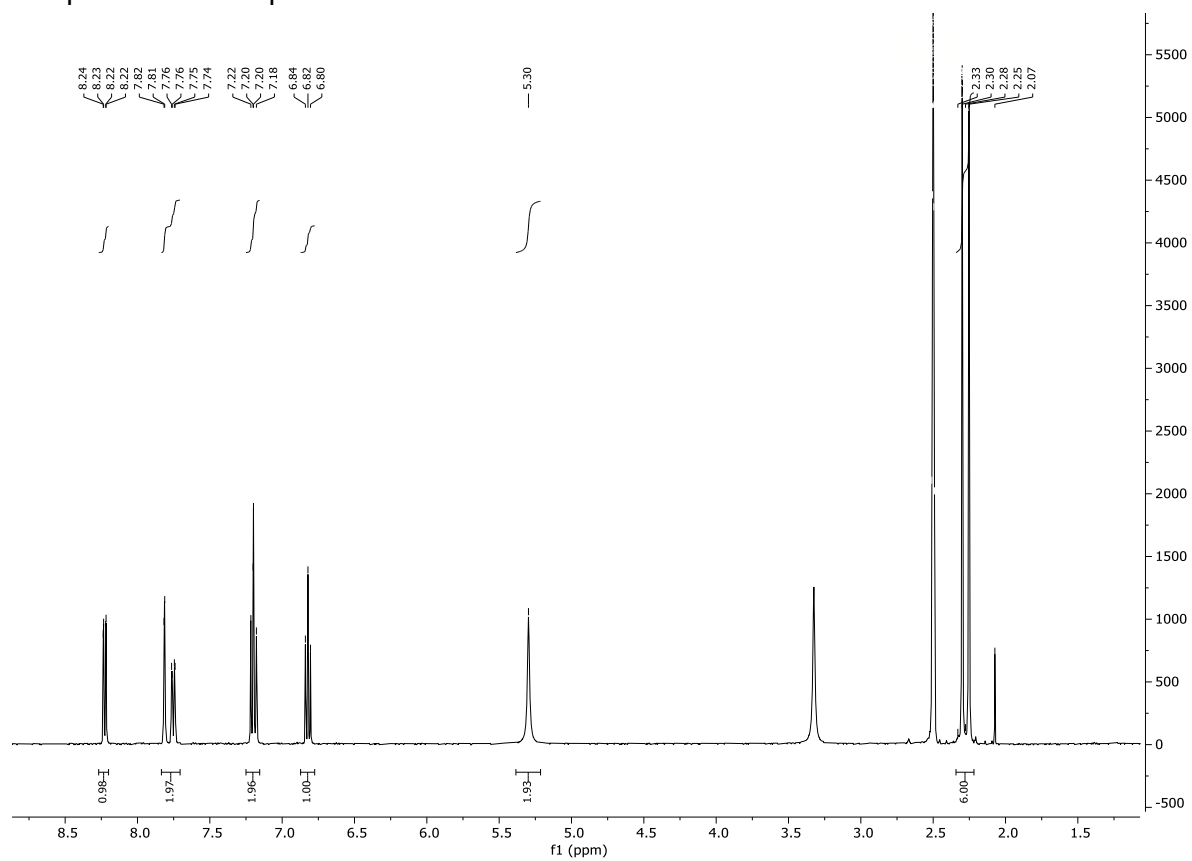
Using Reference Compound: Ethyl 4-(dimethylamino)benzoate (1.09 mg, 99% purity, Mol Weight=193.24)

Sample Integral 1: 6.83836 - 6.92111 ppm, value = 0.11593 (1 nuclides) - Purity = 95.2%

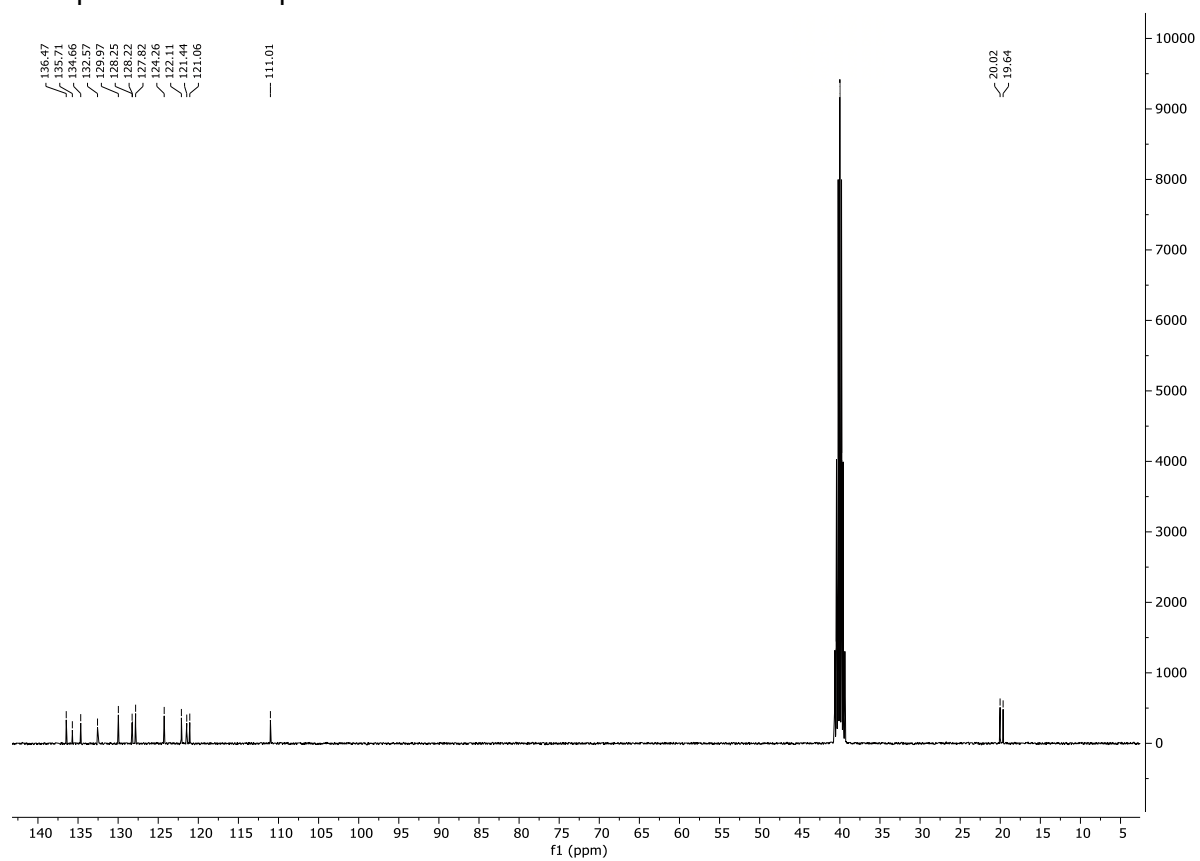
Reference Integral: 6.67629 - 6.77353 ppm, value = 1 (2 nuclides)



¹H spectrum of compound **25**:



¹³C spectrum of compound **25**:



qHNMR spectrum of compound **25**:

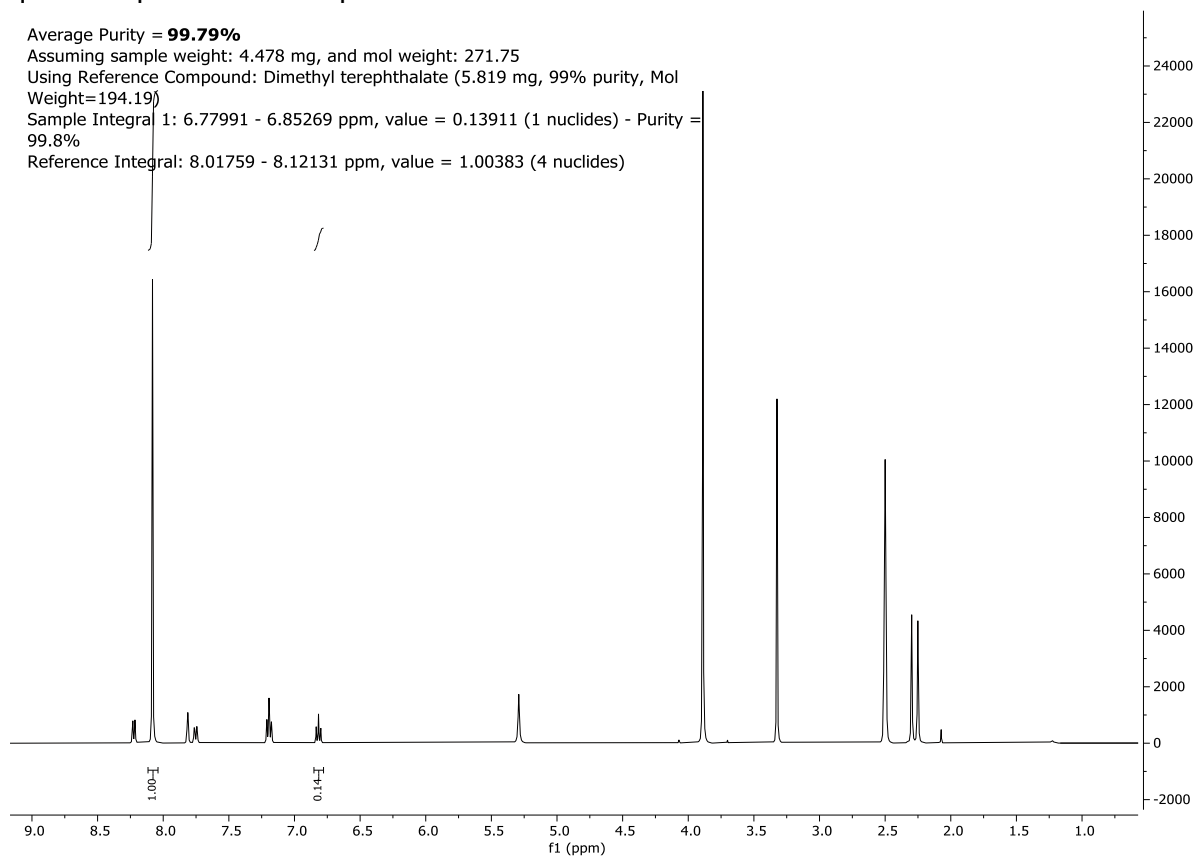
Average Purity = **99.79%**

Assuming sample weight: 4.478 mg, and mol weight: 271.75

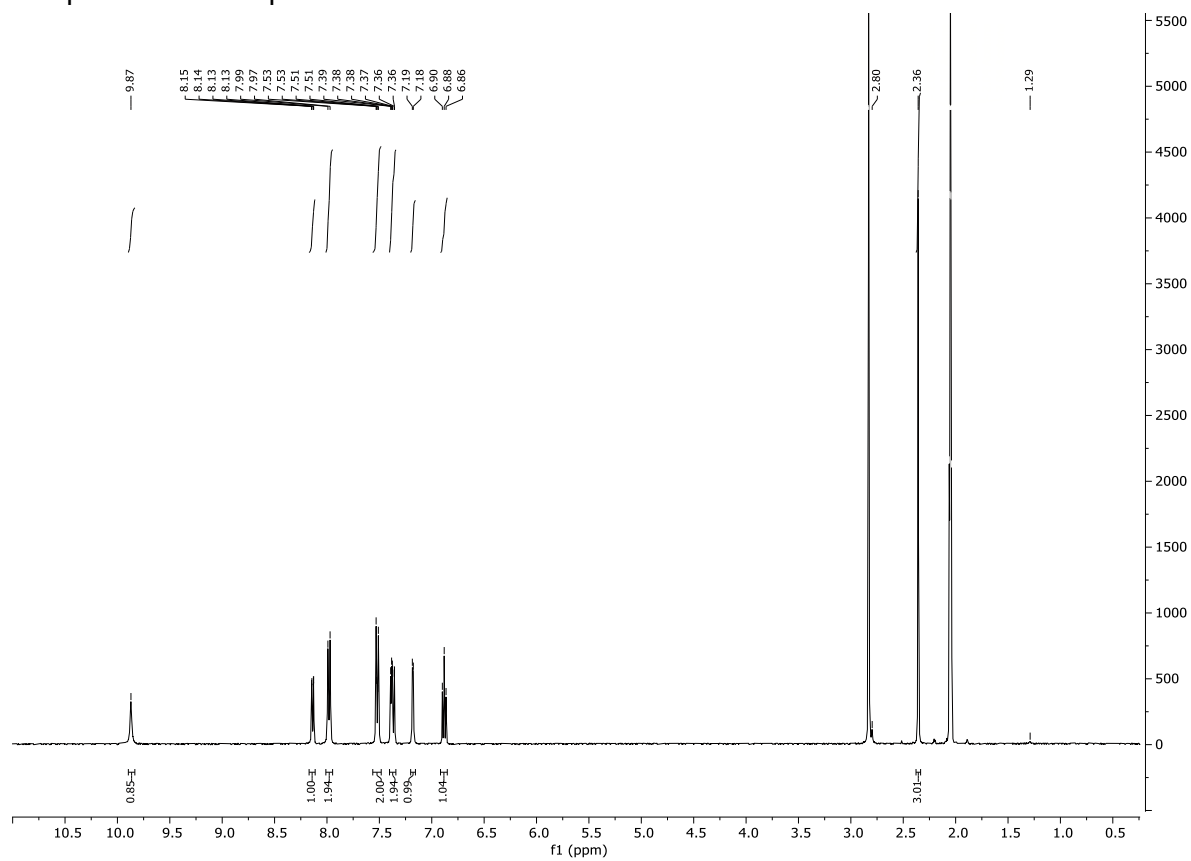
Using Reference Compound: Dimethyl terephthalate (5.819 mg, 99% purity, Mol Weight=194.19)

Sample Integral 1: 6.77991 - 6.85269 ppm, value = 0.13911 (1 nuclides) - Purity = 99.8%

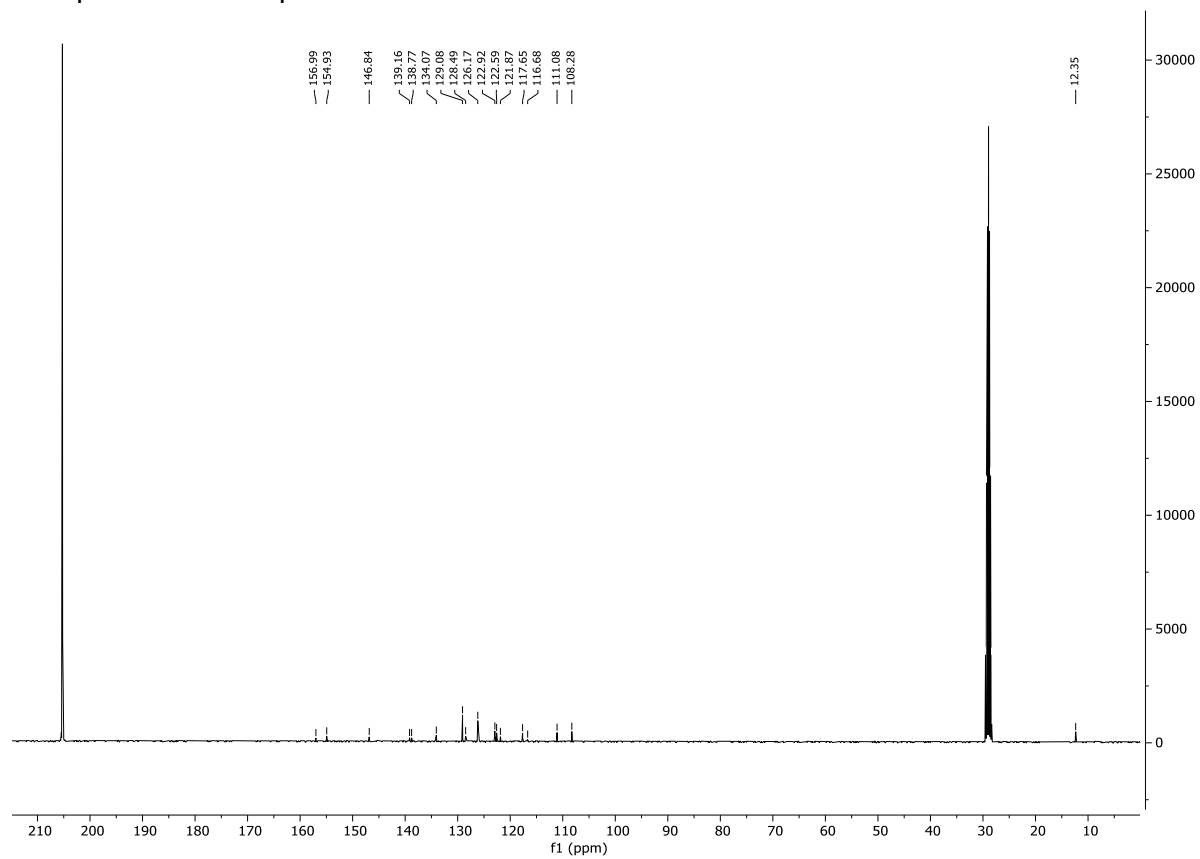
Reference Integral: 8.01759 - 8.12131 ppm, value = 1.00383 (4 nuclides)



¹H spectrum of compound 26:



¹³C spectrum of compound **26**:



qHNMR spectrum of compound **26**:

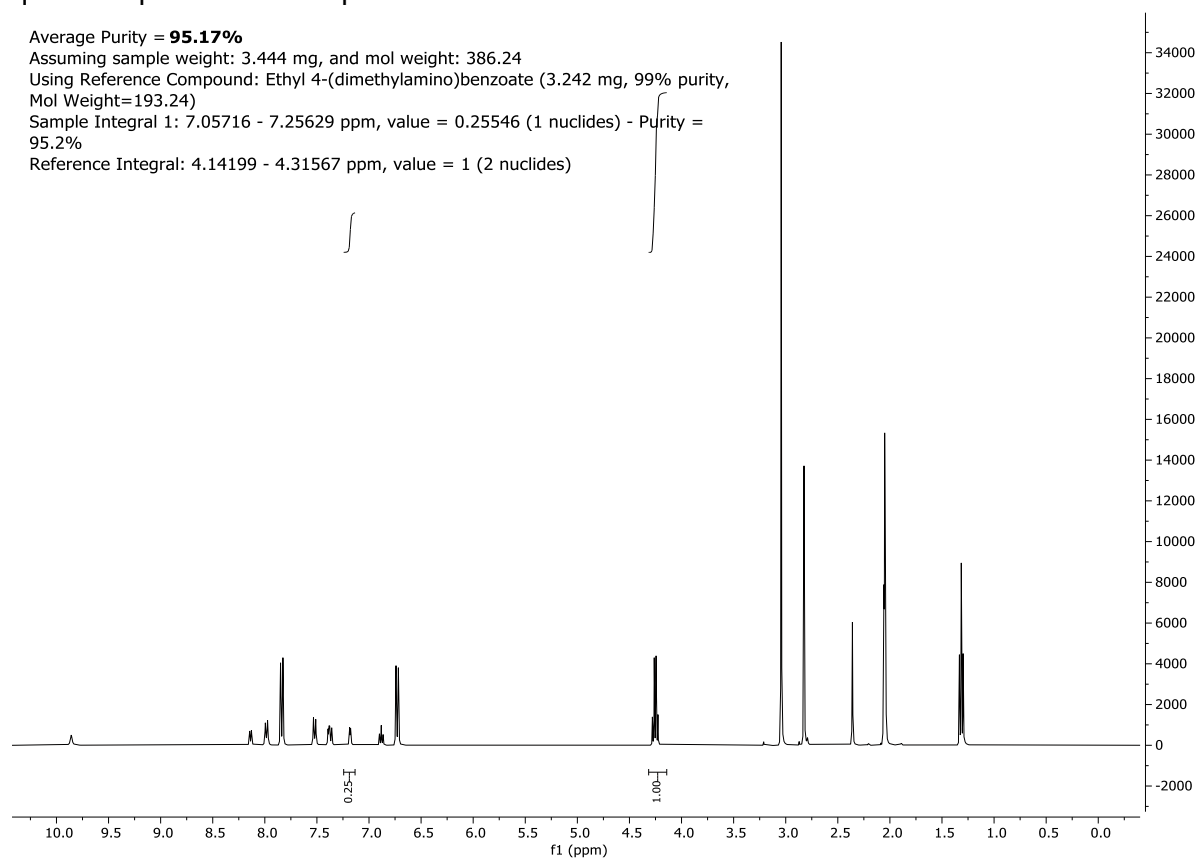
Average Purity = **95.17%**

Assuming sample weight: 3.444 mg, and mol weight: 386.24

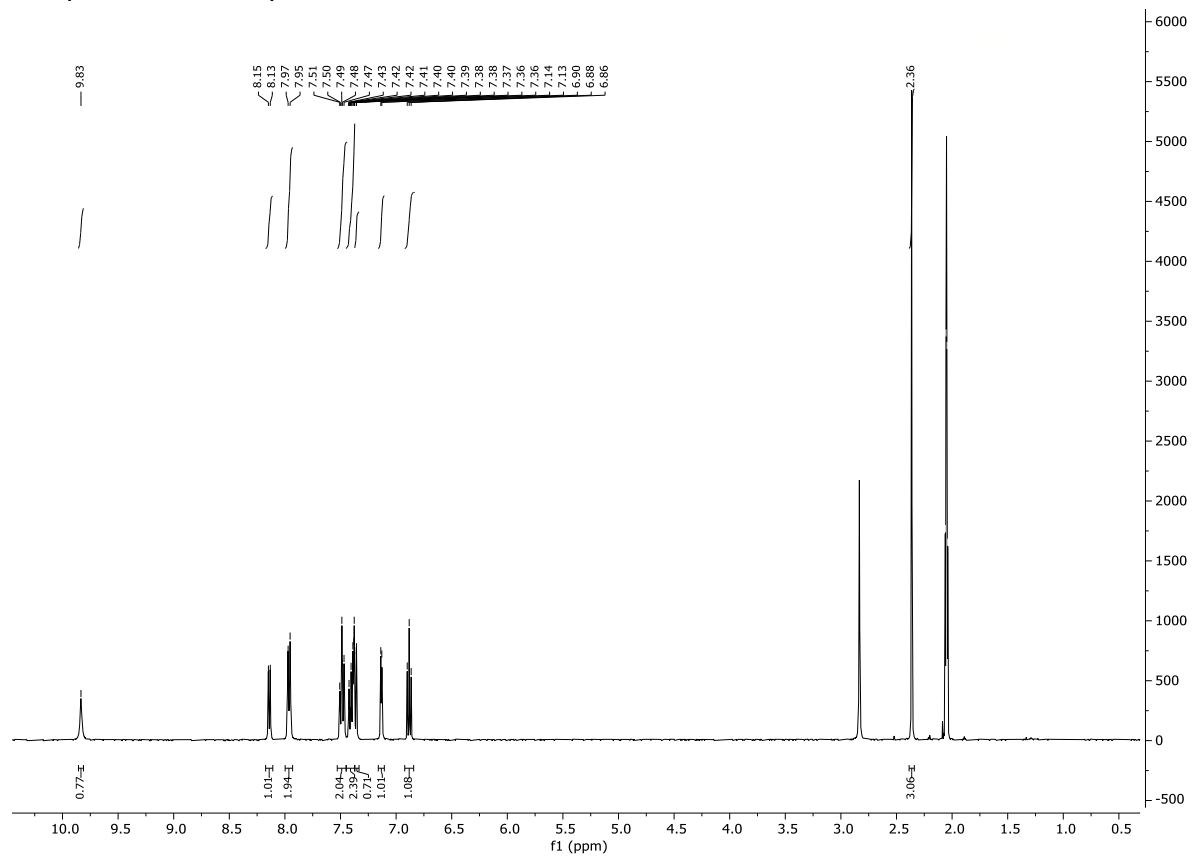
Using Reference Compound: Ethyl 4-(dimethylamino)benzoate (3.242 mg, 99% purity, Mol Weight=193.24)

Sample Integral 1: 7.05716 - 7.25629 ppm, value = 0.25546 (1 nuclides) - Purity = 95.2%

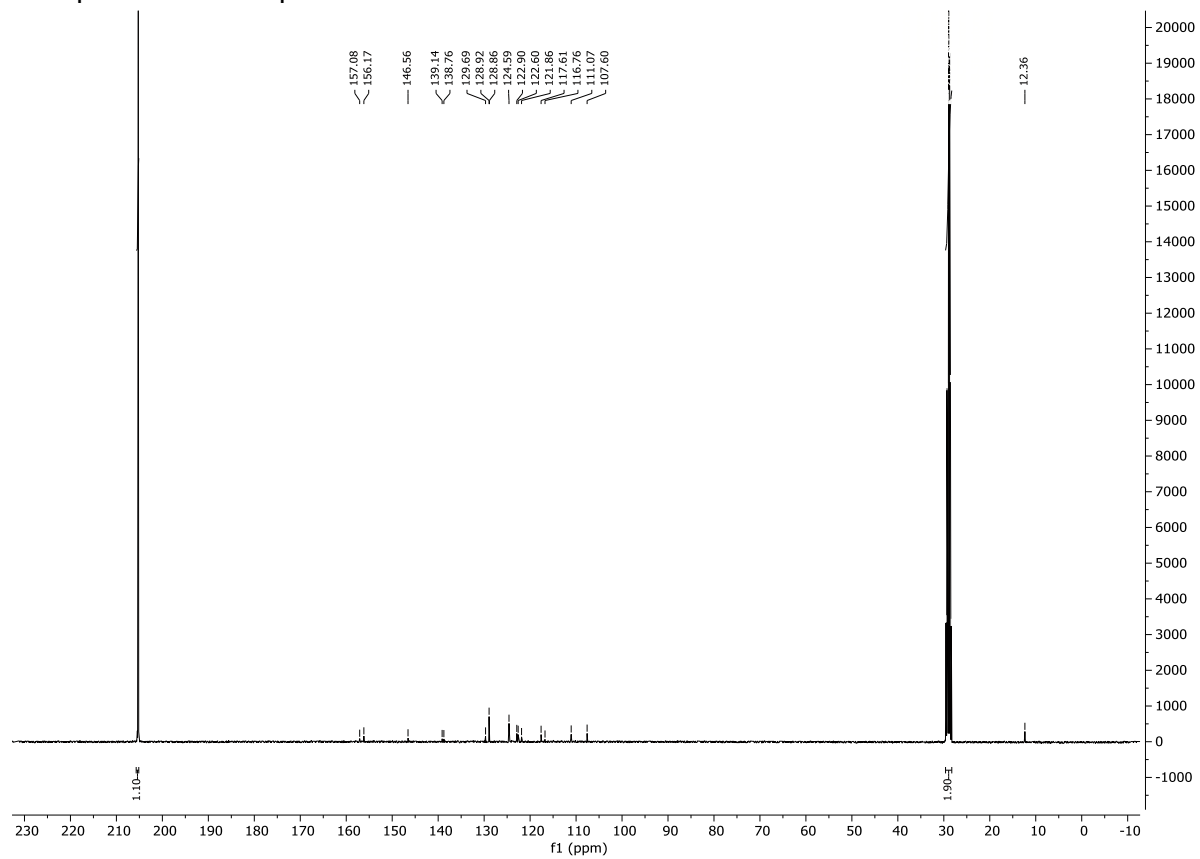
Reference Integral: 4.14199 - 4.31567 ppm, value = 1 (2 nuclides)



¹H spectrum of compound 27:

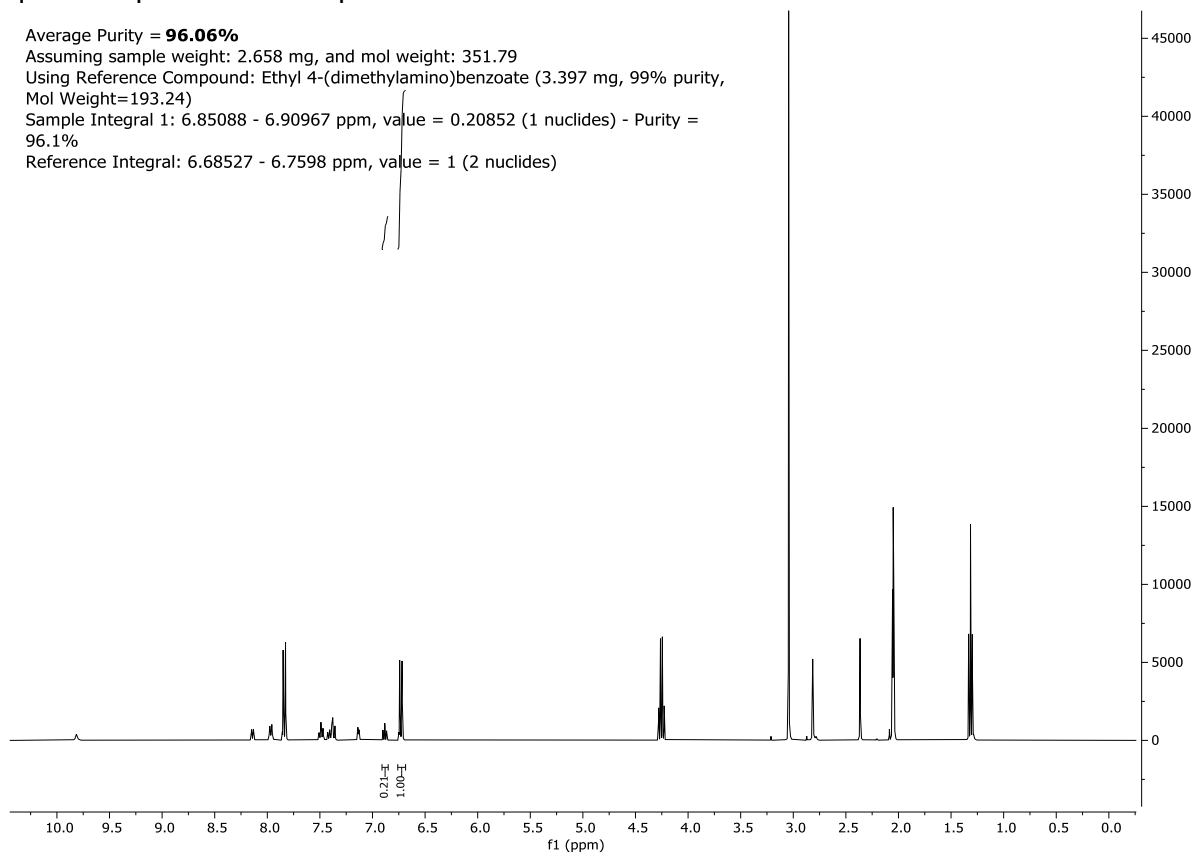


¹³C spectrum of compound **27**:

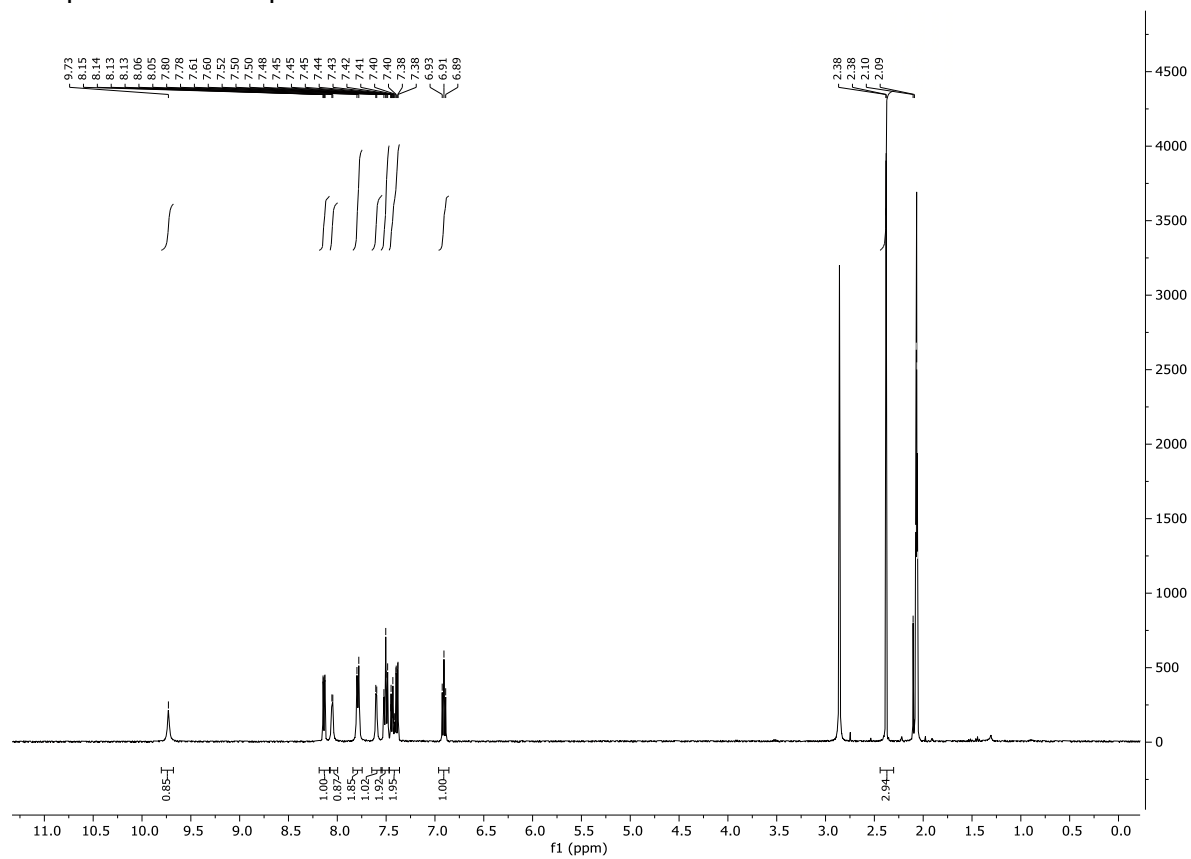


qHNMR spectrum of compound **27**:

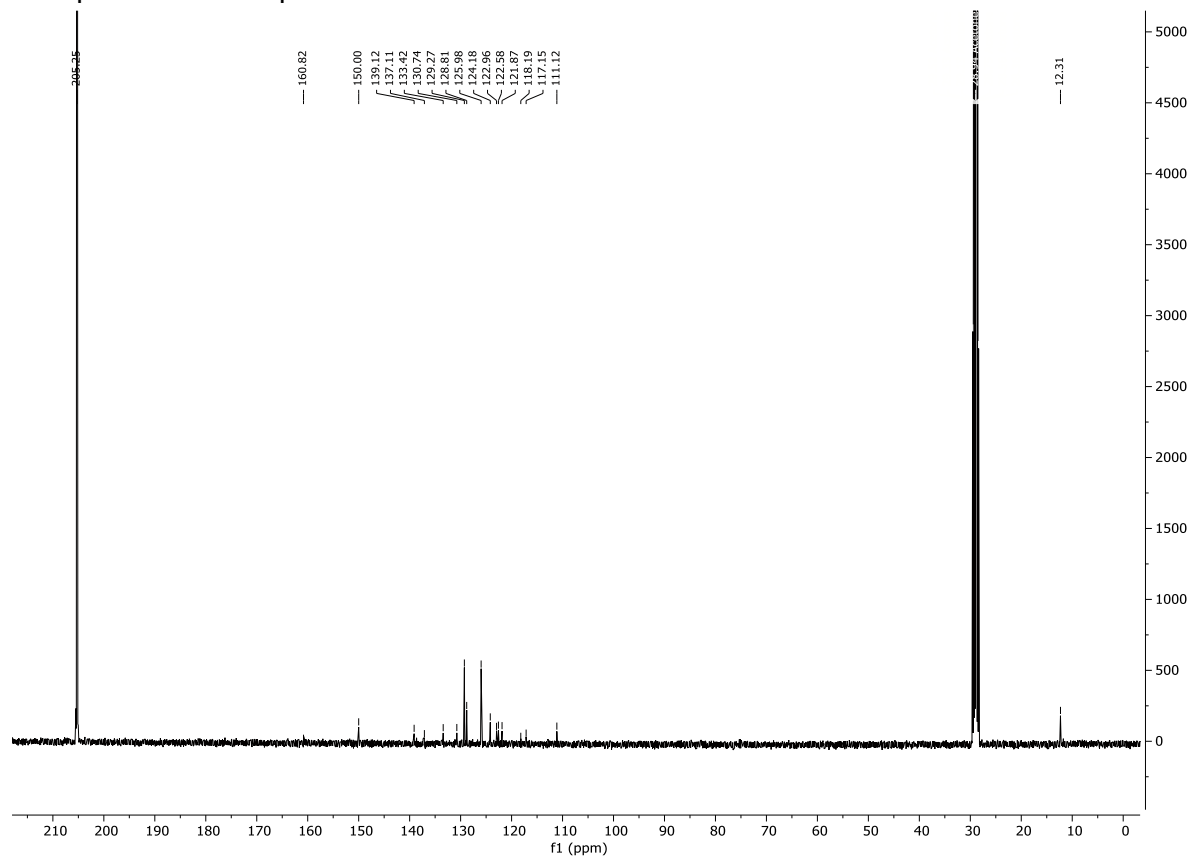
Average Purity = **96.06%**
Assuming sample weight: 2.658 mg, and mol weight: 351.79
Using Reference Compound: Ethyl 4-(dimethylamino)benzoate (3.397 mg, 99% purity,
Mol Weight=193.24)
Sample Integral 1: 6.85088 - 6.90967 ppm, value = 0.20852 (1 nuclides) - Purity =
96.1%
Reference Integral: 6.68527 - 6.7598 ppm, value = 1 (2 nuclides)



¹H spectrum of compound 28:



¹³C spectrum of compound **28**:



qHNMR spectrum of compound **28**:

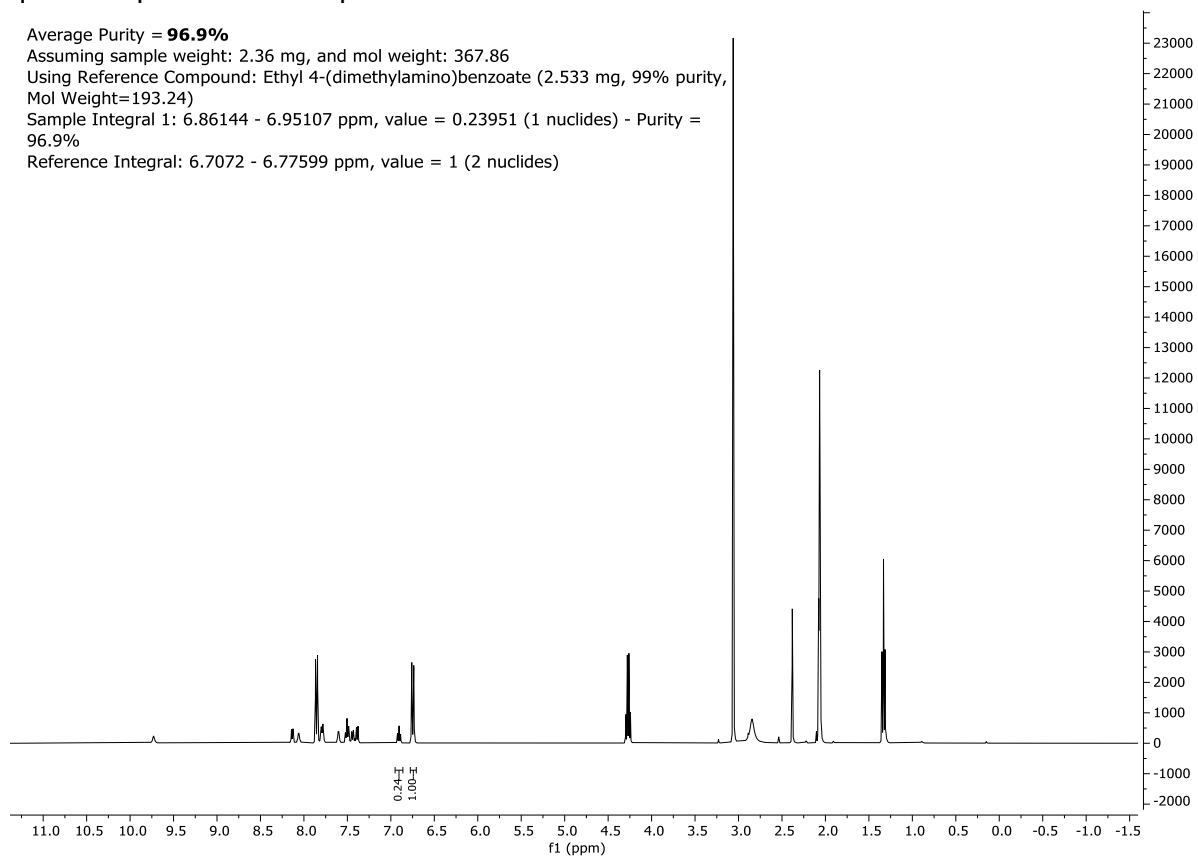
Average Purity = **96.9%**

Assuming sample weight: 2.36 mg, and mol weight: 367.86

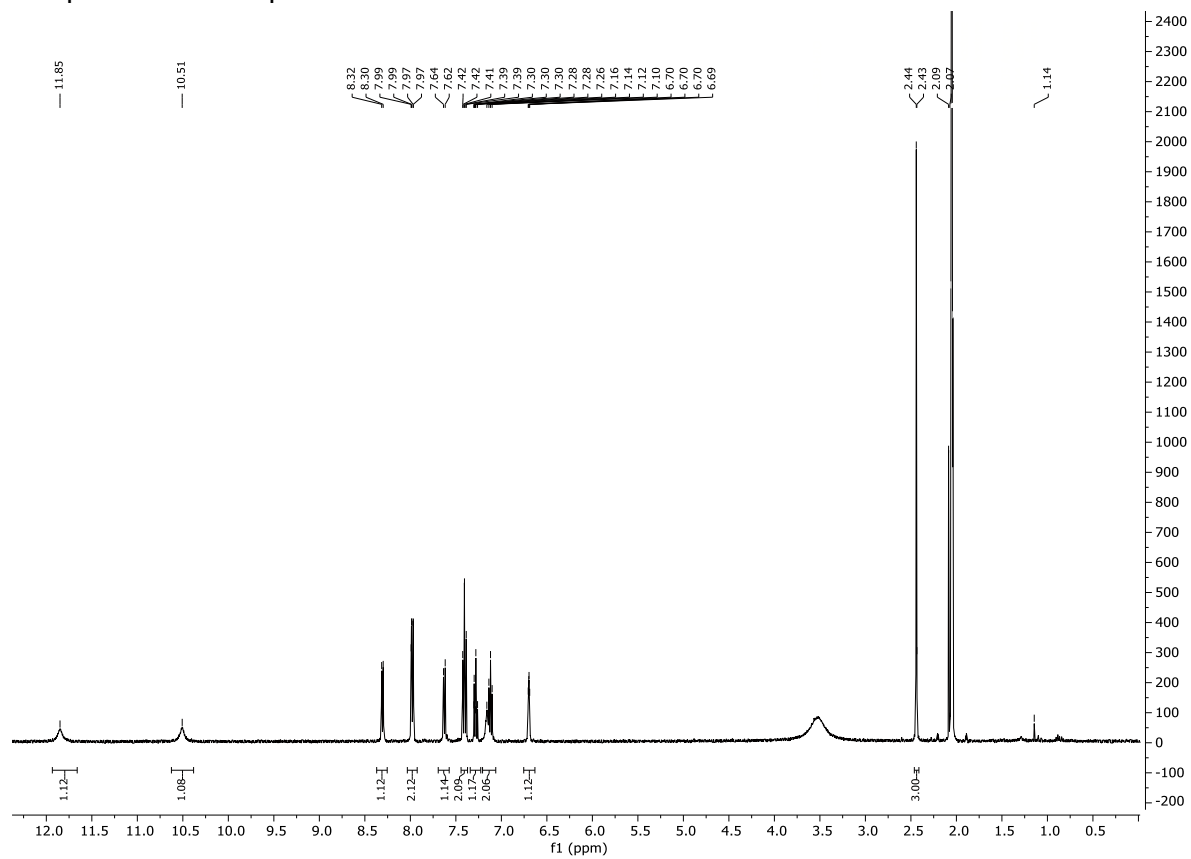
Using Reference Compound: Ethyl 4-(dimethylamino)benzoate (2.533 mg, 99% purity, Mol Weight=193.24)

Sample Integral 1: 6.86144 - 6.95107 ppm, value = 0.23951 (1 nuclide) - Purity = 96.9%

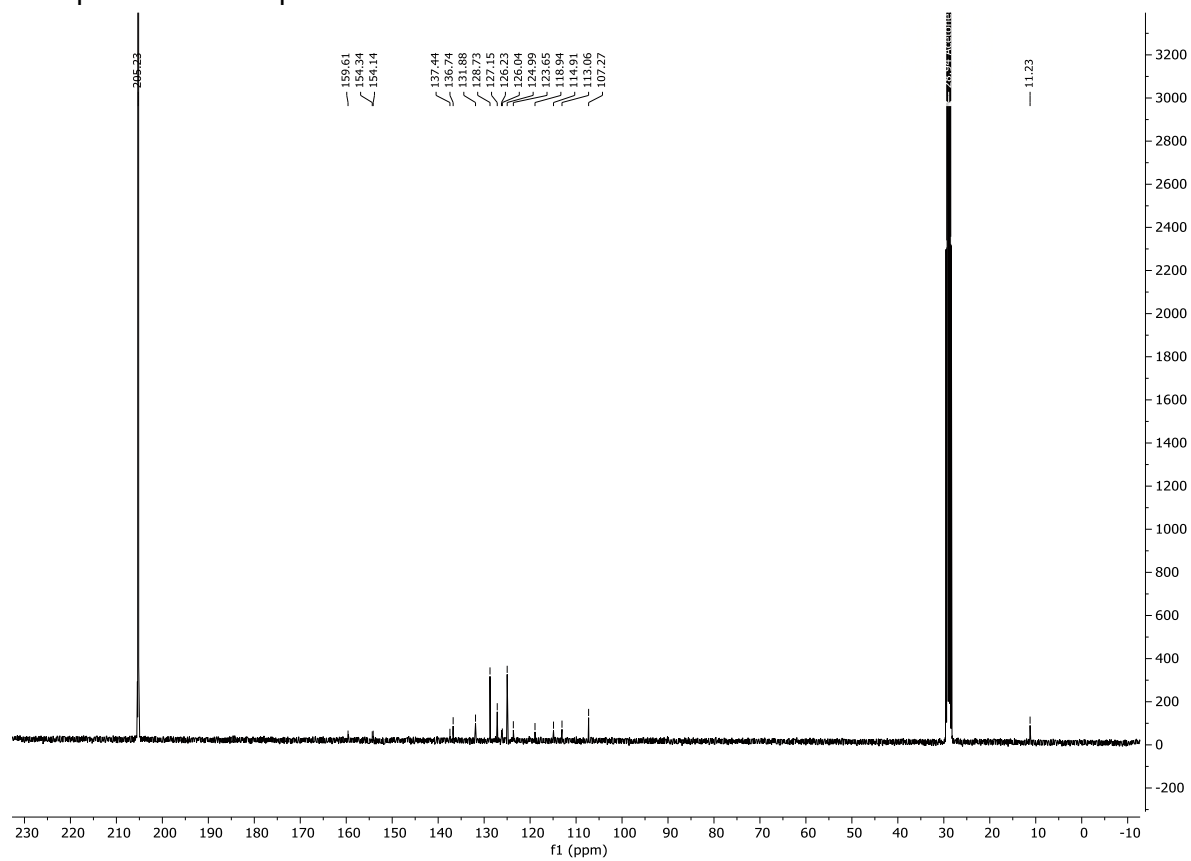
Reference Integral: 6.7072 - 6.77599 ppm, value = 1 (2 nuclides)



¹H spectrum of compound 29:

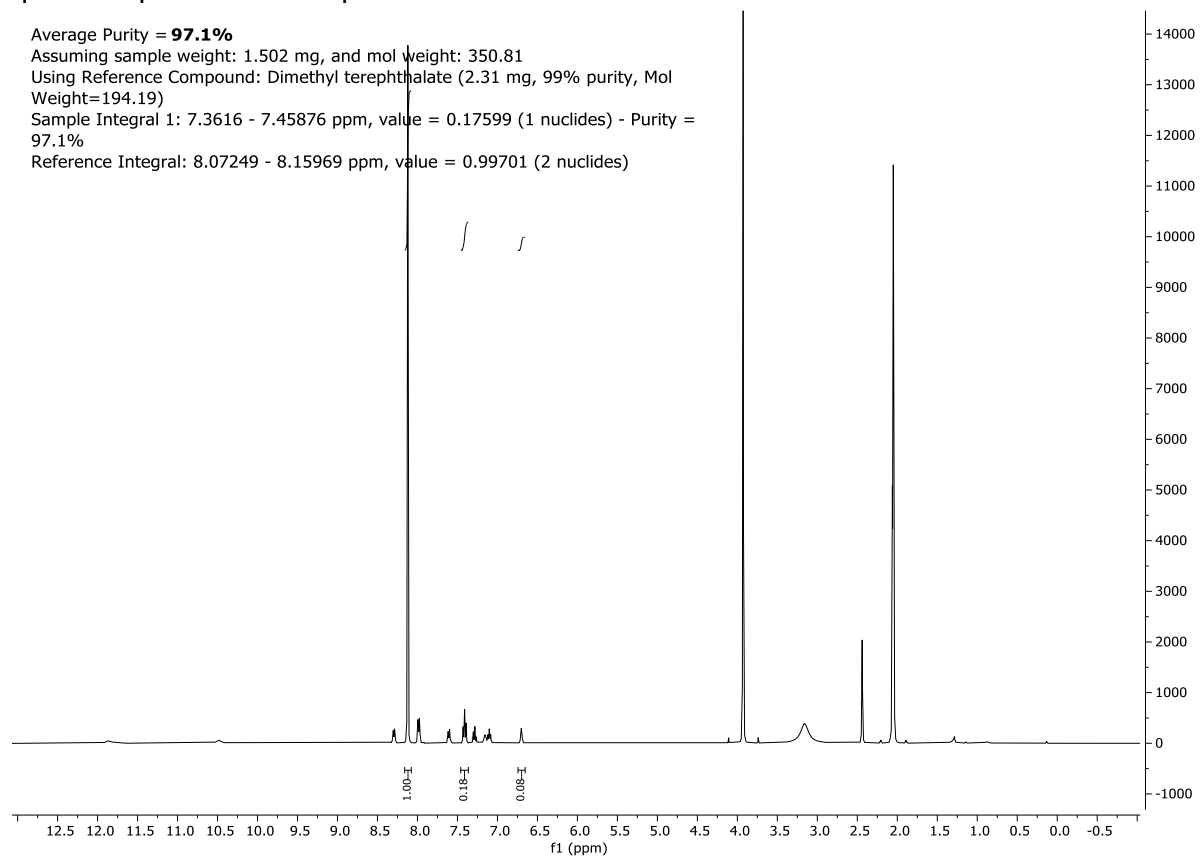


¹³C spectrum of compound **29**:

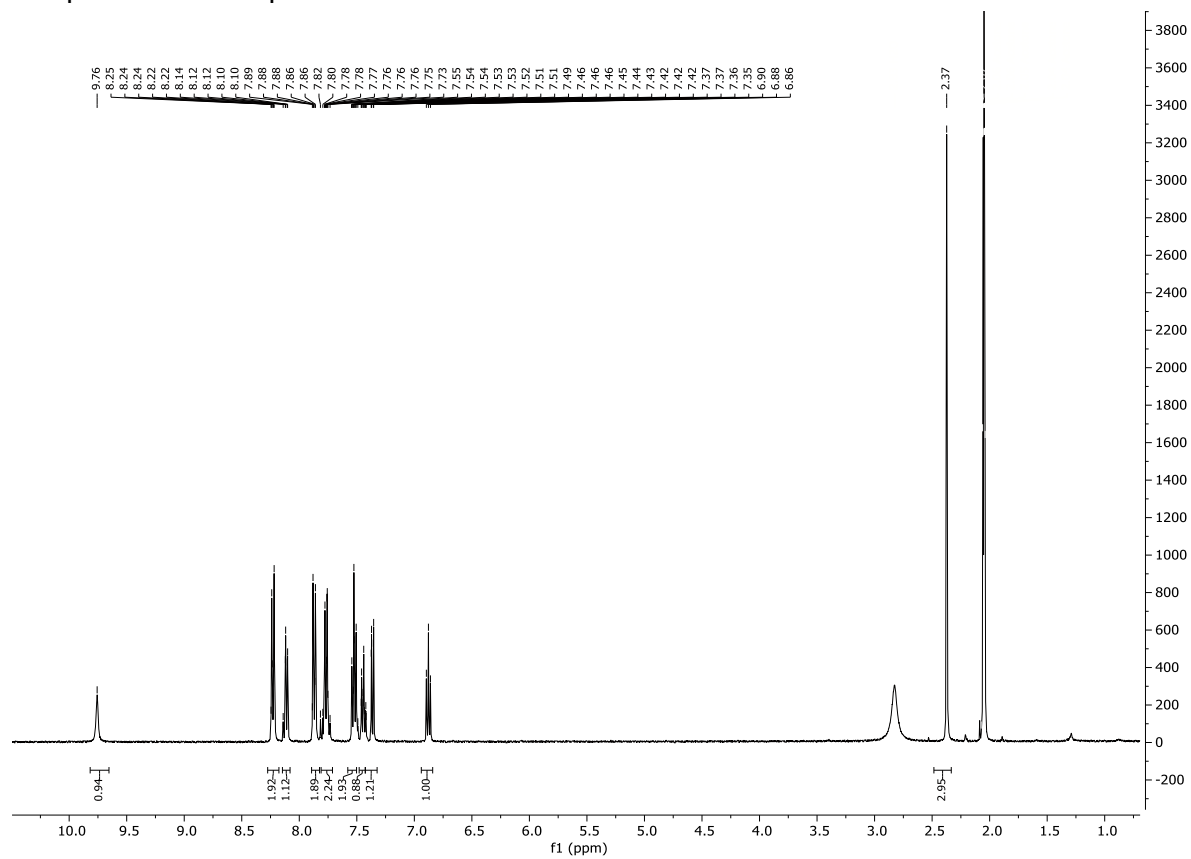


qHNMR spectrum of compound **29**:

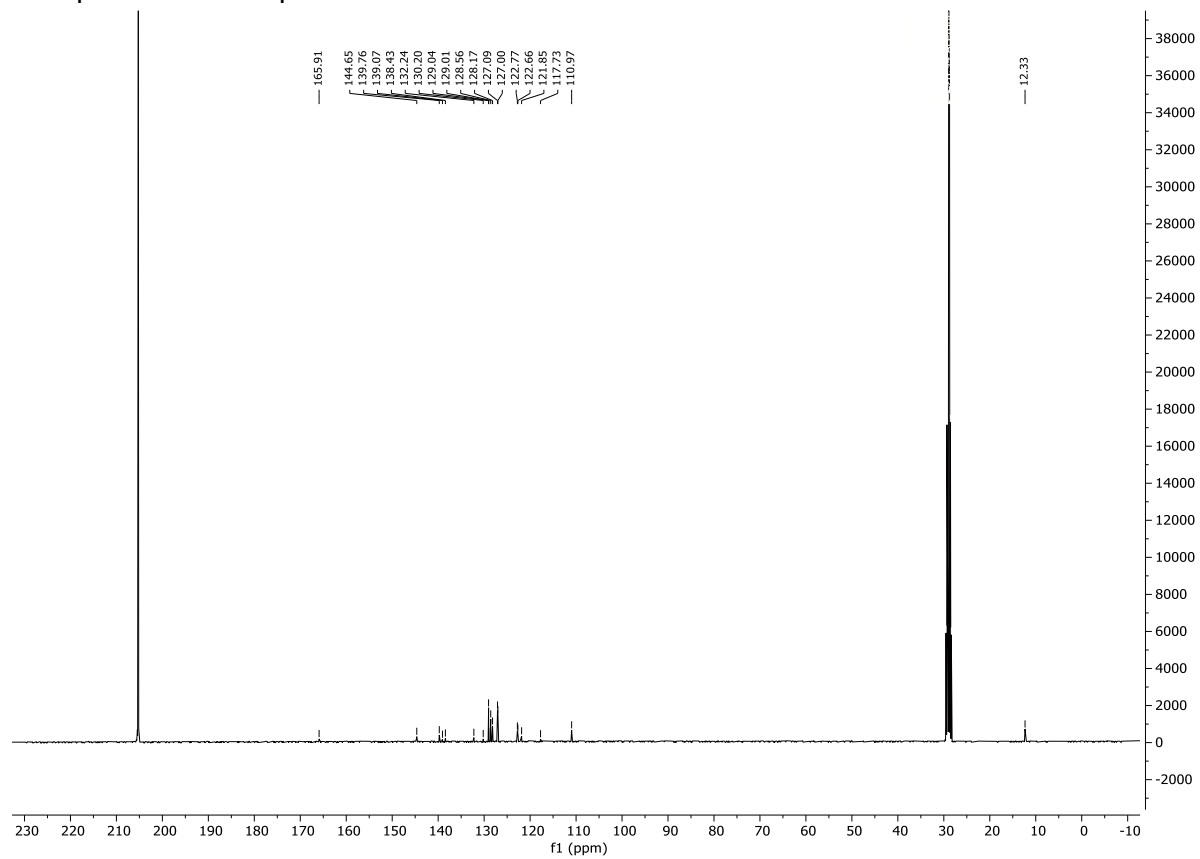
Average Purity = **97.1%**
Assuming sample weight: 1.502 mg, and mol weight: 350.81
Using Reference Compound: Dimethyl terephthalate (2.31 mg, 99% purity, Mol Weight=194.19)
Sample Integral 1: 7.3616 - 7.45876 ppm, value = 0.17599 (1 nuclides) - Purity = 97.1%
Reference Integral: 8.07249 - 8.15969 ppm, value = 0.99701 (2 nuclides)



¹H spectrum of compound **30**:

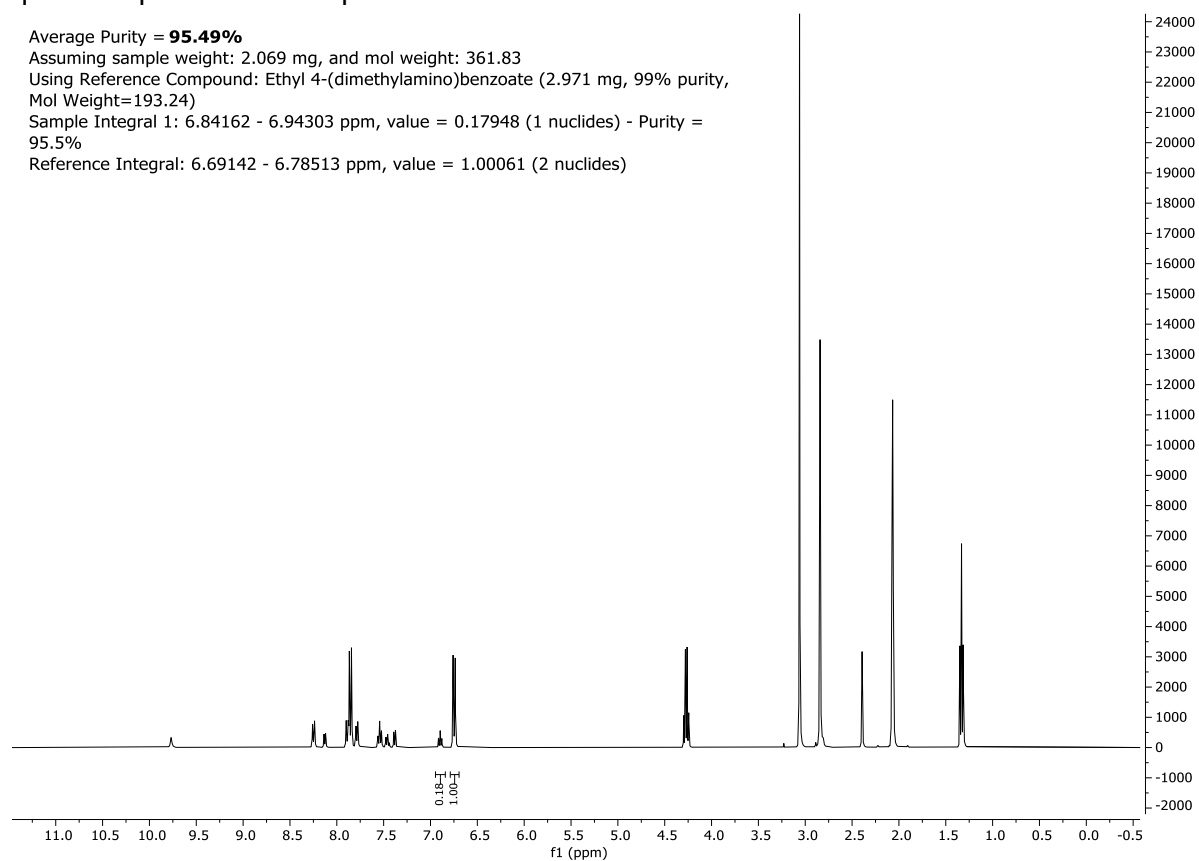


¹³C spectrum of compound **30**:

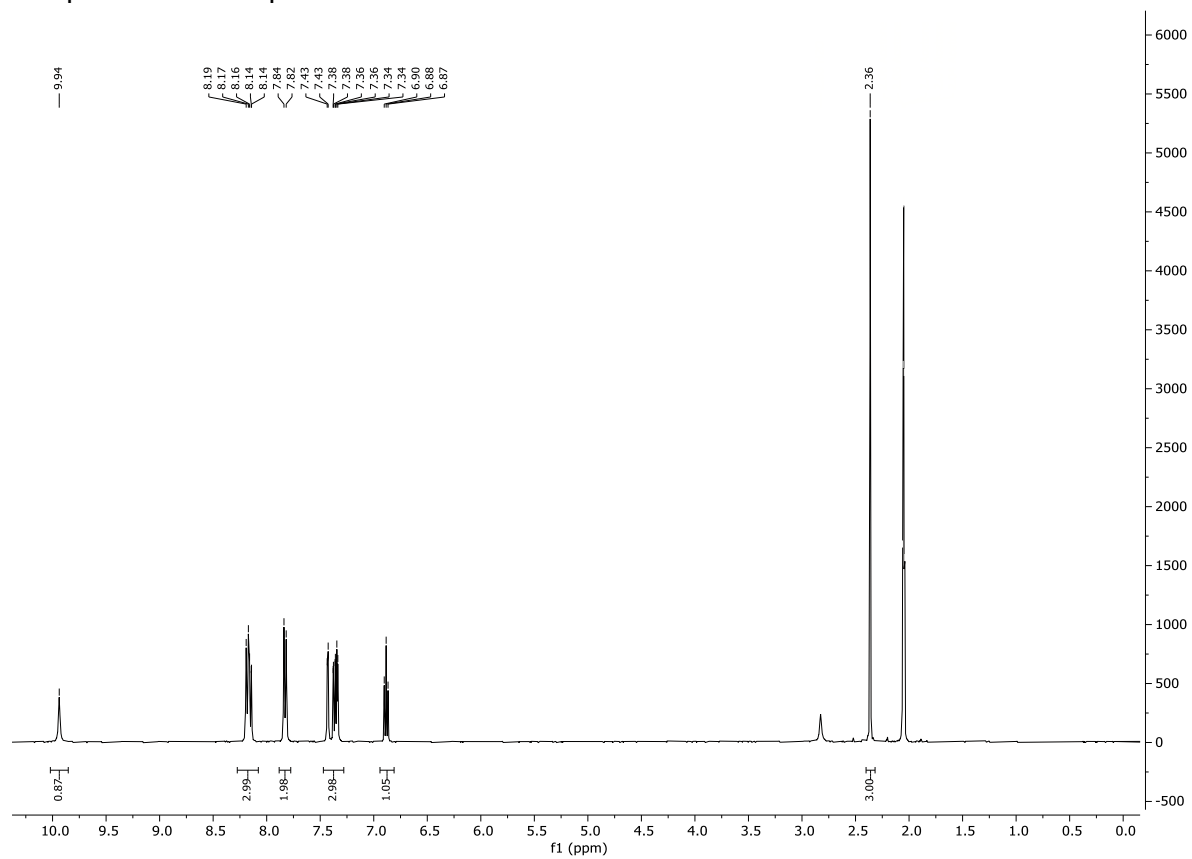


qHNMR spectrum of compound **30**:

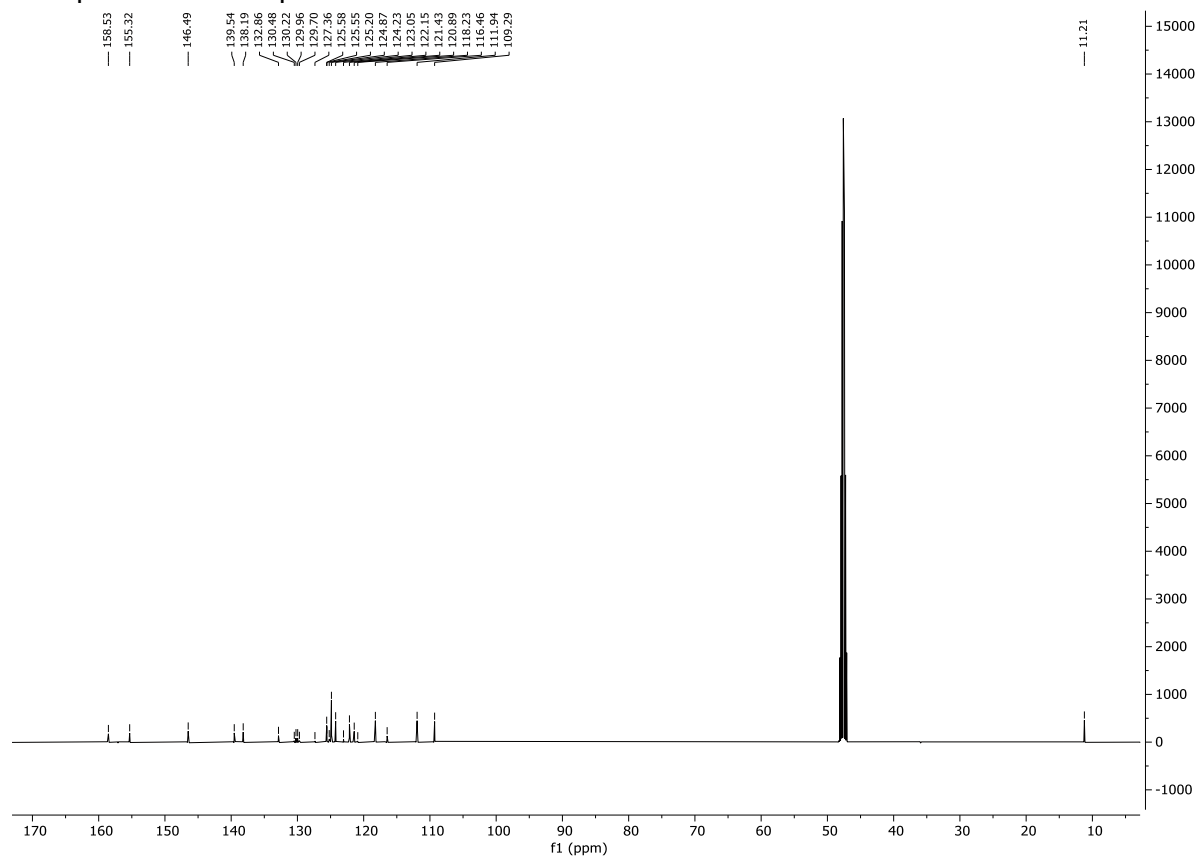
Average Purity = **95.49%**
Assuming sample weight: 2.069 mg, and mol weight: 361.83
Using Reference Compound: Ethyl 4-(dimethylamino)benzoate (2.971 mg, 99% purity,
Mol Weight=193.24)
Sample Integral 1: 6.84162 - 6.94303 ppm, value = 0.17948 (1 nuclides) - Purity =
95.5%
Reference Integral: 6.69142 - 6.78513 ppm, value = 1.00061 (2 nuclides)



¹H spectrum of compound **31**:



¹³C spectrum of compound **31**:



qHNMR spectrum of compound **31**:

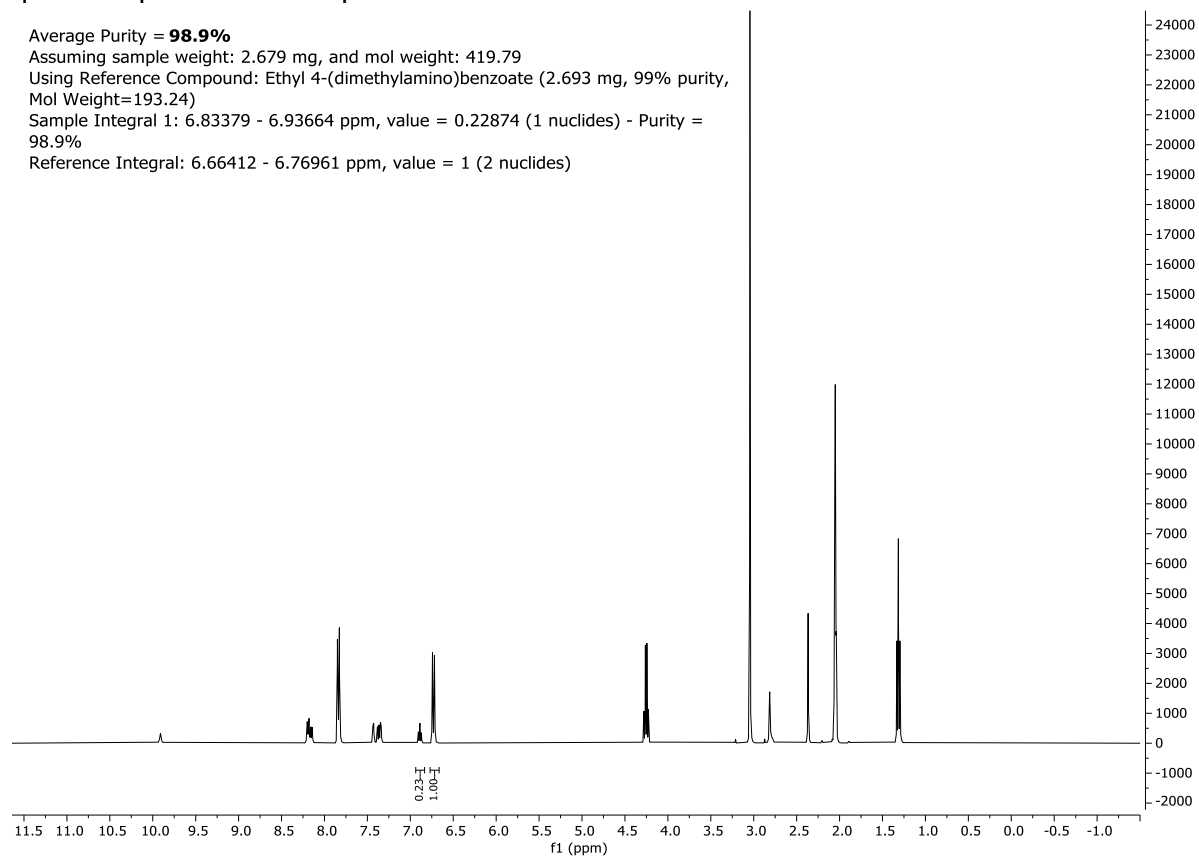
Average Purity = **98.9%**

Assuming sample weight: 2.679 mg, and mol weight: 419.79

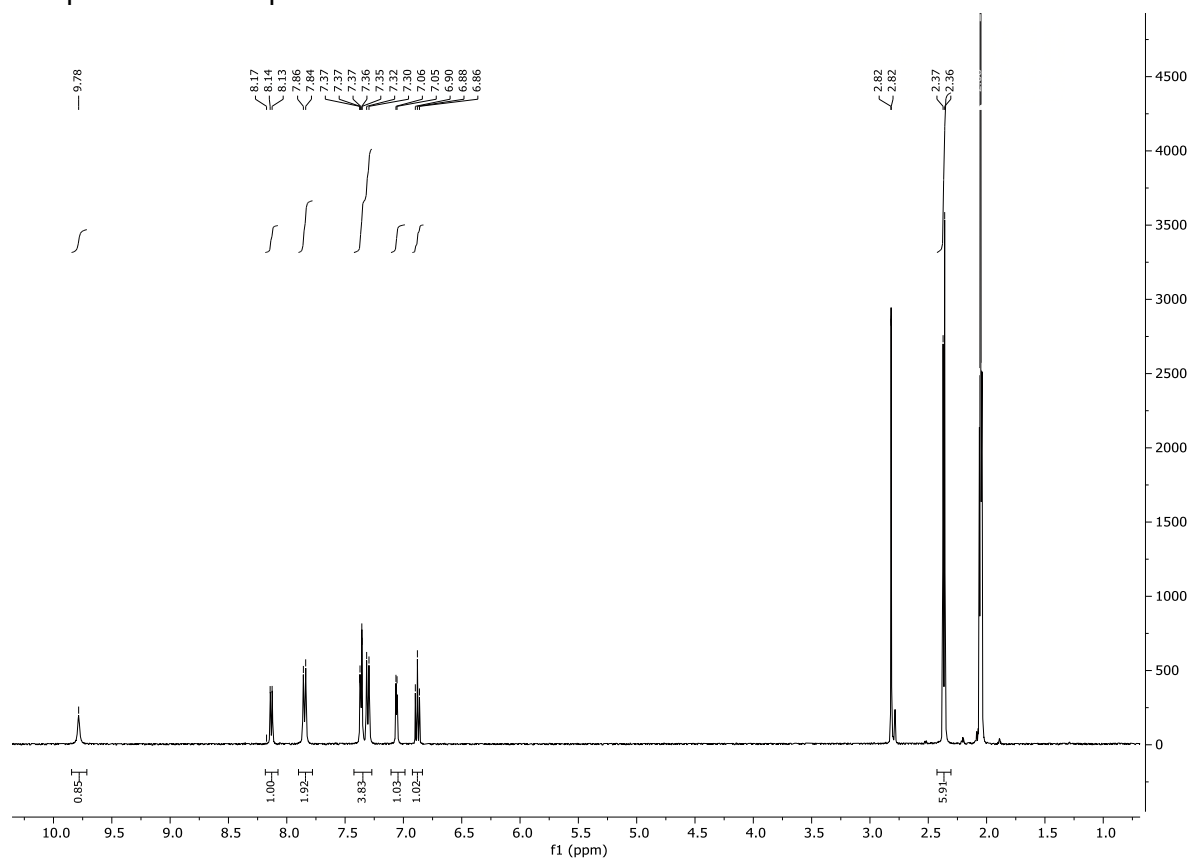
Using Reference Compound: Ethyl 4-(dimethylamino)benzoate (2.693 mg, 99% purity, Mol Weight=193.24)

Sample Integral 1: 6.83379 - 6.93664 ppm, value = 0.22874 (1 nuclides) - Purity = 98.9%

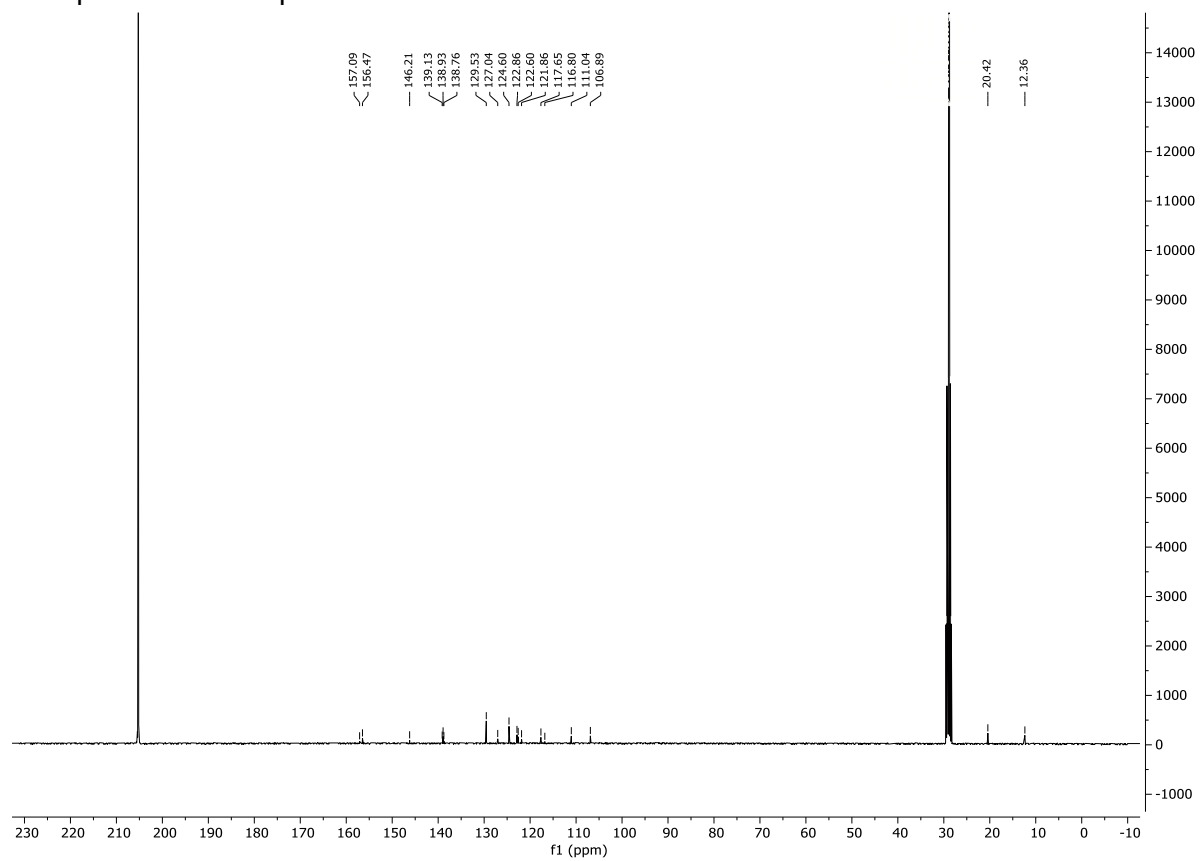
Reference Integral: 6.66412 - 6.76961 ppm, value = 1 (2 nuclides)



¹H spectrum of compound **32**:

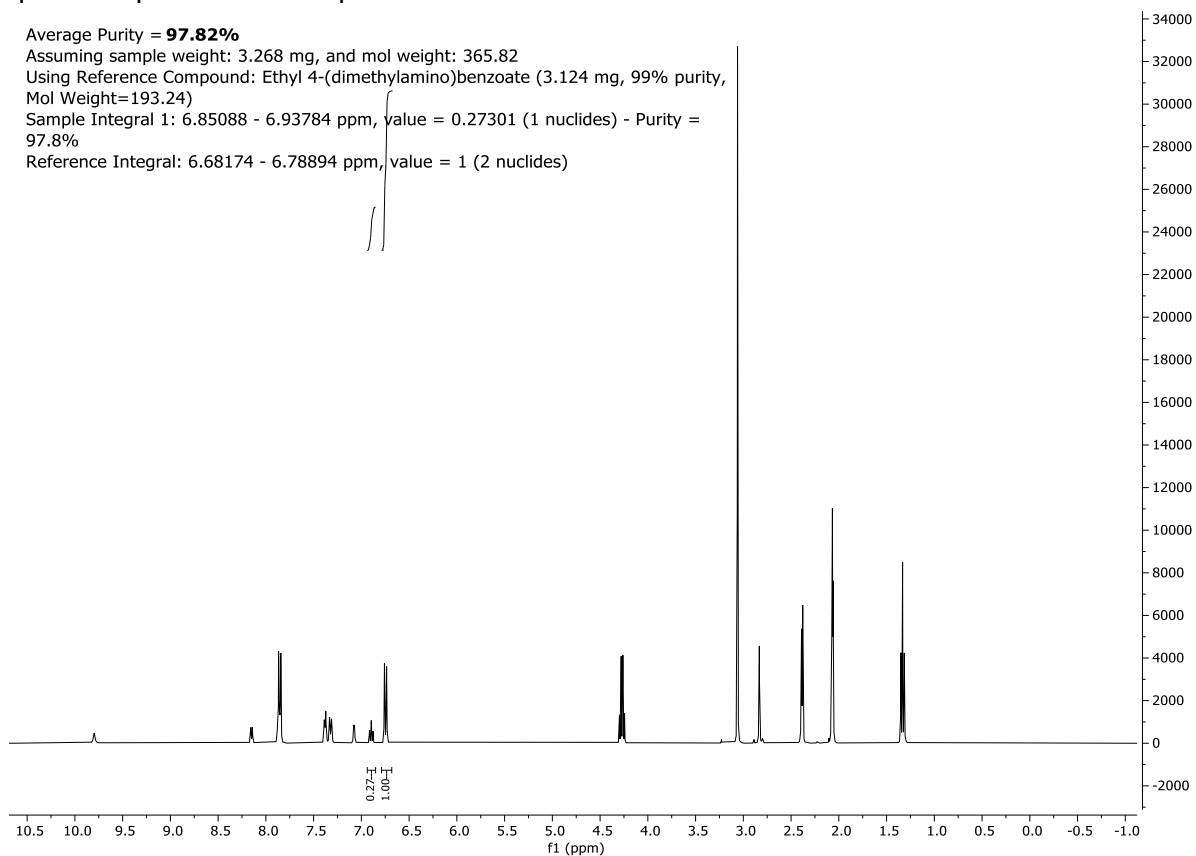


¹³C spectrum of compound **32**:

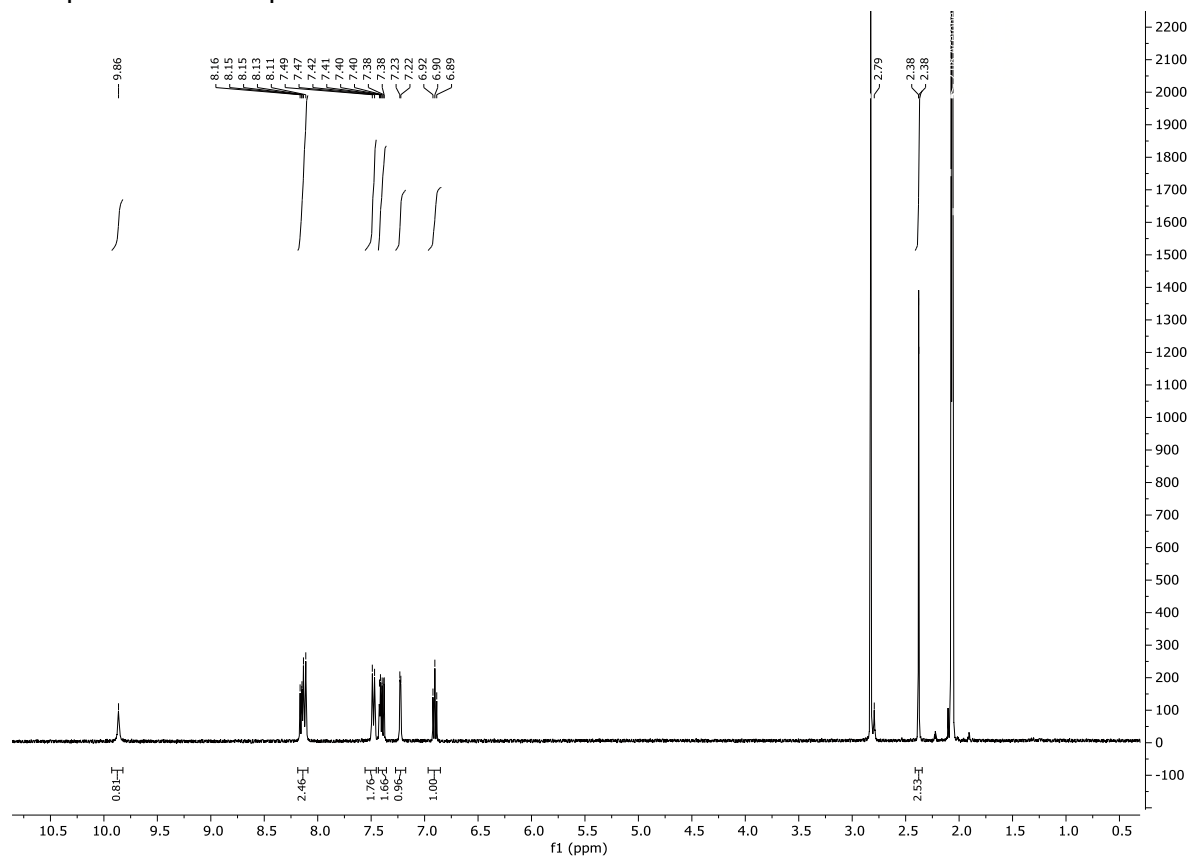


qHNMR spectrum of compound **32**:

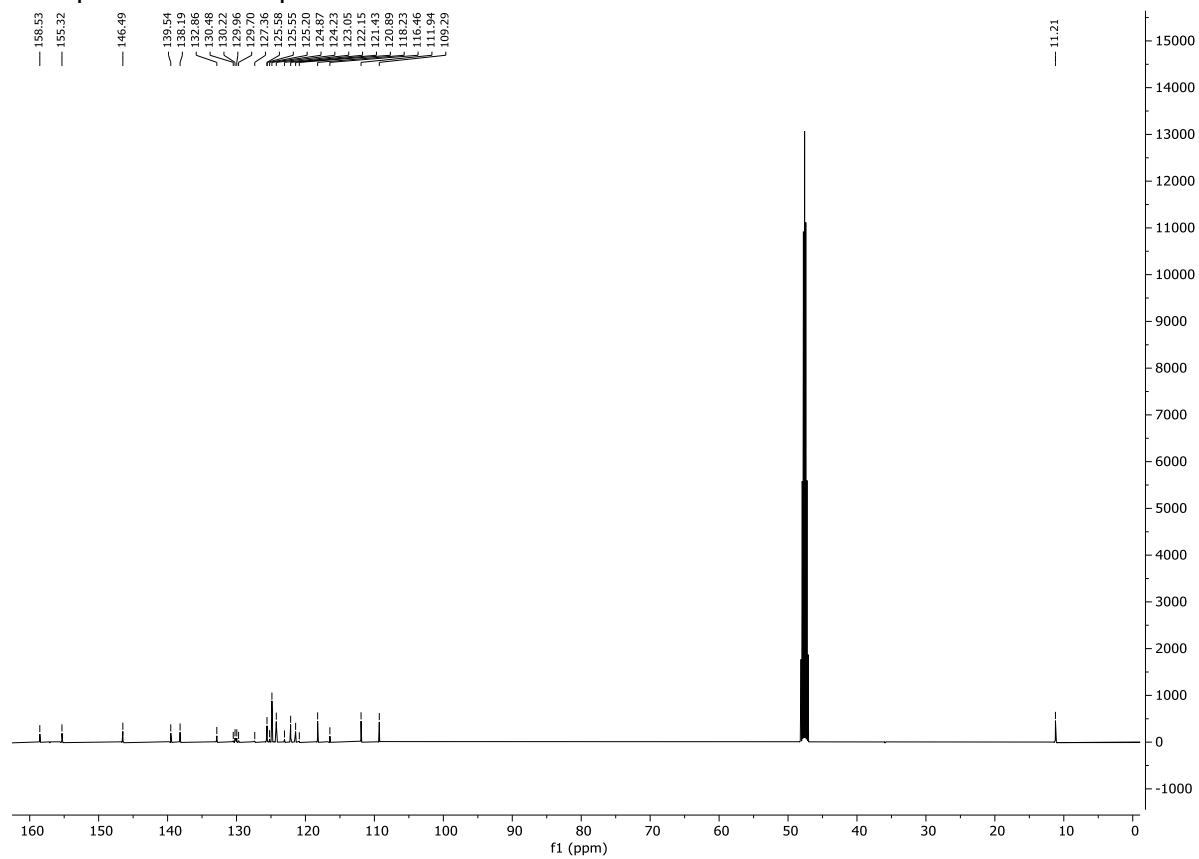
Average Purity = **97.82%**
Assuming sample weight: 3.268 mg, and mol weight: 365.82
Using Reference Compound: Ethyl 4-(dimethylamino)benzoate (3.124 mg, 99% purity,
Mol Weight=193.24)
Sample Integral 1: 6.85088 - 6.93784 ppm, value = 0.27301 (1 nuclides) - Purity = 97.8%
Reference Integral: 6.68174 - 6.78894 ppm, value = 1 (2 nuclides)



¹H spectrum of compound **33**:



¹³C spectrum of compound **33**:



qHNMR spectrum of compound **33**:

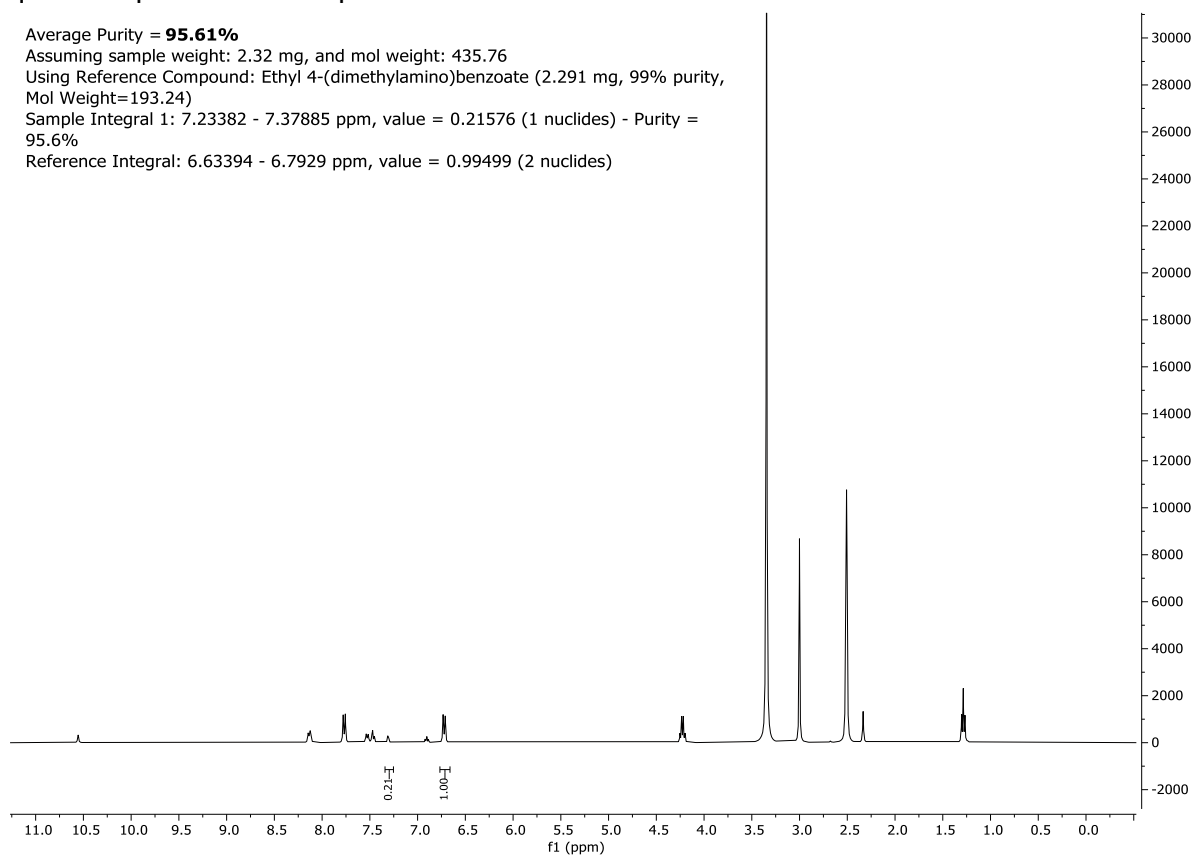
Average Purity = **95.61%**

Assuming sample weight: 2.32 mg, and mol weight: 435.76

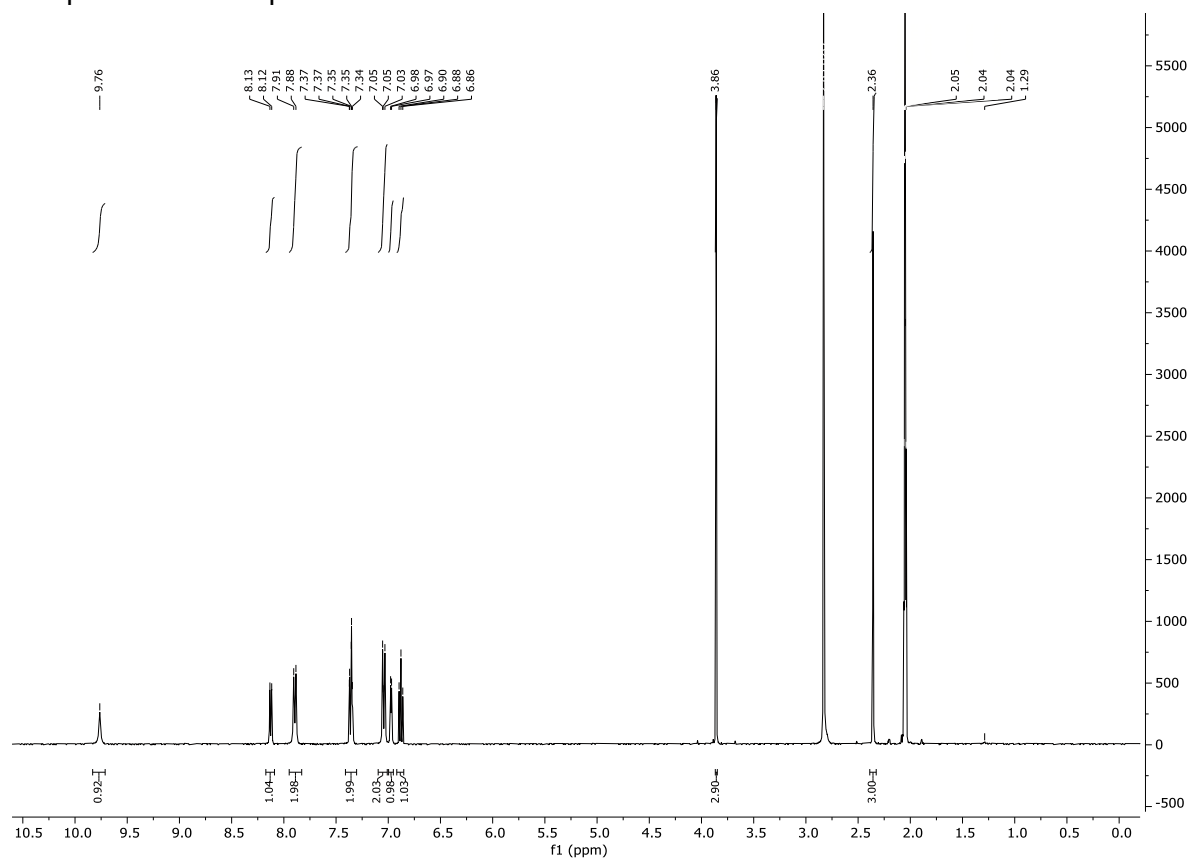
Using Reference Compound: Ethyl 4-(dimethylamino)benzoate (2.291 mg, 99% purity, Mol Weight=193.24)

Sample Integral 1: 7.23382 - 7.37885 ppm, value = 0.21576 (1 nuclides) - Purity = 95.6%

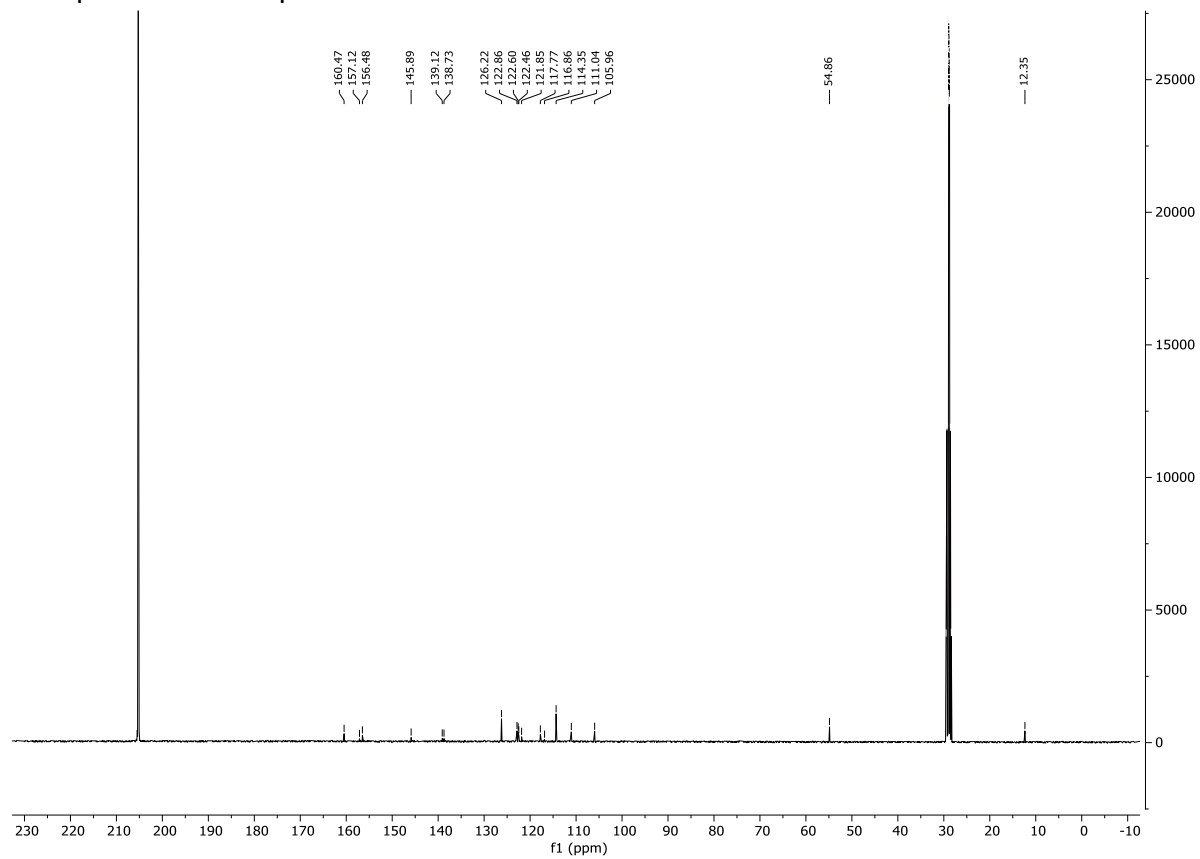
Reference Integral: 6.63394 - 6.7929 ppm, value = 0.99499 (2 nuclides)



¹H spectrum of compound **34**:

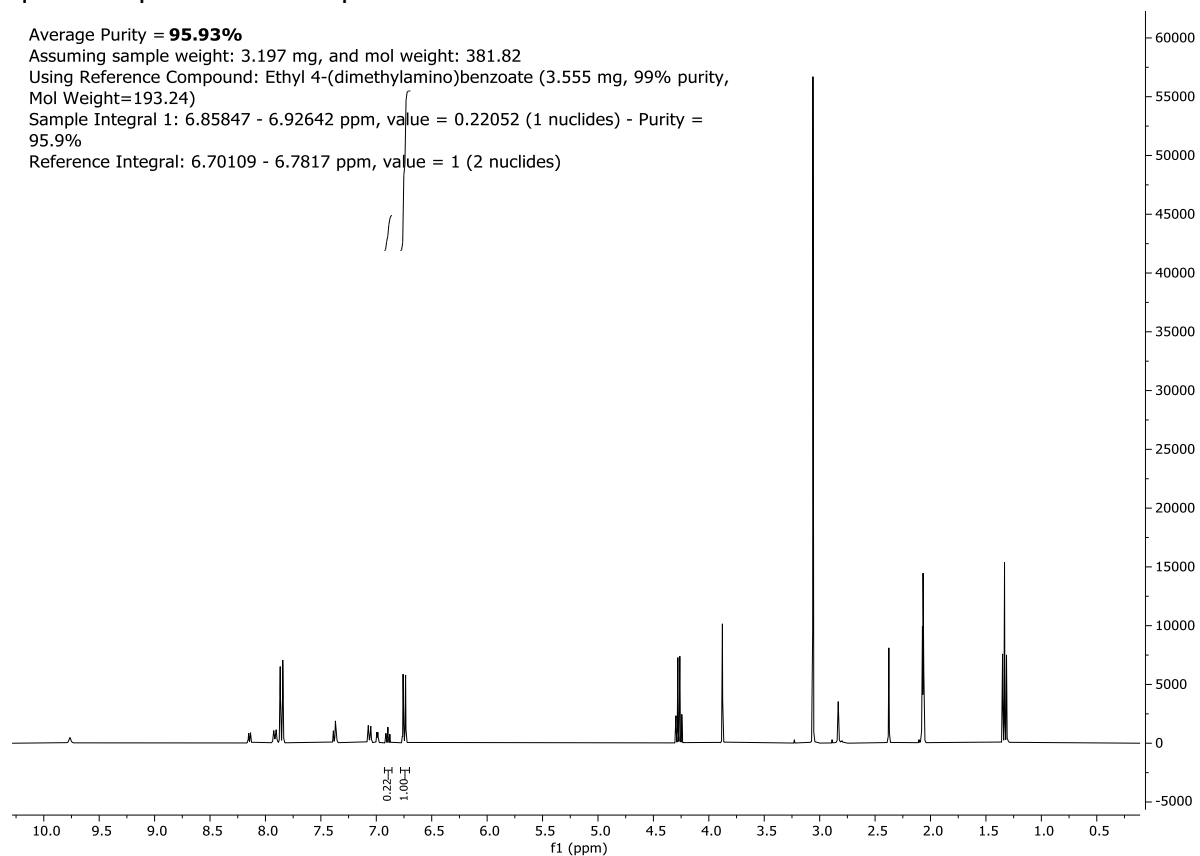


¹³C spectrum of compound **34**:

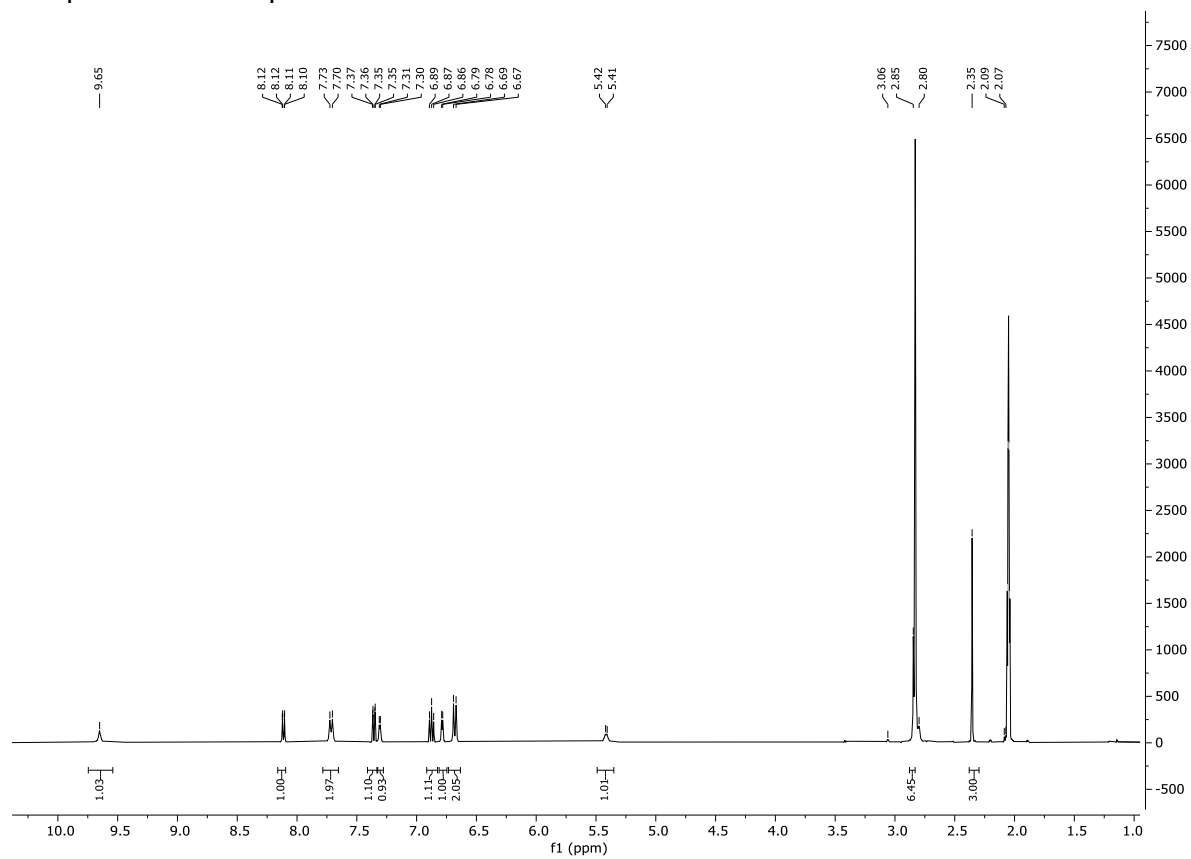


qHNMR spectrum of compound **34**:

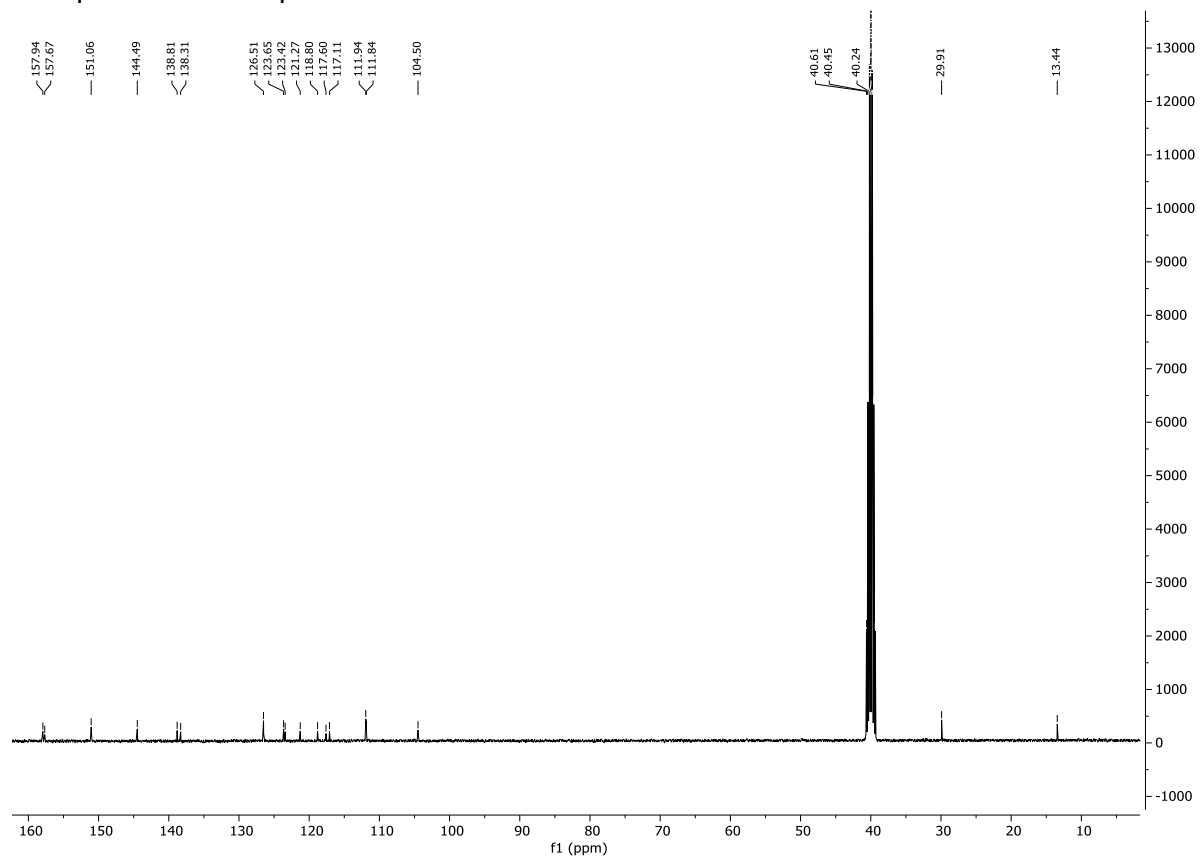
Average Purity = **95.93%**
Assuming sample weight: 3.197 mg, and mol weight: 381.82
Using Reference Compound: Ethyl 4-(dimethylamino)benzoate (3.555 mg, 99% purity,
Mol Weight=193.24)
Sample Integral 1: 6.85847 - 6.92642 ppm, value = 0.22052 (1 nuclides) - Purity = 95.9%
Reference Integral: 6.70109 - 6.7817 ppm, value = 1 (2 nuclides)



¹H spectrum of compound **35**:

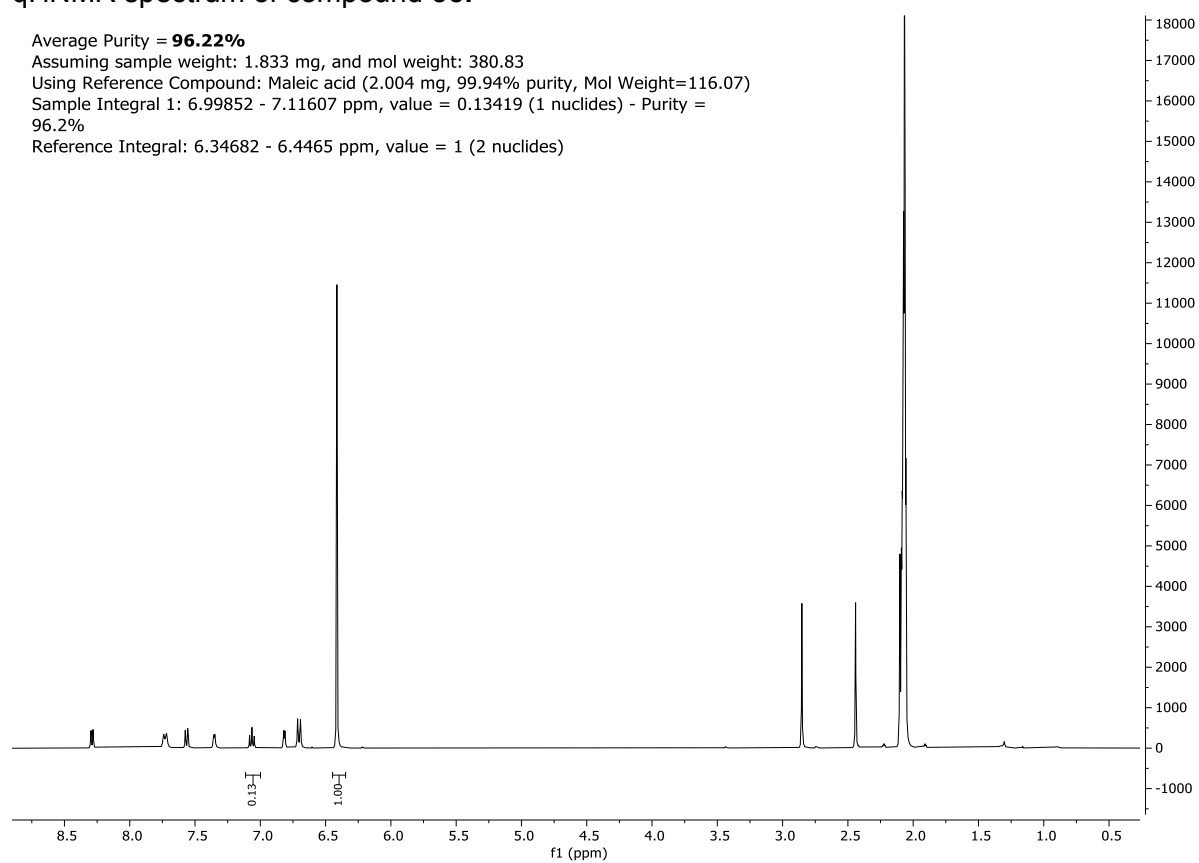


¹³C spectrum of compound **35**:

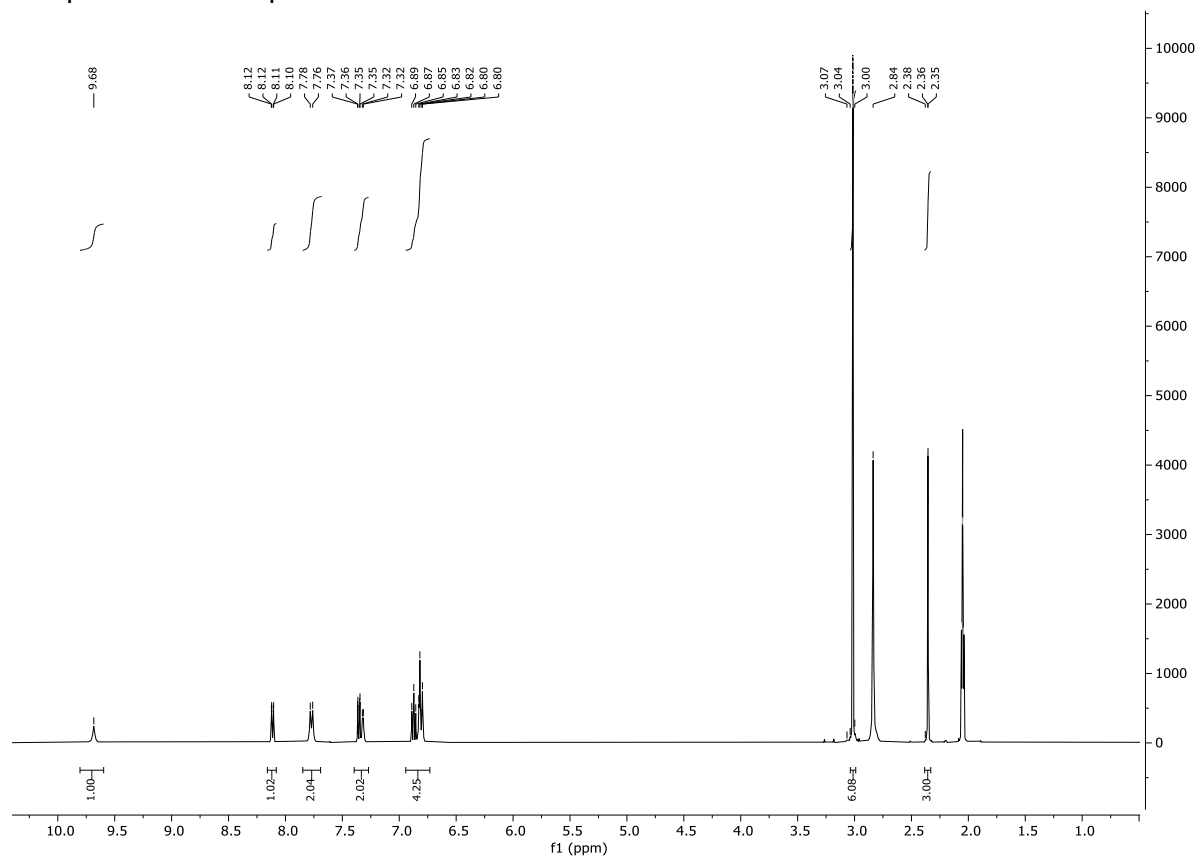


qHNMR spectrum of compound **35**:

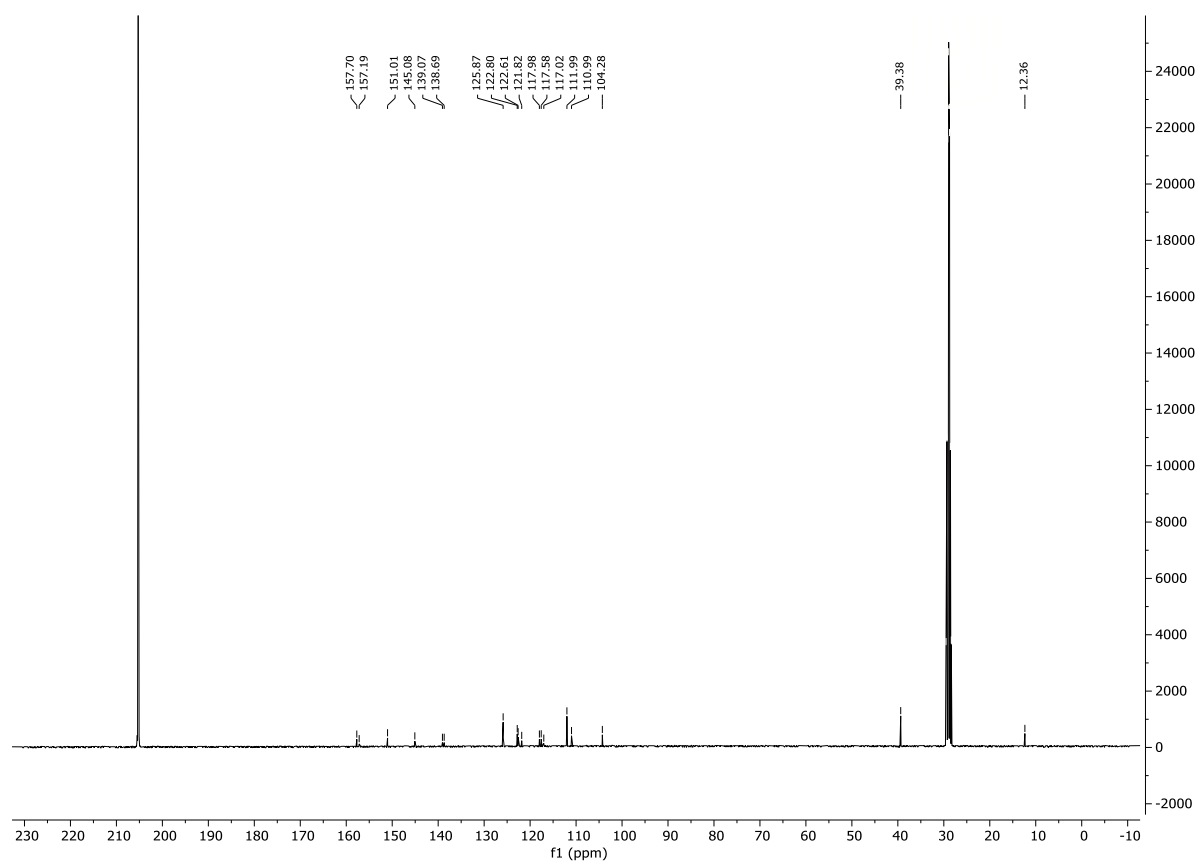
Average Purity = **96.22%**
Assuming sample weight: 1.833 mg, and mol weight: 380.83
Using Reference Compound: Maleic acid (2.004 mg, 99.94% purity, Mol Weight=116.07)
Sample Integral 1: 6.99852 - 7.11607 ppm, value = 0.13419 (1 nuclides) - Purity = 96.2%
Reference Integral: 6.34682 - 6.4465 ppm, value = 1 (2 nuclides)



¹H spectrum of compound **36**:

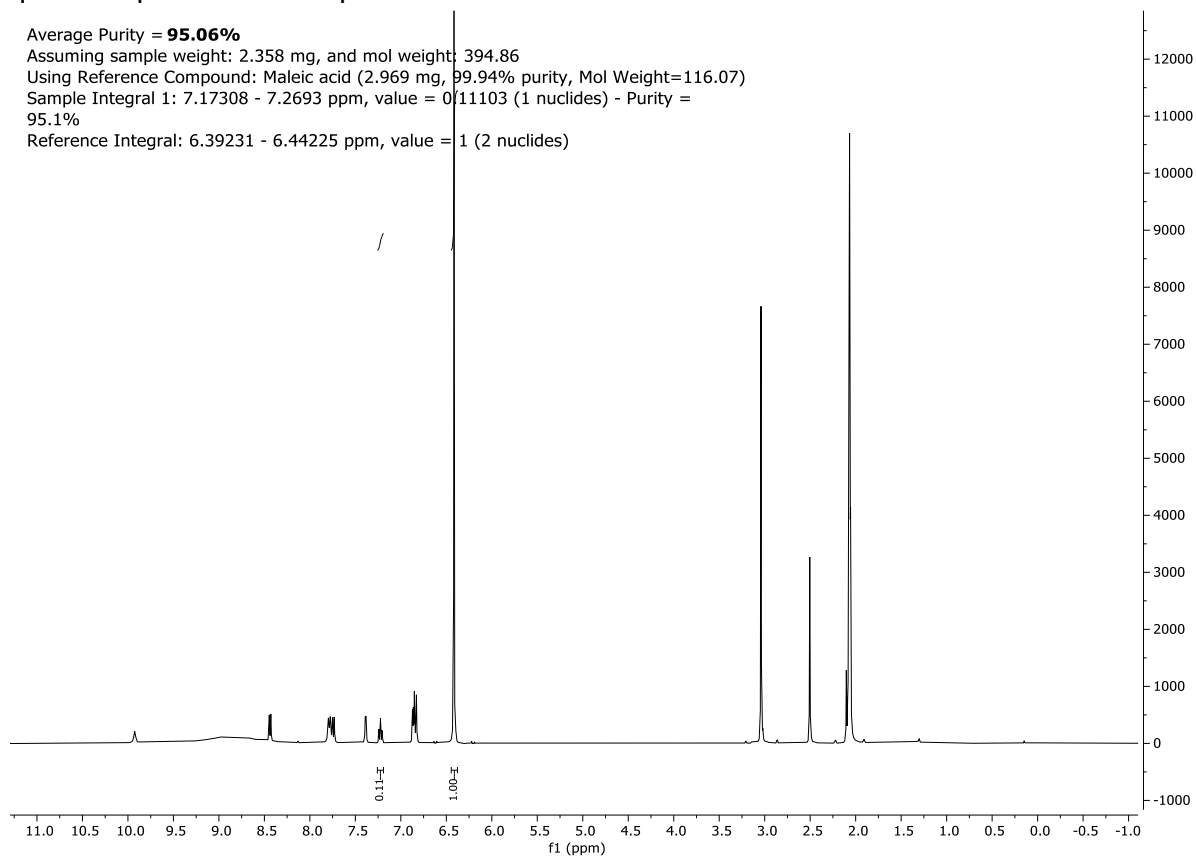


^{13}C spectrum of compound **36**:

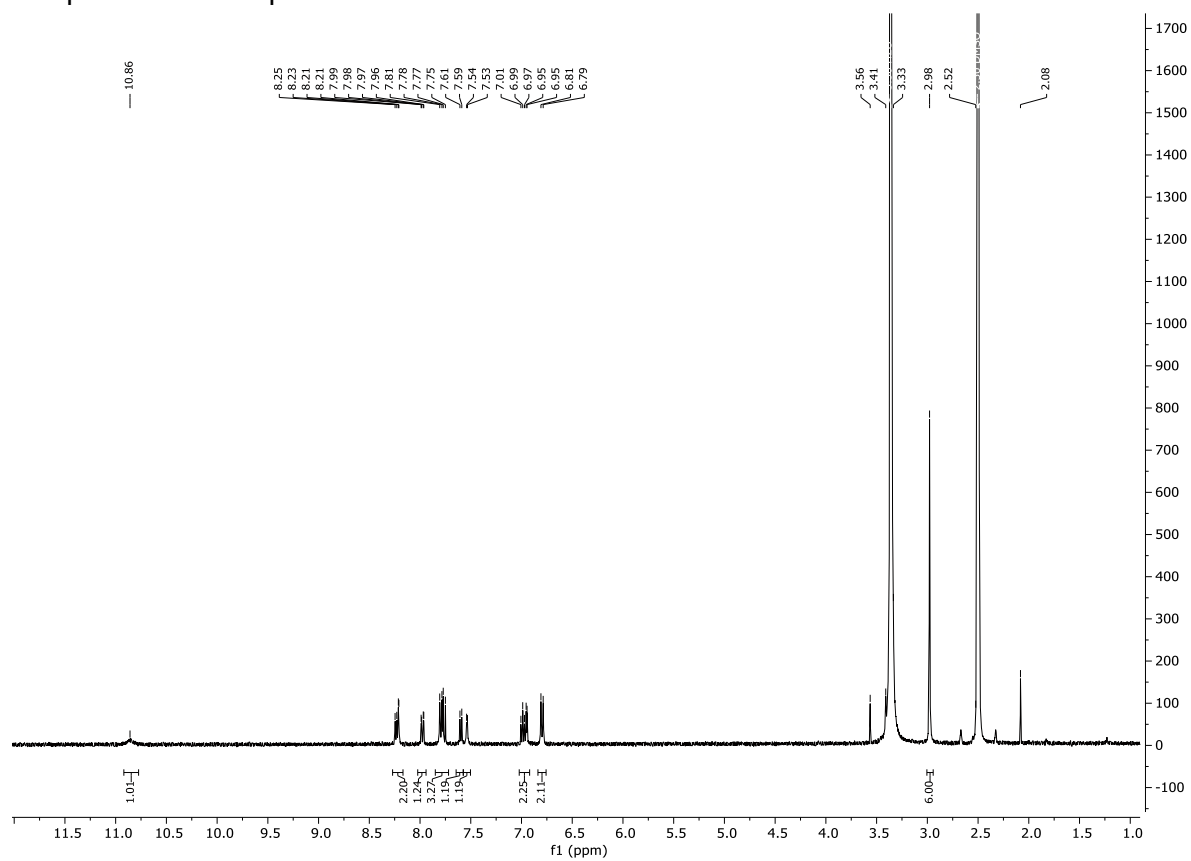


qHNMR spectrum of compound **36**:

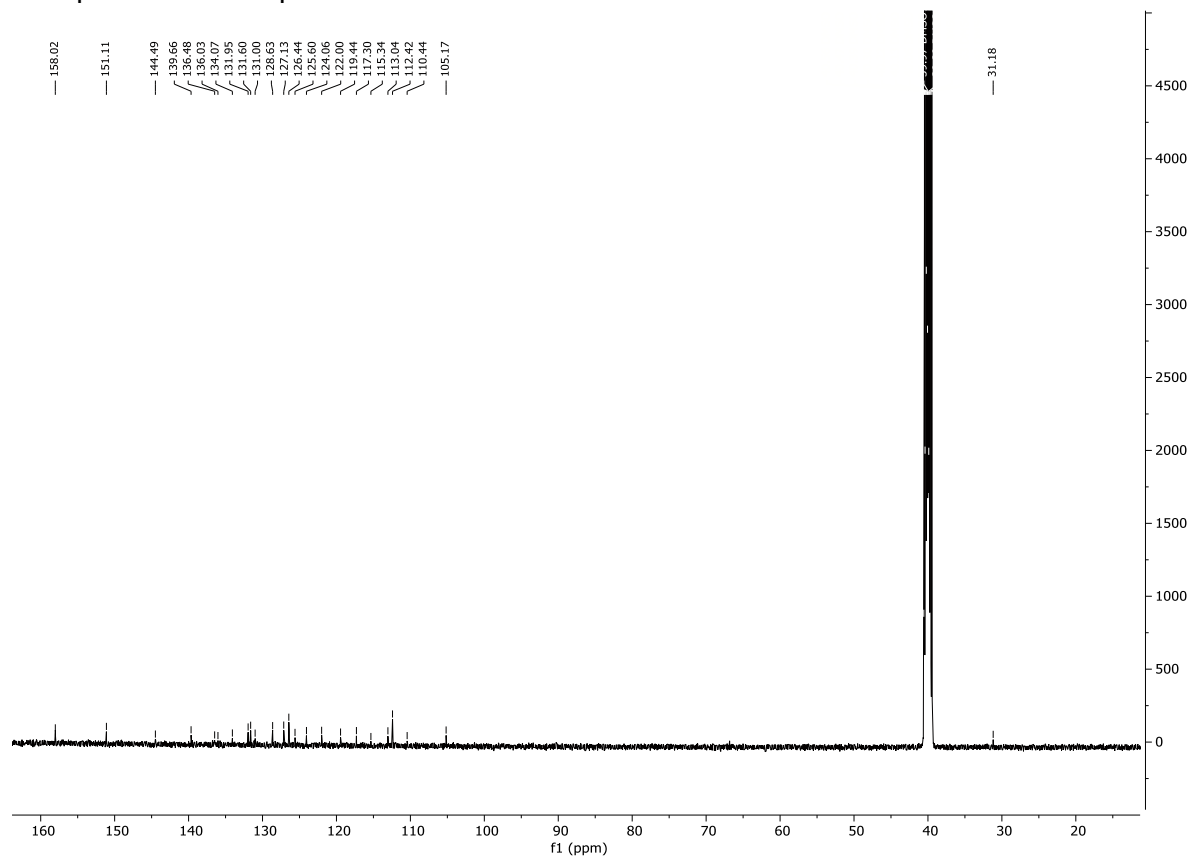
Average Purity = **95.06%**
Assuming sample weight: 2.358 mg, and mol weight: 394.86
Using Reference Compound: Maleic acid (2.969 mg, 99.94% purity, Mol Weight=116.07)
Sample Integral 1: 7.17308 - 7.2693 ppm, value = 0.11103 (1 nuclides) - Purity = 95.1%
Reference Integral: 6.39231 - 6.44225 ppm, value = 1 (2 nuclides)



¹H spectrum of compound **37**:

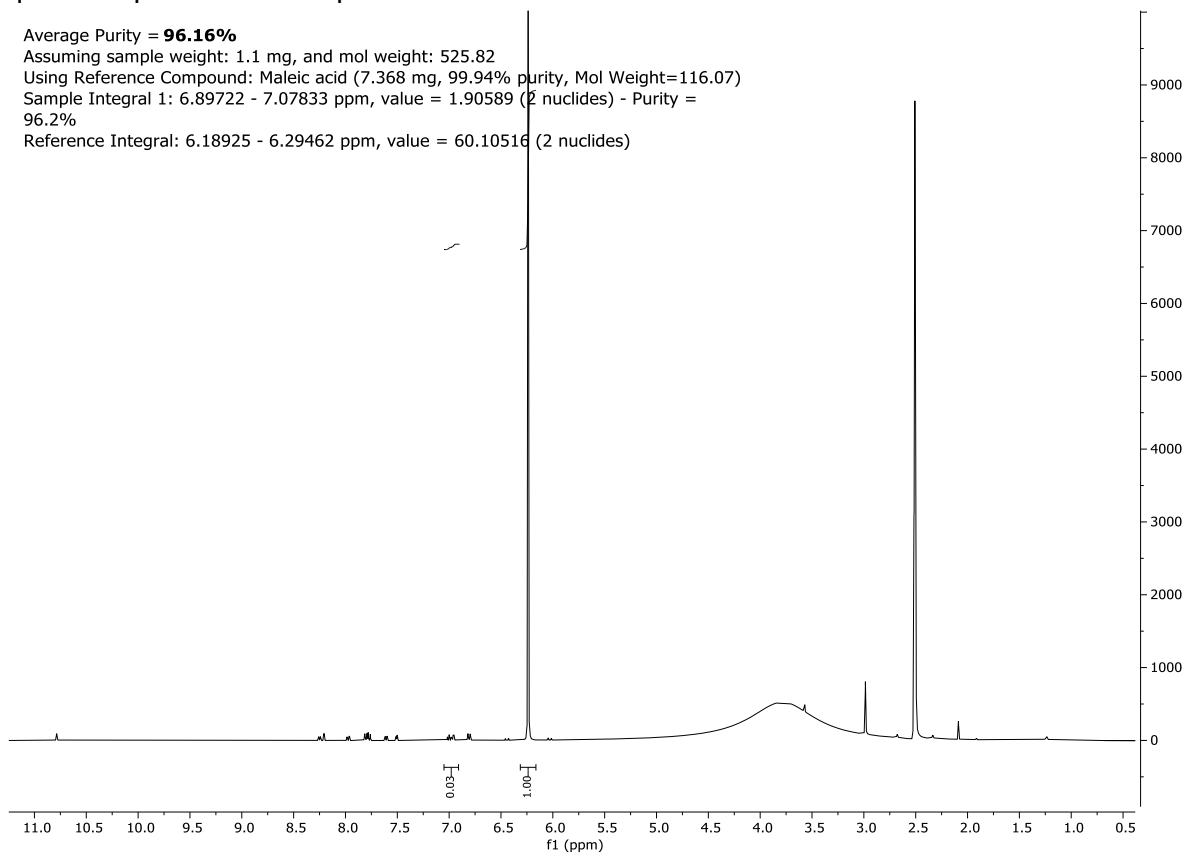


^{13}C spectrum of compound **37**:

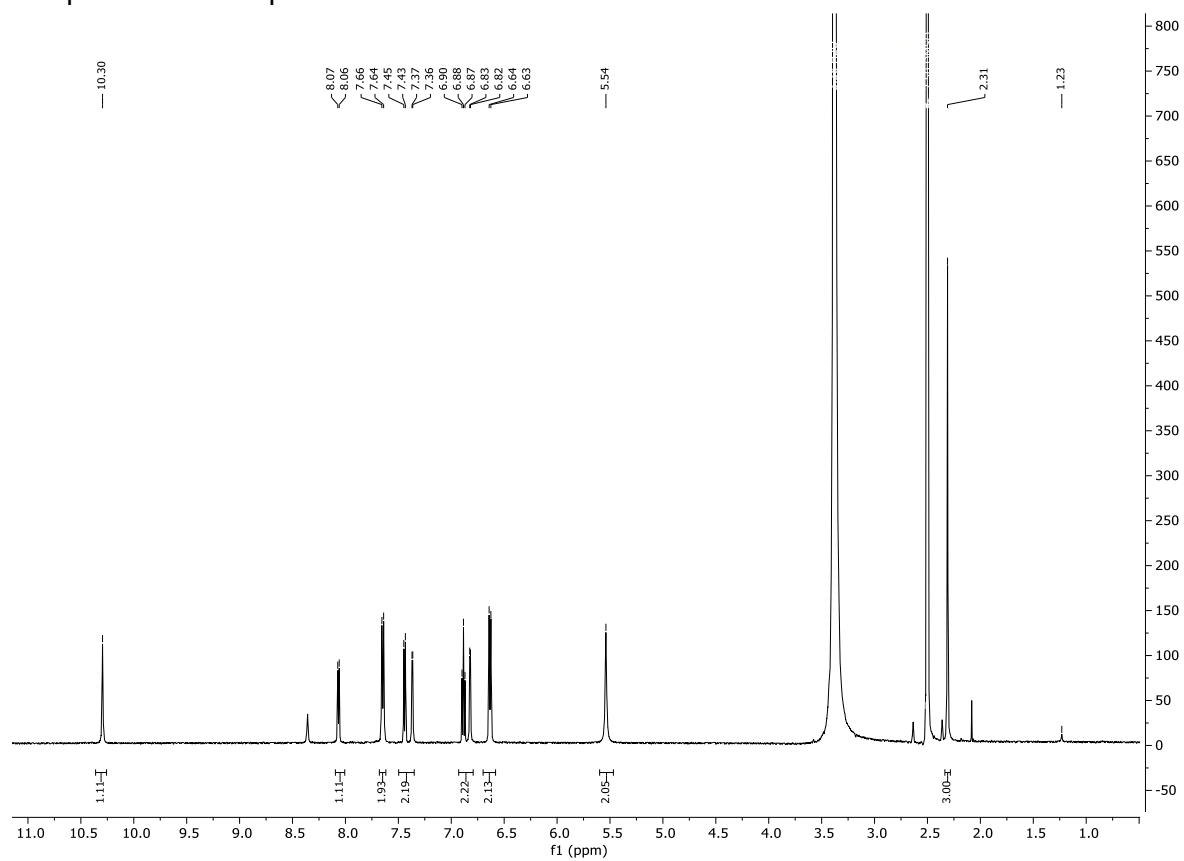


qHNMR spectrum of compound **37**:

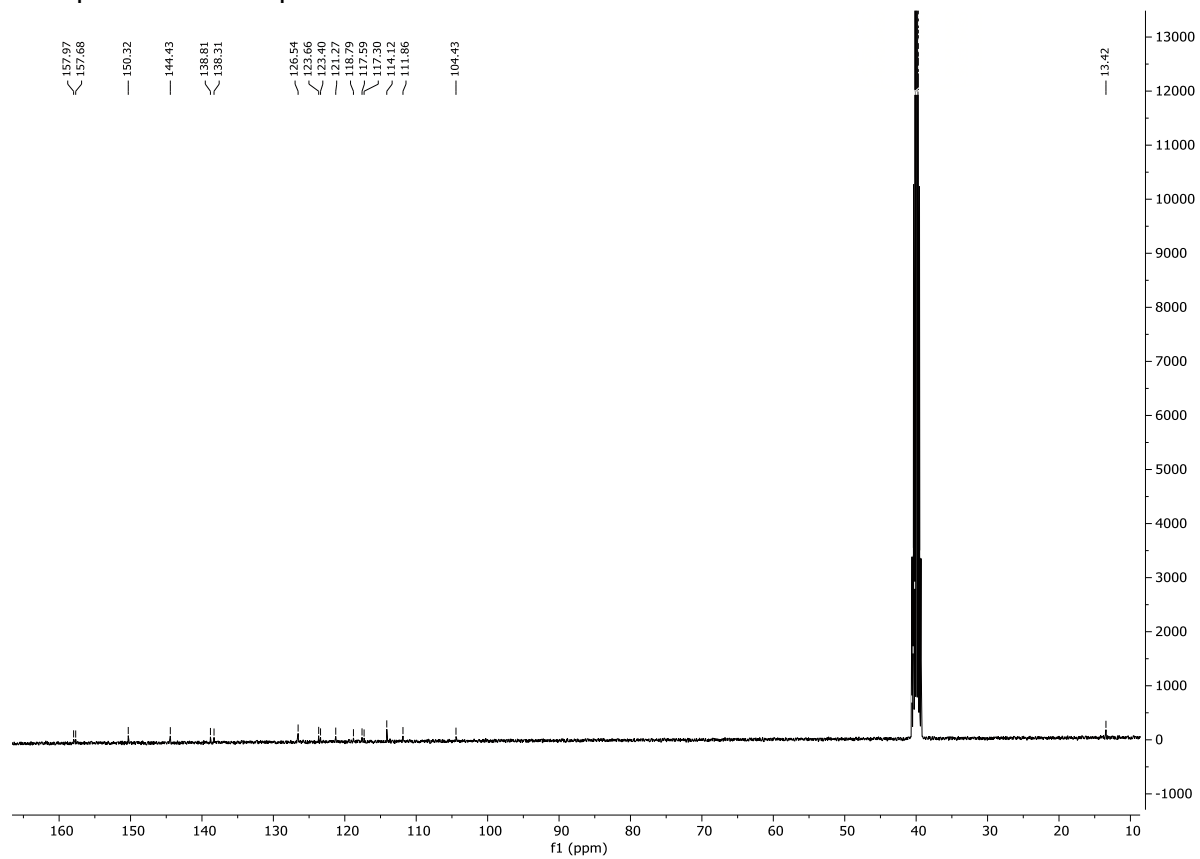
Average Purity = **96.16%**
Assuming sample weight: 1.1 mg, and mol weight: 525.82
Using Reference Compound: Maleic acid (7.368 mg, 99.94% purity, Mol Weight=116.07)
Sample Integral 1: 6.89722 - 7.07833 ppm, value = 1.90589 (2 nuclides) - Purity = 96.2%
Reference Integral: 6.18925 - 6.29462 ppm, value = 60.10516 (2 nuclides)



¹H spectrum of compound **38**:



¹³C spectrum of compound **38**:



qHNMR spectrum of compound **38**:

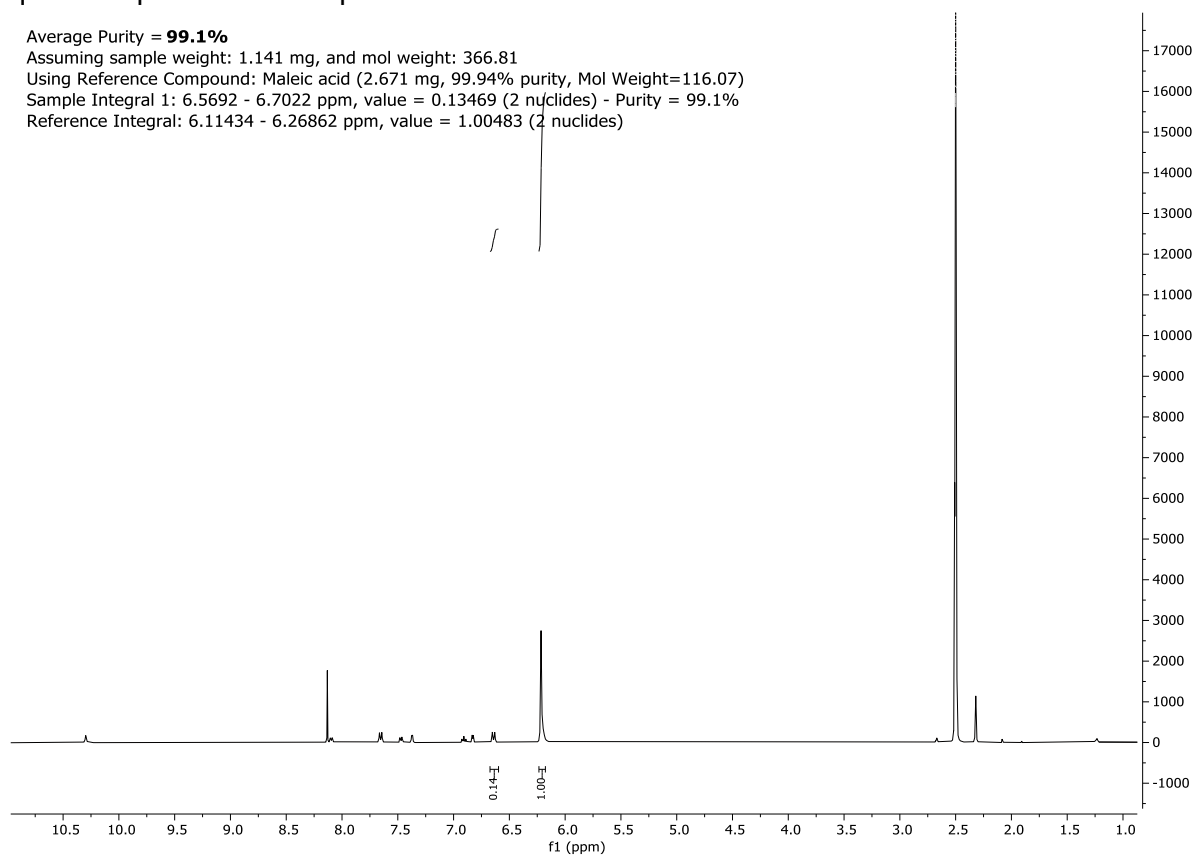
Average Purity = **99.1%**

Assuming sample weight: 1.141 mg, and mol weight: 366.81

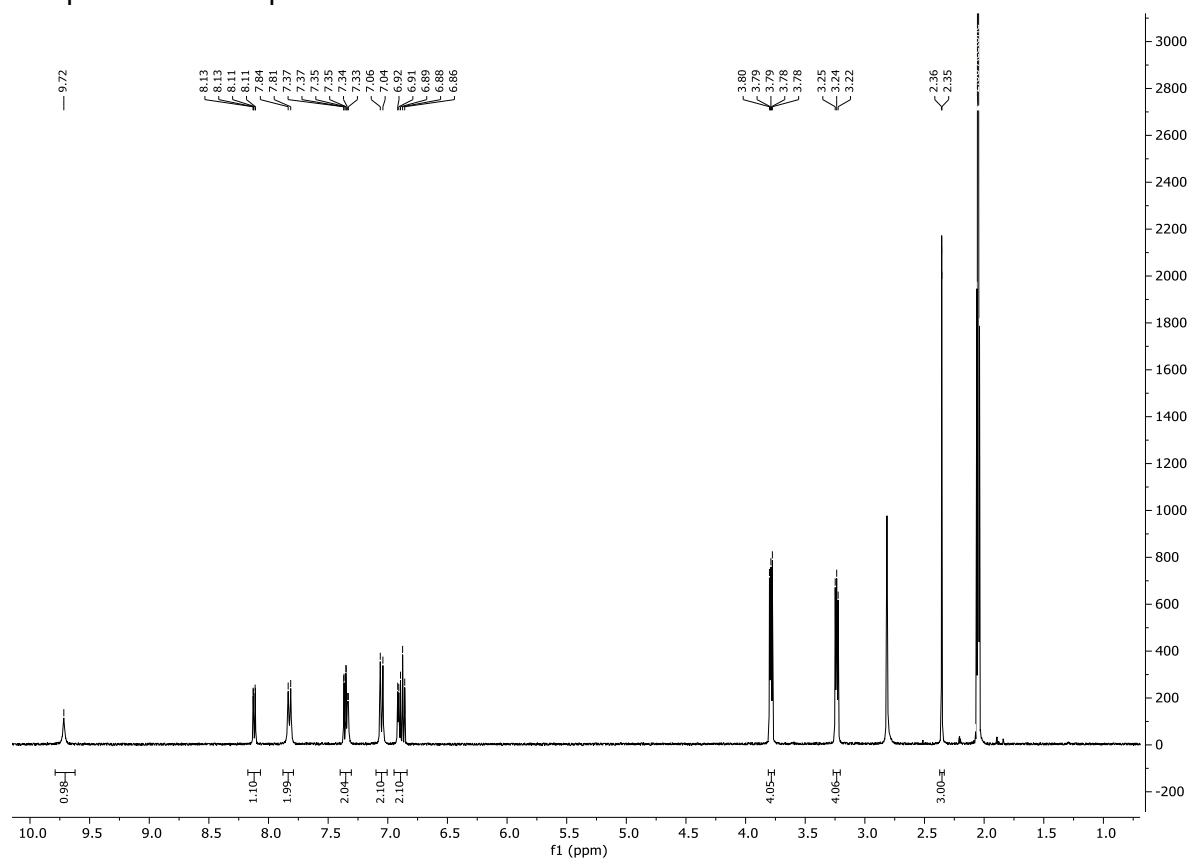
Using Reference Compound: Maleic acid (2.671 mg, 99.94% purity, Mol Weight=116.07)

Sample Integral 1: 6.5692 - 6.7022 ppm, value = 0.13469 (2 nuclides) - Purity = 99.1%

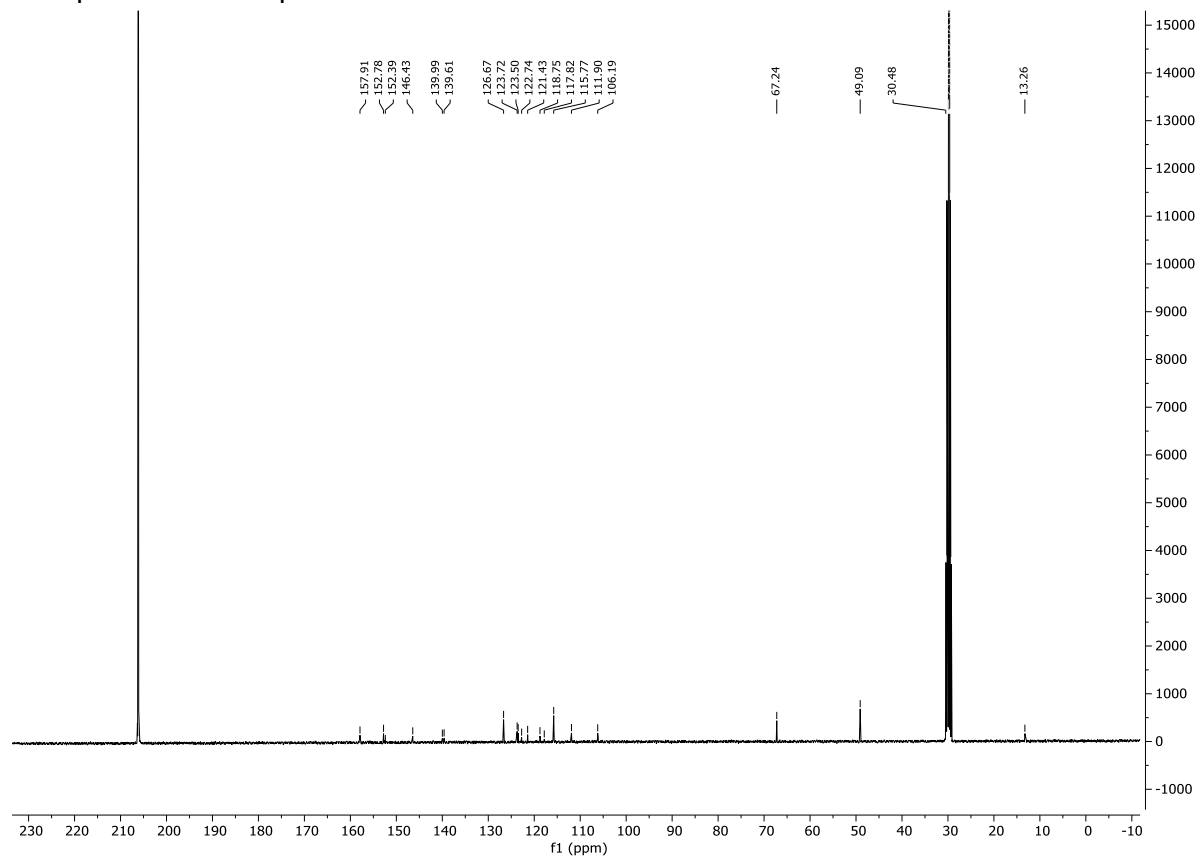
Reference Integral: 6.11434 - 6.26862 ppm, value = 1.00483 (2 nuclides)



¹H spectrum of compound **39**:

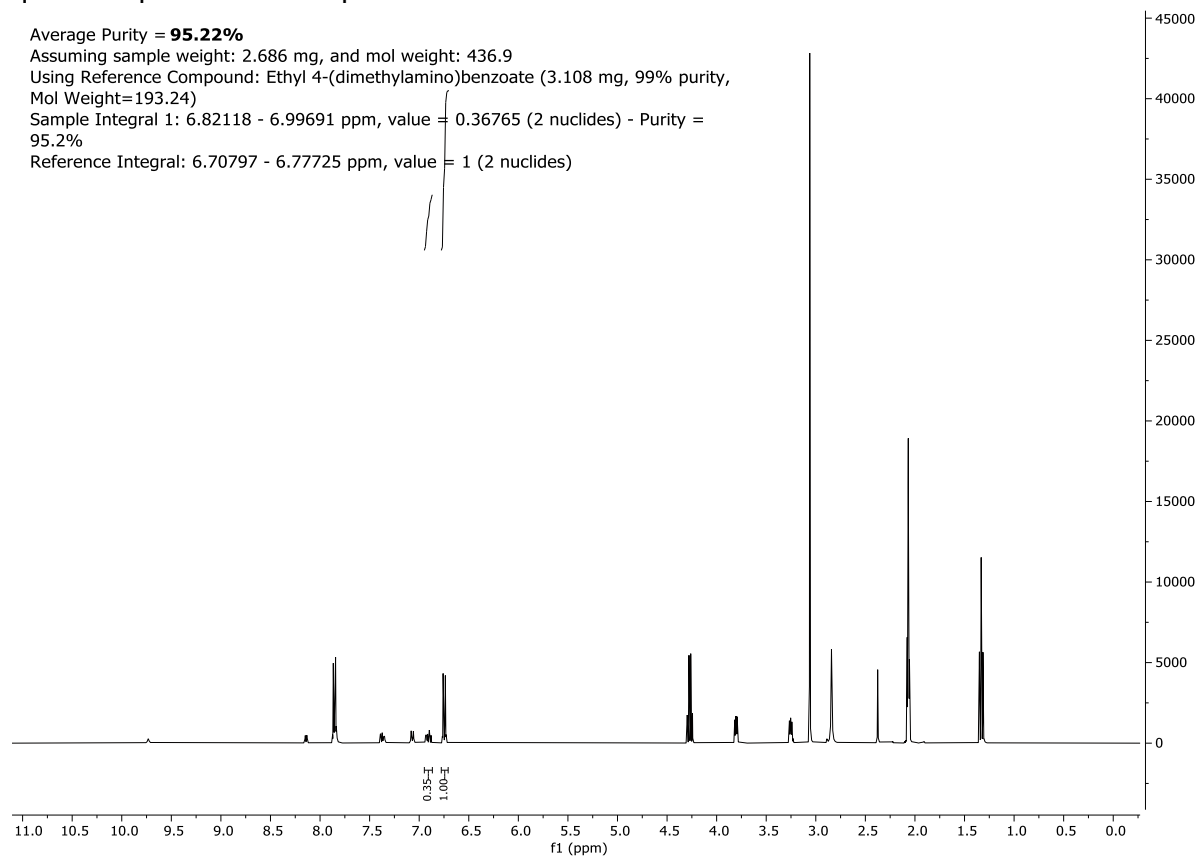


¹³C spectrum of compound **39**:

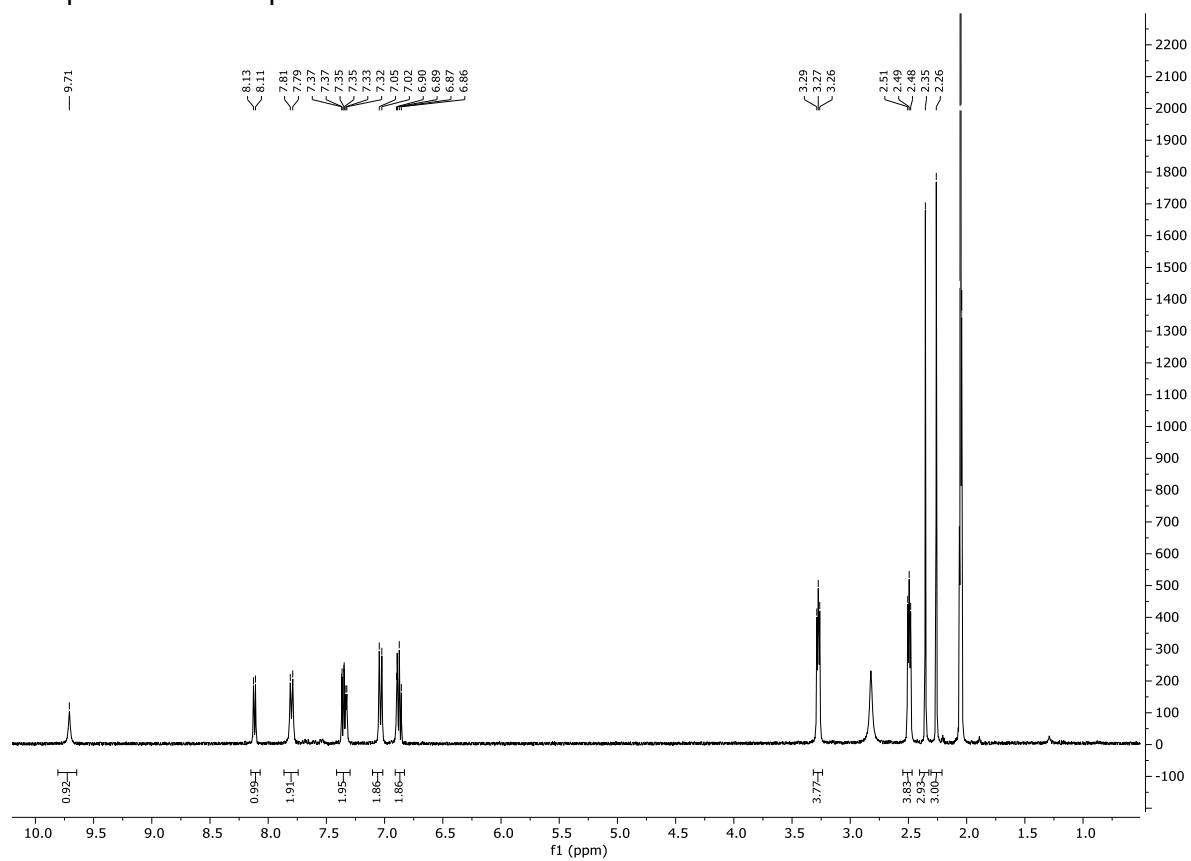


qHNMR spectrum of compound **39**:

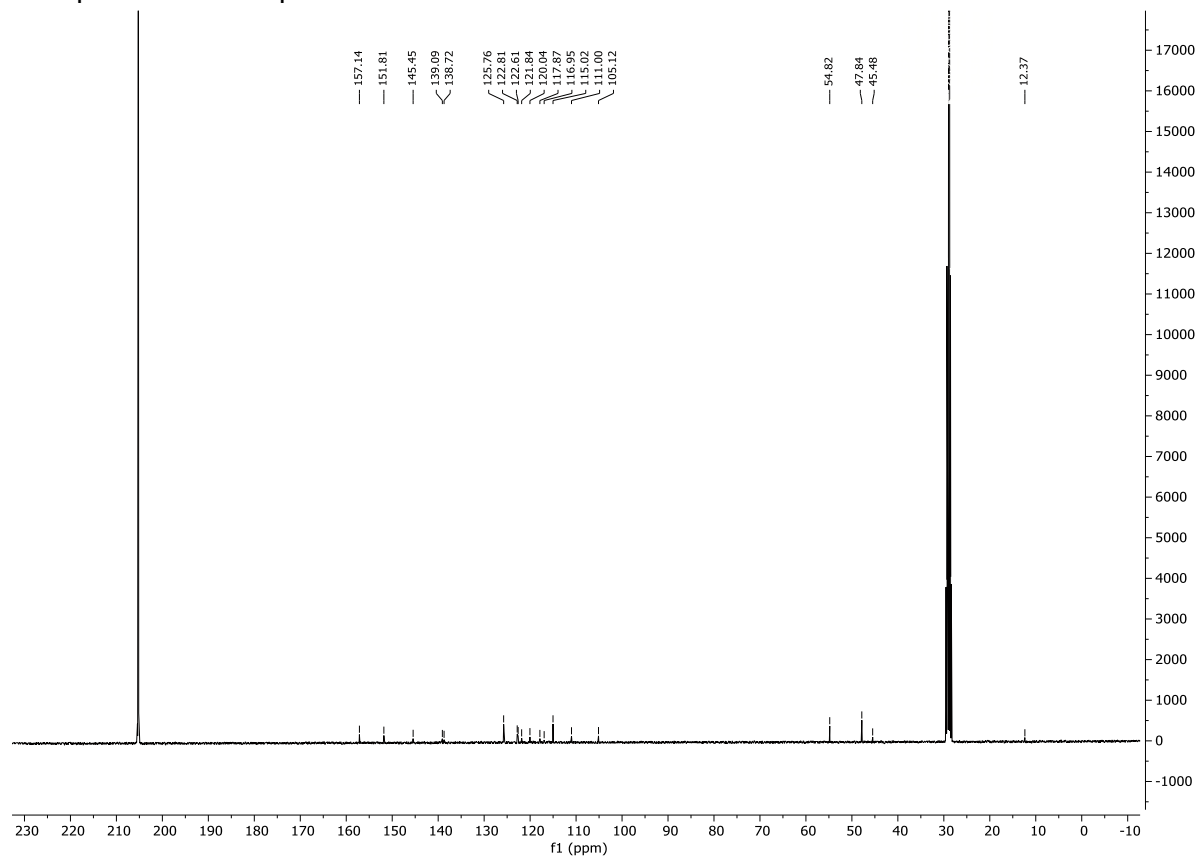
Average Purity = **95.22%**
Assuming sample weight: 2.686 mg, and mol weight: 436.9
Using Reference Compound: Ethyl 4-(dimethylamino)benzoate (3.108 mg, 99% purity,
Mol Weight=193.24)
Sample Integral 1: 6.82118 - 6.99691 ppm, value = 0.36765 (2 nuclides) - Purity = 95.2%
Reference Integral: 6.70797 - 6.77725 ppm, value = 1 (2 nuclides)



¹H spectrum of compound **40**:

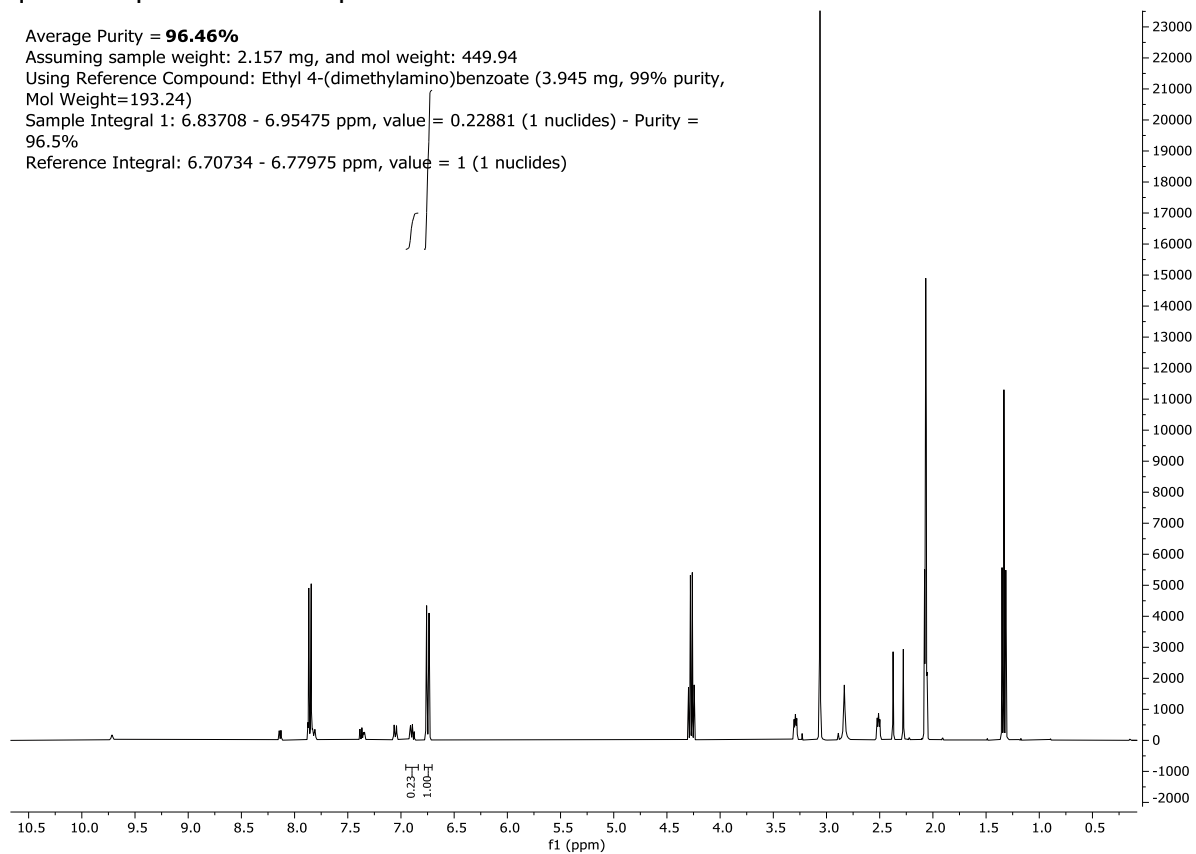


^{13}C spectrum of compound **40**:

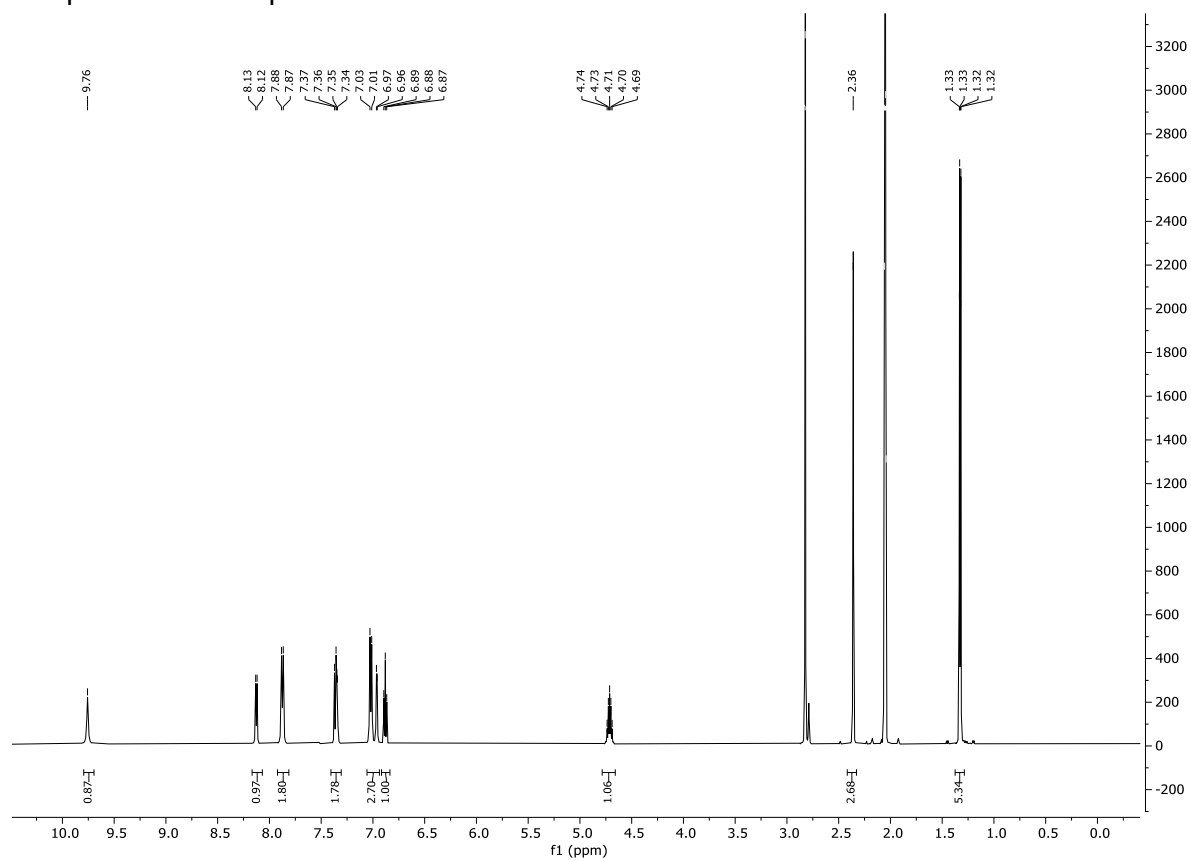


qHNMR spectrum of compound 40:

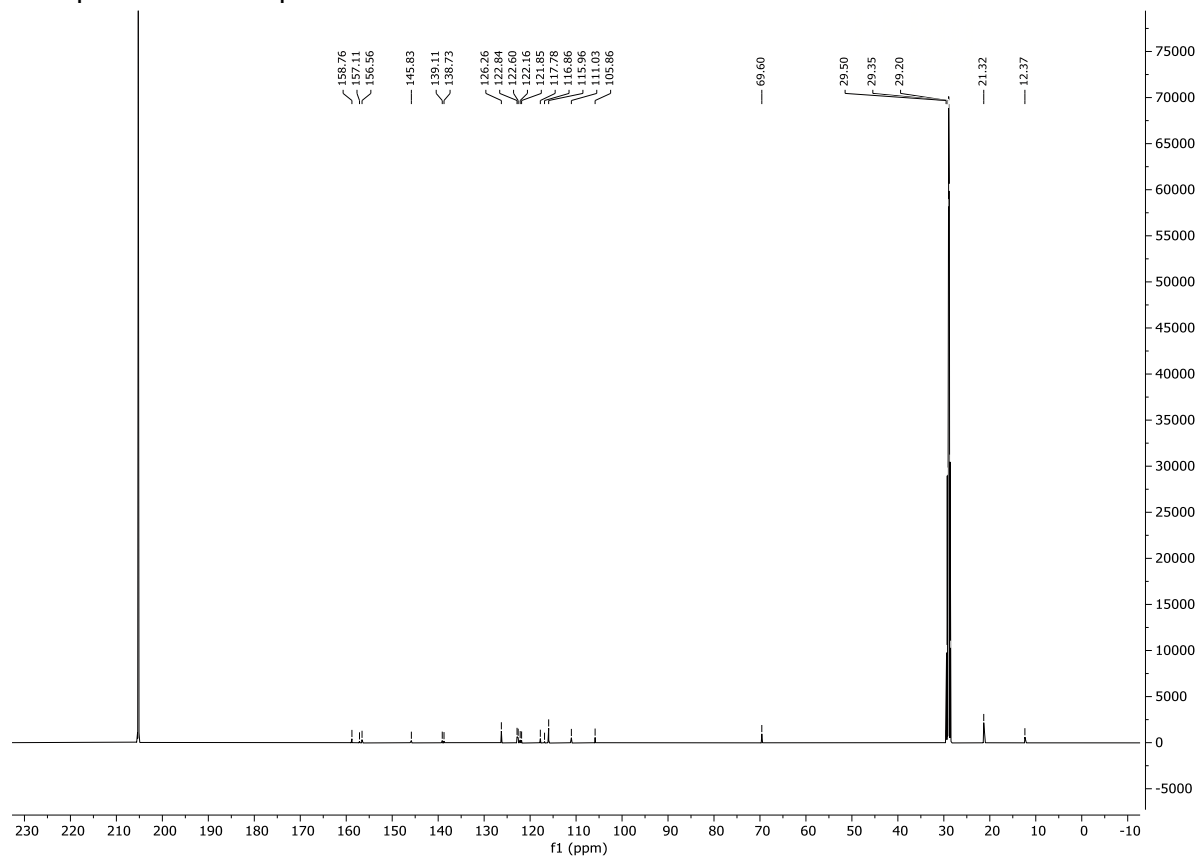
Average Purity = **96.46%**
Assuming sample weight: 2.157 mg, and mol weight: 449.94
Using Reference Compound: Ethyl 4-(dimethylamino)benzoate (3.945 mg, 99% purity,
Mol Weight=193.24)
Sample Integral 1: 6.83708 - 6.95475 ppm, value = 0.22881 (1 nuclides) - Purity = 96.5%
Reference Integral: 6.70734 - 6.77975 ppm, value = 1 (1 nuclides)



¹H spectrum of compound **41**:

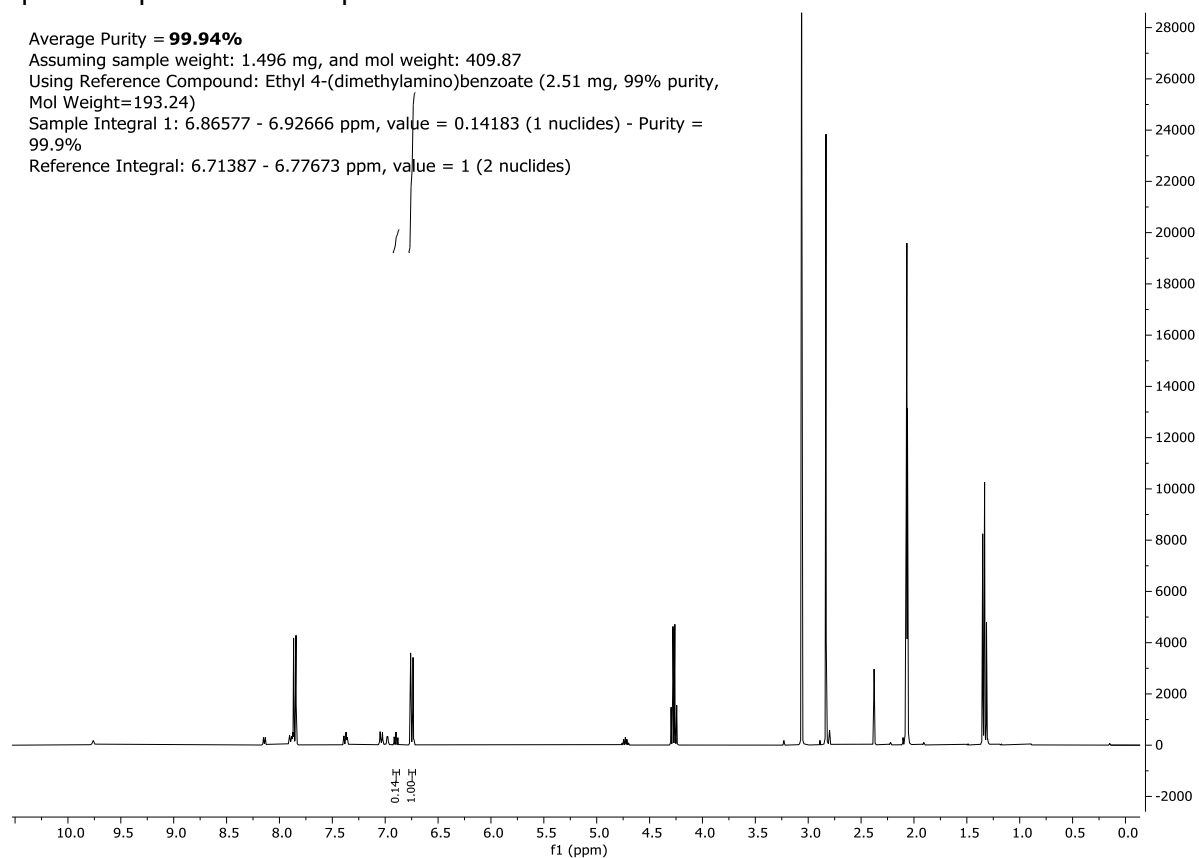


¹³C spectrum of compound **41**:

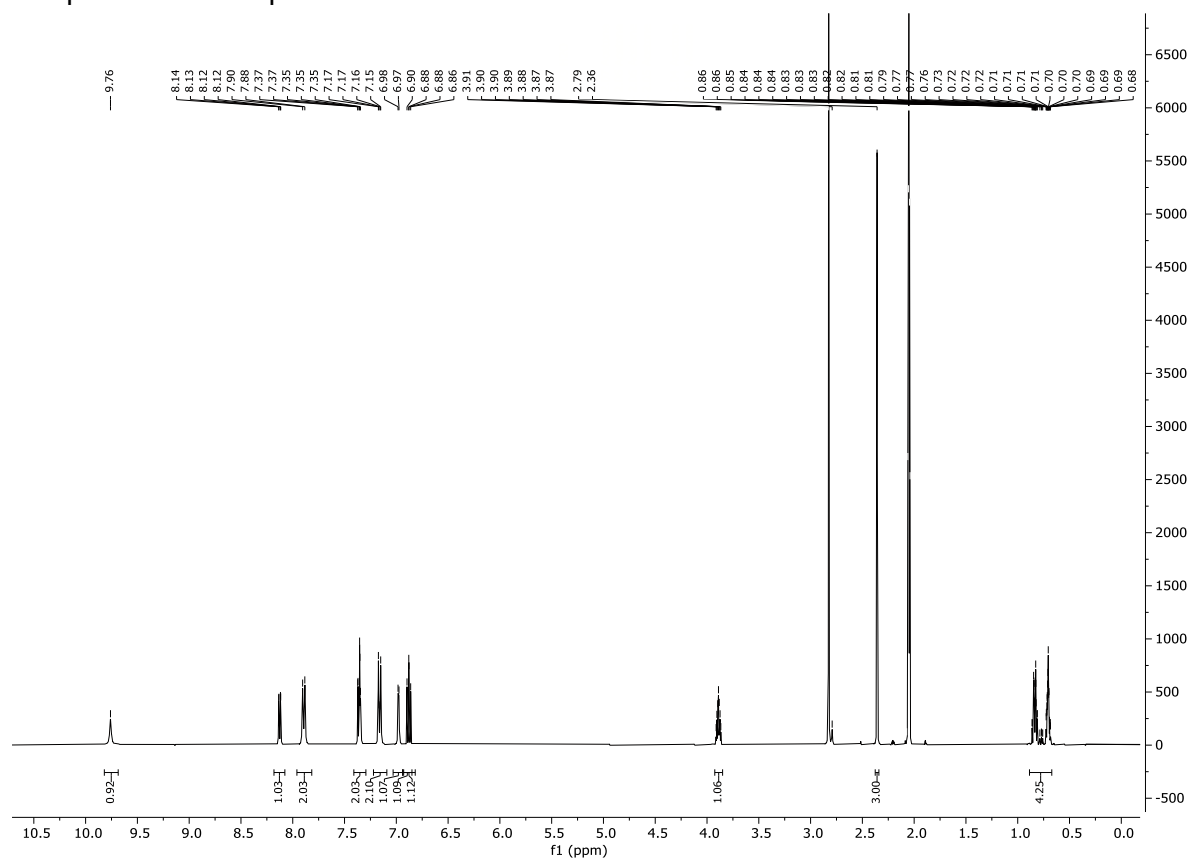


qHNMR spectrum of compound **41**:

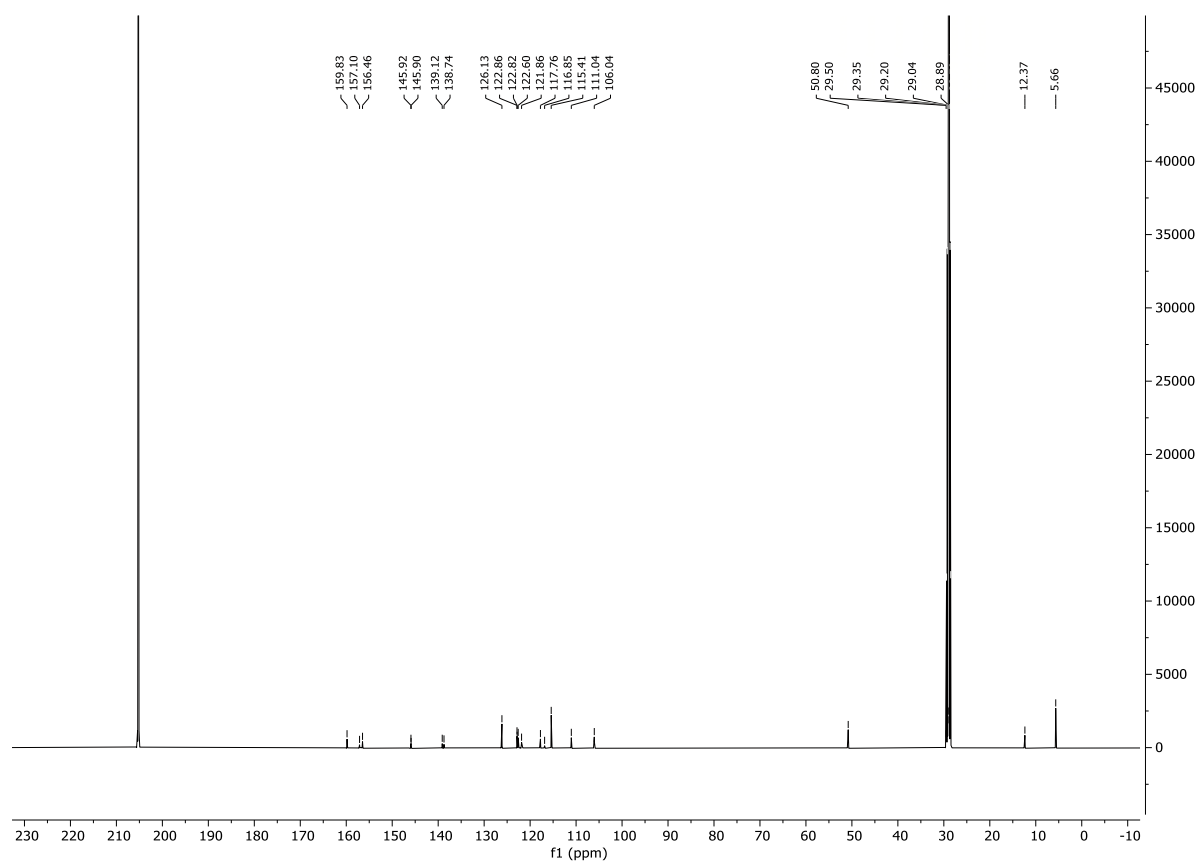
Average Purity = **99.94%**
Assuming sample weight: 1.496 mg, and mol weight: 409.87
Using Reference Compound: Ethyl 4-(dimethylamino)benzoate (2.51 mg, 99% purity, Mol Weight=193.24)
Sample Integral 1: 6.86577 - 6.92666 ppm, value = 0.14183 (1 nuclides) - Purity = 99.9%
Reference Integral: 6.71387 - 6.77673 ppm, value = 1 (2 nuclides)



¹H spectrum of compound 42:



^{13}C spectrum of compound **42**:



qHNMR spectrum of compound **42**:

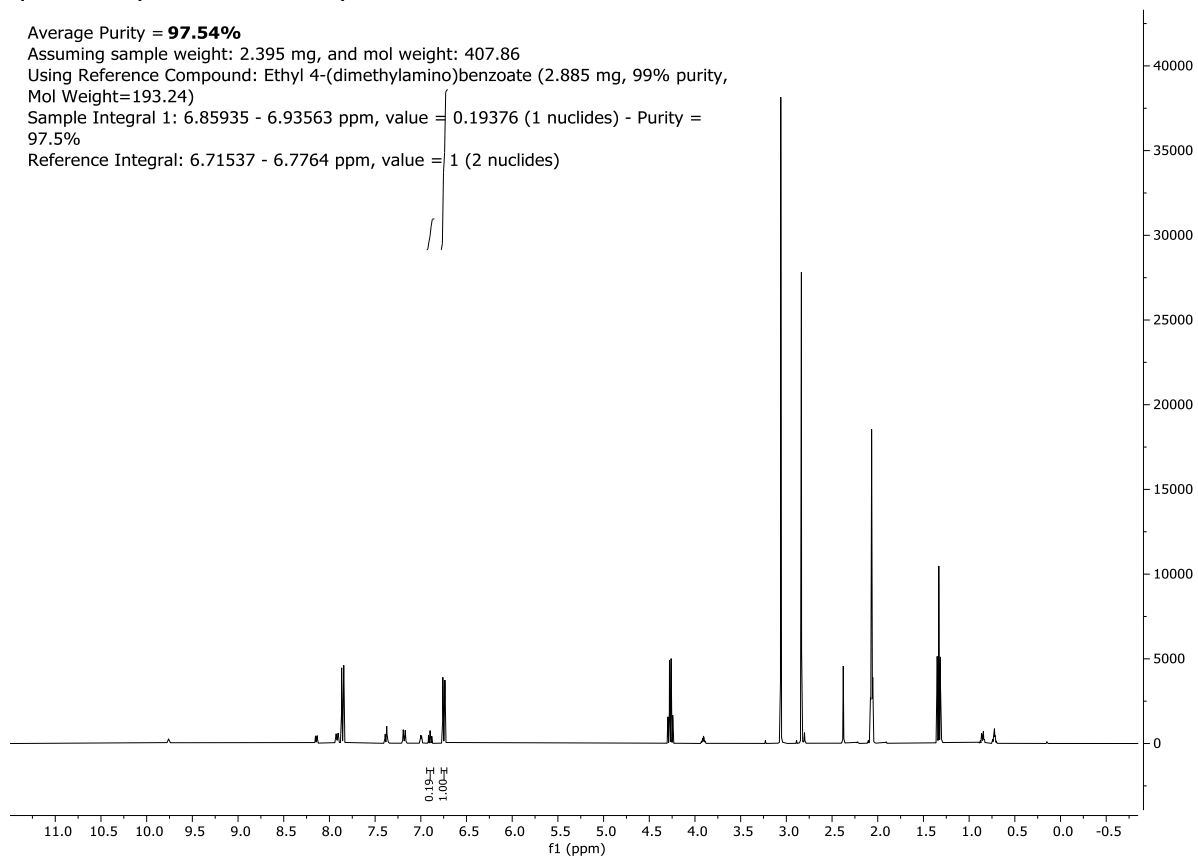
Average Purity = **97.54%**

Assuming sample weight: 2.395 mg, and mol weight: 407.86

Using Reference Compound: Ethyl 4-(dimethylamino)benzoate (2.885 mg, 99% purity, Mol Weight=193.24)

Sample Integral 1: 6.85935 - 6.93563 ppm, value = 0.19376 (1 nuclides) - Purity = 97.5%

Reference Integral: 6.71537 - 6.7764 ppm, value = 1 (2 nuclides)



12.3 Tuning RXR modulators for PGC1 α recruitment

Nawa, F.*; Sai, M.*; Vietor, J.*; Schwarzenbach, R.; Bitic, A.; Wolff, S.; Ildefeld, N.; Pabel, J.; Wein, T.; Marschner, J.A.; Heering, J.; Merk, D. Tuning RXR modulators for PGC1 α recruitment.

Manuscript currently accepted in *J. Med. Chem.* after peer-review. (02.09.2024)

Tuning RXR Modulators for PGC1 α Recruitment

Felix Nawa^{1,#}, Minh Sai^{1,#}, Jan Vietor^{1,#}, Roman Schwarzenbach¹, Anesa Bitić¹, Sina Wolff¹, Niklas Ildefeld², Jörg Pabel¹, Thomas Wein¹, Julian A. Marschner¹, Jan Heering³, Daniel Merk^{1*}

¹ Ludwig-Maximilians-Universität (LMU) München, Department of Pharmacy, 81377 Munich, Germany

² Goethe University Frankfurt, Institute of Pharmaceutical Chemistry, 60438 Frankfurt, Germany

³ Fraunhofer Institute for Translational Medicine and Pharmacology ITMP, 60596 Frankfurt, Germany

F.N., M.S. and J.V. contributed equally

* daniel.merk@cup.lmu.de

ABSTRACT: The molecular activation mechanism of the nuclear retinoid X receptors (RXRs) crucially involves ligand-induced co-repressor release and co-activator recruitment which mediate transcriptional repression or activation. The ability of RXR to bind diverse co-activators suggests that a co-regulator-selective modulation by ligands may open an avenue to tissue- or gene-selective RXR activation. Here, we identified strong induction of peroxisome proliferator-activated receptor gamma co-activator 1-alpha (PGC1 α) binding to RXR by a synthetic agonist but not by the endogenous ligand 9-cis retinoic acid. Structure-guided diversification of this lead resulted in a set of three structurally related RXR agonists with different ability to promote PGC1 α recruitment in cell-free and cellular context. These results demonstrate that selective modulation of co-regulator recruitment to RXR can be achieved with molecular glues and open potential new therapeutic opportunities by targeting ligand-induced RXR-PGC1 α interaction.

KEYWORDS retinoid X receptor; peroxisome proliferator-activated receptor gamma co-activator 1-alpha; nuclear receptor; transcription factor; energy metabolism; cancer

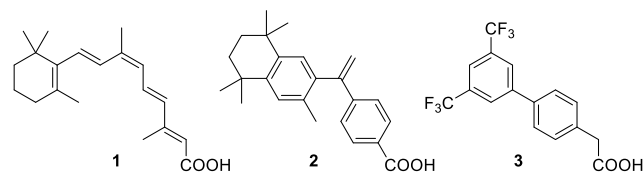
Introduction

Nuclear receptors (NRs) are ligand-sensing transcription factors and regulate gene expression in response to ligand signals¹⁻⁴. On the molecular level, their activity is to a large extent mediated by the recruitment and release of co-activators and co-repressors. NR modulator binding induces conformational changes in the NR ligand binding domain (LBD) that in turn alter the affinity for interaction with co-activators or co-repressors⁴⁻⁷. NR agonists can thus be described as molecular glues stabilizing protein-protein interactions of the target NR with co-activator complexes^{8,9}. The existence of multiple different co-activators and co-repressors capable of interacting with the same NR suggests that this regulatory network may be selectively modulated by different types of NR ligands that induce recruitment of only a subset of possible co-regulators. Such selective modulation might open new therapeutic avenues³ but has been poorly explored to date.

The retinoid X receptors (RXR α , RXR β and RXR γ , NR2B1-3)^{10,11} are a subfamily of NRs recognizing fatty acids and vitamin A metabolites like 9-cis retinoic acid (9-cis RA, **1**, Chart 1) as natural ligands^{12,13}. RXRs exhibit a particularly important role in NR signaling as universal heterodimer partners for various other NRs¹. Therefore, they participate in multiple physiological processes ranging from proliferation and differentiation over metabolic homeostasis to inflammation¹⁴⁻¹⁹. While this suggests therapeutic potential of RXR ligands in diverse indications, the wide involvement in

genomic regulation also entails adverse effects of pharmacological RXR modulation which is evident from the only drug approved synthetic RXR agonist bexarotene (**2**; EC₅₀(RXR α / β / γ) = 0.025/0.028/0.020 μ M)²⁰⁻²³. While many potent and selective RXR agonist and antagonist scaffolds are available^{24,25} and even RXR ligands selectively stabilizing certain heterodimers²⁶⁻²⁹ have been discovered, ligand-induced selective co-regulator recruitment to RXR might be an attractive avenue to achieve more selective modulation that has not been explored.

Chart 1. RXR agonists



NR co-regulators exhibit different expression patterns³⁰⁻³² and since NRs can typically interact with various co-regulators, selective ligand-induced recruitment of only a subset of these interaction partners might enable tissue-specific or even gene-selective modulation with reduced adverse effects. Progress with co-regulator selective ligands has been made for several NRs including, for example, peroxisome proliferator-activated receptor γ (PPAR γ)^{33,34}, farnesoid X receptor (FXR)³⁵ and estrogen receptor (ER)^{36,37}, suggesting that tuning of the ligand-induced co-regulator recruitment

profile may also be possible for RXR but this concept has not been established with suitable ligands, yet.

Here, we discovered that the recently developed RXR agonist **3**³⁸ has substantially different effects on co-regulator recruitment to RXR than the natural agonist **1** and explored the potential of tuning this activity by broad structural modifications on this ligand scaffold. Using a chemically diverse set of analogues of **3** designed in a structure-guided fashion, we found that minor structural differences impacted on the binding of peroxisome proliferator-activated receptor gamma co-activator 1-alpha (PGC1 α) to the RXR LBD demonstrating that RXR ligands can be tuned for selective effects on co-regulator recruitment. This unprecedented ligand-induced interaction of RXR with PGC1 α , which is a key regulator of metabolism and energy homeostasis³⁹⁻⁴¹, may open new opportunities for RXR modulation.

Results & Discussion

Selective modulation of NRs via selective effects on protein-protein interactions with partner receptors or co-regulators is increasingly recognized as a promising avenue to therapeutic innovation in the NR field³. Based on recent studies showing, that different agonist chemotypes of the PPARs and FXR can exhibit different effects on co-regulator recruitment to their target receptors^{35,42}, we hypothesized that selective co-regulator recruitment could also be achieved with different RXR agonist scaffolds. Using 9-cis RA (**1**) and a collection of chemically diverse synthetic RXR modulators, we explored such potential mechanistic differences in the co-regulator recruitment profile of RXRs by observing the ligand-induced interaction of the RXR α LBD (Tb³⁺-cryptate labeled, FRET donor) with a panel of common NR co-regulator peptides (fluorescein-labeled, FRET acceptor) in homogeneous time-resolved fluorescence resonance energy transfer (HTRF) based assays. We found pronounced differences in RXR-co-regulator recruitment profiles (Figure 1) caused by the natural ligand **1** and the synthetic agonist **3**³⁸. 9-cis RA (**1**) recruited several co-activators (SRCs, NCoA6) with intermediate efficacy while displacement of the co-repressor silencing mediator for retinoid and thyroid-hormone receptors (SMRT, NCOR2) emerged as strongest effect. NCOR1 binding to RXR was generally weaker in the HTRF setting and slightly reduced by **1**. **3**, in contrast, exhibited a strong preference for PGC1 α recruitment while its effect on corepressor (NCOR1/2) binding was negligible. This ability of **3** to differentiate between co-regulators and induce recruitment of PGC1 α with strong preference appeared highly attractive as it might offer access to unprecedented RXR modulation.

The appealing effect of **3** on RXR-PGC1 α interaction prompted us to study the structure-activity relationship of this RXR modulator chemotype further. To explore the chemical space around **3**, we employed the co-crystal structure of the RXR α LBD in complex with **3** (pdb ID 6sjm³⁸; Figure 2a) for structure-guided analogue design. Retrospective docking of the previously reported derivatives of **3**³⁸ showed good correlation between potency and docking score (Figure 2b) indicating that a docking-based approach was suitable to reveal analogues of **3** as RXR ligands. We thus generated a virtual library of 15,759 biphenylacetic

acid derivatives (Figure 2c) by in silico fusion of 4-boronophenylacetic acid with commercially available aryl halides. These designs were then docked to the binding site of **3** and ranked based on their score. From the top-ranking 100 molecules, we selected **4-31** for synthesis based on binding mode inspection and chemical diversity.

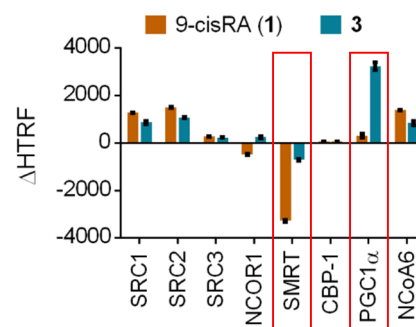


Figure 1. Effects of 9-cis RA (**1**) and **3** on co-regulator recruitment to the RXR α LBD. Compounds were tested at 1 μ M. Data are the mean \pm SD Δ HTRF relative to the ligand free setting; N=4. Red boxes highlight prominent differences.

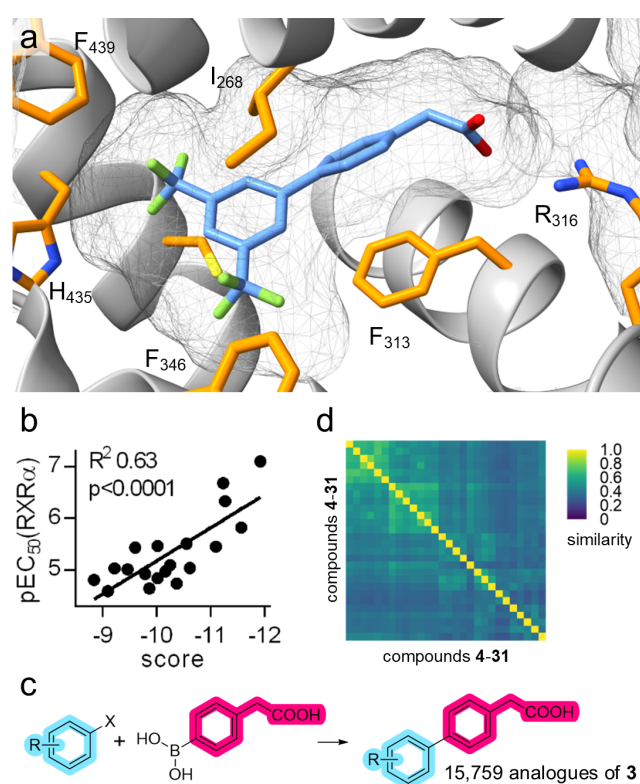
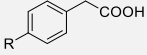
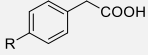
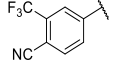
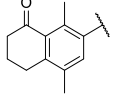
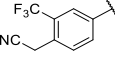
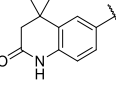
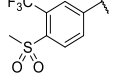
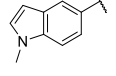
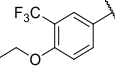
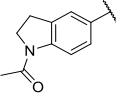
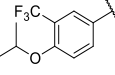
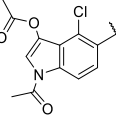
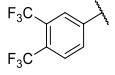
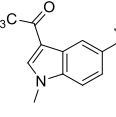
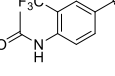
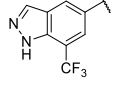
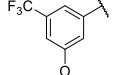
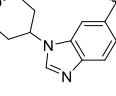
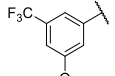
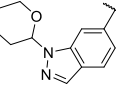
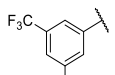
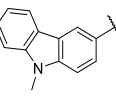
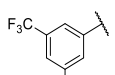
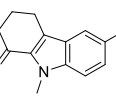
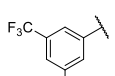
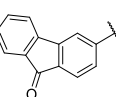
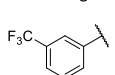
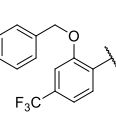
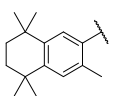
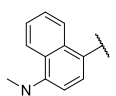


Figure 2. Structure-based design of RXR ligands based on **3**. (a) **3** binds to the highly hydrophobic orthosteric site of RXR α (pdb ID 6sjm³⁸) and forms a single polar contact to Arg316 like most RXR agonists. (b) Retrospective evaluation of **3** and previously tested analogues³⁸ revealed good correlation between potency and docking score. (c) A virtual library of 15,759 biphenylacetic acids was generated for docking to the binding site of **3** in RXR α to identify novel RXR modulators. (d) The computationally favored designs **4-31** were chemically diverse despite sharing the biphenylacetic acid motif. The heatmap shows pairwise Tanimoto similarity computed on Morgan fingerprints.

Table 1. Analogues of RXR agonist 3 from structure-guided design

ID	 R	EC ₅₀ (max. rel. activation) ^a			ID	 R	EC ₅₀ (max. rel. activation) ^a		
		RXR α	RXR β	RXR γ			RXR α	RXR β	RXR γ
4		1.6±0.2 μM (24±1%)	2.0±0.3 μM (31±1%)	11±1 μM (31±2%)	18		15±1 μM (18±1%)	14±3 μM (26±2%)	13±4 μM (24±2%)
5		2.7±0.3 μM (12±1%)	4.2±0.7 μM (18±1%)	11±1 μM (16±1%)	19		inactive (50 μM ^b)	inactive (50 μM ^b)	inactive (50 μM ^b)
6		inactive (15 μM ^b)	inactive (15 μM ^b)	inactive (15 μM ^b)	20		inactive (10 μM ^b)	inactive (10 μM ^b)	inactive (10 μM ^b)
7		4.4±0.5 μM (14±1%)	3.3±0.4 μM (10±1%)	3.0±0.1 μM (14±1%)	21		inactive (100 μM ^b)	inactive (100 μM ^b)	inactive (100 μM ^b)
8		0.29±0.03 μM (29±1%)	1.3±0.1 μM (22±1%)	3.4±0.3 μM (20±1%)	22		inactive (50 μM ^b)	inactive (50 μM ^b)	inactive (50 μM ^b)
9		0.060±0.004 μM (22±1%)	0.4±0.1 μM (22±1%)	0.24±0.03 μM (21±1%)	23		10.1±0.1 μM (31±1%)	10.5±0.3 μM (19±3%)	< 5%
10		inactive (30 μM ^b)	inactive (30 μM ^b)	inactive (30 μM ^b)	24		8.0±0.3 μM (24±1%)	8±1 μM (15±1%)	17±1 μM (20±1%)
11		0.52±0.05 μM (52±3%)	0.8±0.3 μM (32±3%)	4.8±0.3 μM (28±1%)	25		inactive (50 μM ^b)	inactive (50 μM ^b)	inactive (50 μM ^b)
12		0.6±0.1 μM (36±1%)	0.9±0.1 μM (20±1%)	3.0±0.1 μM (30±1%)	26		19±1 μM (29±1%)	23±4 μM (33±3%)	62±7 μM (19±2%)
13		1.4±0.1 μM (32±1%)	> 100 μM	10±1 μM (46±4%)	27		6±1 μM (29±4%)	9±2 μM (21±5%)	> 10 μM
14		2.6±0.3 μM (28±2%)	0.54±0.06 μM (26±1%)	6.1±0.9 μM (25±1%)	28		inactive (30 μM ^b)	inactive (30 μM ^b)	inactive (30 μM ^b)
15		2.0±0.3 μM (19±1%)	3.4±0.6 μM (18±1%)	7.9±0.1 μM (30±2%)	29		inactive (100 μM ^b)	inactive (100 μM ^b)	inactive (100 μM ^b)
16		6.8±0.7 μM (31±2%)	8±1 μM (36±2%)	38±4 μM (92±4%)	30		1.0±0.2 μM (34±1%)	1.1±0.2 μM (24±1%)	2.9±0.1 μM (13±1%)
17		0.53±0.04 μM (53±3%)	0.55±0.04 μM (55±3%)	0.52±0.07 μM (52±3%)	31		14±2 μM (27±3%)	17±3 μM (15±2%)	inactive (30 μM)

^a RXR modulation was determined in uniform Gal4-hybrid reporter gene assays for the RXR α / β / γ subtypes. Max. rel. activation refers to the effect of the reference agonist **2** at 1 μ M. Data are the mean \pm S.E.M.; $n \geq 3$. ^b Highest non-toxic concentration. Data of **3** for comparison³⁸: EC₅₀(RXR α / β / γ) = 0.08/0.15/0.22 μ M.

The structure-guided analogue selection approach prioritized 3,4- and 3,5-disubstituted phenyl groups as well as bi- and tricyclic motifs as 4-substituent of the phenylacetic acid residue (Table 1). Although all designs in the virtual library shared the biphenylacetic acid motif, intermediate chemical diversity of the selected compounds **4-31** was evident from the compounds' pairwise Tanimoto similarity computed on Morgan fingerprints⁴³ (Figure 2d). This collection therefore appeared suitable to explore the SAR of the scaffold with a focus on identifying potent analogues of **3** for mechanistic comparison, and possibly capturing structural determinants of differential co-regulator recruitment.

4-31 were initially tested in uniform Gal4-hybrid reporter gene assays for the three RXR subtypes (Table 1). These cellular assays have been widely used to characterize RXR agonists^{38,44,45} and provide homogeneous and comparable data. They are based on chimeric receptors composed of the Gal4 DNA binding domain from yeast and the respective human RXR LBD which control expression of a Gal4-responsive firefly luciferase reporter gene. Constitutively expressed Renilla luciferase (SV40 promoter) was used for normalization and to monitor test compound toxicity.

Marked activity cliffs were evident for **4-31** in the cellular profiling and revealed preferred motifs. Among the 3,4-disubstituted analogues **4-10**, the 4-isopropoxy-3-trifluoromethyl derivative **8** and the 3,4-bistrifluoromethyl derivative **9** emerged as highly potent RXR agonists while the corresponding cyano (**4**), cyanomethyl (**5**), methylsulfonyl (**6**), and acetamido (**10**) analogues were significantly less active. Interestingly, **8** and **9** additionally displayed a slight preference for RXR α over the RXR β and RXR γ subtypes.

Alkoxy substituents (**11, 12**) were also preferred among the 3,5-substituted derivatives **11-16** while cyano (**13**), fluoro (**14**), acetyl (**15**) and even hydroxymethyl (**16**) substituents were tolerated. Like **8** and **9**, the 3-cyano-5-trifluoromethyl substitution pattern (**13**) achieved considerable preference for RXR α while the 3-fluoro-5-trifluoromethyl analogue **14** interestingly displayed an inverted profile with slight preference for RXR β indicating relevance of the hydrophobic sub-pocket accommodating the lipophilic backbone of the scaffold in driving RXR subtype selective activation.

Although using only structural information from the RXR α :**3** complex our docking-guided strategy prioritized the 3,5,5,8,8-pentamethyl-5,6,7,8-tetrahydronaphthalen-2-yl motif (**17**) contained in the widely used reference agonist bexarotene (**2**) indicating that the approach could generalize within the chemical space of RXR agonists. The bexarotene related design **17** indeed exhibited considerable RXR agonist potency, but the structurally related 1,4-dimethyl-8-oxo-5,6,7,8-tetrahydronaphthalen-2-yl (**18**) and 4,4-dimethyl-2-oxo-1,2,3,4-tetrahydroquinolin-6-yl (**19**) derivatives were substantially less active. Apart from **17**, bulky two- or three-ring systems (**18-29**) were generally less tolerated, despite very promising binding modes and scores in the docking, and marked activity differences were evident

for highly similar motifs especially among indole-based substituents (**20-29**). While the *N*-methylindol-5-yl (**20**), *N*-acetylindolin-5-yl (**21**), and *N*-acetyl-3-acetoxyindol-5-yl (**22**) derivatives were inactive on RXRs, structurally related *N*-methyl-3-trifluoroacetoxyindol-5-yl (**23**) and 7-trifluoromethylindazol-5-yl (**24**) retained RXR agonism with intermediate potency. The structurally related derivatives **25/26** and **27-29** revealed similarly steep SAR further supporting the assumption that minor structural differences in the hydrophobic backbone of the scaffold of **3** had marked impact on RXR modulation.

Docking mainly prioritized analogues of **3** with substituents (or rings) in meta/para positions indicating that the binding site of the RXR α :**3** complex demanded a rather linear ligand geometry. **30** bearing a bulky benzyloxy group in ortho position and the 4-(dimethylamino)naphthalen-1-yl derivative **31** deviating from this predominant geometry interestingly exhibited considerable RXR agonism.

The structure-guided design approach generated structurally diverse RXR agonists based on the scaffold of **3** for comparative mechanistic profiling as intended. Compounds **8, 9** and **17** exhibiting RXR agonism with similarly strong potency and sharing a 3,4-substitution pattern appeared suitable as initial test set to explore mechanistic differences in co-regulator recruitment. Comparative profiling of these RXR modulators in HTRF-based assays (Figure 3a) indeed revealed remarkably different effects on SRC1, SMRT and PGC1 α binding to RXR α . Despite the structural similarity of **8, 9** and **17**, **8** failed to affect PGC1 α binding, while **9** and **17** retained the ability of **3** to promote PGC1 α recruitment with **9** displaying substantially higher efficacy in inducing PGC1 α binding than **17**. This was also evident in dose-response profiling which confirmed a markedly stronger PGC1 α recruitment by **9** compared to **17** (Figure 3b).

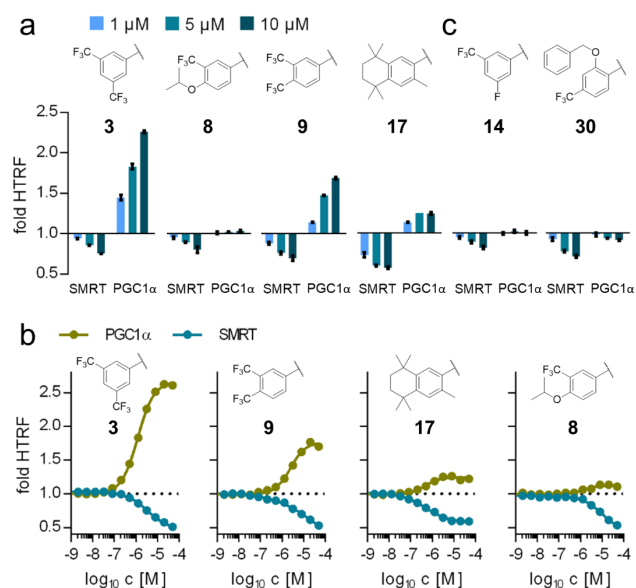


Figure 3. Effects of RXR ligands on the recruitment of co-regulators to the RXR α LBD in HTRF-based systems. (a) Despite

high structural similarity, **8**, **9** and **17** revealed pronounced differences in their effects on co-regulator recruitment. (b) Dose-response profiling demonstrated PGC1 α recruitment by **9** and **17** with considerably higher efficacy for **9**. **3** for comparison. (c) **14** and **30** failed to induce PGC1 α recruitment. All data are the mean \pm SD; n=3.

Building on these findings, we extended the co-regulator recruitment profiling to structurally more diverse analogues (Figure 3c). However, **14**, which exhibited RXR β preference in the cellular assay, and **30**, which has a significantly more angled shape than most other active derivatives of **3**, failed to enhance recruitment of PGC1 α to RXR.

Closer inspection and comparison of the (predicted) binding modes of **3**, **8**, **9** and **17** (Figure 4a) albeit revealing no major differences indicated that **8** and **17** extended further towards His435 in helix 11 than **3** and **9** (Figure 4b). Helix 11 makes multiple contacts with helix 12 which bears the ligand dependent activation function 2 (AF2) of RXR and mediates activation by ligands (Figure 4c). Ligand effects on the position of helix 11 likely translate in shifts of helix 12 which in turn alters the shape and size of the co-activator binding site. The predicted differences in the binding of **3**, **8**, **9** and **17** to the His435 region may thus induce subtle differences in the co-activator binding site via allosteric crosstalk through helices 11 and 12 which could possibly explain the different effects on PGC1 α recruitment.

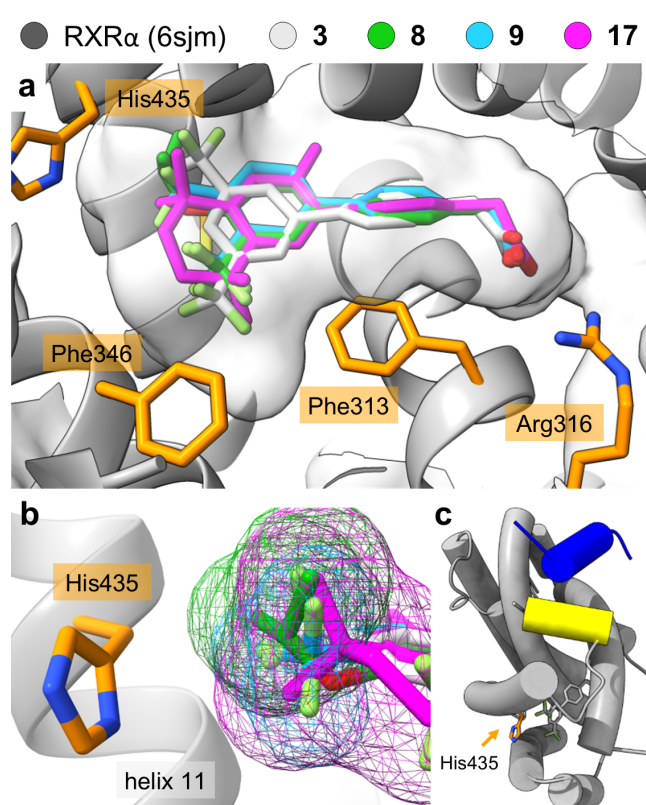


Figure 4. Binding mode comparison of **3**, **8**, **9** and **17**. (a) Docking poses of **8**, **9** and **17** in the binding site of **3** in the RXR α LBD (pdb ID 6sjm³⁸). **3**, **8**, **9** and **17** form highly similar binding modes to RXR α involving a strong ionic contact to Arg316. (b) Differences in the binding of **3**, **8**, **9** and **17** in the His435 region with the ligand surfaces shown as mesh. **8** (green mesh) and **17** (magenta mesh) have higher structural demands in the His435 region than **3** (grey mesh) and **9** (blue mesh) possibly affecting

the position of helix 11. (c) Structural overview of the ternary complex of **3** and nuclear receptor co-activator 2 (blue) bound to the RXR α LBD (pdb ID 6sjm³⁸). Helix 12 is shown in yellow. Different ligand interactions with helix 11 likely affect the position of helix 12 and consequently the co-activator binding region via allosteric crosstalk.

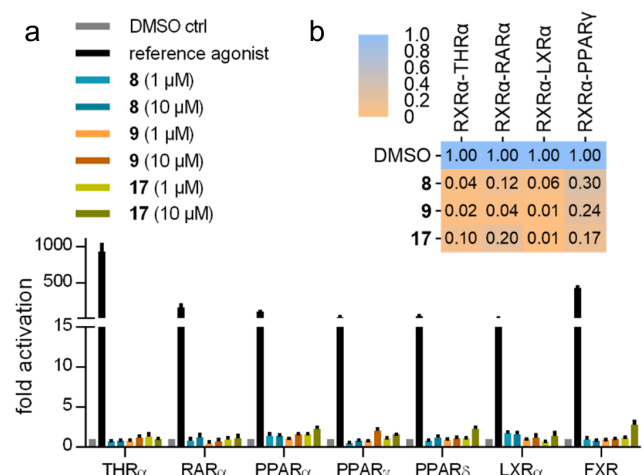


Figure 5. In vitro characterization of **8**, **9** and **17**. (a) **8**, **9** and **17** were inactive on lipid-sensing nuclear receptors related to RXR at 1 and 10 μ M. Data are the mean \pm S.E.M., n=3. (b) Effects of **8**, **9** and **17** (10 μ M each) on the interaction of RXR α with the heterodimer partners THR α , RAR α , LXR α and PPAR γ in a cellular assay observing the binding of VP16-RXR α -LBD to the corresponding Gal4-hybrid receptors of the dimer partners. The heatmap shows the mean rel. reporter activity vs. DMSO; n=3.

These results illustrate that minor structural variations in RXR ligands may result in markedly different ligand-induced co-regulator recruitment and that different molecular mechanisms (co-activator recruitment, co-repressor release) can induce RXR activation by ligands. However, the biological relevance of these findings remained elusive. To validate the suitability of **8**, **9** and **17** as set of chemical tools to study effects of differently modulated RXR-PGC1 α interaction, we characterized and compared their activity profiles in vitro (Figure 5). All three compounds were inactive at 1 and 10 μ M on lipid-activated NRs related to RXR (Figure 5a) demonstrating favorable selectivity. Since RXR can act as dimer with various other NRs, we also evaluated how the compounds affected RXR heterodimerization (Figure 5b) and observed consistently diminished interaction of RXR α with THR α , RAR α , LXR α and PPAR γ in presence of **8**, **9** and **17**. These results highlighted the absence of activity differences in the compound set on related nuclear receptors and their interaction with RXR which would otherwise compromise the use of the set as a tool.

Eventually we aimed to validate the ability of **9** to induce interaction of RXR with PGC1 α in a cellular setting and confirm the compound's suitability as tool to explore the biological impact of this unprecedented RXR modulation (Figure 6). We employed a reporter gene assay with a Gal4-PGC1 α fusion protein for interaction with the Gal4-responsive reporter construct and an RXR α -LBD-VP16 fusion protein lacking the ability to activate the reporter alone (Figure 6a). When binding to DNA-bound Gal4-PGC1 α via the RXR α

LBD, the fused VP16 acts as strong transcriptional inducer. This assay thus enabled observing the interaction of PGC1 α and the RXR α LBD in a cellular context. The RXR modulators **9** and **17** did not activate reporter activity in absence of RXR α -LBD-VP16 but robustly enhanced reporter gene expression when the RXR α fusion protein was present (Figure 6b) demonstrating their ability to induce the RXR α -PGC1 α interaction in a cellular context with high potency (EC_{50} $0.04 \pm 0.02 \mu\text{M}$ (**9**); $0.06 \pm 0.03 \mu\text{M}$ (**17**)). As observed in the cell-free HTRF assay, **9** promoted RXR α -PGC1 α binding more efficiently than **17** (Figure 6b) and the reference RXR agonist **2** had only a weak effect on reporter activity in this setting (Figure 6c).

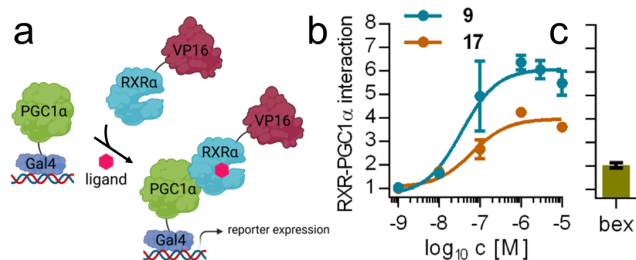


Figure 6. The RXR modulators **9** and **17** induce RXR α -PGC1 α interaction in cellular context. (a) A Gal4-PGC1 α fusion protein, a Gal4-responsive reporter construct and an RXR α -LBD-VP16 fusion protein were used to observe ligand-induced RXR α -PGC1 α interaction in HEK293T cells. Created with Biorender. (b) **9** and **17** robustly enhanced RXR α -PGC1 α interaction dependent reporter activity (EC_{50} $0.04 \pm 0.02 \mu\text{M}$ (**9**); $0.06 \pm 0.03 \mu\text{M}$ (**17**)) while the reference RXR agonist bexarotene ($1 \mu\text{M}$) had only a weak effect (c). Data are mean \pm SD reporter activity in presence of Gal4-PGC1 α and RXR α -LBD-VP16 normalized to the RXR α -LBD-VP16-free setting; $n=3$.

PGC1 α exhibits tissue-selective expression in compartments with high metabolic activity such as adipose tissue and the heart thus partly overlapping with the RXR expression profile^{32,46,47}. It has a prominent role in cellular metabolism by promoting mitochondrial biogenesis and protecting against oxidative stress^{48,49} and is inducible by cold in adipose tissue⁴⁷. Strikingly, PGC1 α was reported to mediate promoter-specific activation of PPAR γ and thyroid hormone receptor β in the uncoupling protein 1 (UCP-1) enhancer, which is a key factor of thermogenesis^{47,49}. PPARs form obligate heterodimers with RXR and both PPAR-RXR heterodimers and RXR homodimers act via the same DR1 response element⁵⁰. Ligand-induced PGC1 α recruitment to RXR might thus enable promoter specific effects, for example, in thermogenesis in adipose tissue. On the other hand, PGC1 α has been linked to tumor growth, metastasis and resistance by modulating and reprogramming cancer cell metabolism⁵¹⁻⁵⁶. While there are also reports of pro-carcinogenic impact of PGC1 α ⁵¹⁻⁵³ several lines of evidence suggest that PGC1 α can counteract metastasis^{54,56} of several cancers and that its suppression is required for metabolic reprogramming⁵⁵. Modulation of PGC1 α activity via ligand-induced interaction with RXR could potentially impact on these mechanisms in cancer. The set of **3**, **8**, **9** and **17** may serve as chemical tool

to probe these hypotheses in phenotypic in vitro settings by comparing the compounds' effects with respect to their ability to induce PGC1 α recruitment.

Conclusion

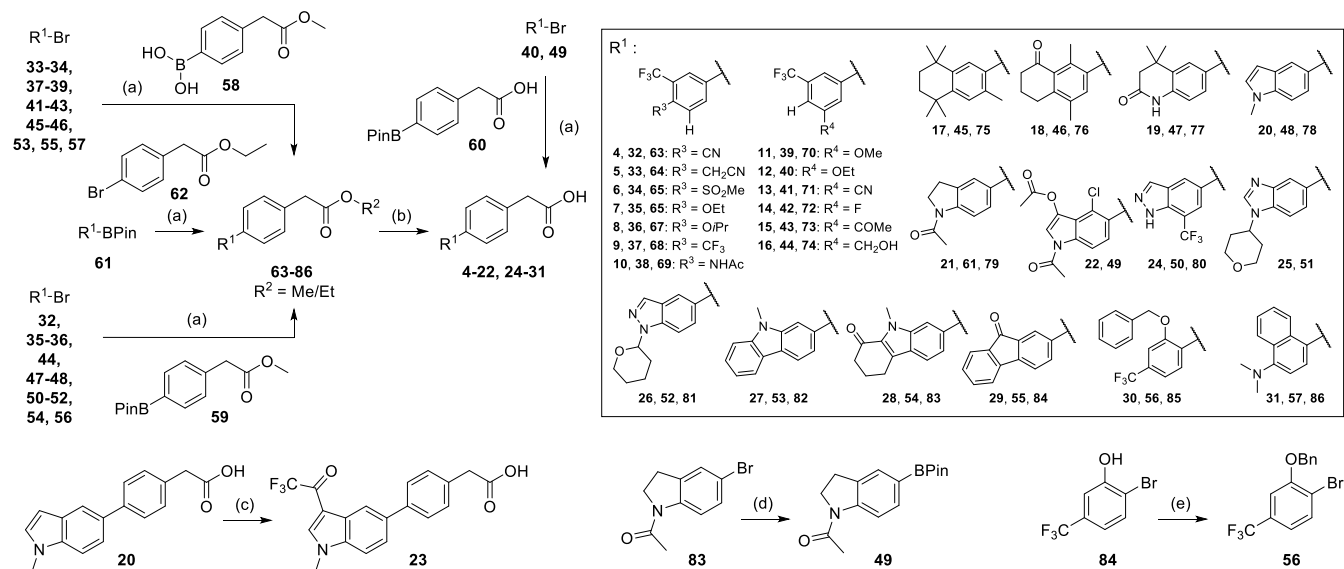
The discovery of substantially different effects of **3** on RXR-PGC1 α interaction compared to the natural ligand 9-cis RA (**1**) suggested that RXR ligands can be tuned for selective modulation of co-regulator recruitment. Building on this observation, we identified analogues of **3** (**8**, **9**, **17**) with varying PGC1 α recruitment efficacy showing that co-regulator recruitment effects can be "dosed" and strengthening the hypothesis that co-regulator selective RXR modulation can be achieved by ligand design. These findings demonstrate that RXR ligands can be shaped to act as molecular glues modulating the binding and release of individual co-regulators. As several molecular mechanisms (co-activator recruitment, co-repressor release) can mediate RXR activation, subtle differences in ligand-induced co-regulator recruitment may enable tissue-selective activation based on cell-type specific expression and roles of certain co-regulators^{30,31}. However, such subtle differences are not distinguishable in reporter gene assays based on which most available RXR agonists have been developed. Future innovation in targeting RXR may therefore rest in deeper mechanistic characterization of ligands and their structural tuning for desired activation mechanisms. Such selective modulation of certain protein-protein interactions of NRs with molecular glues may open new therapeutic avenues.

Despite high structural similarity, the RXR ligands **3**, **8**, **9** and **17** exhibit substantial mechanistic differences in terms of PGC1 α recruitment ranging from strong (**3**) to intermediate (**9**), weak (**17**) and no (**8**) ligand-induced PGC1 α binding. While the structural similarity may be an obstacle to further development of the scaffold and complicate the discovery of other co-regulator selective RXR ligand chemotypes, it is a valuable feature for the application in mechanistic studies. Therefore, the set of **3**, **8**, **9** and **17** emerges as attractive chemical tool to explore the biological relevance of the RXR-PGC1 α interaction and the impact of different ligand effects.

Chemistry

Compounds **4-22** and **24-31** were prepared according to Scheme 1 by Suzuki reaction of commercially available aryl bromides **32-57** with (4-boronophenyl)acetate derivatives **58-60** or boronic ester **61** with ethyl (4-bromophenyl)acetate (**62**). Suzuki coupling was achieved using XPhos Pd G2 pre-catalyst in good to excellent yields with the exception of reactions using the free carboxylic acid **60**. The obtained esters **63-86** were hydrolyzed under alkaline conditions to provide the free carboxylic acids **4-11**, **13-21**, **24** and **26-31**. **12** and **22** were directly prepared as free acids in the Suzuki reaction to avoid side reactions observed during ester hydrolysis. **25** was obtained directly from the Suzuki reaction between **51** and **59** followed by hydrolysis in one pot. Compound **23** was synthesized by trifluoroacetylation of **20**. The building blocks **49** was obtained by borylation of the aryl bromide **83**, and **57** was prepared by benzylation of the phenol **84**.

Scheme 1. Synthesis of the biarylacetic acids 4-31^a



^a Reagents and conditions: (a) K₃PO₄, XPhos Pd G2, 1,4-dioxane/H₂O, reflux, 1.5–24 h or Cs₂CO₃, XPhos Pd G2, toluene/H₂O, reflux, 1.5–24 h, 4–96%; (b) LiOH, MeOH/H₂O, rt, 18 h, 16–90%; (c) trifluoroacetic anhydride, DCM, 0°C, 30 min, 6%; (d) K₂CO₃, B₂Pin₂, Pd(dppf)Cl₂, 1,4-dioxane, 100°C, 2 h, 79%; (e) benzyl bromide, K₂CO₃, DMF, rt, 10 h, 78%.

Experimental

Chemistry

General. All chemicals were of reagent grade, purchased from commercial sources (e.g., Sigma-Aldrich, TCI, BLDpharm) and used without further purification unless otherwise specified. All reactions were conducted under nitrogen or argon atmosphere and in absolute solvents purchased from fisherscientific. Other solvents, especially for work-up procedures, were of reagent grade or purified by distillation (*iso*-hexane, cyclohexane, ethyl acetate (EtOAc), EtOH). Reactions were monitored by thin layer chromatography (TLC) on TLC Silica gel 60 F254 coated aluminum sheets by Merck and visualized under ultraviolet light (254 nm). Purification by column chromatography (CC) was performed on a puriFlash® XS520Plus system (Advion, Ithaca, NY, USA) using high performance spherical silica columns (SIHP, 50 μm) by Interchim and a gradient of *iso*-hexane or cyclohexane to EtOAc. Reversed-phase column chromatography (RP-CC) was performed on a puriFlash® 5.250 system (Advion) using C18HP columns (SIHP, 15 μm) by Interchim and a gradient of H₂O with 10% MeCN to 100% MeCN (HPLC gradient grade). Mass spectra were obtained on a puriFlash®-CMS system (Advion) using atmospheric pressure chemical ionization (APCI). HRMS were obtained with a Thermo Finnigan LTQ FT instrument for electron impact ionization (EI) or electrospray ionization (ESI). NMR spectra were recorded on Bruker Avance III HD 400 MHz or 500 MHz spectrometers equipped with a CryoProbe™ Prodigy broadband probe (Bruker). Chemical shifts are reported in δ values (ppm), coupling constants (*J*) in hertz

(Hz). The purity of the compounds was determined by ¹H-NMR (qHNMR) according to the method described by Pauli *et al.*⁵⁷: a sample of the analyte (1–4 mg) and an internal calibrant (1–4 mg; Purchased from Sigma Aldrich: Ethyl 4 (dimethylamino)benzoate, lot: #BCCC6657; Maleic acid, lot: #BCCH2407; Dimethyl terephthalate, lot: #BCBT9974) were weighed into a 1.5 mL Eppendorf tube with ±0.01 mg accuracy. The mixture was treated with 600 μL of a deuterated solvent (Acetone-*d*₆, DMSO-*d*₆, CD₃OD) and homogenized. The solution was transferred to a 5 mm NMR tube and the sample was submitted for measurement immediately. 2 dummy scans were performed prior to acquisition. Spectra were acquired at room temperature with 64 scans in a spectral range of 30 ppm (7.5–22.5 ppm relative to TMS). The relaxation time was set to 60 s to ensure complete relaxation, the acquisition time was set to 4 s. Recorded spectra were processed by applying zero-filling (256k), apodization (0.1 Hz exponential term), baseline correction (5th order Bernstein polynomial fit) and phase correction (manual). Purity was calculated by the following formula: $P_A [\%] = \frac{n_{IC} \cdot \text{Int}_A \cdot \text{MW}_A \cdot m_{IC}}{n_A \cdot \text{Int}_{IC} \cdot \text{MW}_{IC} \cdot m_A} \cdot P_{IC}$ where *A* denotes the analyte and *IC* denotes the internal calibrant. Integral ranges, masses of compounds and internal calibrants used for purity calculation are noted in the individual spectra. All compounds for biological testing had a purity >95% according to qHNMR.

General procedure for Suzuki Miyaura coupling (GP1). The respective aryl bromide 32–57 (1.0 eq), the respective boronic acid or boronic ester 58–60 (1.2 eq) and a base (3.0 eq) were evacuated for a few minutes. A solvent

mixture was degassed by the freeze-pump-thaw method (3×) and added under Ar. Next the corresponding Pd catalyst (0.10 eq) was added, and the reaction was heated under reflux until the completion of the reaction was indicated by TLC (1.5–24 h). After cooling to rt, the mixture was filtered through Celite and washed with EtOAc. H₂O was added and the aqueous layer was extracted with EtOAc (3×). The organic layers were combined, dried over Na₂SO₄, filtered and evaporated. The crude product was purified by CC/RP-CC.

General procedure for the ester hydrolysis (GP2). The respective alkyl ester **63–86** (1.0 eq) was dissolved in a mixture of an organic solvent and H₂O and LiOH (2.0– 10.0 eq) was added. The reaction was stirred at rt for 18 h and an equal volume aqueous HCl (10%) was added. The aqueous layer was extracted with EtOAc (3×). The organic layers were combined, dried over Na₂SO₄, filtered and evaporated. The crude product was purified by CC/RP-CC or crystallization.

2-(4'-Cyano-3'-trifluoromethyl[1,1'-biphenyl]-4-yl)acetic acid (4). Preparation according to GP2, using methyl 2-(4'-cyano-3'-trifluoromethyl[1,1'-biphenyl]-4-yl)acetate (**63**, 0.11 g, 0.35 mmol, 1.0 eq) and LiOH (0.041 g, 1.7 mmol, 5.0 eq) in THF (5 mL) and H₂O (5 mL). Further purification was performed by RP-CC to obtain **4** (77 mg, 74%) as a colorless solid. *R_f* (iso-hexane/EtOAc = 8:2 + 2% acetic acid) = 0.30. ¹H-NMR (400 MHz, Acetone-*d*₆): δ = 8.27–8.10 (m, 3H), 7.85–7.76 (m, 2H), 7.56–7.48 (m, 2H), 3.74 (s, 2H) ppm. ¹³C-NMR (101 MHz, Acetone-*d*₆): δ = 171.59, 145.76, 136.75, 136.05, 135.75, 132.34 (q, *J* = 32.0 Hz), 130.95, 130.45, 127.39, 125.07 (m), 122.88 (d, *J* = 273.1 Hz), 115.41, 107.83 (m), 40.00 ppm. qHNMR (400 MHz, Acetone-*d*₆, maleic acid as reference): purity = 99%. MS (APCI-): *m/z* 304.5 ([M-H]⁻). HRMS (EI+): *m/z* calculated 305.0664 for C₁₆H₁₀F₃NO₂, found 305.0657 ([M]⁺).

2-(4'-Cyanomethyl-3'-trifluoromethyl[1,1'-biphenyl]-4-yl)acetic acid (5). Preparation according to GP2, using methyl 2-(4'-cyanomethyl-3'-trifluoromethyl[1,1'-biphenyl]-4-yl)acetate (**64**, 0.10 g, 0.31 mmol, 1.0 eq) and LiOH (0.015 g, 0.63 mmol, 2.0 eq) in MeOH (4 mL) and H₂O (2 mL). Further purification was performed by RP-CC to obtain **5** (54 mg, 58%) as a colorless solid. *R_f* (iso-hexane/EtOAc = 7:3 + 2% formic acid) = 0.40. ¹H-NMR (400 MHz, Acetone-*d*₆): δ = 10.80 (br s, 1H), 8.06–8.00 (m, 2H), 7.88–7.81 (m, 1H), 7.76–7.68 (m, 2H), 7.52–7.45 (m, 2H), 4.19 (s, 2H), 3.72 (s, 2H) ppm. ¹³C-NMR (101 MHz, Acetone-*d*₆): δ = 172.55, 142.09, 137.99, 136.39, 132.62, 132.09, 131.14, 129.28 (q, *J* = 30.9 Hz), 129.10 (q, *J* = 1.5 Hz), 127.91, 125.65 (q, *J* = 5.7 Hz), 125.16 (q, *J* = 273.5 Hz), 118.07, 40.85, 21.24 (q, *J* = 2.8 Hz) ppm. qHNMR (400 MHz, Acetone-*d*₆, ethyl 4-(dimethylamino)benzoate as reference): purity = 98%. MS (EI+): *m/z* 319.0 ([M]⁺). HRMS (EI+): *m/z* calculated 319.0820 for C₁₇H₁₂F₃NO₂ found 319.0815 ([M]⁺).

2-(4'-Methylsulfonyl-3'-trifluoromethyl[1,1'-biphenyl]-4-yl)acetic acid (6). Preparation according to GP2, using methyl 2-(4'-methylsulfonyl-3'-trifluoromethyl[1,1'-biphenyl]-4-yl)acetate (**65**, 0.17 g, 0.45 mmol, 1.0 eq) and LiOH (0.022 g, 0.91 mmol, 2.0 eq) in MeOH (6 mL) and H₂O (3 mL). Further purification was performed by RP-CC to obtain **6** (132 mg, 81%) as a colorless solid. *R_f* (iso-hexane/EtOAc = 1:1 + 2% formic acid) = 0.47. ¹H-NMR

(500 MHz, Acetone-*d*₆): δ = 10.86 (br s, 1H), 8.39–8.34 (m, 1H), 8.27–8.19 (m, 2H), 7.84–7.77 (m, 2H), 7.56–7.48 (m, 2H), 3.75 (s, 2H), 3.29 (s, 3H) ppm. ¹³C-NMR (126 MHz, Acetone-*d*₆): δ = 172.45, 147.10, 139.04, 137.46, 136.98, 133.97, 131.81, 131.34, 129.58 (q, *J* = 33.0 Hz), 128.31, 127.36 (q, *J* = 6.3 Hz), 123.95 (q, *J* = 273.2 Hz), 45.34 (q, *J* = 3.0 Hz), 40.84 ppm. qHNMR (400 MHz, Acetone-*d*₆, ethyl 4-(dimethylamino)benzoate as reference): purity = 99%. MS (EI+): *m/z* 357.7 ([M]⁺). HRMS (EI+): *m/z* calculated 358.0487 for C₁₆H₁₃F₃O₄S, found 358.0484 ([M]⁺).

2-(4'-Ethoxy-3'-trifluoromethyl[1,1'-biphenyl]-4-yl)acetic acid (7). Preparation according to GP2, using methyl 2-(4'-ethoxy-3'-trifluoromethyl[1,1'-biphenyl]-4-yl)acetate (**66**, 0.30 g, 0.89 mmol, 1.0 eq) and LiOH (0.21 g, 8.9 mmol, 10.0 eq) in MeOH (24 mL) and H₂O (6 mL). Further purification was performed by RP-CC to obtain **7** (172 mg, 60%) as a colorless solid. *R_f* (cyclohexane/EtOAc 7:3 + 1% acetic acid) = 0.55. ¹H-NMR (500 MHz, Acetone-*d*₆): δ = 10.79 (br s, 1H), 7.90–7.83 (m, 2H), 7.65–7.59 (m, 2H), 7.42 (d, *J* = 8.1 Hz, 2H), 7.31 (d, *J* = 8.5 Hz, 1H), 4.25 (q, *J* = 7.0 Hz, 2H), 3.69 (s, 2H), 1.43 (t, *J* = 6.9 Hz, 3H) ppm. ¹³C-NMR (126 MHz, Acetone-*d*₆): δ = 172.67, 157.24 (q, *J* = 1.7 Hz), 138.73, 135.19, 133.61, 132.90–132.74 (m), 130.95, 127.41, 125.86 (q, *J* = 5.3 Hz), 124.88 (q, *J* = 271.8 Hz), 119.48 (q, *J* = 30.3 Hz), 114.85, 65.40, 40.86, 14.89 ppm. qHNMR (400 MHz, DMSO-*d*₆, ethyl 4-(dimethylamino)benzoate as reference): purity = 99%. MS (APCI+): *m/z* 325.0 ([M+H]⁺). HRMS (EI+): *m/z* calculated 324.0973 for C₁₇H₁₅F₃O₃, found 324.0992 ([M]⁺).

2-(4'-Isopropoxy-3'-trifluoromethyl[1,1'-biphenyl]-4-yl)acetic acid (8). Preparation according to GP2, using methyl 2-(4'-isopropoxy-3'-trifluoromethyl[1,1'-biphenyl]-4-yl)acetate (**67**, 0.16 g, 0.55 mmol, 1.0 eq) and LiOH (0.054 g, 2.3 mmol, 4.2 eq) in THF (5 mL) and H₂O (5 mL). Further purification was performed by RP-CC to obtain **8** (80 mg, 52%) as a colorless solid. *R_f* (iso-hexane/EtOAc = 8:2 + 2% acetic acid) = 0.51. ¹H-NMR (400 MHz, Acetone-*d*₆): δ = 7.89–7.83 (m, 2H), 7.65–7.57 (m, 2H), 7.42 (d, *J* = 8.2 Hz, 2H), 7.34 (d, *J* = 8.5 Hz, 1H), 4.87 (hept, *J* = 6.1 Hz, 1H), 3.68 (s, 2H), 1.37 (d, *J* = 6.1 Hz, 6H) ppm. ¹³C-NMR (101 MHz, Acetone-*d*₆): δ = 172.71, 156.37 (q, *J* = 2.1 Hz), 138.76, 135.16, 133.44, 132.70, 130.94, 127.38, 125.94 (q, *J* = 5.3 Hz), 123.54 (q, *J* = 271.5 Hz), 120.26 (q, *J* = 30.4 Hz), 115.99, 72.00, 40.88, 22.13 ppm. qHNMR (400 MHz, Acetone-*d*₆, ethyl 4-(dimethylamino)benzoate as reference): purity = 98%. MS (APCI+): *m/z* 338.9 ([M+H]⁺). HRMS (EI+): *m/z* calculated 338.1130 for C₁₈H₁₇F₃O₃, found 338.1123 ([M]⁺).

2-[3',4'-Bis(trifluoromethyl)[1,1'-biphenyl]-4-yl]acetic acid (9). Preparation according to GP2, using methyl 2-[3',4'-bis(trifluoromethyl)[1,1'-biphenyl]-4-yl]acetate (**68**, 0.16 g, 0.44 mmol, 1.0 eq) and LiOH (0.021 g, 0.88 mmol, 2.0 eq) in MeOH (6 mL) and H₂O (3 mL). Further purification was performed by RP-CC to obtain **9** (138 mg, 90%) as a colorless solid. *R_f* (iso-hexane/EtOAc = 7:3 + 2% formic acid) = 0.41. ¹H-NMR (500 MHz, Acetone-*d*₆): δ = 10.80 (br s, 1H), 8.28–8.21 (m, 1H), 8.21–8.14 (m, 1H), 8.13–8.07 (m, 1H), 7.84–7.74 (m, 2H), 7.56–7.47 (m, 2H), 3.74 (s, 2H) ppm. ¹³C-NMR (126 MHz, Acetone-*d*₆): δ = 172.48, 146.22, 137.27, 137.12, 131.78, 131.30, 129.85 (q, *J* = 5.9 Hz), 128.70 (qq, *J* = 32.8, 1.9 Hz), 128.22, 127.24 (q, *J* = 5.9 Hz), 126.46 (qq, *J* =

33.3, 1.8 Hz), 124.20 (qq, $J = 276.1, 2.2$ Hz), 124.0 (qq, $J = 270.8, 2.0$ Hz), 40.85 ppm. qHNMR (400 MHz, Acetone- d_6 , ethyl 4-(dimethylamino)benzoate as reference): purity = 98%. MS (EI+): m/z 348.0 ([M]⁺). HRMS (EI+): m/z calculated 348.0585 for C₁₆H₁₀F₆O₂, found 348.0579 ([M]⁺).

2-(4'-Acetamido-3'-trifluoromethyl[1,1'-biphenyl]-4-yl)acetic acid (10). Preparation according to GP2, using methyl 2-(4'-acetamido-3'-trifluoromethyl[1,1'-biphenyl]-4-yl)acetate (**69**, 0.052 g, 0.15 mmol, 1.0 eq) and LiOH (0.007 g, 0.3 mmol, 2.0 eq) in MeOH (4 mL) and H₂O (2 mL). Further purification was performed by RP-CC to obtain **10** (33 mg, 66%) as a colorless solid. R_f (iso-hexane/EtOAc = 1:1 + 2% formic acid) = 0.53. ¹H-NMR (500 MHz, Acetone- d_6): $\delta = 8.01$ – 7.89 (m, 3H), 7.73 – 7.64 (m, 2H), 7.50 – 7.41 (m, 2H), 3.71 (s, 2H), 2.18 (s, 3H) ppm. ¹³C-NMR (126 MHz, DMSO- d_6): $\delta = 172.58, 169.31, 138.15, 136.56, 135.12, 134.71, 130.82, 130.17, 130.15, 126.74, 125.15$ (q, $J = 29.2$ Hz), 124.02 (q, $J = 5.1$ Hz), 123.53 (q, $J = 273.6$ Hz), $40.27, 22.94$ ppm. qHNMR (400 MHz, Acetone- d_6 , ethyl 4-(dimethylamino)benzoate as reference): purity = 98%. MS (EI+): m/z 337.1 ([M]⁺). HRMS (EI+): m/z calculated 337.0926 for C₁₇H₁₄F₃NO₃ found 337.0926 ([M]⁺).

2-(3'-Methoxy-5'-trifluoromethyl[1,1'-biphenyl]-4-yl)acetic acid (11). Preparation according to GP2, using methyl 2-(3'-methoxy-5'-trifluoromethyl[1,1'-biphenyl]-4-yl)acetate (**70**, 0.16 g, 0.50 mmol, 1.0 eq) and LiOH (0.024 g, 1.0 mmol, 2.0 eq) in MeOH (6 mL) and H₂O (3 mL). Further purification was performed by RP-CC to obtain **11** (130 mg, 85%) as a colorless solid. R_f (iso-hexane/EtOAc = 7:3 + 2% formic acid) = 0.53. ¹H-NMR (400 MHz, Acetone- d_6): $\delta = 10.79$ (br s, 1H), 7.73 – 7.65 (m, 2H), 7.53 – 7.50 (m, 1H), 7.49 – 7.42 (m, 3H), 7.23 – 7.18 (m, 1H), 3.98 (s, 3H), 3.67 (s, 2H) ppm. ¹³C-NMR (101 MHz, Acetone- d_6): $\delta = 172.60, 161.51, 144.32, 138.76, 136.22, 132.65$ (q, $J = 31.7$ Hz), $131.00, 127.98, 125.17$ (q, $J = 272.3$ Hz), 117.03 (q, $J = 1.4$ Hz), 116.42 (q, $J = 3.9$ Hz), 110.32 (q, $J = 3.7$ Hz), $56.20, 40.88$ ppm. qHNMR (400 MHz, Acetone- d_6 , ethyl 4-(dimethylamino)benzoate as reference): purity = 99%. MS (EI+): m/z 310.0 ([M]⁺). HRMS (EI+): m/z calculated 310.0817 for C₁₆H₁₃F₃O₃, found 310.0813 ([M]⁺).

2-(3'-Ethoxy-5'-trifluoromethyl[1,1'-biphenyl]-4-yl)acetic acid (12). Preparation according to GP1 but using 1-bromo-3-ethoxy-5-(trifluoromethyl)benzene (**40**, 0.14 g, 0.50 mmol, 1.0 eq), 4-(carboxymethyl)phenylboronic acid pinacol ester (**60**, 0.16 g, 0.60 mmol, 1.2 eq), XPhos Pd G2 (0.039 g, 0.050 mmol, 0.10 eq) and Cs₂CO₃ (0.49 g, 1.5 mmol, 3.0 eq). Further purification was performed by RP-CC to obtain **12** (18 mg, 11%) as a colorless solid. R_f (cyclohexane/EtOAc 7:3 + 1% acetic acid) = 0.26. ¹H-NMR (400 MHz, Acetone- d_6): $\delta = 7.72$ – 7.64 (m, 2H), 7.53 – 7.48 (m, 1H), 7.48 – 7.42 (m, 3H), 7.21 – 7.15 (m, 1H), 4.23 (q, $J = 7.0$ Hz, 2H), 3.71 (s, 2H), 1.43 (t, $J = 7.0$ Hz, 3H) ppm. ¹³C-NMR (126 MHz, Acetone- d_6): $\delta = 171.81, 159.92, 143.38, 137.88, 135.33, 131.73$ (q, $J = 31.9$ Hz), $130.10, 127.06, 124.29$ (q, $J = 271.8$ Hz), $116.57, 115.39$ (q, $J = 3.9$ Hz), 109.88 (q, $J = 3.9$ Hz), $63.90, 40.05, 14.08$ ppm. qHNMR (400 MHz, DMSO- d_6 , ethyl 4-(dimethylamino)benzoate as reference): purity = 97%. MS (APCI+): m/z 324.6 ([M+H]⁺). HRMS (EI+): m/z calculated 324.0973 for C₁₇H₁₅F₃O₃, found 324.0973 ([M]⁺).

2-(3'-Cyano-5'-trifluoromethyl[1,1'-biphenyl]-4-yl)acetic acid (13). Preparation according to GP2, using methyl 2-(3'-cyano-5'-trifluoromethyl[1,1'-biphenyl]-4-yl)acetate (**71**, 0.13 g, 0.41 mmol, 1.0 eq) and LiOH (0.020 g, 0.83 mmol, 2.0 eq) in MeOH (6 mL) and H₂O (3 mL). Further purification was performed by RP-CC to obtain **13** (20 mg, 16%) as a colorless solid. R_f (iso-hexane/EtOAc = 6:4 + 2% formic acid) = 0.54. ¹H-NMR (500 MHz, Acetone- d_6): $\delta = 8.53$ – 8.20 (m, 2H), 8.20 – 8.08 (m, 1H), 7.86 – 7.73 (m, 2H), 7.61 – 7.39 (m, 2H), 3.74 (s, 2H) ppm. ¹³C-NMR (126 MHz, Acetone- d_6): $\delta = 172.53, 144.09, 137.24, 136.66, 135.00, 132.75$ (q, $J = 33.3$ Hz), $131.30, 128.59$ (q, $J = 3.7$ Hz), 128.33 (q, $J = 3.8$ Hz), $128.16, 124.30$ (q, $J = 272.2$ Hz), $118.09, 115.03, 40.86$ ppm. qHNMR (400 MHz, Acetone- d_6 , ethyl 4-(dimethylamino)benzoate as reference): purity = 97%. MS (EI+): m/z 305.0 ([M]⁺). HRMS (EI+): m/z calculated 305.0664 for C₁₆H₁₀F₃NO₂, found 305.0656 ([M]⁺).

2-(3'-Fluoro-5'-trifluoromethyl[1,1'-biphenyl]-4-yl)acetic acid (14). Preparation according to GP2, using methyl 2-(3'-fluoro-5'-trifluoromethyl[1,1'-biphenyl]-4-yl)acetate (**72**, 0.035 g, 0.11 mmol, 1.0 eq) and LiOH (0.008 g, 0.3 mmol, 3.1 eq) in MeOH (4 mL) and H₂O (2 mL). Further purification was performed by CC to obtain **14** (23 mg, 68%) as a colorless solid. R_f (iso-hexane/EtOAc = 7:3 + 2% formic acid) = 0.37. ¹H-NMR (500 MHz, Acetone- d_6): $\delta = 7.87$ – 7.81 (m, 1H), 7.80 – 7.70 (m, 3H), 7.53 – 7.43 (m, 3H), 3.72 (s, 2H) ppm. ¹³C-NMR (126 MHz, Acetone- d_6): $\delta = 172.54, 163.89$ (d, $J = 246.8$ Hz), 145.48 (d, $J = 8.3$ Hz), 137.43 (d, $J = 2.2$ Hz), $136.89, 133.34$ (qd, $J = 32.9, 8.6$ Hz), $131.17, 128.01, 124.51$ (qd, $J = 272.0, 3.3$ Hz), 120.39 (p, $J = 3.7$ Hz), 118.36 (d, $J = 22.2$ Hz), 111.99 (dq, $J = 25.1, 3.8$ Hz), 40.91 ppm. qHNMR (400 MHz, Acetone- d_6 , ethyl 4-(dimethylamino)benzoate as reference): purity = 98%. MS (EI+): m/z 297.9 ([M]⁺). HRMS (EI+): m/z calculated 298.0617 for C₁₅H₁₀F₄O₂, found 298.0612 ([M]⁺).

2-(3'-Acetyl-5'-trifluoromethyl[1,1'-biphenyl]-4-yl)acetic acid (15). Preparation according to GP2, using methyl 2-(3'-acetyl-5'-trifluoromethyl[1,1'-biphenyl]-4-yl)acetate (**73**, 0.088 g, 0.26 mmol, 1.0 eq) and LiOH (0.013 g, 0.52 mmol, 2.0 eq) in MeOH (4 mL) and H₂O (2 mL). Further purification was performed by RP-CC to obtain **15** (54 mg, 64%) as a colorless solid. R_f (iso-hexane/EtOAc = 7:3 + 2% formic acid) = 0.22. ¹H-NMR (500 MHz, MeOD- d_4): $\delta = 8.45$ – 8.35 (m, 1H), 8.24 – 8.17 (m, 1H), 8.11 (td, $J = 1.8, 0.8$ Hz, 1H), 7.71 – 7.62 (m, 2H), 7.48 – 7.38 (m, 2H), 3.68 (s, 2H), 2.71 (s, 3H) ppm. ¹³C-NMR (126 MHz, MeOD- d_4): $\delta = 198.72, 175.27, 144.01, 139.78, 138.53, 136.88, 132.77$ (q, $J = 32.6$ Hz), $131.38, 131.29$ (q, $J = 1.4$ Hz), 128.62 (q, $J = 3.6$ Hz), $128.31, 125.31$ (q, $J = 271.8$ Hz), 124.45 (q, $J = 3.8$ Hz), $41.57, 26.88$ ppm. qHNMR (400 MHz, MeOH- d_4 , ethyl 4-(dimethylamino)benzoate as reference): purity = 97%. MS (EI+): m/z 322.0 ([M]⁺). HRMS (EI+): m/z calculated 322.0817 for C₁₇H₁₃F₃O₃, found 322.0803 ([M]⁺).

2-(3'-Hydroxymethyl-5'-trifluoromethyl[1,1'-biphenyl]-4-yl)acetic acid (16). Preparation according to GP2, using methyl 2-(3'-hydroxymethyl-5'-trifluoromethyl[1,1'-biphenyl]-4-yl)acetate (**74**, 0.10 g, 0.31 mmol, 1.0 eq) and LiOH (0.037 g, 1.5 mmol, 5.0 eq) in THF (5 mL) and H₂O (5 mL). Further purification was performed by RP-

CC to obtain **16** (58 mg, 61%) as colorless solid. R_f (iso-hexane/EtOAc = 8:2 + 2% formic acid) = 0.30. $^1\text{H-NMR}$ (400 MHz, Acetone- d_6): δ = 7.93 (s, 1H), 7.83 (s, 1H), 7.72–7.67 (m, 3H), 7.49–7.44 (m, 2H), 4.82 (s, 2H), 3.71 (s, 2H) ppm. $^{13}\text{C-NMR}$ (101 MHz, Acetone- d_6): δ = 172.61, 145.71, 142.53, 138.87, 136.05, 131.49 (q, J = 31.8 Hz), 131.05, 129.37, 127.91, 125.48 (q, J = 271.8 Hz), 122.76 – 122.43 (m (overlapping quartets)), 63.90, 40.88 ppm. qHNMR (400 MHz, Acetone- d_6 , maleic acid as reference): purity = 97%. MS (APCI-): m/z 309.5 ([M-H] $^-$). HRMS (ESI-): m/z calculated 309.0744 for $\text{C}_{16}\text{H}_{12}\text{F}_3\text{O}_3$, found 309.0742 ([M-H] $^-$).

2-[4-(3,5,5,8,8-Pentamethyl-5,6,7,8-tetrahydronaphthalen-2-yl)phenyl]acetic acid (17). Preparation according to GP2, using methyl 2-[4-(3,5,5,8,8-pentamethyl-5,6,7,8-tetrahydronaphthalen-2-yl)phenyl]acetate (**75**, 0.26 g, 0.75 mmol, 1.0 eq) and LiOH (0.036 g, 1.5 mmol, 2.0 eq) in MeOH (6 mL), THF (3 mL) and H₂O (3 mL). Further purification was performed by crystallization from MeOH to obtain **17** (167 mg, 66%) as a colorless solid. R_f (iso-hexane/EtOAc = 8:2 + 2% formic acid) = 0.57. $^1\text{H-NMR}$ (400 MHz, DMSO- d_6): δ = 12.35 (s, 1H), 7.33–7.23 (m, 4H), 7.20 (s, 1H), 7.08 (s, 1H), 3.60 (s, 2H), 2.18 (s, 3H), 1.64 (s, 4H), 1.26 (s, 6H), 1.23 (s, 6H) ppm. $^{13}\text{C-NMR}$ (101 MHz, DMSO- d_6): δ = 172.74, 143.22, 141.86, 139.88, 138.34, 133.33, 131.57, 129.16, 128.87, 128.10, 127.33, 40.35, 34.70, 34.68, 33.56, 33.52, 31.62, 19.93 ppm. qHNMR (400 MHz, DMSO- d_6 , dimethylterephthalate as reference): purity = 99%. MS (EI+): m/z 336.09 ([M] $^+$). HRMS (EI+): m/z calculated 336.2089 for $\text{C}_{23}\text{H}_{28}\text{O}_2$, found 336.2082 ([M] $^+$).

2-[4-(1,4-Dimethyl-8-oxo-5,6,7,8-tetrahydronaphthalen-2-yl)phenyl]acetic acid (18). Preparation according to GP2, using methyl 2-[4-(1,4-dimethyl-8-oxo-5,6,7,8-tetrahydronaphthalen-2-yl)phenyl]acetate (**76**, 0.13 g, 0.39 mmol, 1.0 eq) and LiOH (0.047 g, 1.9 mmol, 5.1 eq) in THF (5 mL) and H₂O (5 mL). Further purification was performed by RP-CC to obtain **18** (85 mg, 71%) as a colorless solid. R_f (iso-hexane/EtOAc = 8:2 + 1% acetic acid) = 0.46. $^1\text{H-NMR}$ (400 MHz, Acetone- d_6): δ = 7.43–7.39 (m, 2H), 7.28–7.21 (m, 3H), 3.71 (s, 2H), 2.93 (t, J = 12.4 Hz, 2H), 2.66–2.59 (m, 2H), 2.40 (s, 3H), 2.33 (s, 3H), 2.18–2.09 (m, 2H) ppm. $^{13}\text{C-NMR}$ (101 MHz, Acetone- d_6): δ = 200.04, 171.82, 142.94, 141.27, 140.43, 135.02, 134.69, 133.72, 133.35, 132.63, 129.38, 129.21, 40.55, 40.08, 26.97, 22.38, 18.94, 18.72 ppm. qHNMR (400 MHz, acetone- d_6 , ethyl 4-(dimethylamino)benzoate as reference): purity = 99%. MS (APCI+): m/z 308.5 ([M+H] $^+$). HRMS (ESI-): m/z calculated 307.1339 for $\text{C}_{20}\text{H}_{19}\text{O}_3$, found 307.1336 ([M-H] $^-$).

2-[4-(4,4-Dimethyl-2-oxo-1,2,3,4-tetrahydroquinolin-6-yl)phenyl]acetic acid (19). Preparation according to GP2, using methyl 2-[4-(4,4-dimethyl-2-oxo-1,2,3,4-tetrahydroquinolin-6-yl)phenyl]acetate (**77**, 0.11 mg, 0.33 mmol, 1.0 eq) and LiOH (0.039 g, 1.6 mmol, 5.0 eq) in THF (5 mL) and H₂O (5 mL). Further purification was performed by RP-CC to obtain **19** (70 mg, 69%) as a colorless solid. R_f (iso-hexane/EtOAc = 8:2 + 2% acetic acid) = 0.30. $^1\text{H-NMR}$ (400 MHz, DMSO- d_6): δ = 10.21 (s, 1H), 7.56 (d, J = 8.0 Hz, 2H), 7.53–7.50 (m, 1H), 7.43 (dd, J = 8.2, 2.0 Hz, 1H), 7.31 (d, J = 8.1 Hz, 2H), 6.95 (d, J = 8.2 Hz, 1H), 3.59 (s, 2H), 2.38 (s, 2H), 1.28 (s, 6H) ppm. $^{13}\text{C-NMR}$ (101 MHz, DMSO- d_6): δ = 172.74, 169.36, 138.59, 136.35, 134.32, 133.70, 132.63, 129.89, 126.23, 125.45, 122.62, 115.95, 44.95,

40.33, 33.70, 27.29 ppm. qHNMR (400 MHz, DMSO- d_6 , maleic acid as reference): purity = 99%. MS (APCI+): m/z 310.1 ([M+H] $^+$). HRMS (EI-): m/z calculated 309.1365 for $\text{C}_{19}\text{H}_{19}\text{NO}_3$, found 309.1313 ([M] $^-$).

2-[4-(1-Methyl-1H-indol-5-yl)phenyl]acetic acid (20). Preparation according to GP2, using methyl 2-[4-(1-methyl-1H-indol-5-yl)phenyl]acetate (**78**, 0.022 g, 0.79 mmol, 1.0 eq) and LiOH (0.095 g, 3.9 mmol, 5.0 eq) in MeOH (24 mL) and H₂O (6 mL). Further purification was performed by RP-CC to obtain **20** (128 mg, 61%) as a colorless solid. R_f (cyclohexane/EtOAc 7:3 + 1% acetic acid) = 0.24. $^1\text{H-NMR}$ (400 MHz, DMSO- d_6): δ = 12.36 (s, 1H), 7.83–7.78 (m, 1H), 7.64–7.58 (m, 2H), 7.54–7.47 (m, 1H), 7.47–7.42 (m, 1H), 7.38–7.28 (m, 3H), 6.50–6.45 (m, 1H), 3.81 (s, 3H), 3.59 (s, 2H) ppm. $^{13}\text{C-NMR}$ (101 MHz, DMSO- d_6): δ = 172.81, 140.02, 135.96, 133.02, 131.19, 130.32, 129.80, 128.58, 126.52, 120.30, 118.22, 110.08, 100.75, 40.34, 32.55 ppm. qHNMR (400 MHz, DMSO- d_6 , ethyl 4-(dimethylamino)benzoate as reference): purity = 99%. MS (APCI+): m/z 265.7 ([M+H] $^+$). HRMS (EI+): m/z calculated 265.1103 for $\text{C}_{17}\text{H}_{15}\text{NO}_2$, found 265.1095 ([M] $^+$).

2-[4-(1-Acetylin-dolin-5-yl)phenyl]acetic acid (21). Preparation according to GP2, using ethyl 2-[4-(1-acetylin-dolin-5-yl)phenyl]acetate (**79**, 0.090 g, 0.28 mmol, 1.0 eq) and LiOH (0.033 g, 1.4 mmol, 4.9 eq) in MeOH (24 mL) and H₂O (6 mL). Further purification was performed by RP-CC to obtain **21** (39 mg, 48%) as a colorless solid. R_f (cyclohexane/EtOAc 7:3 + 1% acetic acid) = 0.18. $^1\text{H-NMR}$ (400 MHz, DMSO- d_6): δ = 12.34 (s, 1H), 8.12–8.05 (m, 1H), 7.59–7.55 (m, 2H), 7.53 (s, 1H), 7.48–7.42 (m, 1H), 7.33–7.29 (m, 2H), 4.13 (t, J = 8.5 Hz, 2H), 3.59 (s, 2H), 3.20 (t, J = 8.5 Hz, 2H), 2.17 (s, 3H) ppm. $^{13}\text{C-NMR}$ (101 MHz, DMSO- d_6): δ = 173.16, 169.02, 142.86, 138.79, 135.30, 134.18, 133.15, 130.37, 126.59, 125.84, 123.35, 116.46, 48.86, 40.75, 27.88, 24.45 ppm. qHNMR (400 MHz, DMSO- d_6 , ethyl 4-(dimethylamino)benzoate as reference): purity = 99%. MS (APCI+): m/z 296.0 ([M+H] $^+$). HRMS (EI+): m/z calculated 295.1208 for $\text{C}_{18}\text{H}_{17}\text{NO}_3$, found 295.1200 ([M] $^+$).

2-[4-(3-Acetoxy-1-acetyl-4-chloro-1H-indol-5-yl)phenyl]acetic acid (22). Preparation according to GP1, using 1-acetyl-5-bromo-4-chloro-1H-indol-3-yl acetate (**49**, 0.17 g, 0.60 mmol, 1.0 eq), 4-(carboxymethyl)phenylboronic acid pinacol ester (**60**, 0.16 g, 0.60 mmol, 1.2 eq), K_3PO_4 (0.32 g, 1.5 mmol, 2.5 eq) and XPhos Pd G2 (0.039 g, 0.050 mmol, 0.08 eq) in 1,4-dioxane (12.6 mL) and H₂O (1.4 mL). Further purification was performed by RP-CC to obtain **22** (54 mg, 28%) as a colorless solid. R_f (cyclohexane/EtOAc = 8:2 + 2% acetic acid) = 0.32. $^1\text{H-NMR}$ (400 MHz, Acetone- d_6): δ = 8.47 (d, J = 8.6 Hz, 1H), 7.85 (s, 1H), 7.46–7.41 (m, 4H), 7.39 (d, J = 8.6 Hz, 1H), 3.72 (s, 2H), 2.71 (s, 3H), 2.33 (s, 3H) ppm. $^{13}\text{C-NMR}$ (101 MHz, Acetone- d_6): δ = 172.66, 169.83, 169.71, 138.40, 137.12, 135.33, 134.87, 134.05, 130.63, 130.06, 129.45, 122.83, 122.76, 119.08, 116.01, 41.00, 23.93, 20.81 ppm. qHNMR (400 MHz, Acetone- d_6 , ethyl 4-(dimethylamino)benzoate as reference): purity = 96%. MS (APCI+): m/z 386.3 ([M] $^+$). HRMS (ESI-): m/z calculated 340.0745 and 342.0716 for $\text{C}_{19}\text{H}_{15}\text{ClNO}_3$, found 340.0741 and 342.0711 ([M-CO₂-H] $^-$).

2-[4-[1-Methyl-3-(2,2,2-trifluoroacetyl)-1H-indol-5-yl]phenyl]acetic acid (23). The title compound was synthesized from 2-[4-[1-methyl-1H-indol-5-yl]phenyl]acetic

acid (**20**, 0.12 g, 0.45 mmol, 1.0 eq) by treatment with tri-fluoroacetic anhydride (0.11 mg, 0.50 mmol, 1.1 eq) in CH₂Cl₂ (2 mL) at 0 °C for 30 min. Further purification was performed by RP-CC to obtain **23** (10 mg, 6%) as a colorless solid. *R_f* (cyclohexane/EtOAc 7:3 +1% acetic acid) = 0.13. ¹H-NMR (500 MHz, Acetone-*d*₆): δ = 10.80 (br s, 1H), 8.57 (t, *J* = 1.3 Hz, 1H), 8.40 (q, *J* = 1.9 Hz, 1H), 7.72 (d, *J* = 1.3 Hz, 2H), 7.70–7.67 (m, 2H), 7.49–7.42 (m, 2H), 4.10 (s, 3H), 3.70 (s, 2H) ppm. ¹³C-NMR (126 MHz, Acetone-*d*₆): δ = 174.78 (q, *J* = 34.2 Hz), 172.75, 141.20 (q, *J* = 4.9 Hz), 140.82, 138.18, 137.76, 134.90, 130.88, 128.39, 128.06, 124.69, 120.70, 118.12 (q, *J* = 290.1 Hz), 112.38, 109.64, 40.93, 34.37 ppm. qHNMR (400 MHz, DMSO-*d*₆, ethyl 4-(dimethylamino)benzoate as reference): purity = 96%. MS (APCI+): *m/z* 362.7 ([M+H]⁺). HRMS (EI+): *m/z* calculated 361.0926 for C₁₉H₁₄F₃NO₃, found 361.0924 ([M]⁺).

2-[4-(7-Trifluoromethyl-1H-indazol-5-yl)phenyl]acetic acid (24). Preparation according to GP2, using methyl 2-[4-(7-trifluoromethyl-1H-indazol-5-yl)phenyl]acetate (**80**, 0.11 g, 0.33 mmol, 1.0 eq) and LiOH (0.39 g, 1.7 mmol, 5.0 eq) in THF (5 mL) and H₂O (5 mL). Further purification was performed by RP-CC to obtain **24** (78 mg, 72%) as a colorless solid. *R_f* (iso-hexane/EtOAc = 8:2 + 2% acetic acid) = 0.34. ¹H-NMR (400 MHz, Acetone-*d*₆): δ = 8.38–8.35 (m, 1H), 8.31 (s, 1H), 8.03 (s, 1H), 7.77–7.68 (m, 2H), 7.47 (d, *J* = 8.4 Hz, 2H), 3.71 (s, 2H) ppm. ¹³C-NMR (101 MHz, Acetone-*d*₆): δ = 172.83, 139.31, 135.90, 135.54, 135.36, 134.30, 131.01, 128.02, 127.04, 126.61 (q, *J* = 270.4 Hz), 124.37 (q, *J* = 4.5 Hz), 124.02, 113.62 (q, *J* = 33.9 Hz), 40.93 ppm. qHNMR (400 MHz, DMSO-*d*₆, ethyl 4-(dimethylamino)benzoate as reference): purity = 97%. MS (APCI+): *m/z* 321.1 ([M+H]⁺). HRMS (EI+): *m/z* calculated 320.0773 for C₁₆H₁₁F₃N₂O₂, found 320.0765 ([M]⁺).

2-[4-(1-Tetrahydro-2H-pyran-4-yl-1H-benzo[d]imidazol-5-yl)phenyl]acetic acid (25). Preparation according to GP1, using 6-bromo-1-(tetrahydro-2H-pyran-4-yl)-1H-benzimidazole (**51**, 0.14 mg, 0.50 mmol, 1.0 eq), (4-methoxycarbonylmethylphenyl)boronic acid pinacol ester (**59**, 0.17 g, 0.60 mmol, 1.2 eq), K₃PO₄ (0.32 g, 1.5 mmol, 3.0 eq) and XPhos Pd G2 (0.039 g, 0.050 mmol, 0.10 eq) in 1,4-dioxane (12.6 mL) and H₂O (1.4 mL). Further purification was performed by RP-CC to obtain **25** (20 mg, 12%) as a colorless solid. *R_f* (iso-hexane/EtOAc = 8:2 + 2% acetic acid) = 0.30. ¹H-NMR (400 MHz, MeOD-*d*₄): δ = 8.34 (s, 1H), 7.86 (s, 1H), 7.73 (d, *J* = 8.5 Hz, 1H), 7.66 (d, *J* = 7.9 Hz, 2H), 7.60–7.53 (m, 1H), 7.39 (d, *J* = 8.0 Hz, 2H), 4.81–4.68 (m, 1H), 4.13 (dd, *J* = 11.9, 4.3 Hz, 2H), 3.75–3.66 (m, 2H), 3.65 (s, 2H), 2.31–2.08 (m, 4H) ppm. ¹³C-NMR (101 MHz, DMSO-*d*₆): δ = 172.77, 142.88, 142.20, 139.30, 134.67, 133.96, 133.82, 129.86, 126.98, 120.88, 119.73, 108.69, 66.39, 51.28, 40.37, 32.76 ppm. qHNMR (400 MHz, DMSO-*d*₆, ethyl 4-(dimethylamino)benzoate as reference): purity = 97%. MS (APCI+): *m/z* 337.0 ([M+H]⁺). HRMS (ESI+): *m/z* calculated 337.1547 for C₂₀H₂₁N₂O₃, found 337.1545 ([M+H]⁺).

2-[4-(1-Tetrahydro-2H-pyran-2-yl-1H-indazol-6-yl)phenyl]acetic acid (26). Preparation according to GP2, using methyl 2-[4-(1-tetrahydro-2H-pyran-2-yl-1H-indazol-6-yl)phenyl]acetate (**81**, 0.17 g, 0.49 mmol, 1.0 eq) and LiOH (0.058 g, 2.4 mmol, 5.0 eq) in THF (5 mL) and H₂O (5 mL). Further purification was performed by RP-CC to ob-

tain **26** (106 mg, 65%) as a colorless solid. *R_f* (iso-hexane/EtOAc = 8:2 + 2% formic acid) = 0.35. ¹H-NMR (400 MHz, MeOD-*d*₄): δ = 10.75 (s, 1H), 8.05 (s, 1H), 7.84 (s, 1H), 7.80 (d, *J* = 0.8 Hz, 1H), 7.68–7.62 (m, 2H), 7.47 (d, *J* = 1.4 Hz, 1H), 7.42–7.37 (m, 2H), 5.89 (dd, *J* = 9.9, 2.6 Hz, 1H), 4.05–3.98 (m, 1H), 3.91–3.80 (m, 1H), 3.67 (s, 2H), 2.59–2.46 (m, 1H), 2.14–1.98 (m, 2H), 1.92–1.61 (m, 3H) ppm. ¹³C-NMR (101 MHz, MeOD-*d*₄): δ = 174.12, 140.27, 139.97, 139.82, 134.21, 133.57, 129.57, 127.23, 123.69, 121.20, 120.96, 107.63, 84.74, 67.26, 40.23, 29.27, 24.96, 22.36 ppm. qHNMR (400 MHz, Acetone-*d*₆, maleic acid as reference): purity = 97%. MS (APCI+): *m/z* 337.0 ([M+H]⁺). HRMS (ESI-): *m/z* calculated 335.1401 for C₂₀H₁₉N₂O₃, found 335.1398 ([M-H]⁻).

2-[4-(9-Methyl-9H-carbazol-3-yl)phenyl]acetic acid (27). Preparation according to GP2, using methyl 2-[4-(9-methyl-9H-carbazol-3-yl)phenyl]acetate (**82**, 0.25 g, 0.76 mmol, 1.0 eq) and LiOH (0.036 mg, 1.5 mmol, 2.0 eq) in MeOH (6 mL), THF (3 mL) and H₂O (3 mL). Further purification was performed by crystallization from *n*-heptane to obtain **27** (142 mg, 59%) as a brown solid. *R_f* (iso-hexane/EtOAc = 8:2 + 2% formic acid) = 0.33. ¹H-NMR (400 MHz, DMSO-*d*₆): δ = 12.35 (bs, 1H), 8.47 (s, 1H), 8.25 (d, *J* = 7.8 Hz, 1H), 7.81–7.76 (m, 1H), 7.76–7.70 (m, 2H), 7.69–7.63 (m, 1H), 7.63–7.57 (m, 1H), 7.53–7.44 (m, 1H), 7.40–7.33 (m, 2H), 7.23 (t, *J* = 7.4 Hz, 1H), 3.90 (s, 3H), 3.63 (s, 2H) ppm. ¹³C-NMR (101 MHz, DMSO-*d*₆): δ = 172.82, 141.10, 140.14, 139.46, 133.22, 130.90, 129.91, 126.53, 125.91, 124.62, 122.62, 122.18, 120.48, 118.86, 118.18, 109.52, 109.26, 40.35, 29.09 ppm. qHNMR: (400 MHz, DMSO-*d*₆, dimethylterephthalate as reference): purity = 95%. MS (EI+): *m/z* 315.01 ([M]⁺). HRMS (EI+): *m/z* calculated 315.1259 for C₂₁H₁₇NO₂, found 315.1248 ([M]⁺).

2-[4-(9-Methyl-1-oxo-2,3,4,4a,9,9a-hexahydro-1H-carbazol-7-yl)phenyl]acetic acid (28). Preparation according to GP2, using methyl 2-[4-(9-methyl-1-oxo-2,3,4,4a,9,9a-hexahydro-1H-carbazol-7-yl)phenyl]acetate (**83**, 0.12 g, 0.34 mmol, 1.0 eq) and LiOH (0.041 g, 1.7 mmol, 5.0 eq) in THF (5 mL) and H₂O (5 mL). Further purification was performed by RP-CC to obtain **28** (54 mg, 28%) as a colorless solid. *R_f* (cyclohexane/EtOAc = 9:1 + 2% acetic acid) = 0.39. ¹H-NMR (400 MHz, DMSO-*d*₆): δ = 12.34 (s, 1H), 8.01–7.93 (m, 1H), 7.71 (dd, *J* = 8.8, 1.8 Hz, 1H), 7.66 (d, *J* = 8.1 Hz, 2H), 7.60 (d, *J* = 8.8 Hz, 2H), 7.34 (d, *J* = 8.1 Hz, 2H), 4.02 (s, 3H), 3.60 (s, 2H), 3.03 (t, *J* = 6.0 Hz, 2H), 2.59 (t, *J* = 5.9 Hz, 2H), 2.20–2.09 (m, 2H). ¹³C-NMR (101 MHz, CDCl₃): δ = 192.83, 178.28, 140.98, 139.43, 133.22, 131.88, 131.10, 129.99, 129.96, 127.60, 126.78, 125.28, 119.58, 110.77, 40.88, 40.00, 31.85, 24.84, 21.98 ppm. qHNMR (400 MHz, DMSO-*d*₆, ethyl 4-(dimethylamino)benzoate as reference): purity = 97%. MS (APCI+): *m/z* 334.1 ([M+H]⁺). HRMS (ESI+): *m/z* calculated 334.1438 for C₂₁H₂₀NO₃, found 334.1436 ([M+H]⁺).

2-[4-(9-Oxo-9H-fluoren-2-yl)phenyl]acetic acid (29). Preparation according to GP2, using methyl 2-[4-(9-oxo-9H-fluoren-2-yl)phenyl]acetate (**84**, 0.13 g, 0.39 mmol, 1.0 eq) and LiOH (0.019 g, 0.78 mmol, 2.0 eq) in MeOH (6 mL) and H₂O (3 mL). Further purification was performed by crystallization from MeOH to obtain **29** (29 mg, 24%) as a yellow solid. *R_f* (iso-hexane/Acetone = 9:1 + 2% formic acid) = 0.19. ¹H-NMR (400 MHz, DMSO-*d*₆): δ = 12.40 (br s, 1H), 8.19–

8.13 (m, 1H), 7.96–7.89 (m, 1H), 7.81–7.74 (m, 2H), 7.70–7.65 (m, 2H), 7.65–7.59 (m, 2H), 7.45–7.36 (m, 3H), 3.66 (s, 2H) ppm. ¹³C-NMR (101 MHz, DMSO-*d*₆): δ = 192.69, 172.56, 146.82, 144.85, 143.66, 137.33, 135.75, 135.27, 133.82, 132.07, 130.13, 129.60, 127.48, 126.94, 124.48, 123.81, 121.43, 119.55, 40.33 ppm. qHNMR (400 MHz, DMSO-*d*₆, dimethylterephthalate as reference): purity = 98%. MS (EI+): *m/z* 314.0 ([M]⁺). HRMS (EI+): *m/z* calculated 314.0943 for C₂₁H₁₄O₃, found 314.0939 ([M]⁺).

2-(2'-Benzyloxy-4'-trifluoromethyl[1,1'-biphenyl]-4-yl)acetic acid (30). Preparation according to GP2, using methyl 2-(2'-benzyloxy-4'-trifluoromethyl[1,1'-biphenyl]-4-yl)acetate (**85**, 0.20 g, 0.50 mmol, 1.0 eq) and LiOH (0.060 g, 2.5 mmol, 5.0 eq) in MeOH (24 mL) and H₂O (6 mL). Further purification was performed by RP-CC to obtain **30** (162 mg, 84%) as a pale yellow solid. *R*_f (cyclohexane/EtOAc 7:3 +1% acetic acid) = 0.25. ¹H-NMR (400 MHz, DMSO-*d*₆): δ = 12.42 (s, 1H), 7.56–7.50 (m, 3H), 7.50–7.47 (m, 1H), 7.42–7.27 (m, 8H), 5.25 (s, 2H), 3.61 (s, 2H) ppm. ¹³C-NMR (101 MHz, DMSO-*d*₆): δ = 172.63, 155.44, 136.50, 134.92, 134.68, 134.03, 131.31, 129.16 (overlapping with 129.15), 129.15 (overlapping with 129.16), 129.06 (q, *J* = 31.5 Hz), 128.42, 127.82, 127.43, 124.08 (q, *J* = 272.1 Hz), 117.67 (q, *J* = 3.7 Hz), 109.78 (q, *J* = 3.7 Hz), 70.03, 40.44 ppm. qHNMR (400 MHz, DMSO-*d*₆, ethyl 4-(dimethylamino)benzoate as reference): purity = 96%. MS (APCI+): *m/z* 404.1 ([M+NH₄]⁺). HRMS (EI+): *m/z* calculated 386.1130 for C₂₂H₁₇F₃O₃, found 386.1136 ([M]⁺).

2-{4-[4-(Dimethylamino)naphthalen-1-yl]phenyl}acetic acid (31). Preparation according to GP1, using 4-bromo-*N,N*-dimethylnaphthalen-1-amine (**57**, 0.50 g, 2.0 mmol, 1.0 eq), methyl (4-boronophenyl)acetate (**58**, 0.45 mg, 2.3 mmol, 1.15 eq), Cs₂CO₃ (2.0 g, 6.0 mmol, 3.0 eq) and Pd(PPh₃)₄ (0.23 g, 0.20 mmol, 0.10 eq) in DMF (16 mL) and H₂O (4 mL). Further purification was performed by RP-CC to obtain **31** (25 mg, 4%) as a colorless solid. *R*_f (DCM/MeOH = 97:3) = 0.26. ¹H-NMR (400 MHz, Acetone-*d*₆): δ = 10.79 (br s, 1H), 8.36–8.29 (m, 1H), 7.89–7.81 (m, 1H), 7.55–7.49 (m, 1H), 7.49–7.38 (m, 5H), 7.35 (d, *J* = 7.7 Hz, 1H), 7.20 (d, *J* = 7.7 Hz, 1H), 3.74 (s, 2H), 2.91 (s, 6H) ppm. ¹³C-NMR (126 MHz, CDCl₃): δ = 177.36, 150.25, 140.21, 134.93, 132.89, 132.09, 130.61, 129.39, 128.92, 126.97, 126.63, 126.06, 125.32, 124.47, 113.82, 45.43, 40.91 ppm. qHNMR (400 MHz, Acetone-*d*₆, ethyl 4-(dimethylamino)benzoate as reference): purity = 97%. MS (EI+): *m/z* 305.0 ([M]⁺). HRMS (EI+): *m/z* calculated 305.1416 for C₂₀H₁₉NO₂, found 305.1408 ([M]⁺).

2-Benzyloxy-1-bromo-4-trifluoromethylbenzene (56). 2-bromo-5-(trifluoromethyl)phenol (0.74 g, 3.1 mmol, 1.0 eq), benzyl bromide (0.55 g, 3.2 mmol, 1.05 eq) and K₂CO₃ (0.43 g, 3.1 mmol, 1.0 eq) were dissolved in DMF (2 mL). The reaction mixture was stirred at rt overnight, diluted with EtOAc (15 mL) and washed with a sat. NaHCO₃ solution, H₂O and brine (10 mL each). The organic layer was dried over Na₂SO₄, the volatiles were removed under reduced pressure and the residue was loaded onto Celite and subjected to CC (cyclohexane/EtOAc 100:0 to 80:20) to afford **56** as a colorless solid (797 mg, 78%). *R*_f (*iso*-hexane/EtOAc = 8:2) = 0.68. ¹H-NMR (400 MHz, DMSO-*d*₆): δ = 7.89–7.81 (m, 1H), 7.53–7.47 (m, 3H), 7.46–7.40 (m, 2H), 7.39–7.33 (m, 1H), 7.29–7.25 (m, 1H), 5.33 (s,

2H) ppm. ¹³C-NMR (101 MHz, DMSO-*d*₆): δ = 154.97, 136.09, 134.01, 129.56 (q, *J* = 32.2 Hz), 128.53, 128.07, 127.50, 123.74 (q, *J* = 272.3 Hz), 118.72 (q, *J* = 3.8 Hz), 116.05, 110.65 (q, *J* = 3.8 Hz), 70.52 ppm. MS (APCI+): *m/z* 330.9 ([M+H]⁺).

1-[5-(4,4,5,5-Tetramethyl-1,3,2-dioxaborolan-2-yl)indolin-1-yl]ethan-1-one (61). Preparation according to literature procedure⁵⁸. Bis(pinacolato)diboron (0.22 g, 0.85 mmol, 1.2 eq), anhydrous potassium acetate (0.20 g, 2.1 mmol, 5.0 eq), 1-(5-bromo-2,3-dihydro-1*H*-indol-1-yl)ethan-1-one (0.10 g, 0.42 mmol, 1.0 eq) and Pd(dppf)Cl₂ (0.034 g, 0.042 mmol, 0.10 eq) were dissolved in dioxane (4 mL) and the mixture was refluxed to 105°C for 2 h. Upon cooling to rt, H₂O (20 mL) was added, and the mixture was extracted with ethyl acetate (3 × 15 mL). The combined organic layers were washed with brine, then dried over Na₂SO₄. The volatiles were removed under reduced pressure, the residue was loaded onto Celite and subjected to CC (cyclohexane/EtOAc 98:2 to 65:35) to afford **61** as a colorless solid (95 mg, 79%). ¹H-NMR (400 MHz, DMSO-*d*₆): δ = 8.03 (d, *J* = 8.0 Hz, 1H), 7.51 (s, 1H), 7.48 (d, *J* = 8.0 Hz, 1H), 4.09 (t, *J* = 8.6 Hz, 2H), 3.12 (t, *J* = 8.6 Hz, 2H), 2.16 (s, 3H), 1.27 (s, 13H). ¹³C-NMR: (101 MHz, DMSO-*d*₆): δ = 168.98, 145.58, 134.07, 131.30, 130.86, 115.11, 83.39, 48.25, 26.99, 26.33, 24.95, 24.68, 24.11. MS (APCI+): *m/z* 288.1 ([M+H]⁺).

Methyl 2-(4'-cyano-3'-trifluoromethyl[1,1'-biphenyl]-4-yl)acetate (63). Preparation according to GP1, using 4-bromo-2-(trifluoromethyl)benzotrile (**32**, 0.13 g, 0.50 mmol, 1.0 eq), methyl 2-[4-(4,4,5,5-tetramethyl-1,3,2-dioxaborolan-2-yl)phenyl]acetate (**59**, 0.17 g, 0.60 mmol, 1.2 eq), XPhos Pd G2 (0.039 g, 0.050 mmol, 0.10 eq) and K₃PO₄ (0.32 g, 1.5 mmol, 3.0 eq) in dioxane (9 mL) and H₂O (1 mL). Further purification was performed by CC to obtain **63** (155 mg, 97%) as a colorless solid. *R*_f (*iso*-hexane/EtOAc = 8:2) = 0.35. ¹H-NMR (400 MHz, Acetone-*d*₆) δ = 8.24–8.13 (m, 3H), 7.84–7.77 (m, 2H), 7.52–7.46 (m, 2H), 3.76 (s, 2H), 3.67 (s, 3H) ppm. ¹³C-NMR (400 MHz, Acetone-*d*₆) δ = 172.14, 146.72, 137.33, 137.22, 136.78, 133.38 (q, *J* = 32.3 Hz), 131.99, 131.42, 128.50, 126.09 (q, *J* = 4.7 Hz), 123.90 (q, *J* = 273.3 Hz), 116.42, 109.12–108.70 (m), 52.28, 40.98 ppm. MS (APCI+): *m/z* 319.4 ([M+H]⁺).

Methyl 2-(4'-cyanomethyl-3'-trifluoromethyl-[1,1'-biphenyl]-4-yl)acetate (64). Preparation according to GP1, using 4-(bromo-2-trifluoromethylphenyl)acetoneitrile (**33**, 0.13 g, 0.50 mmol, 1.0 eq), methyl (4-boronophenyl)acetate (**58**, 0.12 g, 0.60 mmol, 1.2 eq), K₃PO₄ (0.32 g, 1.5 mmol, 3.0 eq) and XPhos Pd G2 (0.039 g, 0.050 mmol, 0.10 eq) in 1,4-dioxane (12.6 mL) and H₂O (1.4 mL). Further purification was performed by RP-CC to obtain **64** (104 mg, 62%) as a colorless oil. *R*_f (*iso*-hexane/EtOAc = 8:2) = 0.35. ¹H-NMR (400 MHz, Acetone-*d*₆): δ = 8.06–8.00 (m, 2H), 7.88–7.81 (m, 1H), 7.76–7.67 (m, 2H), 7.49–7.42 (m, 2H), 4.19 (s, 2H), 3.74 (s, 2H), 3.67 (s, 3H) ppm. ¹³C-NMR (101 MHz, Acetone-*d*₆): δ = 172.12, 142.02, 138.10, 136.01, 132.63, 132.09, 131.07, 129.29 (q, *J* = 30.8 Hz), 129.14, 127.97, 125.66 (q, *J* = 5.4 Hz), 125.15 (q, *J* = 273.7 Hz), 118.07, 52.11, 40.87, 21.24 (q, *J* = 2.3 Hz) ppm. MS (APCI+): *m/z* 333.6 ([M+H]⁺).

Methyl 2-(4'-methylsulfonyl-3'-trifluoromethyl[1,1'-biphenyl]-4-yl)acetate (65). Preparation according to

GP1, using 4-bromo-1-methylsulfonyl-2-trifluoromethylbenzene (**34**, 0.15 g, 0.50 mmol, 1.0 eq), methyl (4-boronophenyl)acetate (**58**, 0.12 g, 0.60 mmol, 1.2 eq), K_3PO_4 (0.32 g, 1.5 mmol, 3.0 eq) and XPhos Pd G2 (0.039 g, 0.050 mmol, 0.10 eq) in 1,4-dioxane (12.6 mL) and H_2O (1.4 mL). Further purification was performed by CC to obtain **65** (179 mg, 96%) as a colorless solid. R_f (iso-hexane/EtOAc = 6:4) = 0.45. 1H -NMR (500 MHz, Acetone- d_6): δ = 8.40–8.34 (m, 1H), 8.28–8.18 (m, 2H), 7.85–7.76 (m, 2H), 7.55–7.45 (m, 2H), 3.76 (s, 2H), 3.67 (s, 3H), 3.29 (s, 3H) ppm. ^{13}C -NMR (126 MHz, Acetone- d_6): δ = 172.03, 147.03, 139.09 (q, J = 1.3 Hz), 137.10, 137.07, 133.98, 131.83, 131.28, 129.59 (q, J = 33.0 Hz), 128.38, 127.38 (q, J = 6.4 Hz), 123.94 (q, J = 273.4 Hz), 52.15, 45.34 (q, J = 3.0 Hz), 40.86 ppm. MS (APCI+): m/z 372.8 ([M+H] $^+$).

Methyl 2-(4'-ethoxy-3'-trifluoromethyl)[1,1'-biphenyl]-4-yl)acetate (66). Preparation according to GP1, using 4-bromo-1-ethoxy-2-(trifluoromethyl)benzene (**35**, 0.28 g, 1.0 mmol, 1.0 eq), (4-methoxycarbonylmethylphenyl)boronic acid pinacol ester (**59**, 0.33 g, 1.2 mmol, 1.2 eq), XPhos Pd G2 (0.079 g, 0.10 mmol, 0.10 eq) and Cs_2CO_3 (0.98 mg, 3.0 mmol, 3.0 eq) in toluene (18 mL) and H_2O (2 mL). Further purification was performed by CC to obtain **66** (116 mg, 34%) as a colorless solid. R_f (iso-hexane/EtOAc = 8:2) = 0.57. 1H -NMR (400 MHz, DMSO- d_6): δ = 7.94–7.87 (m, 1H), 7.84–7.79 (m, 1H), 7.66–7.59 (m, 2H), 7.39–7.31 (m, 3H), 4.21 (q, J = 7.0 Hz, 2H), 3.72 (s, 2H), 3.63 (s, 3H), 1.36 (t, J = 7.0 Hz, 3H) ppm. ^{13}C -NMR (101 MHz, DMSO- d_6): δ = 171.57, 155.79, 137.08, 133.59, 132.09, 131.88, 130.02, 126.41, 124.56 (q, J = 5.2 Hz), 123.72 (q, J = 272.1 Hz), 117.62 (q, J = 30.1 Hz), 114.38, 64.43, 51.73, 14.42 ppm. MS (APCI+): m/z 339.0 ([M+H] $^+$).

Methyl 2-(4'-isopropoxy-3'-trifluoromethyl)[1,1'-biphenyl]-4-yl)acetate (67). Preparation according to GP1, using 4-bromo-1-isopropoxy-2-(trifluoromethyl)benzene (**36**, 0.14 g, 0.50 mmol, 1.0 eq), (4-methoxycarbonylmethylphenyl)boronic acid pinacol ester (**59**, 0.17 g, 0.60 mmol, 1.2 eq), XPhos Pd G2 (0.039 g, 0.050 mmol, 0.10 eq) and K_3PO_4 (0.32 g, 1.5 mmol, 3.0 eq) in dioxane (9 mL) and H_2O (1 mL). Further purification was performed by CC to obtain **67** (160 mg, 91%) as a yellow solid. R_f (iso-hexane/EtOAc = 8:2) = 0.21. 1H -NMR (400 MHz, Acetone- d_6): δ = 7.88–7.83 (m, 2H), 7.64–7.59 (m, 2H), 7.42–7.37 (m, 2H), 7.34 (d, J = 8.3 Hz, 1H), 4.91–4.81 (m, 1H), 3.70 (s, 2H), 3.66 (s, 3H), 1.37 (d, J = 6.1 Hz, 6H) ppm. ^{13}C -NMR (101 MHz, DMSO- d_6): δ = 172.21, 156.40 (q, J = 1.9 Hz), 138.89, 134.75, 133.36, 132.71, 130.87, 127.45, 125.98 (q, J = 5.3 Hz), 124.89 (q, J = 271.7 Hz), 121.03 (q, J = 31.8 Hz), 115.99, 72.00, 52.07, 40.86, 22.13 ppm. MS (APCI+): m/z 352.7 ([M+H] $^+$).

Methyl 2-[3',4'-bis(trifluoromethyl)][1,1'-biphenyl]-4-yl)acetate (68). Preparation according to GP1, using 4-bromo-1,2-bis(trifluoromethyl)benzene (**37**, 86 μ L, 0.50 mmol, 1.0 eq), methyl (4-boronophenyl)acetate (**58**, 0.12 g, 0.60 mmol, 1.2 eq), K_3PO_4 (0.32 g, 1.5 mmol, 3.0 eq) and XPhos Pd G2 (0.039 g, 0.050 mmol, 0.10 eq) in 1,4-dioxane (12.6 mL) and H_2O (1.4 mL). Further purification was performed by RP-CC to obtain **68** (169 mg, 94%) as a colorless solid. R_f (iso-hexane/EtOAc = 8:2) = 0.50. 1H -NMR (500 MHz, Acetone- d_6): δ = 8.26–8.21 (m, 1H), 8.21–8.16 (m, 1H), 8.13–8.08 (m, 1H), 7.84–7.74 (m, 2H), 7.52–7.45

(m, 2H), 3.76 (s, 2H), 3.67 (s, 3H) ppm. ^{13}C -NMR (126 MHz, Acetone- d_6): δ = 172.05, 146.15, 137.24, 136.87, 131.80, 131.24, 129.86 (q, J = 6.0 Hz), 128.70 (qq, J = 32.8, 1.9 Hz), 128.29, 127.25 (q, J = 6.0 Hz), 126.49 (qq, J = 33.1, 1.6 Hz), 124.19 (qq, J = 275.1, 2.1 Hz), 124.02 (qq, J = 271.2, 2.0 Hz), 52.14, 40.86 ppm. MS (APCI+): m/z 362.8 ([M+H] $^+$).

Methyl 2-(4'-acetamido-3'-trifluoromethyl)[1,1'-biphenyl]-4-yl)acetate (69). Preparation according to GP1, using *N*-(4-bromo-2-trifluoromethylphenyl)acetamide (**38**, 0.14 g, 0.50 mmol, 1.0 eq), methyl (4-boronophenyl)acetate (**58**, 0.12 g, 0.60 mmol, 1.2 eq), K_3PO_4 (0.32 g, 1.5 mmol, 3.0 eq) and XPhos Pd G2 (0.039 g, 0.050 mmol, 0.10 eq) in 1,4-dioxane (12.6 mL) and H_2O (1.4 mL). Further purification was performed by CC to obtain **69** (109 mg, 62%) as a colorless solid. R_f (iso-hexane/EtOAc = 1:1) = 0.36. 1H -NMR (500 MHz, DMSO- d_6): δ = 9.61 (s, 1H), 7.97–7.92 (m, 1H), 7.92–7.89 (m, 1H), 7.74–7.65 (m, 2H), 7.60–7.55 (m, 1H), 7.44–7.36 (m, 2H), 3.75 (s, 2H), 3.63 (s, 3H), 2.07 (s, 3H) ppm. ^{13}C -NMR (126 MHz, DMSO- d_6): δ = 171.55, 169.34, 138.07, 136.80, 134.76, 134.42, 130.85, 130.82, 130.16, 126.87, 125.17 (q, J = 29.2 Hz), 124.07 (q, J = 4.9 Hz), 123.53 (q, J = 273.4 Hz), 51.78, 25.50, 22.95 ppm. MS (APCI+): m/z 351.3 ([M] $^+$).

Methyl 2-(3'-methoxy-5'-trifluoromethyl)[1,1'-biphenyl]-4-yl)acetate (70). Preparation according to GP1, using 1-bromo-3-methoxy-5-trifluoromethylbenzene (**39**, 82 μ L, 0.50 mmol, 1.0 eq), methyl (4-boronophenyl)acetate (**58**, 0.12 g, 0.60 mmol, 1.2 eq), K_3PO_4 (0.32 g, 1.5 mmol, 3.0 eq) and XPhos Pd G2 (0.039 g, 0.050 mmol, 0.10 eq) in 1,4-dioxane (12.6 mL) and H_2O (1.4 mL). Further purification was performed by RP-CC to obtain **70** (161 mg, 99%) as a colorless oil. R_f (iso-hexane/EtOAc = 8:2) = 0.30. 1H -NMR (400 MHz, Acetone- d_6): δ = 7.72–7.65 (m, 2H), 7.54–7.49 (m, 1H), 7.48–7.45 (m, 1H), 7.45–7.40 (m, 2H), 7.23–7.18 (m, 1H), 3.97 (s, 3H), 3.73 (s, 2H), 3.67 (s, 3H) ppm. ^{13}C -NMR (101 MHz, Acetone- d_6): δ = 172.15, 161.52, 144.25, 138.88, 135.82, 132.66 (q, J = 32.1 Hz), 130.94, 128.05, 123.81 (q, J = 272.1 Hz), 117.04 (q, J = 1.1 Hz), 116.43 (q, J = 4.1 Hz), 110.35 (q, J = 3.7 Hz), 56.21, 52.10, 40.88 ppm. MS (APCI+): m/z 324.7 ([M+H] $^+$).

Methyl 2-(3'-cyano-5'-trifluoromethyl)[1,1'-biphenyl]-4-yl)acetate (71). Preparation according to GP1, using 3-bromo-5-trifluoromethylbenzonitrile (**41**, 73 μ L, 0.50 mmol, 1.0 eq), methyl (4-boronophenyl)acetate (**58**, 0.12 g, 0.60 mmol, 1.2 eq), K_3PO_4 (0.32 g, 1.5 mmol, 3.0 eq) and XPhos Pd G2 (0.039 g, 0.050 mmol, 0.10 eq) in 1,4-dioxane (12.6 mL) and H_2O (1.4 mL). Further purification was performed by RP-CC to obtain **71** (142 mg, 89%) as a colorless solid. R_f (iso-hexane/EtOAc = 8:2) = 0.49. 1H -NMR (500 MHz, Acetone- d_6): δ = 8.43–8.36 (m, 1H), 8.32–8.28 (m, 1H), 8.20–8.12 (m, 1H), 7.86–7.76 (m, 2H), 7.53–7.44 (m, 2H), 3.76 (s, 2H), 3.67 (s, 3H) ppm. ^{13}C -NMR (126 MHz, Acetone- d_6): δ = 172.05, 144.02, 136.81, 136.77, 135.02, 132.76 (q, J = 33.4 Hz), 131.23, 128.61 (q, J = 3.7 Hz), 128.38 (q, J = 4.0 Hz), 128.24, 124.30 (q, J = 272.2 Hz), 118.08, 115.04, 52.14, 40.84 ppm. MS (APCI+): m/z 319.9 ([M+H] $^+$).

Methyl 2-(3'-fluoro-5'-trifluoromethyl)[1,1'-biphenyl]-4-yl)acetate (72). Preparation according to GP1, using 1-bromo-3-fluoro-5-trifluoromethylbenzene (**42**, 80 μ L, 0.50 mmol, 1.0 eq), methyl (4-boronophenyl)acetate (**58**, 0.12 g, 0.60 mmol, 1.2 eq), K_3PO_4 (0.32 g, 1.5 mmol,

3.0 eq) and XPhos Pd G2 (0.039 g, 0.050 mmol, 0.10 eq) in 1,4-dioxane (12.6 mL) and H₂O (1.4 mL). Further purification was performed by RP-CC to obtain **72** (155 mg, 99%) as a yellow oil. *R_f* (iso-hexane/EtOAc = 7:3 + 2% formic acid) = 0.65. ¹H-NMR (500 MHz, Acetone-*d*₆): δ = 7.86–7.82 (m, 1H), 7.79–7.72 (m, 3H), 7.53–7.48 (m, 1H), 7.48–7.44 (m, 2H), 3.74 (s, 2H), 3.67 (s, 3H) ppm. ¹³C-NMR (126 MHz, Acetone-*d*₆): δ = 172.10, 163.89 (d, *J* = 246.8 Hz), 145.39 (d, *J* = 8.1 Hz), 137.56 (d, *J* = 2.2 Hz), 136.44, 133.34 (qd, *J* = 33.0, 8.7 Hz), 131.11, 128.08, 124.50 (qd, *J* = 271.9, 3.1 Hz), 120.40 (p, *J* = 3.7 Hz), 118.37 (d, *J* = 22.3 Hz), 112.04 (dq, *J* = 25.0, 3.9 Hz), 52.13, 40.85 ppm. MS (APCI+): *m/z* 312.4 ([M]⁺).

Methyl 2-(3'-acetyl-5'-trifluoromethyl[1,1'-biphenyl]-4-yl)acetate (73). Preparation according to GP1, using 1-(3-bromo-5-trifluoromethylphenyl)ethan-1-one (**43**, 0.13 g, 0.50 mmol, 1.0 eq), methyl (4-boronophenyl)acetate (**58**, 0.12 g, 0.60 mmol, 1.2 eq), K₃PO₄ (0.32 g, 1.5 mmol, 3.0 eq) and XPhos Pd G2 (0.039 g, 0.050 mmol, 0.10 eq) in 1,4-dioxane (12.6 mL) and H₂O (1.4 mL). Further purification was performed by RP-CC to obtain **73** (96 mg, 57%) as a colorless solid. *R_f* (iso-hexane/EtOAc = 8:2 + 2% formic acid) = 0.33. ¹H-NMR (400 MHz, Acetone-*d*₆): δ = 8.56–8.45 (m, 1H), 8.28–8.14 (m, 2H), 7.84–7.72 (m, 2H), 7.53–7.42 (m, 2H), 3.75 (s, 2H), 3.67 (s, 3H), 2.76 (s, 3H) ppm. ¹³C-NMR (101 MHz, Acetone-*d*₆): δ = 197.08, 172.12, 143.35, 139.62, 138.08, 136.23, 132.04 (q, *J* = 32.4 Hz), 131.18 (q, *J* = 1.1 Hz), 131.13, 128.20, 128.15 (q, *J* = 3.6 Hz), 124.99 (q, *J* = 272.0 Hz), 124.11 (q, *J* = 3.9 Hz), 52.13, 40.87, 27.00 ppm. MS (APCI+): *m/z* 336.4 ([M+H]⁺).

Methyl 2-(3'-hydroxymethyl-5'-trifluoromethyl[1,1'-biphenyl]-4-yl)acetate (74). Preparation according to GP1, using [3-bromo-5-(trifluoromethyl)phenyl]methanol (**44**, 0.13 g, 0.50 mmol, 1.0 eq), (4-methoxycarbonylmethylphenyl)boronic acid pinacol ester (**59**, 0.17 g, 0.60 mmol, 1.2 eq), XPhos Pd G2 (0.039 g, 0.050 mmol, 0.10 eq) and K₃PO₄ (0.32 g, 1.5 mmol, 3.0 eq) in dioxane (9 mL) and H₂O (1 mL). Further purification was performed by CC to obtain **74** (100 mg, 62%) as a colorless solid. *R_f* (iso-hexane/EtOAc = 8:2) = 0.54. ¹H-NMR (400 MHz, Acetone-*d*₆): δ = 7.93 (s, 1H), 7.83 (s, 1H), 7.75–7.68 (m, 3H), 7.47–7.41 (m, 2H), 4.82 (s, 2H), 3.73 (s, 2H), 3.67 (s, 3H) ppm. ¹³C-NMR (101 MHz, Acetone-*d*₆): δ = 171.26, 144.84, 141.57, 138.10, 134.76, 130.75 (d, *J* = 31.6 Hz), 130.09, 128.47 (m), 127.14, 127.08, 124.57 (d, *J* = 271.8 Hz), 121.71 (q, *J* = 3.9 Hz), 62.96, 51.20, 39.98 ppm. MS (APCI+): *m/z* 324.8 ([M+H]⁺).

Methyl 2-[4-(3,5,5,8,8-pentamethyl-5,6,7,8-tetrahydronaphthalen-2-yl)phenyl]acetate (75). Preparation according to GP1, using 6-bromo-1,1,4,4,7-pentamethyl-1,2,3,4-tetrahydronaphthalene (**45**, 0.28 g, 1.0 mmol, 1.0 eq), methyl (4-boronophenyl)acetate (**58**, 0.23 g, 1.2 mmol, 1.2 eq), Na₂CO₃ (0.32 g, 3.0 mmol, 3.0 eq) and Pd(PPh₃)₄ (0.12 g, 0.10 mmol, 0.10 eq) in toluene (4 mL), MeOH (2 mL) and H₂O (1 mL). Further purification was performed by CC to obtain **75** (263 mg, 75%) as a green solid. *R_f* (iso-hexane/EtOAc = 98:2) = 0.75. ¹H-NMR (400 MHz, DMSO-*d*₆): δ = 7.33–7.25 (m, 4H), 7.20 (s, 1H), 7.08 (s, 1H), 3.72 (s, 2H), 3.64 (s, 3H), 2.17 (s, 3H), 1.64 (s, 4H), 1.26 (s, 6H), 1.23 (s, 6H) ppm. ¹³C-NMR (101 MHz, DMSO-*d*₆): δ = 171.67, 143.28, 141.88, 140.11, 138.26, 132.67, 131.58, 129.12, 129.00, 128.12, 127.32, 51.73, 39.53, 34.70, 34.67,

33.57, 33.53, 31.61, 19.92 ppm. MS (APCI+): *m/z* 351.0 ([M+H]⁺).

Methyl 2-[4-(1,4-dimethyl-8-oxo-5,6,7,8-tetrahydronaphthalen-2-yl)phenyl]acetate (76). Preparation according to GP1, using 7-bromo-5,8-dimethyl-3,4-dihydronaphthalen-1(2*H*)-one (**46**, 0.13 g, 0.50 mmol, 1.0 eq), methyl (4-boronophenyl)acetate (**58**, 0.12 g, 0.60 mmol, 1.2 eq), XPhos Pd G2 (0.039 g, 0.050 mmol, 0.10 eq) and K₃PO₄ (0.32 g, 1.5 mmol, 3.0 eq) in 1,4-dioxane (9 mL) and H₂O (1 mL). Further purification was performed by CC to obtain **76** (161 mg, 100%) as a colorless solid. *R_f* (iso-hexane/EtOAc = 7:3) = 0.60. ¹H-NMR (400 MHz, Acetone-*d*₆): δ = 7.38–7.35 (m, 2H), 7.26–7.19 (m, 3H), 3.71 (s, 2H), 3.67 (s, 3H), 2.91 (t, *J* = 6.2 Hz, 2H), 2.64–2.58 (m, 2H), 2.38 (s, 3H), 2.31 (s, 3H), 2.16–2.07 (m, 2H) ppm. ¹³C-NMR (101 MHz, Acetone-*d*₆): δ = 200.02, 171.37, 142.96, 141.21, 140.57, 135.00, 134.68, 133.37, 133.34, 132.64, 129.45, 129.14, 51.18, 40.55, 40.07, 26.98, 22.38, 18.93, 18.72 ppm. MS (APCI+): *m/z* 322.9 ([M+H]⁺).

Methyl 2-[4-(4,4-dimethyl-2-oxo-1,2,3,4-tetrahydroquinolin-6-yl)phenyl]acetate (77). Preparation according to GP1, using 6-bromo-4,4-dimethyl-3,4-dihydroquinolin-2(1*H*)-one (**47**, 0.13 g, 0.50 mmol, 1.0 eq), (4-methoxycarbonylmethylphenyl)boronic acid pinacol ester (**59**, 0.17 g, 0.60 mmol, 1.2 eq), XPhos Pd G2 (0.039 g, 0.050 mmol, 0.10 eq) and K₃PO₄ (0.32 g, 1.5 mmol, 3.0 eq) in 1,4-dioxane (9 mL) and H₂O (1 mL). Further purification was performed by CC to obtain **77** (158 mg, 98%) as a colorless solid. *R_f* (iso-hexane/EtOAc = 6:4) = 0.64. ¹H-NMR (400 MHz, CDCl₃): δ = 9.28 (s, 1H), 7.52–7.49 (m, 2H), 7.48–7.47 (m, 1H), 7.39 (dd, *J* = 8.1, 2.0 Hz, 1H), 7.36–7.32 (m, 2H), 6.89 (d, *J* = 8.1 Hz, 1H), 3.71 (s, 3H), 3.67 (s, 2H), 2.53 (s, 2H), 1.37 (s, 6H) ppm. ¹³C-NMR (101 MHz, CDCl₃): δ = 172.16, 171.21, 139.87, 136.50, 135.36, 133.01, 132.98, 129.87, 127.19, 126.30, 123.47, 116.35, 52.26, 45.44, 40.92, 34.24, 27.86 ppm. MS (APCI+): *m/z* 324.2 ([M+H]⁺).

Methyl 2-[4-(1-methyl-1*H*-indol-5-yl)phenyl]acetate (78). Preparation according to GP1, using 5-bromo-1-methyl-1*H*-indole (**48**, 0.21 g, 1.0 mmol, 1.0 eq), (4-methoxycarbonylmethylphenyl)boronic acid pinacol ester (**59**, 0.33 g, 1.2 mmol, 1.2 eq), XPhos Pd G2 (0.079 g, 0.10 mmol, 0.10 eq) and Cs₂CO₃ (0.98 g, 3.00 mmol, 3.0 eq) in toluene (18 mL) and H₂O (2 mL). Further purification was performed by CC to obtain **78** (226 mg, 56%) as a colorless solid. *R_f* (iso-hexane/EtOAc = 7:3) = 0.45. ¹H-NMR (400 MHz, DMSO-*d*₆): δ = 7.83–7.78 (m, 1H), 7.64–7.60 (m, 2H), 7.52–7.49 (m, 1H), 7.46–7.43 (m, 1H), 7.36–7.30 (m, 3H), 6.50–6.45 (m, 1H), 3.81 (s, 3H), 3.71 (s, 2H), 3.63 (s, 3H) ppm. ¹³C-NMR (101 MHz, DMSO-*d*₆): δ = 172.20, 140.76, 136.47, 132.75, 131.56, 130.82, 130.26, 129.07, 127.12, 120.78, 118.74, 110.57, 101.25, 52.19, 40.46, 33.02 ppm. MS (APCI+): *m/z* 279.7 ([M+H]⁺).

Ethyl 2-[4-(1-acetyldolin-5-yl)phenyl]acetate (79). Preparation according to GP1, using 1-(5-(4,4,5,5-tetramethyl-1,3,2-dioxaborolan-2-yl)indolin-1-yl)ethan-1-one (**61**, 0.095 g, 0.33 mmol, 1.0 eq), ethyl 2-(4-bromophenyl)acetate (**62**, 0.099 g, 0.41 mmol, 1.2 eq), XPhos Pd G2 (0.026 g, 0.033 mmol, 0.10 eq) and Cs₂CO₃ (0.22 g, 0.62 mmol, 1.9 eq) in toluene (18 mL) and H₂O (2 mL). Further purification was performed by CC to obtain **79** (92 mg, 86%) as a light yellow solid. *R_f* (iso-hexane/EtOAc = 7:3) = 0.30. ¹H-NMR

(500 MHz, DMSO- d_6): δ = 8.11–8.06 (m, 1H), 7.60–7.56 (m, 2H), 7.55–7.51 (m, 1H), 7.47–7.43 (m, 1H), 7.34–7.29 (m, 2H), 4.12 (t, J = 8.6 Hz, 2H), 4.09 (q, J = 7.0 Hz, 2H), 3.68 (s, 2H), 3.19 (t, J = 8.5 Hz, 2H), 2.17 (s, 3H), 1.19 (t, J = 7.1 Hz, 3H) ppm. $^{13}\text{C-NMR}$ (126 MHz, DMSO- d_6): δ = 171.16, 168.55, 142.42, 138.50, 134.71, 133.10, 132.68, 129.83, 126.20, 125.39, 122.89, 115.98, 60.29, 48.38, 39.65, 27.40, 23.98, 14.10 ppm. MS (APCI+): m/z 323.9 ([M+H] $^+$).

Methyl 2-[4-(7-trifluoromethyl-1H-indazol-5-yl)phenyl]acetate (80). Preparation according to GP1, using 5-bromo-7-(trifluoromethyl)-1H-indazole (**50**, 0.13 g, 0.50 mmol, 1.0 eq), (4-methoxycarbonylmethylphenyl)boronic acid pinacol ester (**59**, 0.17 g, 0.60 mmol, 1.2 eq), XPhos Pd G2 (0.039 g, 0.050 mmol, 0.10 eq) and K_3PO_4 (0.32 g, 1.5 mmol, 3.0 eq) in 1,4-dioxane (9 mL) and H_2O (1 mL). Further purification was performed by CC to obtain **80** (137 mg, 82%) as a colorless solid. R_f (iso-hexane/EtOAc = 8:2) = 0.30. $^1\text{H-NMR}$ (400 MHz, Acetone- d_6): δ = 12.85 (s, 1H), 8.40–8.34 (m, 1H), 8.30 (s, 1H), 8.05–7.99 (m, 1H), 7.76–7.68 (m, 2H), 7.48–7.40 (m, 2H), 3.73 (s, 2H), 3.67 (s, 3H) ppm. $^{13}\text{C-NMR}$ (101 MHz, Acetone- d_6): δ = 172.23, 139.46, 136.01, 135.58, 134.93, 134.25, 130.95, 128.11, 127.07, 126.62, 125.28 (q, J = 270.9 Hz), 124.37 (q, J = 4.9 Hz), 124.06, 115.74 (q, J = 28.8 Hz), 52.09, 40.87 ppm. MS (APCI+): m/z 335.0 ([M+H] $^+$).

Methyl 2-[4-(1-tetrahydro-2H-pyran-2-yl)-1H-indazol-5-yl]phenyl]acetate (81). Preparation according to GP1, using 6-bromo-1-(tetrahydro-2H-pyran-2-yl)-1H-indazole (**52**, 0.14 g, 0.50 mmol, 1.0 eq), (4-methoxycarbonylmethylphenyl)boronic acid pinacol ester (**59**, 0.17 g, 0.60 mmol, 1.2 eq), XPhos Pd G2 (0.039 g, 0.050 mmol, 0.10 eq) and K_3PO_4 (0.32 g, 1.5 mmol, 3.0 eq) in 1,4-dioxane (9 mL) and H_2O (1 mL). Further purification was performed by CC to obtain **81** (170 mg, 97%) as a colorless solid. R_f (iso-hexane/EtOAc = 8:2) = 0.40. $^1\text{H-NMR}$ (400 MHz, Acetone- d_6): δ = 8.04 (s, 1H), 7.95–7.93 (m, 1H), 7.83 (dd, J = 8.4, 0.8 Hz, 1H), 7.72–7.67 (m, 2H), 7.48 (dd, J = 8.4, 1.4 Hz, 1H), 7.44–7.39 (m, 2H), 5.99–5.91 (m, 1H), 3.96–3.89 (m, 1H), 3.86–3.76 (m, 1H), 3.72 (s, 2H), 3.67 (s, 3H), 2.64–2.53 (m, 1H), 2.19–.09 (m, 1H), 2.09–2.06 (m, 1H), 1.91–1.76 (m, 1H), 1.75–1.58 (m, 2H) ppm. $^{13}\text{C-NMR}$ (101 MHz, Acetone- d_6): δ = 171.35, 140.41, 140.00, 139.10, 133.99, 133.08, 129.87, 127.46, 124.07, 121.11, 120.92, 108.24, 84.70, 66.69, 51.19, 40.03, 25.15, 24.33, 22.46 ppm. MS (APCI+): m/z 351.4 ([M+H] $^+$).

Methyl 2-[4-(9-methyl-9H-carbazol-3-yl)phenyl]acetate (82). Preparation according to GP1, using 3-bromo-9-methyl-9H-carbazole (**53**, 0.26 g, 1.0 mmol, 1.0 eq), methyl (4-boronophenyl)acetate (**58**, 0.23 g, 1.2 mmol, 1.2 eq), Na_2CO_3 (0.32 g, 3.0 mmol, 3.0 eq) and $\text{Pd}(\text{PPh}_3)_4$ (0.12 g, 0.10 mmol, 0.10 eq) in THF (5 mL) and H_2O (1 mL). Further purification was performed by CC to obtain **82** (251 mg, 76%) as a colorless solid. R_f (iso-hexane/EtOAc + 2% triethylamine = 9:1) = 0.23. $^1\text{H-NMR}$ (400 MHz, DMSO- d_6): δ = 8.48 (d, J = 1.8 Hz, 1H), 8.25 (d, J = 7.7 Hz, 1H), 7.79 (dd, J = 8.5, 1.8 Hz, 1H), 7.76–7.72 (m, 2H), 7.67 (d, J = 8.5 Hz, 1H), 7.60 (d, J = 8.2 Hz, 1H), 7.51–7.45 (m, 1H), 7.40–7.35 (m, 2H), 7.23 (t, J = 7.4 Hz, 1H), 3.91 (s, 3H), 3.74 (s, 2H), 3.64 (s, 3H) ppm. $^{13}\text{C-NMR}$ (101 MHz, DMSO- d_6): δ = 171.72, 141.10, 140.17, 139.69, 132.50, 130.78, 129.88, 126.64, 125.92, 124.62, 122.61, 122.17, 120.48, 118.86, 118.22, 109.53,

109.26, 51.73, 39.78, 29.09 ppm. MS (APCI+): m/z 329.8 ([M+H] $^+$).

Methyl 2-[4-(9-methyl-1-oxo-2,3,4,4a,9,9a-hexahydro-1H-carbazol-7-yl)phenyl]acetate (83). Preparation according to GP1, using 6-bromo-9-methyl-2,3,4,9-tetrahydro-1H-carbazol-1-one (**54**, 0.14 g, 0.50 mmol, 1.0 eq), (4-methoxycarbonylmethylphenyl)boronic acid pinacol ester (**59**, 0.17 g, 0.60 mmol, 1.2 eq), XPhos Pd G2 (0.039 g, 0.050 mmol, 0.10 eq) and K_3PO_4 (0.32 g, 1.5 mmol, 3.0 eq) in 1,4-dioxane (9 mL) and H_2O (1 mL). Further purification was performed by CC to obtain **83** (137 mg, 79%) as green solid. R_f (iso-hexane/EtOAc = 9:1 + 2% acetic acid) = 0.39. $^1\text{H-NMR}$ (400 MHz, Acetone- d_6): δ = 7.97–7.94 (m, 1H), 7.72 (dd, J = 8.8, 1.8 Hz, 1H), 7.69–7.64 (m, 2H), 7.56 (dd, J = 8.8, 0.8 Hz, 1H), 7.41–7.36 (m, 2H), 4.08 (s, 3H), 3.70 (s, 2H), 3.67 (s, 3H), 3.08 (t, J = 6.1 Hz, 2H), 2.63–2.56 (m, 2H), 2.27–2.18 (m, 2H) ppm. $^{13}\text{C-NMR}$ (101 MHz, Acetone- d_6): δ = 192.10, 172.33, 141.16, 140.06, 133.96, 133.75, 131.78, 130.69, 129.88, 127.82, 126.84, 126.24, 119.99, 111.72, 52.05, 40.92, 40.57, 31.85, 25.50, 22.30 ppm. MS (APCI+): m/z 348.3 ([M+H] $^+$).

Methyl 2-[4-(9-oxo-9H-fluoren-2-yl)phenyl]acetate (84). Preparation according to GP1, using 2-bromo-9H-fluoren-9-one (**55**, 0.26 g, 1.0 mmol, 1.0 eq), methyl (4-boronophenyl)acetate (**58**, 0.23 g, 1.2 mmol, 1.2 eq), K_2CO_3 (0.42 g, 3.0 mmol, 3.0 eq) and $\text{Pd}(\text{PPh}_3)_4$ (0.12 g, 0.10 mmol, 0.10 eq) in toluene (8 mL) and EtOH (2 mL). Further purification was performed by CC to obtain **84** (175 mg, 53%) as a yellow solid. R_f (iso-hexane/Acetone = 9:1) = 0.20. $^1\text{H-NMR}$ (400 MHz, DMSO- d_6): δ = 8.17 (t, J = 1.2 Hz, 1H), 7.93 (dt, J = 7.4, 0.9 Hz, 1H), 7.81–7.76 (m, 2H), 7.69–7.61 (m, 4H), 7.45–7.38 (m, 3H), 3.78 (s, 2H), 3.64 (s, 3H) ppm. $^{13}\text{C-NMR}$ (101 MHz, DMSO- d_6): δ = 192.68, 171.49, 146.73, 144.85, 143.65, 137.56, 135.28, 135.03, 133.81, 132.11, 130.10, 129.61, 127.52, 127.06, 124.47, 123.81, 121.44, 119.59, 51.78, 40.20 ppm. MS (APCI+): m/z 328.9 ([M+H] $^+$).

Methyl 2-(2'-benzyloxy-4'-trifluoromethyl[1,1'-biphenyl]-4-yl)acetate (85). Preparation according to GP1, using 2-benzyloxy-1-bromo-4-trifluoromethylbenzene (**56**, 0.33 g, 1.00 mmol, 1.0 eq), (4-methoxycarbonylmethylphenyl)boronic acid pinacol ester (**59**, 0.33 g, 1.2 mmol, 1.2 eq), Cs_2CO_3 (0.98 g, 3.0 mmol, 3.0 eq) and XPhos Pd G2 (0.079 g, 0.10 mmol, 0.10 eq) in toluene (18 mL) and H_2O (2 mL). Further purification was performed by CC to obtain **85** (200 mg, 72%) as a colorless solid. R_f (cyclohexane/EtOAc = 7:3) = 0.64. $^1\text{H-NMR}$ (400 MHz, DMSO- d_6): δ = 7.56–7.51 (m, 3H), 7.50–7.48 (m, 1H), 7.41–7.28 (m, 8H), 5.24 (s, 2H), 3.73 (s, 2H), 3.63 (s, 3H) ppm. $^{13}\text{C-NMR}$ (101 MHz, DMSO- d_6): δ = 171.56, 155.45, 136.49, 135.19, 133.91, 131.34, 129.30, 129.14 (q, J = 31.9 Hz), 129.13, 128.42, 128.41, 127.85, 127.45, 124.07 (q, J = 273.5 Hz), 117.68 (q, J = 4.2 Hz), 109.79 (q, J = 3.6 Hz), 70.05, 51.74, 39.80 ppm. MS (APCI+): m/z 400.5 ([M+H] $^+$).

Methyl 2-[4-[4-(dimethylamino)naphthalen-1-yl]phenyl]acetate (86). Preparation according to GP1, using 4-bromo-*N,N*-dimethylnaphthalen-1-amine (**57**, 0.50 g, 2.0 mmol, 1.0 eq), methyl (4-boronophenyl)acetate (**58**, 0.45 g, 2.3 mmol, 1.15 eq), Cs_2CO_3 (2.0 g, 6.0 mmol, 3.0 eq) and $\text{Pd}(\text{PPh}_3)_4$ (0.23 g, 0.20 mmol, 0.10 eq) in DMF (16 mL) and H_2O (4 mL). Further purification was performed by RP-

CC to obtain **86** (203 mg, 32%) as a yellow oil. R_f (*iso*-hexane/EtOAc = 7:3) = 0.72. $^1\text{H-NMR}$ (400 MHz, Acetone- d_6): δ = 8.36–8.29 (m, 1H), 7.89–7.81 (m, 1H), 7.56–7.48 (m, 1H), 7.47–7.38 (m, 5H), 7.34 (d, J = 7.7 Hz, 1H), 7.19 (d, J = 7.7 Hz, 1H), 3.75 (s, 2H), 3.70 (s, 3H), 2.90 (s, 6H) ppm. $^{13}\text{C-NMR}$ (101 MHz, Acetone- d_6): δ = 172.32, 151.52, 140.47, 135.36, 134.32, 133.63, 130.91, 130.20, 129.93, 127.80, 126.95, 126.73, 125.81, 125.36, 114.59, 52.10, 45.41, 41.02 ppm. MS (APCI+): m/z 319.6 ([M+H] $^+$).

In vitro Characterization

Hybrid reporter gene assays. RXR modulation was determined in Gal4 hybrid reporter gene assays in HEK293T cells (German Collection of Microorganisms and Cell Culture GmbH, DSMZ; ACC635) using pFR-Luc (Stratagene, La Jolla, CA, USA; reporter), pRL-SV40 (Promega, Madison, WI, USA; internal control) and pFA-CMV-hRXR α -LBD⁴⁴, pFA-CMV-hRXR β -LBD⁴⁴, or pFA-CMV-hRXR γ -LBD⁴⁴, coding for the hinge region and ligand binding domain of the respective human RXR subtype. Cells were cultured in Dulbecco's modified Eagle's medium (DMEM), high glucose supplemented with 10% fetal calf serum (FCS), sodium pyruvate (1 mM), penicillin (100 U/mL), and streptomycin (100 $\mu\text{g}/\text{mL}$) at 37°C and 5% CO₂ and seeded in 96-well plates (3 \times 10⁴ cells/well). After 24 h, medium was changed to Opti-MEM without supplements and cells were transiently transfected using Lipofectamine LTX reagent (Invitrogen, Carlsbad, CA, USA) according to the manufacturer's protocol. Five hours after transfection, cells were incubated with the test compounds in Opti-MEM supplemented with penicillin (100 U/mL), streptomycin (100 $\mu\text{g}/\text{mL}$) and 0.1% DMSO for 16 h before luciferase activity was measured using the Dual-Glo Luciferase Assay System (Promega) according to the manufacturer's protocol on a Tecan Spark luminometer (Tecan Deutschland GmbH, Crailsheim, Germany). Firefly luminescence was divided by Renilla luminescence and multiplied by 1000 resulting in relative light units (RLU) to normalize for transfection efficiency and cell growth. Fold activation was obtained by dividing the mean RLU of a test sample by the mean RLU of the untreated control, and relative activation was obtained by normalization to the effect of reference RXR agonist bexarotene (**2**) at 1 μM . All samples were tested in at least three biologically independent experiments in duplicates. For dose-response curve fitting and calculation of EC₅₀ values, the equation "[Agonist] vs. response -- Variable slope (four parameters)" was used in GraphPad Prism (version 7.00, GraphPad Software, La Jolla, CA, USA). Selectivity profiling was performed with identical procedures using the corresponding pFA-CMV-NR-LBD clones for THR α , RAR α , PPAR α , PPAR γ , PPAR δ , and FXR as described previously³³.

Co-regulator recruitment assays. The co-regulator recruitment to the biotinylated RXR α LBD (3 nM; expressed, purified, and biotin-labeled as described previously⁵⁹) was determined in a HTRF assay system as described previously⁵⁹ using Tb³⁺-cryptate as streptavidin conjugate (Tb-SA; 6 nM; Cisbio Bioassays; FRET donor) for stable coupling to biotinylated recombinant RXR α LBD protein as well as co-regulator peptides (100 nM, sequences in ⁶⁰) fused to fluorescein (ThermoFisher Scientific, FRET acceptor). Assays were performed in HTRF assay buffer (25 mM HEPES pH 7.5, 150

mM KF, 5% (w/v) glycerol, 5 mM DTT) supplemented with 0.1% (w/v) CHAPS with 1% DMSO and test compounds (in a single concentration or dilution series) or DMSO alone as a negative control in 384 well format using low volume white flat bottom polystyrol microtiter plates (Greiner Bio-One; #784075) with a final volume of 20 μL . All samples were tested in three technical replicates. After 2 h incubation at room temperature, fluorescence intensities (FI) after excitation at 340 nm were recorded at 520 nm for fluorescein acceptor fluorescence and 620 nm for Tb-SA donor fluorescence on a SPARK plate reader (Tecan Deutschland GmbH). FI520nm was divided by FI620nm and multiplied with 10,000 to give a dimensionless HTRF signal which was normalized to the HTRF signal of the DMSO control in the respective setting.

Heterodimerization assays. Ligand effects on heterodimerization of RXR with THR α , RAR α , PPAR γ , LXR α and FXR were observed in a cellular setting using an RXR α -LBD-VP16 fusion expressed from pFTI-CMV-RXR α -LBD⁵⁹, the respective Gal4-hybrid receptors expressed from pFA-CMV-NR-LBD clones for THR α , RAR α , PPAR γ , LXR α , and FXR, and pFR-Luc (Stratagene), pRL-SV40 (Promega) was co-transfected for normalization. HEK293T cells were cultured as described and seeded in 96-well plates (3 \times 10⁴ cells/well) 24 h prior to transfection. Transient transfection, incubation with test compounds, readout and calculation of RLU values was conducted as described above. All samples were tested in at least three biologically independent experiments in duplicates.

Reporter gene assay for the RXR α -PGC1 α interaction. HEK293T cells were cultured as described and seeded in 96-well plates (3 \times 10⁴ cells/well) 24 h prior to transfection. Medium was changed to Opti-MEM without supplements and cells were transiently transfected with pFR-Luc (Stratagene; reporter), pRL-SV40 (Promega; internal control), and Gal4-PGC1 α ⁴⁷ (Addgene, plasmid #8892) with or without pFTI-CMV-hRXR α -LBD⁵⁹ using Lipofectamine LTX reagent (Invitrogen) according to the manufacturer's protocol. Five hours after transfection, cells were incubated with the test compounds in Opti-MEM supplemented with penicillin (100 U/mL), streptomycin (100 $\mu\text{g}/\text{mL}$) and 0.1% DMSO for 16 h before luciferase activity was measured using the Dual-Glo Luciferase Assay System (Promega) according to the manufacturer's protocol on a Tecan Spark luminometer (Tecan). Firefly luminescence was divided by Renilla luminescence and multiplied by 1000 resulting in relative light units (RLU) to normalize for transfection efficiency and cell growth. Fold activation was obtained by dividing the mean RLU of a test sample by the mean RLU of the untreated control, and fold activation for the RXR α -PGC1 α assay was normalized to fold activation in the pFTI-CMV-hRXR α -LBD free setting. All samples were tested in three biologically independent experiments in duplicates. For dose-response curve fitting and calculation of EC₅₀ values, the equation "[Agonist] vs. response -- Variable slope (four parameters)" was used in GraphPad Prism (version 7.00, GraphPad Software).

Computational Methods

Virtual library preparation and docking. All calculations were performed with Schrödinger software version 2019-

4. The 3D structure of RXR α LBD (pdb id 6sjm³⁸) was prepared using the Protein Preparation Wizard in Maestro. The Xray ligand JP175 was selected to identify the active site, resulting in $x=18.2033$, $y=3.9776$ and $z=23.9669$ for the docking grid center. Docking was performed using GLIDE software⁶¹ in standard precision mode (SP). All parameters were left at the default values (SP; flexible ligands; sample ring conformations of ligand; add Epik⁶² state penalties to docking score; scaling of van der Waals radii = 0.8; post docking minimization of five poses per ligand; write out one pose per ligand). Reevaluation of the docking poses using MMGBSA (Molecular Mechanics Generalized Born Surface Area) was performed using the Prime software⁶³. All default parameters in the Prime MM-GBSA module were used except the sampling method was switched to “Minimize side chains only” (-rflexgroup side in the prime_mmgsa command line). Commercially available compounds with bromoaryl substructure were searched in Reaxys (filter setting = “SigmaAldrich”) and fused with 4-boronophenylacetic acid using the “RDKit Two Component Reaction” node⁶⁴ in KNIME⁶⁵, resulting in 15,759 virtual ligands with the desired biphenyl substructure. 3D conversion of the virtual library using ligprep yielded 19,222 molecules for docking. Chiral information in the 2D input structure was retained when present, otherwise all possible stereoisomers were generated. The forcefield OPLS4 was used and the correct protonation between pH 6 to 8 was calculated with Epik⁶². Docking of the virtual library into the ligand binding site of 6sjm resulted in 13,917 poses with docking scores between -12.829 and -1.808.

ASSOCIATED CONTENT

Supporting Information

Supporting Information (pdf) contains Table S1 and NMR spectra of **4-31**.

Docking (zip) contains the predicted binding modes of **4-31** in the RXR α ligand binding site as individual pdb files.

Molecular formula strings (csv) contains molecular structures of **4-31** and associated activity data.

This material is available free of charge on the ACS Publications website.

AUTHOR INFORMATION

Corresponding Author

* daniel.merk@cup.lmu.de

Notes

There are no competing interests to declare.

ACKNOWLEDGMENT

This project was supported by the German Research Foundation (DFG, ME 5481/1-1). Gal4-PGC1 α was a gift from Bruce Spiegelman (Addgene plasmid # 8892).

ABBREVIATIONS

9-cis RA, 9-cis retinoic acid; HTRF, homogeneous time-resolved fluorescence resonance energy transfer; LBD, ligand binding

domain; NR, nuclear receptor; PGC1 α , peroxisome proliferator-activated receptor gamma co-activator 1-alpha; RXR, retinoid X receptor; SMRT, silencing mediator for retinoid and thyroid-hormone receptor.

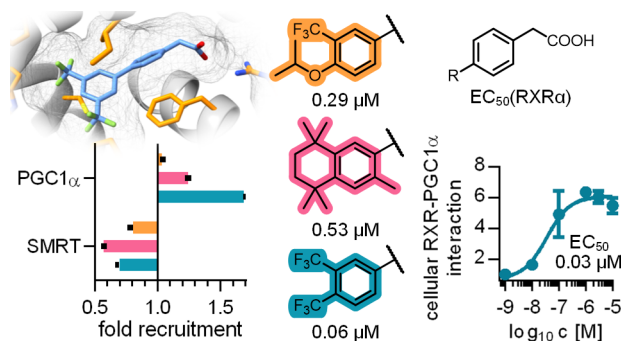
REFERENCES

- Evans, R. M.; Mangelsdorf, D. J. Nuclear Receptors, RXR, and the Big Bang. *Cell* **2014**, *157* (1), 255–266.
- Weikum, E. R.; Liu, X.; Ortlund, E. A. The Nuclear Receptor Superfamily: A Structural Perspective. *Protein Sci.* **2018**, *27* (11), 1876–1892.
- De Bosscher, K.; Desmet, S. J.; Clarisse, D.; Estébanez-Perpiña, E.; Brunsveld, L. Nuclear Receptor Crosstalk — Defining the Mechanisms for Therapeutic Innovation. *Nat. Rev. Endocrinol.* **2020**, *16* (7), 363–377.
- Isigkeit, L.; Merk, D. Opportunities and Challenges in Targeting Orphan Nuclear Receptors. *Chem. Commun.* **2023**, *59*, 4551–4561.
- Millard, C. J.; Watson, P. J.; Fairall, L.; Schwabe, J. W. R. An Evolving Understanding of Nuclear Receptor Coregulator Proteins. *J. Mol. Endocrinol.* **2013**, *51* (3), T23–T36.
- Gallastegui, N.; Mackinnon, J. A. G.; Fletterick, R. J.; Estébanez-Perpiñá, E. Advances in Our Structural Understanding of Orphan Nuclear Receptors. *Trends Biochem. Sci.* **2015**, *40* (1), 25–35.
- Merk, D.; Sreeramulu, S.; Kudlinzki, D.; Saxena, K.; Linhard, V.; Gande, S. L.; Hiller, F.; Lamers, C.; Nilsson, E.; Aagaard, A.; Wissler, L.; Dekker, N.; Bamberg, K.; Schubert-Zsilavec, M.; Schwalbe, H. Molecular Tuning of Farnesoid X Receptor Partial Agonism. *Nat. Commun.* **2019**, *10* (1), 2915.
- Lumba, S.; Cutler, S.; McCourt, P. Plant Nuclear Hormone Receptors: A Role for Small Molecules in Protein-Protein Interactions. *Annu. Rev. Cell Dev. Biol.* **2010**, *26*, 445–469.
- De Vink, P. J.; Andrei, S. A.; Higuchi, Y.; Ottmann, C.; Milroy, L. G.; Brunsveld, L. Cooperativity Basis for Small-Molecule Stabilization of Protein-Protein Interactions. *Chem. Sci.* **2019**, *10* (10), 2869–2874.
- Germain, P.; Chambon, P.; Eichele, G.; Evans, R. M.; Lazar, M. A.; Leid, M.; De Lera, A. R.; Lotan, R.; Mangelsdorf, D. J.; Gronemeyer, H. International Union of Pharmacology. LXIII. Retinoid X Receptors. *Pharmacol. Rev.* **2006**, *58* (4), 760–772.
- de Lera, A. R.; Bourguet, W.; Altucci, L.; Gronemeyer, H. Design of Selective Nuclear Receptor Modulators: RAR and RXR as a Case Study. *Nat. Rev. Drug Discov.* **2007**, *6* (10), 811–820.
- de Lera, Á.; Krezel, W.; Rühl, R. An Endogenous Mammalian Retinoid X Receptor Ligand, at Last! *ChemMedChem* **2016**, *11* (10), 1027–1037.
- Chaikuad, A.; Pollinger, J.; Rühl, M.; Ni, X.; Kilu, W.; Heering, J.; Merk, D. Comprehensive Set of Tertiary Complex Structures and Palmitic Acid Binding Provide Molecular Insights into Ligand Design for RXR Isoforms. *Int. J. Mol. Sci.* **2020**, *21* (22), 8457.
- Sharma, S.; Shen, T.; Chitranshi, N.; Gupta, V. V.; Basavarajappa, D.; Sarkar, S.; Mirzaei, M.; You, Y.; Krezel, W.; Graham, S. L.; Gupta, V. V. Retinoid X Receptor: Cellular and Biochemical Roles of Nuclear Receptor with a Focus on Neuropathological Involvement. *Mol. Neurobiol.* **2022**, *59* (4), 2027–2050.
- Willems, S.; Zaienne, D.; Merk, D. Targeting Nuclear Receptors in Neurodegeneration and Neuroinflammation. *J. Med. Chem.* **2021**, *64* (14), 9592–9638.
- Leal, A. S.; Reich, L. A.; Moerland, J. A.; Zhang, D.; Liby, K. T. Potential Therapeutic Uses of Retinoids. *Adv. Pharmacol.* **2021**, *91*, 141–183.
- Leal, A. S.; Hung, P. Y.; Chowdhury, A. S.; Liby, K. T. Retinoid X Receptor Agonists as Selective Modulators of the Immune System for the Treatment of Cancer. *Pharmacol. Ther.* **2023**, *252*, 108561.
- Shao, M.; Lu, L.; Wang, Q.; Ma, L.; Tian, X.; Li, C.; Li, C.; Guo, D.; Wang, Q.; Wang, W.; Wang, Y. The Multi-Faceted Role of Retinoid X Receptor in Cardiovascular Diseases. *Biomed. Pharmacother.* **2021**, *137*, 111264.

- (19) De Cosmo, S.; Mazzoccoli, G. Retinoid X Receptors Intersect the Molecular Clockwork in the Regulation of Liver Metabolism. *Front. Endocrinol. (Lausanne)*. **2017**, *8*, 24.
- (20) Boehm, M. F.; Zhang, L.; Zhi, L.; McClurg, M. R.; Berger, E.; Wagoner, M.; Mais, D. E.; Suto, C. M.; Davies, P. J. A.; Heyman, R. A.; Nadzan, A. M. Design and Synthesis of Potent Retinoid X Receptor Selective Ligands That Induce Apoptosis in Leukemia Cells. *J. Med. Chem.* **1995**, *38* (16), 3146–3155.
- (21) De Weij Vries-Van Der Weij, J.; De Haan, W.; Hu, L.; Kuif, M.; Oei, L.; Van Der Hoorn, J. W. A.; Havekes, L.; Princen, H.; Romijn, J.; Smit, J.; Rensen, P. Bexarotene Induces Dyslipidemia by Increased Very Low-Density Lipoprotein Production and Cholesteryl Ester Transfer Protein-Mediated Reduction of High-Density Lipoprotein. *Endocrinology* **2009**, *150* (5), 2368–2375.
- (22) Sherman, S. I.; Gopal, J.; Haugen, B. R.; Chiu, A. C.; Whaley, K.; Nowlakha, P.; Duvic, M. Central Hypothyroidism Associated with Retinoid X Receptor–Selective Ligands. *N. Engl. J. Med.* **1999**, *340* (14), 1075–1079.
- (23) Takamura, Y.; Kato, I.; Fujita-Takahashi, M.; Azuma-Nishii, M.; Watanabe, M.; Nozaki, R.; Akehi, M.; Sasaki, T.; Hirano, H.; Kakuta, H. Teratogenicity and Fetal-Transfer Assessment of the Retinoid X Receptor Agonist Bexarotene. *ACS Pharmacol. Transl. Sci.* **2022**, *5* (9), 811–818.
- (24) Watanabe, M.; Kakuta, H. Retinoid X Receptor Antagonists. *Int. J. Mol. Sci.* **2018**, *19* (8), 2354.
- (25) Brtko, J.; Dvorak, Z. Natural and Synthetic Retinoid X Receptor Ligands and Their Role in Selected Nuclear Receptor Action. *Biochimie* **2020**, *179*, 157–168.
- (26) Scheepstra, M.; Andrei, S. A.; de Vries, R. M. J. M.; Meijer, F. A.; Ma, J.-N.; Burstein, E. S.; Olsson, R.; Ottmann, C.; Milroy, L.-G.; Brunsveld, L. Ligand Dependent Switch from RXR Homo- to RXR-NURR1 Heterodimerization. *ACS Chem. Neurosci.* **2017**, *8* (9), 2065–2077.
- (27) Wang, J.; Bi, W.; Zhao, W.; Varghese, M.; Koch, R. J.; Walker, R. H.; Chandraratna, R. A.; Sanders, M. E.; Janesick, A.; Blumberg, B.; Ward, L.; Ho, L.; Pasinetti, G. M. Selective Brain Penetrable Nurr1 Transactivator for Treating Parkinson's Disease. *Oncotarget* **2016**, *7* (7), 7469–7479.
- (28) Pérez, E.; Bourguet, W.; Gronemeyer, H.; de Lera, A. R. Modulation of RXR Function through Ligand Design. *Biochim. Biophys. Acta - Mol. Cell Biol. Lipids* **2012**, *1821* (1), 57–69.
- (29) Lagu, B.; Pio, B.; Lebedev, R.; Yang, M.; Pelton, P. D. RXR–LXR Heterodimer Modulators for the Potential Treatment of Dyslipidemia. *Bioorg. Med. Chem. Lett.* **2007**, *17* (12), 3497–3503.
- (30) York, B.; Sagen, J. V.; Tsimelzon, A.; Louet, J. F.; Chopra, A. R.; Reineke, E. L.; Zhou, S.; Stevens, R. D.; Wenner, B. R.; Ilkayeva, O.; Bain, J. R.; Xu, J.; Hilsenbeck, S. G.; Newgard, C. B.; O'Malley, B. W. Research Resource: Tissue- and Pathway-Specific Metabolomic Profiles of the Steroid Receptor Coactivator (SRC) Family. *Mol. Endocrinol.* **2013**, *27* (2), 366–380.
- (31) Dasgupta, S.; Lonard, D. M.; O'Malley, B. W. Nuclear Receptor Coactivators: Master Regulators of Human Health and Disease. *Annu. Rev. Med.* **2014**, *65* (1), 279–292.
- (32) Delerive, P.; Wu, Y.; Burris, T. P.; Chin, W. W.; Suen, C. S. PGC-1 Functions as a Transcriptional Coactivator for the Retinoid X Receptors. *J. Biol. Chem.* **2002**, *277* (6), 3913–3917.
- (33) Arifi, S.; Marschner, J. A.; Pollinger, J.; Isigkeit, L.; Heitel, P.; Kaiser, A.; Obeser, L.; Höfner, G.; Proschak, E.; Knapp, S.; Chaikuad, A.; Heering, J.; Merk, D. Targeting the Alternative Vitamin E Metabolite Binding Site Enables Noncanonical PPAR γ Modulation. *J. Am. Chem. Soc.* **2023**, *145* (27), 14802–14810.
- (34) Willems, S.; Gellrich, L.; Chaikuad, A.; Kluge, S.; Werz, O.; Heering, J.; Knapp, S.; Lorkowski, S.; Schubert-Zsilavecz, M.; Merk, D. Endogenous Vitamin E Metabolites Mediate Allosteric PPAR γ Activation with Unprecedented Co-Regulatory Interactions. *Cell Chem. Biol.* **2021**, *28* (10), 1489–1500.e8.
- (35) Heering, J.; Jores, N.; Kilu, W.; Schallmayer, E.; Peelen, E.; Muehler, A.; Kohlhof, H.; Vitt, D.; Linhard, V.; Gande, S. L.; Chaikuad, A.; Sreeramulu, S.; Schwalbe, H.; Merk, D. Mechanistic Impact of Different Ligand Scaffolds on FXR Modulation Suggests Avenues to Selective Modulators. *ACS Chem. Biol.* **2022**, *17* (11), 3159–3168.
- (36) Pearce, K. H.; Iannone, M. A.; Simmons, C. A.; Gray, J. G. Discovery of Novel Nuclear Receptor Modulating Ligands: An Integral Role for Peptide Interaction Profiling. *Drug Discov. Today* **2004**, *9* (17), 741–751.
- (37) Iannone, M. A.; Simmons, C. A.; Kadwell, S. H.; Svoboda, D. L.; Vanderwall, D. E.; Deng, S. J.; Consler, T. G.; Shearin, J.; Gray, J. G.; Pearce, K. H. Correlation between In Vitro Peptide Binding Profiles and Cellular Activities for Estrogen Receptor-Modulating Compounds. *Mol. Endocrinol.* **2004**, *18* (5), 1064–1081.
- (38) Pollinger, J.; Schierle, S.; Gellrich, L.; Ohrndorf, J.; Kaiser, A.; Heitel, P.; Chaikuad, A.; Knapp, S.; Merk, D. A Novel Biphenyl-Based Chemotype of Retinoid X Receptor Ligands Enables Subtype and Heterodimer Preferences. *ACS Med. Chem. Lett.* **2019**, *10* (9), 1346–1352.
- (39) Scarpulla, R. C. Metabolic Control of Mitochondrial Biogenesis through the PGC-1 Family Regulatory Network. *Biochim. Biophys. Acta - Mol. Cell Res.* **2011**, *1813* (7), 1269–1278.
- (40) Boström, P.; Wu, J.; Jedrychowski, M. P.; Korde, A.; Ye, L.; Lo, J. C.; Rasbach, K. A.; Boström, E. A.; Choi, J. H.; Long, J. Z.; Kajimura, S.; Zingaretti, M. C.; Vind, B. F.; Tu, H.; Cinti, S.; Højlund, K.; Gygi, S. P.; Spiegelman, B. M. A PGC-1 α -Dependent Myokine That Drives Brown-Fat-like Development of White Fat and Thermogenesis. *Nature* **2012**, *481* (7382), 463–468.
- (41) Liu, C.; Lin, J. D. PGC-1 Coactivators in the Control of Energy Metabolism. *Acta Biochim. Biophys. Sin. (Shanghai)*. **2011**, *43* (4), 248–257.
- (42) Kamata, S.; Honda, A.; Kashiwagi, N.; Shimamura, A.; Yashiro, S.; Komori, Y.; Hosoda, A.; Akahoshi, N.; Ishii, I. Different Coactivator Recruitment to Human PPAR α / δ / γ Ligand-Binding Domains by Eight PPAR Agonists to Treat Nonalcoholic Fatty Liver Disease. *Biomedicines* **2024**, *12* (3), 624.
- (43) Morgan, H. L. The Generation of a Unique Machine Description for Chemical Structures-A Technique Developed at Chemical Abstracts Service. *J. Chem. Doc.* **1965**, *5* (2), 107–113.
- (44) Heitel, P.; Gellrich, L.; Kalinowsky, L.; Heering, J.; Kaiser, A.; Ohrndorf, J.; Proschak, E.; Merk, D. Computer-Assisted Discovery and Structural Optimization of a Novel Retinoid X Receptor Agonist Chemotype. *ACS Med. Chem. Lett.* **2019**, *10* (2), 203–208.
- (45) Adouvi, G.; Nawa, F.; Ballarotto, M.; Rüger, L. A.; Knümann, L.; Kasch, T.; Arifi, S.; Schubert-Zsilavecz, M.; Willems, S.; Marschner, J. A.; Pabel, J.; Merk, D. Structural Fusion of Natural and Synthetic Ligand Features Boosts RXR Agonist Potency. *J. Med. Chem.* **2023**.
- (46) Knutti, D.; Kaul, A.; Kralli, A. A Tissue-Specific Coactivator of Steroid Receptors, Identified in a Functional Genetic Screen. *Mol. Cell Biol.* **2000**, *20* (7), 2411–2422.
- (47) Puigserver, P.; Wu, Z.; Park, C. W.; Graves, R.; Wright, M.; Spiegelman, B. M. A Cold-Inducible Coactivator of Nuclear Receptors Linked to Adaptive Thermogenesis. *Cell* **1998**, *92* (6), 829–839.
- (48) Qian, L.; Zhu, Y.; Deng, C.; Liang, Z.; Chen, J.; Chen, Y.; Wang, X.; Liu, Y.; Tian, Y.; Yang, Y. Peroxisome Proliferator-Activated Receptor Gamma Coactivator-1 (PGC-1) Family in Physiological and Pathophysiological Process and Diseases. *Signal Transduct. Target. Ther.* **2024**, *9* (1), 50.
- (49) Puigserver, P.; Spiegelman, B. M. Peroxisome Proliferator-Activated Receptor- γ Coactivator 1 α (PGC-1 α): Transcriptional Coactivator and Metabolic Regulator. *Endocr. Rev.* **2003**, *24* (1), 78–90.
- (50) Tata, J. R. Signalling through Nuclear Receptors. *Nat. Rev. Mol. Cell Biol.* **2002**, *3* (9), 702–710.
- (51) Bhalla, K.; Hwang, B. J.; Dewi, R. E.; Ou, L.; Twaddel, W.; Fang, H. Bin; Vafai, S. B.; Vazquez, F.; Puigserver, P.; Boros, L.; Girmun, G. D. PGC1 α Promotes Tumor Growth by Inducing Gene Expression Programs Supporting Lipogenesis. *Cancer Res.* **2011**, *71* (21), 6888–6898.
- (52) Lebleu, V. S.; O'Connell, J. T.; Gonzalez Herrera, K. N.; Wikman, H.; Pantel, K.; Haigis, M. C.; De Carvalho, F. M.; Damascena, A.

- Domingos Chinen, L. T.; Rocha, R. M.; Asara, J. M.; Kalluri, R. PGC-1 α Mediates Mitochondrial Biogenesis and Oxidative Phosphorylation in Cancer Cells to Promote Metastasis. *Nat. Cell Biol.* **2014**, *16* (10), 992–1003.
- (53) Vellinga, T. T.; De Boer, V. C. J.; Fatrai, S.; Van Schelven, S.; Trumpi, K.; Verheem, A.; Snoeren, N.; Emmink, B. L.; Koster, J.; Rinkes, I. H. M. B.; Kranenburg, O. SIRT1/PGC1 α -Dependent Increase in Oxidative Phosphorylation Supports Chemotherapy Resistance of Colon Cancer. *Clin. Cancer Res.* **2015**, *21* (12), 2870–2879.
- (54) Luo, C.; Lim, J. H.; Lee, Y.; Granter, S. R.; Thomas, A.; Vazquez, F.; Widlund, H. R.; Puigserver, P. A PGC1 α -Mediated Transcriptional Axis Suppresses Melanoma Metastasis. *Nature* **2016**, *537* (7620), 422–426.
- (55) LaGory, E. L.; Wu, C.; Taniguchi, C. M.; Ding, C. K. C.; Chi, J. T.; von Eyben, R.; Scott, D. A.; Richardson, A. D.; Giaccia, A. J. Suppression of PGC-1 α Is Critical for Reprogramming Oxidative Metabolism in Renal Cell Carcinoma. *Cell Rep.* **2015**, *12* (1), 116–127.
- (56) Torrano, V.; Valcarcel-Jimenez, L.; Cortazar, A. R.; Liu, X.; Urosevic, J.; Castillo-Martin, M.; Fernández-Ruiz, S.; Morciano, G.; Caro-Maldonado, A.; Guiu, M.; Zúñiga-García, P.; Graupera, M.; Bellmunt, A.; Pandya, P.; Lorente, M.; Martín-Martín, N.; David Sutherland, J.; Sanchez-Mosquera, P.; Bozal-Basterra, L. et al. The Metabolic Co-Regulator PGC1 α Suppresses Prostate Cancer Metastasis. *Nat. Cell Biol.* **2016**, *18* (6), 645–656.
- (57) Pauli, G. F.; Chen, S. N.; Simmler, C.; Lankin, D. C.; Gödecke, T.; Jaki, B. U.; Friesen, J. B.; McAlpine, J. B.; Napolitano, J. G. Importance of Purity Evaluation and the Potential of Quantitative ^1H NMR as a Purity Assay. *J. Med. Chem.* **2014**, *57* (22), 9220–9231.
- (58) Yin, L.; Hu, Q.; Emmerich, J.; Lo, M. M. C.; Metzger, E.; Ali, A.; Hartmann, R. W. Novel Pyridyl- or Isoquinoliny-Substituted Indolines and Indoles as Potent and Selective Aldosterone Synthase Inhibitors. *J. Med. Chem.* **2014**, *57* (12), 5179–5189.
- (59) Kilu, W.; Merk, D.; Steinhilber, D.; Proschak, E.; Heering, J. Heterodimer Formation with Retinoic Acid Receptor RXR α Modulates Coactivator Recruitment by Peroxisome Proliferator-Activated Receptor PPAR γ . *J. Biol. Chem.* **2021**, *297* (1), 100814.
- (60) Willems, S.; Kilu, W.; Ni, X.; Chaikuad, A.; Knapp, S.; Heering, J.; Merk, D. The Orphan Nuclear Receptor Nurr1 Is Responsive to Non-Steroidal Anti-Inflammatory Drugs. *Commun. Chem.* **2020**, *3*, 85.
- (61) Friesner, R. A.; Banks, J. L.; Murphy, R. B.; Halgren, T. A.; Klicic, J. J.; Mainz, D. T.; Repasky, M. P.; Knoll, E. H.; Shelley, M.; Perry, J. K.; Shaw, D. E.; Francis, P.; Shenkin, P. S. Glide: A New Approach for Rapid, Accurate Docking and Scoring. 1. Method and Assessment of Docking Accuracy. *J. Med. Chem.* **2004**, *47* (7), 1739–1749.
- (62) Shelley, J. C.; Cholleti, A.; Frye, L. L.; Greenwood, J. R.; Timlin, M. R.; Uchimaya, M. Epik: A Software Program for PKa Prediction and Protonation State Generation for Drug-like Molecules. *J. Comput. Aided. Mol. Des.* **2007**, *21* (12), 681–691.
- (63) Borrelli, K. W.; Cossins, B.; Guallar, V. Exploring Hierarchical Refinement Techniques for Induced Fit Docking with Protein and Ligand Flexibility. *J. Comput. Chem.* **2010**, *31* (6), 1224–1235.
- (64) RDKit: Open-Source Cheminformatics; [Http://www.rdkit.org](http://www.rdkit.org). 2017.
- (65) Berthold, M. R.; Cebon, N.; Dill, F.; Gabriel, T. R.; Kötter, T.; Meinel, T.; Ohl, P.; Thiel, K.; Wiswedel, B. KNIME - the Konstanz Information Miner: Version 2.0 and Beyond. *SIGKDD Explor. Newsl* **2006**, *11*, 26–31.

Table of Contents graphic



- Supporting Information -

Tuning RXR Modulators for PGC1 α Recruitment

Felix Nawa^{1,#}, Minh Sai^{1,#}, Jan Vietor^{1,#}, Roman Schwarzenbach¹, Anesa Bitić¹, Sina Wolff¹, Niklas Ildefeld², Jörg Pabel¹, Thomas Wein¹, Julian A. Marschner¹, Jan Heering³, Daniel Merk^{1*}

¹ Ludwig-Maximilians-Universität (LMU) München, Department of Pharmacy, 81377 Munich, Germany

² Goethe University Frankfurt, Institute of Pharmaceutical Chemistry, 60438 Frankfurt, Germany

³ Fraunhofer Institute for Translational Medicine and Pharmacology ITMP, 60596 Frankfurt, Germany

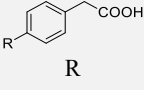
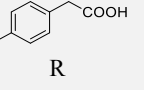
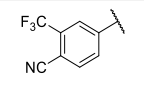
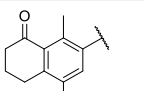
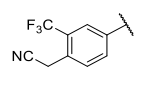
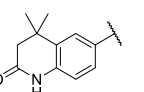
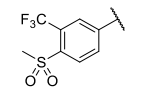
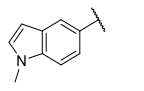
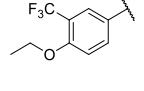
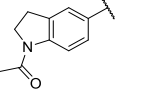
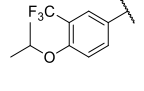
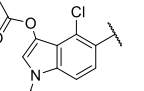
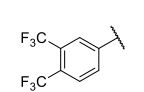
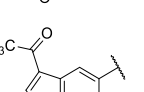
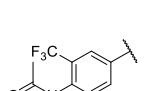
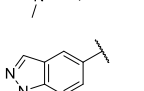
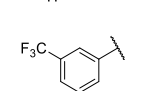
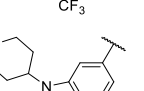
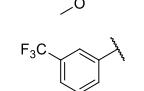
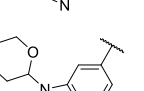
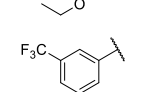
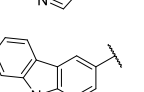
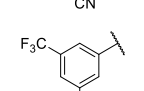
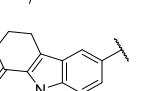
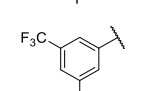
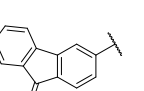
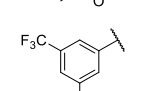
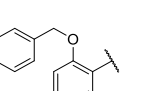
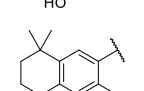
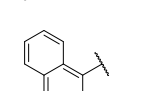
F.N., M.S. and J.V. contributed equally

* daniel.merk@cup.lmu.de

Table of Contents

Table S1	S2
NMR spectra of compounds 4-31	S3
References	S59

Table S1. Potencies and docking scores of analogues **4-31** for RXR α

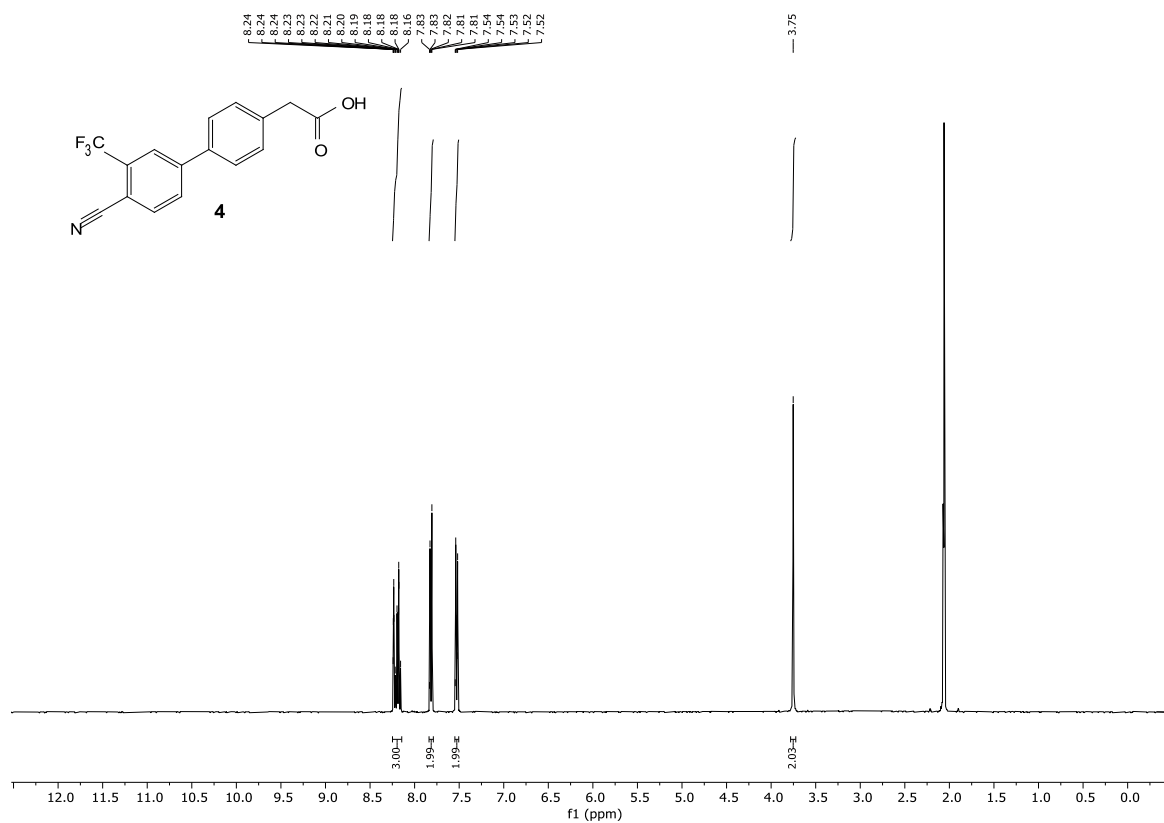
ID		EC ₅₀ (RXR α) ^a	Docking score		ID		EC ₅₀ (RXR α) ^a	Docking score	
			OPLS4 ^c	MM/GBSA ^d Δ G-Bind				OPLS4 ^c	MM/GBSA ^d Δ G-Bind
4		1.6±0.2 μ M	-11.96	-58.37	18		15±1 μ M	-11.81	-69.52
5		2.7±0.3 μ M	-11.91	-62.43	19		inactive (50 μ M ^b)	-11.78	-62.65
6		inactive (15 μ M ^b)	-12.01	-56.16	20		inactive (10 μ M ^b)	-11.02	-50.09
7		4.4±0.5 μ M	-11.89	-61.86	21		inactive (100 μ M ^b)	-11.65	-54.36
8		0.29±0.03 μ M	-12.05	-62.50	22		inactive (50 μ M ^b)	-12.01	-57.19
9		0.060±0.004 μ M	-11.95	-59.05	23		10.1±0.1 μ M	-12.83	-55.67
10		inactive (30 μ M ^b)	-12.05	-57.03	24		8.0±0.3 μ M	-11.78	-56.81
11		0.52±0.05 μ M	-11.66	-58.57	25		inactive (50 μ M ^b)	-11.95	-64.04
12		0.6±0.1 μ M	-11.77	-60.22	26		19±1 μ M	-11.99	-63.28
13		1.4±0.1 μ M	-11.85	-57.65	27		6±1 μ M	-11.78	-62.20
14		2.6±0.3 μ M	-11.73	-54.94	28		inactive (30 μ M ^b)	-12.49	-59.49
15		2.0±0.3 μ M	-12.00	-58.01	29		inactive (100 μ M ^b)	-11.69	-61.82
16		6.8±0.7 μ M	-11.90	-61.08	30		1.0±0.2 μ M	-12.16	-62.40
17		0.53±0.04 μ M	-12.35	-72.42	31		14±2 μ M	-11.93	-64.85

^a RXR α modulation was determined in a Gal4-Nurr1 hybrid reporter gene assay. Data are the mean±S.E.M.; n≥3. ^b Highest non-toxic concentration. Docking scores were calculated from the co-crystal structure with lead **3** (pdb id 6sjm¹) using either ^c OPLS4² or ^d GBSA³.

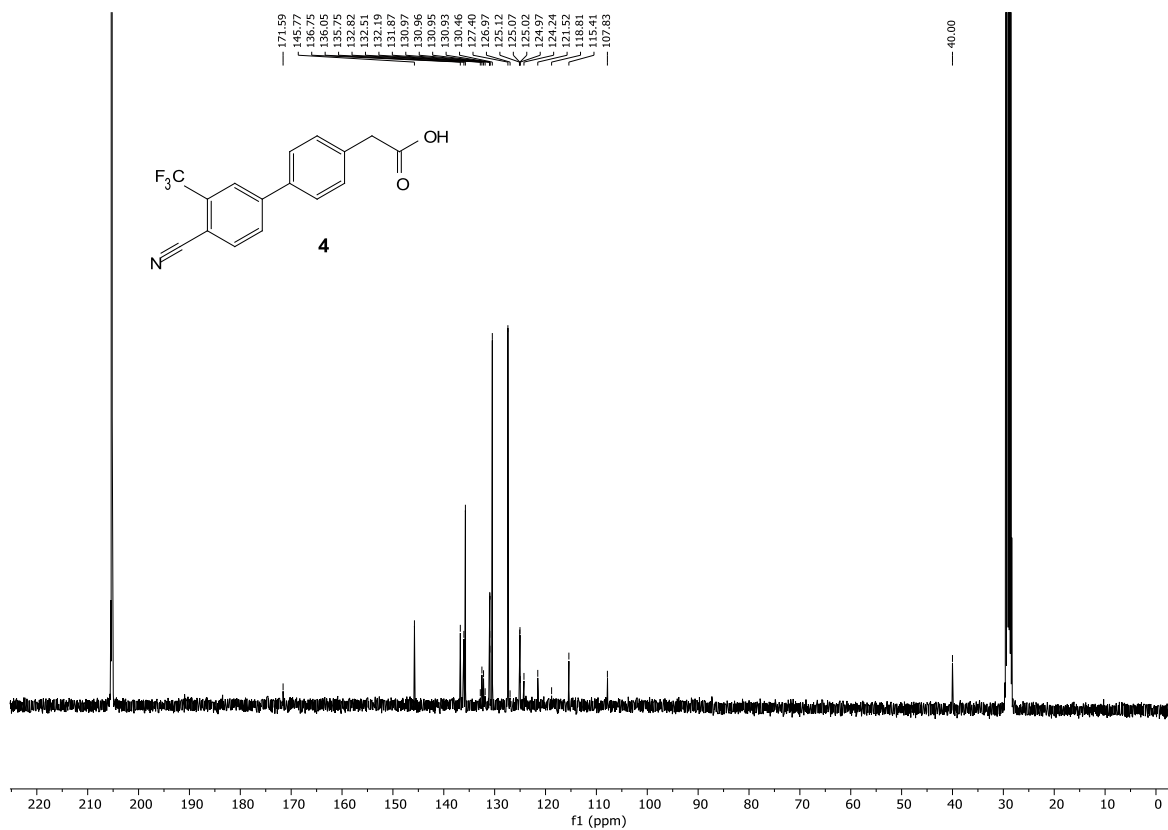
NMR spectra of compounds 4-31

Compound 4:

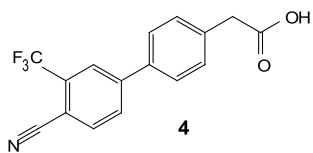
¹H-NMR:



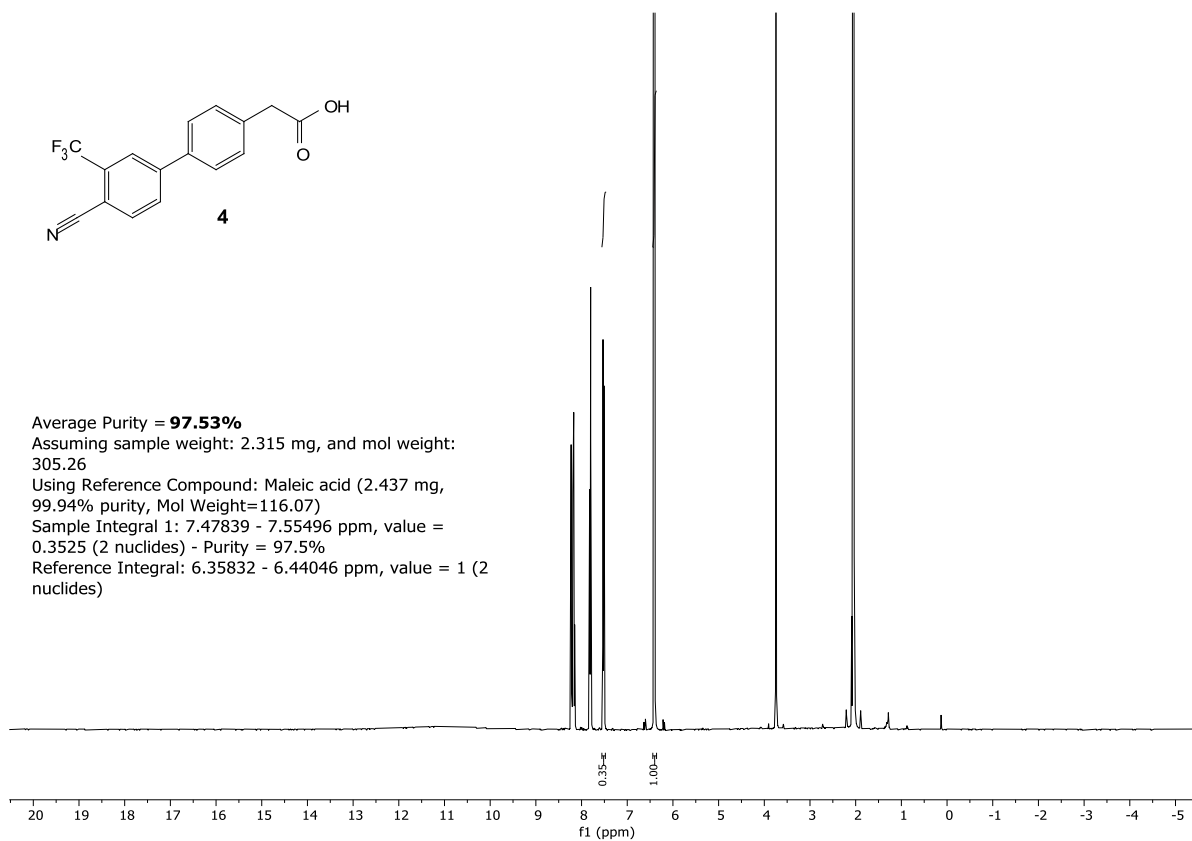
¹³C-NMR:



¹H-NMR:

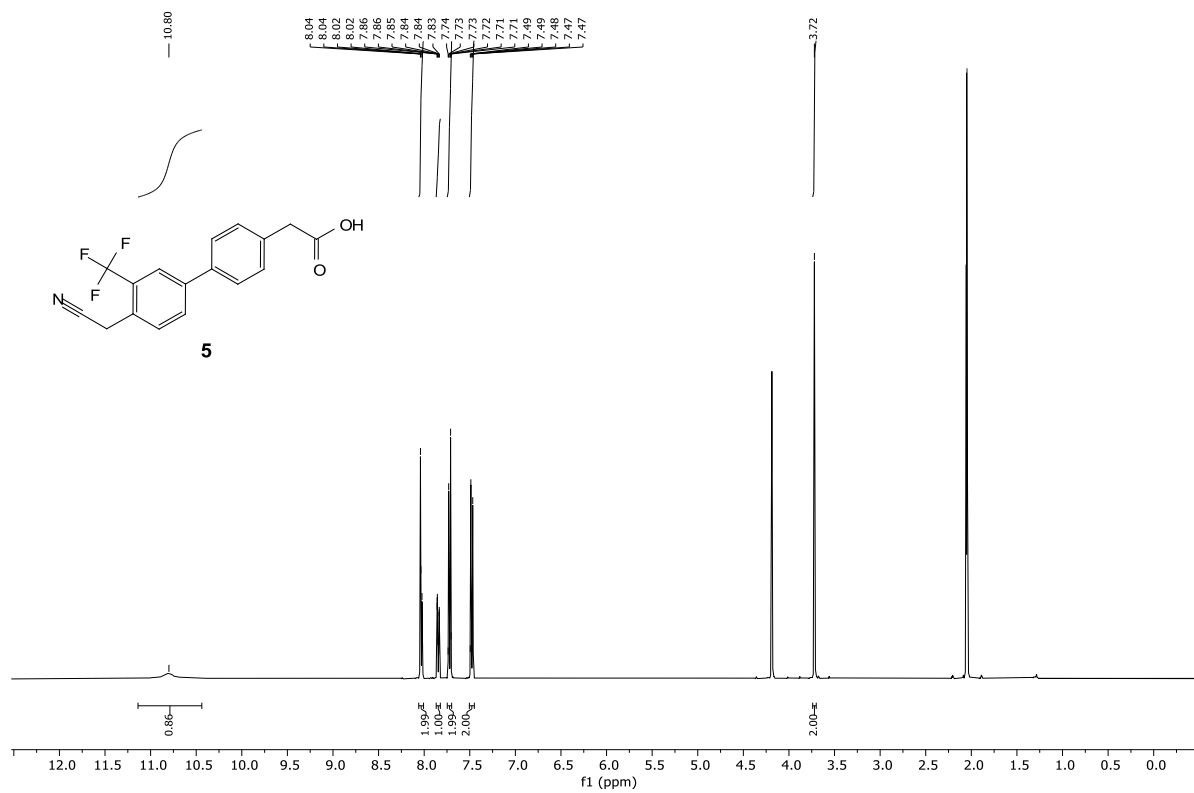


Average Purity = **97.53%**
Assuming sample weight: 2.315 mg, and mol weight:
305.26
Using Reference Compound: Maleic acid (2.437 mg,
99.94% purity, Mol Weight=116.07)
Sample Integral 1: 7.47839 - 7.55496 ppm, value =
0.3525 (2 nuclides) - Purity = 97.5%
Reference Integral: 6.35832 - 6.44046 ppm, value = 1 (2
nuclides)

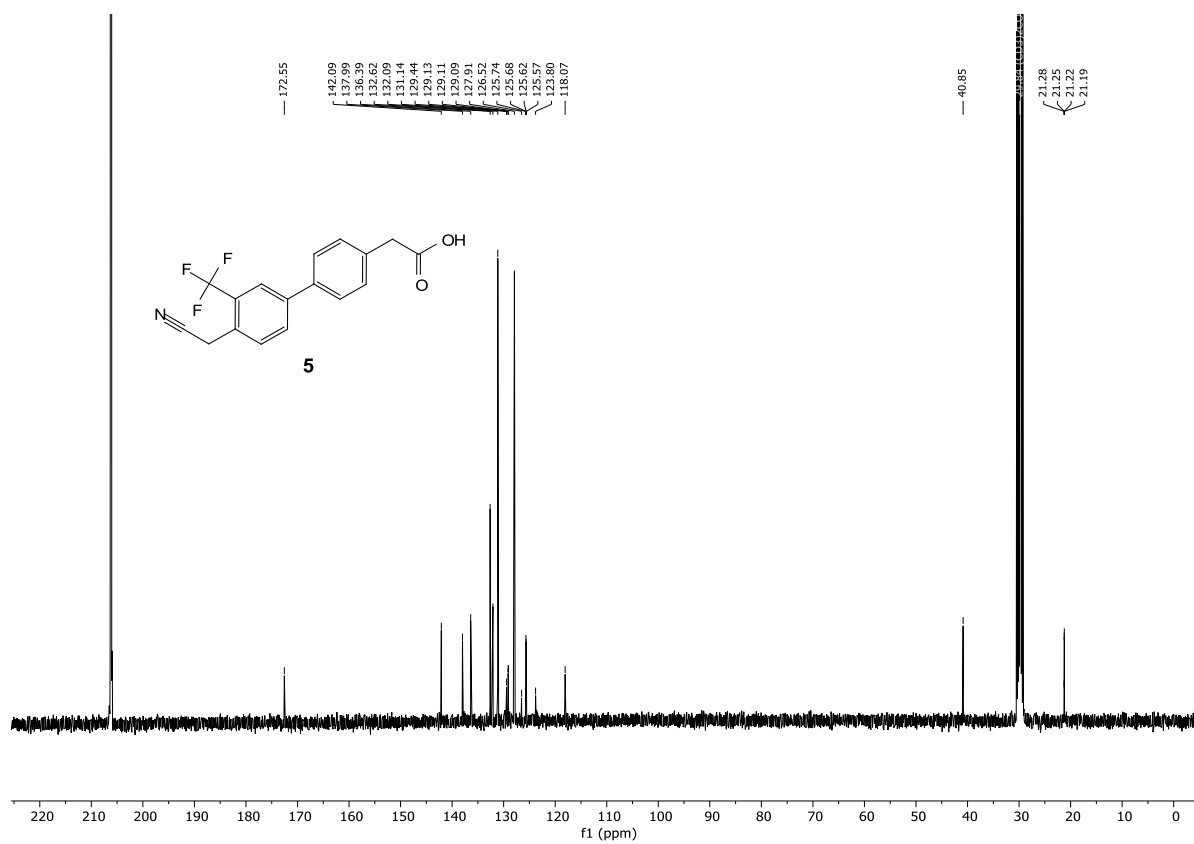


Compound 5:

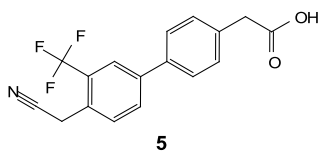
¹H-NMR:



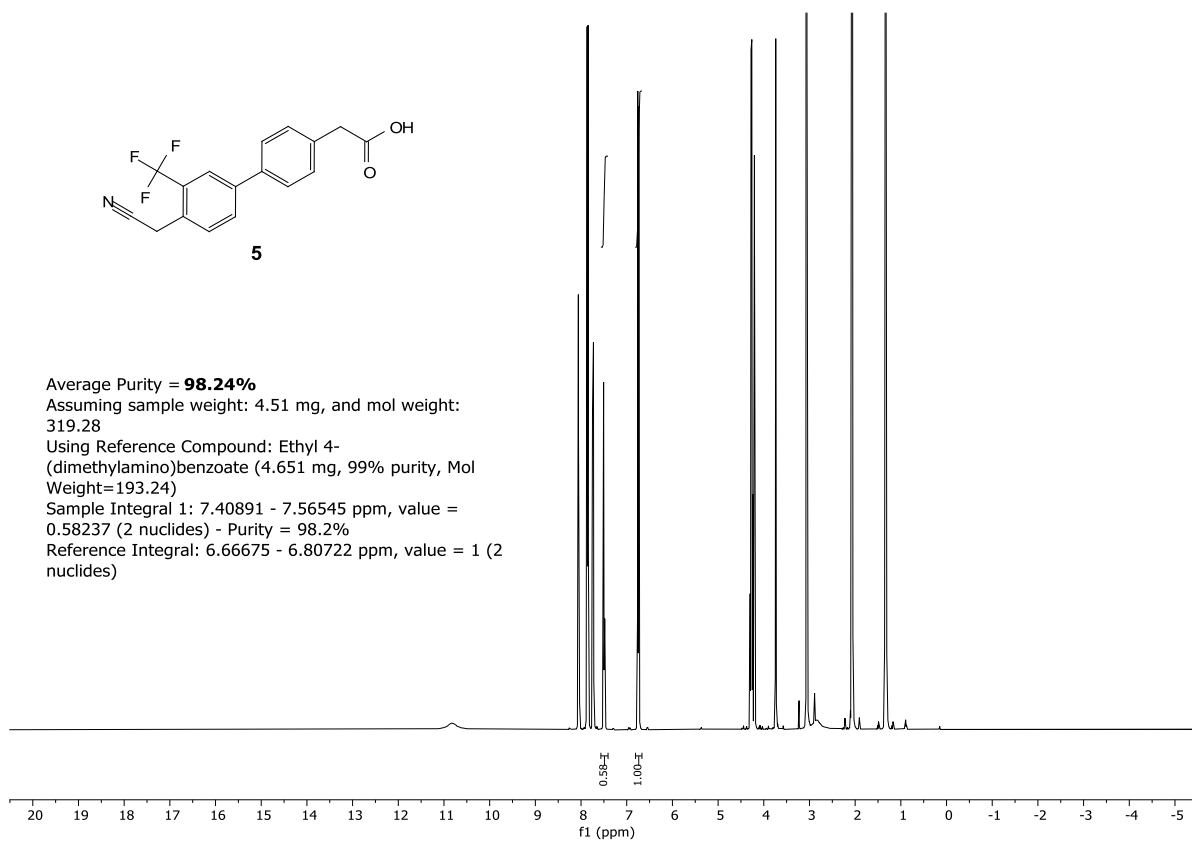
¹³C-NMR:



¹H-qNMR:

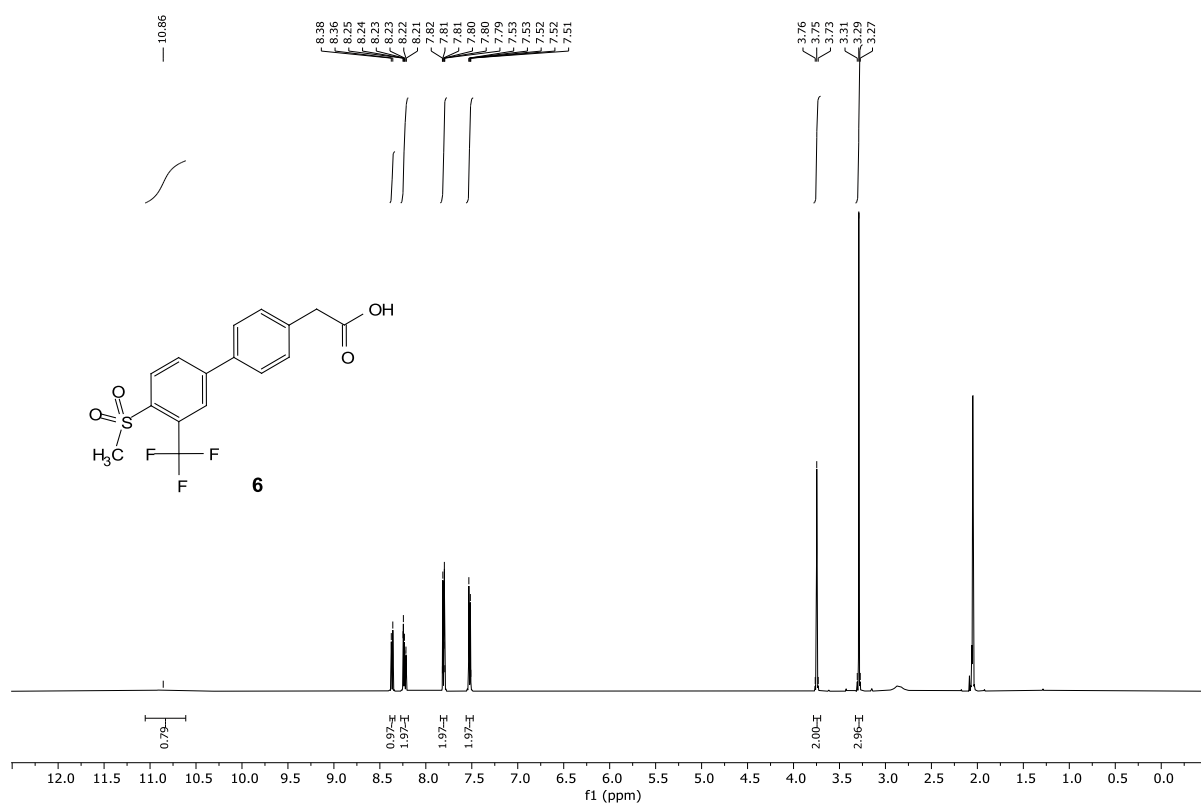


Average Purity = **98.24%**
Assuming sample weight: 4.51 mg, and mol weight:
319.28
Using Reference Compound: Ethyl 4-
(dimethylamino)benzoate (4.651 mg, 99% purity, Mol
Weight=193.24)
Sample Integral 1: 7.40891 - 7.56545 ppm, value =
0.58237 (2 nuclides) - Purity = 98.2%
Reference Integral: 6.66675 - 6.80722 ppm, value = 1 (2
nuclides)

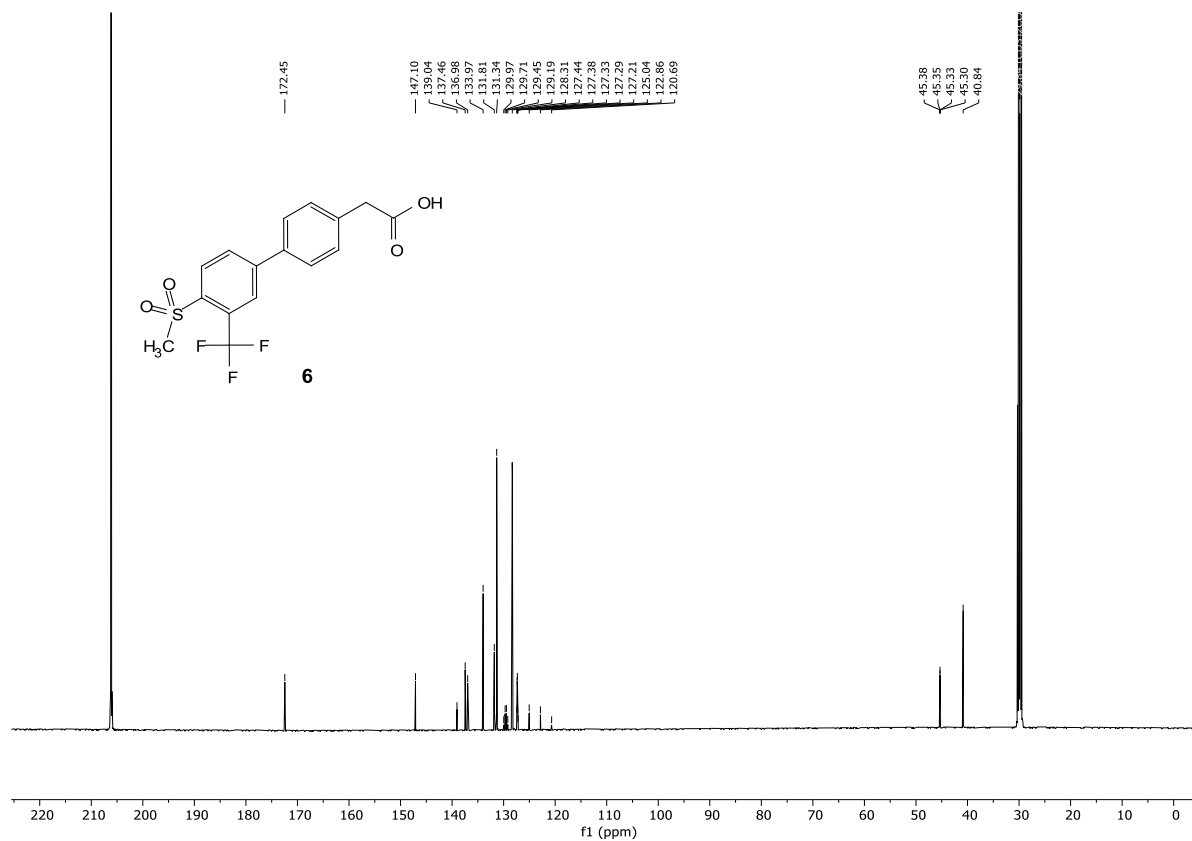


Compound 6:

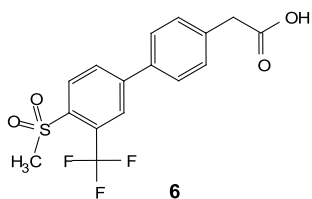
¹H-NMR:



¹³C-NMR:



¹H-qNMR:



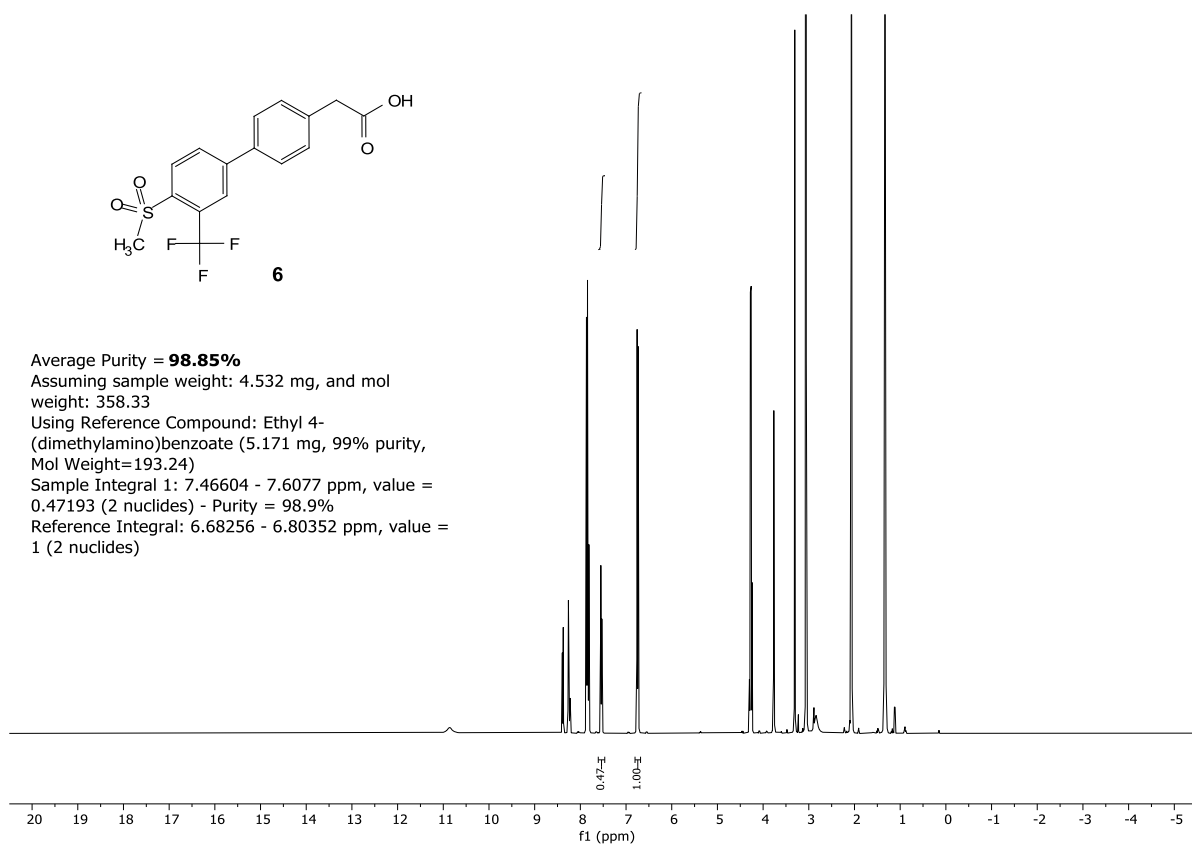
Average Purity = **98.85%**

Assuming sample weight: 4.532 mg, and mol weight: 358.33

Using Reference Compound: Ethyl 4-(dimethylamino)benzoate (5.171 mg, 99% purity, Mol Weight=193.24)

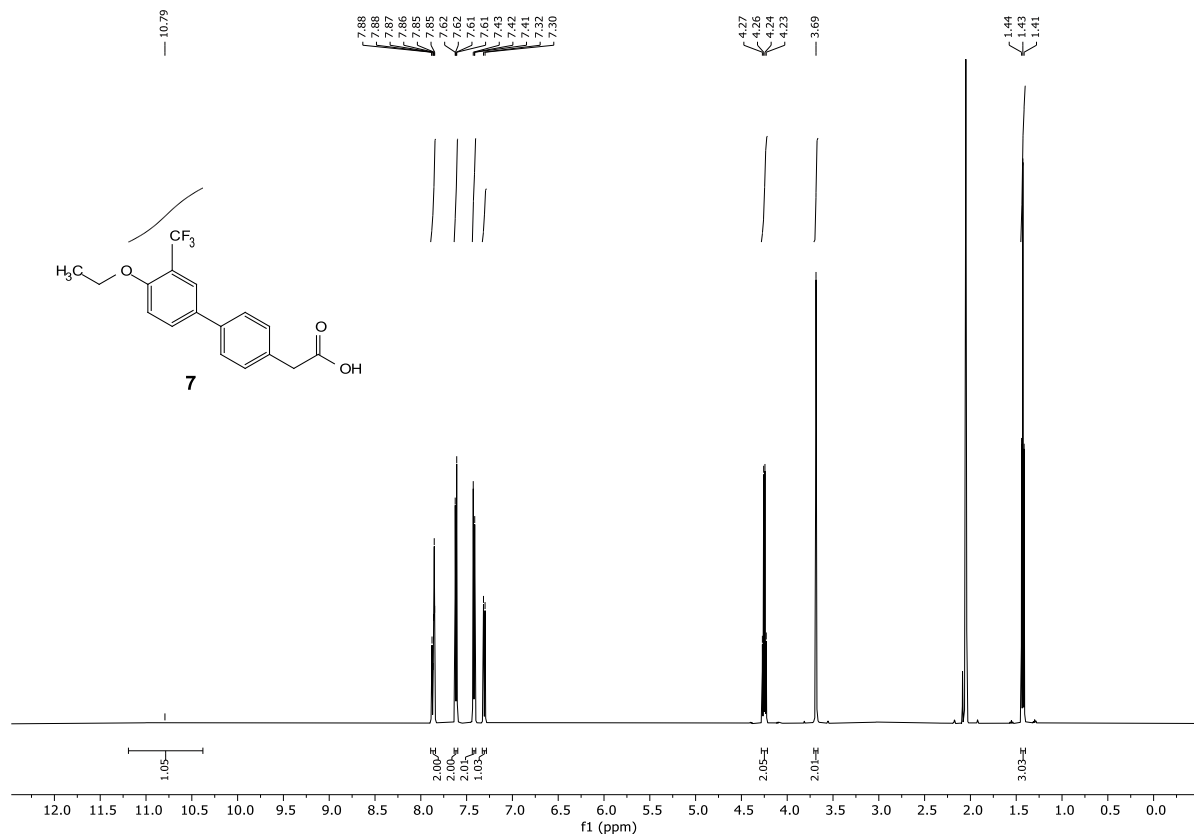
Sample Integral 1: 7.46604 - 7.6077 ppm, value = 0.47193 (2 nuclides) - Purity = 98.9%

Reference Integral: 6.68256 - 6.80352 ppm, value = 1 (2 nuclides)

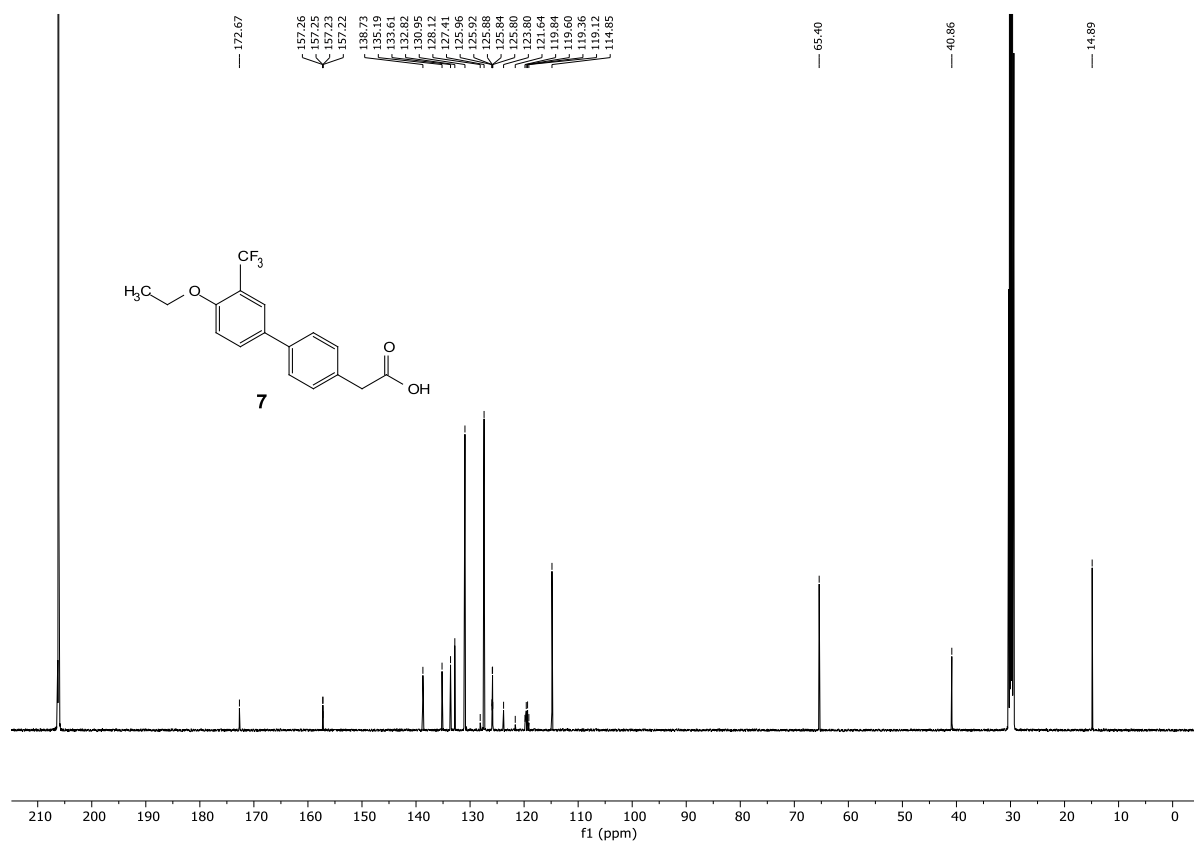


Compound 7:

¹H-NMR:

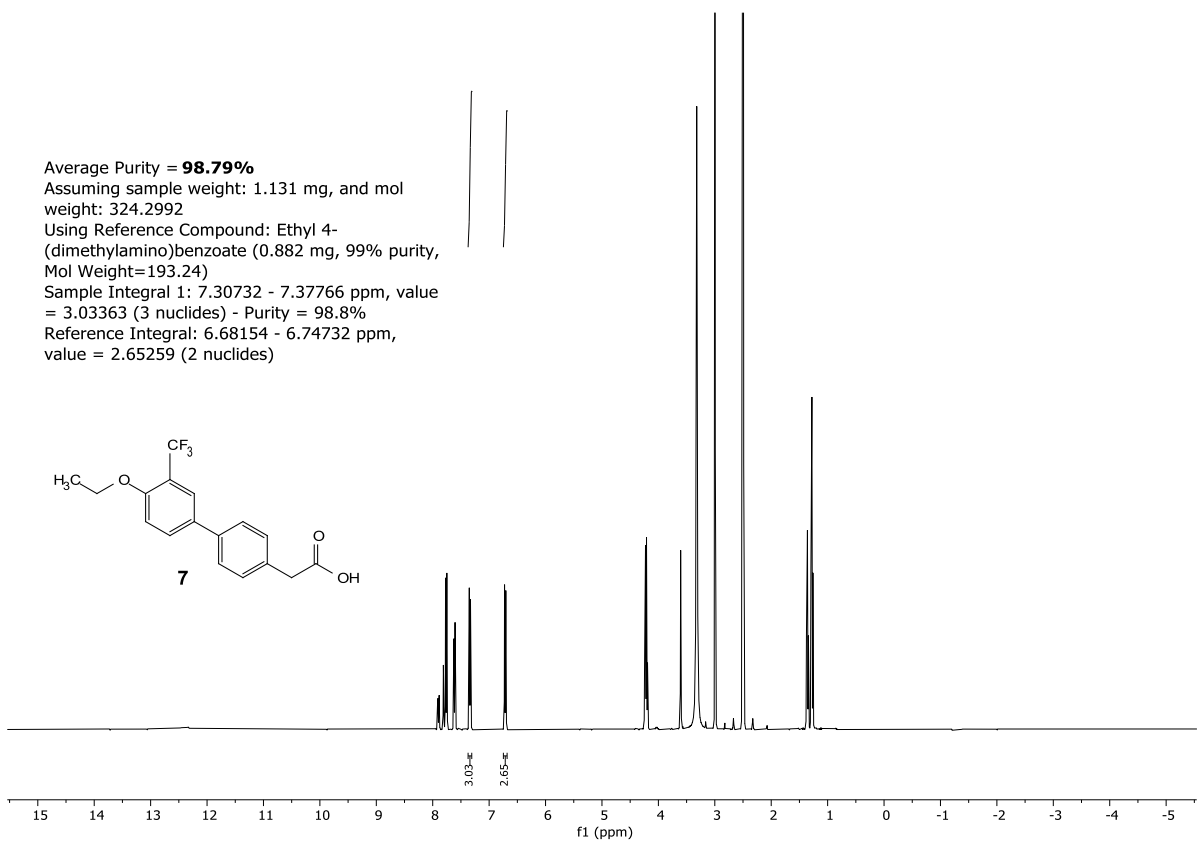


¹³C-NMR:



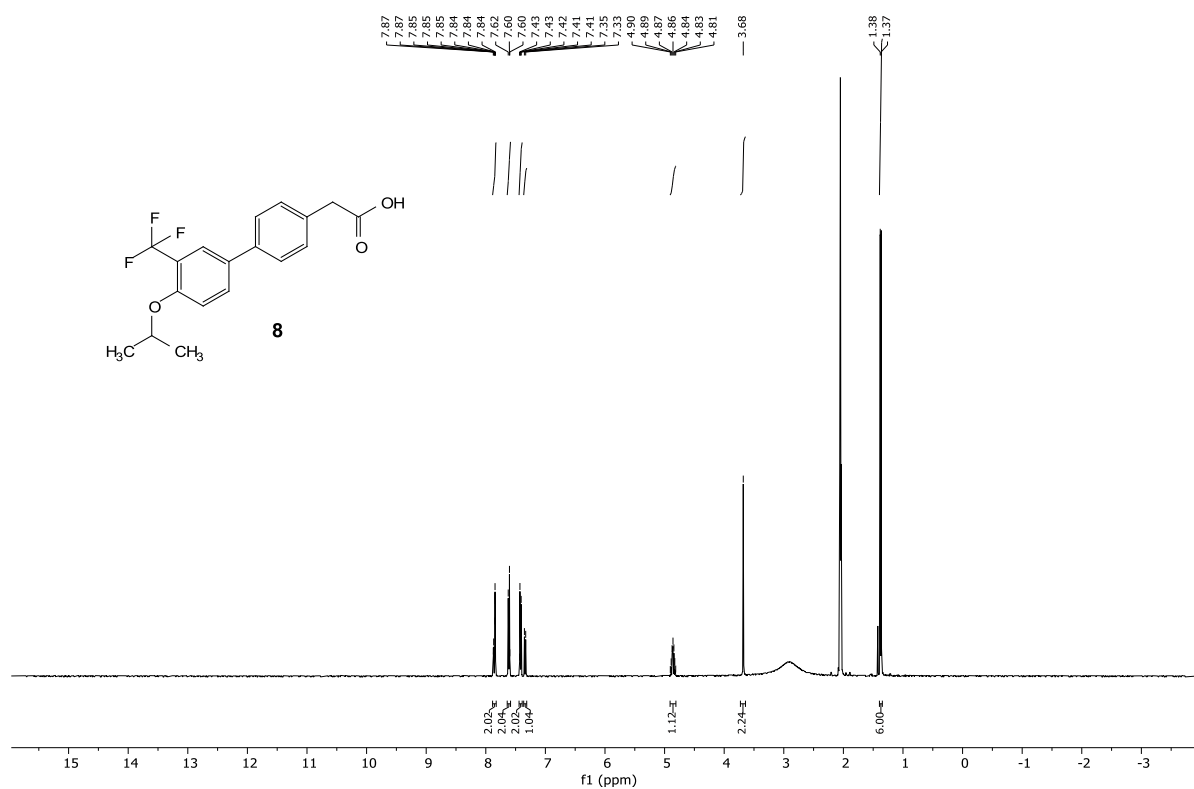
¹H-qNMR:

Average Purity = **98.79%**
Assuming sample weight: 1.131 mg, and mol weight: 324.2992
Using Reference Compound: Ethyl 4-(dimethylamino)benzoate (0.882 mg, 99% purity, Mol Weight=193.24)
Sample Integral 1: 7.30732 - 7.37766 ppm, value = 3.03363 (3 nuclides) - Purity = 98.8%
Reference Integral: 6.68154 - 6.74732 ppm, value = 2.65259 (2 nuclides)

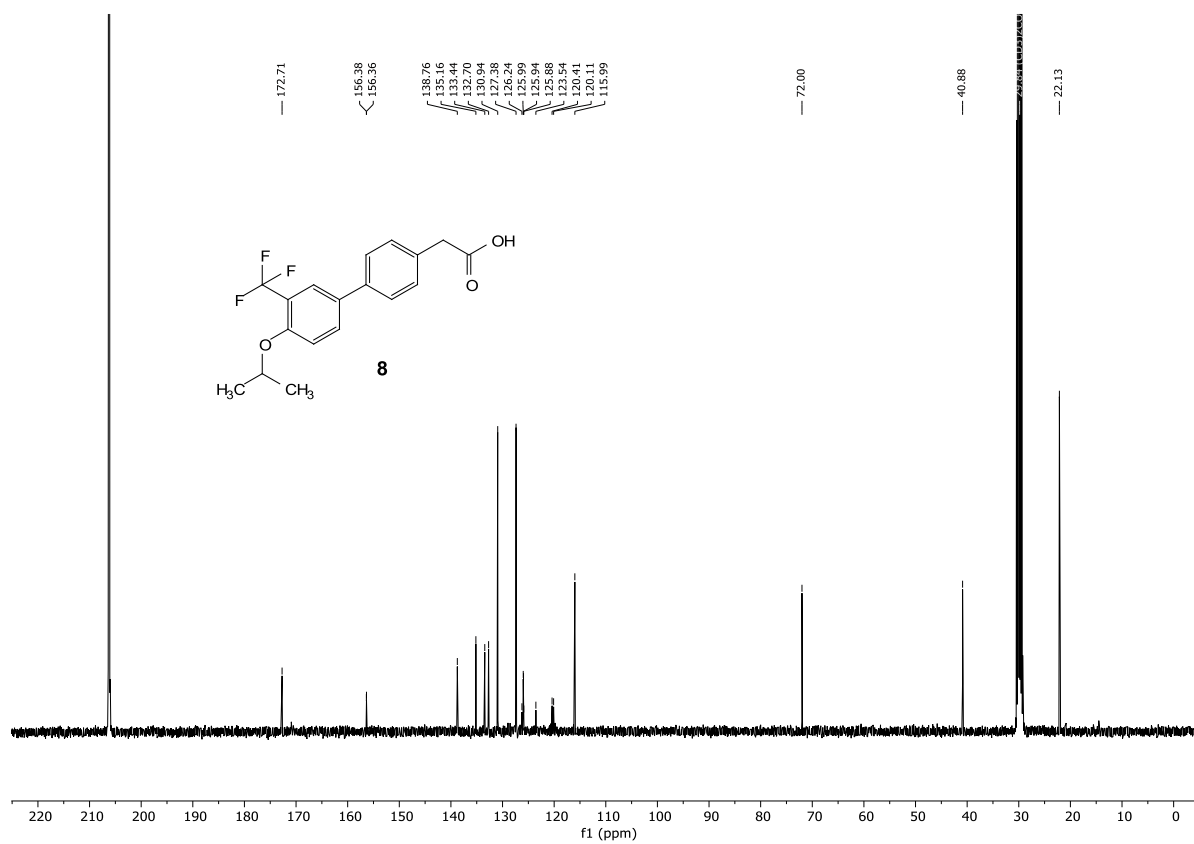


Compound 8:

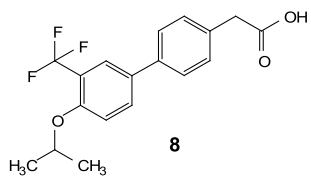
¹H-NMR:



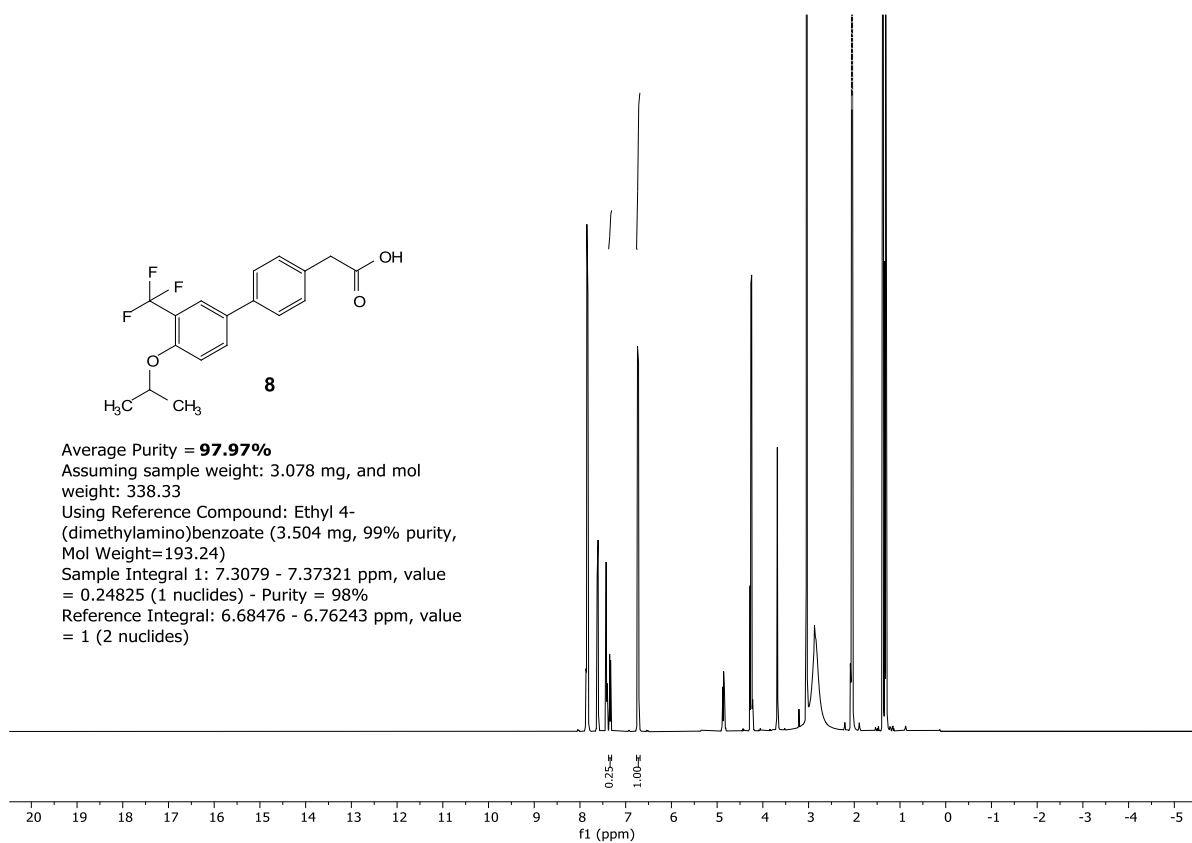
¹³C-NMR:



¹H-NMR:

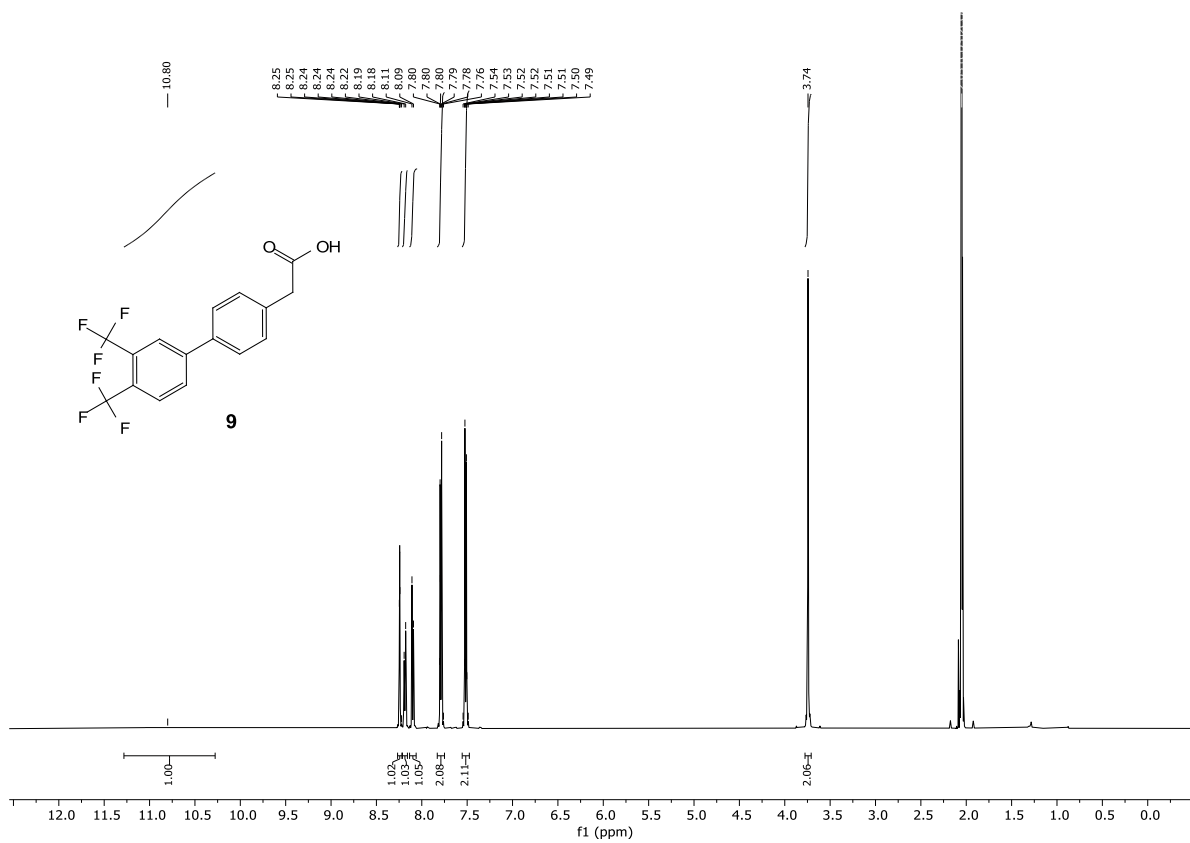


Average Purity = **97.97%**
Assuming sample weight: 3.078 mg, and mol weight: 338.33
Using Reference Compound: Ethyl 4-(dimethylamino)benzoate (3.504 mg, 99% purity, Mol Weight=193.24)
Sample Integral 1: 7.3079 - 7.37321 ppm, value = 0.24825 (1 nuclides) - Purity = 98%
Reference Integral: 6.68476 - 6.76243 ppm, value = 1 (2 nuclides)

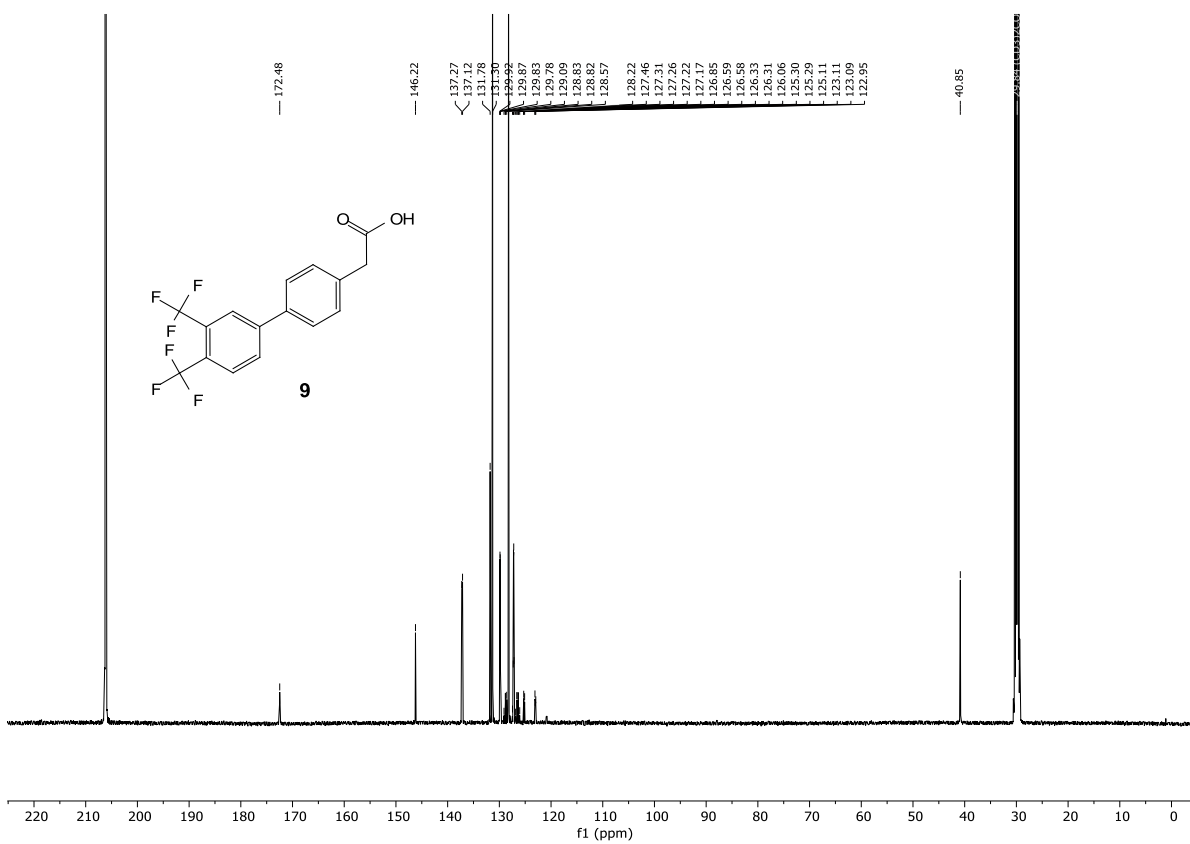


Compound 9:

¹H-NMR:

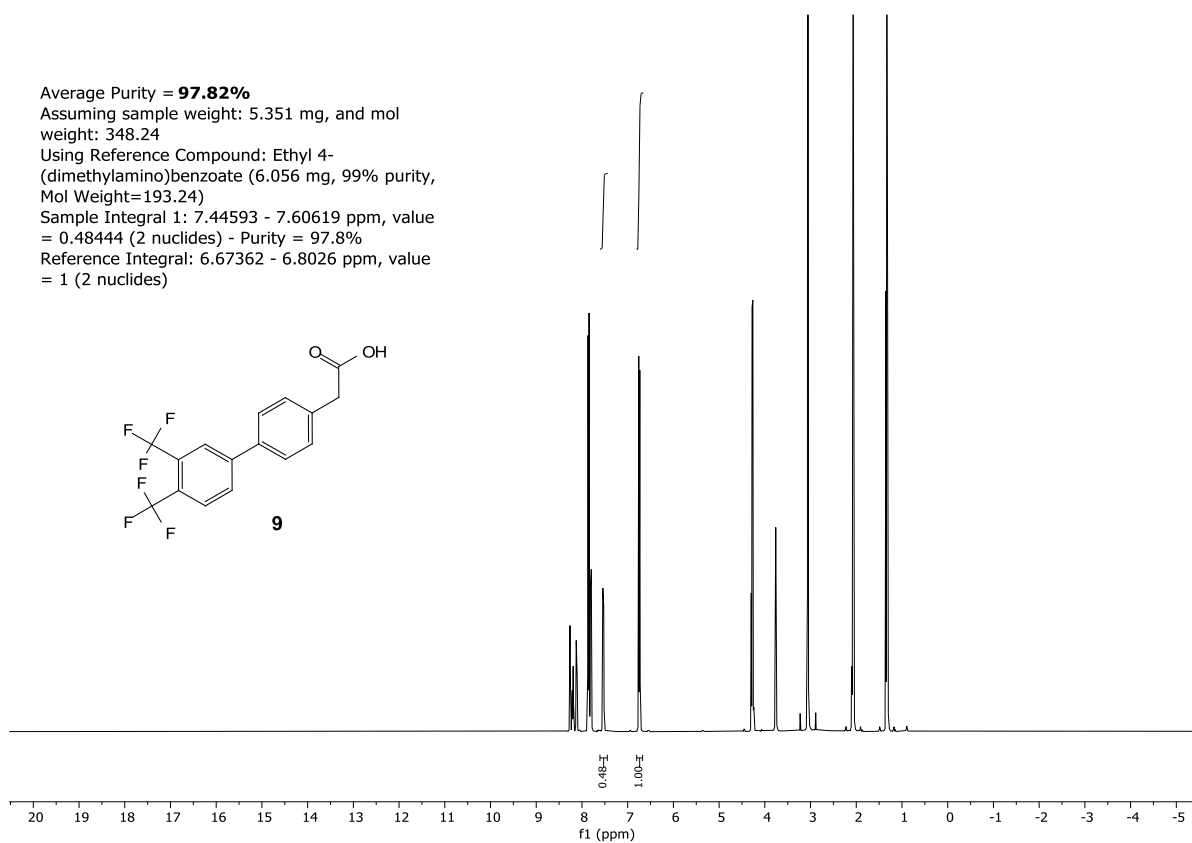
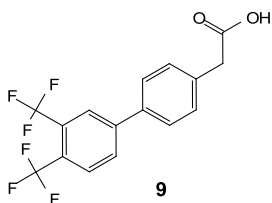


¹³C-NMR:



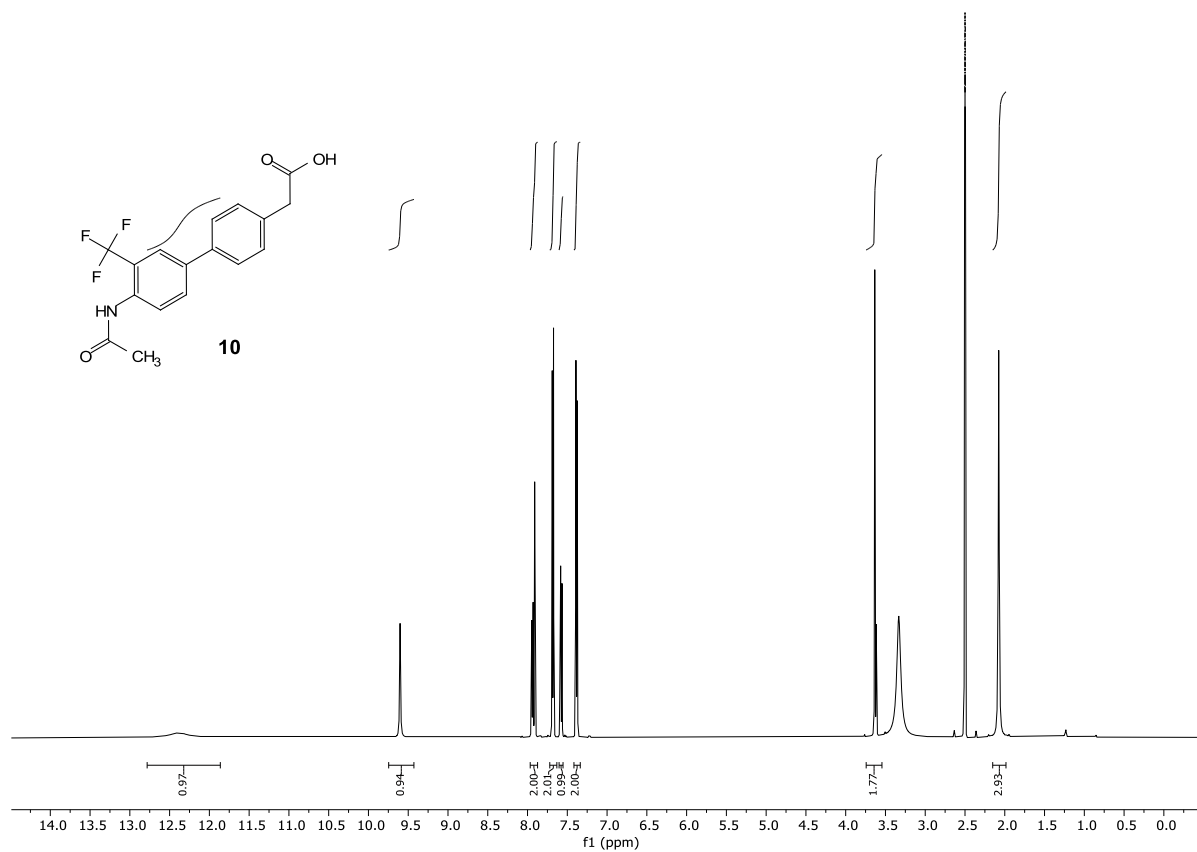
¹H-NMR:

Average Purity = **97.82%**
Assuming sample weight: 5.351 mg, and mol weight: 348.24
Using Reference Compound: Ethyl 4-(dimethylamino)benzoate (6.056 mg, 99% purity, Mol Weight=193.24)
Sample Integral 1: 7.44593 - 7.60619 ppm, value = 0.48444 (2 nuclides) - Purity = 97.8%
Reference Integral: 6.67362 - 6.8026 ppm, value = 1 (2 nuclides)

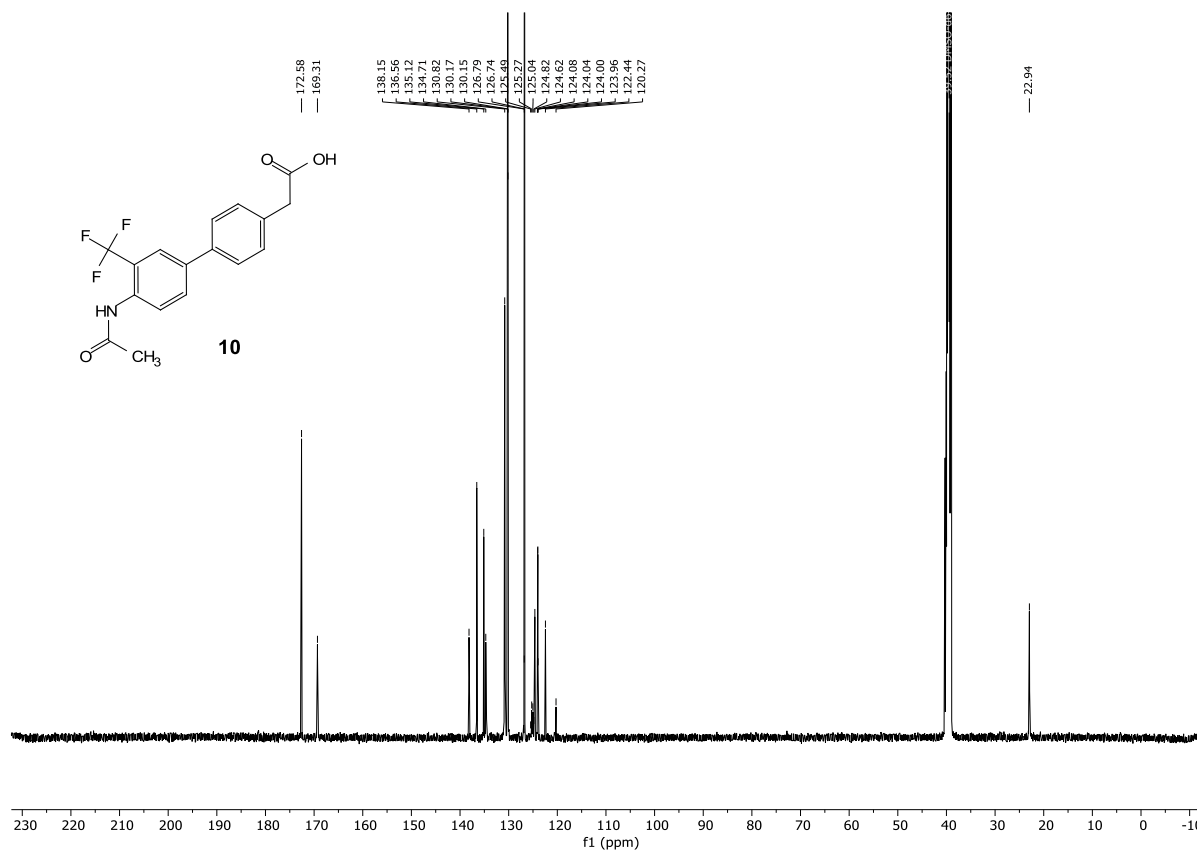


Compound **10**:

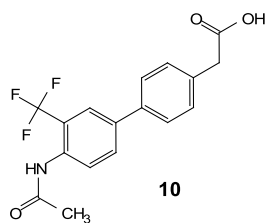
$^1\text{H-NMR}$:



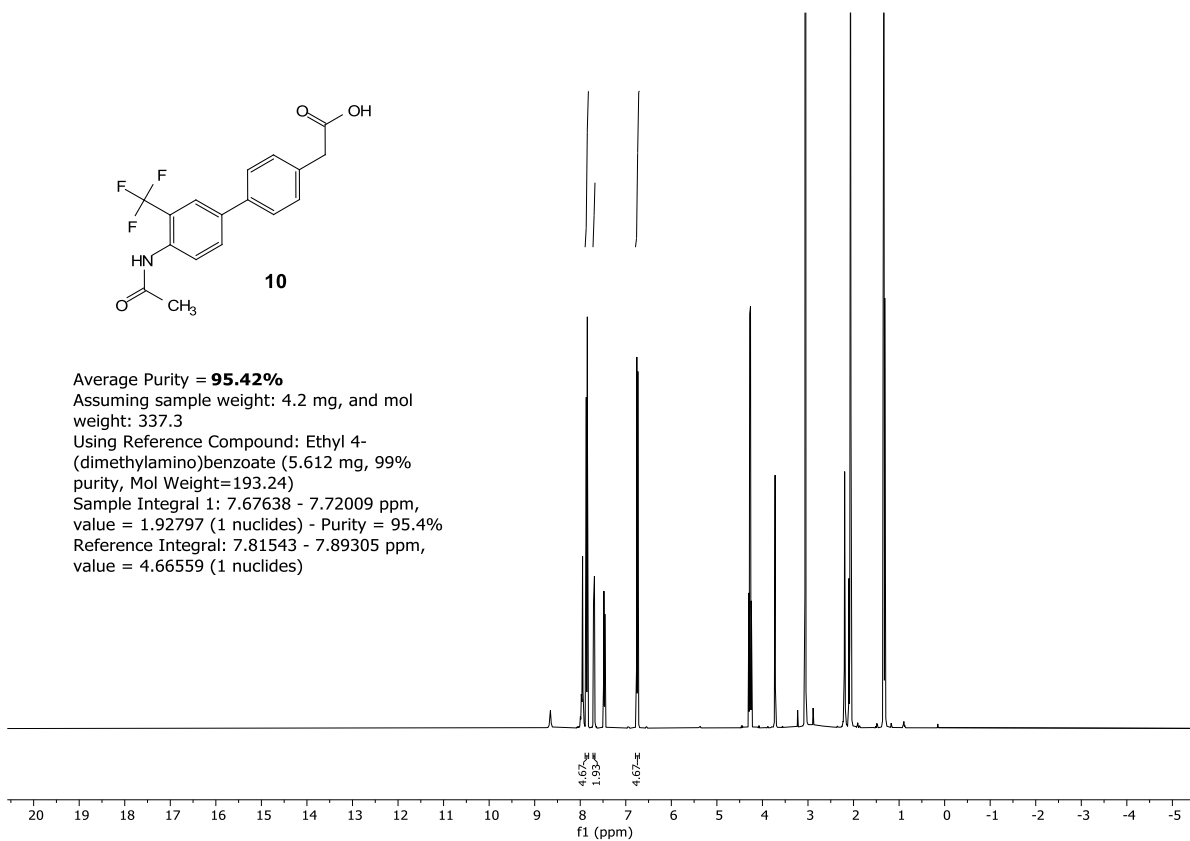
$^{13}\text{C-NMR}$:



¹H-qNMR:

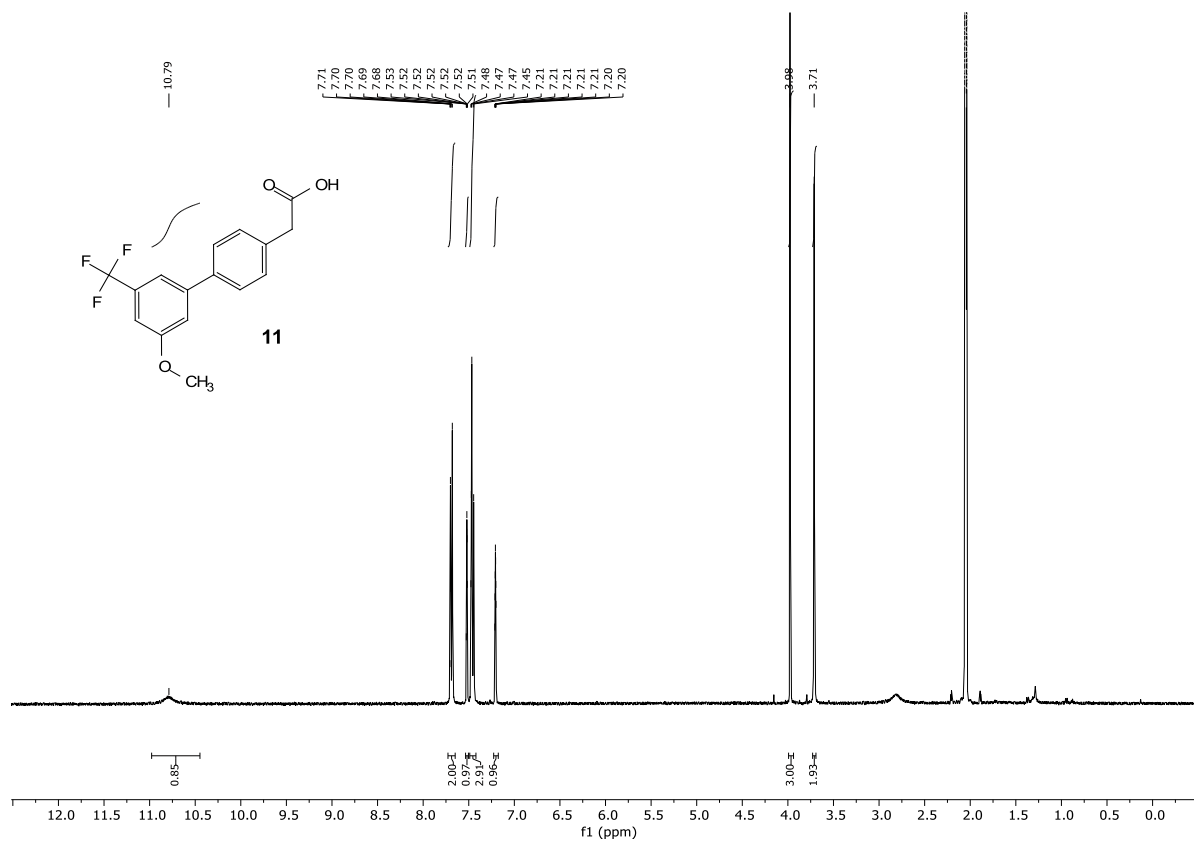


Average Purity = **95.42%**
Assuming sample weight: 4.2 mg, and mol weight: 337.3
Using Reference Compound: Ethyl 4-(dimethylamino)benzoate (5.612 mg, 99% purity, Mol Weight=193.24)
Sample Integral 1: 7.67638 - 7.72009 ppm, value = 1.92797 (1 nuclides) - Purity = 95.4%
Reference Integral: 7.81543 - 7.89305 ppm, value = 4.66559 (1 nuclides)

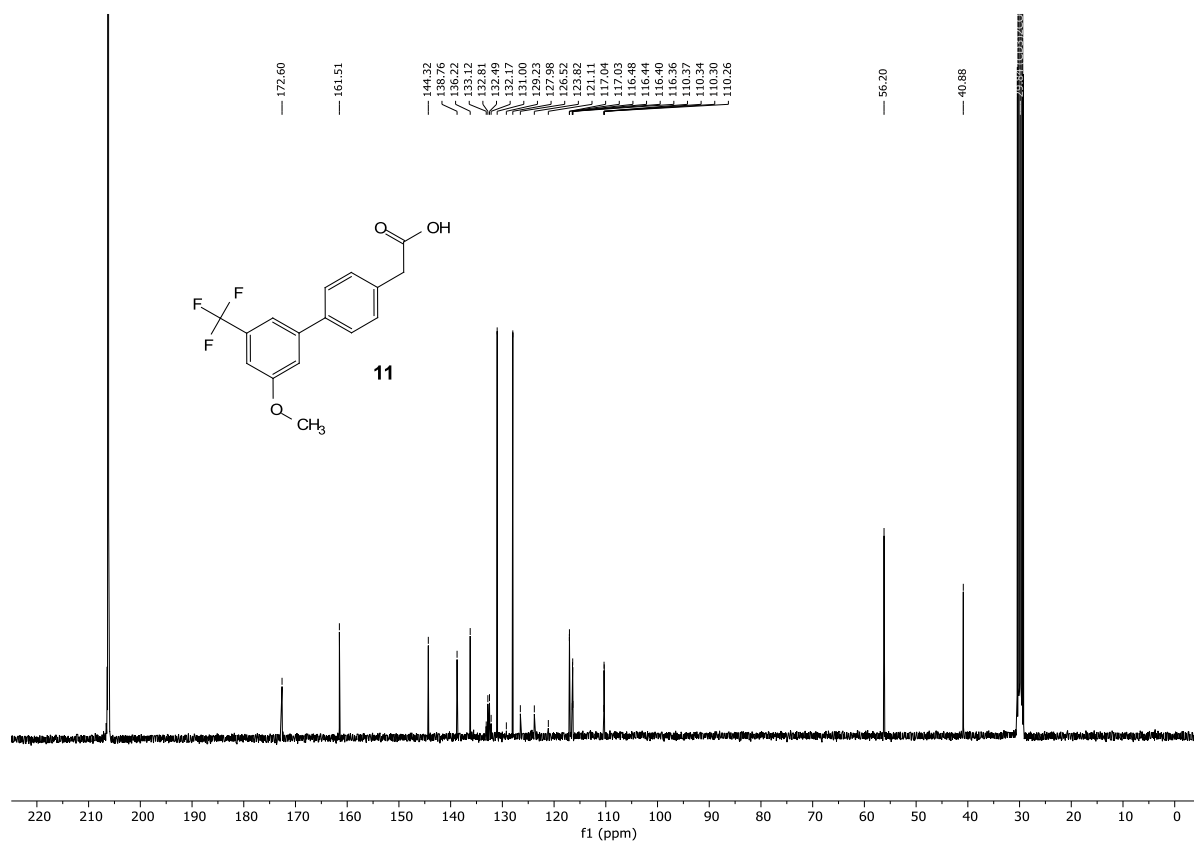


Compound 11:

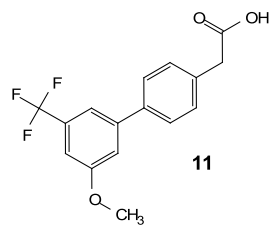
¹H-NMR:



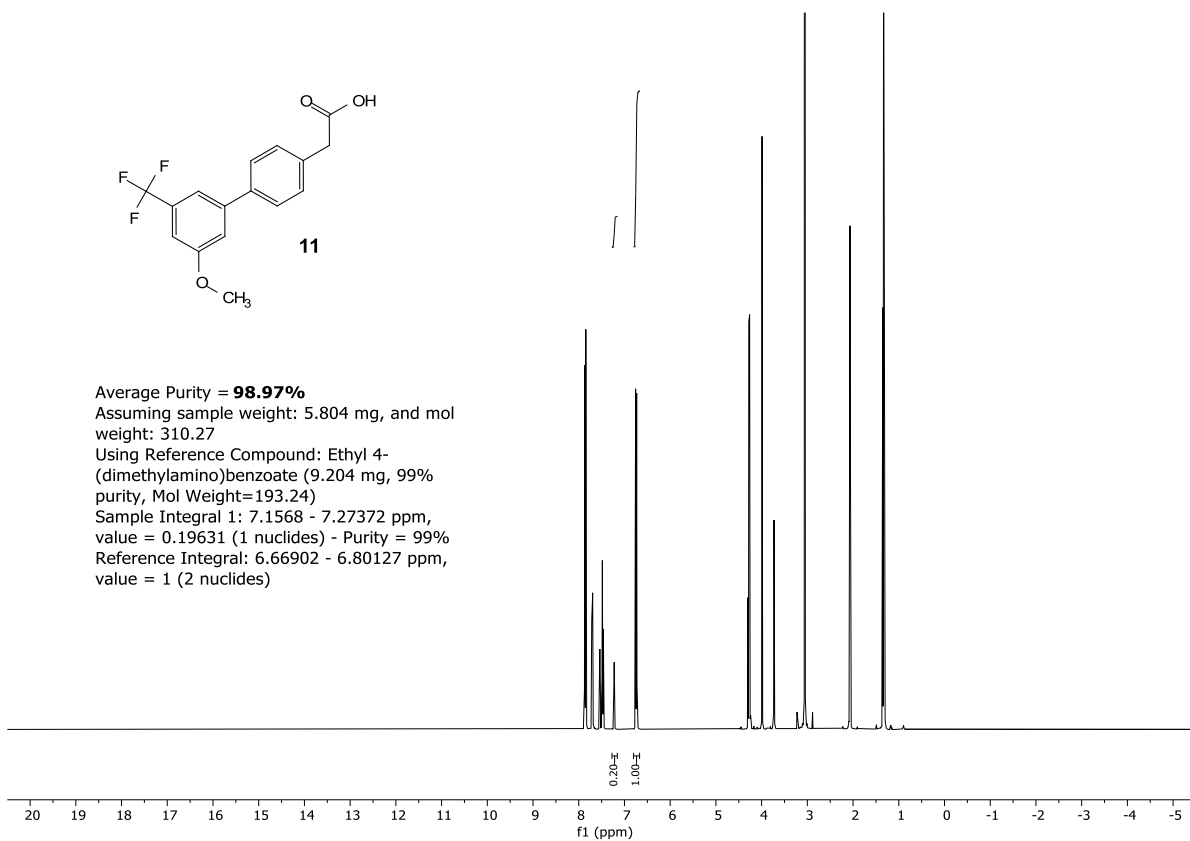
¹³C-NMR:



¹H-NMR:

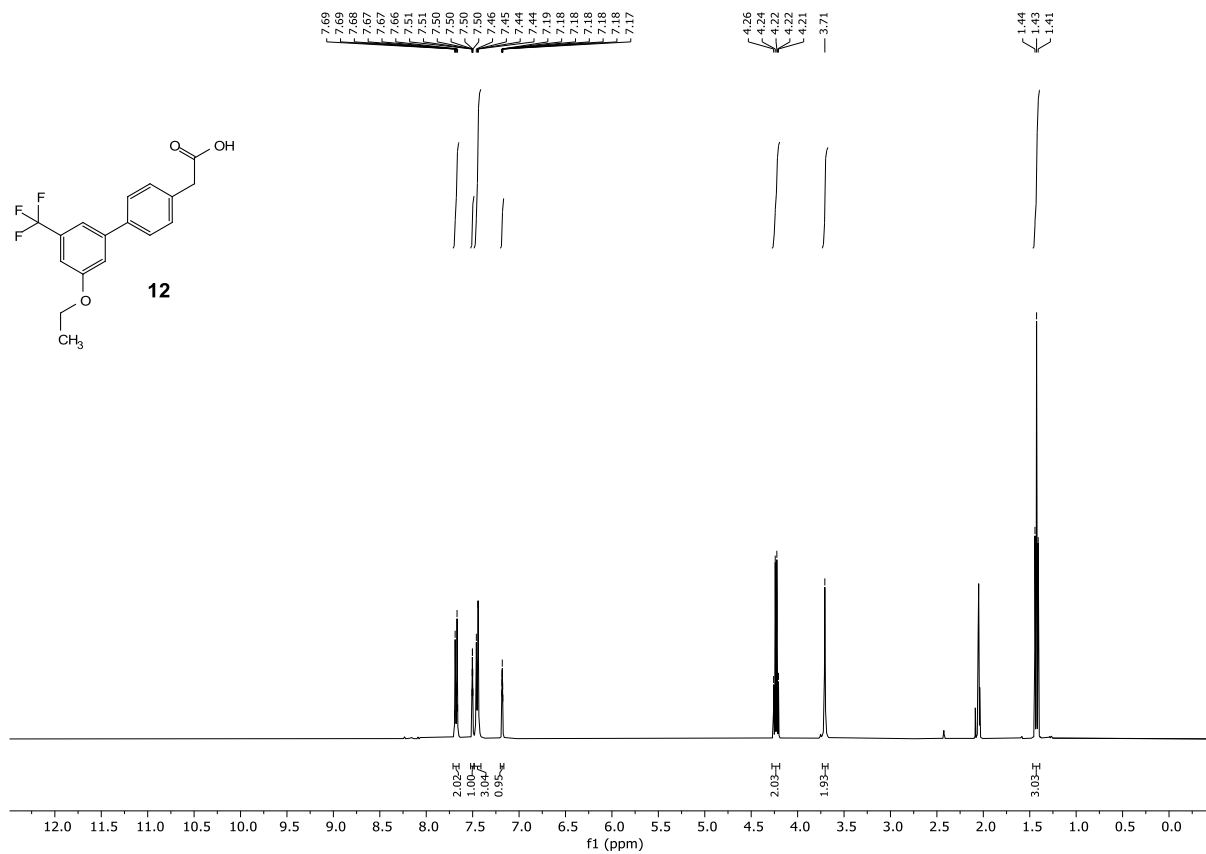


Average Purity = **98.97%**
Assuming sample weight: 5.804 mg, and mol weight: 310.27
Using Reference Compound: Ethyl 4-(dimethylamino)benzoate (9.204 mg, 99% purity, Mol Weight=193.24)
Sample Integral 1: 7.1568 - 7.27372 ppm, value = 0.19631 (1 nuclides) - Purity = 99%
Reference Integral: 6.66902 - 6.80127 ppm, value = 1 (2 nuclides)

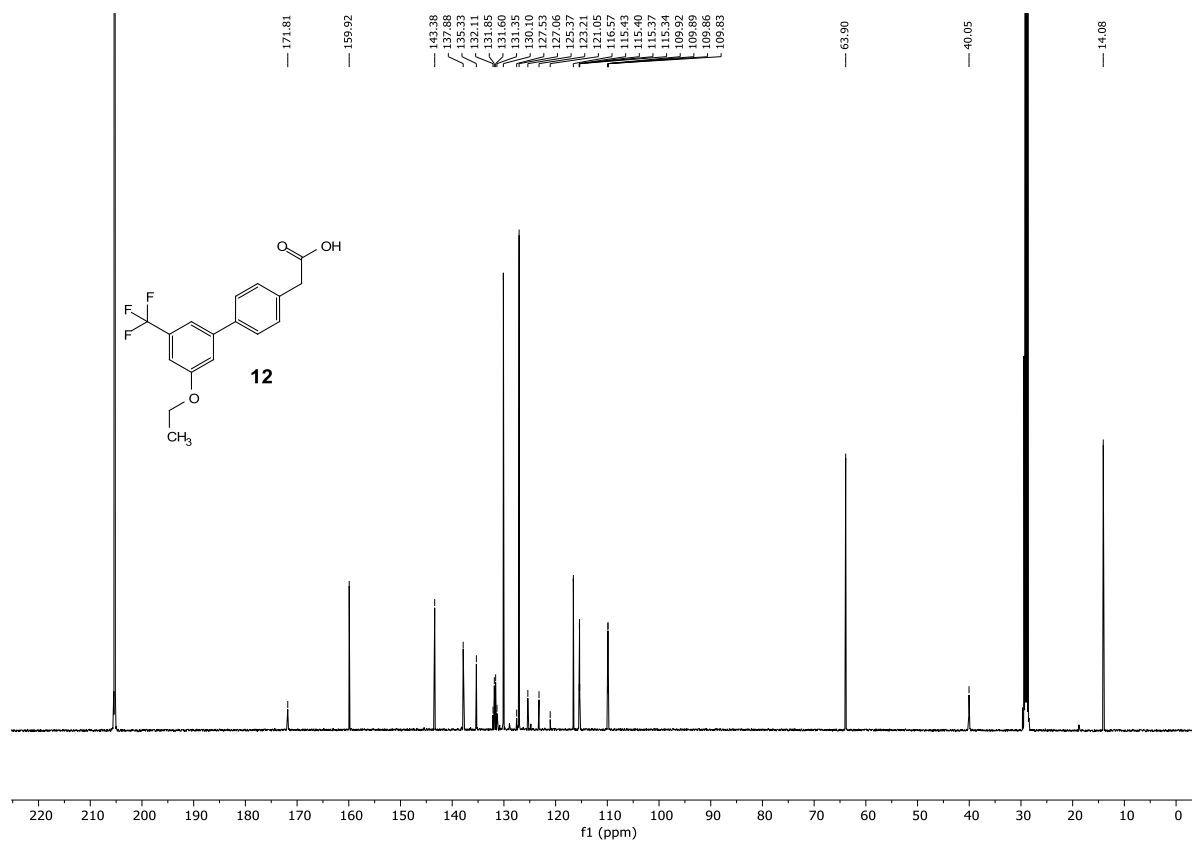


Compound 12:

¹H-NMR:

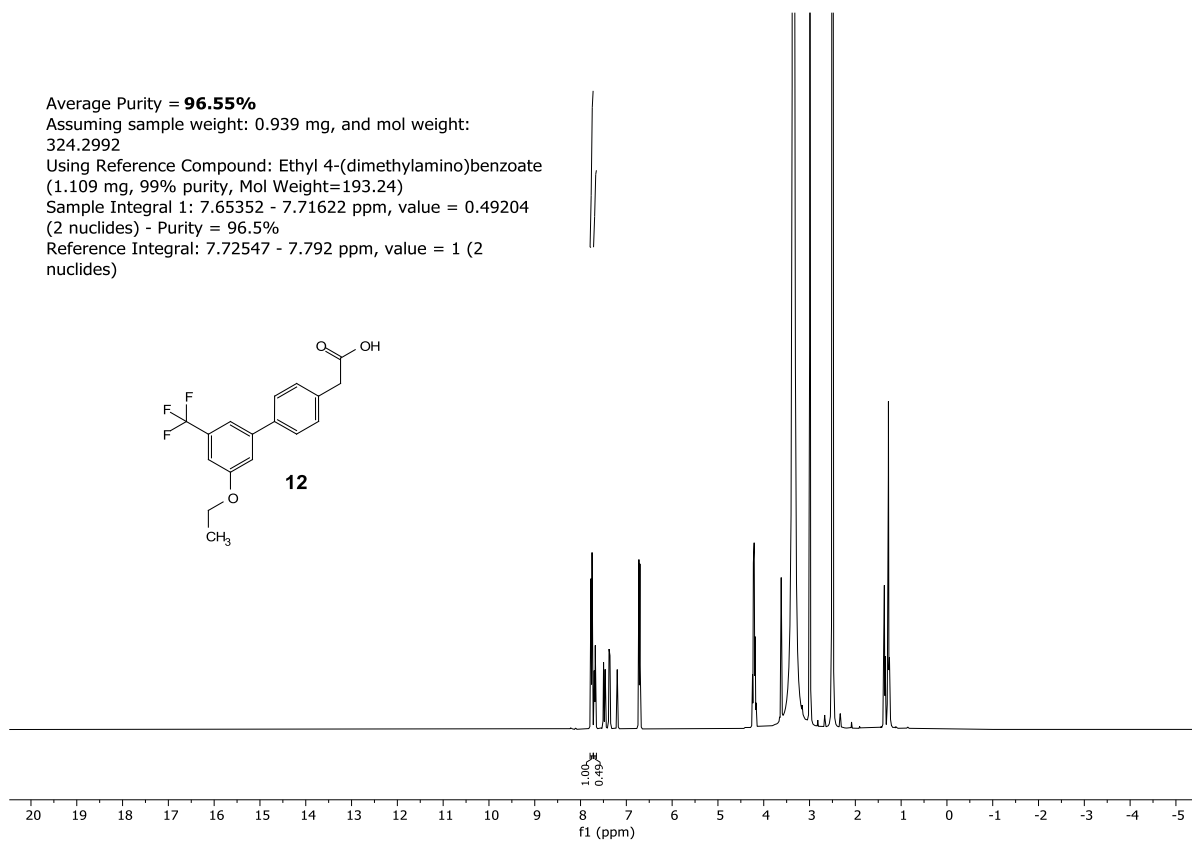
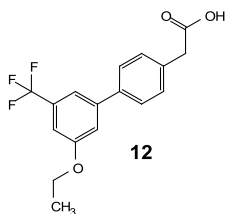


¹³C-NMR:



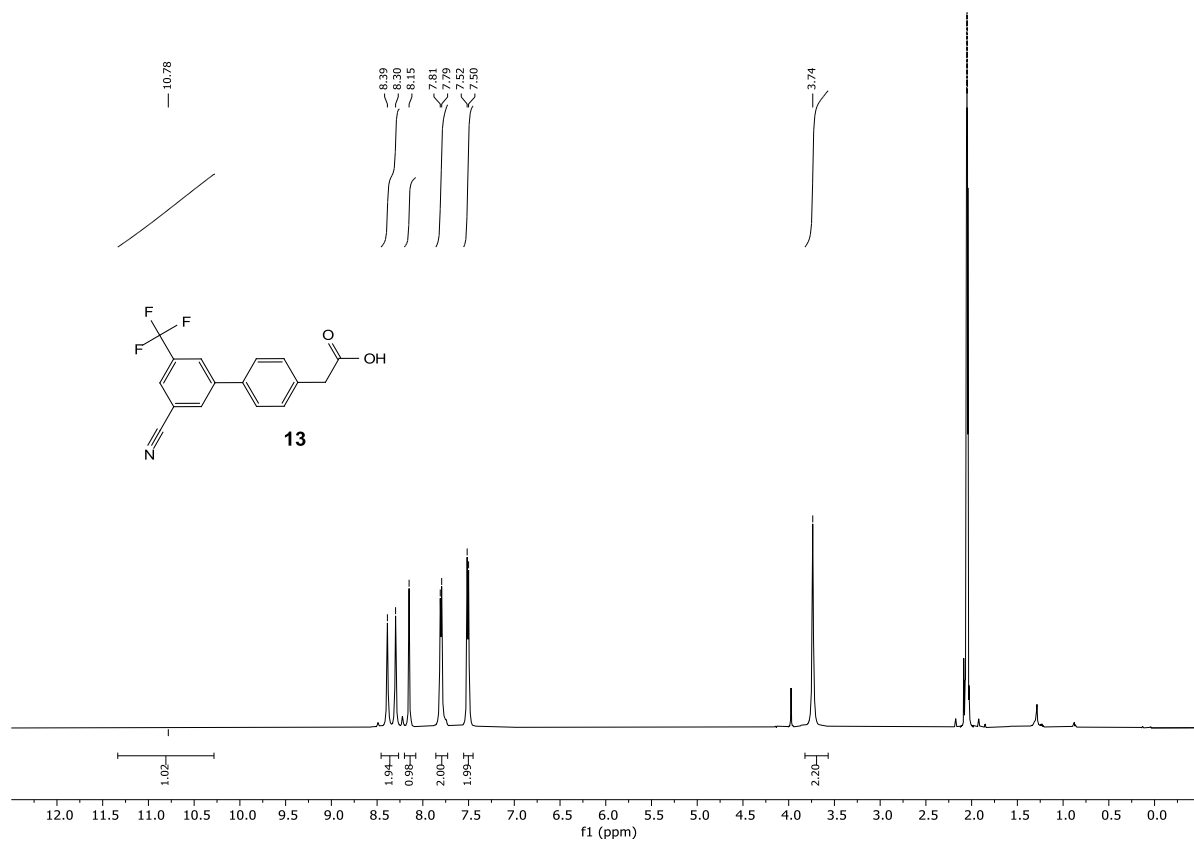
¹H-qNMR:

Average Purity = **96.55%**
Assuming sample weight: 0.939 mg, and mol weight:
324.2992
Using Reference Compound: Ethyl 4-(dimethylamino)benzoate
(1.109 mg, 99% purity, Mol Weight=193.24)
Sample Integral 1: 7.65352 - 7.71622 ppm, value = 0.49204
(2 nuclides) - Purity = 96.5%
Reference Integral: 7.72547 - 7.792 ppm, value = 1 (2
nuclides)

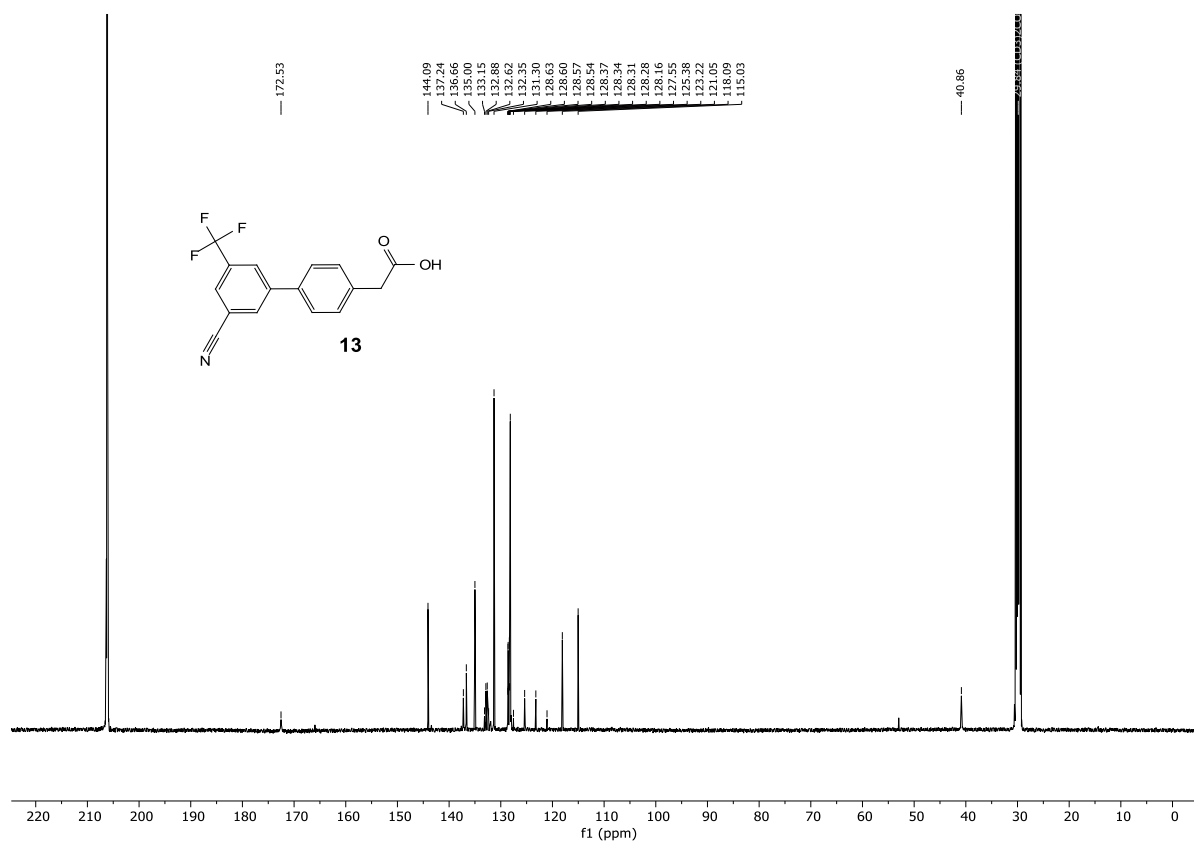


Compound 13:

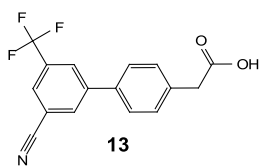
¹H-NMR:



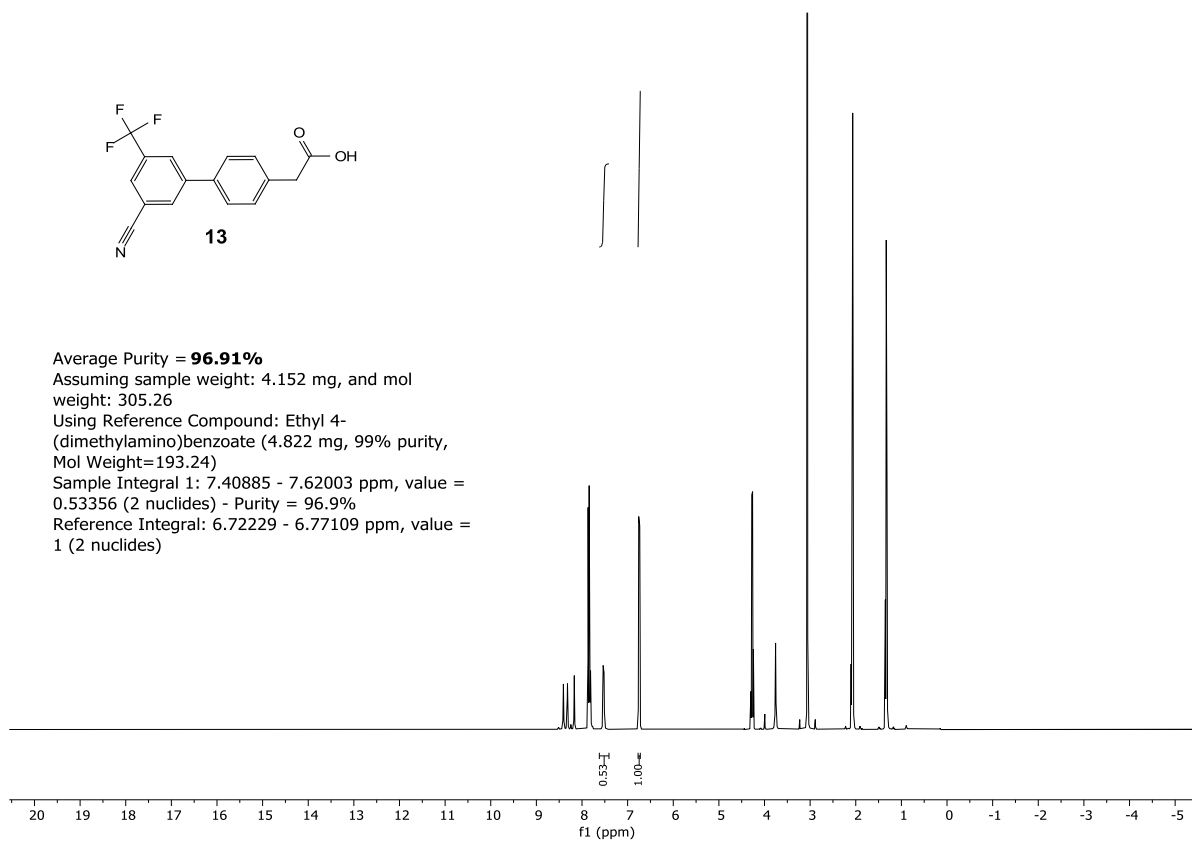
¹³C-NMR:



¹H-qNMR:

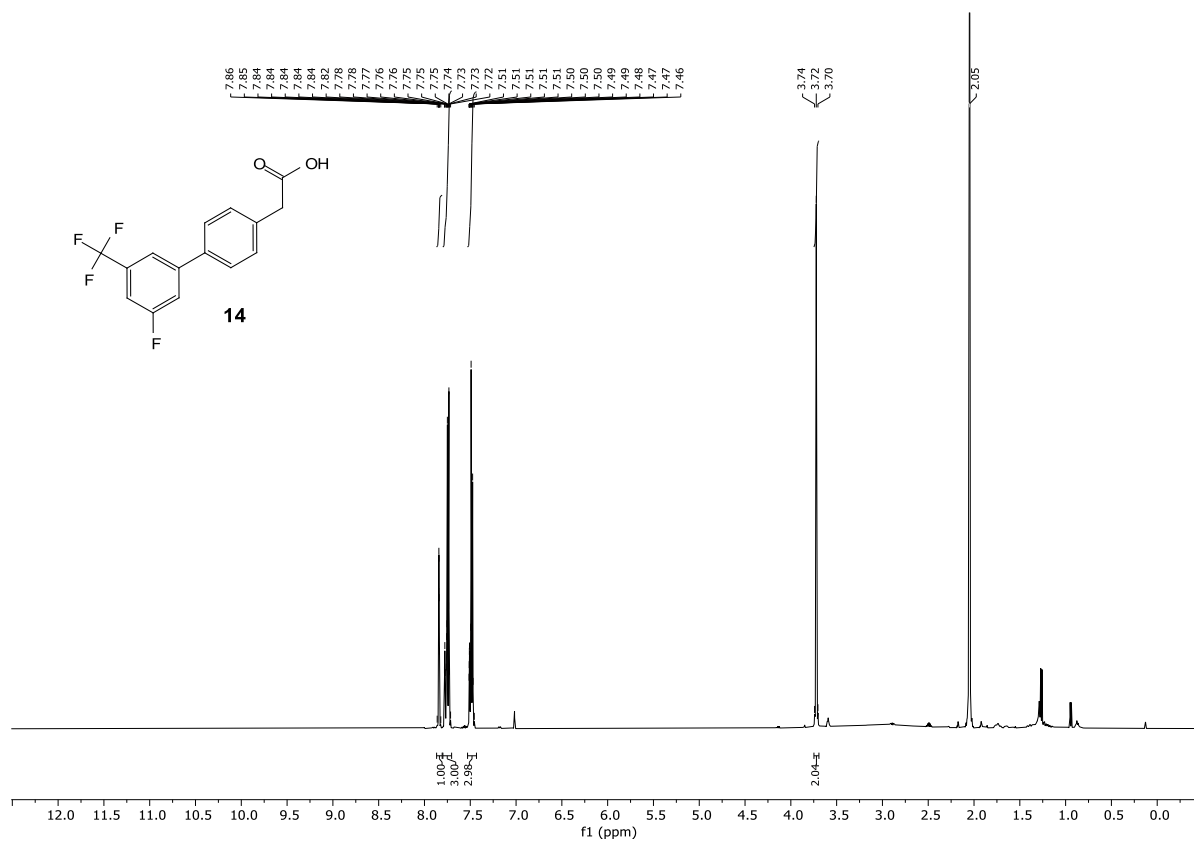


Average Purity = **96.91%**
Assuming sample weight: 4.152 mg, and mol weight: 305.26
Using Reference Compound: Ethyl 4-(dimethylamino)benzoate (4.822 mg, 99% purity, Mol Weight=193.24)
Sample Integral 1: 7.40885 - 7.62003 ppm, value = 0.53356 (2 nuclides) - Purity = 96.9%
Reference Integral: 6.72229 - 6.77109 ppm, value = 1 (2 nuclides)

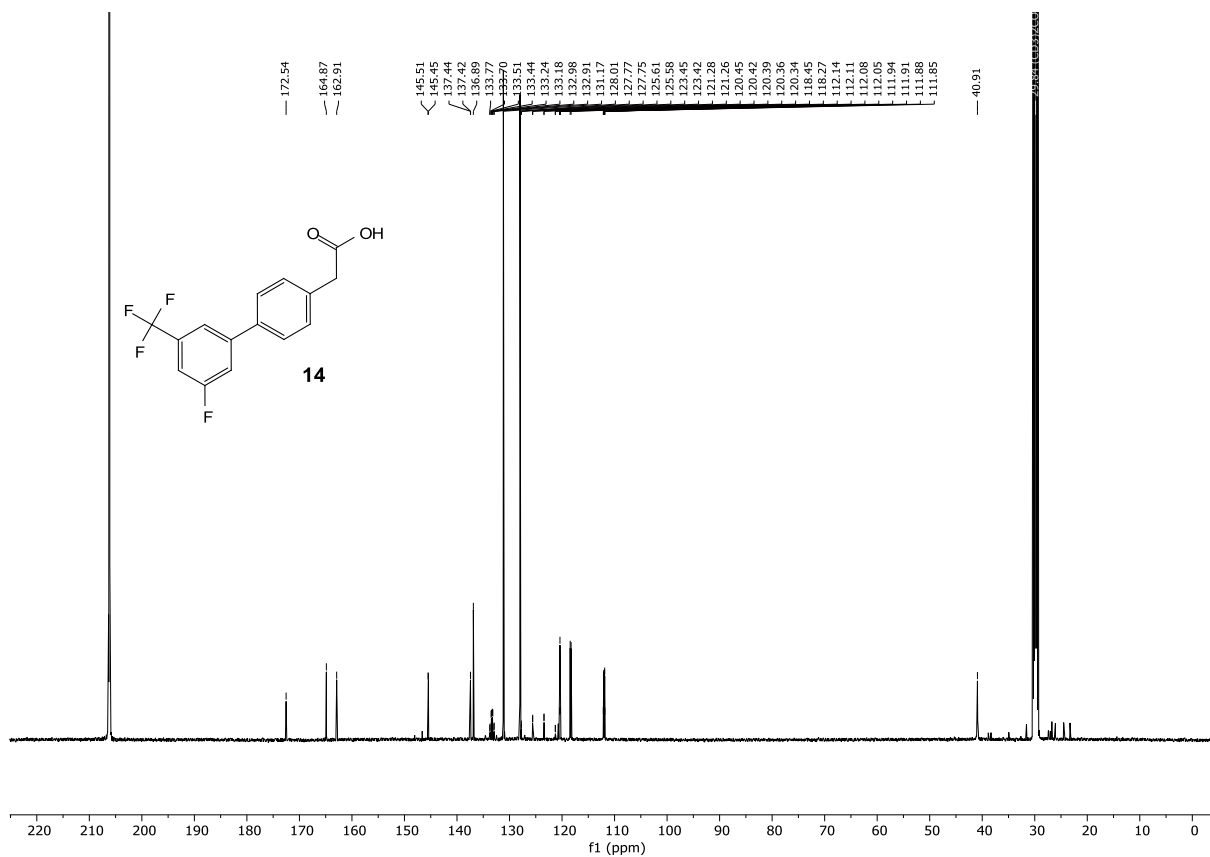


Compound **14**:

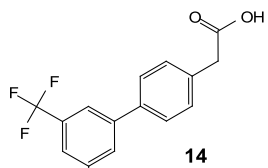
¹H-NMR:



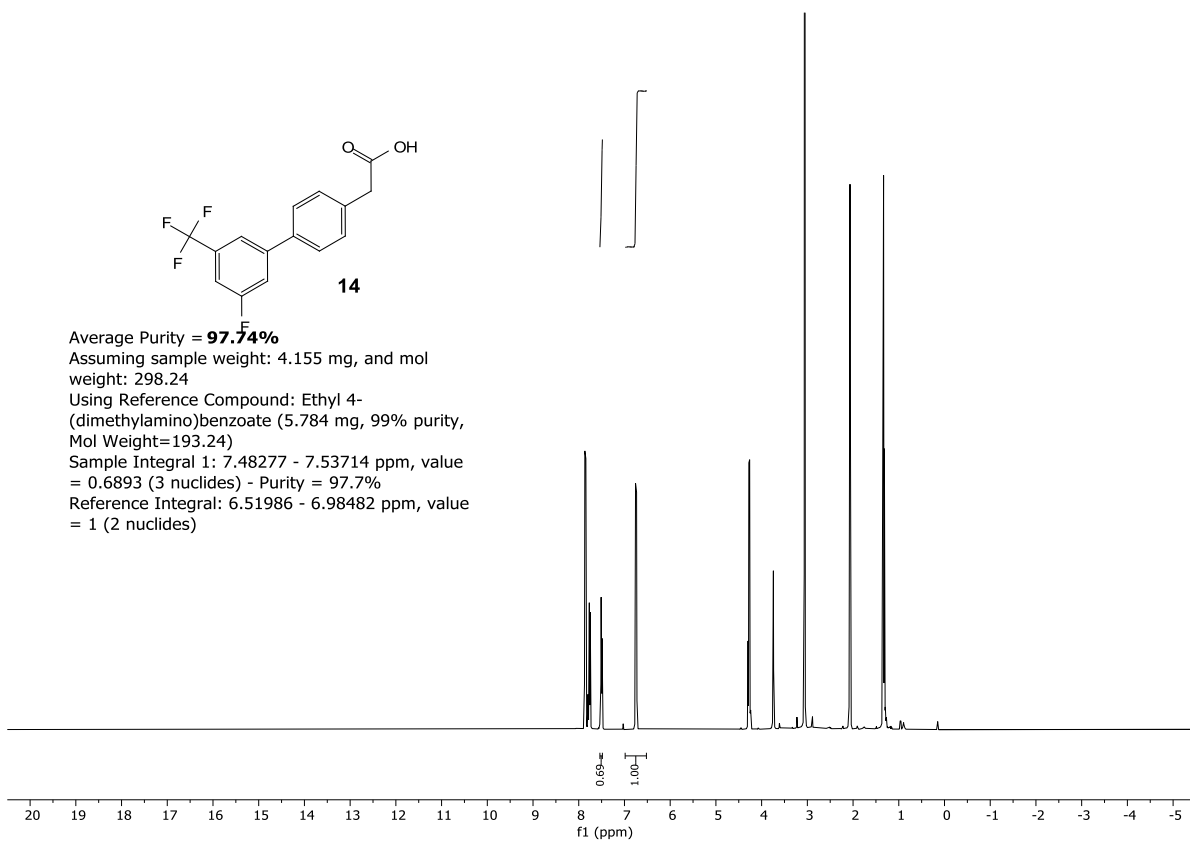
¹³C-NMR:



¹H-qNMR:

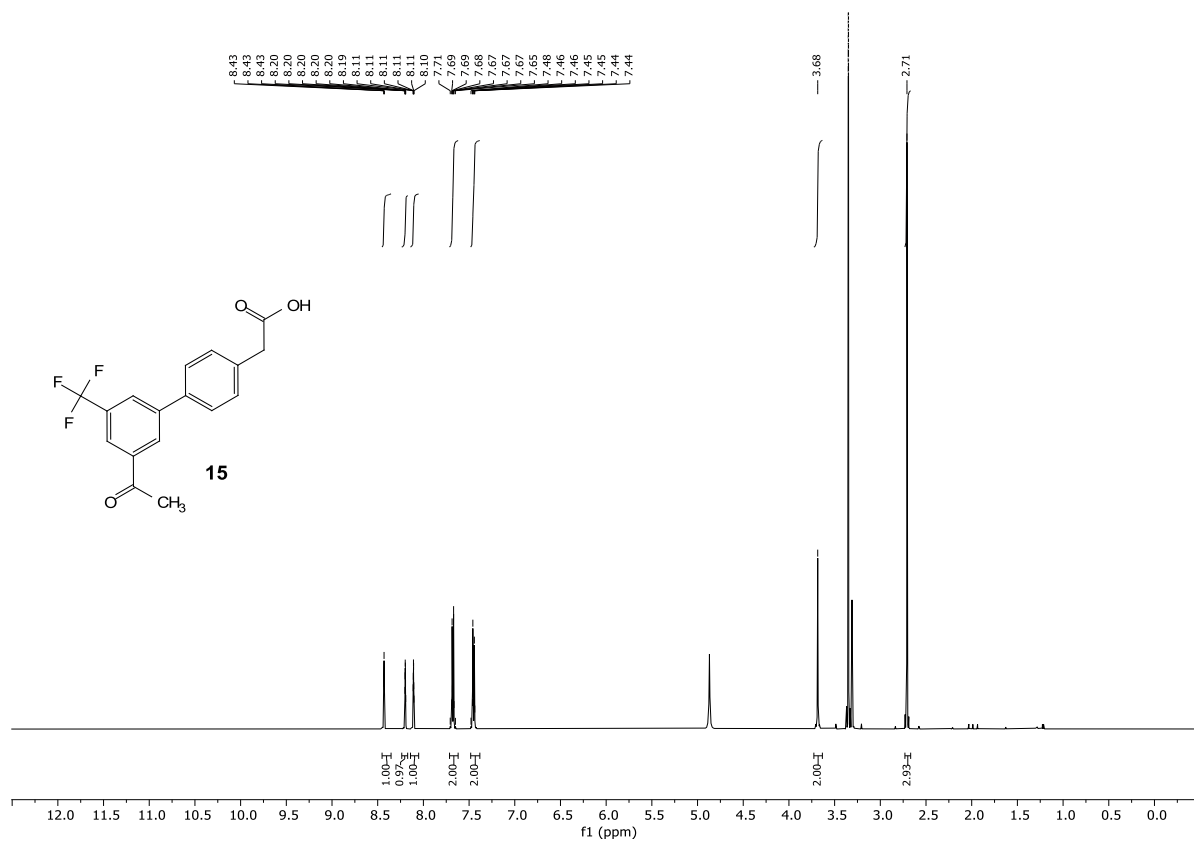


Average Purity = **97.74%**
Assuming sample weight: 4.155 mg, and mol weight: 298.24
Using Reference Compound: Ethyl 4-(dimethylamino)benzoate (5.784 mg, 99% purity, Mol Weight=193.24)
Sample Integral 1: 7.48277 - 7.53714 ppm, value = 0.6893 (3 nuclides) - Purity = 97.7%
Reference Integral: 6.51986 - 6.98482 ppm, value = 1 (2 nuclides)

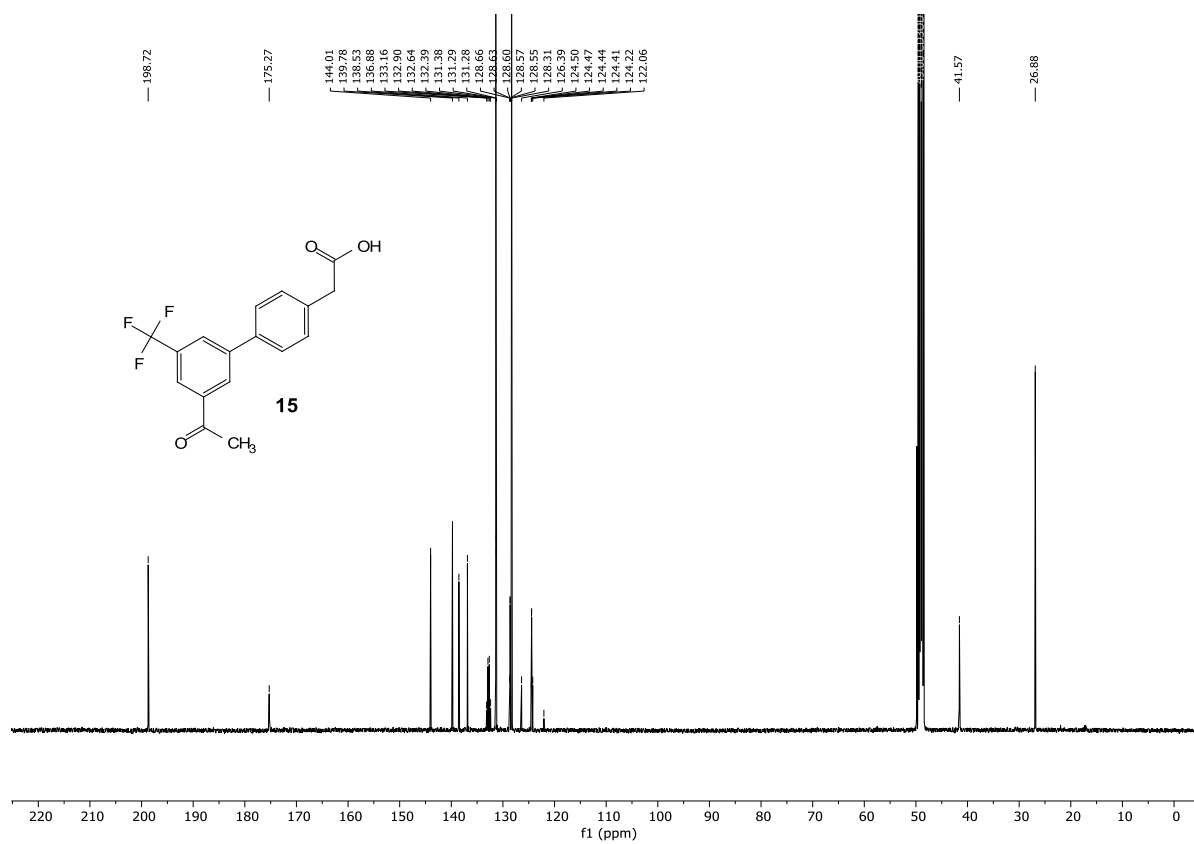


Compound 15:

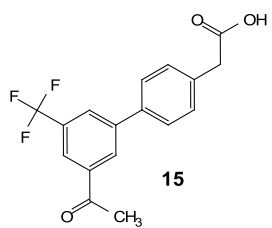
¹H-NMR:



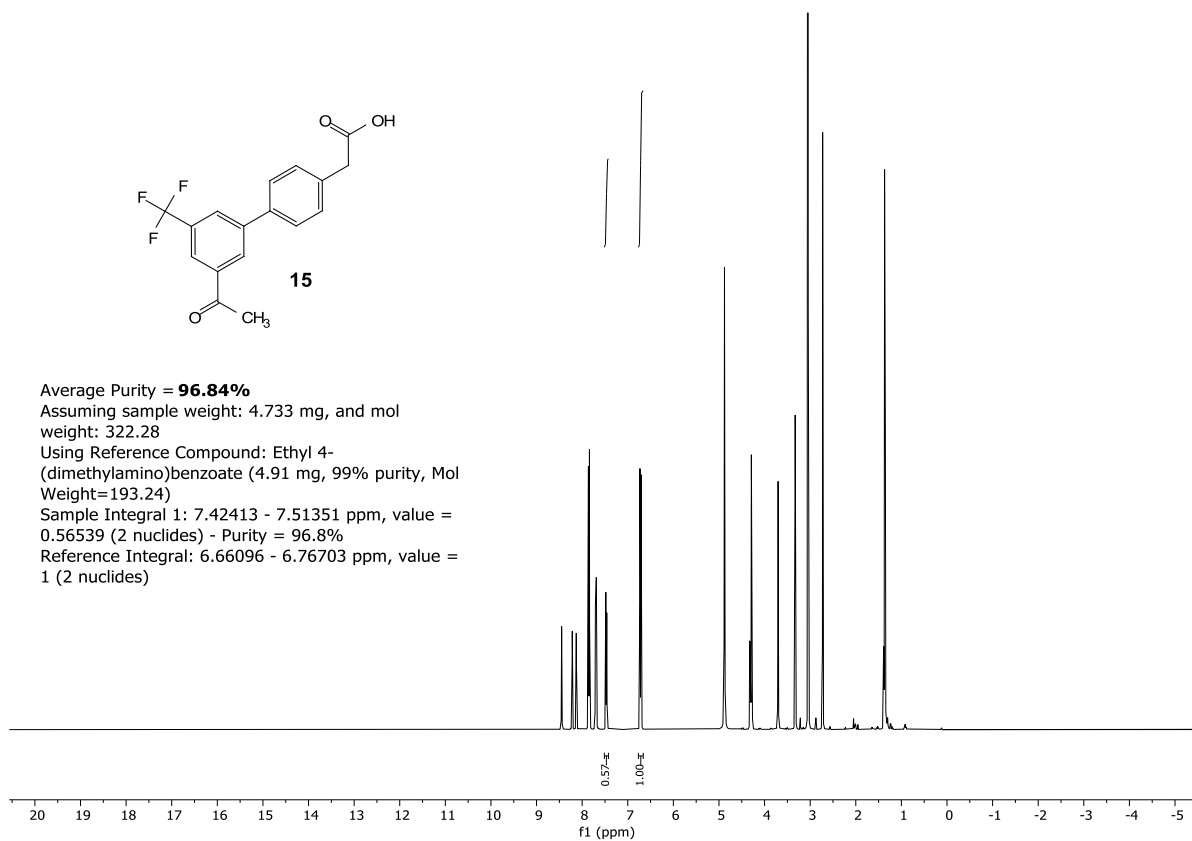
¹³C-NMR:



¹H-NMR:

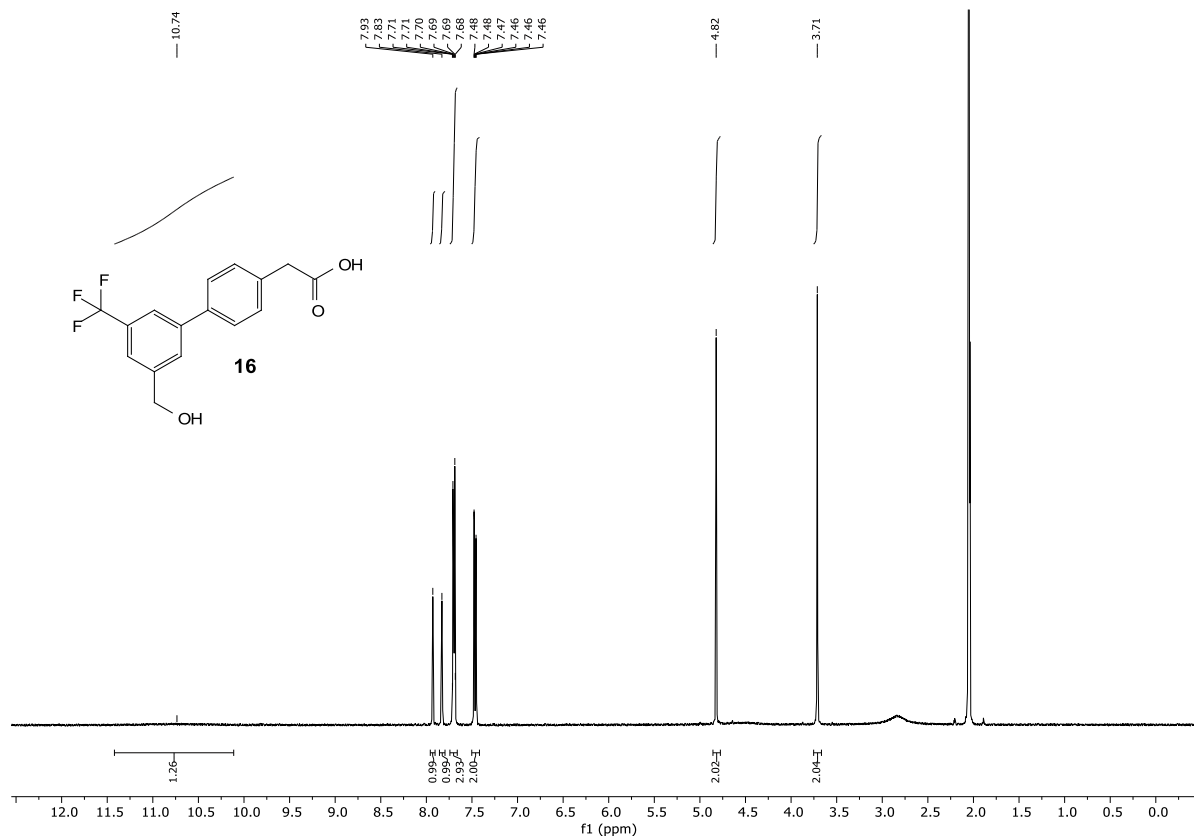


Average Purity = **96.84%**
Assuming sample weight: 4.733 mg, and mol weight: 322.28
Using Reference Compound: Ethyl 4-(dimethylamino)benzoate (4.91 mg, 99% purity, Mol Weight=193.24)
Sample Integral 1: 7.42413 - 7.51351 ppm, value = 0.56539 (2 nuclides) - Purity = 96.8%
Reference Integral: 6.66096 - 6.76703 ppm, value = 1 (2 nuclides)

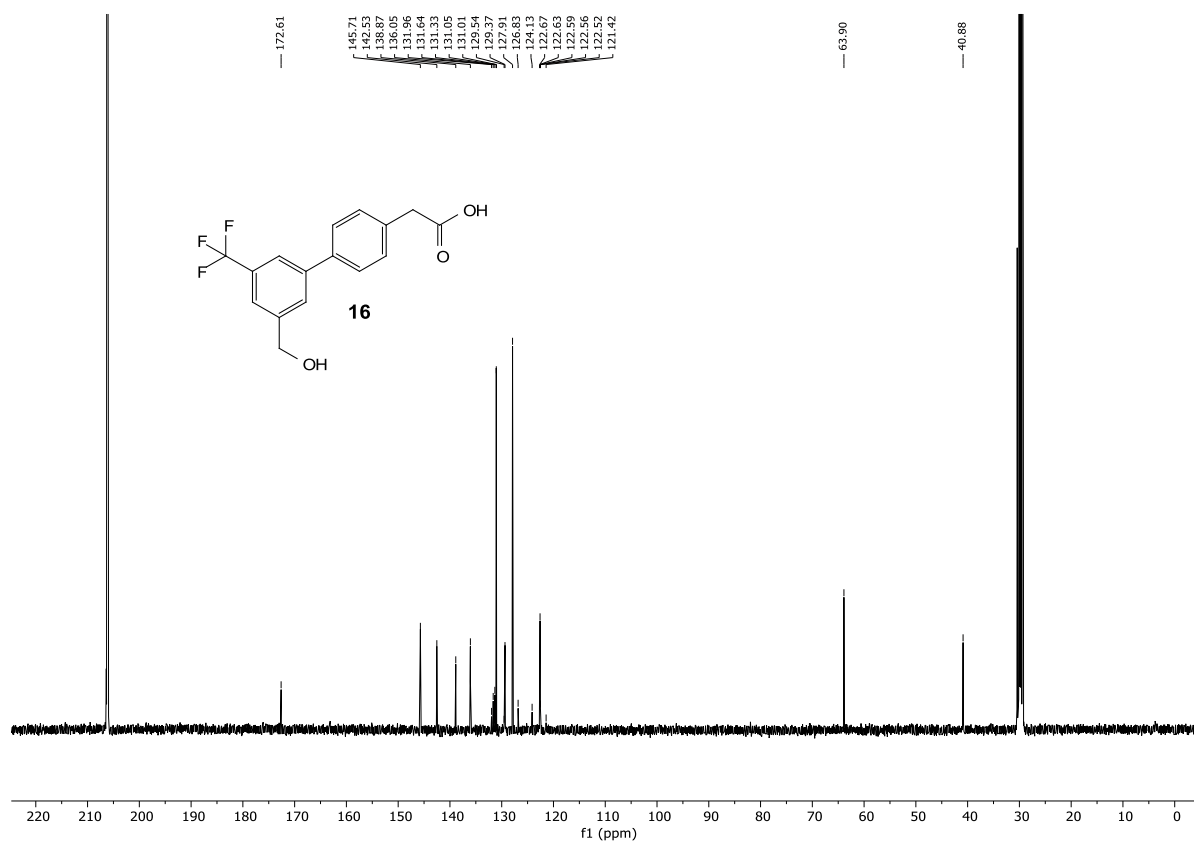


Compound 16:

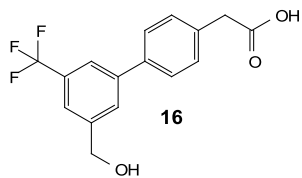
¹H-NMR:



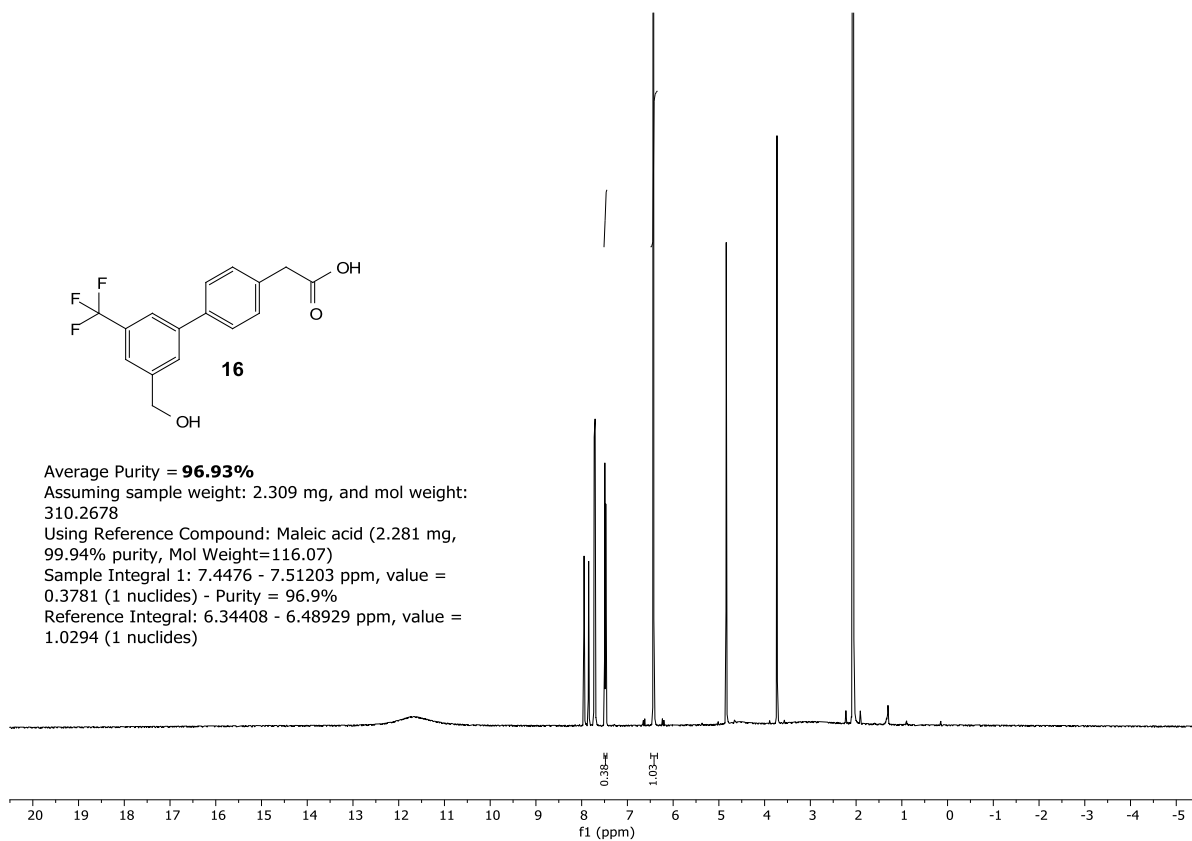
¹³C-NMR:



¹H-qNMR:

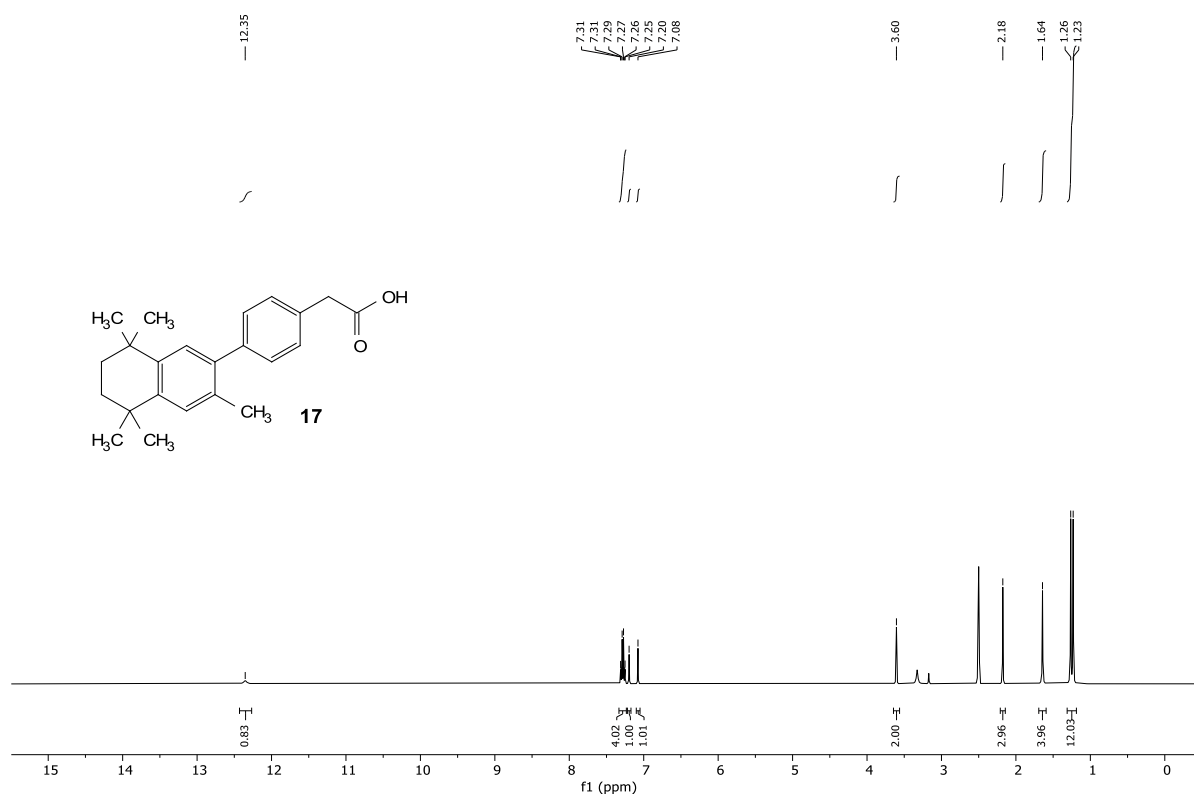


Average Purity = **96.93%**
Assuming sample weight: 2.309 mg, and mol weight:
310.2678
Using Reference Compound: Maleic acid (2.281 mg,
99.94% purity, Mol Weight=116.07)
Sample Integral 1: 7.4476 - 7.51203 ppm, value =
0.3781 (1 nuclides) - Purity = 96.9%
Reference Integral: 6.34408 - 6.48929 ppm, value =
1.0294 (1 nuclides)

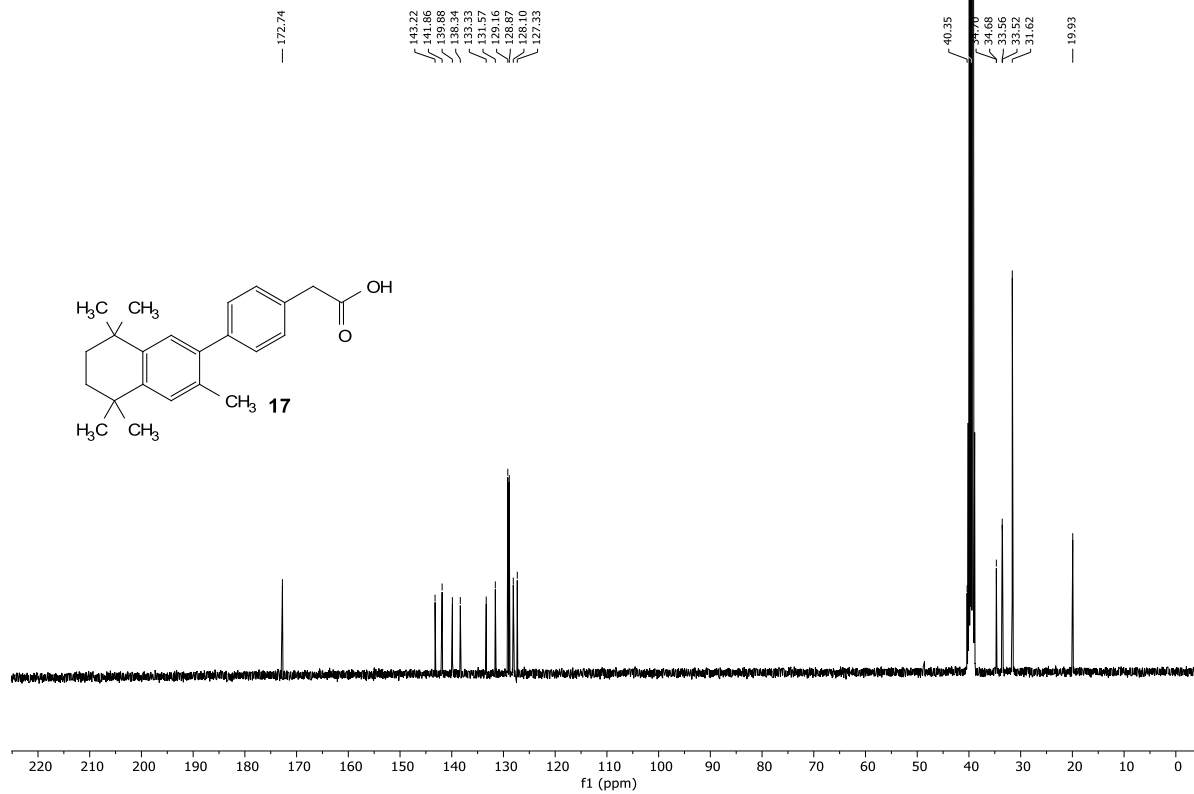


Compound 17:

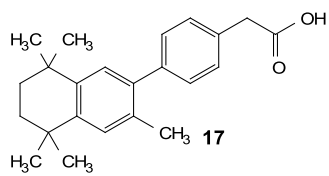
¹H-NMR:



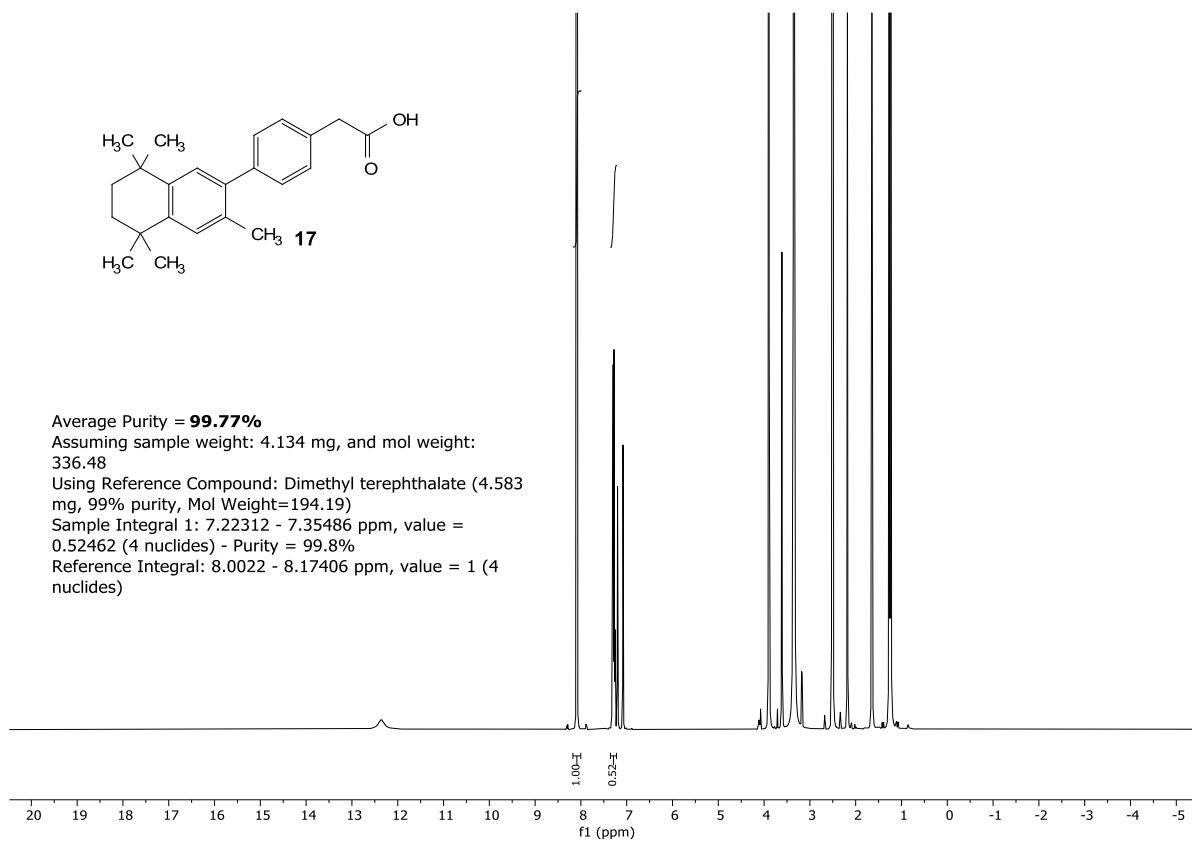
¹³C-NMR:



¹H-NMR:

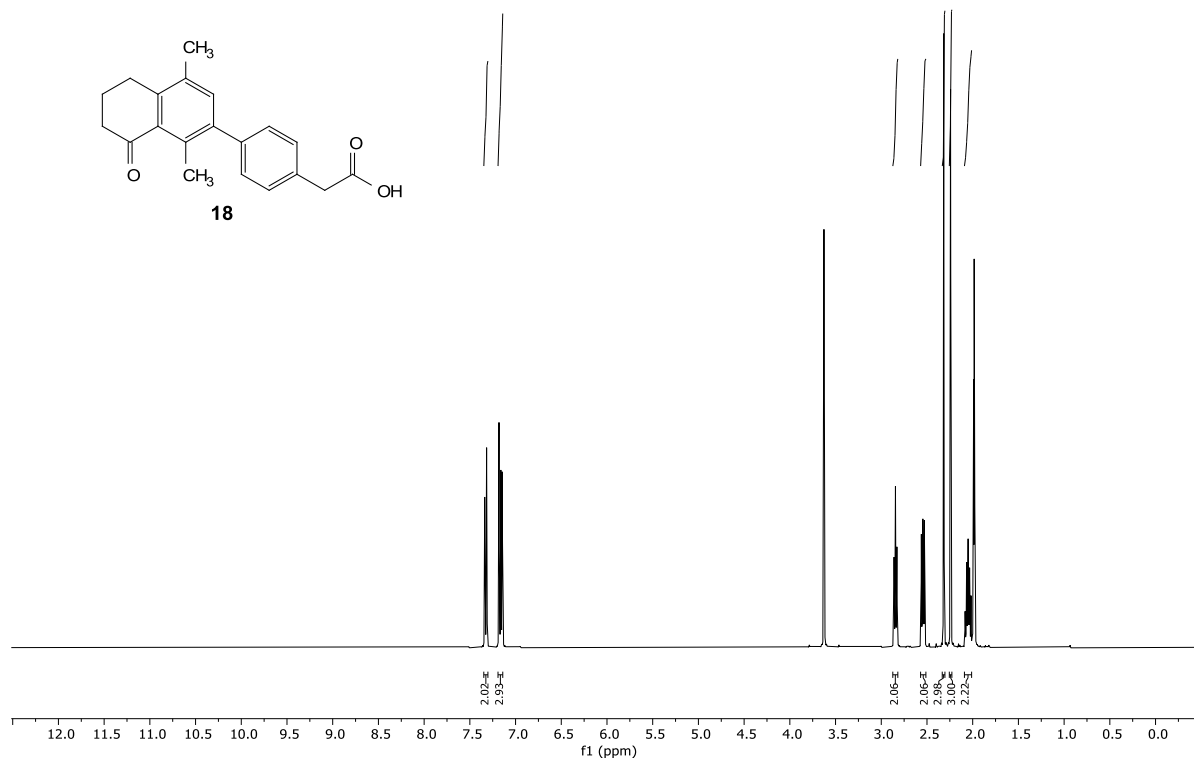


Average Purity = **99.77%**
Assuming sample weight: 4.134 mg, and mol weight:
336.48
Using Reference Compound: Dimethyl terephthalate (4.583
mg, 99% purity, Mol Weight=194.19)
Sample Integral 1: 7.22312 - 7.35486 ppm, value =
0.52462 (4 nuclides) - Purity = 99.8%
Reference Integral: 8.0022 - 8.17406 ppm, value = 1 (4
nuclides)

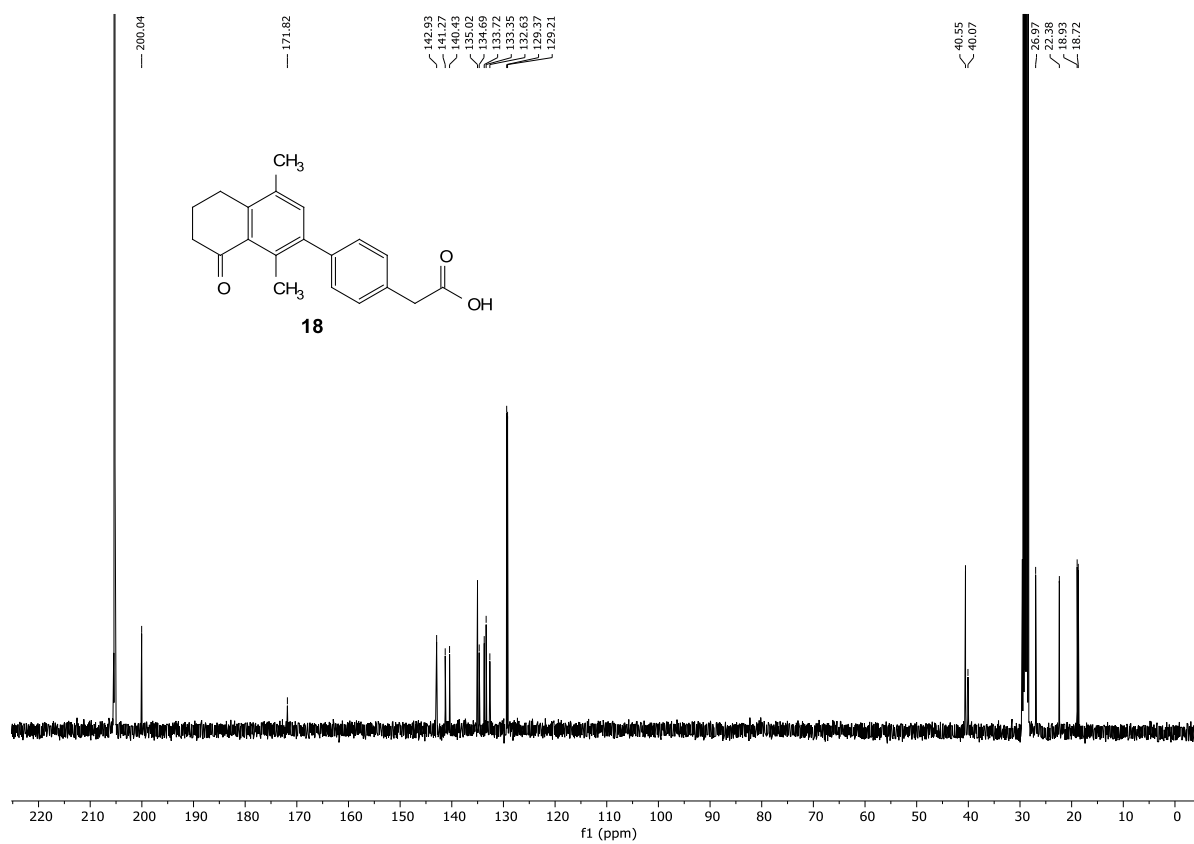


Compound 18:

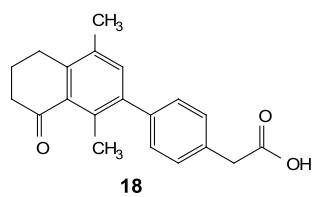
¹H-NMR:



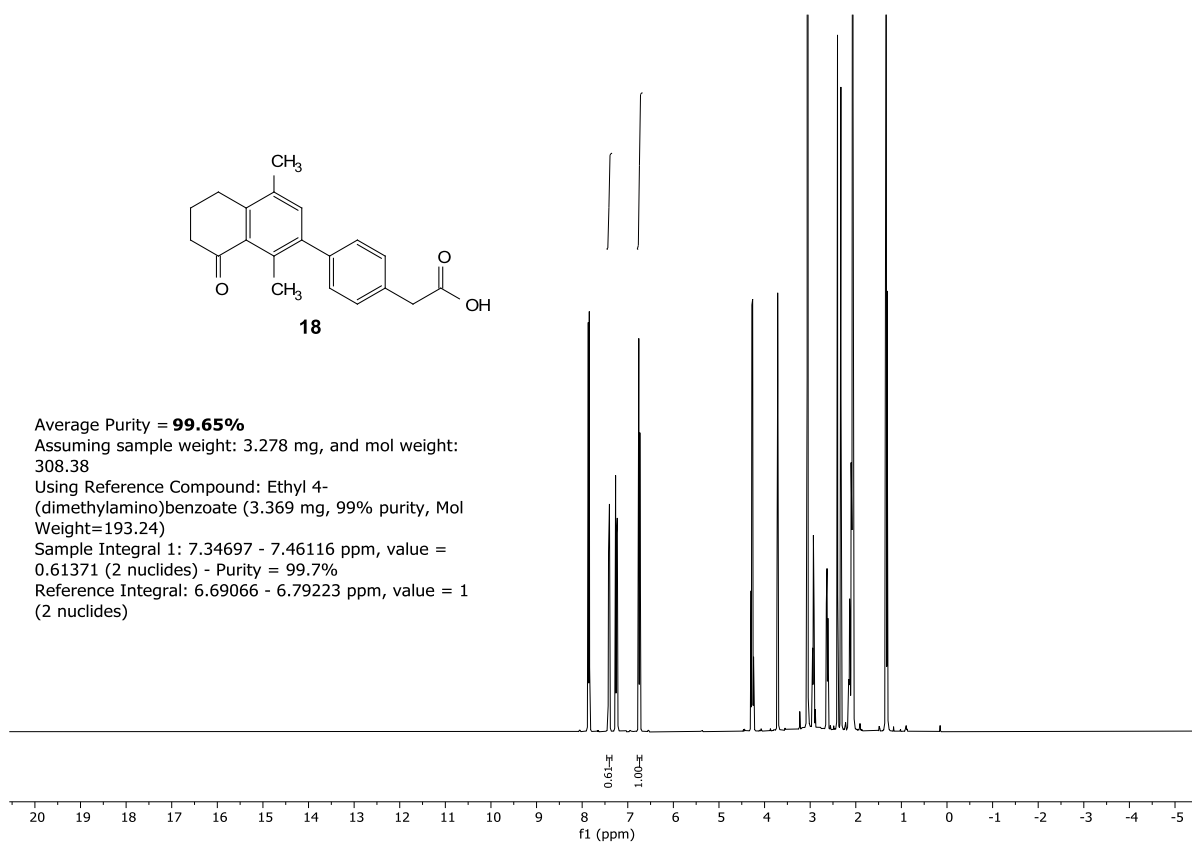
¹³C-NMR:



¹H-qNMR:

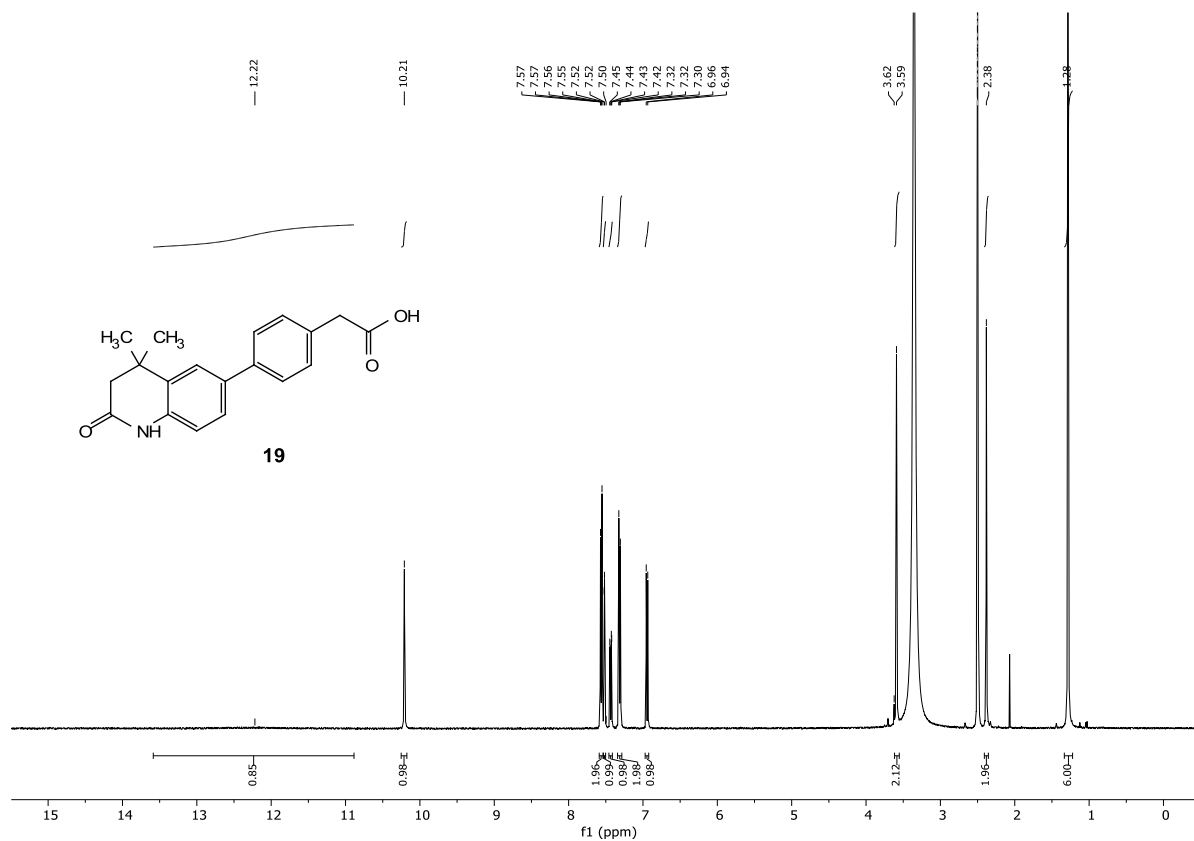


Average Purity = **99.65%**
Assuming sample weight: 3.278 mg, and mol weight:
308.38
Using Reference Compound: Ethyl 4-
(dimethylamino)benzoate (3.369 mg, 99% purity, Mol
Weight=193.24)
Sample Integral 1: 7.34697 - 7.46116 ppm, value =
0.61371 (2 nuclides) - Purity = 99.7%
Reference Integral: 6.69066 - 6.79223 ppm, value = 1
(2 nuclides)

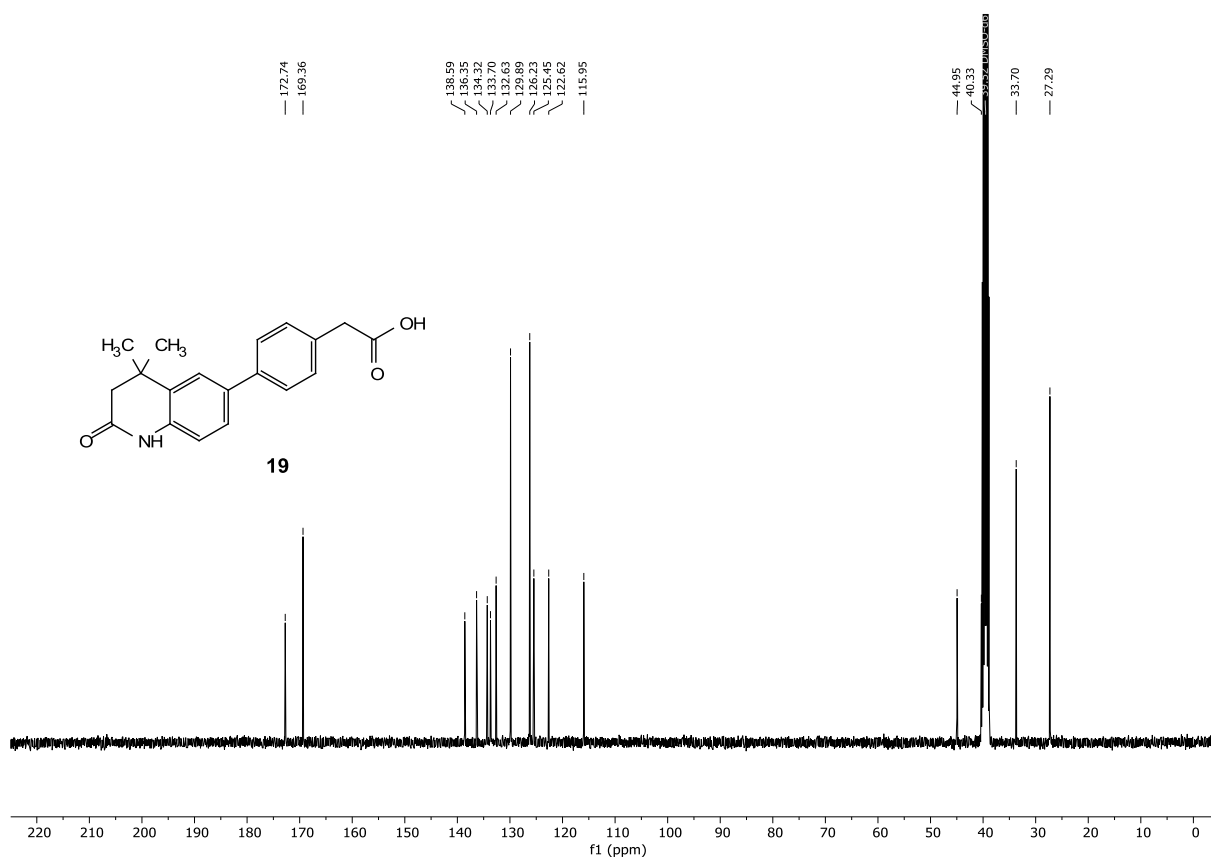


Compound 19:

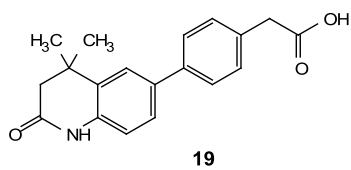
¹H-NMR:



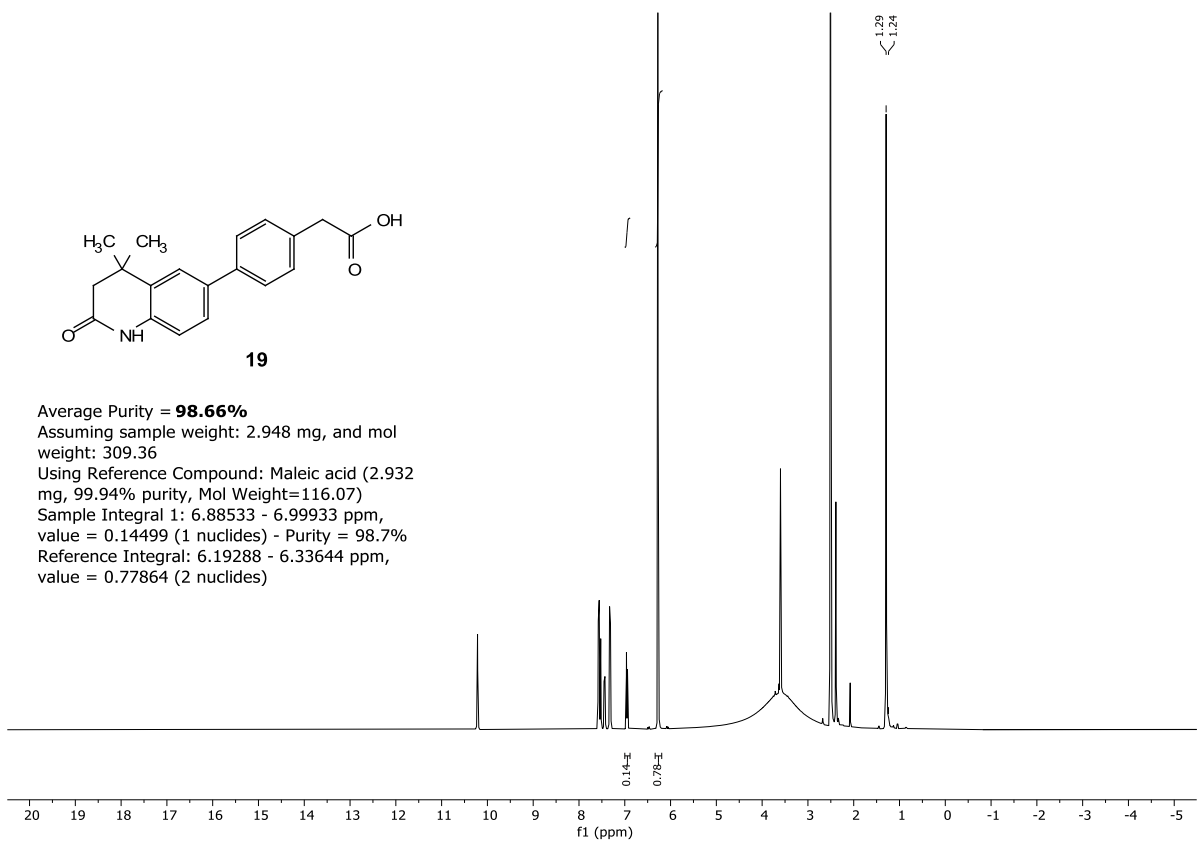
¹³C-NMR:



¹H-qNMR:

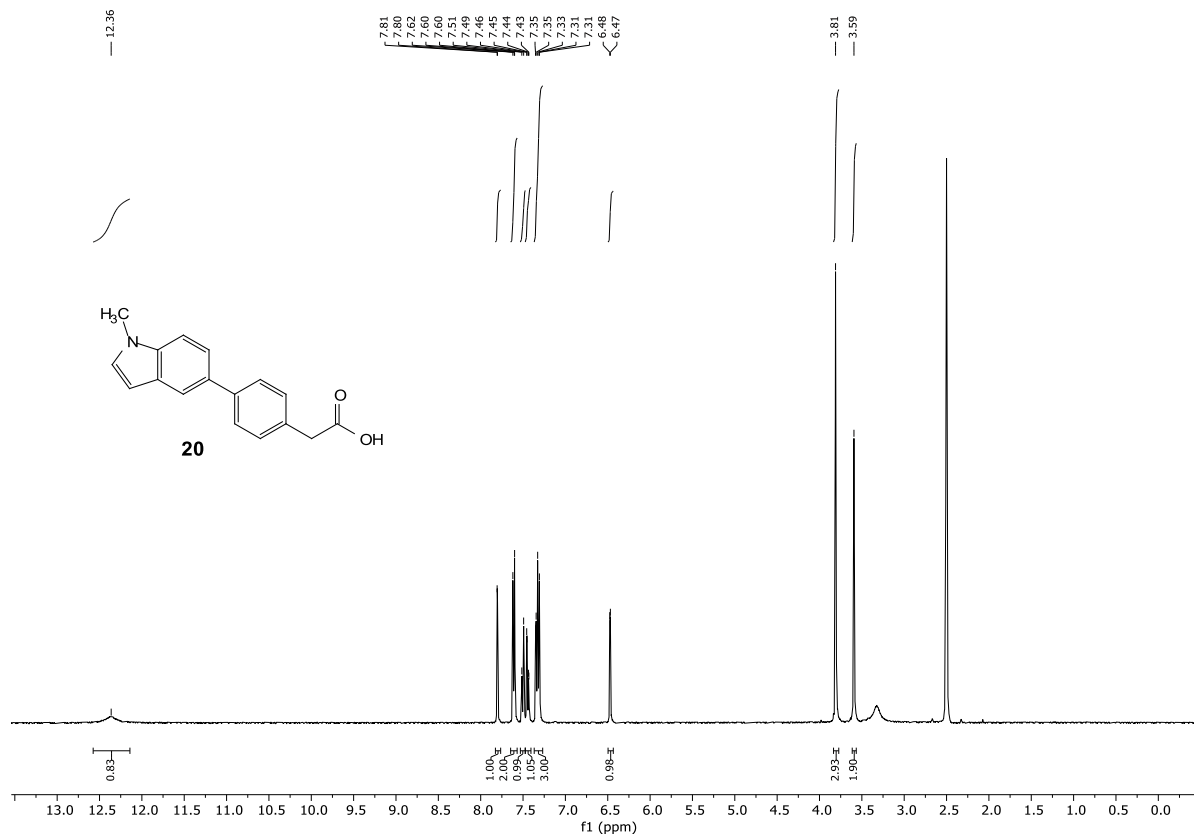


Average Purity = **98.66%**
Assuming sample weight: 2.948 mg, and mol weight: 309.36
Using Reference Compound: Maleic acid (2.932 mg, 99.94% purity, Mol Weight=116.07)
Sample Integral 1: 6.88533 - 6.99933 ppm, value = 0.14499 (1 nuclides) - Purity = 98.7%
Reference Integral: 6.19288 - 6.33644 ppm, value = 0.77864 (2 nuclides)

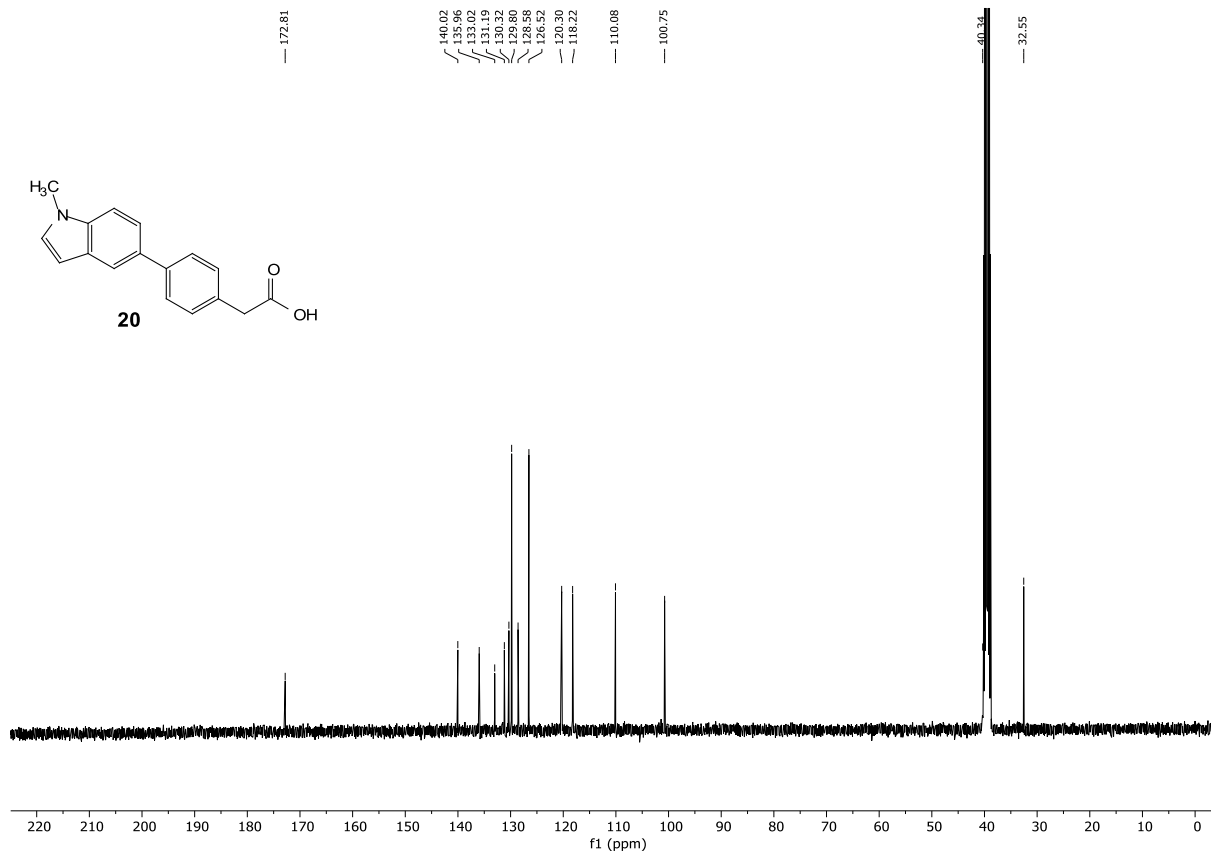


Compound 20:

¹H-NMR:

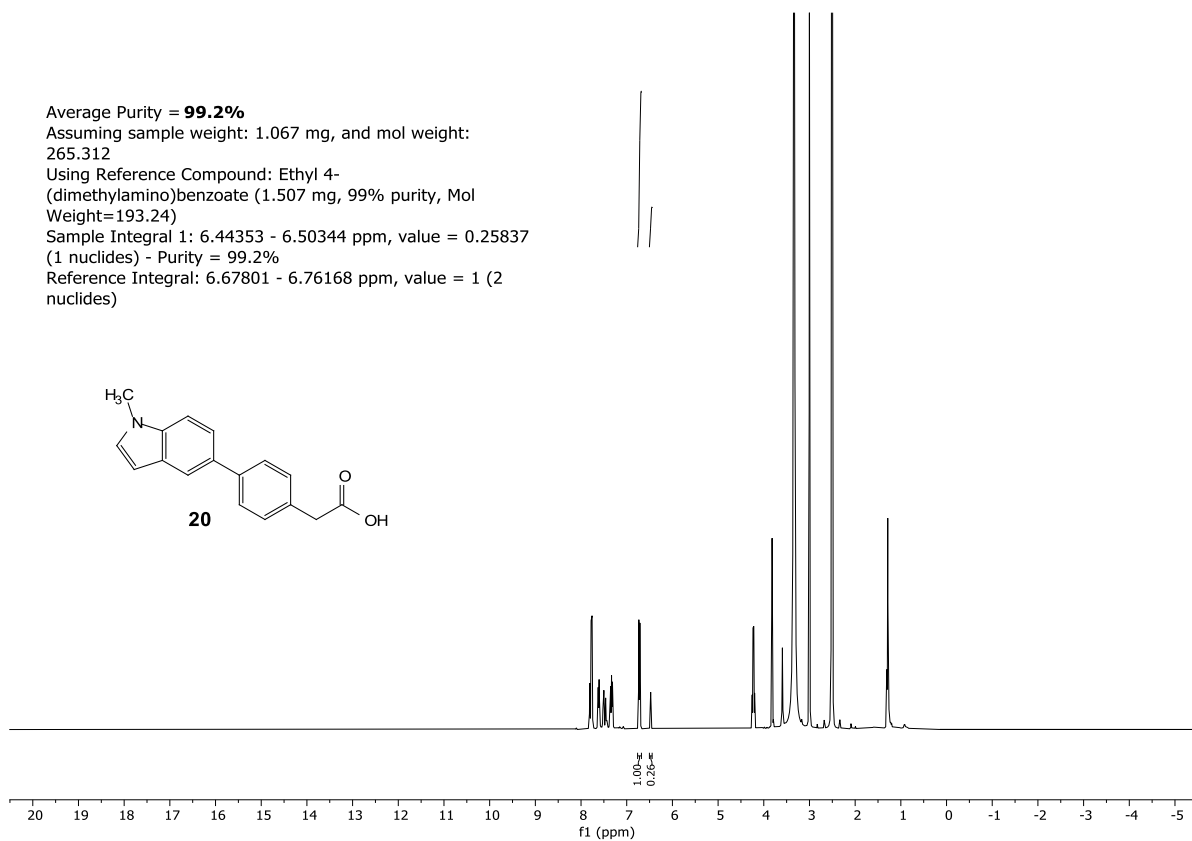
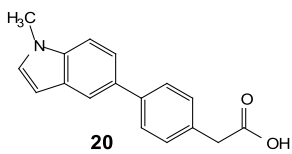


¹³C-NMR:



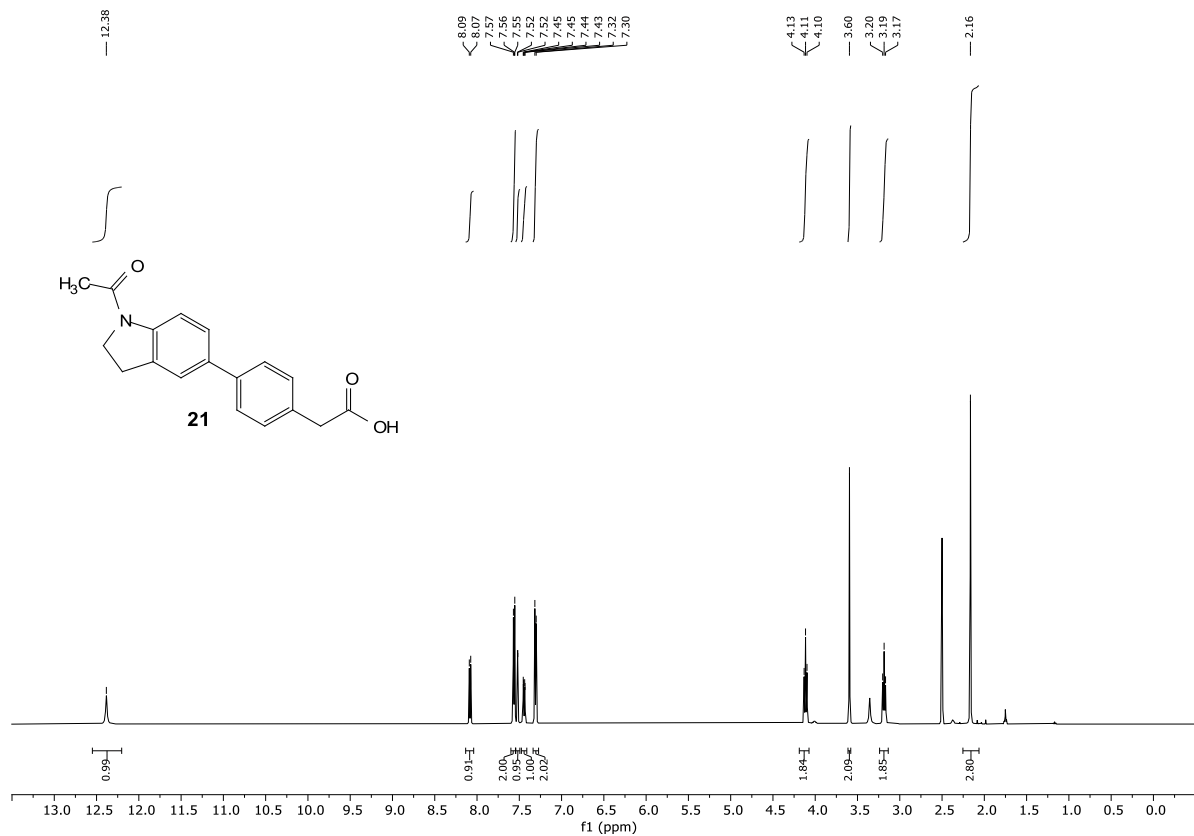
¹H-NMR:

Average Purity = **99.2%**
Assuming sample weight: 1.067 mg, and mol weight:
265.312
Using Reference Compound: Ethyl 4-
(dimethylamino)benzoate (1.507 mg, 99% purity, Mol
Weight=193.24)
Sample Integral 1: 6.44353 - 6.50344 ppm, value = 0.25837
(1 nuclides) - Purity = 99.2%
Reference Integral: 6.67801 - 6.76168 ppm, value = 1 (2
nuclides)

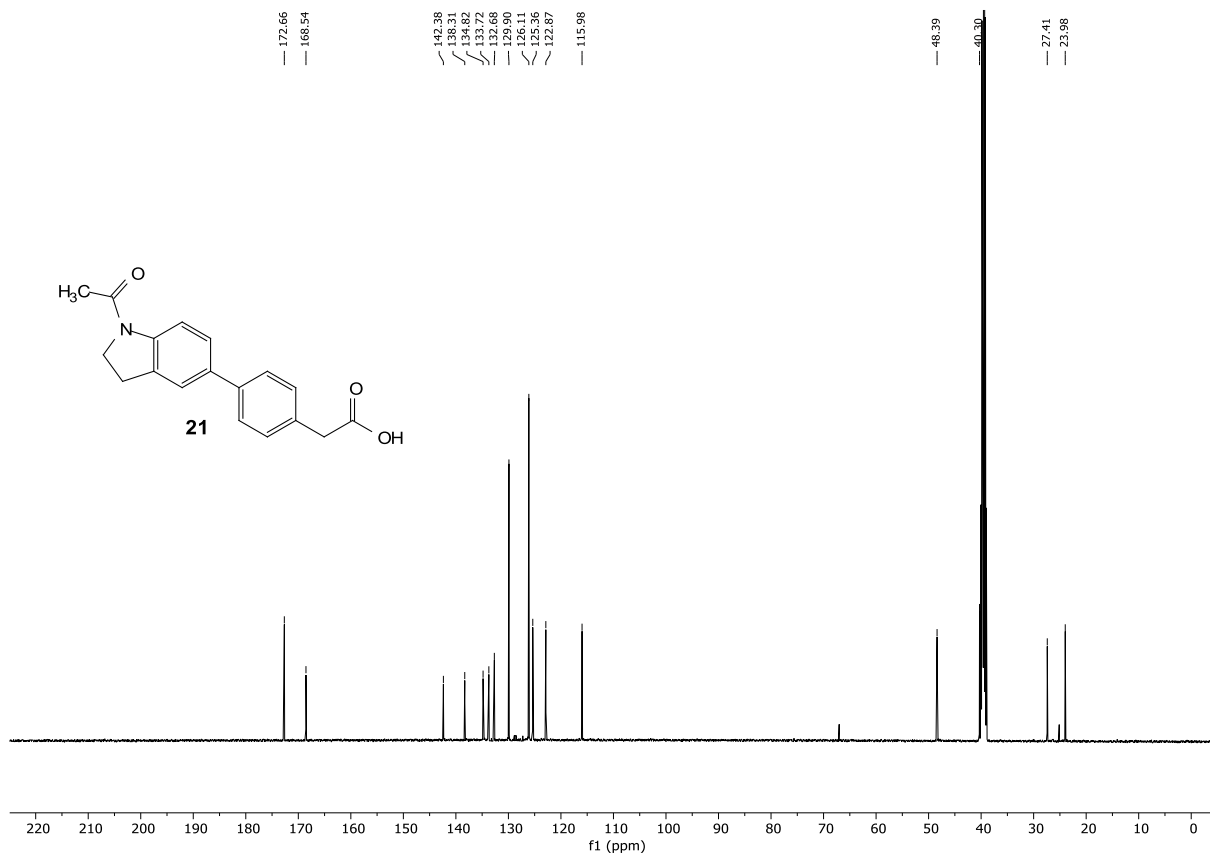


Compound 21:

¹H-NMR:



¹³C-NMR:



¹H-NMR:

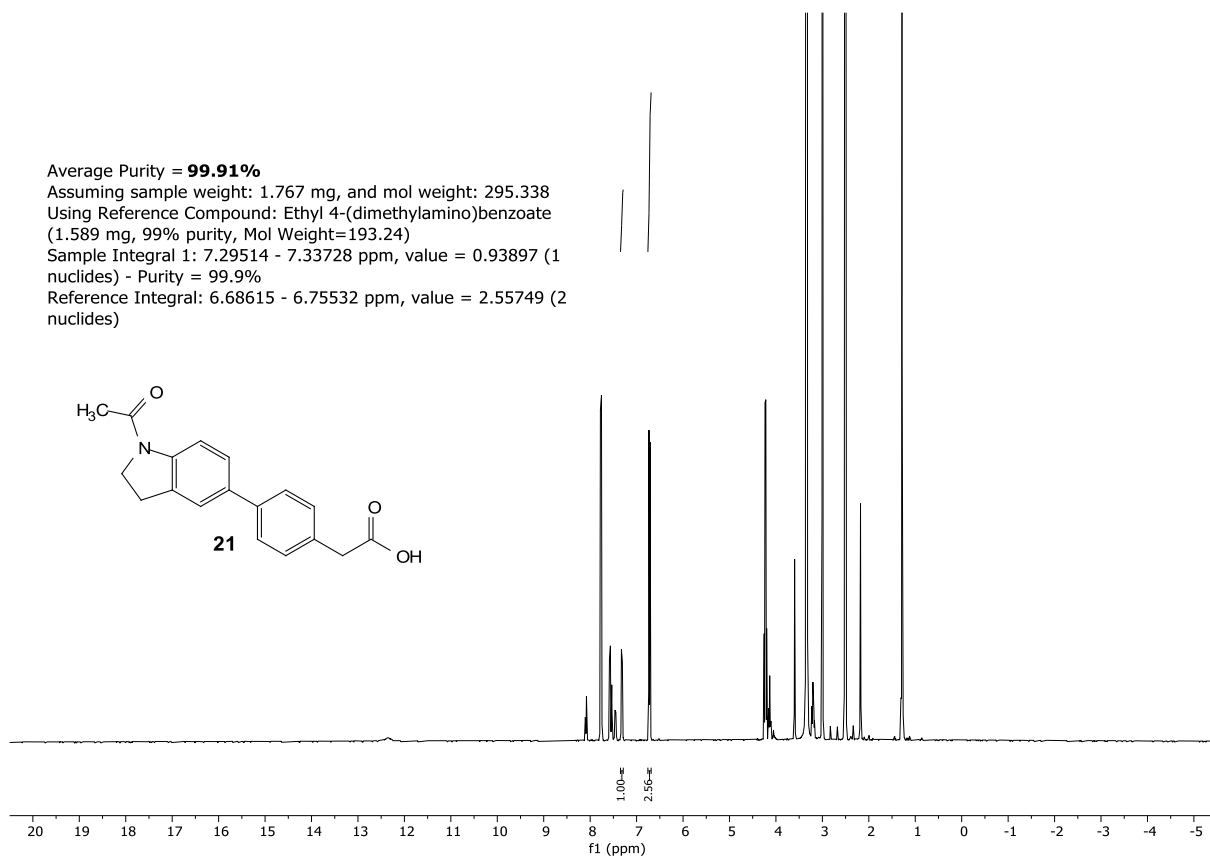
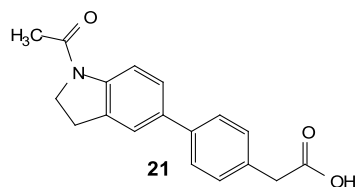
Average Purity = **99.91%**

Assuming sample weight: 1.767 mg, and mol weight: 295.338

Using Reference Compound: Ethyl 4-(dimethylamino)benzoate
(1.589 mg, 99% purity, Mol Weight=193.24)

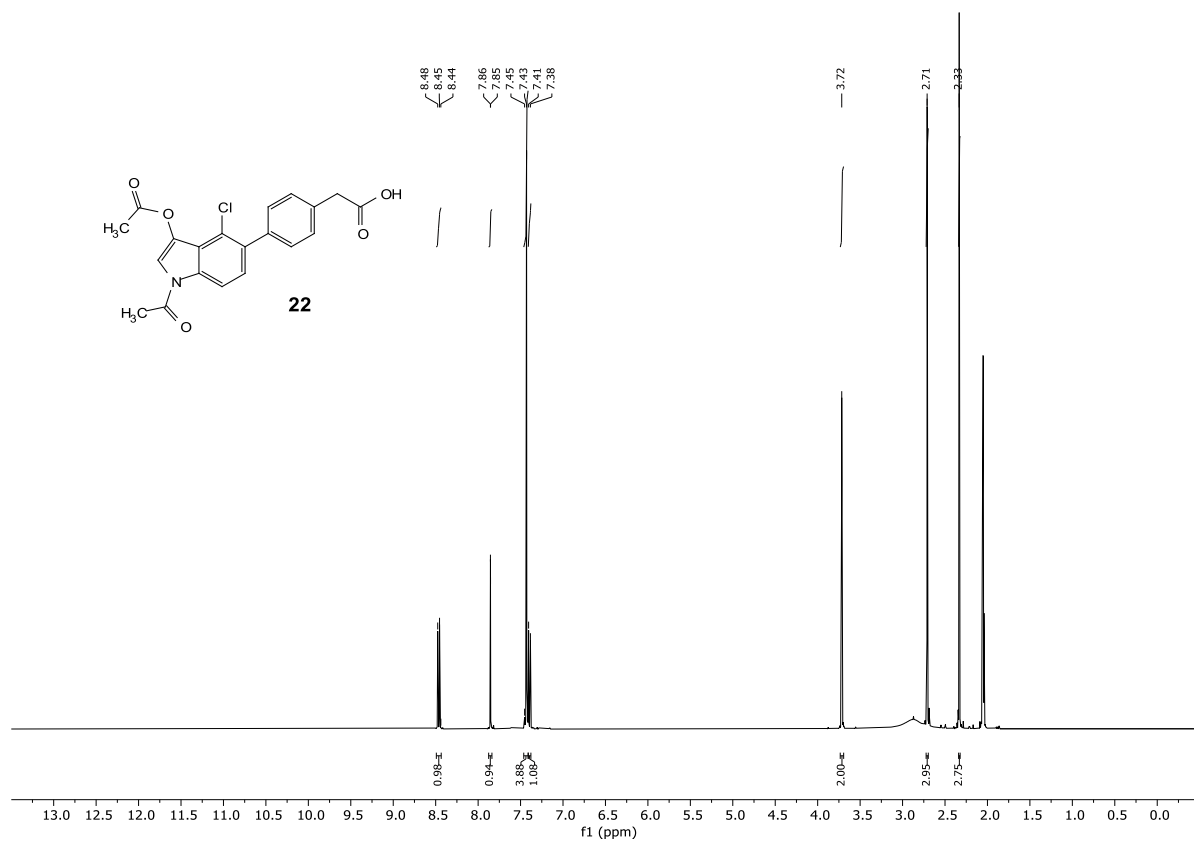
Sample Integral 1: 7.29514 - 7.33728 ppm, value = 0.93897 (1
nuclides) - Purity = 99.9%

Reference Integral: 6.68615 - 6.75532 ppm, value = 2.55749 (2
nuclides)

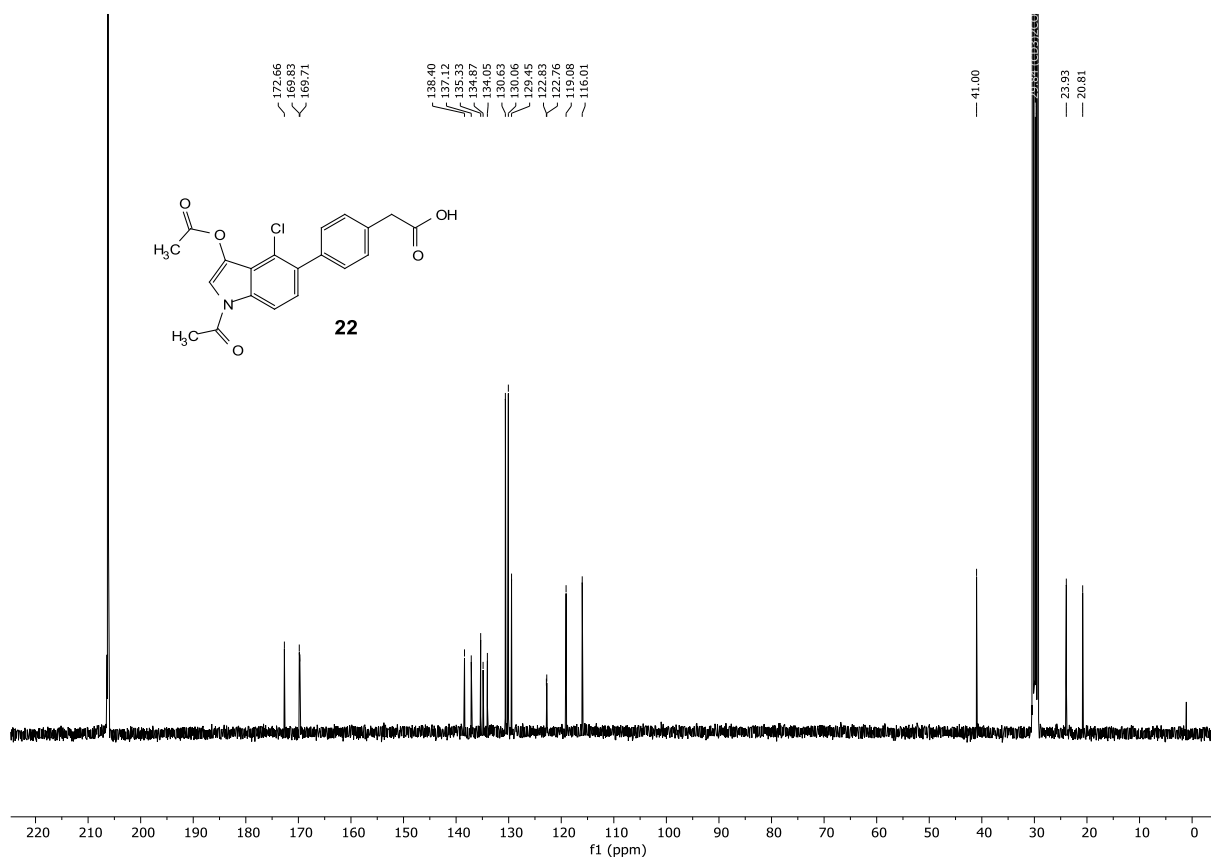


Compound **22**:

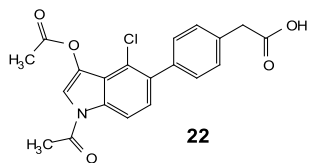
¹H-NMR:



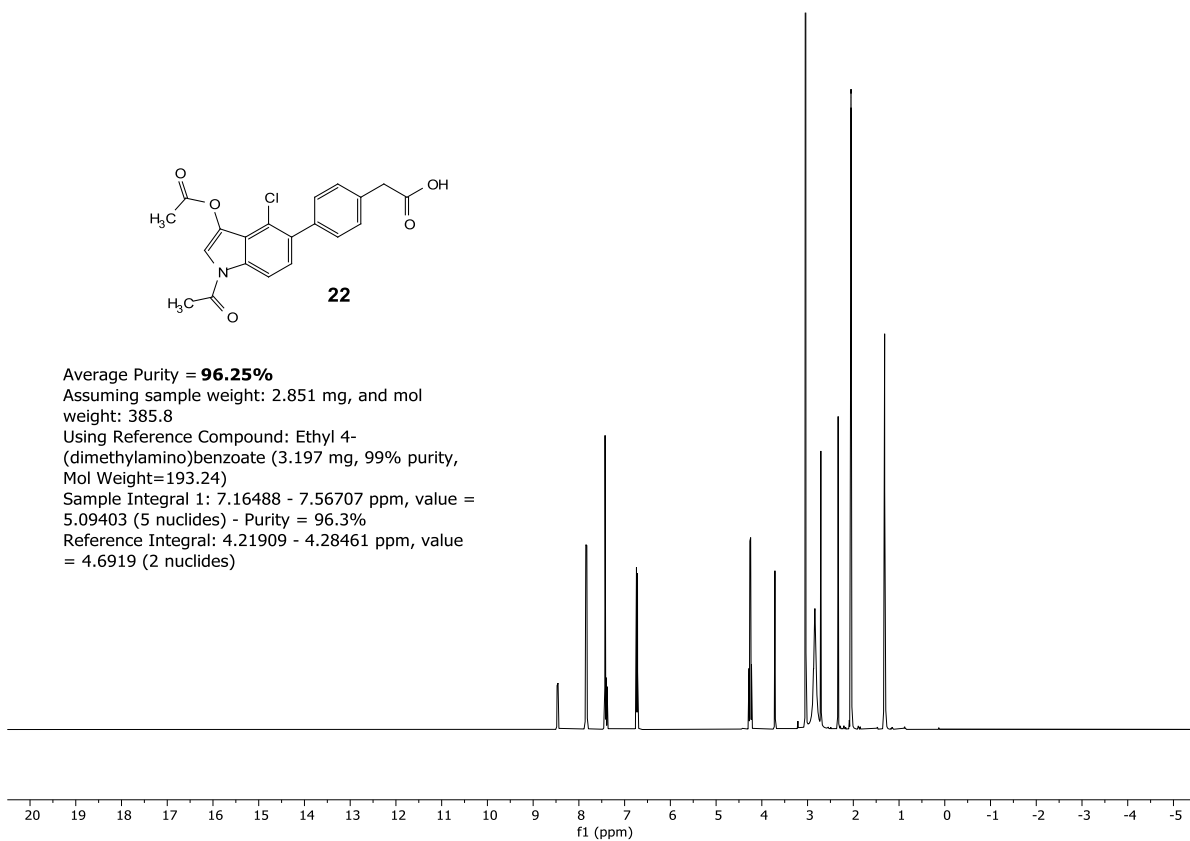
¹³C-NMR:



¹H-qNMR:

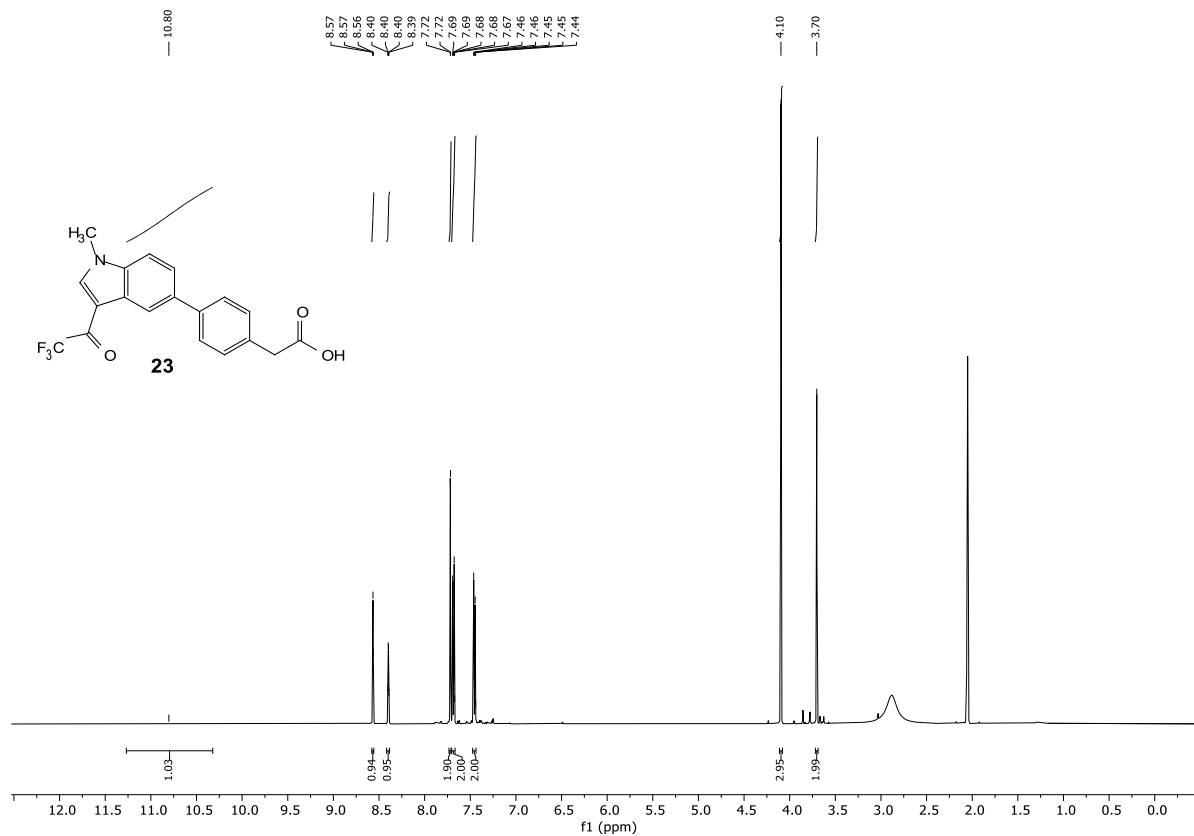


Average Purity = **96.25%**
Assuming sample weight: 2.851 mg, and mol weight: 385.8
Using Reference Compound: Ethyl 4-(dimethylamino)benzoate (3.197 mg, 99% purity, Mol Weight=193.24)
Sample Integral 1: 7.16488 - 7.56707 ppm, value = 5.09403 (5 nuclides) - Purity = 96.3%
Reference Integral: 4.21909 - 4.28461 ppm, value = 4.6919 (2 nuclides)

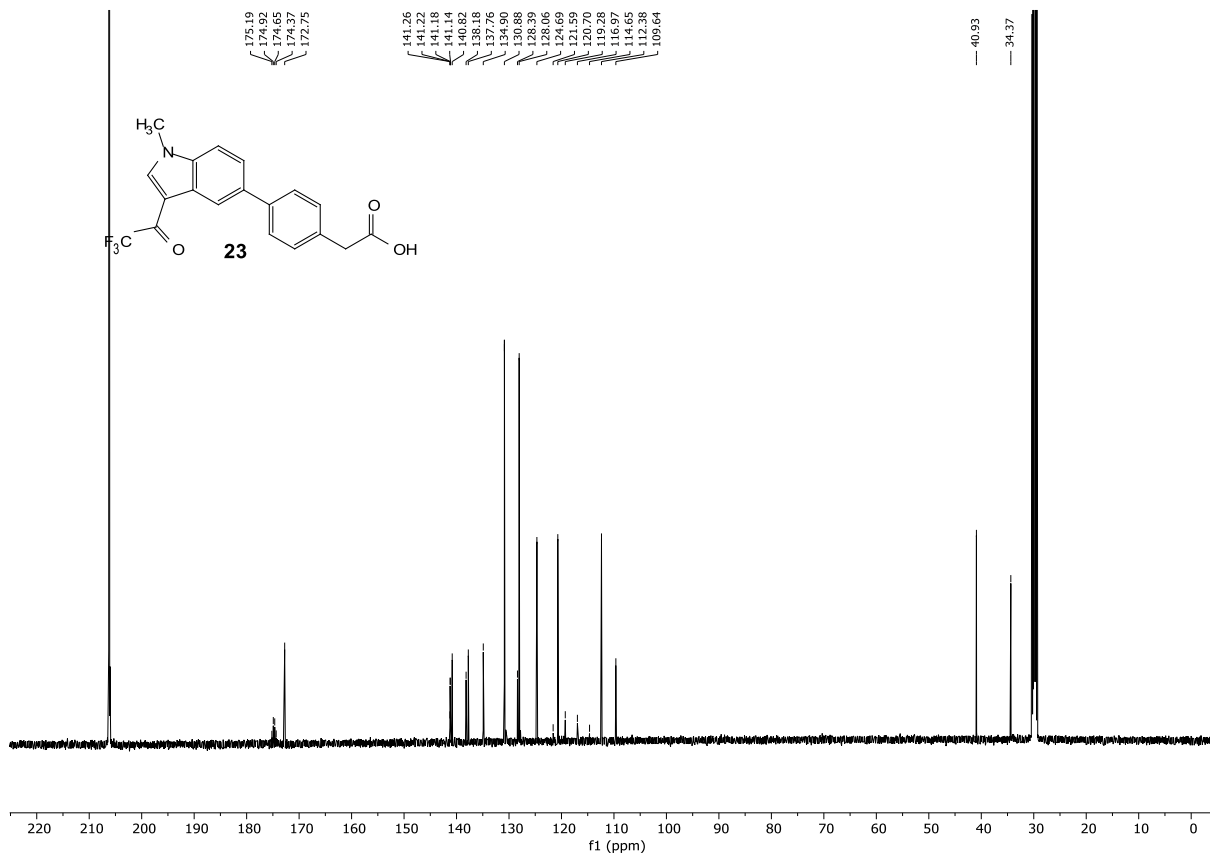


Compound 23:

¹H-NMR:



¹³C-NMR:



¹H-qNMR:

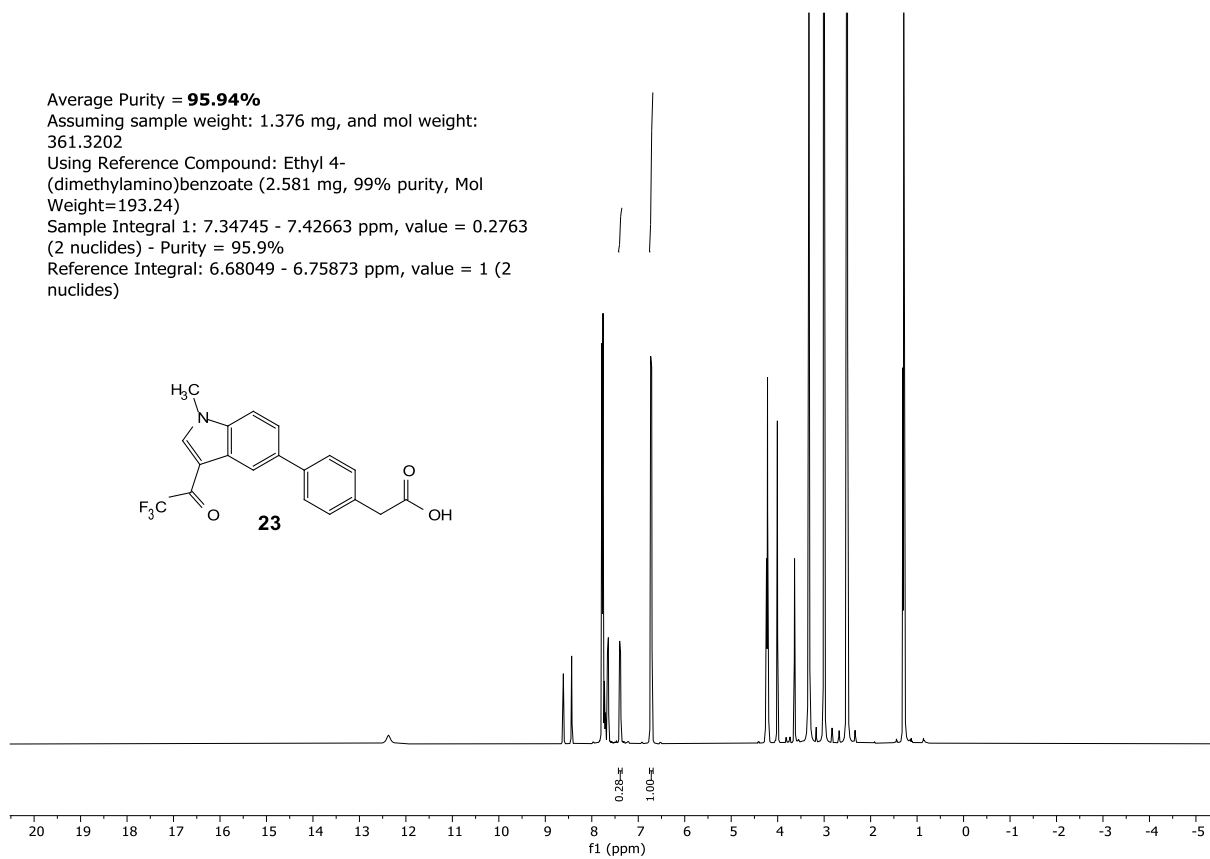
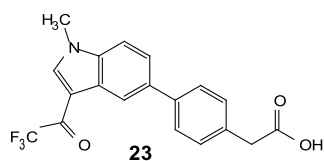
Average Purity = **95.94%**

Assuming sample weight: 1.376 mg, and mol weight:
361.3202

Using Reference Compound: Ethyl 4-(
dimethylamino)benzoate (2.581 mg, 99% purity, Mol
Weight=193.24)

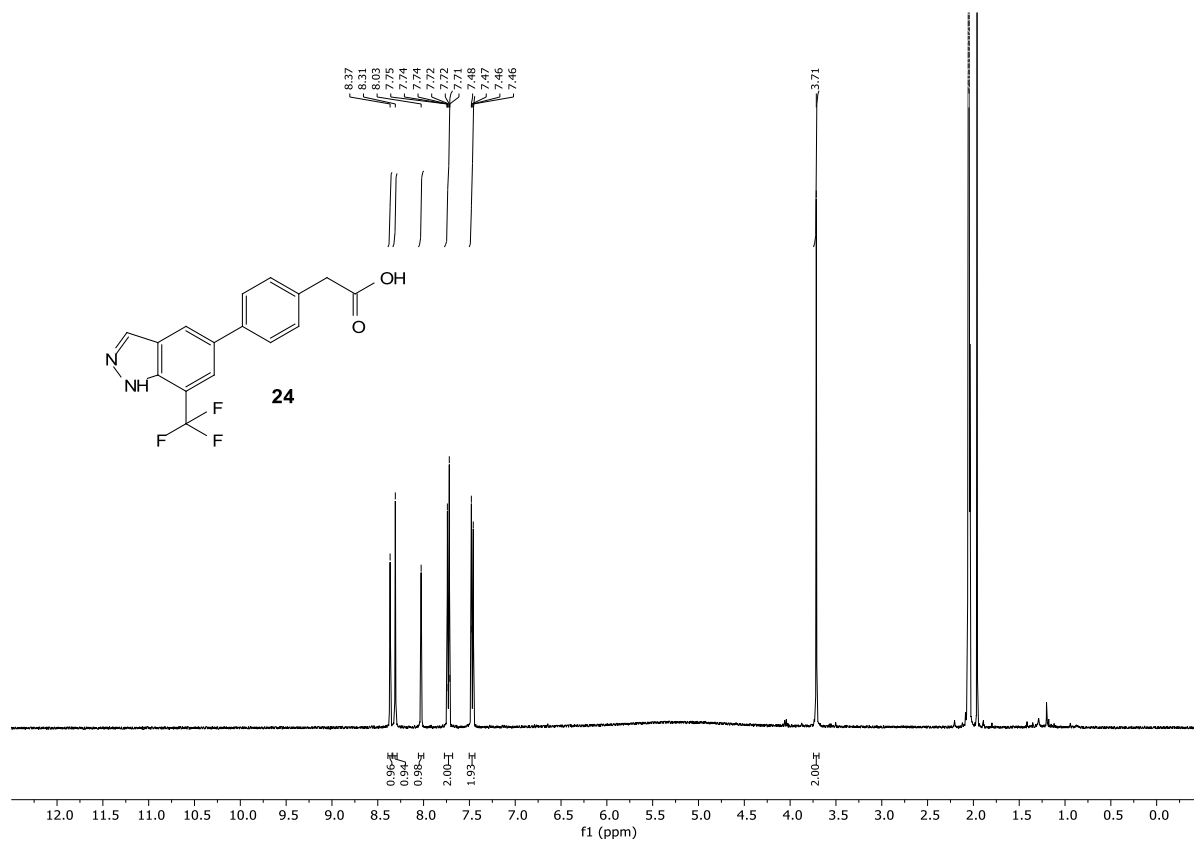
Sample Integral 1: 7.34745 - 7.42663 ppm, value = 0.2763
(2 nuclides) - Purity = 95.9%

Reference Integral: 6.68049 - 6.75873 ppm, value = 1 (2
nuclides)

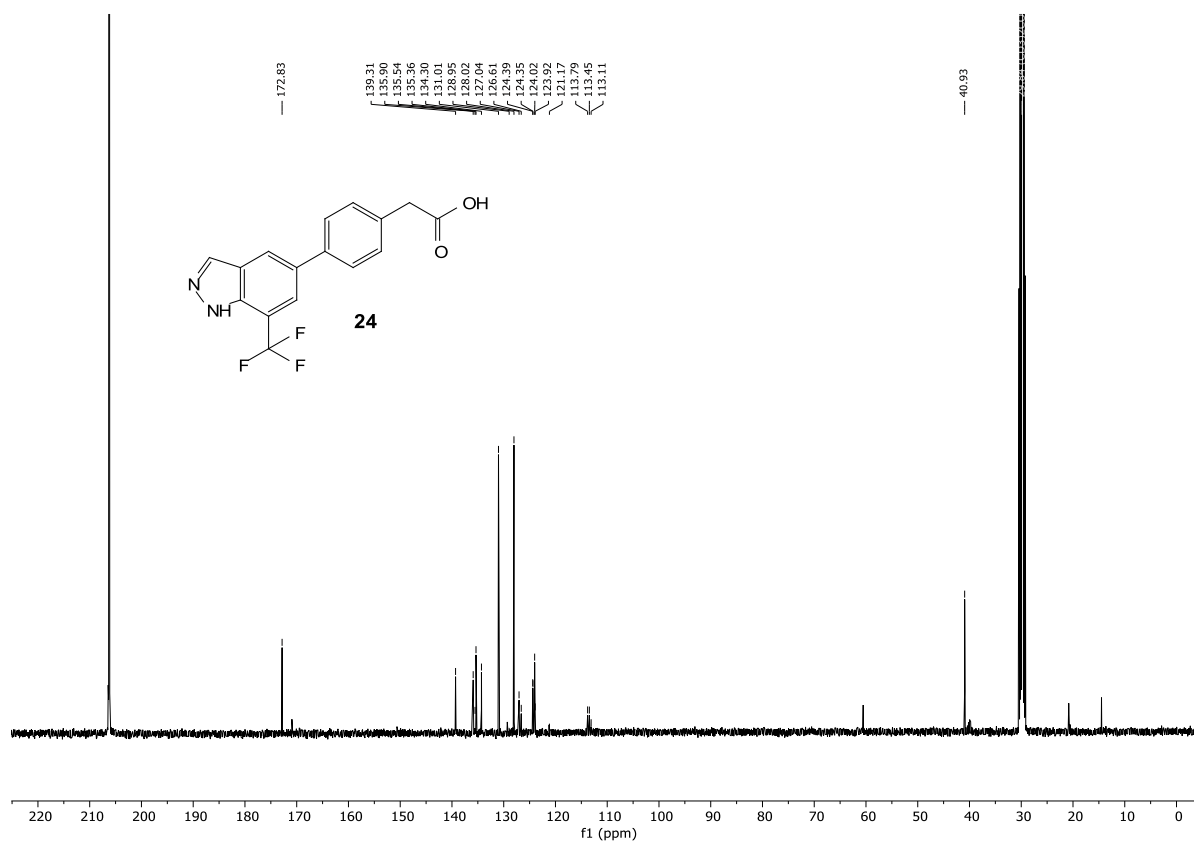


Compound **24**:

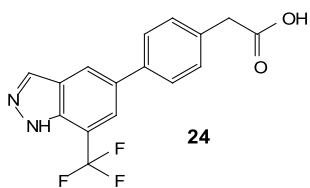
¹H-NMR:



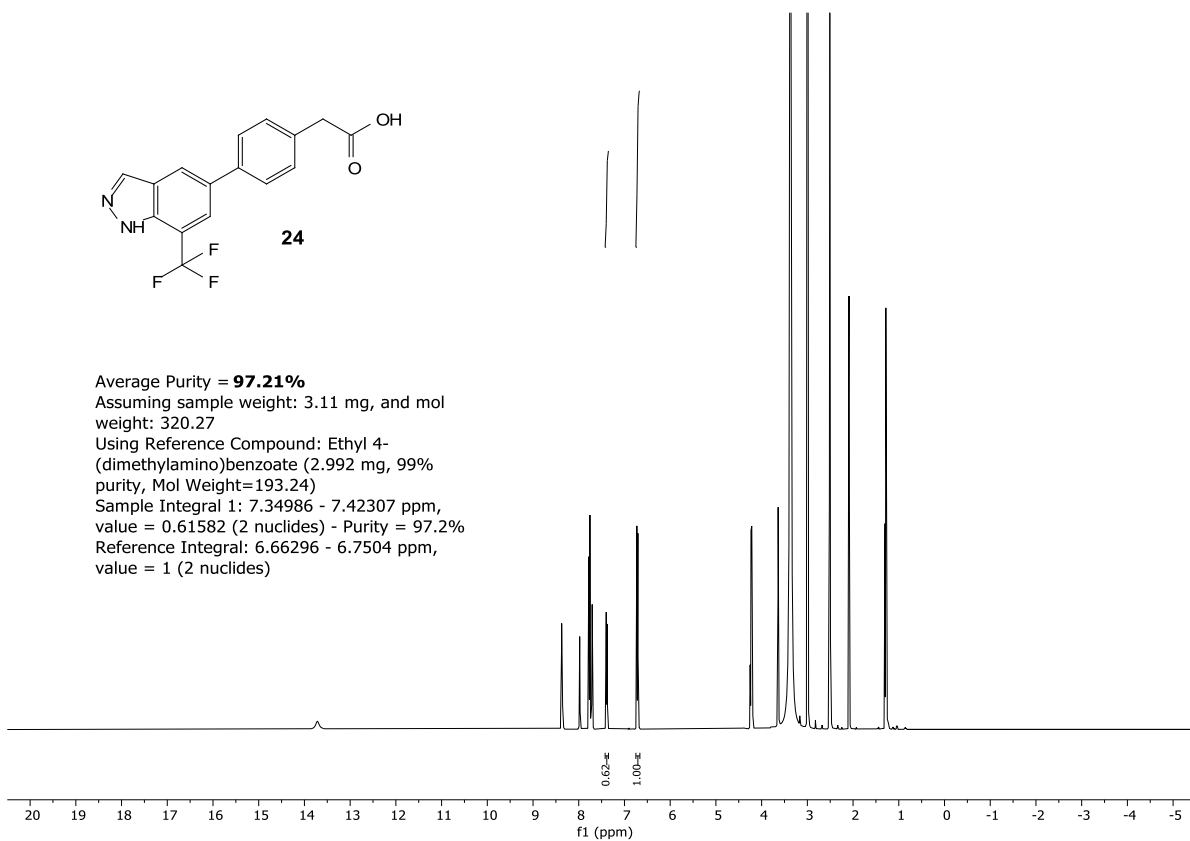
¹³C-NMR:



¹H-qNMR:

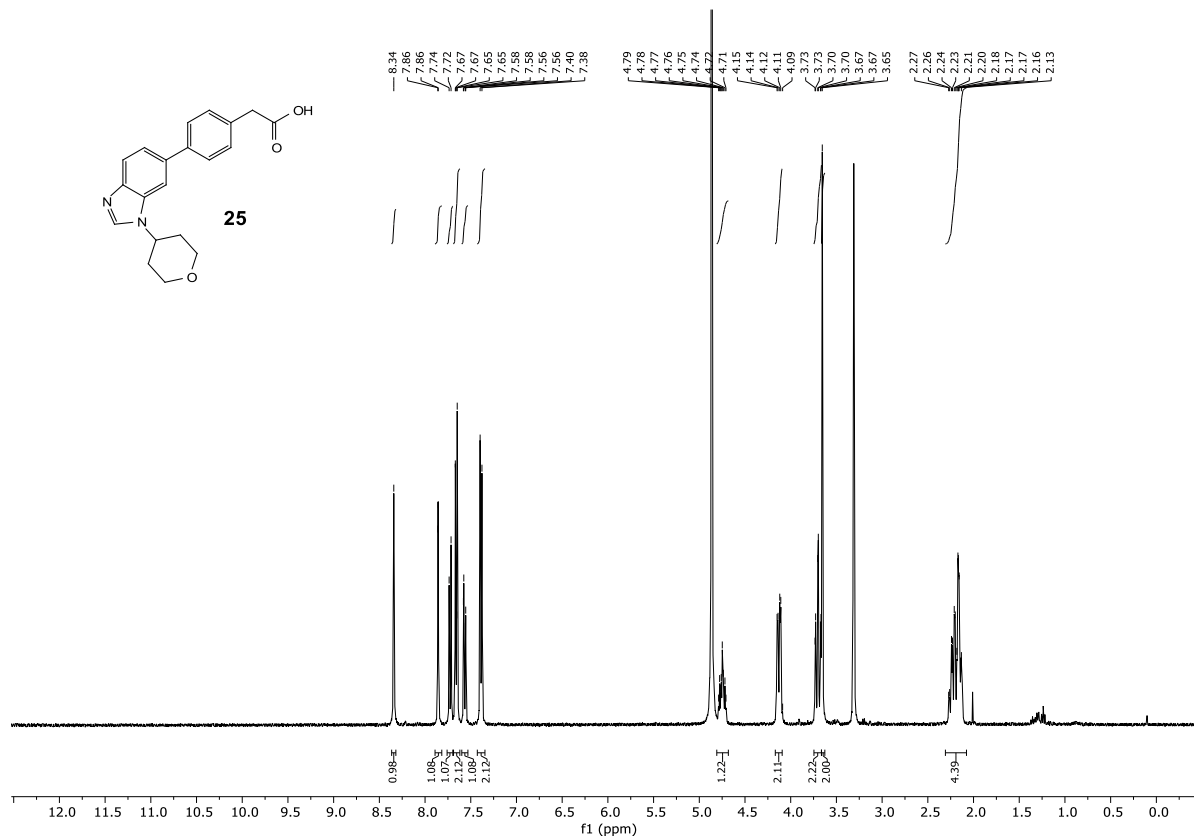


Average Purity = **97.21%**
Assuming sample weight: 3.11 mg, and mol weight: 320.27
Using Reference Compound: Ethyl 4-(dimethylamino)benzoate (2.992 mg, 99% purity, Mol Weight=193.24)
Sample Integral 1: 7.34986 - 7.42307 ppm, value = 0.61582 (2 nuclides) - Purity = 97.2%
Reference Integral: 6.66296 - 6.7504 ppm, value = 1 (2 nuclides)

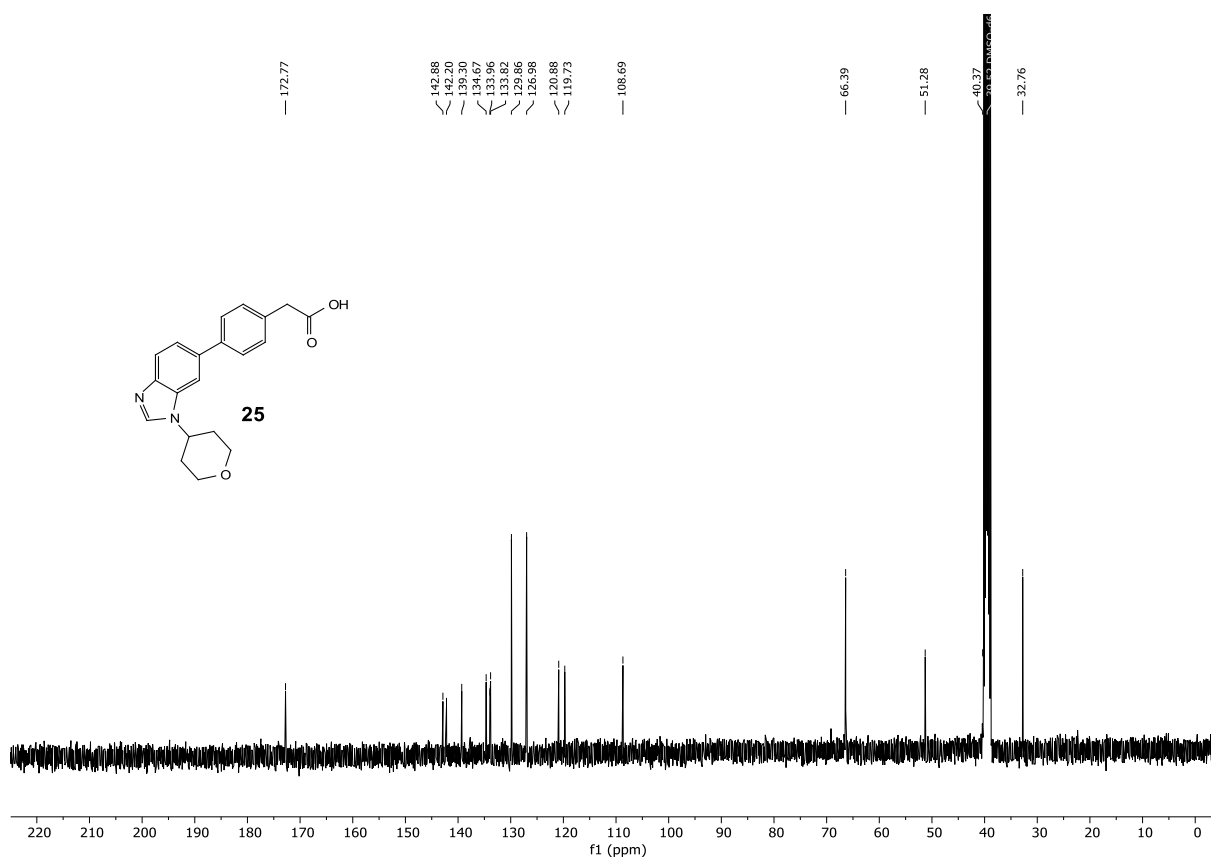


Compound **25**:

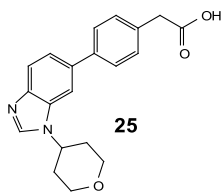
¹H-NMR:



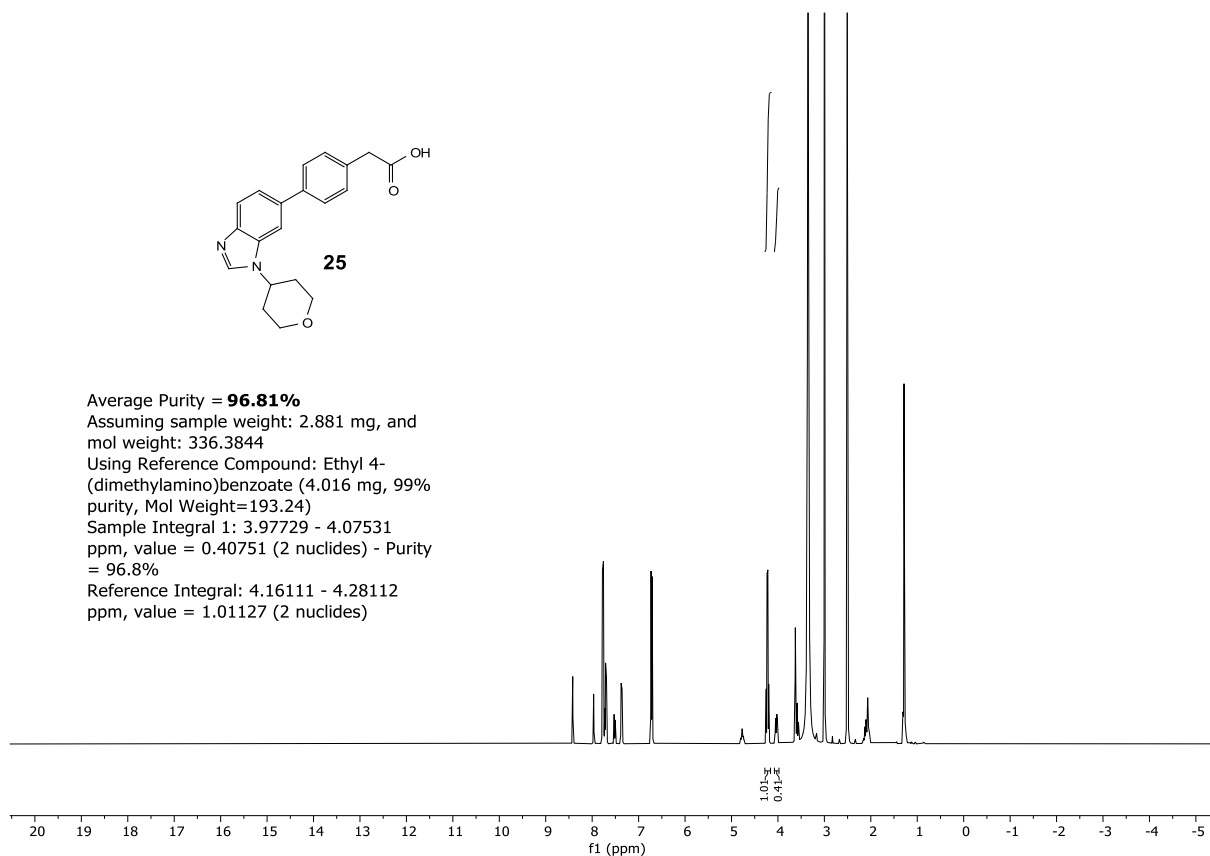
¹³C-NMR:



¹H-qNMR:

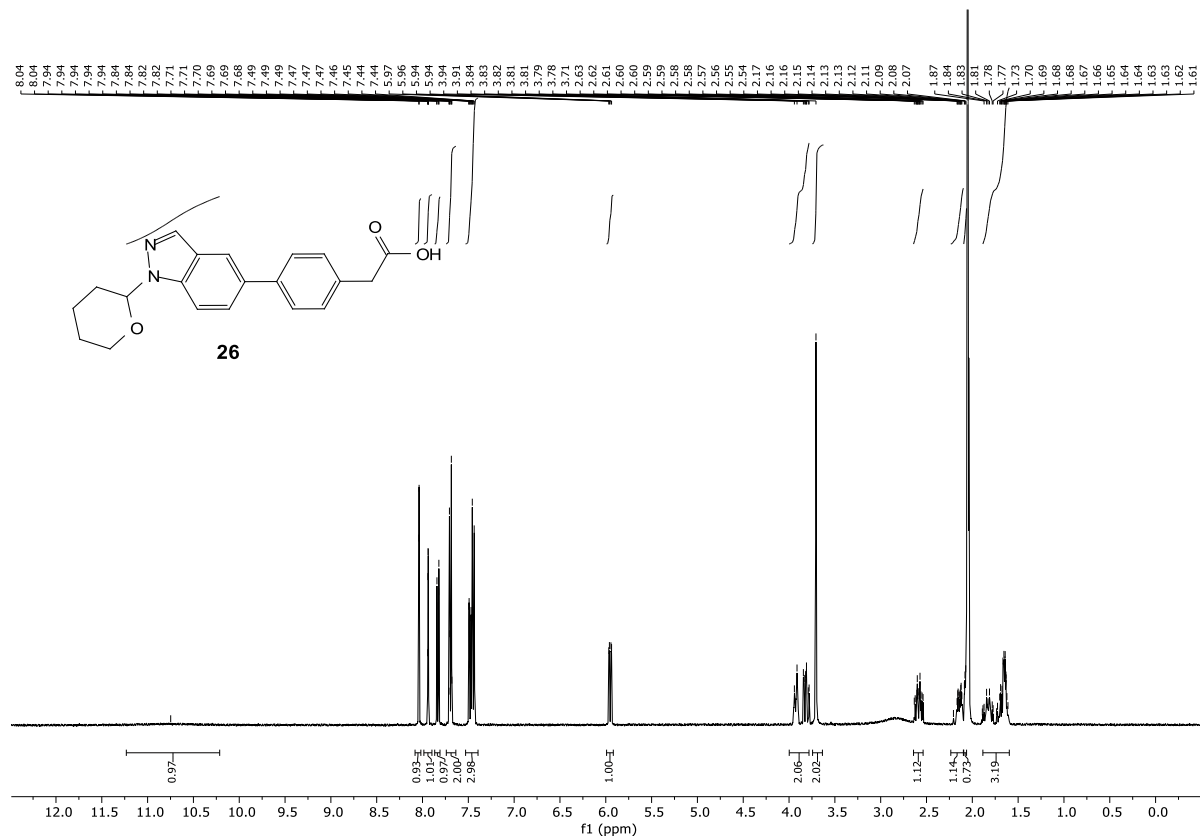


Average Purity = **96.81%**
Assuming sample weight: 2.881 mg, and
mol weight: 336.3844
Using Reference Compound: Ethyl 4-
(dimethylamino)benzoate (4.016 mg, 99%
purity, Mol Weight=193.24)
Sample Integral 1: 3.97729 - 4.07531
ppm, value = 0.40751 (2 nuclides) - Purity
= 96.8%
Reference Integral: 4.16111 - 4.28112
ppm, value = 1.01127 (2 nuclides)

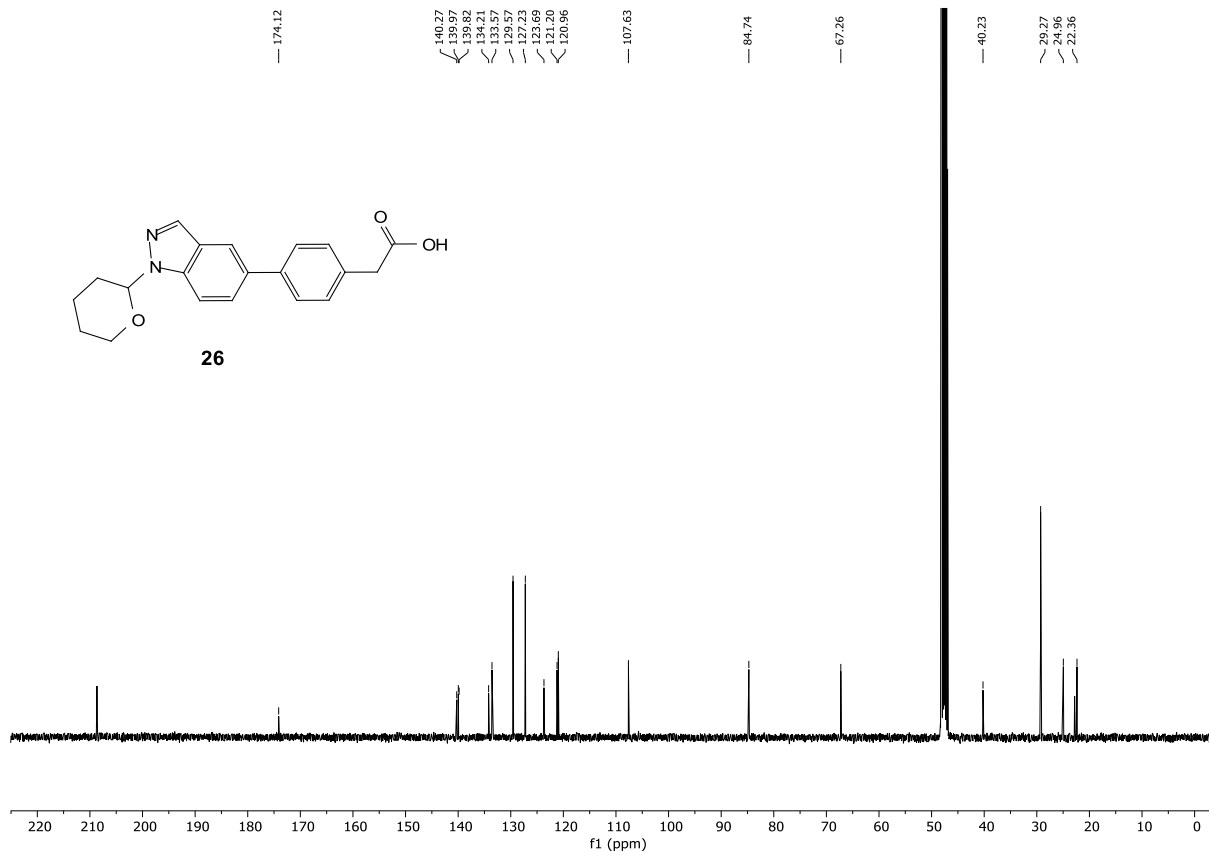


Compound 26:

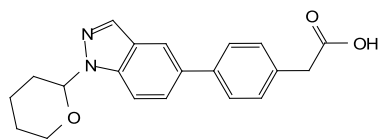
¹H-NMR:



¹³C-NMR:

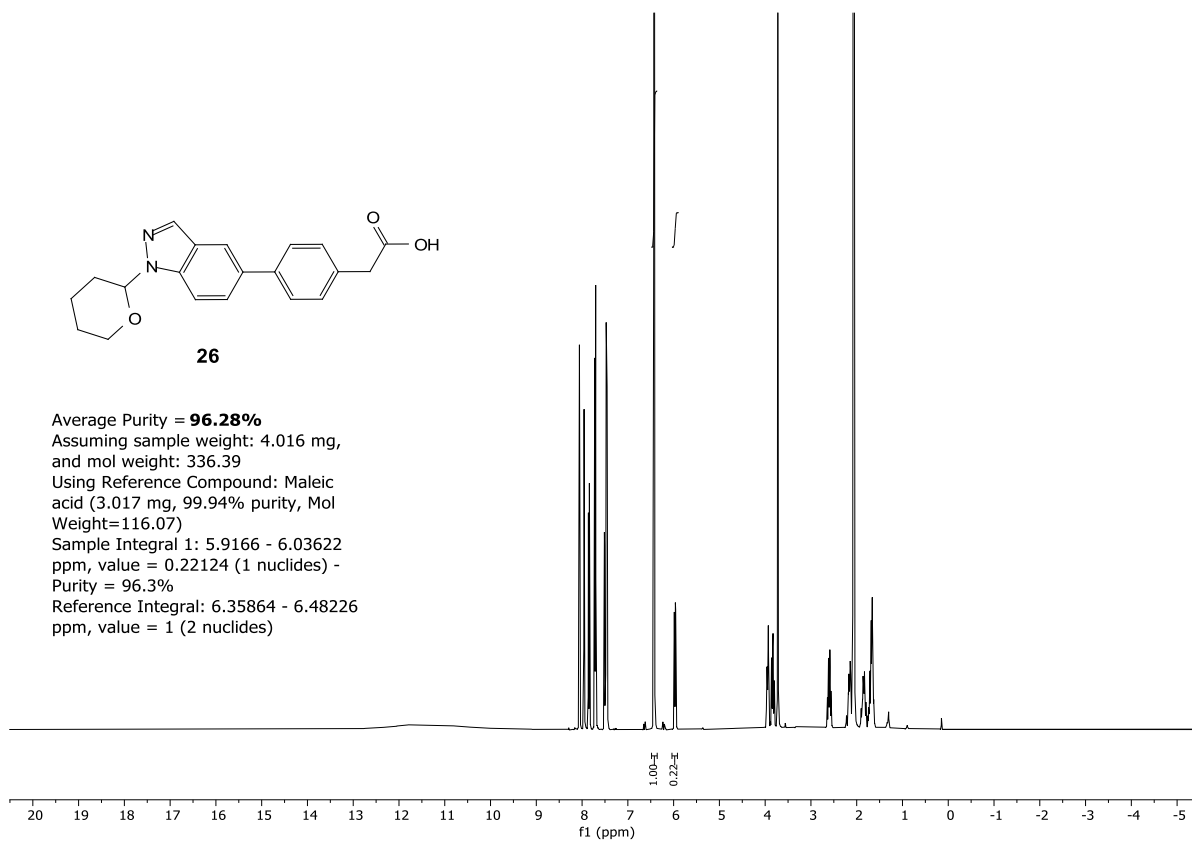


¹H-qNMR:



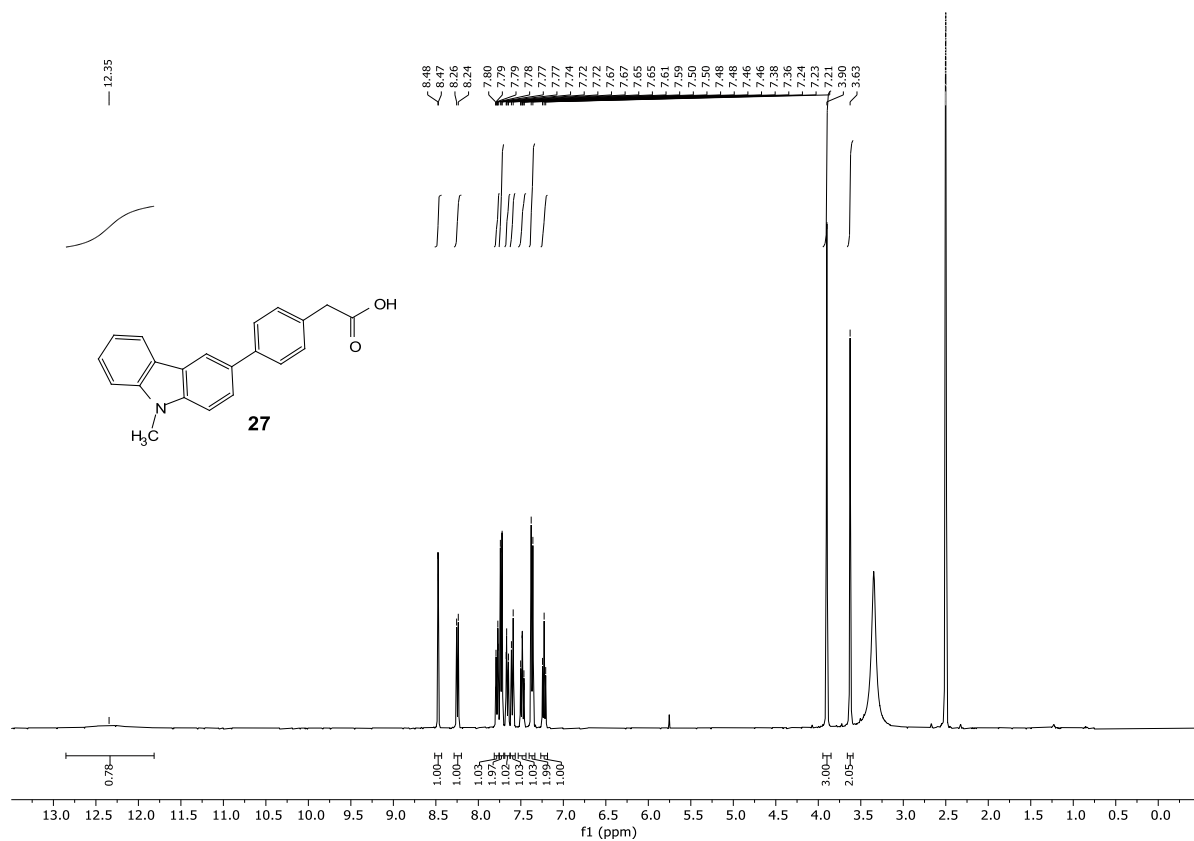
26

Average Purity = **96.28%**
Assuming sample weight: 4.016 mg,
and mol weight: 336.39
Using Reference Compound: Maleic
acid (3.017 mg, 99.94% purity, Mol
Weight=116.07)
Sample Integral 1: 5.9166 - 6.03622
ppm, value = 0.22124 (1 nuclides) -
Purity = 96.3%
Reference Integral: 6.35864 - 6.48226
ppm, value = 1 (2 nuclides)

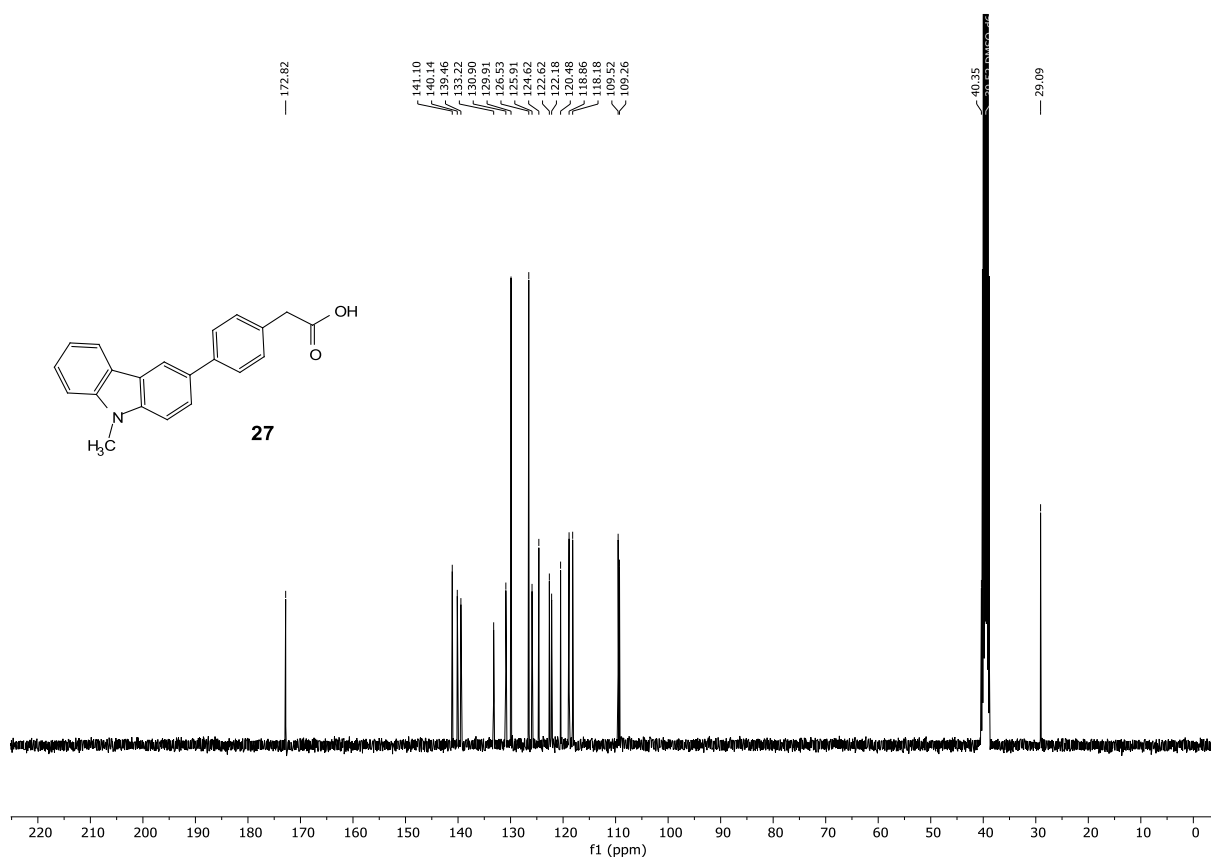


Compound 27:

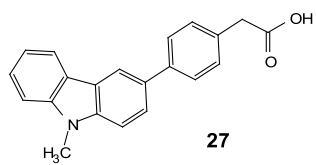
¹H-NMR:



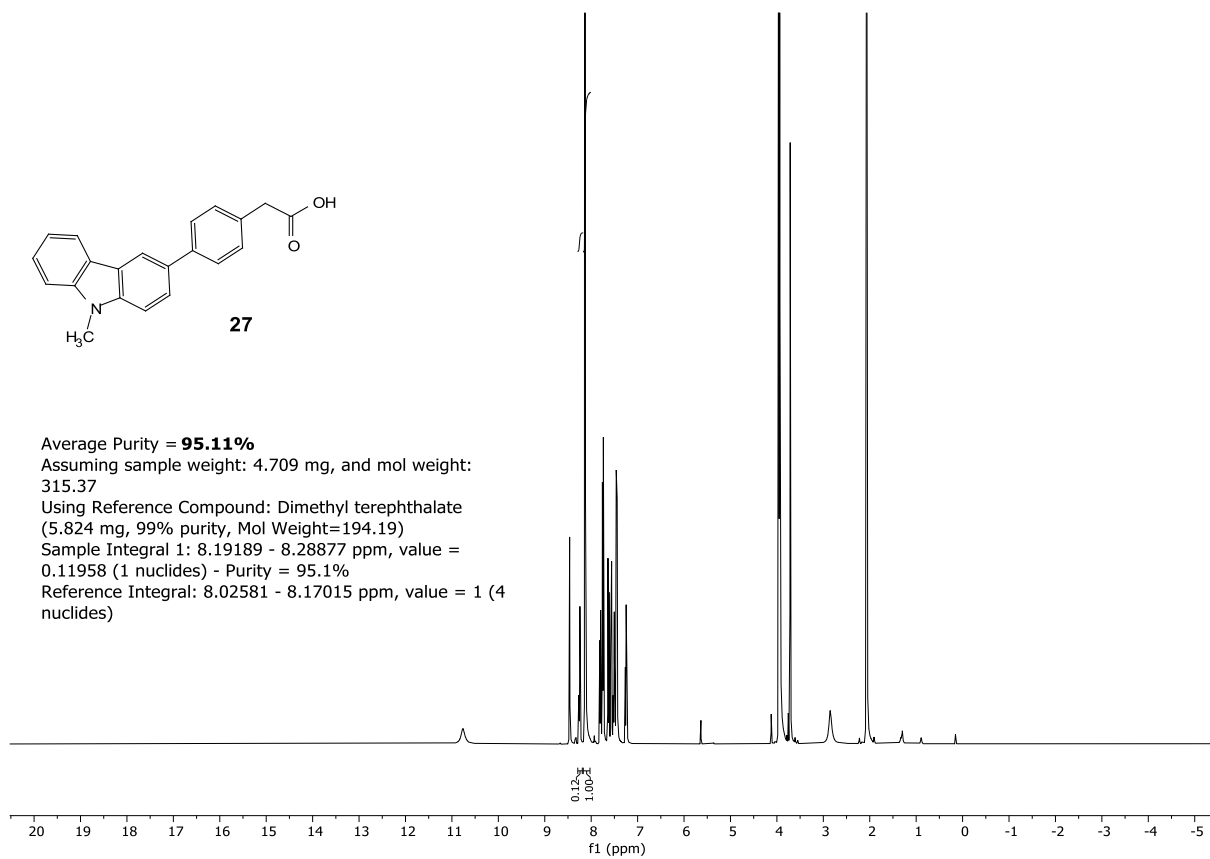
¹³C-NMR:



¹H-qNMR:

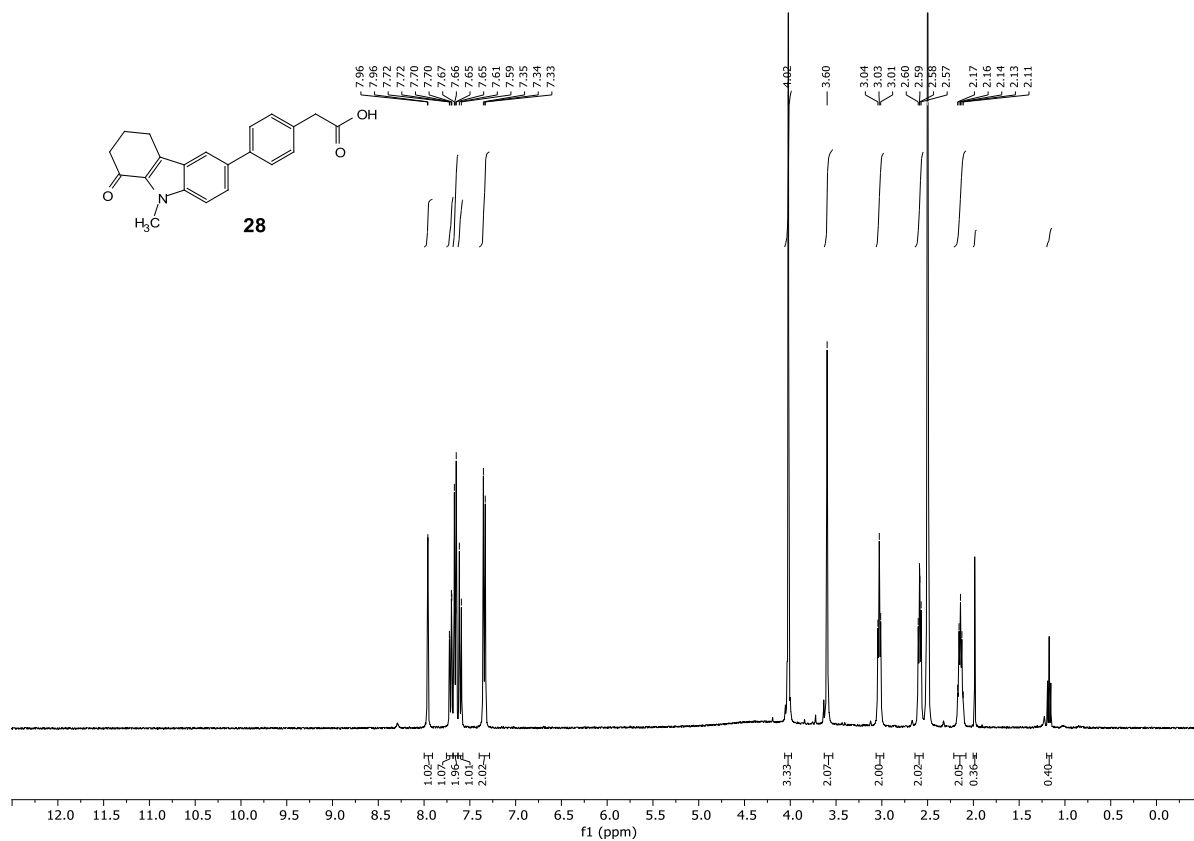


Average Purity = **95.11%**
Assuming sample weight: 4.709 mg, and mol weight:
315.37
Using Reference Compound: Dimethyl terephthalate
(5.824 mg, 99% purity, Mol Weight=194.19)
Sample Integral 1: 8.19189 - 8.28877 ppm, value =
0.11958 (1 nuclides) - Purity = 95.1%
Reference Integral: 8.02581 - 8.17015 ppm, value = 1 (4
nuclides)

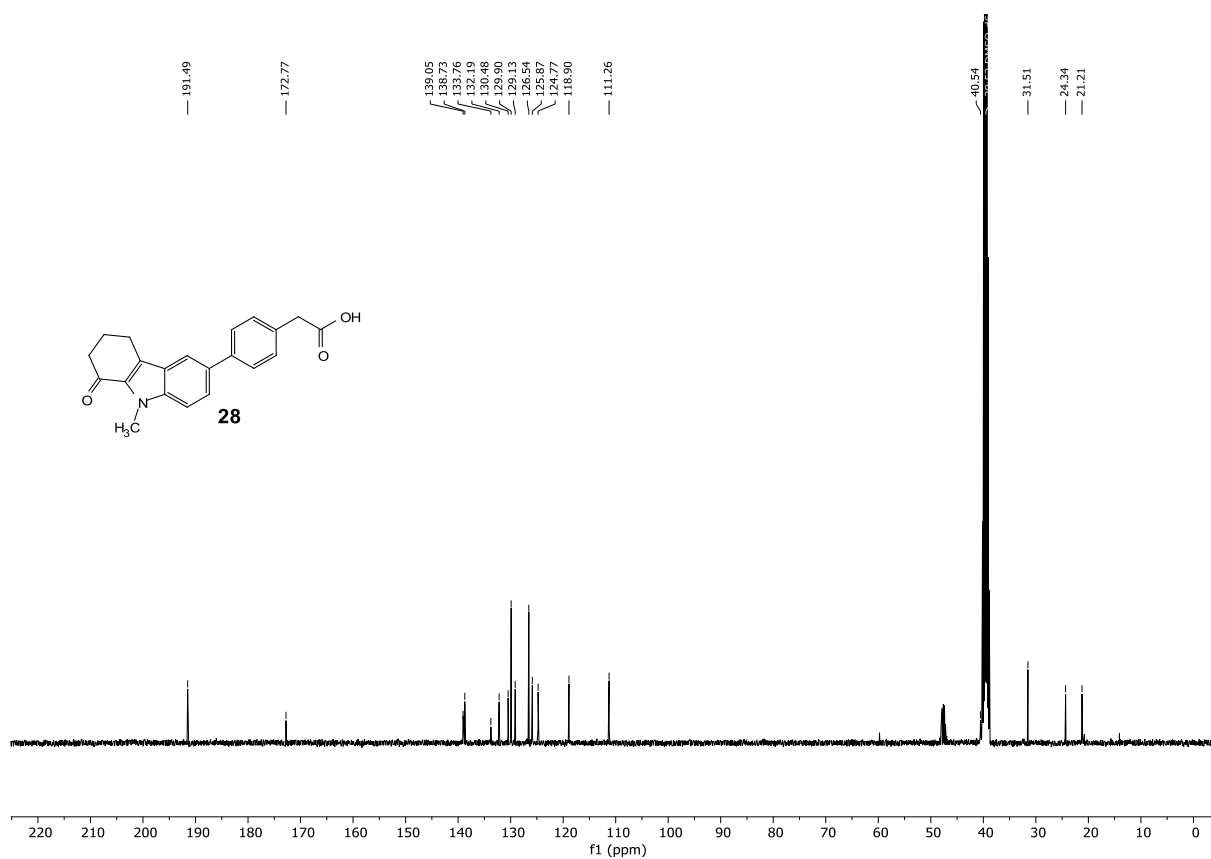


Compound **28**:

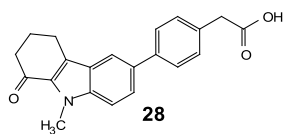
¹H-NMR:



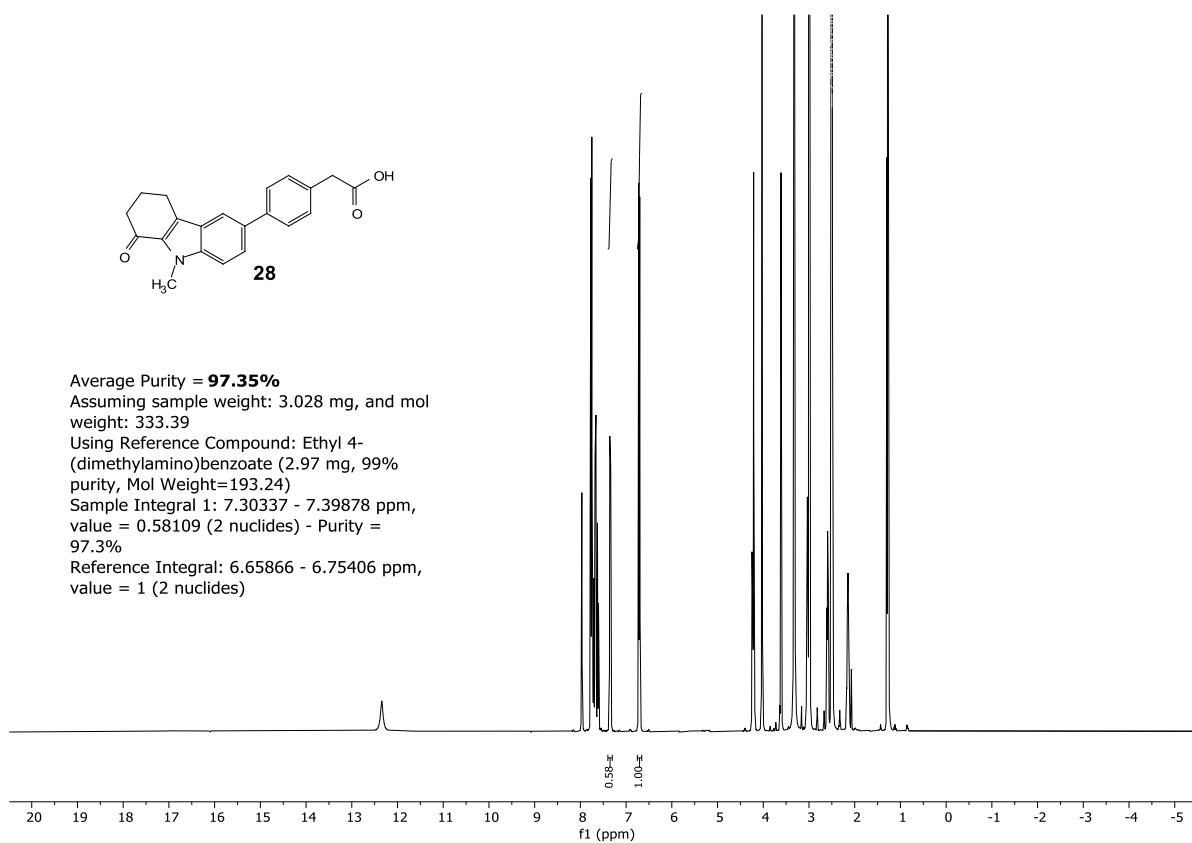
¹³C-NMR:



¹H-qNMR:

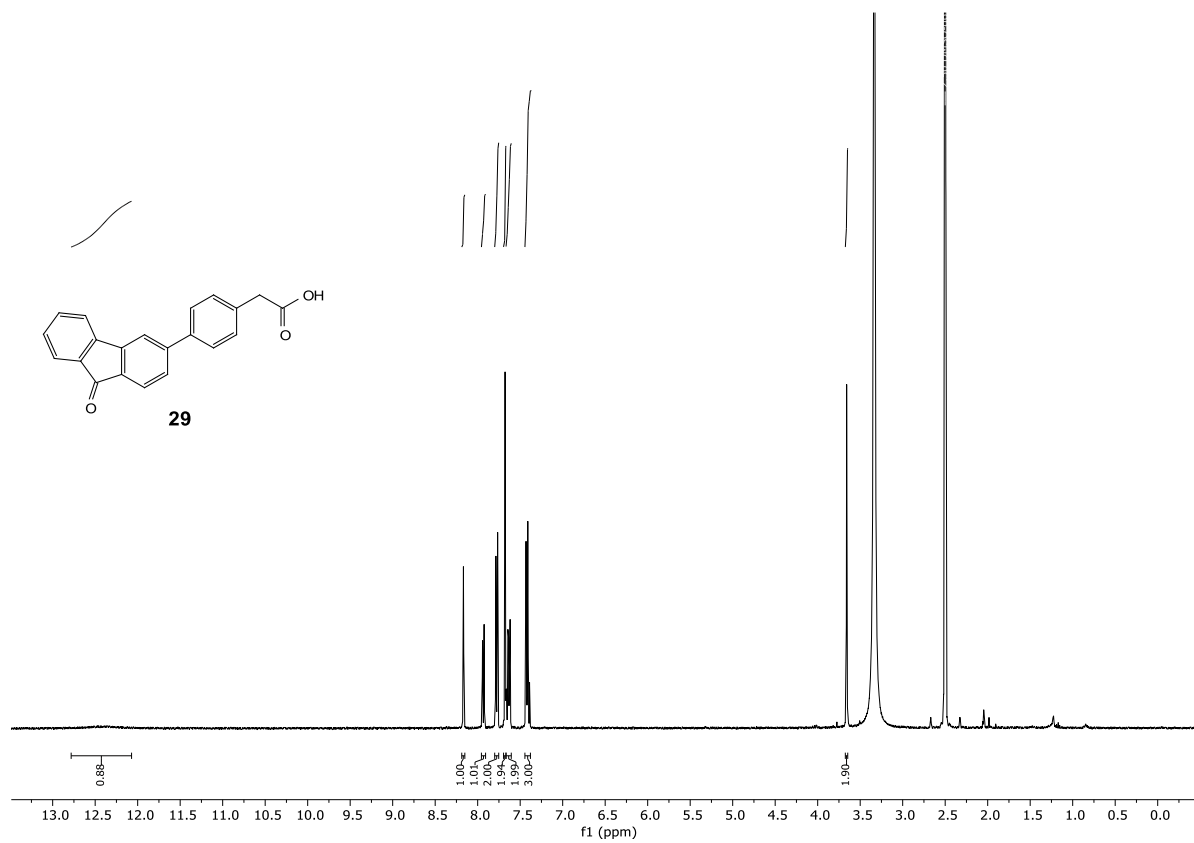


Average Purity = **97.35%**
Assuming sample weight: 3.028 mg, and mol weight: 333.39
Using Reference Compound: Ethyl 4-(dimethylamino)benzoate (2.97 mg, 99% purity, Mol Weight=193.24)
Sample Integral 1: 7.30337 - 7.39878 ppm, value = 0.58109 (2 nuclides) - Purity = 97.3%
Reference Integral: 6.65866 - 6.75406 ppm, value = 1 (2 nuclides)

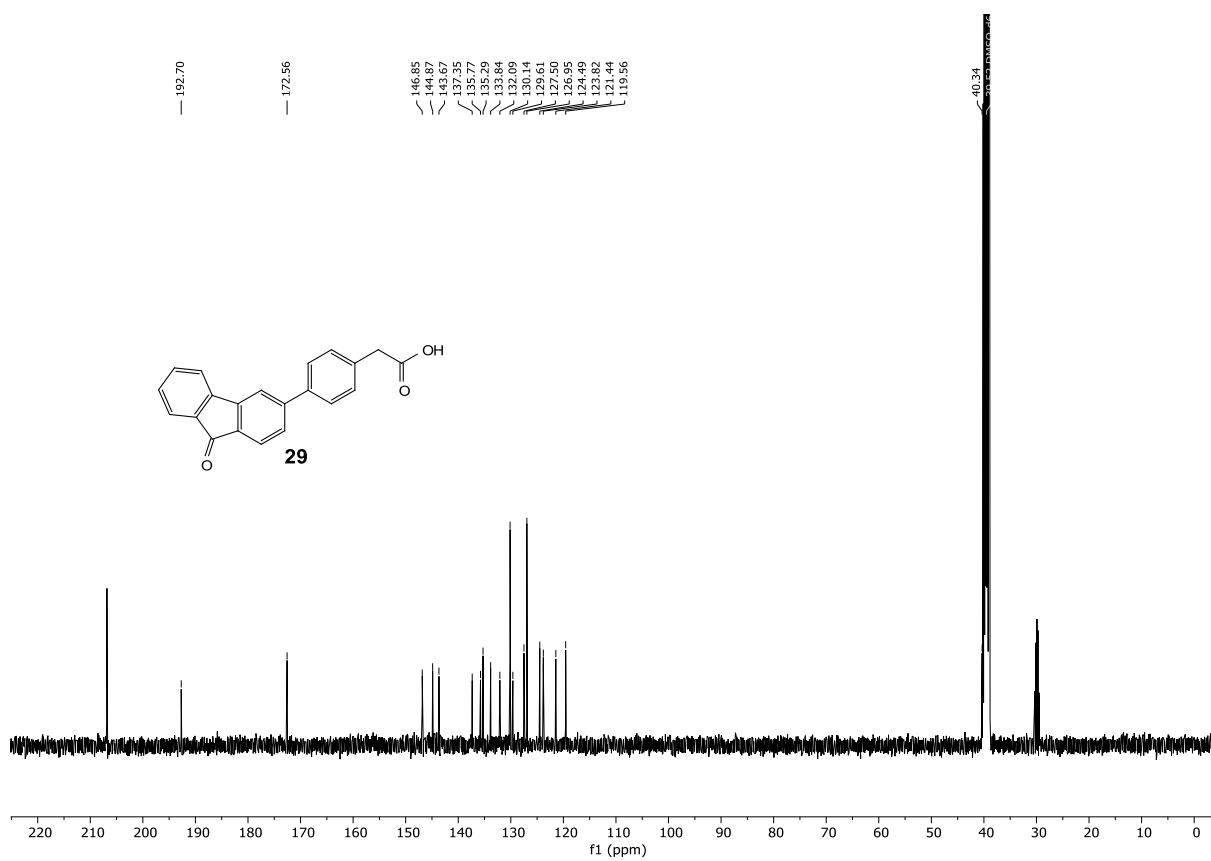


Compound **29**:

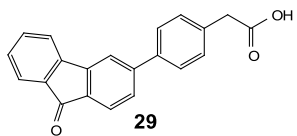
¹H-NMR:



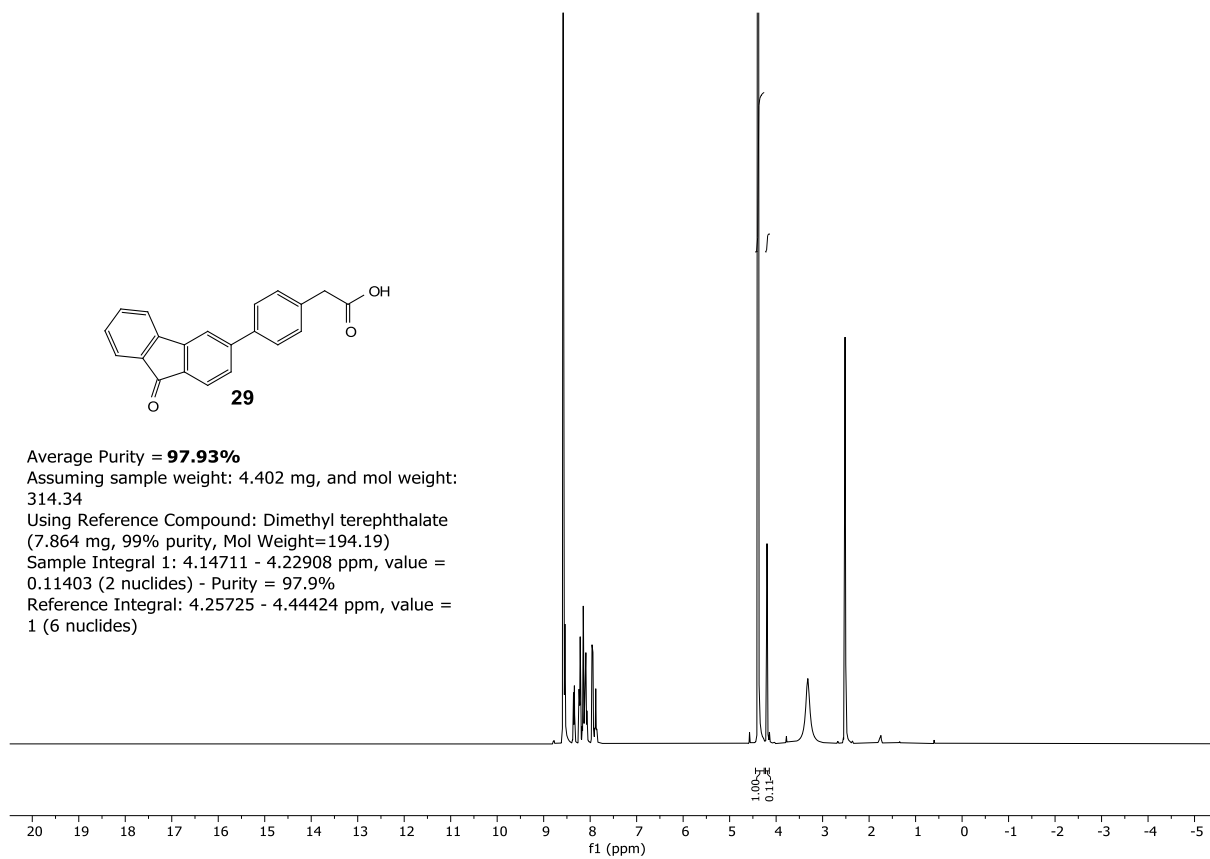
¹³C-NMR:



¹H-qNMR:

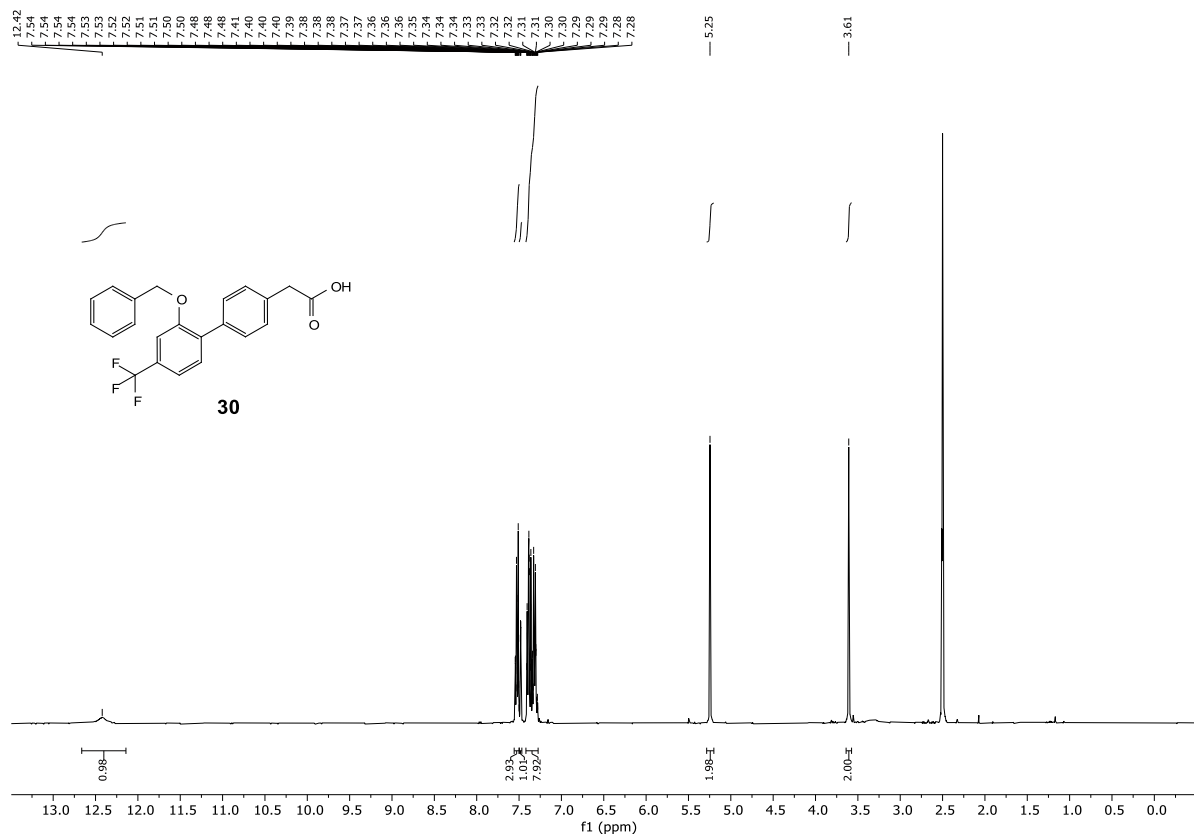


Average Purity = **97.93%**
Assuming sample weight: 4.402 mg, and mol weight:
314.34
Using Reference Compound: Dimethyl terephthalate
(7.864 mg, 99% purity, Mol Weight=194.19)
Sample Integral 1: 4.14711 - 4.22908 ppm, value =
0.11403 (2 nuclides) - Purity = 97.9%
Reference Integral: 4.25725 - 4.44424 ppm, value =
1 (6 nuclides)

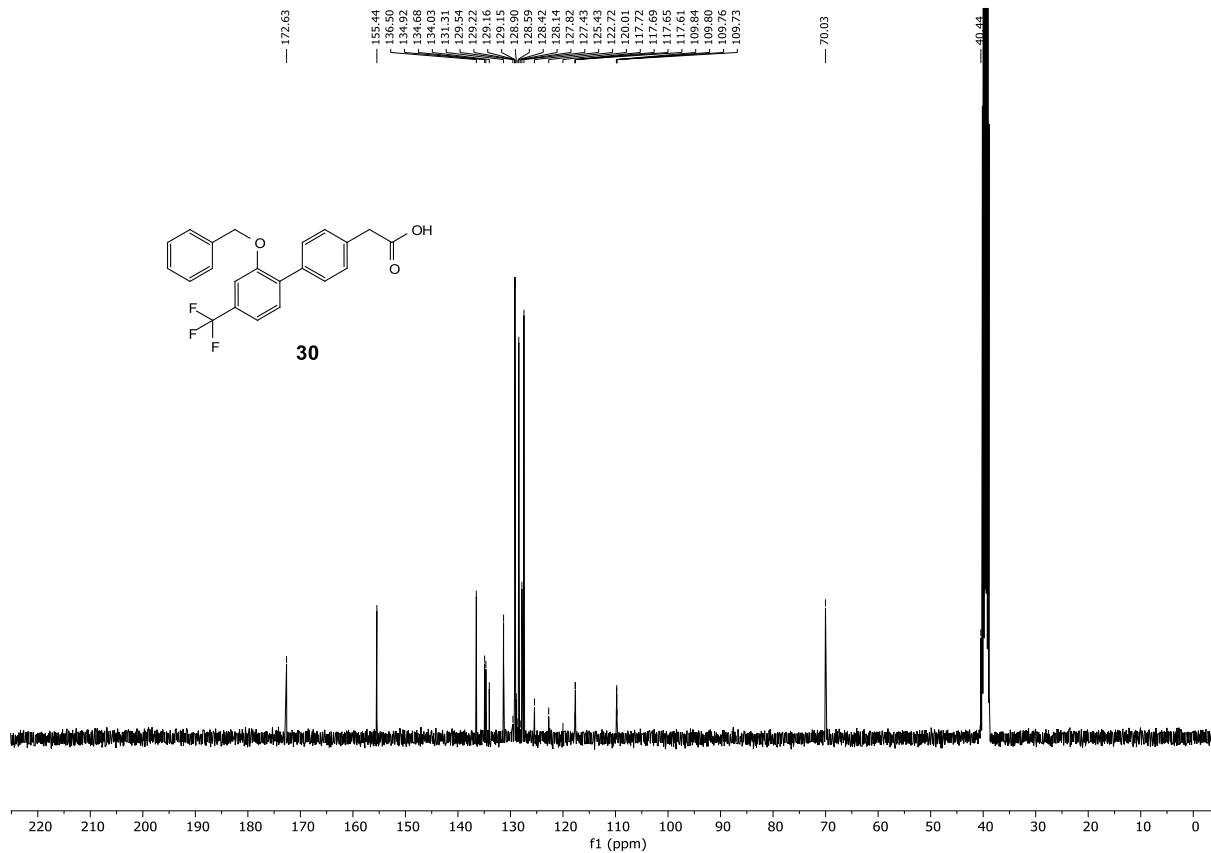


Compound 30:

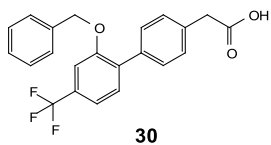
¹H-NMR:



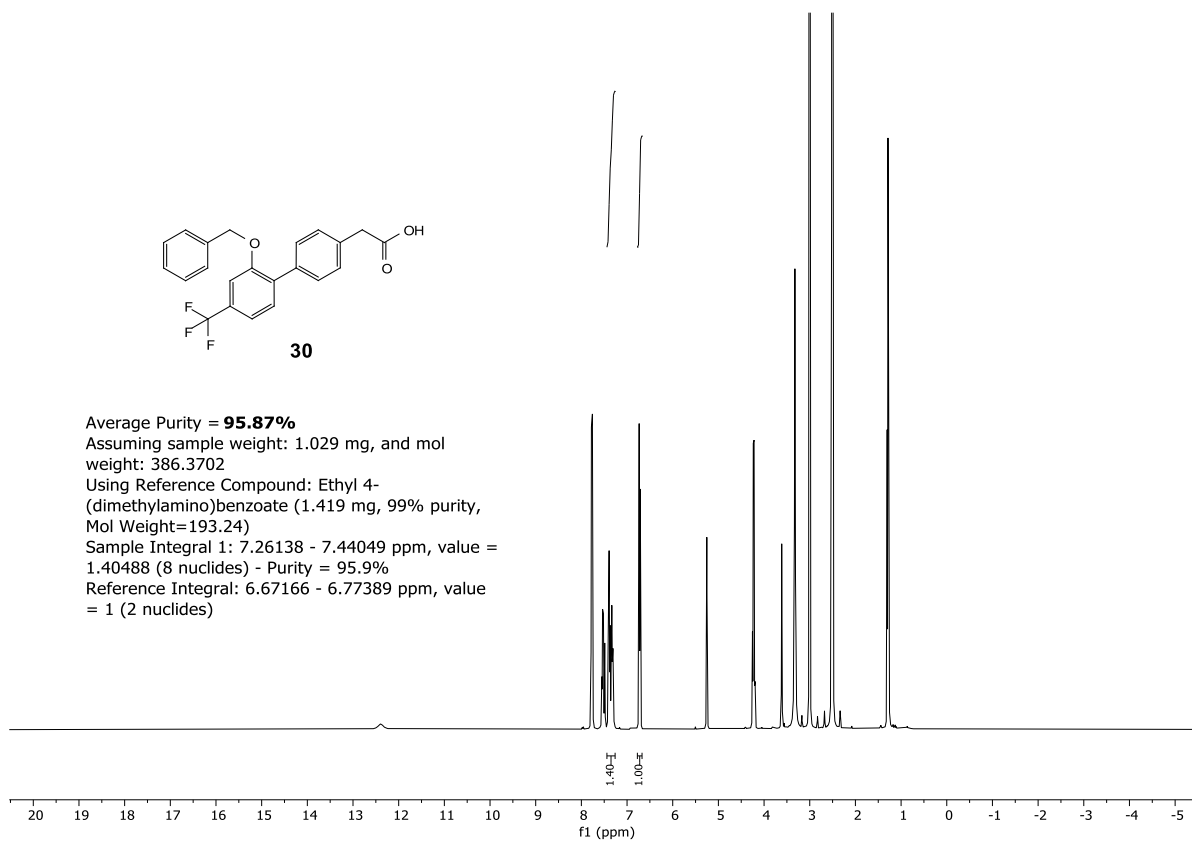
¹³C-NMR:



¹H-qNMR:

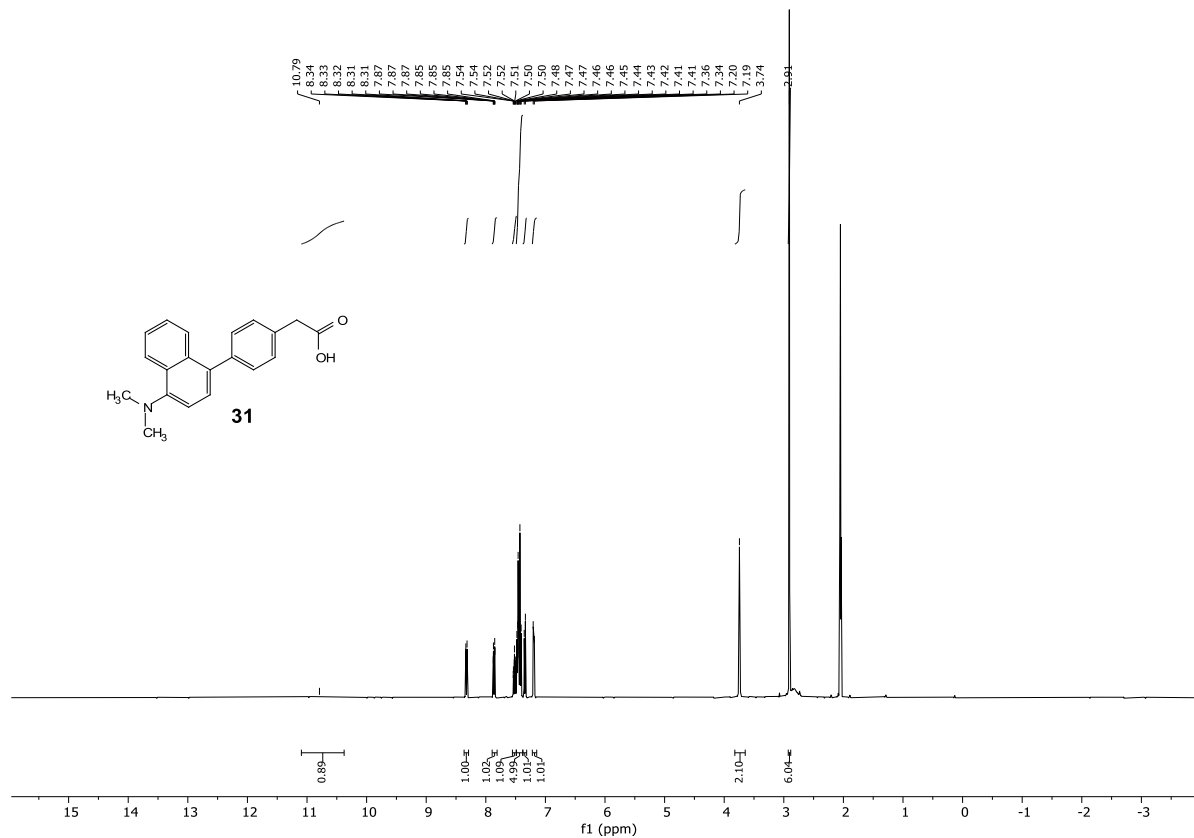


Average Purity = **95.87%**
Assuming sample weight: 1.029 mg, and mol weight: 386.3702
Using Reference Compound: Ethyl 4-(dimethylamino)benzoate (1.419 mg, 99% purity, Mol Weight=193.24)
Sample Integral 1: 7.26138 - 7.44049 ppm, value = 1.40488 (8 nuclides) - Purity = 95.9%
Reference Integral: 6.67166 - 6.77389 ppm, value = 1 (2 nuclides)

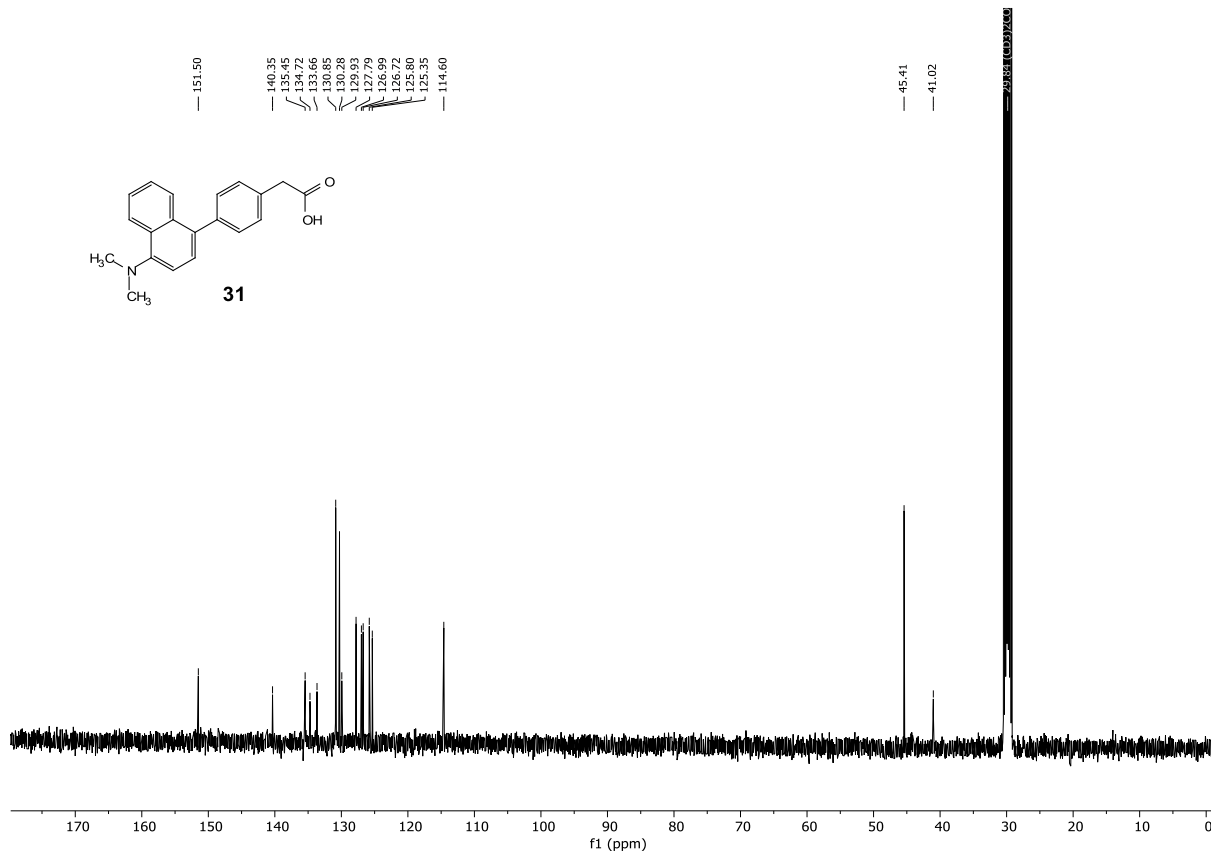


Compound **31**:

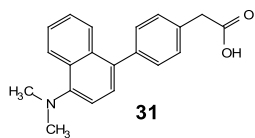
¹H-NMR:



¹³C-NMR:



¹H-qNMR:



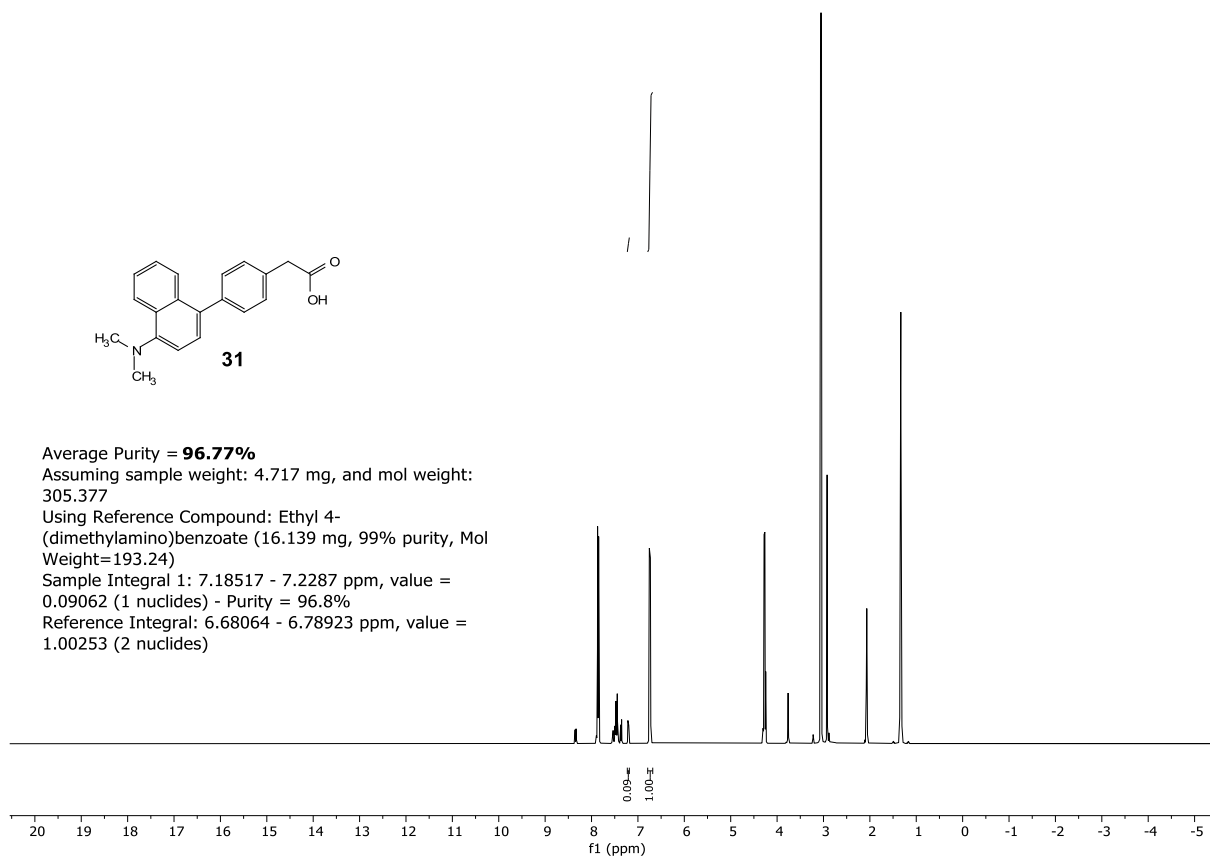
Average Purity = **96.77%**

Assuming sample weight: 4.717 mg, and mol weight:
305.377

Using Reference Compound: Ethyl 4-
(dimethylamino)benzoate (16.139 mg, 99% purity, Mol
Weight=193.24)

Sample Integral 1: 7.18517 - 7.2287 ppm, value =
0.09062 (1 nuclides) - Purity = 96.8%

Reference Integral: 6.68064 - 6.78923 ppm, value =
1.00253 (2 nuclides)



References

- (1) Pollinger, J.; Schierle, S.; Gellrich, L.; Ohrndorf, J.; Kaiser, A.; Heitel, P.; Chaikuad, A.; Knapp, S.; Merk, D. A Novel Biphenyl-Based Chemotype of Retinoid X Receptor Ligands Enables Subtype and Heterodimer Preferences. *ACS Med. Chem. Lett.* **2019**, *10* (9), 1346–1352. doi: 10.1021/acsmchemlett.9b00306.
- (2) Shelley, J. C.; Cholleti, A.; Frye, L. L.; Greenwood, J. R.; Timlin, M. R.; Uchimaya, M. Epik: A Software Program for PKa Prediction and Protonation State Generation for Drug-like Molecules. *J. Comput. Aided. Mol. Des.* **2007**, *21* (12), 681–691. doi: 10.1007/s10822-007-9133-z.
- (3) Borrelli, K. W.; Cossins, B.; Guallar, V. Exploring Hierarchical Refinement Techniques for Induced Fit Docking with Protein and Ligand Flexibility. *J. Comput. Chem.* **2010**, *31* (6), 1224–1235. doi: 10.1002/jcc.21409.

12.4 Azologs of the fatty acid mimetic drug cinalukast enable light-induced PPAR α activation

Sai, M.; van Herwijnen, N.; Merk, D. Azologs of the fatty acid mimetic drug cinalukast enable light-induced PPAR α activation. *ChemMedChem*, 2024, e20240032 (2024).

Reprinted with permission from Sai, M.; van Herwijnen, N.; Merk, D. Azologs of the fatty acid mimetic drug cinalukast enable light-induced PPAR α activation. *ChemMedChem*, 2024, e20240032 (2024).

Azologs of the Fatty Acid Mimetic Drug Cinalukast Enable Light-Induced PPAR α Activation

Minh Sai,^[a] Niels van Herwijnen,^[a] and Daniel Merk^{*[a]}

Photo-switchable nuclear receptor modulators (“photohormones”) enable spatial and temporal control over transcription factor activity and are valuable precision tools for biological studies. We have developed a new photohormone chemotype by incorporating a light-switchable motif in the scaffold of a cinalukast-derived PPAR α ligand and tuned light-controlled

activity by systematic structural variation. An optimized photohormone exhibited PPAR α agonism in its light-induced (*Z*)-configuration and strong selectivity over related lipid-activated transcription factors representing a valuable addition to the collection of light-controlled tools to study nuclear receptor activity.

Introduction

The peroxisome proliferator-activated receptor (PPAR) α is a fatty acid sensing transcription factor and a master metabolic regulator.^[1] It is found in tissues with high metabolic activity like liver and adipose tissue and governs fatty acid catabolism by β -oxidation, lipid transport and gluconeogenesis.^[2–4] Fibrates acting as PPAR α agonists have therapeutic relevance as lipid lowering agents and glitazars activating the PPAR α and γ isoforms are evaluated for the treatment of the highly prevalent metabolism associated fatty liver disease (MAFLD).^[5–7] Additionally, there is preliminary evidence for a beneficial role of PPAR α activation, for example, in chronic obstructive pulmonary disease^[8] and neuroinflammation^[9,10] indicating further potential. Nevertheless, available PPAR α agonists are also associated with adverse effects among which rhabdomyolysis is most critical.^[11]

Photopharmacology is a promising approach to achieve spatial and temporal control over protein activity utilizing photo-switchable bioactive molecules.^[12,13] Such agents are typically obtained by incorporation of a molecular photo-switch like an azobenzene motif in the scaffold of a ligand of the protein of interest.^[12,13] This concept has been successfully implemented for multiple types of protein targets and in the control of various biological processes.^[14] Light-controlled bioactive molecules are very valuable as high-precision tools and may have unprecedented therapeutic potential owing to their ability to be locally activated.

We have previously developed a photo-switchable PPAR α agonist that was active in the stable (*E*)-configuration and could be deactivated by light-induced isomerization to the (*Z*)-configuration.^[15] While this compound valuably enabled optical control of PPAR α activity in cells, (*Z*)-active photohormones are preferable for optical control since full photo-switching to 100% (*Z*)-configuration is not achieved with azobenzenes.^[13] Based on the CysLT₁R antagonist cinalukast, we have previously developed the PPAR α agonist **1** (Figure 1) lacking activity on original target CysLT₁R following the approach of selective optimization of side-activities (SOSA).^[16,17] The structure of **1** comprising a styrylthiazole motif appeared suitable for azologization and the potential development of a novel light-controlled PPAR α ligand. By replacing the styrylthiazole of **1** by a stilbene or an azobenzene motif, we successfully obtained photoswitchable PPAR α modulators (**2**, **3**) that could be engineered to a light-activated agonist by variation of the hydrophobic substitution pattern. With >10-fold higher potency in the light-induced (*Z*)-configuration, the obtained photohormone **9** emerges as a valuable tool to study PPAR α biology.

Results and Discussion

Chemistry

The stilbene analogue **2** of **1** was prepared over five steps according to Scheme 1. 3-Bromobenzaldehyde (**14**) and 3,4-

[a] M. Sai, N. van Herwijnen, Prof. Dr. D. Merk
Ludwig-Maximilians-Universität München
Department of Pharmacy
81377 Munich, Germany
E-mail: daniel.merk@cup.lmu.de

Supporting information for this article is available on the WWW under <https://doi.org/10.1002/cmdc.202400327>

© 2024 The Authors. ChemMedChem published by Wiley-VCH GmbH. This is an open access article under the terms of the Creative Commons Attribution License, which permits use, distribution and reproduction in any medium, provided the original work is properly cited.

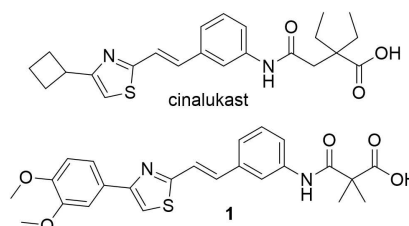
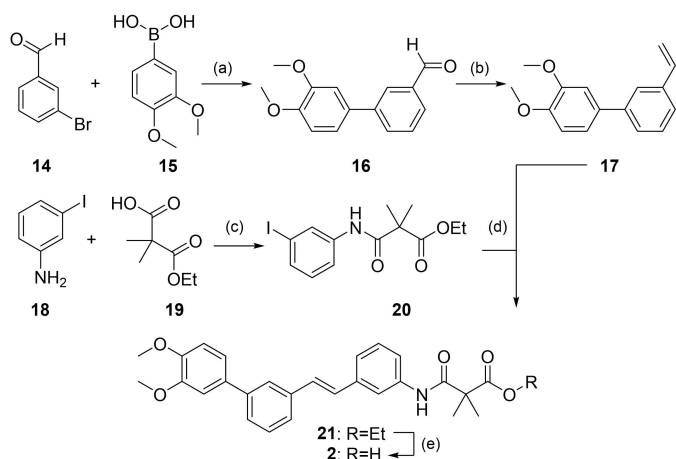


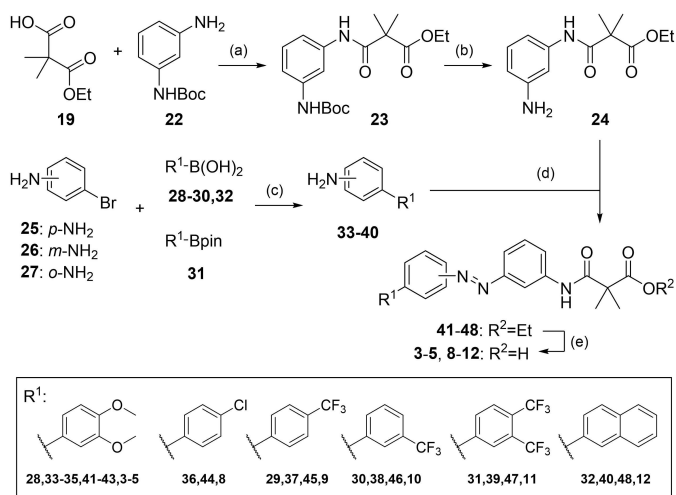
Figure 1. Chemical structures of cinalukast and the cinalukast-derived PPAR α agonist **1**.



Scheme 1. Synthesis of **2**. Reagents & Conditions: (a) XPhos Pd G2, K_3PO_4 , water/dioxane, reflux, overnight, 83%; (b) methyltriphenylphosphonium bromide, $KOtBu$, THF, $0^\circ C \rightarrow rt$, overnight, 94%; (c) HATU, DIPEA, DMF, rt, overnight, 95%; (d) $Pd(OAc)_2$, K_3PO_4 , DMA, $140^\circ C$, overnight, 42%; (e) $LiOH$, water/THF, rt, overnight, 72%.

dimethoxyphenylboronic acid (**15**) were coupled in a Suzuki reaction and the product **16** was treated with methyltriphenylphosphonium bromide in a Wittig reaction to obtain **17**. Additionally, amide coupling of 3-iodoaniline (**18**) and ethyl 2,2-dimethylmalonate (**19**) afforded **20** which was reacted with **17** under Heck conditions to the ester precursor **21** and alkaline ester hydrolysis of **21** yielded **2**.

The azobenzene derivatives **3–5** and **8–12** were prepared according to Scheme 2. The amine **24** comprising the acidic head group was obtained by amide coupling of **19** and *N*-Boc-3-phenylenediamine (**22**), followed by deprotection. The corresponding amines **33–40** representing the lipophilic backbones were prepared by Suzuki reaction of the bromoanilines **25–27** with the boronates **28–32**. Subsequent Baeyer-Mills coupling



Scheme 2. Synthesis of azobenzene derivatives **3–5** and **8–12**. Reagents & Conditions: (a) HATU, DIPEA, DMF, rt, overnight, quant.; (b) TFA, rt, overnight, quant.; (c) XPhos Pd G2, K_3PO_4 , water/dioxane, reflux, overnight, 44–95%; (d) Oxone, DCM, rt, 1–3 h, then DCM, HOAc, rt, 1–2 days, 3–59%; (e) $LiOH$, water/THF, rt, overnight, 40–95%.

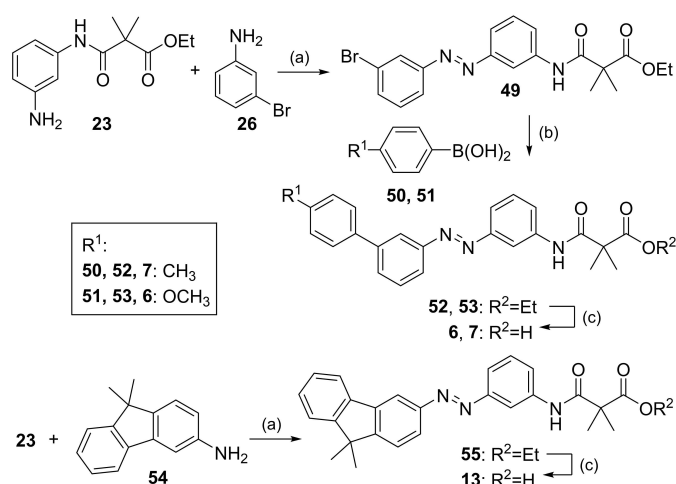
was carried out by oxidation of **24** with Oxone®, and subsequent reaction of the nitroso intermediate with the amines **33–40** to obtain **41–48** which afforded the desired photo-switchable PPAR modulators **3–5** and **8–12** after alkaline ester hydrolysis.

For the preparation of azobenzenes **6** and **7**, the reaction sequence was adapted and Baeyer-Mills coupling was performed first with **23** and 3-bromoaniline (**26**) to obtain the diazobenzene **49** (Scheme 3). Subsequently, **49** was reacted with the boronic acids **50** and **51** in Suzuki reactions yielding **52** and **53** and ester hydrolysis afforded compounds **6** and **7**. Similarly, **13** was prepared from **23** by Baeyer-Mills coupling with 9,9-dimethyl-9*H*-fluoren-3-amine (**54**) to **55** and subsequent ester hydrolysis to **13** (Scheme 3).

Photohormone Development and Profiling

To probe the potential of the scaffold of **1** to obtain photohormones, we prepared the stilbene analogue **2** (Figure 2a) which is bistable in (*E*)- and (*Z*)-configuration. Screening of **2** on lipid-sensing nuclear receptors revealed agonism of both isomers on $RAR\alpha$, PPARs and FXR. In line with the activity of the template compound **1**, PPAR α agonism emerged as most pronounced activity of **2** validating our design hypothesis. Encouraged by this profile, we prepared and tested the azobenzene analogue **3** (Figure 2b), which also exhibited robust PPAR agonism with preference for PPAR α and was more selective over $RAR\alpha$ and FXR than **2**. Full dose-response profiling (Table 1) confirmed (*E*)-**3** as potent PPAR α agonist (EC_{50} 3 μM) with lower efficacy of the (*Z*)-isomer. **3** exhibited favorable photophysical characteristics enabling efficient and repeated photo-switching (Supplementary Figure 1) and thus appeared suitable as lead for photohormone development.

Based on its favorable photophysical characteristics and light-dependent activity we selected the azobenzene **3** as lead



Scheme 3. Synthesis of azobenzene derivatives **6**, **7** and **13**. Reagents & Conditions: (a) Oxone, DCM, rt, 1 h, then DCM, HOAc, rt, 2 days, 59–60%; (b) XPhos Pd G2, K_3PO_4 , water/dioxane, reflux, overnight, 91–94%; (c) $LiOH$, water/THF, rt, overnight, 77–99%.

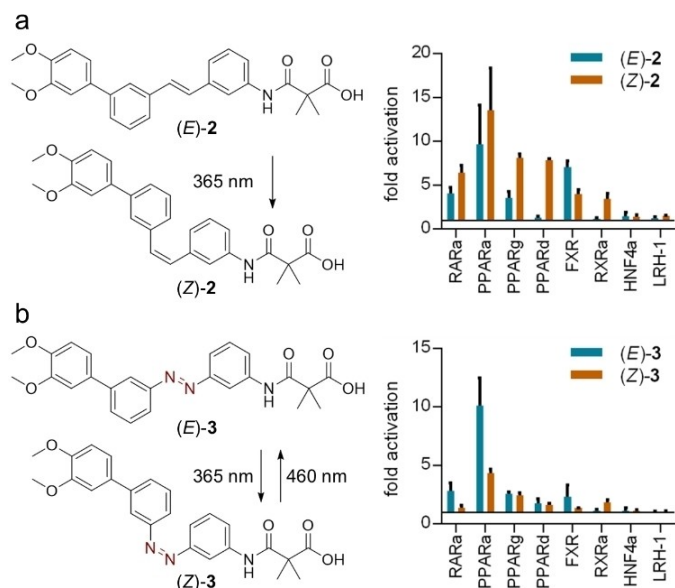


Figure 2. Nuclear receptor modulation by **2** and **3**. (a) The stilbene analogue **2** ($3 \mu\text{M}$) of **1** exhibited agonism on $\text{RAR}\alpha$, PPARs and FXR with $\text{PPAR}\alpha$ activation as most prominent activity. (b) The azobenzene **3** ($10 \mu\text{M}$) exhibited stronger preference for $\text{PPAR}\alpha$. Data are the mean \pm S.E.M. fold nuclear receptor activation vs. DMSO ctrl; $n \geq 3$.

Table 1. Photo-switchable analogues of **1**.

Structure	$\text{EC}_{50}(\text{PPAR}\alpha)$; (max. rel. act.) ^[a]	
	(E)	(Z) ^[b]
	$2.4 \pm 0.4 \mu\text{M}$ ($17 \pm 2\%$)	$1.3 \pm 0.1 \mu\text{M}$ ($48 \pm 2\%$)
	$3 \pm 1 \mu\text{M}$ ($26 \pm 1\%$)	$4 \pm 2 \mu\text{M}$ ($17 \pm 4\%$)
	$6 \pm 1 \mu\text{M}$ ($15 \pm 2\%$)	$7 \pm 1 \mu\text{M}$ ($8.1 \pm 0.8\%$)
	inactive ($10 \mu\text{M}$)	inactive ($10 \mu\text{M}$)

[a] $\text{PPAR}\alpha$ agonism was determined in a Gal4 hybrid reporter gene assay; data are the mean \pm S.E.M.; $n \geq 3$. Relative activation refers to the activity of GW7647 at $1 \mu\text{M}$ defined as 100% activation. [b] A cell DISCO^[18] was used to maintain the (Z)-configuration.

for further structural evaluation and initially focused on varying the scaffold geometry (Table 1). The corresponding para-analogue **4** offered improved photophysical characteristics with a red-shifted (405 nm, Supplementary Figure 1) maximum for (E) to (Z) switching but reduced $\text{PPAR}\alpha$ agonism. The ortho-derivative **5**, in contrast, revealed poor (E) to (Z) switching efficiency and was inactive on $\text{PPAR}\alpha$.

We thus retained the favored meta-regiochemistry of **3** and moved our attention to substituents on the lipophilic backbone (Table 2). Removal of one methoxy substituent in **6** was well tolerated with a slight increase in potency indicating that double substitution was not required. Evaluation of alternative groups in 4-position revealed slightly enhanced potency and (Z)-preference for the 4-methyl derivative **7** and a further improved activity difference between the (E)- and (Z)-isomers for the 4-chloro analogue **8**. The 4-trifluoromethyl derivative **9** retained high potency on $\text{PPAR}\alpha$ in the light-induced (Z)-configuration while its dark-adapted (E)-isomer was significantly less active thus providing the desired light-activated $\text{PPAR}\alpha$ agonist profile.

Moving the trifluoromethyl group to the 3-position (**10**) and 3,4-bistrifluoromethyl substitution (**11**) were tolerated in terms of $\text{PPAR}\alpha$ agonist potency but reduced the favorable (Z)-

Table 2. Evaluation of the lipophilic substitution pattern.

R		$\text{EC}_{50}(\text{PPAR}\alpha)$; (max. rel. act.) ^[a]	
		(E)	(Z) ^[b]
3		$3 \pm 1 \mu\text{M}$ ($26 \pm 1\%$)	$4 \pm 2 \mu\text{M}$ ($17 \pm 4\%$)
6		$2.3 \pm 0.4 \mu\text{M}$ ($18 \pm 2\%$)	$3.1 \pm 0.5 \mu\text{M}$ ($20 \pm 2\%$)
7		$2.2 \pm 0.2 \mu\text{M}$ ($36 \pm 2\%$)	$1.5 \pm 0.1 \mu\text{M}$ ($32 \pm 1\%$)
8		$3.6 \pm 0.5 \mu\text{M}$ ($40 \pm 3\%$)	$1.2 \pm 0.1 \mu\text{M}$ ($30 \pm 1\%$)
9		$> 20 \mu\text{M}$	$1.5 \pm 0.2 \mu\text{M}$ ($39 \pm 2\%$)
10		$4 \pm 1 \mu\text{M}$ ($37 \pm 8\%$)	$3 \pm 1 \mu\text{M}$ ($38 \pm 7\%$)
11		$5 \pm 1 \mu\text{M}$ ($15 \pm 3\%$)	$3.1 \pm 0.2 \mu\text{M}$ ($33 \pm 1\%$)
12		$4.8 \pm 0.4 \mu\text{M}$ ($23 \pm 2\%$)	$3.7 \pm 0.5 \mu\text{M}$ ($21 \pm 2\%$)
13		inactive ($10 \mu\text{M}$)	inactive ($10 \mu\text{M}$)

[a] $\text{PPAR}\alpha$ agonism was determined in a Gal4 hybrid reporter gene assay; data are the mean \pm S.E.M.; $n \geq 3$. Relative activation refers to the activity of GW7647 at $1 \mu\text{M}$ defined as 100% activation. [b] A cell DISCO^[18] was used to maintain the (Z)-configuration.

preference compared to **9**. A β -naphthyl motif (**12**) to mimic the 3,4-disubstitution pattern and concomitantly expand the chromophore for a longer switching wavelength also retained potent PPAR α agonism but with less (*Z*)-preference. Further structural extension to a bulky 9,9-dimethyl-9*H*-fluoren-2-yl substituent (**13**) was not tolerated. These SAR results thus indicated that PPAR α agonism tolerated various substitution patterns on the favored scaffold of **3** but that only a relatively bulky, electron-withdrawing and hydrophobic 4-substituent provided the desired (*Z*)-preference. The light-activated 4-trifluoromethyl derivative **9** thus emerged from this series as PPAR α targeted photohormone with most favorable characteristics for further evaluation.

9 offered favorable photophysical characteristics for application as chemical tool (Figure 3a–d) with efficient switching between (*E*)- to (*Z*)-configurations (Figure 3b), no fatigue over

multiple cycles of switching (Figure 3c), and a long thermal relaxation half-life of 28.5 h for the light-induced (*Z*)-isomer (Figure 3d). In vitro profiling additionally revealed strong selectivity for PPAR α over related lipid-activated nuclear receptors for both (*E*)- and (*Z*)-**9** (Figure 3e).

To validate the applicability of **9** as light-activatable tool in cellular settings, we compared the effects of (*E*)-**9** and the light-activated (*Z*)-**9** on temporally monitored PPAR α activity in cells using a fluorescent reporter (Figure 3f). The dark-adapted (*E*)-**9** induced no PPAR α -dependent mCherry expression at 10 μ M whereas light-activated (*Z*)-**9** mediated continuously increasing reporter expression over time.

Conclusions

Using the cinalukast analogue **1** as lead, we have obtained a new light-switchable PPAR α agonist scaffold by incorporation of an azobenzene motif. The PPAR α ligand **9** offers favorable light-activated agonism with >10-fold activity difference between the (*E*)- and (*Z*)-configurations and high reversible switching efficiency. Such photo-regulated PPAR α agonist offering spatially and time-resolved control^[18] over PPAR α activity may be useful to further explore the role and potential of the transcription factor in phenotypic in vitro settings for which **9** provides favorable chemical tool characteristics with the inactive dark-adapted or light-induced (435 nm) (*E*)-configuration as integrated negative control. Moreover, spatially resolved activity of potential future light-controlled PPAR α agonist drugs could be an attractive avenue to overcome side effects of PPAR α activation such as rhabdomyolysis^[11] and gallstone formation,^[19] especially in indications enabling topical application.^[20] **9** thus emerges as an orthogonal tool to previously developed PPAR α modulators and as valuable new photohormone scaffold for further optimization.

Experimental

Chemistry

General. All chemicals were of reagent grade, purchased from commercial sources (e.g., Sigma-Aldrich, TCI, BLDpharm) and used without further purification unless otherwise specified. All reactions were conducted under nitrogen or argon atmosphere and in absolute solvents purchased from Sigma-Aldrich. Other solvents, especially for work-up procedures, were of reagent grade or purified by distillation (cyclohexane (CH), ethyl acetate (EA), ethanol (EtOH)). Reactions were monitored by thin layer chromatography (TLC) on Silica gel 60 F254 coated aluminum sheets by Merck and visualized under ultraviolet light (254 nm) or by using ninhydrin or Ehrlich's reagent stains. Purification by column chromatography (CC) was performed on a puriFlash® XS520Plus system (Advion, Ithaca, NY, USA) using high performance spherical silica columns (SIHP, 50 μ m) by Interchim and a gradient of CH to EA, Reversed-phase column chromatography was performed on a puriFlash® 5.250 system (Advion) using C18HP columns (SIHP, 15 μ m) by Interchim and a gradient of H₂O with 10% acetonitrile (MeCN) to 100% MeCN (HPLC gradient grade). Mass spectra were obtained on a puriFlash®-CMS system (Advion) using atmospheric pressure

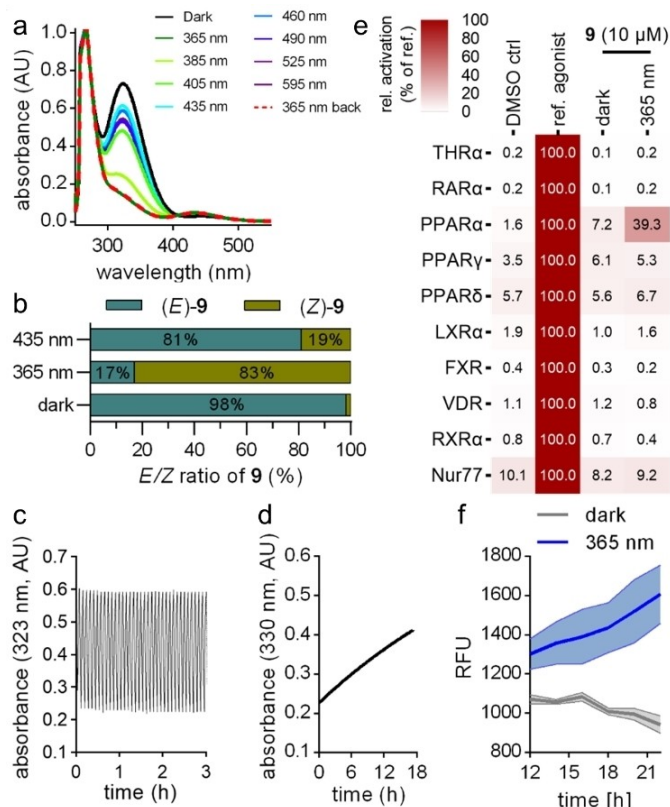


Figure 3. Profiling of the PPAR α targeted photohormone **9**. (a) UV/vis absorbance spectra of **9** (30 μ M in DMSO) measured after irradiation at the indicated wavelengths. (b) (*E/Z*)-configuration ratios of **9** in the dark adapted state and after irradiation at 365 nm or 435 nm determined by ¹H-NMR based on the (CH₃)₂-integral of the oxopropanoic acid motif. (c) **9** could be reversibly switched between the (*E*)- and (*Z*)-configuration over multiple cycles by alternating irradiation at 365 and 435 nm. Absorbance was measured at 323 nm. (d) (*Z*)-**9** showed slow thermal relaxation at 37 °C ($t_{1/2}$ = 28.5 h). (e) **9** was selective for PPAR α over related lipid-activated nuclear receptors. Data are the mean \pm S.E.M. relative nuclear receptor activation; $n = 3$. (f) Light-activated (*Z*)-**9** caused continuous PPAR α activation over time while (*E*)-**9** had no effect. Compounds were tested at 10 μ M in a fluorescent (mCherry) reporter gene assay. Fluorescence intensity was measured every two hours and normalized to the untreated control (0.1% DMSO) of the respective dark or illuminated setting. A cell DISCO¹⁸ was used to induce the active (*Z*)-configuration of **9**. The graph shows the mean (lines) and S.E.M. (shadows); $n = 3$.

chemical ionization (APCI). HRMS spectra were obtained with a Thermo Finnigan LTQ FT instrument for electron impact ionization (EI) or electrospray ionization (ESI). NMR spectra were recorded in deuterated solvents on Bruker Avance III HD 400 MHz or 500 MHz spectrometers equipped with a CryoProbe™ Prodigy broadband probe (Bruker). Chemical shifts are reported in δ values (ppm) relative to residual protium in the NMR solvent ($^1\text{H-NMR}$: acetone- d_6 : δ = 2.04 ppm; CDCl_3 : δ = 7.26 ppm; DMSO- d_6 : δ = 2.50 ppm; MeOD- d_4 : δ = 3.31 ppm, $^{13}\text{C-NMR}$: acetone- d_6 : δ = 206.26, 29.84 ppm; CDCl_3 : δ = 77.16 ppm; DMSO- d_6 : δ = 39.52 ppm; MeOD- d_4 : δ = 49.0 ppm), coupling constants (J) in hertz (Hz). The purity of test compounds was determined by quantitative ^1H NMR (qH NMR) according to the method described by Pauli et al.^[21] with internal calibration. To ensure accurate determination of peak area ratio, the qH NMR measurements were conducted under conditions allowing for complete relaxation. Ethyl 4-(dimethylamino)benzoate (LOT#BCCC6657, purity 99.63%) and maleic acid (LOT#BCBM8127V, purity 99.94%) were used as internal standards in MeOD- d_4 , DMSO- d_6 , or acetone- d_6 . All compounds for biological testing had a purity > 95% according to quantitative NMR.

General procedure A for Suzuki reaction. The respective aryl bromide (1.00–1.20 eq), respective boronate (1.00–1.20 eq), XPhos G2/3 (0.10–0.25 eq) and tripotassium phosphate (3.00 eq) were dissolved in a solvent mixture dioxane and water (0.13 M, 9:1) which was degassed by the freeze-pump-thaw method (three times) under argon. The reaction was stirred under reflux overnight. After cooling to room temperature, the mixture was filtered through Celite and washed with EA (20 mL). H_2O (30 mL) was added and the aqueous layer was extracted with EA (10 mL) three times. The organic layers were combined, dried over MgSO_4 , filtered and concentrated. The crude product was purified by CC and potentially reverse CC.

General procedure B for Baeyer-Mills coupling. The respective amine (1.00–2.00 eq), and Oxone® (6.00 eq) were dissolved in a solvent mixture of methylene chloride (DCM) and H_2O (0.1 M, 1:1). The mixture was stirred for 1–3 h at room temperature until the corresponding nitrosoarene intermediate was formed according to TLC. The mixture was then washed with 2 N aqueous HCl, saturated NaHCO_3 solution and brine. The organic layers were dried over MgSO_4 and filtered, and the solvent was evaporated under reduced pressure. The crude nitroso compound was dissolved in DCM (0.1 M) and the second amine (1.00–2.00 eq), and acetic acid (0.1 M) were added. The mixture was stirred for 12–48 h at room temperature. After TLC indicated completion, the solvent was evaporated under reduced pressure and the crude product was purified by CC and potentially reverse CC.

General procedure C for alkaline hydrolysis. The respective ester (1.00 eq) and lithium hydroxide (5.00 eq) were dissolved in a solvent mixture of tetrahydrofuran and H_2O (0.05 M, 1:1). The mixture was stirred at room temperature overnight. The solvents were evaporated and the crude was dissolved in EA. 2 N aqueous HCl was added, phases were separated, and the aqueous layer was extracted with EA three times. The combined organic layers were dried over MgSO_4 , filtered and concentrated. The crude product was purified by CC and potentially reverse CC.

(E)-2,2-Dimethyl-3-oxo-3-((3-((4-(trifluoromethyl)-[1,1'-biphenyl]-3-yl)diazanyl)phenyl)amino)propanoic acid (9). Preparation according to general procedure C using ethyl 2,2-dimethyl-3-oxo-3-((3-((4-(trifluoromethyl)-[1,1'-biphenyl]-3-yl)diazanyl)phenyl)amino)propanoate (**45**, 105 mg, 0.217 mmol, 1.00 eq) and lithium hydroxide (26.0 mg, 1.08 mmol, 5.00 eq) to yield compound **9** as an orange solid (85 mg, 86%). R_f = 0.39 (3:1 CH:EA + 1% FA). ^1H NMR (400 MHz, MeOD- d_4): δ 8.25–8.21 (m, 1H), 8.21–8.17 (m, 1H), 7.96–7.92 (m, 1H), 7.89 (d, J = 8.0 Hz, 2H), 7.85–7.80 (m, 1H), 7.77 (d, J = 8.2 Hz, 2H), 7.74–7.62 (m, 3H), 7.50 (t, J =

8.0 Hz, 1H), 1.55 (s, 6H). ^{13}C NMR (126 MHz, MeOD- d_4): δ 178.2, 174.3, 154.2, 154.1, 145.1, 141.8, 140.6, 130.9, 130.8, 130.6 (q, J = 32.3 Hz), 130.3, 128.6, 126.8 (q, J = 4.0 Hz), 125.3 (q, J = 270.6 Hz), 124.6, 123.4, 122.4, 120.5, 115.6, 52.1, 24.0. qH NMR (400 MHz, MeOD- d_4 , ethyl 4-(dimethylamino)benzoate as reference): purity = 95%. HRMS (ESI+): m/z calculated 456.1530 for $\text{C}_{24}\text{H}_{21}\text{N}_3\text{O}_3\text{F}_3$, found: 456.1526 ($[\text{M} + \text{H}]^+$).

Ethyl ((3-aminophenyl)amino)-2,2-dimethyl-3-oxopropanoate (24). Ethyl 3-((3-((tert-butoxycarbonyl)amino)phenyl)amino)-2,2-dimethyl-3-oxopropanoate (**23**, 635 mg, 1.81 mmol, 1.00 eq) was dissolved in chloroform (5 mL) and trifluoroacetic acid (TFA, 1.39 mL, 18.1 mmol, 10 eq) was added to the solution. The reaction was stirred at room temperature overnight. The solvents were evaporated under reduced pressure, the crude product was dissolved in EA and washed with 2 N aqueous NaOH solution. The organic layer was dried over MgSO_4 , concentrated, and purified by CC using a gradient of CH:EA + 1% TAE (2:1 to 1:2) to give **24** as a yellow oil (363 mg, 80% yield). R_f = 0.46 (1:2 CH:EA + 1% TAE). ^1H NMR (500 MHz, CDCl_3): δ 8.46 (s, 1H), 7.17 (t, J = 2.2 Hz, 1H), 7.08 (t, J = 8.0 Hz, 1H), 6.75–6.64 (m, 1H), 6.48–6.38 (m, 1H), 4.23 (q, J = 0.7 Hz, 2H), 3.69 (s, 2H), 1.30 (t, J = 0.7 Hz, 3H). ^{13}C NMR (101 MHz, CDCl_3): δ 175.6, 169.8, 147.4, 139.0, 129.8, 111.2, 109.9, 106.7, 62.1, 50.6, 24.0, 14.2. MS (ASAP+): m/z 250.6 ($[\text{M} + \text{H}]^+$).

4'-(Trifluoromethyl)-[1,1'-biphenyl]-3-amine (37). Preparation according to general procedure A using 4-(trifluoromethyl)phenylboronic acid (**29**, 570 mg, 3.00 mmol, 1.00 eq), 3-bromoaniline (**26**, 619 mg, 3.60 mmol, 1.20 eq), XPhos Pd G3 (324 mg, 0.375 mmol, 0.125 eq) and tribasic potassium phosphate (1910 mg, 9.00 mmol, 3.00 eq) to yield compound **37** as a yellow oil (675 mg, 95%). R_f = 0.31 (3:1 CH:EA). ^1H NMR (500 MHz, acetone- d_6): δ 7.80 (d, J = 8.9 Hz, 2H), 7.76 (d, J = 8.9 Hz, 2H), 7.18 (t, J = 7.8 Hz, 1H), 7.04–6.99 (m, 1H), 6.94–6.90 (m, 1H), 6.76–6.72 (m, 1H), 4.80 (s, 2H). ^{13}C NMR (126 MHz, acetone- d_6): δ 150.1, 146.6, 141.0, 130.6, 129.3 (q, J = 32.4 Hz), 128.2, 126.4 (q, J = 3.8 Hz), 125.6 (q, J = 271.1 Hz), 116.4, 115.3, 113.7. MS (ASAP+): m/z 237.6 ($[\text{M} + \text{H}]^+$).

(E)-Ethyl 2,2-dimethyl-3-oxo-3-((3-((4-(trifluoromethyl)-[1,1'-biphenyl]-3-yl)diazanyl)phenyl)amino)propanoate (45). Preparation according to general procedure B using ethyl 3-((3-aminophenyl)amino)-2,2-dimethyl-3-oxopropanoate (**24**, 535 mg, 2.14 mmol, 1.00 eq) and Oxone® (2628 mg, 8.55 mmol, 6.00 eq) to prepare the nitrosoarene intermediate and 4'-(trifluoromethyl)-[1,1'-biphenyl]-4-amine (**37**, 675 mg, 2.85 mmol, 2.00 eq) to yield compound **45** as a yellow solid (115 mg, 11%). R_f = 0.47 (4:1 CH:EA). ^1H NMR (400 MHz, acetone- d_6): δ 9.11 (s, 1H), 8.37 (t, J = 2.0 Hz, 1H), 8.27 (t, J = 1.7 Hz, 1H), 8.06–7.97 (m, 3H), 7.97–7.92 (m, 1H), 7.90–7.82 (m, 3H), 7.77–7.71 (m, 2H), 7.55 (t, J = 8.0 Hz, 1H), 4.20 (q, J = 7.1 Hz, 2H), 1.56 (s, 6H), 1.24 (t, J = 7.1 Hz, 3H). ^{13}C NMR (101 MHz, acetone- d_6): δ 174.2, 171.5, 154.0, 153.7, 144.8, 141.5, 141.1, 131.0, 130.8, 130.8 (q, J = 31.8 Hz), 130.3, 128.7, 126.8 (q, J = 4.0 Hz), 125.4 (q, J = 258.8 Hz), 123.8, 123.2, 122.4, 120.0, 114.5, 61.8, 51.9, 23.7, 14.4. MS (ASAP+): m/z 483.1 ($[\text{M}]^+$).

Photophysical Characterization

UV/vis absorbance spectra were recorded on an Agilent Technologies Cary 60 using rectangular cuvettes (Agilent, Santa Clara, USA). A pE-4000 illumination (10 mW/cm², CoolLED, Andover, GB) was applied to induce photoisomerization by light irradiation at a specified wavelength (365–590 nm). The LED was pointed directly onto the top of the sample cuvette (30 μM DMSO). Absorption spectra were recorded at different irradiation wavelengths (λ = 365–595 nm) starting from no irradiation. For photostability experiments, the maximum absorption wavelength (λ_{max} (**9**) = 323 nm) was monitored with a repeated irradiation program set with 365 nm (2.5 min) and 435 nm (2.5 min) and was cycled for > 3 h. The

thermal relaxation was observed by absorbance measurement at $\lambda = 330$ nm for > 15 h. Sample **9** was first irradiated with 365 nm for 15 min to induce complete switching into the (*Z*)-isomer, and then the sample were allowed to switch back to the (*E*)-isomer.

In Vitro Characterization

Hybrid reporter gene assays. Nuclear receptor modulation was determined in Gal4 hybrid reporter gene assays in HEK293T cells (German Collection of Microorganisms and Cell Culture GmbH, DSMZ) using pFR-Luc (Stratagene, La Jolla, CA, USA; reporter), pRL-SV40 (Promega, Madison, WI, USA; internal control) and one pFA-CMV-hNR-LBD clone,^[22] coding for the hinge region and ligand binding domain of the canonical isoform of the respective human nuclear receptor (pFA-CMV-THR α -LBD,^[23] pFA-CMV-RAR α -LBD,^[24] pFA-CMV-PPAR α -LBD,^[25] pFA-CMV-PPAR γ -LBD,^[25] pFA-CMV-PPAR δ -LBD,^[25] pFA-CMV-LXR α -LBD,^[26] pFA-CMV-FXR-LBD,^[27] pFA-CMV-VDR-LBD^[27] pFA-CMV-hRXR α -LBD,^[28] pFA-CMV-hNur77-LBD^[22]). Cells were cultured in Dulbecco's modified Eagle's medium (DMEM), high glucose supplemented with 10% fetal calf serum (FCS), sodium pyruvate (1 mM), penicillin (100 U/mL), and streptomycin (100 μ g/mL) at 37 °C and 5% CO₂ and seeded in 96-well plates (3 \times 10⁴ cells/well). After 24 h, medium was changed to Opti-MEM without supplements and cells were transiently transfected using Lipofectamine LTX reagent (Invitrogen, Carlsbad, CA, USA) according to the manufacturer's protocol. Five hours after transfection, cells were incubated with the test compounds in Opti-MEM supplemented with penicillin (100 U/mL), streptomycin (100 μ g/mL) and 0.1% DMSO for 16 h before luciferase activity was measured using the Dual-Glo Luciferase Assay System (Promega) according to the manufacturer's protocol on a Tecan Spark luminometer (Tecan Deutschland GmbH, Crailsheim, Germany). Firefly luminescence was divided by Renilla luminescence and multiplied by 1000 resulting in relative light units (RLU) to normalize for transfection efficiency and cell growth. Fold activation was obtained by dividing the mean RLU of test compound by the mean RLU of the untreated control. All samples were tested in at least three biologically independent experiments in duplicates. For dose-response curve fitting and calculation of EC₅₀ values, the equation "[Agonist] vs. response-Variable slope (four parameters)" was used in GraphPad Prism (version 7.00, GraphPad Software, La Jolla, CA, USA). The following reference agonists were used: triiodothyronine (1 μ M, THR α); tretinoin (1 μ M, RAR α); GW7647 (1 μ M, PPAR α); rosiglitazone (1 μ M, PPAR γ); L165, 041 (1 μ M, PPAR δ); TO901317 (1 μ M, LXR α); GW4064 (1 μ M, FXR); calcitriol (1 μ M, VDR); bexarotene (1 μ M, RXR α); compound **29** from^[29] (1 μ M, Nur77). A Gal4-responsive mCherry reporter (pUAS-mCherry-NLS; Addgene entry 87695^[30]) was used with pFA-CMV-PPAR α -LBD^[25] to determine PPAR α activity over time in HEK293T cells. Cells were cultured, transfected and incubated with test compounds 5 h after transfection as described for the standard reporter gene assays. mCherry fluorescence intensity (FI) was then measured at various time points on a Tecan Spark luminometer after excitation at 585/10 nm with the emission wavelength of 610/10 nm in bottom reading mode. FI of test samples were normalized to FI of the untreated control of the respective dark or illuminated setting and multiplied with 1000 to obtain relative fluorescence units (RFU). GW7647 (1 μ M) was used as positive control and exhibited comparable PPAR α activation in the dark and illuminated condition (not shown). Cellular characterization of the light-induced (*Z*)-configuration of the azobenzene test compound was performed with preirradiated compound (irradiation for 3 min at $\lambda = 365$ nm before incubation) and using a Cell DISCO^[18] system (with 10 ms light pulses every 10 s, $\lambda = 360$ nm) to maintain the compound in the (*Z*)-state.

Supporting Information

The Supporting Information contains Supplementary Figures, synthetic procedures, and analytical data. Additional references^[21] are cited in the Supplementary Information.

Acknowledgements

pUAS-mCherry-NLS (Addgene plasmid 87695)^[30] was a gift from Robert Campbell. Open Access funding enabled and organized by Projekt DEAL.

Conflict of Interests

The authors declare no conflict of interest.

Data Availability Statement

The data that support the findings of this study are available from the corresponding author upon reasonable request.

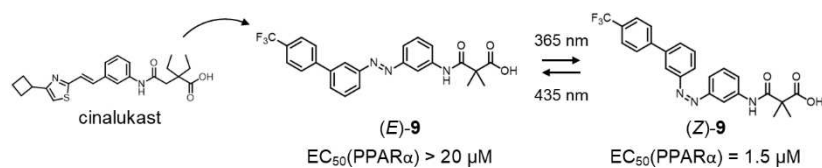
Keywords: transcription factor · peroxisome proliferator-activated receptor · photopharmacology · photohormone

- [1] L. Michalik, J. Auwerx, J. P. Berger, V. K. Chatterjee, C. K. Glass, F. J. Gonzalez, P. A. Grimaldi, T. Kadowaki, M. A. Lazar, S. O'Rahilly, C. N. A. Palmer, J. Plutzky, J. K. Reddy, B. M. Spiegelman, B. Staels, W. Wahli, *Pharmacol. Rev.* **2006**, *58*, 726–741.
- [2] M. Pawlak, P. Lefebvre, B. Staels, *J. Hepatol.* **2015**, *62*, 720–733.
- [3] J. D. Brown, J. Plutzky, *Circulation* **2007**, *115*, 518–533.
- [4] J. Vamecq, N. Latruffe, *Lancet* **1999**, *354*, 141–148.
- [5] S. Gawrieh, M. Noureddin, N. Loo, R. Mohseni, V. Awasty, K. Cusi, K. V. Kowdley, M. Lai, E. Schiff, D. Parmar, P. Patel, N. Chalasani, *Hepatology* **2021**, *74*, 1809–1824.
- [6] L. Gellrich, D. Merk, *Nucl. Recept.* **2017**, *4*, 101310.
- [7] R. Robillard, C. Fontaine, G. Chinetti, J. C. Fruchart, B. Staels, *Handb. Exp. Pharmacol.* **2005**, *170*, 389–406.
- [8] H. Li, W. Pei, Y. Wang, Y. Zhang, Z. Yang, X. Wang, *Front. Biosci. - Landmark* **2024**, *29*, 68.
- [9] M. A. Esmaili, S. Yadav, R. K. Gupta, G. R. Waggoner, A. Deloach, N. Y. Calingasan, M. Flint Beal, M. Kiaei, *Hum. Mol. Genet.* **2016**, *25*, 317–327.
- [10] J. Xu, M. K. Racke, P. D. Drew, *J. Neurochem.* **2007**, *103*, 1801–1810.
- [11] J. Wu, Y. Song, H. Li, J. Chen, *Eur. J. Clin. Pharmacol.* **2009**, *65*, 1169–1174.
- [12] P. Kobauri, F. J. Dekker, W. Szymanski, B. L. Feringa, *Angew. Chem. Int. Ed.* **2023**, *62*, e202300681.
- [13] M. J. Fuchter, *J. Med. Chem.* **2020**, *63*, 11436–11447.
- [14] K. Hüll, J. Morstein, D. Trauner, *Chem. Rev.* **2018**, *118*, 10710–10747.
- [15] K. Hinnah, S. Willems, J. Morstein, J. Heering, F. W. W. Hartrampf, J. Broichhagen, P. Leippe, D. Merk, D. Trauner, *J. Med. Chem.* **2020**, *63*, 10908–10920.
- [16] J. Pollinger, S. Schierle, S. Neumann, J. Ohrndorf, A. Kaiser, D. Merk, *ChemMedChem* **2019**, *14*, 1343–1348.
- [17] T. Langer, C. G. Wermuth, in *Polypharmacology Drug Discov.*, John Wiley & Sons, Inc., Hoboken, NJ, USA, **2012**, pp. 227–243.
- [18] M. Borowiak, W. Nahaboo, M. Reynders, K. Nekolla, P. Jalinot, J. Hasserodt, M. Rehberg, M. Delattre, S. Zahler, A. Vollmar, D. Trauner, O. Thorn-Seshold, *Cell* **2015**, *162*, 403–411.
- [19] M. Botta, M. Audano, A. Sahebkar, C. R. Sirtori, N. Mitro, M. Ruscica, *Int. J. Mol. Sci.* **2018**, *19*, 1197.

- [20] S. Kippenberger, S. M. Loitsch, M. Grundmann-Kollmann, S. Simon, T. A. Dang, K. Hardt-Weinelt, R. Kaufmann, A. Bernd, *J. Invest. Dermatol.* **2001**, *117*, 1430–1436.
- [21] G. F. Pauli, S. N. Chen, C. Simmler, D. C. Lankin, T. Gödecke, B. U. Jaki, J. B. Friesen, J. B. McAlpine, J. G. Napolitano, *J. Med. Chem.* **2014**, *57*, 9220–9231.
- [22] S. Willems, W. Kilu, X. Ni, A. Chaikuad, S. Knapp, J. Heering, D. Merk, *Commun. Chem.* **2020**, *3*, 85.
- [23] L. Gellrich, P. Heitel, J. Heering, W. Kilu, J. Pollinger, T. Goebel, A. Kahnt, S. Arifi, W. Pogoda, A. Paulke, D. Steinhilber, E. Proschak, M. Wurglics, M. Schubert-Zsilavecz, A. Chaikuad, S. Knapp, I. Bischoff, R. Fürst, D. Merk, *J. Med. Chem.* **2020**, *63*, 6727–6740.
- [24] J. Pollinger, L. Gellrich, S. Schierle, W. Kilu, J. Schmidt, L. Kalinowsky, J. Ohrndorf, A. Kaiser, J. Heering, E. Proschak, D. Merk, *J. Med. Chem.* **2019**, *62*, 2112–2126.
- [25] O. Rau, M. Wurglics, A. Paulke, J. Zitzkowski, N. Meindl, A. Bock, T. Dingermann, M. Abdel-Tawab, M. Schubert-Zsilavecz, *Planta Med.* **2006**, *72*, 881–887.
- [26] D. Flesch, S.-Y. Cheung, J. Schmidt, M. Gabler, P. Heitel, J. S. Kramer, A. Kaiser, M. Hartmann, M. Lindner, K. Lüddens-Dämgen, J. Heering, C. Lamers, H. Lüddens, M. Wurglics, E. Proschak, M. Schubert-Zsilavecz, D. Merk, *J. Med. Chem.* **2017**, *60*, 7199–7205.
- [27] J. Schmidt, F.-M. Klingler, E. Proschak, D. Steinhilber, M. Schubert-Zsilavecz, D. Merk, *Sci. Rep.* **2015**, *5*, 14782.
- [28] P. Heitel, L. Gellrich, L. Kalinowsky, J. Heering, A. Kaiser, J. Ohrndorf, E. Proschak, D. Merk, *ACS Med. Chem. Lett.* **2019**, *10*, 203–208.
- [29] J. Vietor, C. Gege, T. Stiller, R. Busch, E. Schallmayer, H. Kohlhof, G. Höfner, J. Pabel, J. A. Marschner, D. Merk, *J. Med. Chem.* **2023**, *66*, 6391–6402.
- [30] W. Zhang, A. W. Lohman, Y. Zhuravlova, X. Lu, M. D. Wiens, H. Hoi, S. Yaganoglu, M. A. Mohr, E. N. Kitova, J. S. Klassen, P. Pantazis, R. J. Thompson, R. E. Campbell, *Nat. Methods* **2017**, *14*, 391–394.

Manuscript received: April 30, 2024
Revised manuscript received: June 16, 2024
Accepted manuscript online: June 19, 2024
Version of record online: ■■■, ■■■

RESEARCH ARTICLE



A new photohormone scaffold was developed based by incorporation of a photo-switchable azobenzene moiety in a cinalukast-derived PPAR α

ligand and optimized to exhibit selective PPAR α agonism in the light-induced (Z)-configuration.

M. Sai, N. van Herwijnen, Prof. Dr. D. Merk*

1 – 8

Azologs of the Fatty Acid Mimetic Drug Cinalukast Enable Light-Induced PPAR α Activation



ChemMedChem

Supporting Information

Azologs of the Fatty Acid Mimetic Drug Cinalukast Enable Light-Induced PPAR α Activation

Minh Sai, Niels van Herwijnen, and Daniel Merk*

- Supporting Information -

Azologs of the fatty acid mimetic drug cinalukast enable light-induced PPAR α activation

Minh Sai¹, Niels van Herwijnen¹, Daniel Merk^{1*}

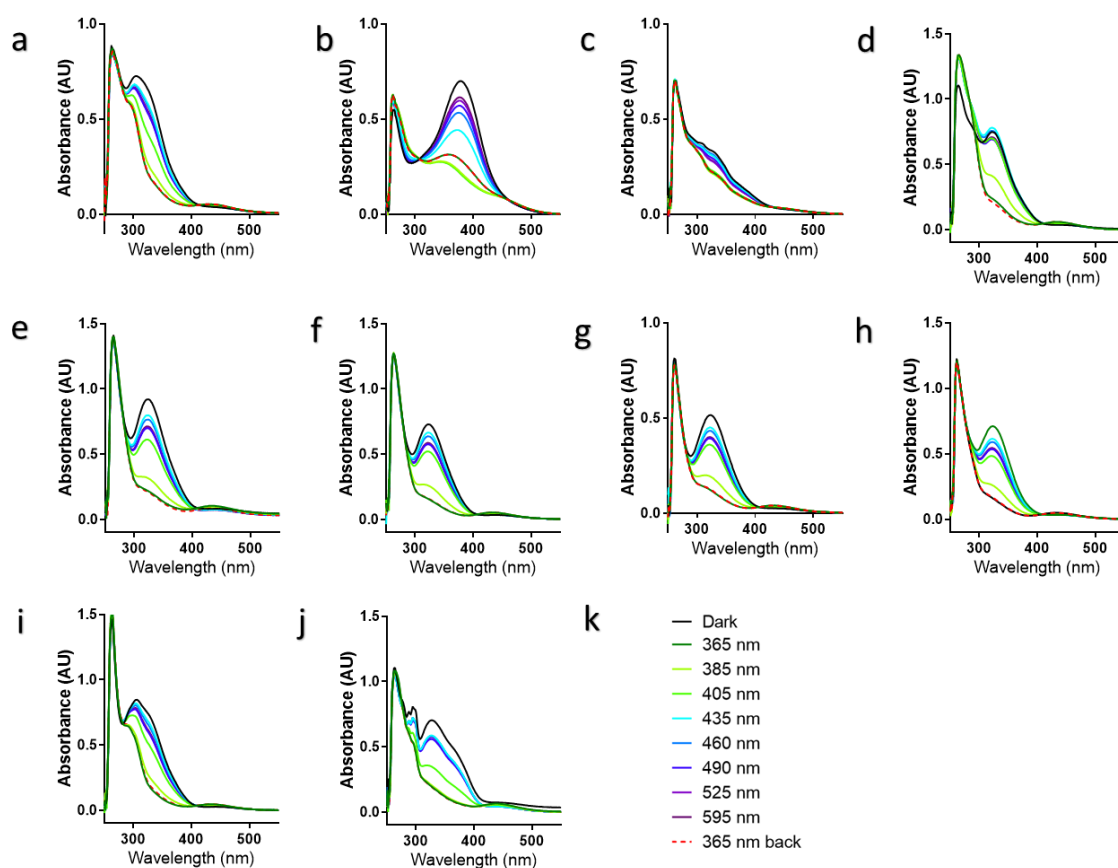
¹ Ludwig-Maximilians-Universität (LMU) München, Department of Pharmacy, 81377 Munich, Germany

* daniel.merk@cup.lmu.de

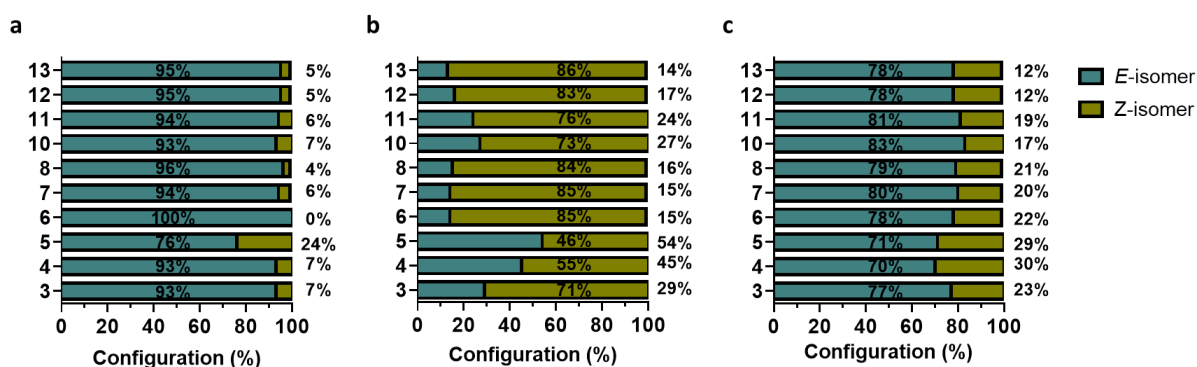
Table of Contents

Supplementary Figures	2
Synthetic Procedures and Analytical Data	3
qHNMR spectra of 2-13	13
Supplementary References	25

Supplementary Figures



Supplementary Figure 1. UV-VIS-absorbance spectra of **3-8** and **10-13** (30 μM in DMSO) measured after irradiation at the indicated wavelengths ((k) $\lambda=365\text{-}595$ nm). (a) compound **3**, (b) compound **4**, (c) compound **5**, (d) compound **6**, (e) compound **7**, (f) compound **8**, (g) compound **10**, (h) compound **11**, (i) compound **12**, (j) compound **13**.



Supplementary Figure 2. *E/Z*-configuration ratios of **3-8** and **10-13** in the dark-adapted state (a) and after irradiation at 365 nm (b) or 435 nm (c) determined by $^1\text{H-NMR}$ based on the $(\text{CH}_3)_2$ -integral of the oxopropanoic acid motif.

Synthetic Procedures and Analytical Data

General. All chemicals were of reagent grade, purchased from commercial sources (e.g., Sigma-Aldrich, TCI, BLDpharm) and used without further purification unless otherwise specified. All reactions were conducted under nitrogen or argon atmosphere and in absolute solvents purchased from Sigma-Aldrich. Other solvents, especially for work-up procedures, were of reagent grade or purified by distillation (cyclohexane (CH), ethyl acetate (EA), ethanol (EtOH)). Reactions were monitored by thin layer chromatography (TLC) on TLC Silica gel 60 F254 coated aluminum sheets by Merck and visualized under ultraviolet light (254 nm) or by using ninhydrin or Ehrlichs reagent stains. Purification by column chromatography (CC) was performed on a puriFlash® XS520Plus system (Advion, Ithaca, NY, USA) using high performance spherical silica columns (SIHP, 50 μ m) by Interchim and a gradient of CH to EA, Reversed-phase column chromatography was performed on a puriFlash® 5.250 system (Advion) using C18HP columns (SIHP, 15 μ m) by Interchim and a gradient of H₂O with 10% acetonitrile (MeCN) to 100% MeCN (HPLC gradient grade). Mass spectra were obtained on a puriFlash®-CMS system (Advion) using atmospheric pressure chemical ionization (APCI). HRMS were obtained with a Thermo Finnigan LTQ FT instrument for electron impact ionization (EI) or electrospray ionization (ESI). NMR spectra were recorded on Bruker Avance III HD 400 MHz or 500 MHz spectrometers equipped with a CryoProbe™ Prodigy broadband probe (Bruker). Chemical shifts are reported in δ values (ppm) relative to residual protium signals in the NMR solvent (¹H-NMR: acetone-*d*₆: δ = 2.04 ppm; CDCl₃: δ = 7.26 ppm; DMSO-*d*₆: δ = 2.50 ppm; MeOD-*d*₄: δ = 3.31 ppm, ¹³C-NMR: acetone-*d*₆: δ = 206.26, 29.84 ppm; CDCl₃: δ = 77.16 ppm; DMSO-*d*₆: δ = 39.52 ppm; MeOD-*d*₄: δ = 49.0 ppm), coupling constants (*J*) in hertz (Hz). The purity of the compounds was determined by quantitative ¹H NMR (qHNMR) according to the method described by Pauli et al.¹ with internal calibration. To ensure accurate determination of peak area ratio, the qHNMR measurements were conducted under conditions allowing for complete relaxation. Ethyl 4-(dimethylamino)benzoate (LOT#BCCC6657, purity 99.63%) and maleic acid (LOT#BCBM8127V, purity 99.94%) were used as internal standards in MeOD-*d*₄, DMSO-*d*₆, or acetone-*d*₆. All compounds for biological testing had a purity >95% according to quantitative NMR.

General procedure A for Suzuki reaction

The respective aryl bromide (1.00-1.20 eq), respective boronate (1.00-1.20 eq), X Phos G_{2/3} (0.10-0.25 eq) and tripotassium phosphate (3.00 eq) were dissolved in a solvent mixture dioxane and water (0.13 M, 9:1) which was degassed by the freeze-pump-thaw method (three times) under argon. The reaction was stirred under reflux overnight. After cooling to room temperature, the mixture was filtered through Celite and washed with EA (20 mL). H₂O (30 mL) was added and the aqueous layer was extracted with EA (10 mL) three times. The organic layers were combined, dried over MgSO₄, filtered and concentrated. The crude product was purified by CC and potentially reverse CC.

General procedure B for Baeyer-Mills coupling

The respective amine (1.00-2.00 eq), and OXONE® (6.00 eq) were dissolved in a solvent mixture of methylene chloride (DCM) and H₂O (0.1 M, 1:1). The mixture was stirred for 1-3 h at room temperature until the corresponding nitrosoarene intermediate was formed according to TLC. The mixture was then washed with 2 N aqueous HCl, saturated NaHCO₃ solution and brine. The organic layers were dried over MgSO₄ and filtered and the solvent was evaporated. The crude nitroso compound was dissolved in DCM (0.1 M) and the second amine (1.00-2.00 eq) and acetic acid (0.1 M) were added to the solution. The mixture was stirred for 12-48 h at room temperature. After TLC indicated completion, the solvent was evaporated and the crude product was purified by CC and potentially reverse CC.

General procedure C for alkaline hydrolysis

The respective ester (1.00 eq) and lithium hydroxide (5.00 eq) were dissolved in a mixture of tetrahydrofuran and H₂O (0.05 M, 1:1). The mixture was stirred at room temperature overnight. After completion, the solvents were evaporated and the crude was dissolved in EA. 2 N aqueous HCl was added, phases were separated and the aqueous layer was extracted with EA three times. The organic layers were combined, dried over MgSO₄, filtered and concentrated. The crude product was purified by CC and potentially reverse CC.

(E)-3-((3-(2-(3',4'-Dimethoxy-[1,1'-biphenyl]-3-yl)vinyl)phenyl)amino)-2,2-dimethyl-3-oxopropanoic acid (2). Preparation according to general procedure C using ethyl (E)-3-((3-(2-(3',4'-dimethoxy-[1,1'-biphenyl]-3-yl)vinyl)phenyl)amino)-2,2-dimethyl-3-oxopropanoate (**21**, 456 mg, 0.963 mmol, 1.00 eq) and lithium hydroxide (115 mg, 4.81 mmol, 5.00 eq) to yield compound **2** as a colorless solid (310 mg, 72%). *R*_f = 0.42 (1:1 CH:EA+1% formic acid (FA)). ¹H NMR (400 MHz, MeOD-*d*₄): δ 7.84 – 7.81 (m, 1H), 7.75 – 7.71 (m, 1H), 7.54 – 7.50 (m, 1H), 7.50 – 7.45 (m, 1H), 7.43 – 7.38 (m, 2H), 7.37 – 7.27 (m, 2H), 7.25 – 7.19 (m, 4H), 7.04 (d, *J* = 8.5 Hz, 1H), 3.92 (s, 3H), 3.88 (s, 3H), 1.55 (s, 6H). ¹³C NMR (101 MHz, MeOD-*d*₄): δ 177.3, 173.8, 150.8, 150.3, 142.8, 139.9, 139.5, 139.2, 135.5, 130.2, 130.1, 130.0, 129.6, 127.2, 126.2, 125.8, 124.0, 121.6, 120.7, 120.2, 113.3, 112.1, 56.6, 56.6, 52.0, 24.0. qHNMR (400 MHz, MeOD-*d*₄, ethyl 4-(dimethylamino)benzoate as reference): purity = 95%. HRMS (ESI+): *m/z* calculated 446.1962 for C₂₇H₂₈NO₅⁺, found: 446.1961 ([M+H]⁺).

(E)-3-((3-((3',4'-Dimethoxy-[1,1'-biphenyl]-3-yl)diazenyl)phenyl)amino)-2,2-dimethyl-3-oxopropanoic acid (3). Preparation according to general procedure C using ethyl (E)-3-((3-((3',4'-dimethoxy-[1,1'-biphenyl]-3-yl)diazenyl)phenyl)amino)-2,2-dimethyl-3-oxopropanoate (**41**, 140 mg, 0.294 mmol, 1.00 eq) and lithium hydroxide (35.2 mg, 1.74 mmol, 5.00 eq) to yield compound **3** as a brown solid (62 mg, 47%). *R*_f = 0.31 (2:1 CH:EA+1% FA). ¹H NMR (500 MHz, MeOD-*d*₄): δ 8.23 (s, 1H), 8.12 (s, 1H), 7.88 – 7.82 (m, 1H), 7.80 – 7.75 (m, 1H), 7.74 – 7.71 (m, 1H), 7.71 – 7.65 (m, 1H), 7.60 (t, *J* = 7.9 Hz, 1H), 7.51 (t, *J* = 8.0 Hz, 1H), 7.31 – 7.26 (m, 2H), 7.08 (d, *J* = 8.7 Hz, 1H), 3.94 (s, 3H), 3.89 (s, 3H), 1.56 (s, 6H). ¹³C NMR (101 MHz, MeOD-*d*₄): δ 179.6, 175.3, 154.4, 154.3, 150.9, 150.6, 143.4, 140.7, 134.6, 130.7, 130.5, 130.4, 124.5, 122.2, 122.0, 120.8, 120.5, 115.5, 113.3, 112.0, 56.6, 56.5, 52.5, 24.7. qHNMR (400 MHz, DMSO-*d*₆, ethyl 4-(dimethylamino)benzoate as reference): purity = 96%. HRMS (ESI+): *m/z* calculated 448.1867 for C₂₅H₂₆N₃O₅⁺, found: 448.1865 ([M+H]⁺).

(E)-3-((3-((3',4'-Dimethoxy-[1,1'-biphenyl]-4-yl)diazenyl)phenyl)amino)-2,2-dimethyl-3-oxopropanoic acid (4). Preparation according to general procedure C using ethyl (E)-3-((3-((3',4'-dimethoxy-[1,1'-biphenyl]-4-yl)diazenyl)phenyl)amino)-2,2-dimethyl-3-oxopropanoic acid (**42**, 28 mg, 0.06 mmol, 1.00 eq) and lithium hydroxide (7.1 mg, 0.29 mmol, 5.00 eq) to yield compound **4** as a yellow solid (24 mg, 95%). *R*_f = 0.24 (3:1 CH:EA+1% FA). ¹H NMR (500 MHz, MeOD-*d*₄): δ 8.20 (s, 1H), 7.99 (d, *J* = 8.3 Hz, 2H), 7.81 (d, *J* = 8.3 Hz, 2H), 7.75 – 7.66 (m, 2H), 7.51 (t, *J* = 8.0 Hz, 1H), 7.34 – 7.27 (m, 2H), 7.08 (d, *J* = 8.9 Hz, 1H), 3.94 (s, 3H), 3.90 (s, 3H), 1.56 (s, 6H). ¹³C NMR (101 MHz, DMSO-*d*₆): δ 163.2, 161.1, 152.4, 150.6, 149.2, 149.2, 143.0, 140.4, 131.5, 129.6, 127.2, 123.1, 122.2, 119.3, 118.8, 112.2, 111.8, 110.4, 55.6, 55.6, 50.4, 24.5. qHNMR (400 MHz, MeOD-*d*₄, ethyl 4-(dimethylamino)benzoate as reference): purity = 95%. HRMS (ESI+): *m/z* calculated 448.1867 for C₂₅H₂₆N₃O₅⁺, found: 448.1862 ([M+H]⁺).

(E)-3-((3-((3',4'-Dimethoxy-[1,1'-biphenyl]-2-yl)diazenyl)phenyl)amino)-2,2-dimethyl-3-oxopropanoic acid (5). Preparation according to general procedure C using ethyl-3-((3-((3',4'-dimethoxy-[1,1'-biphenyl]-2-yl)diazenyl)phenyl)amino)-2,2-dimethyl-3-oxopropanoate (**43**, 38 mg, 0.08 mmol, 1.00 eq) and lithium hydroxide (9.57 mg, 0.40 mmol, 5.00 eq) to yield compound **5** as an orange solid (25 mg, 70%). *R*_f = 0.40 (3:1 CH:EA+1% FA). ¹H NMR (500 MHz, MeOD-*d*₄): δ 8.04 (t, *J* = 1.9 Hz, 1H), 7.69 – 7.64 (m, 2H), 7.63 – 7.52 (m, 3H), 7.47 –

7.40 (m, 2H), 7.05 – 6.98 (m, 3H), 3.89 (s, 3H), 3.77 (s, 3H), 1.54 (s, 6H). ¹³C NMR (126 MHz, MeOD-*d*₄): δ 175.5, 168.5, 155.6, 154.8, 151.1, 150.2, 149.7, 142.1, 140.8, 133.0, 132.1, 131.8, 130.4, 128.8, 124.9, 124.3, 119.5, 117.0, 116.9, 116.2, 112.5, 57.4, 56.5, 24.7. qHNMR (400 MHz, MeOD-*d*₄, maleic acid as reference): purity = 95%. HRMS (ESI+): *m/z* calculated 448.1867 for C₂₅H₂₆N₃O₅⁺, found: 448.1864 ([M+H]⁺).

(E)-3-((3-((4'-Methoxy-[1,1'-biphenyl]-3-yl)diazenyl)phenyl)amino)-2,2-dimethyl-3-oxopropanoic acid (6). Preparation according to general procedure C using ethyl (*E*)-3-((3-((4'-methoxy-[1,1'-biphenyl]-3-yl)diazenyl)phenyl)amino)-2,2-dimethyl-3-oxopropanoate (**52**, 64 mg, 0.144 mmol, 1.00 eq) and lithium hydroxide (17.2 mg, 0.720 mmol, 5.00 eq) to yield compound **6** as an orange solid (46 mg, 77%). R_f = 0.26 (3:1 CH:EA+1% FA). ¹H NMR (500 MHz, MeOD-*d*₄): δ 8.22 (t, *J* = 2.0 Hz, 1H), 8.12 (t, *J* = 1.9 Hz, 1H), 7.88 – 7.79 (m, 1H), 7.78 – 7.67 (m, 3H), 7.67 – 7.63 (m, 2H), 7.59 (t, *J* = 7.8 Hz, 1H), 7.52 (t, *J* = 8.0 Hz, 1H), 7.08 – 7.00 (m, 2H), 3.85 (s, 3H), 1.56 (s, 6H). ¹³C NMR (126 MHz, MeOD-*d*₄): δ 175.9, 172.6, 159.8, 153.0, 153.0, 142.0, 139.3, 132.5, 129.3, 129.0, 129.0, 127.7, 123.3, 120.6, 120.5, 119.2, 114.4, 114.0, 54.4, 50.7, 22.5. qHNMR (400 MHz, MeOD-*d*₄, maleic acid as reference): purity = 96%. HRMS (ESI+): *m/z* calculated 418.1761 for C₂₄H₂₄N₃O₄⁺, found 418.1757 ([M + H]⁺).

(E)-2,2-Dimethyl-3-((3-((4'-methyl-[1,1'-biphenyl]-3-yl)diazenyl)phenyl)amino)-3-oxopropanoic acid (7). Preparation according to general procedure C using ethyl (*E*)-2,2-dimethyl-3-((3-((4'-methyl-[1,1'-biphenyl]-3-yl)diazenyl)phenyl)amino)-3-oxopropanoate (**53**, 64 mg, 0.149 mmol, 1.00 eq) and lithium hydroxide (17.8 mg, 0.745 mmol, 5.00 eq) to yield compound **7** as an orange solid (51 mg, 85%). R_f = 0.31 (3:1 CH:EA+1% FA). ¹H NMR (500 MHz, MeOD-*d*₄): δ 8.22 (t, *J* = 2.0 Hz, 1H), 8.14 (t, *J* = 1.9 Hz, 1H), 7.92 – 7.83 (m, 1H), 7.80 – 7.67 (m, 3H), 7.64 – 7.57 (m, 3H), 7.52 (t, *J* = 8.0 Hz, 1H), 7.31 (d, *J* = 7.8 Hz, 2H), 2.40 (s, 3H), 1.56 (s, 6H). ¹³C NMR (126 MHz, MeOD-*d*₄): δ 175.9, 172.6, 153.0, 152.9, 142.2, 139.3, 137.5, 137.2, 129.3, 129.3, 129.2, 129.0, 126.5, 123.4, 120.92, 120.7, 119.2, 114.4, 50.7, 22.5, 19.7. qHNMR (400 MHz, MeOD-*d*₄, maleic acid as reference): purity = 100%. HRMS (ESI+): *m/z* calculated 402.1812 for C₂₄H₂₄N₃O₃⁺, found 402.1808 ([M+H]⁺).

(E)-3-((3-((4'-Chloro-[1,1'-biphenyl]-3-yl)diazenyl)phenyl)amino)-2,2-dimethyl-3-oxopropanoic acid (8). Preparation according to general procedure C using ethyl (*E*)-3-((3-((4'-chloro-[1,1'-biphenyl]-3-yl)diazenyl)phenyl)amino)-2,2-dimethyl-3-oxopropanoate (**44**, 21 mg, 0.047 mmol, 1.00 eq) and lithium hydroxide (5.59 mg, 0.233 mmol, 5.00 eq) to yield compound **8** as an orange solid (8 mg, 41%). R_f = 0.36 (3:1 CH:EA+1% FA). ¹H NMR (500 MHz, MeOD-*d*₄) δ 8.22 (t, *J* = 2.0 Hz, 1H), 8.13 (t, *J* = 1.9 Hz, 1H), 7.92 – 7.86 (m, 1H), 7.79 – 7.75 (m, 1H), 7.73 – 7.67 (m, 4H), 7.62 (t, *J* = 7.8 Hz, 1H), 7.53 – 7.45 (m, 3H), 1.55 (s, 6H). ¹³C NMR (126 MHz, MeOD-*d*₄): δ 178.6, 174.6, 154.4, 154.3, 142.3, 140.7, 140.2, 135.0, 130.9, 130.7, 130.4, 130.1, 129.6, 124.7, 123.0, 122.2, 120.6, 115.7, 52.3, 24.3. qHNMR (400 MHz, MeOD-*d*₄, maleic acid as reference): purity = 98%. HRMS (ESI+): *m/z* calculated 422.1266 for C₂₃H₂₀ClN₃O₃⁺, found 422.1263 ([M+H]⁺).

(E)-2,2-Dimethyl-3-oxo-3-((3-((4'-(trifluoromethyl)-[1,1'-biphenyl]-3-yl)diazenyl)phenyl)amino)propanoic acid (9). Preparation according to general procedure C using ethyl (*E*)-2,2-dimethyl-3-oxo-3-((3-((4'-(trifluoromethyl)-[1,1'-biphenyl]-3-yl)diazenyl)phenyl)amino)propanoate (**45**, 105 mg, 0.217 mmol, 1.00 eq) and lithium hydroxide (26.0 mg, 1.08 mmol, 5.00 eq) to yield compound **9** as an orange solid (85 mg, 86%). R_f = 0.39 (3:1 CH:EA+1% FA). ¹H NMR (400 MHz, MeOD-*d*₄): δ 8.25 – 8.21 (m, 1H), 8.21 – 8.17 (m, 1H), 7.96 – 7.92 (m, 1H), 7.89 (d, *J* = 8.0 Hz, 2H), 7.85 – 7.80 (m, 1H), 7.77 (d, *J* = 8.2 Hz, 2H), 7.74 – 7.62 (m, 3H), 7.50 (t, *J* = 8.0 Hz, 1H), 1.55 (s, 6H). ¹³C NMR (126 MHz, MeOD-*d*₄): δ 178.2, 174.3, 154.2, 154.1, 145.1, 141.8, 140.6, 130.9, 130.8, 130.6 (q, *J* = 32.3 Hz), 130.3, 128.6, 126.8 (q, *J* = 4.0 Hz), 125.3 (q, *J* = 270.6 Hz), 124.6, 123.4, 122.4, 120.5, 115.6, 52.1,

24.0. qHNMR (400 MHz, MeOD-*d*₄, ethyl 4-(dimethylamino)benzoate as reference): purity = 95%. HRMS (ESI+): *m/z* calculated 456.1530 for C₂₄H₂₁N₃O₃F₃⁺, found: 456.1526 ([M+H]⁺).

(*E*)-2,2-Dimethyl-3-oxo-3-((3-((3'-(trifluoromethyl)-[1,1'-biphenyl]-3-yl)diazenyl)phenyl)amino)propanoic acid (10). Preparation according to general procedure C using ethyl (*E*)-2,2-dimethyl-3-oxo-3-((3-((3'-(trifluoromethyl)-[1,1'-biphenyl]-3-yl)diazenyl)phenyl)amino)propanoate (**46**, 130 mg, 0.27 mmol, 1.00 eq) and lithium hydroxide (32.2 mg, 1.35 mmol, 5.00 eq) to yield compound **10** as a yellow solid (79 mg, 65%). R_f = 0.28 (3:1 CH:EA+1% FA). ¹H NMR (400 MHz, MeOD-*d*₄): δ 8.24 – 8.21 (m, 1H), 8.18 – 8.12 (m, 1H), 7.98 – 7.91 (m, 3H), 7.83 – 7.79 (m, 1H), 7.73 – 7.63 (m, 5H), 7.49 (t, *J* = 8.0 Hz, 1H), 1.54 (s, 6H). ¹³C NMR (101 MHz, MeOD-*d*₄): δ 179.7, 175.1, 154.4, 154.3, 142.6, 142.0, 140.7, 132.4 (q, *J* = 32.4 Hz), 131.9, 131.9, 131.1, 131.0, 130.9, 125.5 (q, *J* = 4.0 Hz), 124.7, 124.6 (d, *J* = 3.8 Hz), 124.3 (q, *J* = 271.8 Hz), 123.4, 122.4, 120.6, 115.6, 52.4, 24.5. qHNMR (400 MHz, MeOD-*d*₄, ethyl 4-(dimethylamino)benzoate as reference): purity = 96%. HRMS (ESI+): *m/z* calculated 456.1530 for C₂₄H₂₁F₃O₃N₃⁺, found: 456.1527 ([M+H]⁺).

(*E*)-3-((3-((3',4'-Bis(trifluoromethyl)-[1,1'-biphenyl]-3-yl)diazenyl)phenyl)amino)-2,2-dimethyl-3-oxopropanoic acid (11). Preparation according to general procedure C using ethyl (*E*)-3-((3-((3',4'-bis(trifluoromethyl)-[1,1'-biphenyl]-3-yl)diazenyl)phenyl)amino)-2,2-dimethyl-3-oxopropanoate (**47**, 100 mg, 0.181 mmol, 1.00 eq) and lithium hydroxide (21.7 mg, 0.905 mmol, 5.00 eq) to yield compound **11** as a yellow solid (71 mg, 75%). R_f = 0.29 (3:1 CH:EA+1% FA). ¹H NMR (400 MHz, MeOD-*d*₄): δ 8.24 – 8.22 (m, 1H), 8.21 – 8.13 (m, 3H), 8.05 (d, *J* = 8.2 Hz, 1H), 8.00 – 7.96 (m, 1H), 7.89 – 7.84 (m, 1H), 7.73 – 7.66 (m, 3H), 7.49 (t, *J* = 8.0 Hz, 1H), 1.55 (s, 6H). ¹³C NMR (126 MHz, MeOD-*d*₄): δ 179.0, 174.7, 166.1, 154.4, 154.2, 146.0, 140.8, 140.3, 132.2, 131.4, 131.0, 130.5, 130.1 (q, *J* = 5.9 Hz), 129.5 (q, *J* = 31.2 Hz), 127.8 (q, *J* = 34.3 Hz), 127.5 (q, *J* = 5.9 Hz), 124.8, 124.3, 122.7, 121.4 (d, *J* = 256.2 Hz), 120.7, 115.7, 52.3, 24.4. qHNMR (400 MHz, MeOD-*d*₄, ethyl 4-(dimethylamino)benzoate as reference): purity = 95%. HRMS (ESI+): *m/z* calculated 524.1403 for C₂₅H₂₀F₆N₃O₃⁺, found 524.1399 ([M+H]⁺).

(*E*)-2,2-Dimethyl-3-((3-((3-(naphthalen-2-yl)phenyl)diazenyl)phenyl)amino)-3-oxopropanoic acid (12). Preparation according to general procedure C using ethyl (*E*)-2,2-dimethyl-3-((3-((3-(naphthalen-2-yl)phenyl)diazenyl)phenyl)amino)-3-oxopropanoate (**48**, 80 mg, 0.172 mmol, 1.00 eq) and lithium hydroxide (20.6 mg, 0.860 mmol, 5.00 eq) to yield compound **12** as an orange solid (48 mg, 64%). R_f: 0.31 (3:1 CH:EA+1% FA). ¹H NMR (400 MHz, MeOD-*d*₄): δ 8.28 (t, *J* = 1.8 Hz, 1H), 8.24 (t, *J* = 2.0 Hz, 1H), 8.21 – 8.16 (m, 1H), 8.00 – 7.82 (m, 6H), 7.76 – 7.64 (m, 3H), 7.54 – 7.48 (m, 3H), 1.55 (s, 6H). ¹³C NMR (126 MHz, MeOD-*d*₄): δ 178.0, 173.5, 153.0, 152.9, 142.1, 139.7, 137.4, 133.8, 133.0, 129.7, 129.5, 129.1, 128.4, 128.0, 127.3, 126.1, 125.9, 125.5, 124.8, 123.2, 121.4, 121.2, 119.2, 114.2, 51.0, 23.0. qHNMR (400 MHz, MeOD-*d*₄, maleic acid as reference): purity = 96%. HRMS (ESI+): *m/z* calculated 438.1812 for C₂₇H₂₄N₃O₃⁺, found 438.1810 ([M+H]⁺).

(*E*)-3-((3-((9,9-Dimethyl-9H-fluoren-3-yl)diazenyl)phenyl)amino)-2,2-dimethyl-3-oxopropanoic acid (13). Preparation according to general procedure C using ethyl (*E*)-3-((3-((9,9-dimethyl-9H-fluoren-3-yl)diazenyl)phenyl)amino)-2,2-dimethyl-3-oxopropanoate (**55**, 274.0 mg, 0.602 mmol, 1.00 eq) and lithium hydroxide (72.1 mg, 3.01 mmol, 5.00 eq) to yield compound **7** as an orange solid (261 mg, 99%). R_f = 0.26 (3:1 CH:EA+1% FA). ¹H NMR (500 MHz, MeOD-*d*₄): δ 8.30 – 8.28 (m, 1H), 8.25 (t, *J* = 2.0 Hz, 1H), 7.96 – 7.91 (m, 1H), 7.90 – 7.86 (m, 1H), 7.77 – 7.74 (m, 1H), 7.73 – 7.65 (m, 2H), 7.54 (t, *J* = 8.0 Hz, 2H), 7.42 – 7.35 (m, 2H), 1.59 (s, 6H), 1.55 (s, 6H). ¹³C NMR (126 MHz, MeOD-*d*₄) δ 175.9, 173.8, 157.0, 153.8, 153.1, 152.4, 140.4, 139.3, 138.2, 129.0, 127.7, 127.0, 123.4, 123.2, 123.0, 122.4, 120.0, 119.2, 114.4, 112.6, 50.7, 46.6, 26.0, 22.6. qHNMR (400 MHz, MeOD-*d*₄, maleic acid as

reference) purity = 97%. HRMS (ESI+): m/z calculated 428.1969 for $C_{26}H_{26}N_3O_3^+$, found 428.1964 ($[M+H]^+$).

Precursors

3',4'-Dimethoxy-[1,1'-biphenyl]-3-carbaldehyde (16). Preparation according to general procedure A using 3,4-dimethoxyphenylboronic acid (**15**, 1180 mg, 6.49 mmol, 1.00 eq), *m*-bromo-benzaldehyde (**14**, 1000 mg, 5.41 mmol, 1.00 eq), XPhos Pd G₂ (425.3 mg, 0.54 mmol, 0.10 eq) and tribasic potassium phosphate (3442 mg, 16.22 mmol, 3.0 eq) to yield compound **16** as a brown oil (1081 mg, 83%). R_f = 0.38 (3:1 CH:EA). ¹H NMR (400 MHz, acetone-*d*₆): δ 7.80 – 7.77 (m, 1H), 7.77 – 7.71 (m, 1H), 7.57 (t, J = 7.9 Hz, 1H), 7.38 – 7.33 (m, 1H), 7.30 – 7.26 (m, 1H), 7.25 – 7.20 (m, 1H), 7.05 (d, J = 8.4 Hz, 1H), 3.89 (s, 3H), 3.85 (s, 3H). ¹³C NMR (101 MHz, CDCl₃): δ 192.2, 149.2, 149.0, 141.8, 136.7, 132.6, 132.4, 129.3, 128.3, 127.4, 119.4, 111.4, 110.1, 55.9, 55.8. MS (ASAP+): m/z 242.7 ($[M+H]^+$).

3,4-Dimethoxy-3'-vinyl-1,1'-biphenyl (17). Methyltriphenylphosphonium bromide (3930 mg, 11.00 mmol, 2.50 eq) was dissolved in tetrahydrofuran (THF, 20 mL) in a three-necked round bottom flask purged with nitrogen. Potassium tert-butoxide (1234 mg, 11.00 mmol, 2.50 eq) was added in portions to the solution at 0°C, and the mixture was stirred for 15 min at room temperature. Then 3',4'-dimethoxy-[1,1'-biphenyl]-3-carbaldehyde (**16**, 1075 mg, 4.44 mmol, 1.00 eq) dissolved in THF (10 mL) was added to the solution at 0°C. The resulting mixture was allowed to reach room temperature and stirred continuously overnight. The mixture was filtered through Celite 545 and the solvent was removed under reduced pressure. The crude product was dissolved in 2 N aqueous HCl and the aqueous mixture was extracted with EA three times. The organic layers were combined, dried over MgSO₄, filtered and concentrated. The crude product was purified by CC using a gradient of CH:EA (4:1 to 3:1) to give **17** as a yellow oil (998 mg, 94%). R_f = 0.51 (3:1 CH:EA). ¹H NMR (400 MHz, acetone-*d*₆): δ 7.71 – 7.70 (m, 1H), 7.55 – 7.51 (m, 1H), 7.43 – 7.35 (m, 2H), 7.26 (d, J = 2.2 Hz, 1H), 7.21 (dd, J = 8.3, 2.1 Hz, 1H), 7.03 (d, J = 8.3 Hz, 1H), 6.83 (dd, J = 17.5, 11.1 Hz, 1H), 5.94 – 5.85 (m, 1H), 5.31 – 5.24 (m, 1H), 3.90 (s, 3H), 3.85 (s, 3H). ¹³C NMR (101 MHz, acetone-*d*₆): δ 150.7, 150.2, 142.2, 139.0, 137.9, 134.5, 129.8, 127.1, 125.5, 125.3, 120.1, 114.4, 113.1, 111.8, 56.2, 56.2. MS (ASAP+): m/z 240.7 ($[M+H]^+$).

Ethyl 3-((3-iodophenyl)amino)-2,2-dimethyl-3-oxopropanoate (20). 3-Ethoxy-2,2-dimethyl-3-oxopropanoic acid (**19**, 0.454 mL, 3.19 mmol, 1.20 eq) and 1-[bis(dimethylamino)methylene]-1*H*-1,2,3-triazolo[4,5-*b*]pyridinium 3-oxide hexafluorophosphate (HATU, 1214 mg, 3.19 mmol, 1.20 eq) were dissolved in DMF (10 mL). Ethyldiisopropylamine (DIPEA, 413 mg, 3.19 mmol, 1.20 eq) was added and the mixture was stirred at room temperature for 40 min. 3-Iodoaniline (**18**, 594 mg, 2.36 mmol, 1.00 eq) was then added and the mixture was stirred at room temperature overnight. The solvent was then removed under reduced pressure, the residue was dissolved in EA and washed with 2 N aqueous HCl and 2 N aqueous NaOH solution. The combined organic layers were dried over MgSO₄, the solvent evaporated under reduced pressure and the crude product was purified by CC using a gradient CH:EA (3:1 to 0:1) to give **20** as a yellow oil (908 mg, 95%). R_f = 0.46 (1:2 CH:EA+1% triethylamine (TAE)). ¹H NMR (400 MHz, CDCl₃): δ 8.77 (s, 1H), 8.00 – 7.96 (m, 1H), 7.50 – 7.46 (m, 1H), 7.45 – 7.42 (m, 1H), 7.03 (t, J = 8.0 Hz, 1H), 4.24 (q, J = 7.2 Hz, 2H), 1.54 (s, 6H), 1.31 (t, J = 7.2 Hz, 3H). ¹³C NMR (101 MHz, CDCl₃): δ 175.8, 170.0, 139.1, 133.5, 130.6, 128.8, 119.2, 94.3, 62.3, 50.5, 24.1, 14.1. MS (ASAP+): m/z 361.4 ($[M]^+$).

Ethyl (E)-3-((3-(2-(3',4'-dimethoxy-[1,1'-biphenyl]-3-yl)vinyl)phenyl)amino)-2,2-dimethyl-3-oxopropanoate (21). Ethyl 3-((3-iodophenyl)amino)-2,2-dimethyl-3-oxopropanoate (**20**, 908 mg, 2.51 mmol, 1.00 eq), 3,4-dimethoxy-3'-vinyl-1,1'-biphenyl (**17**, 724 mg, 3.01 mmol, 1.20

eq), tribasic potassium phosphate (746 mg, 3.51 mmol, 1.40 eq) and palladium(II)acetate (28.2 mg, 0.125 mmol, 0.05 equiv.) were dissolved in DMA (10 mL) in an oven dried round bottom flask purged with nitrogen and refluxed overnight. The mixture was then filtered through Celite 545 and the solvent was removed under reduced pressure. The crude was dissolved in EA and washed with 2 N aqueous NaOH solution. The organic layer was dried over MgSO₄, the solvent was removed under reduced pressure and the crude product was purified by CC using a gradient of CH:EA (2:1 to 1:2) to give **21** as a yellow oil (502 mg, 42%). R_f = 0.18 (5:1 CH:EA). ¹H NMR (400 MHz, acetone-*d*₆): δ 8.86 (s, 1H), 8.00 – 7.96 (m, 1H), 7.92 – 7.86 (m, 1H), 7.59 – 7.52 (m, 3H), 7.43 (t, *J* = 7.7 Hz, 1H), 7.37 – 7.29 (m, 5H), 7.27 – 7.24 (m, 1H), 7.05 (d, *J* = 8.4 Hz, 1H), 4.19 (q, *J* = 7.2 Hz, 2H), 3.92 (s, 3H), 3.86 (s, 3H), 1.54 (s, 6H), 1.24 (t, *J* = 7.1 Hz, 3H). ¹³C NMR (101 MHz, acetone-*d*₆): δ 174.4, 171.2, 150.7, 150.3, 142.3, 140.4, 138.9, 138.8, 134.5, 130.0, 129.8, 129.7, 129.6, 126.9, 125.9, 125.7, 123.0, 120.3, 120.1, 118.9, 113.1, 111.8, 61.8, 56.2, 56.2, 51.8, 23.7, 14.4. MS (ASAP+): *m/z* 473.2 ([M]⁺).

Ethyl 3-((3-((tert-butoxycarbonyl)amino)phenyl)amino)-2,2-dimethyl-3-oxopropanoate (23). 3-Ethoxy-2,2-dimethyl-3-oxopropanoic acid (**19**, 0.369 mL, 2.59 mmol, 1.20 eq) and 1-[bis(dimethylamino)methylene]-1*H*-1,2,3-triazolo[4,5-*b*]pyridinium 3-oxide hexafluorophosphate (HATU, 986 mg, 2.59 mmol, 1.20 eq) were dissolved in DMF (5 mL). Ethyldiisopropylamine (DIPEA, 335 mg, 2.59 mmol, 1.20 eq) was added and the mixture was stirred at room temperature for 40 min. *N*-BOC-*m*-phenylenediamine (**22**, 450 mg, 2.16 mmol, 1.00 eq) was then added and the mixture was stirred at room temperature overnight. The solvent was removed under reduced pressure, the residue was dissolved in EA and washed with 2 N aqueous HCl and 2 N aqueous NaOH solution. The combined organic layers were dried over MgSO₄, concentrated under reduced pressure and the crude product was purified by CC using a gradient CH:EA (3:1 to 0:1) to give **20** as a colorless solid (643 mg, 85%). R_f = 0.41 (3:1 CH:EA). ¹H NMR (400 MHz, CDCl₃): δ 8.53 (s, 1H), 7.72 – 7.66 (m, 1H), 7.25 – 7.18 (m, 2H), 7.10 – 7.04 (m, 1H), 6.50 (s, 1H), 4.23 (q, *J* = 7.2 Hz, 2H), 1.54 (s, 6H), 1.51 (s, 9H), 1.30 (t, *J* = 7.1 Hz, 3H). ¹³C NMR (101 MHz, CDCl₃): δ 175.5, 169.9, 152.8, 139.1, 138.7, 129.6, 114.6, 114.4, 110.0, 80.8, 62.1, 50.6, 28.5, 27.1, 24.0, 14.2. MS (ASAP+): *m/z* 350.7 ([M+H]⁺).

Ethyl 3-((3-((tert-butoxycarbonyl)amino)phenyl)amino)-2,2-dimethyl-3-oxopropanoate (24). Ethyl-3-((3-((tert-butoxycarbonyl)amino)phenyl)amino)-2,2-dimethyl-3-oxopropanoate (**23**, 635 mg, 1.81 mmol, 1.00 eq) was dissolved in chloroform (5 mL) and trifluoroacetic acid (TFA, 1.39 mL, 18.1 mmol, 10 eq) was added to the solution. The mixture was stirred overnight at room temperature. The solvents were then removed under reduced pressure, the crude product was dissolved in EA and washed with 2 N aqueous NaOH solution. The organic layer was dried over MgSO₄ and concentrated and the crude product was purified by CC using a gradient of CH:EA+1% of TAE (2:1 to 1:2) to give **24** as a yellow oil (363 mg, 80% yield). R_f = 0.46 (1:2 CH:EA+1% TAE). ¹H NMR (400 MHz, CDCl₃): δ 8.46 (s, 1H), 7.17 (t, *J* = 2.2 Hz, 1H), 7.08 (t, *J* = 8.0 Hz, 1H), 6.75 – 6.64 (m, 1H), 6.48 – 6.38 (m, 1H), 4.23 (q, *J* = 0.7 Hz, 2H), 3.69 (s, 2H), 1.54 (s, 6H), 1.30 (t, *J* = 0.7 Hz, 3H). ¹³C NMR (101 MHz, CDCl₃): δ 175.6, 169.8, 147.4, 139.0, 129.8, 111.2, 109.9, 106.7, 62.1, 50.6, 24.0, 14.2. MS (ASAP+): *m/z* 250.6 ([M+H]⁺).

3',4'-Dimethoxy-[1,1'-biphenyl]-3-amine (33). Preparation according to general procedure A using 3,4-dimethoxyphenylboronic acid (**28**, 240 mg, 1.32 mmol, 1.20 eq), 3-bromoaniline (**26**, 190 mg, 1.10 mmol, 1.00 eq), XPhos Pd G₂ (425.3 mg, 0.54 mmol, 0.10 eq) and tribasic potassium phosphate (3442 mg, 16.22 mmol, 3.0 eq) to yield compound **33** as a yellow oil (110 mg, 44%). R_f = 0.33 (3:1 CH:EA). ¹H NMR (400 MHz, acetone-*d*₆): δ 7.16 – 7.14 (m, 3H), 7.00 – 6.96 (m, 1H), 6.92 (t, *J* = 2.0 Hz, 1H), 6.86 – 6.80 (m, 1H), 6.64 – 6.58 (m, 1H), 4.65 (s, 2H), 3.87 (s, 3H), 3.83 (s, 3H). ¹³C NMR (101 MHz, acetone-*d*₆): δ 150.8, 150.7, 143.2, 132.8, 130.8, 128.0, 123.2, 123.1, 120.2, 119.3, 113.1, 111.7, 56.3, 56.2. MS (ASAP+): *m/z* 229.8 ([M+H]⁺).

3',4'-Dimethoxy-[1,1'-biphenyl]-2-amine (34). Preparation according to general procedure A using 3,4-dimethoxyphenylboronic acid (**28**, 793 mg, 4.36 mmol, 1.00 eq), 2-bromoaniline (**27**, 900 mg, 5.23 mmol, 1.20 eq), XPhos Pd G₂ (429 mg, 0.545 mmol, 0.125 eq) and tribasic potassium phosphate (2776 mg, 13.10 mmol, 3.00 eq) to yield compound **34** as a yellow oil (455 mg, 46%). R_f = 0.24 (3:1 CH:EA). ¹H NMR (400 MHz, MeOD-*d*₄): δ 7.11 – 7.01 (m, 3H), 7.00 – 6.98 (m, 1H), 6.99 – 6.92 (m, 1H), 6.85 – 6.78 (m, 1H), 6.78 – 6.70 (m, 1H), 3.87 (s, 3H), 3.85 (s, 3H). ¹³C NMR (101 MHz, MeOD-*d*₄): δ 149.2, 148.3, 143.9, 132.7, 129.8, 127.8, 127.7, 121.2, 118.2, 115.7, 112.6, 111.9, 55.1, 55.1. MS (ASAP+): *m/z* 229.7 ([M+H]⁺).

3',4'-Dimethoxy-[1,1'-biphenyl]-4-amine (35). Preparation according to general procedure A using 3,4-dimethoxyphenylboronic acid (**28**, 793 mg, 4.36 mmol, 1.00 eq), 4-bromoaniline (**25**, 900 mg, 5.23 mmol, 1.20 eq), XPhos Pd G₂ (429 mg, 0.545 mmol, 0.125 eq) and tribasic potassium phosphate (2776 mg, 13.10 mmol, 3.00 eq) to yield compound **35** as a yellow oil (520 mg, 52%). R_f = 0.15 (2:1 CH:EA). ¹H NMR (400 MHz, MeOD-*d*₄): δ 7.37 – 7.30 (m, 2H), 7.12 – 7.03 (m, 2H), 6.96 (d, *J* = 8.3 Hz, 1H), 6.81 – 6.74 (m, 2H), 3.88 (s, 3H), 3.84 (s, 3H). ¹³C NMR (101 MHz, MeOD-*d*₄): δ 150.6, 149.2, 147.8, 136.3, 132.3, 128.3, 119.7, 116.9, 113.4, 111.4, 56.6, 56.5. MS (ASAP+): *m/z* 229.3 ([M]⁺).

4-(Trifluoromethyl)-[1,1'-biphenyl]-3-amine (37). Preparation according to general procedure A using 4-(trifluoromethyl)phenylboronic acid (**29**, 570 mg, 3.00 mmol, 1.00 eq), 3-bromoaniline (**26**, 619 mg, 3.60 mmol, 1.20 eq), XPhos Pd G₃ (324 mg, 0.375 mmol, 0.125 eq) and tribasic potassium phosphate (1910 mg, 9.00 mmol, 3.00 eq) to yield compound **37** as a yellow oil (675 mg, 95%). R_f = 0.31 (3:1 CH:EA). ¹H NMR (500 MHz, acetone-*d*₆): δ 7.80 (d, *J* = 8.9 Hz, 2H), 7.76 (d, *J* = 8.9 Hz, 2H), 7.18 (t, *J* = 7.8 Hz, 1H), 7.04 – 6.99 (m, 1H), 6.94 – 6.90 (m, 1H), 6.76 – 6.72 (m, 1H), 4.80 (s, 2H). ¹³C NMR (126 MHz, acetone-*d*₆): δ 150.1, 146.6, 141.0, 130.6, 129.3 (q, *J* = 32.4 Hz), 128.2, 126.4 (q, *J* = 3.8 Hz), 125.6 (q, *J* = 271.1 Hz), 116.4, 115.3, 113.7. MS (ASAP+): *m/z* 237.6 ([M+H]⁺).

3-(Trifluoromethyl)-[1,1'-biphenyl]-3-amine (38). Preparation according to general procedure A using 3-(trifluoromethyl)phenylboronic acid (**30**, 460 mg, 2.42 mmol, 1.20 eq), 3-bromoaniline (**26**, 344 mg, 2.00 mmol, 1.00 eq), XPhos Pd G₃ (216 mg, 0.25 mmol, 0.25 eq) and tribasic potassium phosphate (1274 mg, 6.00 mmol, 3.00 eq) to yield compound **38** as a yellow oil (444 mg, 94%). R_f = 0.53 (4:1 CH:EA). ¹H NMR (500 MHz, acetone-*d*₆): δ 7.92 – 7.83 (m, 2H), 7.73 – 7.61 (m, 2H), 7.18 (t, *J* = 7.8 Hz, 1H), 7.03 – 7.00 (m, 1H), 6.94 – 6.90 (m, 1H), 6.77 – 6.69 (m, 1H), 4.80 (s, 2H). ¹³C NMR (126 MHz, acetone-*d*₆): δ 150.1, 143.7, 141.0, 131.4, 131.3 (q, *J* = 31.6 Hz), 130.6, 130.5, 126.5 (q, *J* = 271.3 Hz), 124.5 (q, *J* = 4.0 Hz), 124.1 (q, *J* = 4.0 Hz), 116.2, 115.1, 113.6. MS (ASAP+): *m/z* 237.4 ([M]⁺).

3',4'-Bis(trifluoromethyl)-[1,1'-biphenyl]-3-amine (39). Preparation according to general procedure A using 3',4'-bis(trifluoromethyl)phenylboronic acid (**31**, 901 mg, 2.60 mmol, 1.00 eq), 3-bromoaniline (**26**, 537 mg, 3.12 mmol, 1.20 eq), XPhos Pd G₃ (280 mg, 0.325 mmol, 0.125 eq) and tribasic potassium phosphate (2776 mg, 13.10 mmol, 3.00 eq) to yield compound **39** as a yellow oil (718 mg, 91%). R_f = 0.31 (3:1 CH:EA). ¹H NMR (500 MHz, acetone-*d*₆): δ 8.13 (s, 1H), 8.11 – 8.02 (m, 2H), 7.22 (t, *J* = 7.8 Hz, 1H), 7.11 – 7.07 (m, 1H), 7.02 – 6.97 (m, 1H), 6.83 – 6.78 (m, 1H), 4.89 (s, 2H). ¹³C NMR (126 MHz, acetone-*d*₆): δ 150.3, 147.2, 139.4, 131.6, 130.8, 129.7 (q, *J* = 5.9 Hz), 128.5 (d, *J* = 30.6 Hz), 127.0 (q, *J* = 6.1 Hz), 126.2 (d, *J* = 32.0 Hz), 124.2 (d, *J* = 274.1 Hz), 124.1 (d, *J* = 271.9 Hz), 116.4, 116.0, 113.6. MS (ASAP+): *m/z* 305.6 ([M+H]⁺).

3-(Naphthalen-2-yl)aniline (40). Preparation according to general procedure A using 2-naphthaleneboronic acid (**32**, 1033 mg, 6.00 mmol, 1.00 eq), 3-bromoaniline (**26**, 1032 mg, 6.00 mmol, 1.00 eq), XPhos Pd G₃ (647 mg, 0.75 mmol, 0.25 eq) and with tribasic potassium phosphate (3821 mg, 18.00 mmol, 3.00 eq) to yield compound **40** as a brown solid (6945 mg, 72%). R_f = 0.46 (3:1 CH:EA). ¹H NMR (400 MHz, acetone-*d*₆): δ 8.13 – 8.06 (m, 1H), 8.00 –

7.89 (m, 3H), 7.77 (dd, $J = 8.5, 1.9$ Hz, 1H), 7.56 – 7.44 (m, 3H), 7.18 (t, $J = 7.8$ Hz, 1H), 7.10 (t, $J = 2.1$ Hz, 1H), 7.04 – 6.99 (m, 1H), 6.75 – 6.68 (m, 1H), 4.75 (s, 2H). ^{13}C NMR (101 MHz, acetone- d_6): δ 149.9, 142.5, 140.0, 134.8, 133.6, 130.4, 129.1, 129.0, 128.4, 127.1, 126.6, 126.3, 126.0, 116.6, 114.5, 114.0. MS (ASAP+): m/z 219.7 ($[\text{M}+\text{H}]^+$).

Ethyl (E)-3-((3-((3',4'-dimethoxy-[1,1'-biphenyl]-3-yl)diazenyl)phenyl)amino)-2,2-dimethyl-3-oxopropanoate (41). Preparation according to general procedure B using ethyl 3-((3-aminophenyl)amino)-2,2-dimethyl-3-oxopropanoate (**24**, 116 mg, 0.462 mmol, 1.00 eq) and OXONE® (861 mg, 2.60 mmol, 6.00 eq) for forming the nitrosoarene intermediate and 3',4'-dimethoxy-[1,1'-biphenyl]-3-amine (**33**, 322 mg, 1.40 mmol, 3.00 eq) to yield compound **41** as a yellow solid (45 mg, 21%). $R_f = 0.61$ (2:1 CH:EA). ^1H NMR (400 MHz, acetone- d_6): δ 9.10 (s, 1H), 8.38 – 8.30 (m, 1H), 8.21 – 8.15 (m, 1H), 7.90 – 7.80 (m, 3H), 7.75 – 7.68 (m, 1H), 7.64 (t, $J = 7.8$ Hz, 1H), 7.54 (t, $J = 8.1$ Hz, 1H), 7.38 – 7.35 (m, 1H), 7.34 – 7.29 (m, 1H), 7.09 (d, $J = 8.2$ Hz, 1H), 4.19 (q, $J = 7.1$ Hz, 2H), 3.94 (s, 3H), 3.88 (s, 3H), 1.56 (s, 6H), 1.24 (t, $J = 7.1$ Hz, 3H). ^{13}C NMR (101 MHz, acetone- d_6): δ 174.2, 171.5, 154.0, 153.8, 150.8, 150.6, 143.1, 141.1, 133.7, 130.6, 130.3, 130.3, 123.7, 122.2, 121.2, 120.2, 120.0, 114.3, 113.2, 111.8, 61.8, 56.3, 56.2, 51.9, 23.7, 14.4. MS (ASAP+): m/z 475.7 ($[\text{M}+\text{H}]^+$).

Ethyl (E)-3-((3-((3',4'-dimethoxy-[1,1'-biphenyl]-4-yl)diazenyl)phenyl)amino)-2,2-dimethyl-3-oxopropanoate (42). Preparation according to general procedure B using ethyl 3-((3-aminophenyl)amino)-2,2-dimethyl-3-oxopropanoate (**24**, 284 mg, 1.14 mmol, 1.00 eq) and OXONE® (2093 mg, 6.81 mmol, 6.00 eq) for forming the nitrosoarene intermediate and 3',4'-dimethoxy-[1,1'-biphenyl]-4-amine (**35**, 520 mg, 2.27 mmol, 2.00 eq) to yield compound **42** as a yellow solid (28 mg, 5%). $R_f = 0.33$ (2:1 CH:EA). ^1H NMR (500 MHz, acetone- d_6): δ 9.09 (s, 1H), 8.34 – 8.29 (m, 1H), 7.99 (d, $J = 8.7$ Hz, 2H), 7.91 – 7.86 (m, 2H), 7.86 – 7.82 (m, 1H), 7.72 – 7.67 (m, 1H), 7.53 (t, $J = 8.0$ Hz, 1H), 7.38 – 7.36 (m, 1H), 7.36 – 7.30 (m, 1H), 7.09 (d, $J = 8.4$ Hz, 1H), 4.20 (q, $J = 7.1$ Hz, 2H), 3.94 (s, 3H), 3.88 (s, 3H), 1.56 (s, 6H), 1.24 (t, $J = 7.1$ Hz, 3H). ^{13}C NMR (126 MHz, acetone- d_6): δ 174.2, 171.5, 153.9, 152.1, 150.8, 150.8, 144.7, 141.1, 133.3, 130.3, 128.2, 124.2, 123.5, 120.4, 119.9, 114.2, 113.1, 111.7, 61.8, 56.2, 56.2, 51.9, 23.7, 14.4. MS (ASAP+): m/z 475.5 ($[\text{M}]^{++}$).

Ethyl (E)-3-((3-((3',4'-dimethoxy-[1,1'-biphenyl]-2-yl)diazenyl)phenyl)amino)-2,2-dimethyl-3-oxopropanoate (43). Preparation according to general procedure B using ethyl 3-((3-aminophenyl)amino)-2,2-dimethyl-3-oxopropanoate (**24**, 243 mg, 0.97 mmol, 1.00 eq) and OXONE® (1789 mg, 5.82 mmol, 6.00 eq) for forming the nitrosoarene intermediate and 3',4'-dimethoxy-[1,1'-biphenyl]-2-amine (**34**, 445 mg, 1.94 mmol, 2.00 eq) to yield compound **43** as a yellow solid (16 mg, 4%). $R_f = 0.35$ (2:1 CH:EA). ^1H NMR (500 MHz, acetone- d_6): δ 9.05 (s, 1H), 8.21 – 8.15 (m, 1H), 7.58 – 7.54 (m, 2H), 7.50 – 7.45 (m, 2H), 7.44 – 7.39 (m, 2H), 7.16 – 7.12 (m, 4H), 4.18 (q, $J = 7.0$ Hz, 2H), 3.88 (s, 3H), 3.83 (s, 3H), 1.53 (s, 6H), 1.22 (t, $J = 7.1$ Hz, 3H). ^{13}C NMR (126 MHz, acetone- d_6): δ 174.2, 171.4, 150.8, 150.6, 150.2, 149.7, 149.6, 142.1, 134.9, 132.4, 131.9, 131.7, 130.2, 124.4, 123.5, 119.1, 116.8, 115.8, 115.7, 112.3, 61.8, 56.2, 56.1, 23.6, 23.6, 14.4. MS (ASAP+): m/z 475.5 ($[\text{M}+\text{H}]^{++}$).

Ethyl (E)-3-((3-((4'-chloro-[1,1'-biphenyl]-3-yl)diazenyl)phenyl)amino)-2,2-dimethyl-3-oxopropanoate (44). Preparation according to general procedure B using ethyl 3-((3-aminophenyl)amino)-2,2-dimethyl-3-oxopropanoate (**24**, 596 mg, 2.38 mmol, 2.00 eq) and OXONE® (2195 mg, 7.14 mmol, 6.00 eq) for forming the nitrosoarene intermediate and 4'-chloro-[1,1'-biphenyl]-4-amine (**36**, 286 mg, 1.19 mmol, 1.00 eq) to yield compound **44** as an orange solid (21 mg, 4%). $R_f = 0.68$ (3:1 CH:EA). ^1H NMR (500 MHz, acetone- d_6): δ 9.10 (s, 1H), 8.36 (t, $J = 2.0$ Hz, 1H), 8.19 (t, $J = 1.9$ Hz, 1H), 7.97 – 7.91 (m, 1H), 7.88 – 7.79 (m, 3H), 7.74 – 7.66 (m, 2H), 7.56 – 7.50 (m, 3H), 4.22 – 4.16 (m, 2H), 1.56 (s, 6H), 1.27 – 1.21 (m, 3H). ^{13}C NMR (126 MHz, acetone- d_6): δ 173.3, 170.6, 153.1, 152.9, 140.9, 140.2, 138.8, 133.5,

130.0, 129.6, 129.4, 129.1, 128.7, 122.9, 121.8, 121.1, 119.0, 113.6, 61.0, 51.0, 22.8, 13.5. MS (ASAP+): m/z 449.5 ([M+H]⁺).

Ethyl (E)-2,2-dimethyl-3-oxo-3-((3-((4'-(trifluoromethyl)-[1,1'-biphenyl]-3-yl)diazanyl)phenyl)amino)propanoate (45). Preparation according to general procedure B using ethyl 3-((3-aminophenyl)amino)-2,2-dimethyl-3-oxopropanoate (**24**, 535 mg, 2.14 mmol, 1.00 eq) and OXONE® (2628 mg, 8.55 mmol, 6.00 eq) for forming the nitrosoarene intermediate and 4'-(trifluoromethyl)-[1,1'-biphenyl]-4-amine (**37**, 675 mg, 2.85 mmol, 2.00 eq) to yield compound **45** as a yellow solid (115 mg, 11%). R_f = 0.47 (4:1 CH:EA). ¹H NMR (400 MHz, acetone-*d*₆): δ 9.11 (s, 1H), 8.37 (t, J = 2.0 Hz, 1H), 8.27 (t, J = 1.7 Hz, 1H), 8.06 – 7.97 (m, 3H), 7.97 – 7.92 (m, 1H), 7.90 – 7.82 (m, 3H), 7.77 – 7.71 (m, 2H), 7.55 (t, J = 8.0 Hz, 1H), 4.20 (q, J = 7.1 Hz, 2H), 1.56 (s, 6H), 1.24 (t, J = 7.1 Hz, 3H). ¹³C NMR (101 MHz, acetone-*d*₆): δ 174.2, 171.5, 154.0, 153.7, 144.8, 141.5, 141.1, 131.0, 130.8, 130.8 (q, J = 31.8 Hz), 130.3, 128.7, 126.8 (q, J = 4.0 Hz), 125.4 (q, J = 258.8 Hz) 123.8, 123.2, 122.4, 120.0, 114.5, 61.8, 51.9, 23.7, 14.4. MS (ASAP+): m/z 483.1 ([M]⁺).

Ethyl (E)-2,2-dimethyl-3-oxo-3-((3'-(trifluoromethyl)-[1,1'-biphenyl]-3-yl)diazanyl)phenyl)amino)propanoate (46). Preparation according to general procedure B using ethyl 3-((3-aminophenyl)amino)-2,2-dimethyl-3-oxopropanoate (**24**, 440 mg, 1.76 mmol, 1.00 eq) and OXONE® (3242 mg, 10.54 mmol, 6.00 eq) for forming the nitrosoarene intermediate and 3'-(trifluoromethyl)-[1,1'-biphenyl]-4-amine (**38**, 834 mg, 3.52 mmol, 2.00 eq) to yield compound **46** as a yellow solid (140 mg, 17%). R_f = 0.62 (3:1 CH:EA). ¹H NMR (400 MHz, acetone-*d*₆): δ 9.11 (s, 1H), 8.38 – 8.35 (m, 1H), 8.28 – 8.26 (m, 1H), 8.13 – 8.08 (m, 2H), 8.01 – 7.97 (m, 1H), 7.97 – 7.93 (m, 1H), 7.88 – 7.84 (m, 1H), 7.79 – 7.76 (m, 2H), 7.75 – 7.73 (m, 1H), 7.73 – 7.71 (m, 1H), 7.55 (t, J = 8.0 Hz, 1H), 4.20 (q, J = 7.1 Hz, 2H), 1.56 (s, 6H), 1.24 (t, J = 7.1 Hz, 3H). ¹³C NMR (101 MHz, acetone-*d*₆): δ 174.2, 171.5, 154.0, 153.8, 142.0, 141.5, 141.1, 131.9 (q, J = 2.5 Hz), 131.4 (q, J = 32.7 Hz), 131.0, 130.9, 130.8, 130.3, 125.4 (q, J = 3.9 Hz), 125.3 (q, J = 271.8 Hz), 124.5 (q, J = 3.8 Hz), 123.8, 123.0, 122.4, 120.0, 114.5, 61.9, 51.9, 23.7, 14.4. MS (ASAP+): m/z 483.1 ([M]⁺).

Ethyl (E)-3-((3-((3',4'-bis(trifluoromethyl)-[1,1'-biphenyl]-3-yl)diazanyl)phenyl)amino)-2,2-dimethyl-3-oxopropanoate (47). Preparation according to general procedure B using ethyl 3-((3-aminophenyl)amino)-2,2-dimethyl-3-oxopropanoate (**24**, 439 mg, 1.76 mmol, 1.00 eq) and OXONE® (2158 mg, 7.92 mmol, 6.00 eq) for forming the nitrosoarene intermediate and 3',4'-bis-(trifluoromethyl)-[1,1'-biphenyl]-4-amine (**39**, 715 mg, 2.34 mmol, 2.00 eq) to yield compound **47** as a yellow solid (109 mg, 11%). R_f = 0.31 (4:1 CH:EA). ¹H NMR (400 MHz, acetone-*d*₆): δ 9.11 (s, 1H), 8.42 – 8.30 (m, 4H), 8.17 (d, J = 8.3 Hz, 1H), 8.07 – 7.99 (m, 2H), 7.87 – 7.82 (m, 1H), 7.79 (t, J = 7.8 Hz, 1H), 7.75 – 7.70 (m, 1H), 7.55 (t, J = 8.0 Hz, 1H), 4.20 (q, J = 7.1 Hz, 2H), 1.56 (s, 6H), 1.24 (t, J = 7.1 Hz, 3H). ¹³C NMR (101 MHz, acetone-*d*₆): δ 174.2, 171.5, 154.1, 153.7, 145.6, 141.1, 139.9, 132.2, 131.2, 131.0, 130.3 130.3 – 127.5 (m), 130.0 (q, J = 6.1 Hz), 128.9 (q, J = 32.5 Hz), 127.6 (q, J = 5.8 Hz), 127.4 (q, J = 32.7 Hz), 124.3 – 121.4 (m), 123.9, 123.7, 122.9, 120.0, 114.5, 61.9, 51.9, 23.7, 14.4. MS (ASAP+): m/z 551.3 ([M]⁺).

Ethyl (E)-2,2-dimethyl-3-((3-((3-(naphthalen-2-yl)phenyl)diazanyl)phenyl)amino)-3-oxopropanoate (48). Preparation according to general procedure B using ethyl 3-((3-aminophenyl)amino)-2,2-dimethyl-3-oxopropanoate (**24**, 250 mg, 1.00 mmol, 1.00 eq) and OXONE® (1789 mg, 5.82 mmol, 6.00 eq) for forming the nitrosoarene intermediate and 3-(naphthalen-2-yl)aniline (**40**, 638 mg, 2.91 mmol, 3.00 eq) to yield compound **48** as an orange solid (80 mg, 18%). R_f = 0.35 (3:1 CH:EA). ¹H NMR (400 MHz, acetone-*d*₆): δ 9.11 (s, 1H), 8.38 (t, J = 2.0 Hz, 1H), 8.37 – 8.35 (m, 1H), 8.34 – 8.32 (m, 1H), 8.11 – 7.93 (m, 6H), 7.90 – 7.82 (m, 1H), 7.78 – 7.70 (m, 2H), 7.60 – 7.51 (m, 3H), 4.20 (q, J = 7.1 Hz, 2H), 1.56 (s, 6H), 1.24 (t, J = 7.1 Hz, 3H). ¹³C NMR (101 MHz, acetone-*d*₆): δ 173.4, 170.6, 153.2, 152.9, 142.1,

140.2, 137.3, 133.9, 133.1, 130.0, 129.9, 129.4, 128.7, 128.4, 127.6, 126.5, 126.3, 125.9, 125.1, 122.8, 121.6, 121.4, 119.1, 113.5, 61.0, 51.0, 22.8, 13.5. MS (ASAP+): m/z 465.6 ([M+H]⁺).

Ethyl (E)-3-((3-((3-bromophenyl)diazenyl)phenyl)amino)-2,2-dimethyl-3-oxopropanoate (49). Preparation according to general procedure B using ethyl 3-((3-aminophenyl)amino)-2,2-dimethyl-3-oxopropanoate (**24**, 350 mg, 1.40 mmol, 1.00 eq) and OXONE® (2582 mg, 8.40 mmol, 6.00 eq) for forming the nitrosoarene intermediate and 3-bromoaniline (**26**, 722 mg, 4.20 mmol, 3.00 eq) to yield compound **49** as an orange solid (350 mg, 60%). R_f = 0.32 (3:1 CH:EA). ¹H NMR (400 MHz, acetone-*d*₆): δ 9.15 (s, 1H), 8.33 (t, J = 2.0 Hz, 1H), 8.04 (t, J = 1.9 Hz, 1H), 7.98 – 7.93 (m, 1H), 7.89 – 7.81 (m, 1H), 7.77 – 7.67 (m, 2H), 7.61 – 7.51 (m, 2H), 4.19 (q, J = 7.2 Hz, 2H), 1.54 (s, 6H), 1.23 (t, J = 7.1 Hz, 3H). ¹³C NMR (101 MHz, acetone-*d*₆): δ 173.3, 170.7, 153.6, 152.6, 140.2, 133.8, 131.2, 129.5, 124.0, 123.3, 123.1, 122.7, 119.3, 113.6, 61.0, 51.0, 22.7, 13.5. MS (ASAP+): m/z 417.5 ([M+H]⁺).

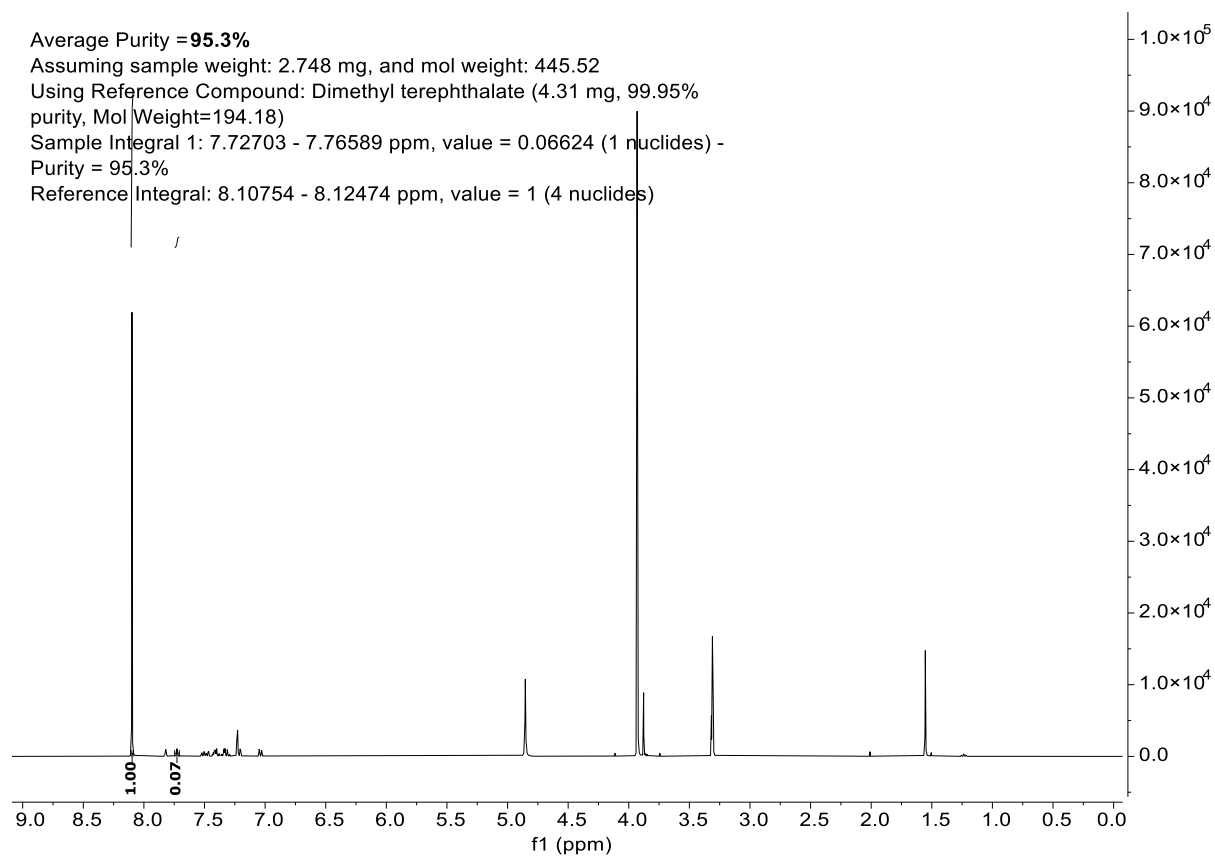
Ethyl (E)-3-((3-((4'-methoxy-[1,1'-biphenyl]-3-yl)diazenyl)phenyl)amino)-2,2-dimethyl-3-oxopropanoate (52). Preparation according to general procedure A using ethyl (E)-3-((3-((3-bromophenyl)diazenyl)phenyl)amino)-2,2-dimethyl-3-oxopropanoate (**49**, 68.5 mg, 0.164 mmol, 1.00 eq), 4-methoxyphenylboronic acid (**51**, 25.3 mg, 0.164 mmol, 1.00 eq), XPhos Pd G₂ (12.9 mg, 0.016 mmol, 0.10 eq) and tribasic potassium phosphate (104 mg, 0.492 mmol, 3.0 eq) to yield compound **52** as a brown oil (69 mg, 94%). R_f = 0.47 (3:1 CH:EA). ¹H NMR (400 MHz, acetone-*d*₆): δ 9.09 (s, 1H), 8.34 (t, J = 2.0 Hz, 1H), 8.16 (t, J = 0.5 Hz, 1H), 7.90 – 7.79 (m, 3H), 7.77 – 7.68 (m, 3H), 7.68 – 7.62 (m, 1H), 7.54 (t, J = 8.0 Hz, 1H), 7.11 – 7.04 (m, 2H), 4.20 (q, J = 7.1 Hz, 2H), 3.87 (s, 3H), 1.56 (s, 6H), 1.24 (t, J = 7.1 Hz, 3H). ¹³C NMR (101 MHz, acetone-*d*₆): δ 174.2, 171.5, 154.0, 153.8, 141.7, 141.1, 139.7, 134.4, 130.9, 130.4, 130.3, 130.0, 129.6, 123.7, 122.7, 122.0, 119.9, 114.5, 61.8, 51.9, 44.3, 23.6, 14.4. MS (ASAP+): m/z 445.5 ([M+H]⁺).

Ethyl (E)-2,2-dimethyl-3-((3-((4'-methyl-[1,1'-biphenyl]-3-yl)diazenyl)phenyl)amino)-3-oxopropanoate (53). Preparation according to general procedure A using ethyl (E)-3-((3-((3-bromophenyl)diazenyl)phenyl)amino)-2,2-dimethyl-3-oxopropanoate (**49**, 68.5 mg, 0.164 mmol, 1.00 eq), 4-tolylboronic acid (**50**, 23.0 mg, 0.164 mmol, 1.00 eq), XPhos Pd G₂ (12.9 mg, 0.016 mmol, 0.10 eq) and tribasic potassium phosphate (104 mg, 0.492 mmol, 3.0 eq) to yield compound **53** as a red oil (64 mg, 91%). R_f = 0.51 (3:1 CH:EA). ¹H NMR (400 MHz, acetone-*d*₆): δ 9.10 (s, 1H), 8.34 (t, J = 2.0 Hz, 1H), 8.18 (t, J = 0.5 Hz, 1H), 7.93 – 7.81 (m, 3H), 7.74 – 7.70 (m, 1H), 7.70 – 7.64 (m, 3H), 7.54 (t, J = 8.0 Hz, 1H), 7.37 – 7.31 (m, 2H), 4.19 (q, J = 7.1 Hz, 2H), 2.40 (s, 3H), 1.56 (s, 6H), 1.24 (t, J = 7.1 Hz, 3H). ¹³C NMR (101 MHz, acetone-*d*₆): δ 173.3, 170.6, 153.1, 152.9, 142.1, 140.2, 137.6, 137.1, 129.8, 129.7, 129.5, 129.4, 126.8, 122.8, 121.1, 121.0, 120.0, 119.0, 113.5, 61.0, 51.0, 22.8, 20.2, 13.5. MS (ASAP+): m/z 429.5 ([M+H]⁺).

Ethyl (E)-3-((3-((9,9-dimethyl-9H-fluoren-3-yl)diazenyl)phenyl)amino)-2,2-dimethyl-3-oxopropanoate (55). Preparation according to general procedure B using ethyl 3-((3-aminophenyl)amino)-2,2-dimethyl-3-oxopropanoate (**24**, 596 mg, 2.38 mmol, 1.00 eq) and OXONE® (2195 mg, 7.14 mmol, 6.00 eq) for forming the nitrosoarene intermediate and 9,9-dimethyl-9H-fluoren-3-amine (**54**, 722 mg, 4.20 mmol, 3.00 eq) to yield compound **55** as an orange solid (320 mg, 59%). R_f = 0.45 (3:1 CH:EA). ¹H NMR (400 MHz, acetone-*d*₆): δ 9.10 (s, 1H), 8.40 – 8.29 (m, 2H), 8.04 – 7.92 (m, 2H), 7.86 – 7.79 (m, 1H), 7.79 – 7.67 (m, 2H), 7.61 – 7.49 (m, 2H), 7.45 – 7.35 (m, 2H), 4.20 (q, J = 7.2 Hz, 2H), 1.56 (s, 6H), 1.55 (s, 6H), 1.25 (t, J = 7.2 Hz, 3H). ¹³C NMR (126 MHz, acetone-*d*₆): δ 173.4, 170.6, 157.0, 154.0, 153.0, 152.4, 140.5, 140.2, 138.2, 129.4, 128.1, 127.3, 123.4, 123.2, 122.8, 122.5, 120.5, 118.9, 113.5, 113.3, 61.0, 51.0, 46.8, 26.62 22.8, 13.5. MS (ASAP+): m/z 455.6 ([M+H]⁺).

gHNMR spectra of **2-13**

(*E*)-3-((3-(2-(3',4'-Dimethoxy-[1,1'-biphenyl]-3-yl)vinyl)phenyl)amino)-2,2-dimethyl-3-oxopropanoic acid (**2**):



(E)-3-((3-((3',4'-Dimethoxy-[1,1'-biphenyl]-3-yl)diazenyl)phenyl)amino)-2,2-dimethyl-3-oxopropanoic acid (3):

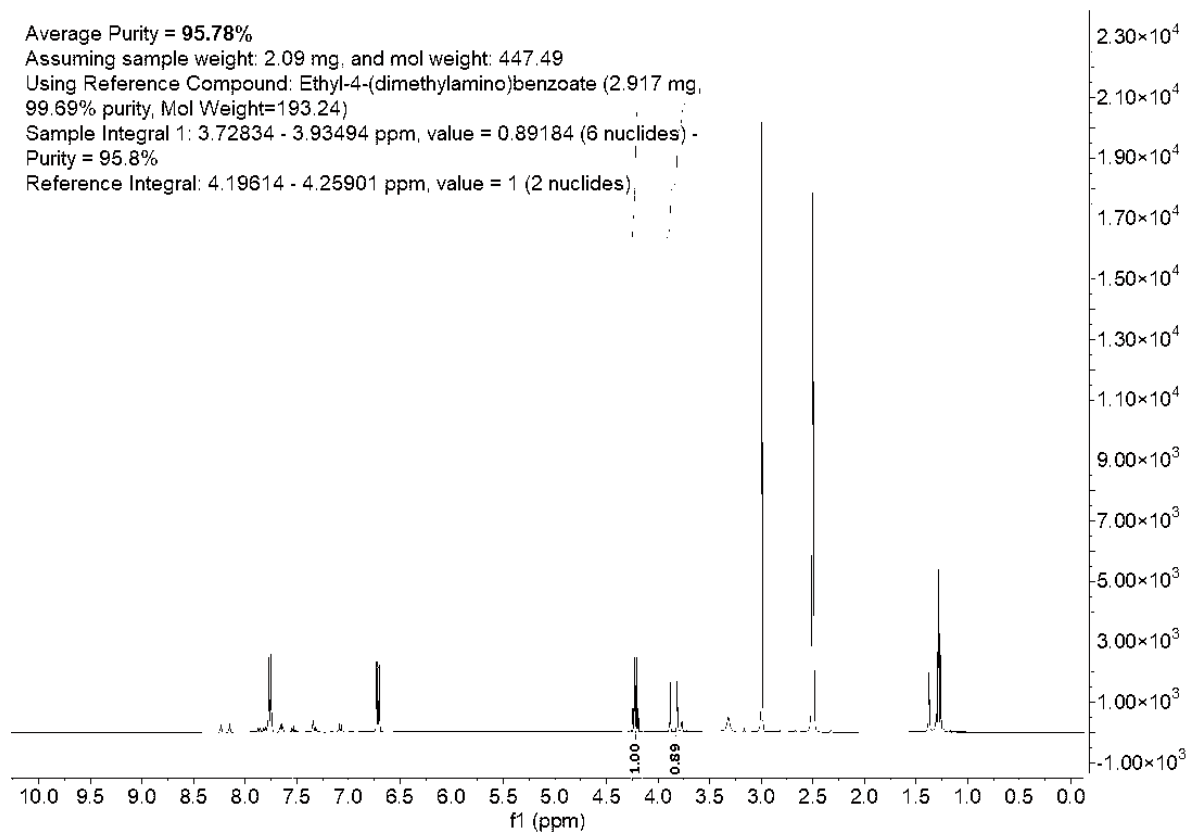
Average Purity = 95.78%

Assuming sample weight: 2.09 mg, and mol weight: 447.49

Using Reference Compound: Ethyl-4-(dimethylamino)benzoate (2.917 mg, 99.69% purity, Mol Weight=193.24)

Sample Integral 1: 3.72834 - 3.93494 ppm, value = 0.89184 (6 nuclides) - Purity = 95.8%

Reference Integral: 4.19614 - 4.25901 ppm, value = 1 (2 nuclides)



(E)-3-((3-((3',4'-Dimethoxy-[1,1'-biphenyl]-4-yl)diazenyl)phenyl)amino)-2,2-dimethyl-3-oxopropanoic acid (4):

Average Purity = **95.06%**

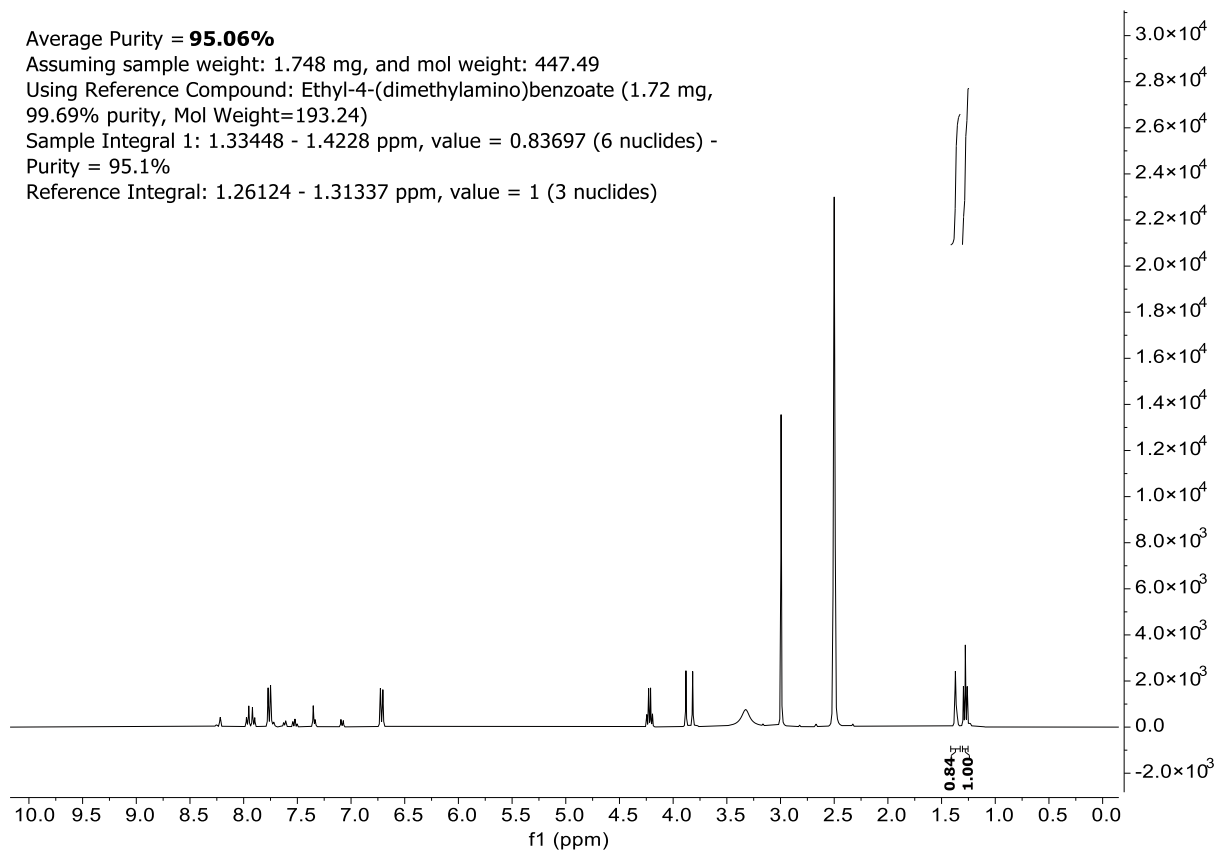
Assuming sample weight: 1.748 mg, and mol weight: 447.49

Using Reference Compound: Ethyl-4-(dimethylamino)benzoate (1.72 mg, 99.69% purity, Mol Weight=193.24)

Sample Integral 1: 1.33448 - 1.4228 ppm, value = 0.83697 (6 nuclides) -

Purity = 95.1%

Reference Integral: 1.26124 - 1.31337 ppm, value = 1 (3 nuclides)



(E)-3-((3-((3',4'-Dimethoxy-[1,1'-biphenyl]-2-yl)diazenyl)phenyl)amino)-2,2-dimethyl-3-oxopropanoic acid (5):

Average Purity = **95.32%**

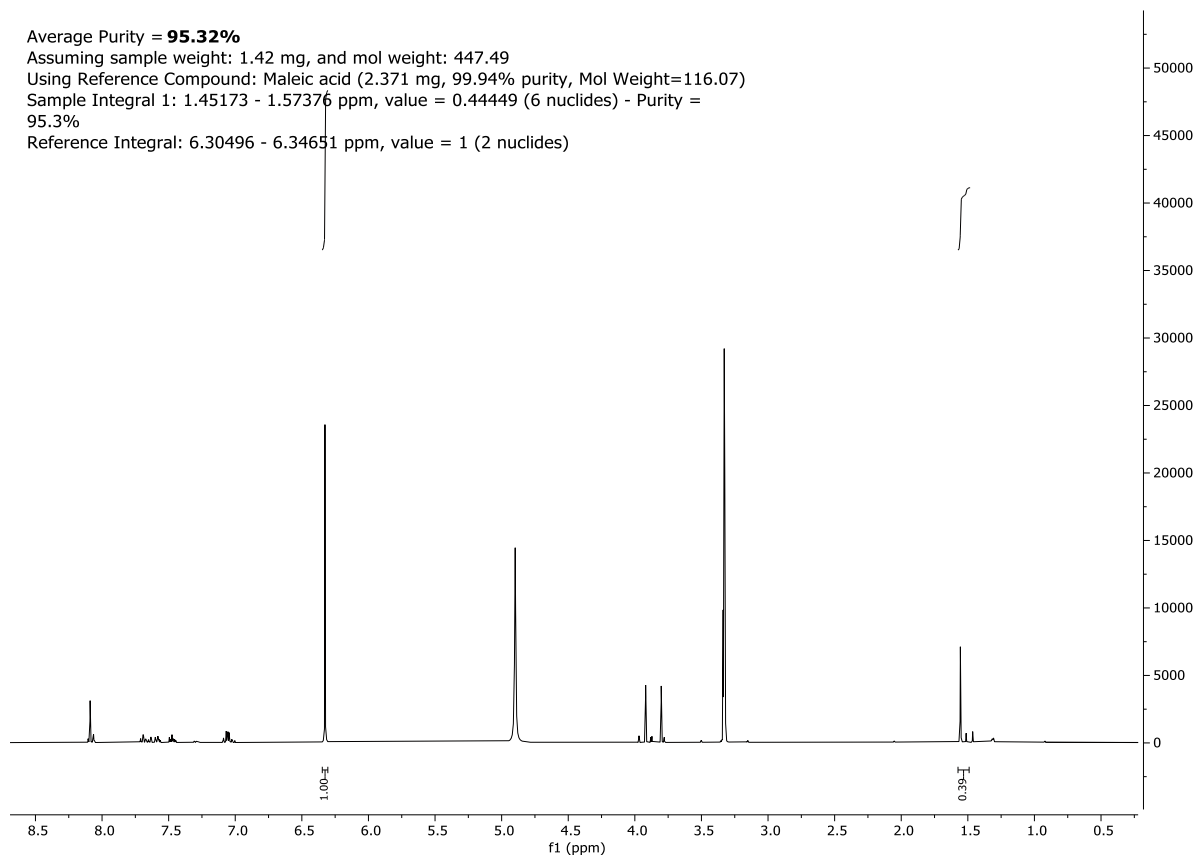
Assuming sample weight: 1.42 mg, and mol weight: 447.49

Using Reference Compound: Maleic acid (2.371 mg, 99.94% purity, Mol Weight=116.07)

Sample Integral 1: 1.45173 - 1.57376 ppm, value = 0.44449 (6 nuclides) - Purity =

95.3%

Reference Integral: 6.30496 - 6.34651 ppm, value = 1 (2 nuclides)



(E)-3-((3-((4'-Methoxy-[1,1'-biphenyl]-3-yl)diazenyl)phenyl)amino)-2,2-dimethyl-3-oxopropanoic acid (6):

Average Purity = **96.28%**

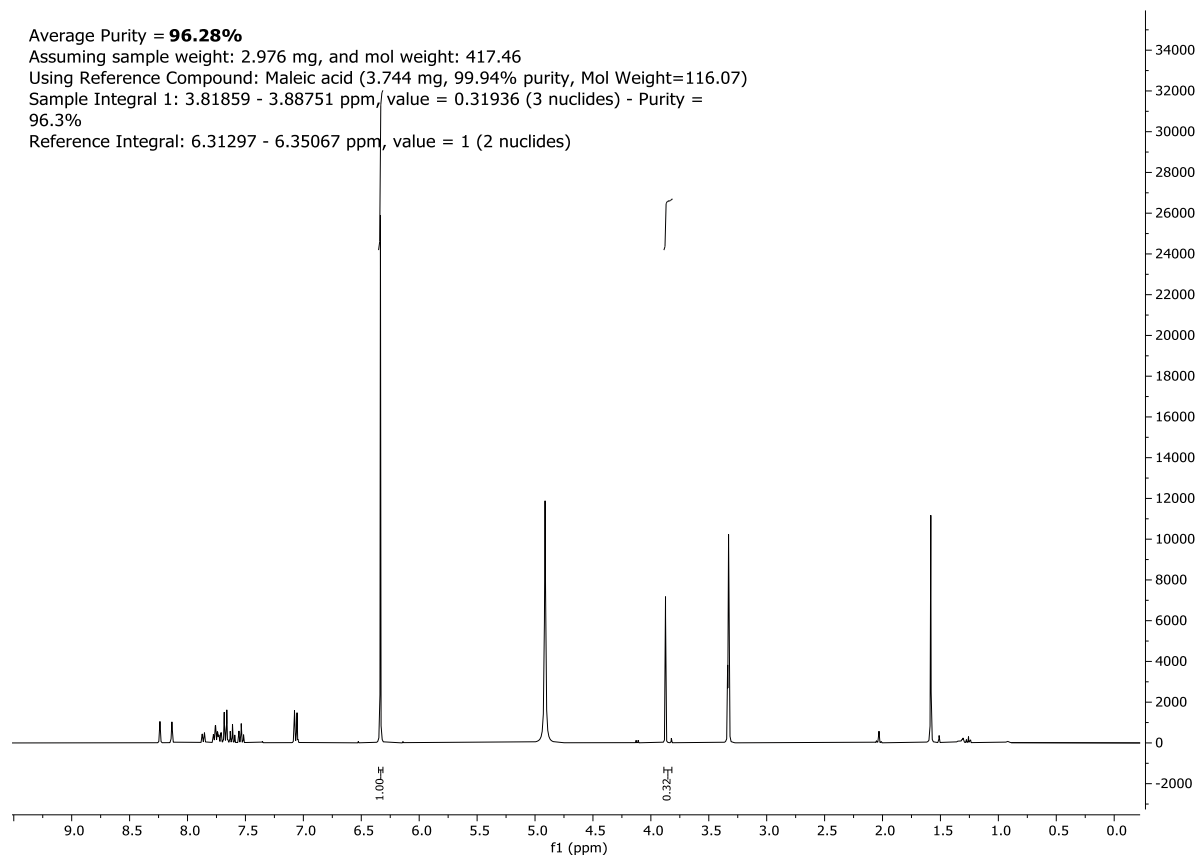
Assuming sample weight: 2.976 mg, and mol weight: 417.46

Using Reference Compound: Maleic acid (3.744 mg, 99.94% purity, Mol Weight=116.07)

Sample Integral 1: 3.81859 - 3.88751 ppm, value = 0.31936 (3 nuclides) - Purity =

96.3%

Reference Integral: 6.31297 - 6.35067 ppm, value = 1 (2 nuclides)



(E)-2,2-Dimethyl-3-((3-((4'-methyl-[1,1'-biphenyl]-3-yl)diazenyl)phenyl)amino)-3-oxopropanoic acid (7):

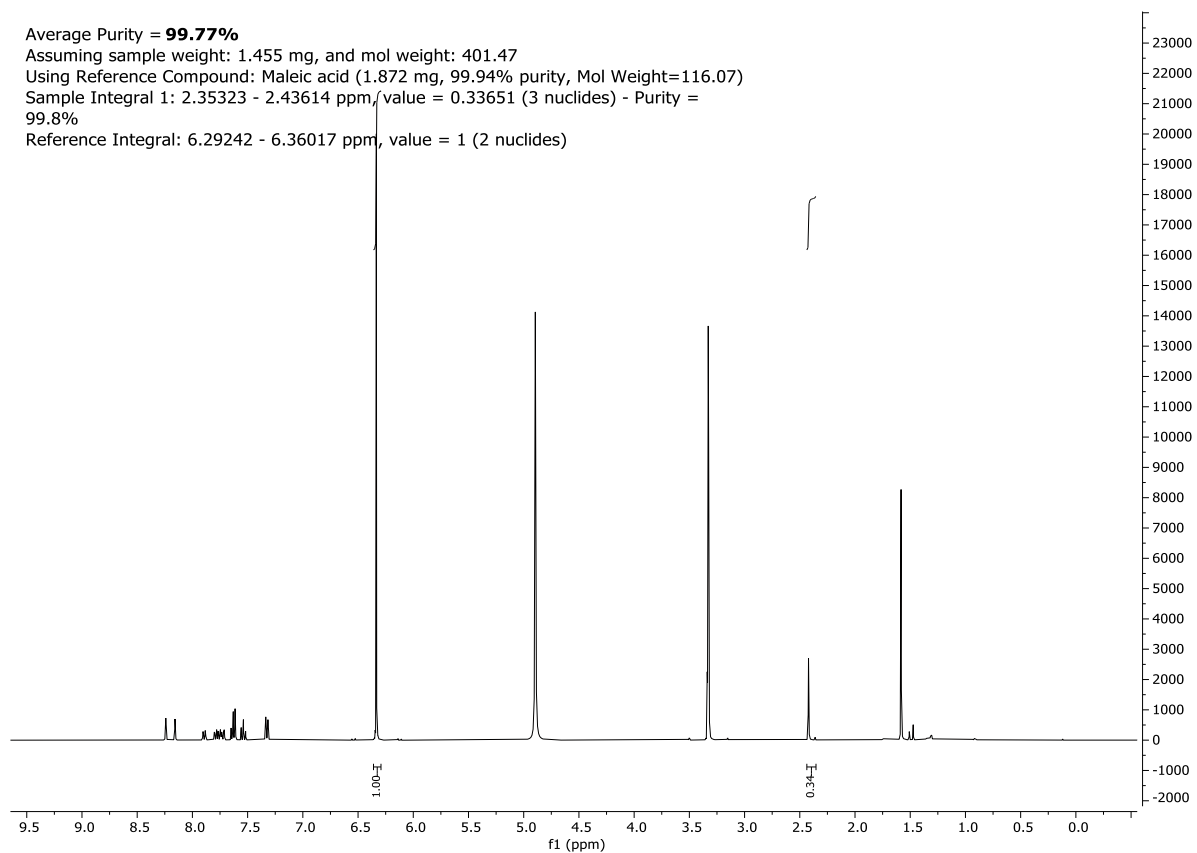
Average Purity = **99.77%**

Assuming sample weight: 1.455 mg, and mol weight: 401.47

Using Reference Compound: Maleic acid (1.872 mg, 99.94% purity, Mol Weight=116.07)

Sample Integral 1: 2.35323 - 2.43614 ppm, value = 0.33651 (3 nuclides) - Purity = 99.8%

Reference Integral: 6.29242 - 6.36017 ppm, value = 1 (2 nuclides)



(E)-3-((3-((4'-Chloro-[1,1'-biphenyl]-3-yl)diazenyl)phenyl)amino)-2,2-dimethyl-3-oxopropanoic acid_minph269 (8):

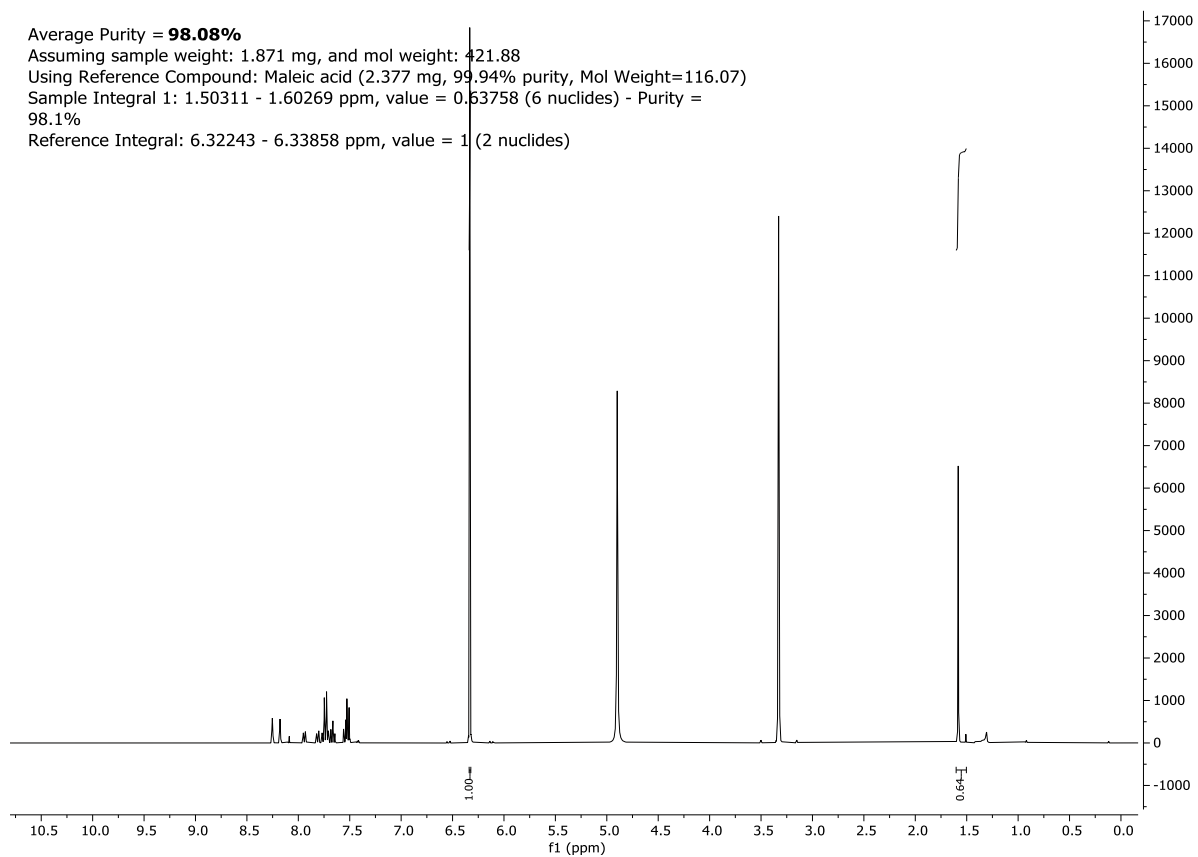
Average Purity = **98.08%**

Assuming sample weight: 1.871 mg, and mol weight: 421.88

Using Reference Compound: Maleic acid (2.377 mg, 99.94% purity, Mol Weight=116.07)

Sample Integral 1: 1.50311 - 1.60269 ppm, value = 0.53758 (6 nuclides) - Purity = 98.1%

Reference Integral: 6.32243 - 6.33858 ppm, value = 1 (2 nuclides)



(E)-2,2-Dimethyl-3-oxo-3-((3-((4'-(trifluoromethyl)-[1,1'-biphenyl]-3-yl)diazenyl)phenyl)amino)propanoic acid (9):

Average Purity = **96.17%**

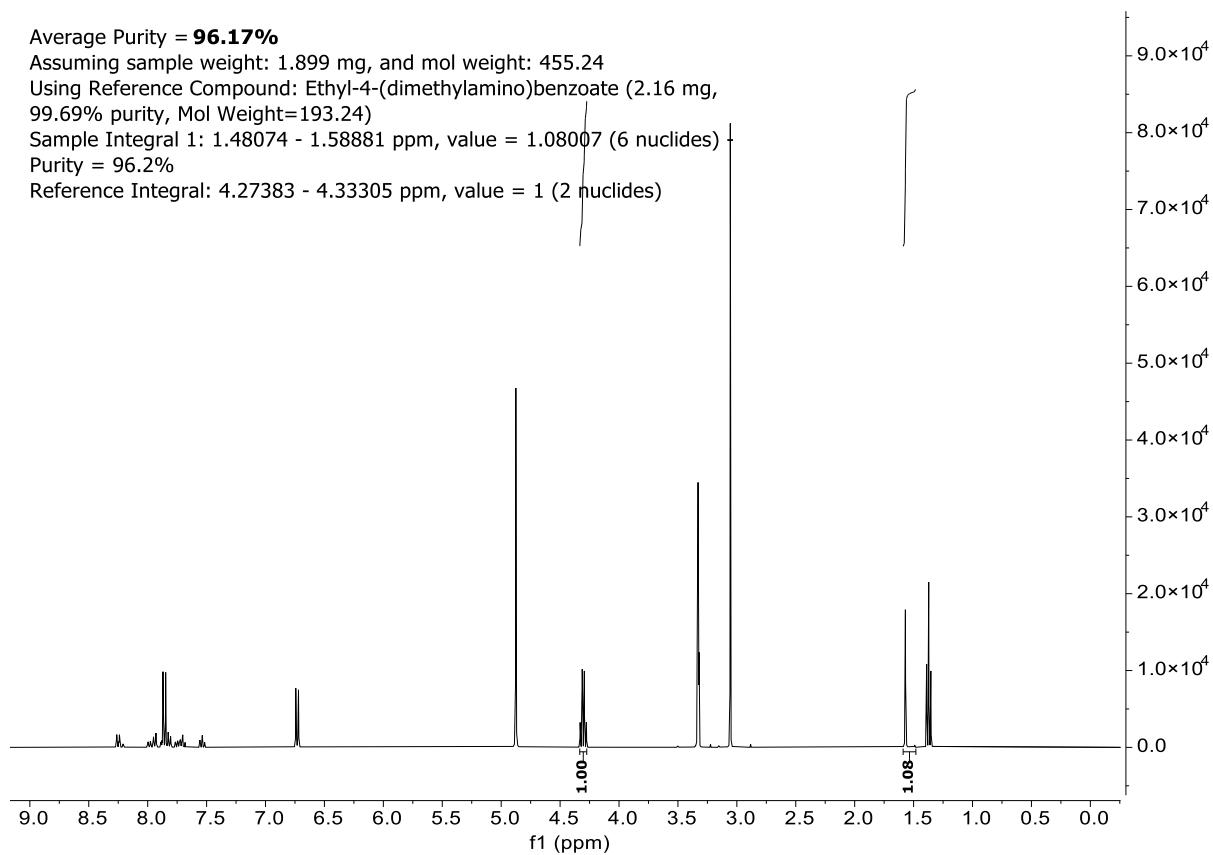
Assuming sample weight: 1.899 mg, and mol weight: 455.24

Using Reference Compound: Ethyl-4-(dimethylamino)benzoate (2.16 mg, 99.69% purity, Mol Weight=193.24)

Sample Integral 1: 1.48074 - 1.58881 ppm, value = 1.08007 (6 nuclides)

Purity = 96.2%

Reference Integral: 4.27383 - 4.33305 ppm, value = 1 (2 nuclides)



(E)-2,2-Dimethyl-3-oxo-3-((3-((3'-(trifluoromethyl)-[1,1'-biphenyl]-3-yl)diazenyl)phenyl)amino)propanoate (10):

Average Purity = **95.61%**

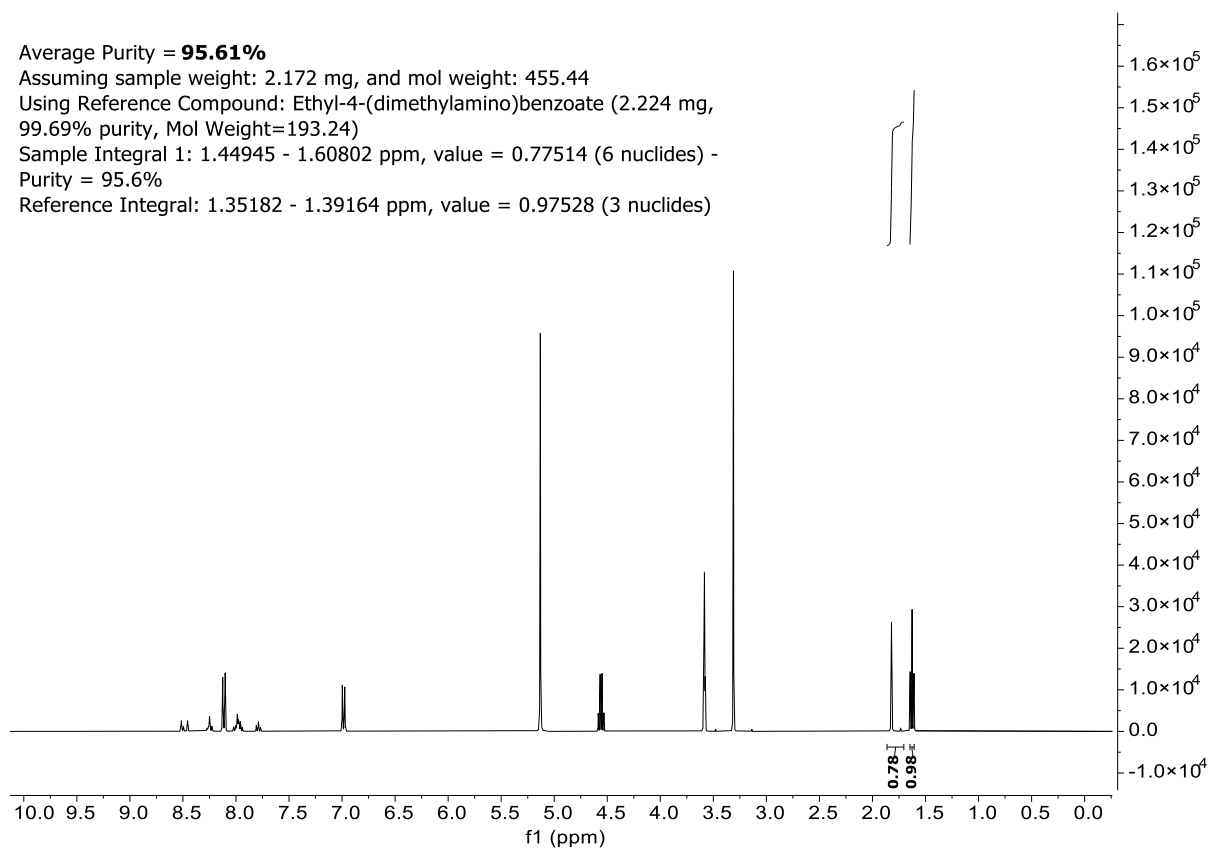
Assuming sample weight: 2.172 mg, and mol weight: 455.44

Using Reference Compound: Ethyl-4-(dimethylamino)benzoate (2.224 mg, 99.69% purity, Mol Weight=193.24)

Sample Integral 1: 1.44945 - 1.60802 ppm, value = 0.77514 (6 nuclides) -

Purity = 95.6%

Reference Integral: 1.35182 - 1.39164 ppm, value = 0.97528 (3 nuclides)



(E)-3-((3-((3',4'-Bis(trifluoromethyl)-[1,1'-biphenyl]-3-yl)diazenyl)phenyl)amino)-2,2-dimethyl-3-oxopropanoic acid (11**):**

Average Purity = **95.25%**

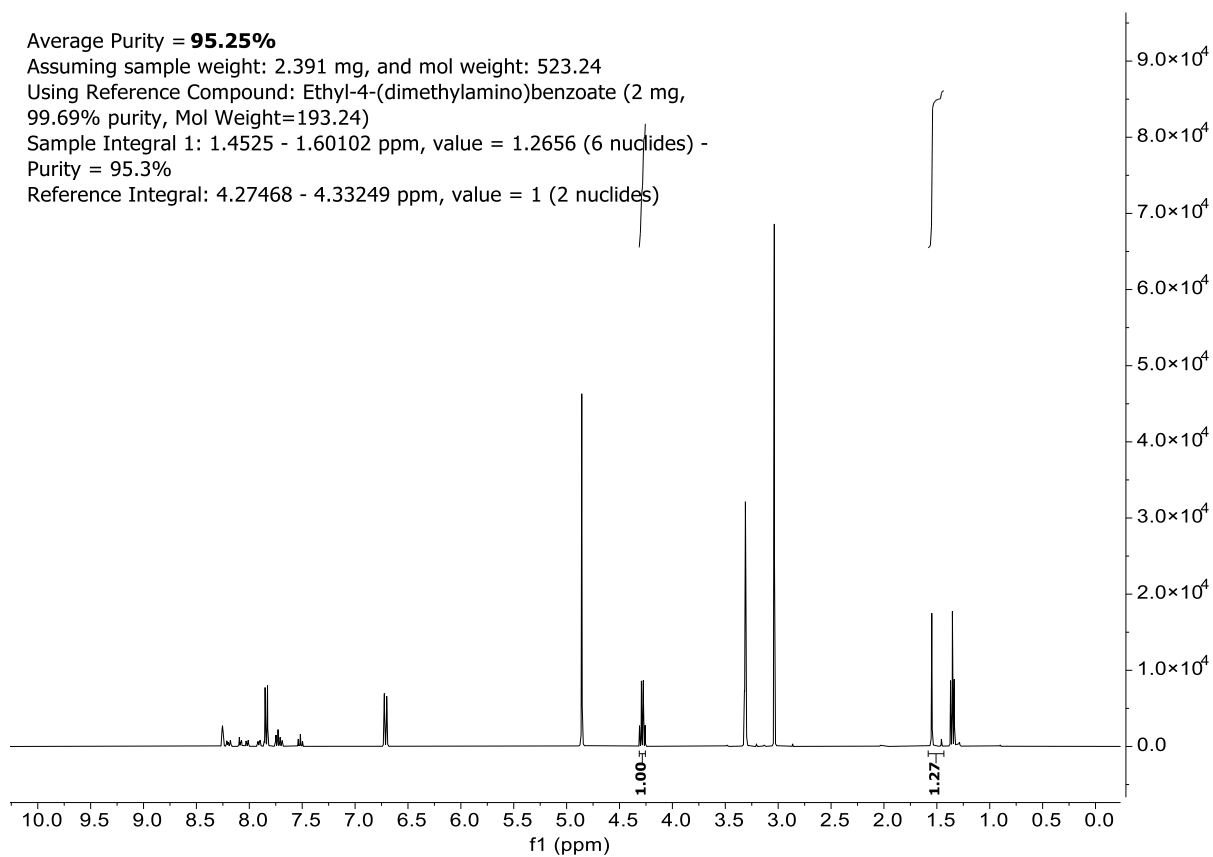
Assuming sample weight: 2.391 mg, and mol weight: 523.24

Using Reference Compound: Ethyl-4-(dimethylamino)benzoate (2 mg, 99.69% purity, Mol Weight=193.24)

Sample Integral 1: 1.4525 - 1.60102 ppm, value = 1.2656 (6 nuclides) -

Purity = 95.3%

Reference Integral: 4.27468 - 4.33249 ppm, value = 1 (2 nuclides)



(E)-2,2-Dimethyl-3-((3-((3-(naphthalen-2-yl)phenyl)diazenyl)phenyl)amino)-3-oxopropanoic acid (12):

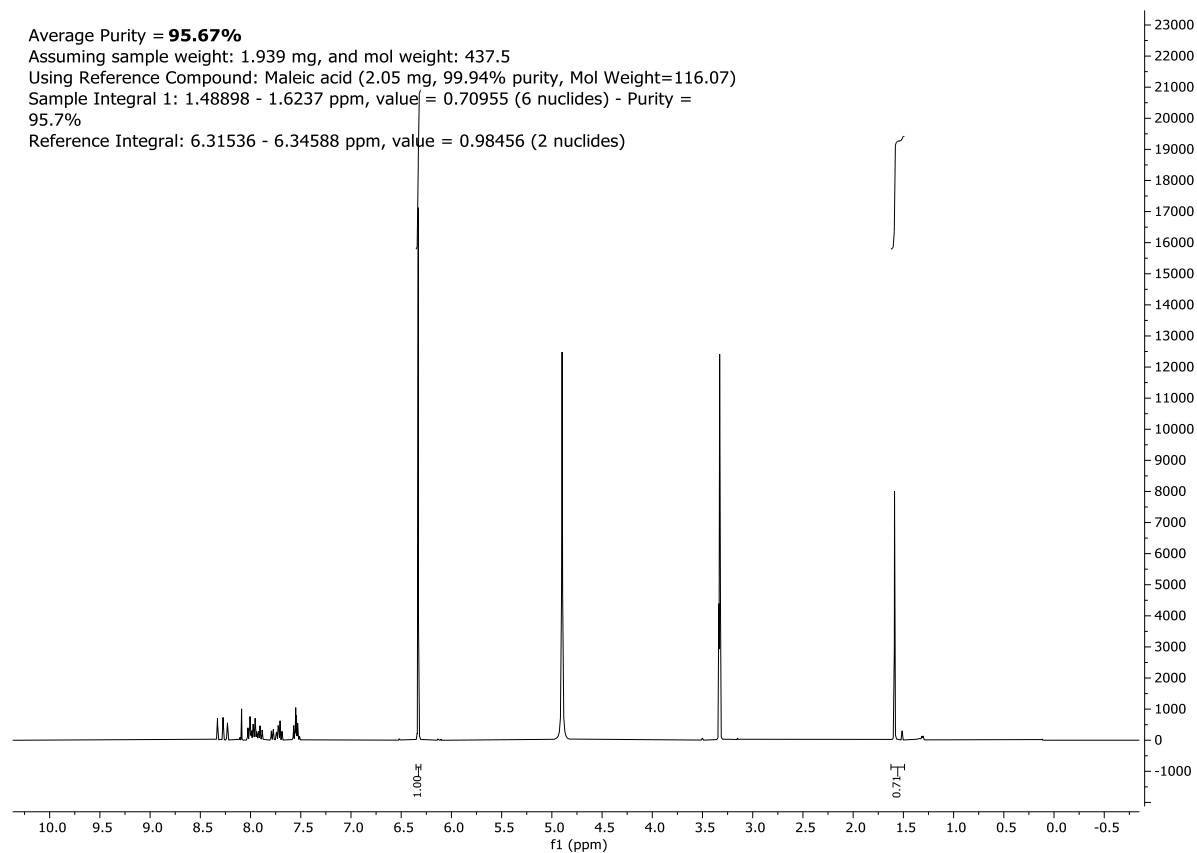
Average Purity = **95.67%**

Assuming sample weight: 1.939 mg, and mol weight: 437.5

Using Reference Compound: Maleic acid (2.05 mg, 99.94% purity, Mol Weight=116.07)

Sample Integral 1: 1.48898 - 1.6237 ppm, value = 0.70955 (6 nuclides) - Purity = 95.7%

Reference Integral: 6.31536 - 6.34588 ppm, value = 0.98456 (2 nuclides)



(E)-3-((3-((9,9-Dimethyl-9H-fluoren-3-yl)diazenyl)phenyl)amino)-2,2-dimethyl-3-oxopropanoic acid (13):

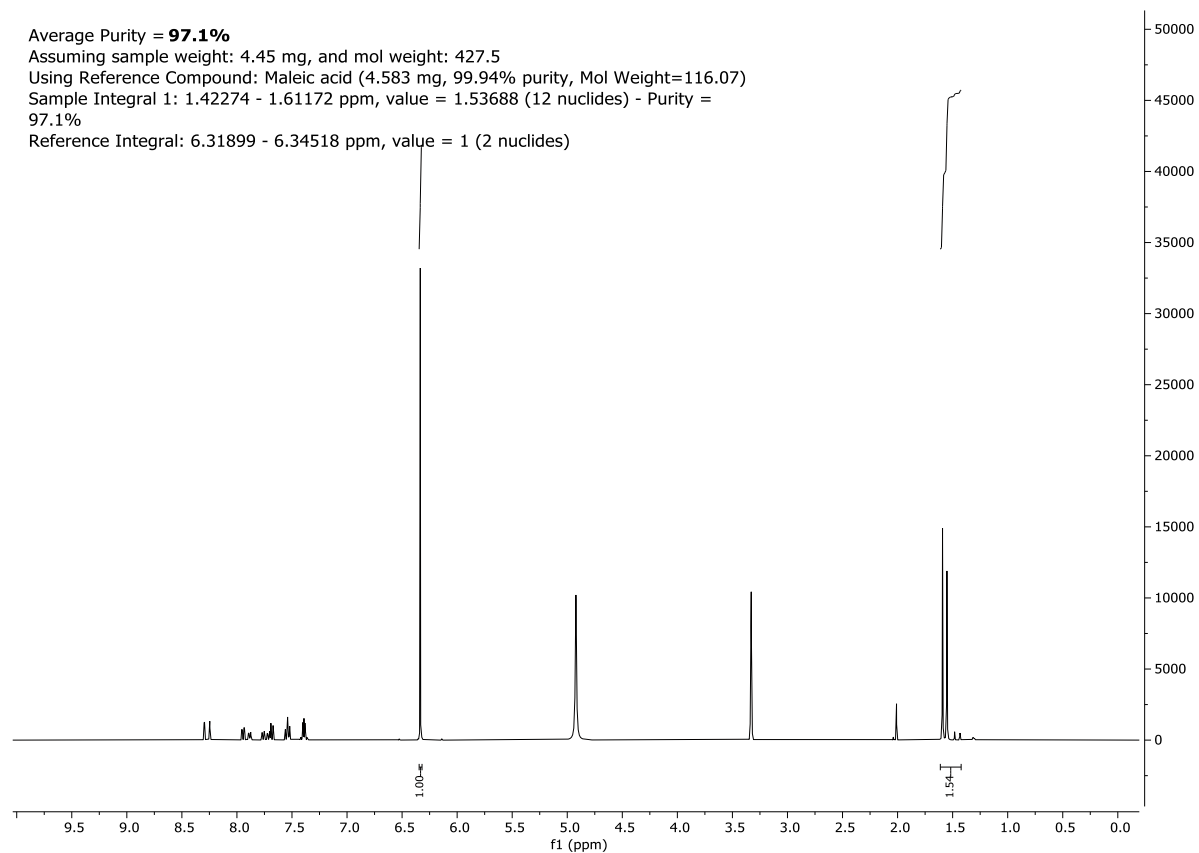
Average Purity = **97.1%**

Assuming sample weight: 4.45 mg, and mol weight: 427.5

Using Reference Compound: Maleic acid (4.583 mg, 99.94% purity, Mol Weight=116.07)

Sample Integral 1: 1.42274 - 1.61172 ppm, value = 1.53688 (12 nuclides) - Purity = 97.1%

Reference Integral: 6.31899 - 6.34518 ppm, value = 1 (2 nuclides)



Supplementary References

¹G. F. Pauli, S. N. Chen, C. Simmler, D. C. Lankin, T. Gödecke, B. U. Jaki, J. B. Friesen, J. B. McAlpine, J. G. Napolitano, *J. Med. Chem.* 2014, *57*, 9220–9231